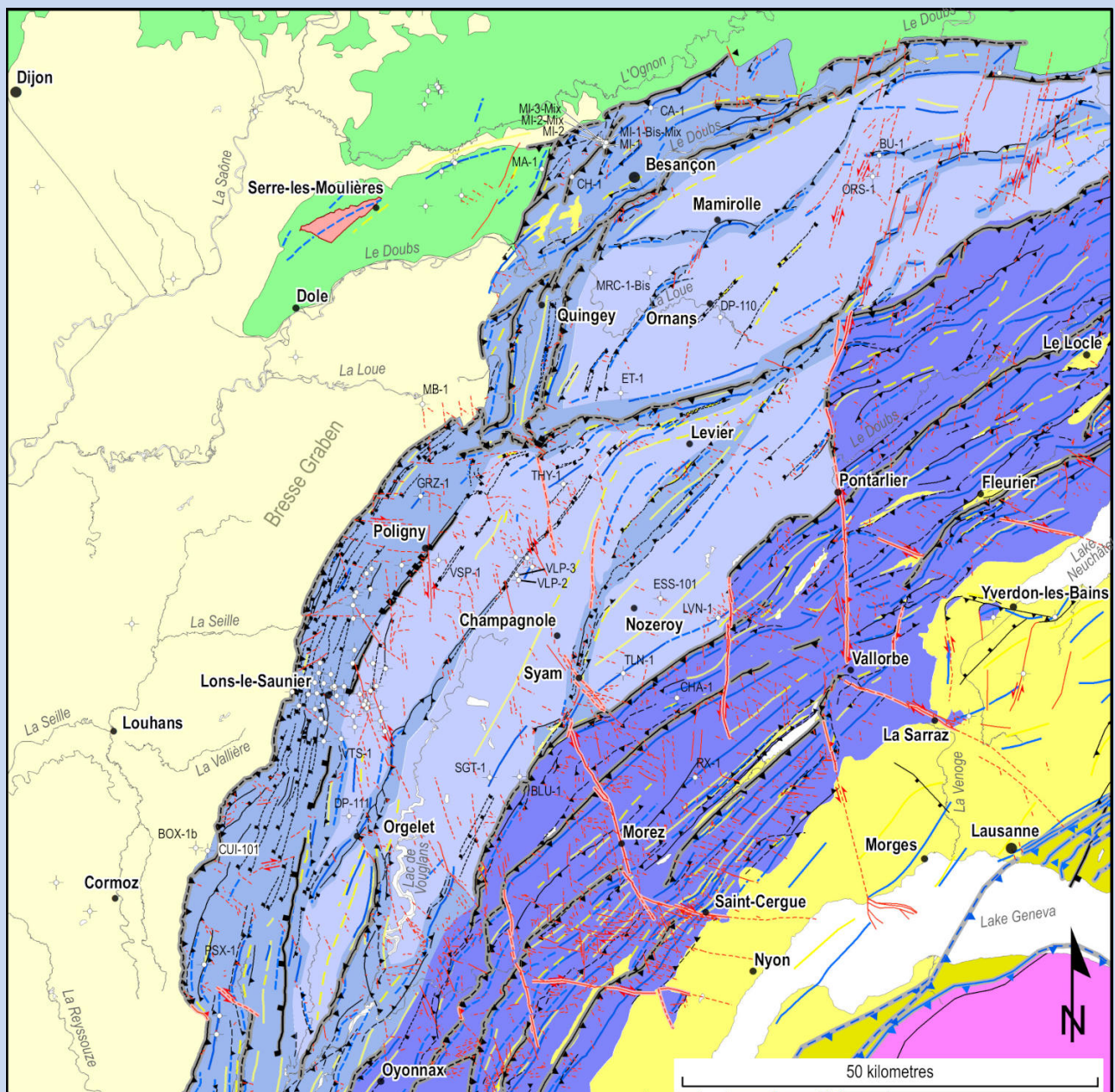


Marc SCHORI

The Development of the Jura Fold-and-Thrust Belt: pre-existing Basement Structures and the Formation of Ramps



Department of Geosciences - Earth Sciences
University of Fribourg (Switzerland)

The Development of the Jura Fold-and-Thrust Belt: pre-existing Basement Structures and the Formation of Ramps

Thesis

presented to the Faculty of Science and Medicine of the University of Fribourg (Switzerland)
in consideration for the award of the academic grade of
Doctor of Philosophy in Earth Sciences

by

MARC SCHORI

from

Biel/Bienne, Switzerland

Thesis No: 4394
media f sa
2021

Accepted by the Faculty of Science and Medicine of the University of Fribourg (Switzerland) upon the recommendation of :

Prof. tit. Jon Mosar	Université de Fribourg (CH)	Thesis supervisor
Prof. Anneleen Foubert	Université de Fribourg (CH)	Marraine
Dr. Anna Sommaruga	Université de Fribourg (CH)	Expert
Prof. Olivier Fabbri	Université de Franche-Comté (F)	Expert
Prof. Guido Schreurs	Universität Bern (CH)	Expert
Prof. Vincent Serneels	Université de Fribourg (CH)	President of the jury

Fribourg, 18. October 2021

Thesis supervisor



Prof. Jon Mosar

Dean



Prof. Gregor Rainer

CONTENTS

CONTENTS	3
ACKNOWLEDGEMENTS	9
ABSTRACT	11
NOMENCLATURE	15
1 INTRODUCTION	17
1.1 MOTIVATION AND OBJECTIVES	17
1.2 STUDY AREA	18
1.3 METHODOLOGY	18
1.4 STRUCTURE OF THE MANUSCRIPT	18
2 GEOLOGICAL CONTEXT	21
2.1 REGIONAL GEOLOGICAL SETTING	21
2.2 STRUCTURAL OVERVIEW MAPS	21
2.2.1 Previous structural maps	21
2.2.2 New structural maps	23
2.2.3 Eastern, Central and Southern Jura	23
2.2.4 Southern and northern Plateau Jura	23
2.2.5 Tabular Jura	23
2.2.6 Faisceaux and plateaus	24
2.2.7 Normal faults in the cover of the Jura Mountains	27
2.3 DÉCOLLEMENT DYNAMICS OF THE NORTHERN ALPINE FORELAND	27
2.4 BASAL DÉCOLLEMENT IN TRIASSIC EVAPORITES	28
2.5 TECTONIC EVOLUTION OF CENTRAL AND WESTERN EUROPE	28
2.5.1 Variscan orogeny and post-Variscan collapse	28
2.5.2 Overview of Palaeozoic trends	31
2.5.3 Triassic basin and opening of Alpine Tethys in Jurassic	31
2.5.4 Cretaceous plate collision and lithospheric folding	33
2.5.5 Evolution of the Alpine flexural basin system	33
2.5.6 Cenozoic rifting	33
2.5.7 Formation of the Jura Mountains	34
2.5.8 Recent basement tectonics	34
2.6 LITHOSPHERIC DEFORMATION IN THE ALPINE FORELAND: PROCESSES / MECHANISMS	34

2.6.1	Intraplate lithospheric folding	34
2.6.2	European Cenozoic rifting	34
2.6.3	Foreland basin systems	35
2.7	STRATIGRAPHY	38
2.7.1	Basement, basal décollement and cover	38
2.7.2	Mesozoic sediments of the Jura	38
2.7.3	Cenozoic sedimentation	39
3	BOREHOLE INVENTORY	43
3.1	AIM OF INVENTORY	43
3.2	HISTORICAL BACKGROUND	43
3.3	METHODS, LOGGING AND DEFINITIONS	44
3.3.1	General	44
3.3.2	Thickness used for isopach maps	45
3.3.3	Ambiguous limits of lithostratigraphic groups	45
3.3.4	Triassic evaporites	46
3.4	BOREHOLE OVERVIEW	47
3.5	BOREHOLE BASED SECTION ACROSS LONS-LE-SAUNIER, EXTERNAL JURA	48
3.6	DIFFERENTIAL SUBSIDENCE IN THE BRESSE GRABEN	48
3.6.1	Structural context	48
3.6.2	Methodology	48
3.6.3	Observations	48
3.6.4	Discussion	49
4	THICKNESS MODELS OF STRATIGRAPHIC GROUPS	51
4.1	INTRODUCTION	51
4.2	METHODOLOGY	51
4.2.1	General procedure	51
4.2.2	Tools and technique	52
4.3	TRIASSIC SERIES	52
4.3.1	Buntsandstein Group	53
4.3.2	Muschelkalk Group	55
4.3.3	Keuper Group	56
4.4	JURASSIC SERIES	58
4.4.1	Lias Group	58
4.4.2	Dogger Group	59
4.4.3	Lower Malm Group	61
4.4.4	Upper Malm Group	61
4.5	CRETACEOUS SERIES	64
4.6	TOTAL MESOZOIC THICKNESS	65
4.7	TERTIARY GROUP	66
4.8	CONCLUSION	68
4.8.1	Tectonic signatures in the Mesozoic and Cenozoic cover	68
4.8.2	Tectonic thickening of Mesozoic units in Cenozoic times	68
4.8.3	Cenozoic erosion and consequences on the formation of the JFTB	68
5	GEOLOGICAL CROSS-SECTIONS	71
5.1	INTRODUCTION	71
5.2	METHODS	71
5.3	SECTION A: CUISEAUX – PLATEAU DE CHAMPAGNOLE – INTERNAL JURA	72
5.4	SECTION B: FAISCEAU LÉDONIEN – PLATEAU DE NOZEROTY	72
5.5	SECTION C: FAISCEAU DE QUINGEY	74
5.6	SECTION D: FAISCEAU DES AVANT-MONTS – PLATEAU D'ORNANS WEST	74

5.7	SECTION E: FAISCEAU BISONTIN – PLATEAU D'ORNANS EAST	77
5.8	DISCUSSION	77
5.9	CONCLUSIONS	78
6	TOPOGRAPHY OF THE PRE-MESOZOIC BASEMENT	81
6.1	INTRODUCTION	81
6.2	METHODS	81
6.2.1	Faults in the pre-Mesozoic basement	81
6.2.2	Base Mesozoic model	82
6.2.3	Calculation of flexural foreland basin	82
6.3	RESULTS	83
6.3.1	Top basement model	83
6.3.2	Top basement cross-sections	86
6.3.3	Basement dips of structural domains	87
6.3.4	Signature of the flexural basin system	88
6.3.5	Migration of the flexural basin system	90
6.4	DISCUSSION	92
6.4.1	Inherited Palaeozoic structures controlling deformation in the Jura	92
6.4.2	Eo-Oligocene rifting	93
6.4.3	Oligo-Miocene foredeep evolution	93
6.4.4	Basement dip and structural domains	94
6.5	CONCLUSIONS	94
7	DATING AND CHRONOLOGY OF TECTONIC EVENTS	97
7.1	INTRODUCTION	97
7.1.1	Aim of chapter	97
7.1.2	Dating of the Jura: an overview	97
7.1.3	U-Pb calcite dating	100
7.1.4	Veins and slickensides associated with faults	101
7.1.5	Previous studies	101
7.2	METHODOLOGY	101
7.3	RESULT	102
7.3.1	Structural context of sampling location	102
7.3.2	Sample description	102
7.3.3	U-Pb ages of sample	102
7.4	DISCUSSION	102
7.4.1	Interpretation of slickenfibres	102
7.4.2	Interpretation of vein calcite	104
7.5	CONCLUSION	104
8	INSIGHT FROM ANALOGUE MODELS	107
8.1	INTRODUCTION	108
8.2	REGIONAL SETTING	109
8.2.1	Jura Mountains fold-and-thrust belt	109
8.2.2	Mechanical stratigraphy	110
8.2.3	Inherited basement faults	110
8.2.4	Lineaments in the Jura Mountains	111
8.3	EXAMPLES OF BASEMENT-FAULT RELATED STRUCTURES	111
8.3.1	Basement-fault controlled frontal faisceau	111
8.3.2	Basement-fault induced cover structures	111
8.4	WORKING HYPOTHESIS	112
8.5	MATERIAL AND METHODS	112
8.5.1	Material properties in analogue models	112
8.5.2	Model scaling	113
8.5.3	Experimental set-up	113

8.5.4	Modelling procedure	114
8.5.5	Model analysis	114
8.6	ANALOGUE MODEL RESULTS	114
8.6.1	Flat-base models	114
8.6.2	Evolution of structures related to basement step formation	115
8.6.3	Frontal steps	116
8.6.4	Oblique downward-step model	117
8.6.5	Oblique upward-step models	118
8.6.6	CT-scanned oblique upward-step model	121
8.6.7	Oblique upward-step model with reduced cover	122
8.7	DISCUSSION	123
8.7.1	Summary of model results	123
8.7.2	Comparison to previous oblique-ramp models	123
8.7.3	Local and regional rotations of structures	123
8.7.4	Natural examples of step-controlled structures	125
8.7.5	Summary of natural structures	128
8.8	CONCLUSIONS	128
8.9	APPENDIX A	129
8.10	REFERENCES	132
9	KINEMATIC MODELLING	135
9.1	INTRODUCTION	135
9.2	METHODS	135
9.3	COMPILATION OF EXTENSIONAL STRUCTURES FROM MODELS AND NATURE	135
9.4	A KINEMATIC MODEL OF THE SOUTHERN PLATEAU JURA	138
9.4.1	Context	138
9.4.2	Model results	138
9.4.3	Discussion	138
9.4.4	Conclusions	140
10	CONCLUSIONS	143
	BIBLIOGRAPHY	147
	APPENDICES	161
A	DATA DESCRIPTION	163
A.1	LIST OF BOREHOLES	164
A.2	AERIAL MAPS AND ELEVATION MODELS	170
A.2.1	Satellite and aerial photography	170
A.2.2	Terrain models	170
A.3	CONTENTS OF SUPPLEMENTARY MATERIAL	172
A.4	DATA INTEGRATION FLOW-CHART	173
B	ADDITIONAL MODELS	175
B.1	GRAVITY MODEL	175
B.1.1	Methods	175
B.1.2	Results	179
B.2	EROSION MODEL OF THE MESOZOIC COVER	180
B.2.1	Method	180
B.2.2	Result	181
B.3	MIO-PLIOCENE DISPLACEMENT MODEL	182
B.3.1	Evaluation of previous displacement models	182
B.3.2	Documentation of new displacement model	182
B.4	LINEAMENT RESTORATION AND INTERPRETED BASEMENT FAULTS	192

B.5	DUPLEX STRUCTURES IN THE BASAL DÉCOLLEMENT	194
C	OVERVIEWS	195
C.1	ELEVATION MAP OF THE JURA MOUNTAINS	196
C.2	INTERNATIONAL CHRONOSTRATIGRAPHIC CHART	197
D	CURRICULUM VITAE	199

ACKNOWLEDGEMENTS

I thank my supervisor Jon Mosar for making this project possible. I appreciate his open and sociable ways to discuss topics and I thank him for sharing his ever honest and forthright opinions. In much the same way, I am immensely grateful to Guido Schreurs, who proofed to be a valuable contact outside Fribourg. These two persons awoke my interest in tectonics of the Jura Mountains in the first place. I deeply enjoyed to be part of the working group in Fribourg. Anna Sommaruga advised me brilliantly and especially in the beginning of this project, her support was precious beyond measure. I appreciate her networking skills, which are almost as valuable as her exactitude, tenacity and pleasantness.

I am indebted to Marius Gruber helping me with a lot of technical starters support and the introduction into the social structures of the institute. Omar Radaideh is thanked for valuable support, his expertise in topography and fault analysis and gravity data treatment as well as many shared meal and cheerful company during more than four years in Fribourg. He ever brought me up to date with the latest rumours, a source of information that never failed me.

Sandra Borderie is thanked for discussions about modelling mechanics and kinematics of wedges, but also for her readiness to help teaching, company during field-courses and EGU 2019. I thank Valentin Rime, my office mate, for many stimulating debates and discussions and for being my living WhatsApp of the institute. It was a great pleasure having him on board during practical courses. I much appreciate the memories of a shared apartment during the KingDom course in London, climbing at Pont de Pérolles, a ski tour and a windy afternoon cycling trip. Louis Hauvette is thanked for Kingdom Suite support and geophysical explanations.

Alexander Vaira is thanked for invaluable computer support, tenacity to solve licensing problems and a healthy amount of flexibility. Christoph Neururer provided valuable technical support and I appreciate his interest and effort that he put into our mini-project to reconfigure the sandbox modelling apparatus of Jon.

Frank Zwaan convinced me to sandbox model our Jura questions during an excursion in Corsica, which proved to

be very fruitful and I am thankful for his help and virulent enthusiasm. At this point, I also like to thank the courteous team of the CT-scanner in Bern, Nicole and Judith.

I am thankful to Nathan Looser, who invested his precious time for screening and dating my samples of the Jura Mountains. My thanks are extended to Nathan's supervisor Stefano Bernasconi, and I appreciate the stimulating exchanges between our research groups.

Cathrine Mottram and Leonie Weiss are thanked for a field trip across the Jura Mountains and exchange of information, a helmet, wine and Muesli. I hope that the collected samples during this trip will yield many more interesting deformation ages. Luca Smeraglia, Flavien Choulet and Olivier Fabbri are thanked for an interesting field visit and explanations of the Fuans and Morteau thrusts. Yves Gouffon is thanked for interesting discussions about the new tectonic map of Switzerland.

And of course there are still many more people that were on hand with help and advice in the course of this project, even if they may not have noticed, and I am indebted to Martinus Abednego, Christian Foth, Cedric Botter, Robin Fentimen, Richard Spitz, Bruno Lauper, Nicole Scheidt, Benjamin Verbeeken, Adéline Marro, Naomi Vouillamoz, Eva de Boever, Anneleen Foubert, Herfried Madritsch, Christian Hauk, Daniel Egli, Stephan Wohlwend, Tobias Reber, Andreas Ebert, Lukasz Gregorczyk, Emelie Hägerstedt, Urs Marti of swisstopo, Peter Jordan, Olivier Lacombe, Guillaume Martelet of BRGM, Martin Mazurek, Timy Schmid, Jean-Charles Schaeggis and Jean-Philippe Blouet.

Great big thanks go to Coline Molaret, Christin Hilbich, Marlene Kronenburg, Laura Niggli and Tobias Wechsler for an unforgettable Chilean experience in high-altitude geophysics.

My partner Barbara Zihlmann was a constant source of energy and supported me steadfastly during this project. We share many happy memories living in between our lakeside island and the seaside big-city until we settled on the rural mountain. I am immensely grateful for our little daughter.

ABSTRACT

Pre-existing faults in the pre-Mesozoic basement are believed to play an important role in controlling deformation of the thin-skinned Jura Mountains fold-and-thrust belt (JFTB), which constitutes the northernmost extension of the Western and Central European Alps. The JFTB was detached in Triassic evaporites during Middle Miocene and Pliocene compression, exerted by the Alps. Prior to this, the Northern Alpine Foreland (NAF) was intensely pre-structured by faults, partially inherited from Palaeozoic times, that were active during the Mesozoic and Cenozoic structural evolution of continental Europe.

In order to understand the connection between the thin-skinned JFTB formation and pre-existing basement structures, different datasets were compiled: this study provides an up-to-date homogenised structural map of the whole JFTB, a unified deep-borehole database, thickness models across the JFTB and surroundings of 9 lithostratigraphic units (comprising Mesozoic and Tertiary sediments), geological cross-sections across the External Jura, an elevation model of the top of the pre-Mesozoic basement, new U-Pb calcite ages of a slickenfibres and a vein in the External Jura, a brittle-viscous analogue modelling study testing basement controlled oblique-ramps and a kinematic forward model of a section in the External Jura that integrates pre-JFTB extensional phases.

The décollement of the JFTB is predominantly in salt-bearing units of the Middle and Upper Triassic evaporites (or evaporites of the Muschelkalk Group and Keuper Group, respectively). The main décollement level in the Eastern Jura concentrates within the Middle Triassic evaporite layers, whereas in the Central and Southern Jura, the main décollement is in Upper Triassic evaporites (Deville 2021; Philippe et al. 1996). This correlates with thickness centres on isopach maps. Furthermore, isopach maps suggest that the Middle Jurassic Group (Dogger Group) predominantly hosts upper detachments in the Eastern Jura, whereas upper detachments in the Central and Southern Jura are rather in the Lower Jurassic Group (Lias Group).

In the Mesozoic cover of the External Jura, normal fault systems are documented, which are mainly connected

to the formation of the European Cenozoic Rift System (ECRIS), which has an Eo-Oligocene age (Illies 1972; Ziegler 1992a). Extensional structures in the Mesozoic cover, which are linked to the formation of the Cenozoic rift system, are mostly identified within *faisceaux* of the Central Jura and are transported north-westwards above the basal décollement in Triassic evaporites, away from their origin in the basement. The pre-Mesozoic basement underneath the External Jura shows sudden regional offsets (basement faults) with vertical throws of up to 450 m to 600 m. These offsets in the External Jura are mainly attributed to the formation of the ECRIS and to Oligo-Miocene flexural faulting during the migration of the Alpine fore-deep. Therefore, basement faults in the External Jura are suggested to pre-date the Mio-Pliocene formation of the JFTB. Basement offsets due to the formation of the ECRIS can form both, upward basement steps and downward basement steps in the direction of transport of the JFTB. Basement faults in connection with the formation of the flexural Alpine foreland basin rather provide upward basement steps. Analogue models testing oblique cover structures controlled by basement faults and comparison to natural structures in the Internal Jura suggest that pre-existing basement steps of several hundred metres also exist beneath the Internal Jura and the Molasse Basin. Basement steps in these domains are rather proposed to originate from flexural faulting in Oligocene times. Basement faults active during Cenozoic times are proposed to have predominantly followed inherited structural seeds of the Variscan orogeny.

The front of the JFTB is essentially pre-determined by the formation of the ECRIS. Underneath the western front of the JFTB (*Faisceau lédonien*, Revermont), the NNE–SSW striking Bresse Graben border fault zone shows cumulative vertical offsets of up to ~2.8 km. This was an exceedingly high downward step in the direction of tectonic transport of the JFTB and blocked a further propagation of the front of the JFTB. Downward steps that localised the front of the JFTB are also detected underneath the northern front of the JFTB, connected to the Rhine–Bresse Transfer Zone (RBTZ, underneath the *Faisceau*

des Avant-Monts) and the Upper Rhine Graben (URG, underneath the Ferrette Zone). In addition, uplift of ECRIS rift shoulders (up to ~930 m) that started in Eocene times led to several hundred metres erosion of Mesozoic sediments towards the front of the future Jura. Uplift in connection with the Alpine forebulge caused decidedly less erosion than uplift in connection with ECRIS rift shoulders, because flexural uplift did not exceed about 350 m and the forebulge did not remain stationary. The topography of the pre-Mesozoic basement suggests that the present-day forebulge crest lies to the north of the JFTB in the RBTZ. Accordingly, the northern portion of the central External Jura lies in the present day forebulge depo-zone whereas the rest of the JFTB (Southern Jura, southern Central Jura, Internal Jura, Eastern Jura) is in the present-day foredeep. The pre-Mesozoic basement underneath the External Jura shows moderate inclinations that are commonly 1.5° or smaller. Underneath the Internal Jura, basement inclinations are mostly between 2° and 3°. The low basement inclination of the External Jura seemed to have fostered the formation of kilometric plateaus.

In summary, this study confirms an important influence of the basement on the structural development of the JFTB and different structural domains of the JFTB can be partially connected to local basement configurations. New faults in the pre-Mesozoic basement of the Jura Mountains (and Molasse Basin) are proposed. Orientations and throws of basement faults are characterised and lithospheric processes that led to their formation are evaluated. The concepts of this study may be applied to other thin-skinned fold-and-thrust belts worldwide that formed above pre-existing basement structures.

ZUSAMMENFASSUNG

Der Jura Falten- und Überschiebungsgürtel (fold-and-thrust belt) ist die nördlichste Erweiterung der westlichen und zentralen Alpen im tektonischen Sinn. Er besteht aus der deformierten, dünnen Sedimenthaut des europäischen nördlichen Alpenvorlandes, welches während dem mittleren Miozän bis unteren Pliozän in triassischen Evaporiten abgeschert wurde als Folge Nordwest gerichteter alpiner Kompression. Vor der Entstehung des Juragebirges war das nördliche Alpenvorland bereits maßgeblich vorstrukturiert und enthielt Brüche, teilweise aus dem Paläozoikum stammend, die während der mesozoisch-känozoischen strukturellen Entwicklung der europäischen Lithosphäre wiederholt aktiv waren. Laubscher (1961) schlägt vor, dass die Deformation des Jura Falten- und Überschiebungsgürtels erheblich durch präexistente Brüche im prämesozoischen Sockel gesteuert wurde.

Um die Verbindung zwischen Juragebirge und vorher existierenden Sockelstrukturen zu verstehen, wurden verschiedene Datensätze angelegt: diese Studie enthält eine aktualisierte und homogenisierte Strukturkarte des Juragebirges, ein vereinheitlichtes Tiefenbohrlochinventar, Mächtigkeitskarten des Juragebirges und Umgebung von neun lithostratigrafischen mesozoischen und känozoischen Einheiten, geologische Profile durch den externen Jura, eine Höhenkarte des vormesozoischen Sockels,

neue U-Pb Kalzitalter von einem Rutschharnisch und einer Kalzitader im externen Jura, eine Analogmodellstudie, welche den Einfluss von Sockelsprüngen auf schräge Rampen testet und schließlich, ein vorwärts modelliertes, geologisches Profil durch den externen Jura.

Die basale Überschiebung des Juras befindet sich hauptsächlich in Halit führenden Einheiten triassischer Evaporite. Die Überschiebung konzentriert sich in den mittleren triassischen Evaporitschichten (Evaporite der Muschelkalk-Gruppe) im östlichen Jura, wohingegen sich die basale Überschiebung im zentralen und südlichen Jura vorwiegend in den oberen triassischen Evaporiteinheiten (Evaporite der Keuper-Gruppe) befindet (Deville 2021; Philippe u. a. 1996). Die Präsenz der Überschiebung korreliert mit Mächtigkeitszunahmen (Überdickungen) der jeweiligen triassischen lithologischen Einheit. Zudem weisen Überdickungen der mittleren Juraschichten (Dogger Gruppe) auf obere Überschiebungsbahnen im östlichen Jura hin, während sich obere Überschiebungsbahnen im zentralen und südlichen Juragebirge eher in den unteren Juraschichten (Lias Gruppe) befinden.

Die mesozoische Sedimentdecke des externen Juras enthält Abschiebungssysteme, welche auf die Eo- und Oligozäne Entstehung des europäischen känozoischen Riftsystems zurückgeführt werden (Illies 1972; Ziegler 1992a). Extensionsstrukturen in der mesozoischen Sedimentdecke, die im Zusammenhang mit dem känozoischen Riftsystem stehen, werden hauptsächlich innerhalb von Faisceaux des zentralen Juras dokumentiert. Sie sind über der basalen Abscherung des Juragebirges Richtung Nordwest transportiert, weg von ihren Wurzeln im Sockel. Unter dem externen Jura werden Sprünge im vormesozoischen Sockel identifiziert, welche maximale vertikale Versätze zwischen 450 m bis 600 m aufweisen. Im externen Jura sind diese Versätze hauptsächlich auf die Entstehung des europäischen känozoischen Riftsystems zurückzuführen und auf Abschiebungen im Zusammenhang mit der Oligozänen bis Miozänen Migration der Vortiefe (foredeep). Somit werden Sockelbrüche unter dem externen Jura als prä-existent verstanden. Sockelversätze im Zusammenhang mit dem känozoischen Riftsystem formen auf- sowie absteigende Sockelstufen in Transportrichtung des Juragebirges. Sockelbrüche im Zusammenhang mit dem nordalpinen Vorlandbecken formen hauptsächlich aufsteigende Sockelstufen. Analogmodelle mit Sockelbrüchen und Vergleiche mit natürlichen Strukturen im internen Jura weisen darauf hin, dass Sockelbrüche mit Versätzen von mehreren hundert Metern (mindestens ca. 400 m) auch unter dem internen Jura und dem Molassebecken vorkommen. Allerdings sind diese Sockelbrüche hauptsächlich auf die Migration der Vortiefe während des Oligozäns zurückzuführen. Sockelbrüche die während des Känozoikums aktiv waren scheinen vorwiegend Strukturen zu folgen, die bereits während der variszischen Orogenese angelegt wurden.

Die Front des Juragebirges ist erheblich durch Brüche des europäischen känozoischen Riftsystems vorgegeben. Unter der westlichen Front des Juragebirges (Faisceau lédonien, Revermont) zeigt die SSW–NNO orientierte Randbruchzone des Bressegrabens kumulative vertikale Versätze von bis zu ca. 2.8 Kilometer. Diese ausserordentlich

hohe, absteigende Sockelstufe (in tektonischer Transportrichtung des Juragebirges) verhinderte ein weiteres Fortschreiten der Jurafront. Eine Lokalisierung der Jurafront an absteigenden Sockelstufen wird ausserdem unter der nördlichen Front des Juragebirges beobachtet (in Verbindung mit der Rhein–Bresse Transferzone), sowie in der Ferrette Zone (in Verbindung mit dem Oberen Rheingraben). Hebung der Riftschultern des Bresse- und Rheingrabens (max. ~930 m unter dem Juragebirge) setzte bereits im Eozän ein und führte zu mehreren hundert Metern Erosion mesozoischer Sedimente im Frontalbereich des Juragebirges, vor seiner Entstehung. Tektonische Hebung im Zusammenhang mit der Vorlandwölbung (forebulge) war maximal 350 m und blieb ausserdem nicht stationär, deshalb führte die Vorlandwölbung zu deutlich weniger Erosion als Hebung in Zusammenhang mit Riftschultern.

Die Topografie des vormesozoischen Sockels deutet darauf hin, dass der Scheitel der heutigen Vorlandwölbung nördlich des Juragebirges liegt, in der Rhein-Bresse Transferzone. Somit liegt der nördliche Teil des zentralen, externen Juras auf der heutigen Vorlandwölbung, wohingegen der Rest des Juragebirges (südlicher Jura, südlicher Teil des zentralen Juras und östlicher Jura) in der heutigen Vertiefung liegt. Die Oberfläche des vormesozoischen Sockels unter dem externen Jura zeigt moderate Einfallswinkel von meist 1.5° und weniger, Richtung Nordwest und Südost. Diese kleinen Einfallswinkel scheinen die Entstehung der kilometerweiten Plateaus des externen Juras begünstigt zu haben. Unter dem internen Jura fällt der Sockel im Schnitt 2° bis 3° Richtung Südost ein.

Zusammenfassend bestätigt diese Studie einen bedeutenden Einfluss des Sockels auf die strukturelle Entwicklung des Juragebirges und einzelne strukturelle Einheiten des Juragebirges können auf lokale Sockelkonfigurationen zurückgeführt werden. Neue Brüche im vormesozoischen Sockel des Juragebirges (und auch im Sockel des Molassebeckens) werden vorgeschlagen. Orientierungen und vertikale Versätze von Sockelbrüchen werden charakterisiert und verursachende lithosphärische Prozesse werden eruiert. Die erarbeiteten Konzepte dieser Studie können auf andere Falten- und Überschiebungsgürtel angewendet werden, welche über einem vorstrukturierten Sockel entstanden sind.

NOMENCLATURE

AM	Avant-Monts s.l. comprising the area between Dole and Besançon (i.e. LSZ and FAM).		Terrain Models (DTM) represent the bare ground, without buildings or plants.
ArcGIS	Geographic Information System Suite by ESRI.	DNF	Doubs Normal Fault, restricted to the mechanical basement beneath the External Jura. The normal fault dips to the NNW and lies south of Besançon.
ASTER	Advanced Spaceborne Thermal Emission and Reflection Radiometer		
Bas	Pre-Mesozoic crystalline basement	Do	Dogger Group (Middle Jurassic)
BEPH	French Office of Exploration and Production of Hydrocarbons	DTM	Digital Terrain Model, representing the bare ground without buildings or plants
BF	Black Forest Massif, eastern rift shoulder of the Upper Rhine Graben (URG).	ECM	External Crystalline Massifs, crystalline basement exposed within the External Alps, comprising the Belledonne, Mont Blanc, Aiguilles Rouges, Aar and Gotthard massifs.
BG	Bresse Graben, graben segment of the European Cenozoic Rift System (ECRIS).	ECORS	""Étude Continentale et Océanique par Réflexion et Réfraction Sismique""
BGF	«Banque Gravimétrique de la France»	ECRIS	European Cenozoic Rift System
BGI	«Bureau gravimétrique international»	EPSG	A geodetic parameter dataset defined by the European Petroleum Survey Group (EPSG).
BRGM	The «Bureau de Recherches Géologiques et Minières» is the French authority for geological data. It was formerly called «Bureau de Recherches Géologiques et Géophysiques» (BRGG). See website on http://infoterre.brgm.fr .	ESRI	Environmental Systems Research Institute
BSJA	Burgundy-Swabian Jura Anticline, lithospheric buckle fold proposed in Bourgeois et al. (2007) due to tectonic uplift of the southern part of the Upper Rhine Graben (URG) since 17 Ma.	FAM	The Faisceau des Avant-Monts is the eastern part of the Avant-Monts s.l., which was detached within Triassic evaporites (Madritsch et al., 2008). It corresponds to the Besançon Zone defined in Madritsch et al. (2008).
Bss	Buntsandstein Group (Lower Triassic)	FZ	Ferrette Zone
BZ	Besançon Zone (definition in Madritsch et al. 2008), corresponding to the FAM in this study.	GA25	Geological Atlas of Switzerland 1:25000, map sheets published by swisstopo.
CFT	Constance-Frick Trough	GDEM	Global Digital Elevation Model
Cr	Cretaceous Group	GIS	Geographic Information System
DEM	Digital Elevation Model, representation of terrain data in an elevation computer model. A DEM can be a digital surface model (DSM) that represents all objects on the earth surface, whereas Digital	IGF1967	International Gravity Formula 1967
		IGN	""Institut national de l'information géographique et forestière""

IGSN71	International Gravity Standardization Net 1971	Nagra	National Cooperative for the Disposal of Radioactive Waste, see www.nagra.ch .
JFTB	Jura fold-and-thrust belt	NASA	National Aeronautics and Space Administration of the U.S. federal government
JGM	Jura Gravity Model, Bouguer grids rendered for this study.	NTB	Nagra Technischer Bericht (technical report)
Ke	Keuper Group (Upper Triassic)	OMM	Obere Meeresmolasse (= Upper Marine Molasse in English)
LA-ICP-MS	Laser Ablation Inductively Coupled Plasma Mass Spectrometry	OSM	Obere Süswassermolasse (= Upper Freshwater Molasse in English)
Li	Lias Group (Lower Jurassic)	PC	Permian and Carboniferous trough sediments
LiDAR	Light Detection And Ranging, method for measuring distances	QGIS	Formerly Quantum GIS, free open-source Geographic Information System, https://qgis.org .
LMa	Lower Malm Group (Early Upper Jurassic)	RAP	""Régie Autonome des Pétroles""
LSH	La Serre Horst, referring to the exposed La Serre Massif to the NE of the Jura Mountains. The LSH lies within the tectonic LSZ defined in this study.	RBTZ	The Rhine–Bresse Transfer Zone links the southern URG and northern BG. It is also called Burgundy Transform Zone (e.g. Schumacher 2002).
LSZ	La Serre Zone, western part of the Avant-Monts s.l., which was not detached within Triassic evaporites (Madritsch et al., 2008). It corresponds to the Avant-Mont Zone defined in Madritsch et al. (2008).	SMB	Swiss Molasse Basin, part of the MB. A large portion of the SMB (west of Zurich) was detached in Mio-Pliocene times together with its Mesozoic substratum.
MB	Molasse Basin, flexural basin containing the Oligocene to Miocene cycles of the UMM, USM, OMM and OSM. It corresponds to the Northern Alpine Foreland Basin (NAFB). The Molasse Basin encompasses parts of Germany, Austria, Switzerland and France. The western part of the MB (Switzerland and France) was detached together with its Mesozoic substratum during Mio-Pliocene times.	SRTM	Shuttle Radar Topography Mission, a space shuttle mission that obtained earth-surface topographic data.
METI	Messaging Extraterrestrial Intelligence, non-profit research organization	Ter	Tertiary Group
Mk	Muschelkalk Group (Middle Triassic)	TJ	Tabular Jura, exposed autochthonous Mesozoic cover of the southern Black Forest and Vosges (including RBTZ), as well as La Serre Zone (LSZ) and Ile Crémieu (IC).
MSWD	Mean squared weighted deviation, measure of goodness of fit of a statistical model	UMa	Upper Malm Group (Late Upper Jurassic)
NAB	Nagra Arbeitsbericht (work report)	UMM	Untere Meeresmolasse (= Lower Marine Molasse in English)
NAF	Northern Alpine Foreland, referring to the Alpine flexural basin system, which includes the foredeep (= NAFB), the forebulge and backbulge depozones, as well as the deflected European lithosphere underneath. The detached western portion of the NAF (= detached NAF) corresponds to the JFTB and the detached western Molasse Basin (MB) including its Mesozoic substratum.	URG	Upper Rhine Graben, graben segment of the ECRIS roughly in between Mannheim and Basel. The URG has a NNE-SSW orientation, lying in between the exposed massifs of the Vosges and Black Forest (BF), which constitute the rift-shoulders.
NAFB	Northern Alpine Foreland Basin, referring to the Molasse Basin north of the Western and Central Alps, spanning France, Switzerland, Austria and Germany. The western NAFB, comprising the majority of the Swiss Molasse Basin (SMB), the French Molasse Basin and the Jura Molasse, detached together with its Mesozoic substratum in Mio-Pliocene times.	USGS	United States Geological Survey
		USM	Untere Süswassermolasse (= Lower Freshwater Molasse in English)
		VZ	Vorfaltenzone, north-eastern most portion of the JFTB, lying above the Constance-Frick Permo-Carboniferous trough.
		WGS84	World Geodetic System, defined in the revision of 1984.

1 - INTRODUCTION

1.1 MOTIVATION AND OBJECTIVES

The Jura Mountains fold-and-thrust belt (JFTB) is a mountain range north-west of the European Alps. The Jura is shared by France and Switzerland and represents one of the most extensively studied fold-and-thrust belts globally, doubtlessly due to an outstanding infrastructure in moderate altitudes below 1720 m a.s.l., at a mean of roughly 700 m a.s.l. The Jura is a living space, with agriculture and industrial centres. The Jura landscape with its exposed limestone cliffs, gorges, winding rivers, windy lakes, green pastures and picturesque nature reserves is intensely explored every year by hikers, canoeists, sailors, climbers, paragliders, hang-gliders, speleologists, skier, cross-country skier and other adventurers of all sorts.

Geologically, the JFTB was intensely explored by the French oil industry, which acquired numerous seismic lines and exploratory wells. The first gas fields were exploited as early as 1906 in Ambérieu (Heritier 1994), 1922 in Vaux-en-Bugey (Schoeffler 1941) and 1946 in Revigny (Heritier 1994; Lienhardt 1962). Further investigations followed in the 1950ies lasting up to the 1980ies, such as in the region of Lons-le-Saunier (Michel et al. 1953; Poujol and Michel 1958) or Valempoulières (PREPA 1963). However, most occurrences of hydrocarbons were rather disappointing with only few exploitable gas or oil and the oil industry lost interest in the Jura Mountains. Today, it is mainly the cement and salt industries that exploit the geological resources in the Jura.

The main geological challenges for maintaining the commercial infrastructure are often connected to karst and water pathways, important for potable water and agriculture. In this respect, the shallow aquifers are of great interest. The knowledge about much deeper fracture systems and water pathways in the basement of the Jura is important for future deep geothermal projects, the first of which is currently in the phase of exploration in Haute-Sorne, lying in the basin of Delémont (Switzerland). The targeted depth of this borehole is between 4 and 5 km, deep in the crystalline basement of the Jura. Establishing a successful geothermal infrastructure will certainly be

an important milestone in the course of the transition to sustainable energy. Understanding the formation of the Jura, in particular its connection to basement structures, is therefore maybe as vital as never before.

Scientifically, the formation of the Jura Mountains is still controversially discussed. Today, most authors interpret the Jura as a thin-skinned fold-and-thrust belt, which means that only the Mesozoic and Cenozoic sedimentary cover is deformed, above a rigid and crystalline pre-Mesozoic basement that contains local grabens filled with Permian-Carboniferous sediments (Burkhard 1990; Buxtorf 1916; Laubscher 1961; Philippe 1995; Sommaruga 1997, 1999). It is not entirely clear how far and where the basement was involved in the formation of the Jura. There are pre-existing extensional structures in the basement that must have affected the deformation of the rather young JFTB (Laubscher 1961). Exploring the control or geometry of pre-existing basement structures is complex as they may only be inferred from structures in the transported and deformed Jura cover, which are for example known as deformation lines or lineaments in the Eastern Jura (Laubscher 2008a,b; Meier 2010; Steinmann 1892). In addition, some few locations across the JFTB are suspected to show basement inversion post-dating the JFTB (Guellec et al. 1990; Madritsch 2008; Ustaszewski 2004). To verify structures at the depth of the basement is complex, as the resolution of seismic lines is often not sufficient.

The deformation across the JFTB is heterogeneous, sometimes clearly controlled by pre-existing structures and sometimes rather not. Also, different structural domains across the JFTB are partially controlled by varying frictions of the JFTB décollement. Many studies revealing interesting geological aspects of the JFTB focus on local structures and their regional importance across the whole of the JFTB is often unclear. There is clearly a need for unified information that allows a data-supported discussion.

The aim of this study is therefore (1) to solidify the geological data set by providing regional but sufficiently detailed maps and cross-sections across the JFTB and surroundings, (2) to identify structures in the detached cover of the

JFTB that are possibly controlled by faults in the footwall, (3) to assess the involvement of the basement at different stages and finally (4), to test the interplay between thin-skinned and basement involved deformation. The focus of this study is set on understanding the long-term evolution of the area of the Jura Mountains and the processes that led to the present day mountain range.

1.2 STUDY AREA

The study area (Fig. 2.1) encompasses the Jura Mountains fold-and-thrust belt (JFTB) and surroundings, namely the Swiss and French Molasse Basin (MB) and the rift segments of the European Cenozoic Rift System (ECRIS), which is to say the southern Upper Rhine Graben (URG), the Bresse Graben (BG) and the Rhine-Bresse Transfer Zone (RBTZ) linking the two grabens. The Mesozoic and Cenozoic sediments of the JFTB and the adjacent Swiss and French (or Savoy) Molasse Basin were detached in Mio-Pliocene times above a basal décollement in Triassic evaporites (Buxtorf 1916; Laubscher 1961). The JFTB and detached Molasse Basin (with its Mesozoic substratum) are the detached western sedimentary portion of the proximal Northern Alpine Foreland (NAF, see subdivision in Fig. 2.1). In a tectonic sense, the detached NAF is an extension of the Alps and constitutes the front of the present day Central and Western European Alps. In this study, NAF refers to the Alpine flexural basin system (Decelles 2012; DeCelles and Giles 1996, see definition in Chapter 2.6.3) before the formation of the JFTB and MB, including the deflected lithosphere underneath. Note that this definition is not restricted to the foredeep-depozone, but includes the forebulge and backbulge depo-zones as well. Therefore, the NAF includes all of the study area, comprising the future Molasse Basin and JFTB, as well as the URG and BG and even the exposed massifs of the Black Forest and Vosges. The NAF stands in contrast to the Northern Alpine Foreland Basin (NAFB), which only addresses the Tertiary deposits of the foredeep depo-zone, or the Molasse Basin correspondingly.

1.3 METHODOLOGY

Geological data is compiled in a geo-referenced database, including field data, cross-sections from previous studies, borehole data, geophysical data, as well as structural and geological maps. The database is created with GIS software ArcMap 10.6 and QGIS 2.14.9 and individual map layers are either stored as vectorised Shapefiles or rasterised TIF-files.

A new structural map is created for the JFTB, with re-evaluated traces of folds, thrusts and faults as well as re-evaluated limits of structural zones. Special focus is set on distinguishing faults that affect the pre-Mesozoic basement and faults that are restricted to the detached cover. A regional, digital borehole database is created, which is dockable to GIS systems. The relational database is created in MS Access 2016 and scripts are developed in order to check the consistency of borehole data, export graph-

ical logs and a PDF-file documentation (the database and PDF-file are available in Supplementary Material C).

An ArcPy-based (provided with ArcGIS 10.6) script suite is developed in Python 2.7 in order to collect geological data from the GIS and borehole database and to interpolate vertical thickness maps and a top basement model. Data preparation is done in ArcMap, QGIS and Move 2019.1, the latter is also used for kinematic forward modelling of a cross-section. Models for palinspastic restoration of maps are prepared in the ArcGIS suite and automated restoration of maps and Shapefiles is based on a Python 2.7 script suite that is developed for this purpose.

Brittle-viscous analogue models are conducted in the laboratory of the University of Bern, Switzerland. Sandbox models are documented by top-view interval photographs and one model is documented in the CT-scanner at the Institute of Forensic Medicine, University of Bern, Switzerland. Cathodoluminescence (CL) microscopy and U-Pb dating of calcite in faults are conducted by Nathan Looser at ETH Zurich, Switzerland.

1.4 STRUCTURE OF THE MANUSCRIPT

The manuscript is sub-divided into ten chapters. Complementary to this, the Appendix B provides a Bouguer anomaly map of the study area, a new displacement model and an interpretative basement fault map from palinspastic restoration of lineaments in the JFTB. These maps and models are partially used in the main chapters. Additionally, this study contains two enclosures providing a description of boreholes (Supplementary Material C) and a new geological map 1:500'000 (Enclosure 01) created for this study.

In Chapter 1, the motivation of the thesis is explained and the aims are defined. Chapter 2 starts with a geological description of the study area (providing structural overview maps with different emphasis) and its tectonic evolution since Variscan times. It also specifies some important lithospheric deformation processes that are vital for the study area and which are addressed in the subsequent chapters. Furthermore, Chapter 2 gives an overview of Variscan trends that are imprinted in the basement of the study area. At the end of Chapter 2, a brief stratigraphic overview is given and a definition of the lithostratigraphic units used in this study.

This is followed by Chapters 3 to 6, which are dedicated to lithological and structural data collection and a unified, regional interpolation of different datasets. These chapters describe a borehole database, thickness maps, geological cross-sections and a top basement model. Chapter 6 additionally investigates the spatial evolution of the Alpine flexural basin system, which I consider a key data-set for interpretations and discussions in Chapters 7 to 9.

Chapter 7 and 8 are analytical and experimental approaches to unravel and understand structures of the JFTB. In Chapter 7, the age of structures in the JFTB is addressed on behalf of new calcite ages from U-Pb dating and compiled ages from previous studies. Chapter 8 shows the results of an analogue modelling study that investigates the control of basement faults on the deformation of a thin-skinned cover. The results help to under-

stand «lineaments» of the JFTB (deformation lines such as the Schwarzwald line or Vicques line, see Meier 2010). In Appendix B.4, I use insights from Chapter 8 to develop the concept of JFTB lineaments, and I provide a lineament restoration map that suggests yet undetected basement faults in the Internal Jura and the Molasse Basin. Finally, a kinematic forward model is presented in Chapter 9, which shows the evolution of a cross-section in the External Jura, based on data and concepts elaborated in the previous chapters. In the last Chapter 10, overall conclusions are drawn.

With this structure of the manuscript, I hope to take the reader through an engaging and stringent story about the response of the JFTB to its pre-structured substratum.

2 - GEOLOGICAL CONTEXT

2.1 REGIONAL GEOLOGICAL SETTING

The JFTB forms an arc-shaped mountain range of ~300 km width and a maximum transect length of ~75 km (Fig. 2.1a and b). The Jura constitutes the outermost front of the Central and Western European Alps (Fig. 2.1a). Together with the western portion of the Molasse Basin (French / Savoy and Swiss Molasse Basin, SMB), the Jura Mountains were part of the western NAF that detached in Triassic evaporites in Miocene to Pliocene (Buxtorf 1916; Jordan 1992; Jordan and Nuesch 1989; Laubscher 1961; Lienhardt 1962; Michel et al. 1953). Note that the detached Mesozoic substratum of the Molasse Basin is not part of the Molasse Basin. The limit between Molasse Basin and JFTB is defined at the erosional limit of the Plateau Molasse (Fig. 2.1b). In the same way, the south-eastern limit of the Molasse Basin is given by the erosional limit of the External Alps (e.g. the Préalpes Klippen, Subalpine Chains, Helvetic and Ultrahelvetic nappes, Fig. 2.1b). The detached NAF reaches from Voreppe in the SW to about Winterthur in the east (Fig. 2.1a).

The extent of the regional décollement of the Jura Mountains was particularly defined by the presence of Triassic evaporites (Laubscher 1961; Philippe 1995; Philippe et al. 1996; Sommaruga 1997), deposited in an epicontinental, shallow basin (Boigk and Schöneich 1974; Philippe et al. 1996; Sommaruga 1999; Sommaruga et al. 2017; Ziegler and Dèzes 2005). The JFTB décollement concentrated in salt systems, predominantly occurring in Upper Triassic units in the Central and Southern Jura (Fig. 2.1) and in the Middle Triassic series in the Eastern Jura (Debrand-Passard et al. 1984; Deville 2021; Guellec et al. 1990; Jordan 1992; Laubscher 1961, 1986; Philippe et al. 1996; Sommaruga et al. 2017). The front of the Jura thrusts over the edges of the European Cenozoic Rift System (ECRIS, Dèzes et al. 2004; Ziegler and Dèzes 2005, see Fig. 2.9), in particular the Bresse Graben (BG) in the west of the JFTB and the Upper Rhine Graben (URG) to the north, as well as the interjacent Rhine-Bresse Transfer Zone (RBTZ, also known as Burgundy Transfer Zone in Ziegler and Dèzes 2005) linking the two grabens (Fig.

2.1a). The JFTB is classically divided into a highly deformed internal structural domain (Internal Jura, also High Jura, Haute-Chaîne or Faisceau helvétique Fig. 2.1a) and a considerable less deformed external domain (External Jura, see classifications in Chauve and Perriaux 1974; Trümpy 1980). The Internal Jura (Fig. 2.1) is estimated to be displaced up to 30 km to the NW in its central segment (Affolter and Gratier 2004; Burkhard 1990; Laubscher 1965; Philippe et al. 1996), featuring well developed ramp and fault-propagation folds that partially led to duplication of the Mesozoic cover (Fig. 2.1b, Sommaruga 1997). The External Jura (Fig. 2.1) is subdivided into highly deformed zones showing thrusts and narrow folds that are called “faisceaux” (meaning bundles in French, see Fig. 2.1a) and into gently folded but intact plateaus (Fig. 2.1a). The plateaus of the External Jura are Mesozoic blocks of several hundred square kilometres, embedded within faisceaux (Fig. 2.1a). The southern plateaus reveal WNW directed displacements of about 10 km, which is deduced from balanced cross-sections (Philippe et al. 1996) and the front of the western Central Jura at Lons-le-Saunier (Fig. 2.1a) overthrusts Tertiary sediments of the BG by a distance of 5 to 7 kilometres (Blanc et al. 1991; Chauve et al. 1988; Laubscher 1961; Michel et al. 1953). Frontal faisceaux occupy a special position in the tectonic history of the Jura Mountains, since they inherited their structural orientations from extensional structures of the ECRIS (Bièvre and Mercier 2010; Chauve and Perriaux 1974; Glangeaud 1951; Martin and Mercier 1996; Philippe et al. 1996).

2.2 STRUCTURAL OVERVIEW MAPS

2.2.1 Previous structural maps

In the past, structural maps of Chauve and Perriaux (1974) and Trümpy (1980) were often used as reference maps (e.g. Philippe 1995 or Sommaruga 1997). As for example, Philippe (1995) presented a tectonic map based on structural domains of Chauve and Perriaux (1974), whereas the tectonic map of Sommaruga (1997) rather follows Trümpy

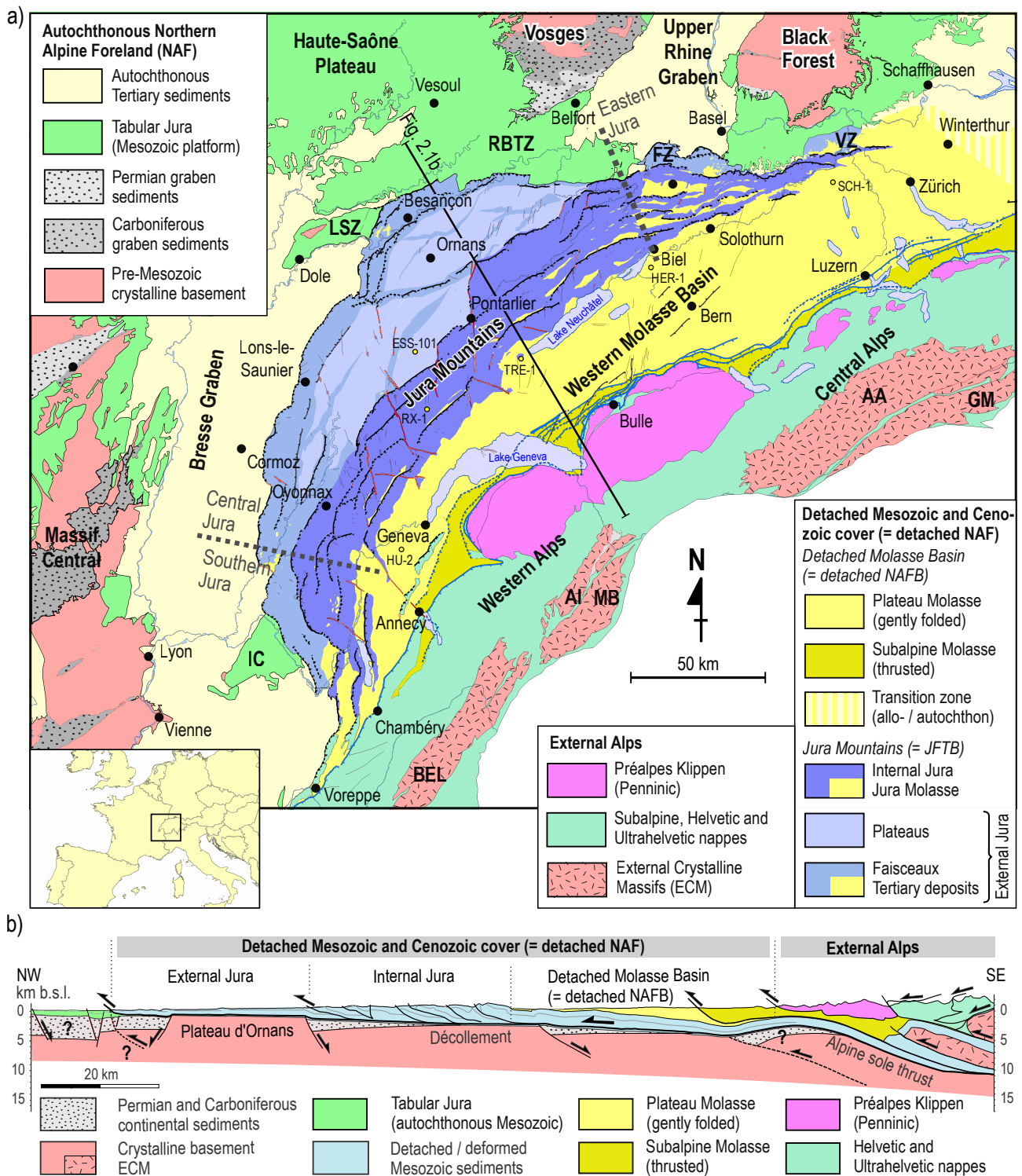


Fig. 2.1 – a) Tectonic overview map of the study area, showing the Jura Mountains and surroundings. Dotted lines indicate the limits between Southern, Central and Eastern Jura as used in this study. b) Regional cross-section modified from Sommaruga et al. (2017). AA: Aar Massif, AI: Aiguilles Rouges Massif, BEL: Belledonne Massif, FZ: Ferrette Zone, GM: Gotthard Massif, IC: Île Crémieu, LSZ: La Serre Zone, MB: Mont Blanc Massif, NAF: Northern Alpine Foreland, NAFB: Northern Alpine Foreland Basin, RBTZ: Rhine Bresse Transfer Zone, VZ: Vorfaltenzone, also known as Herzog-Börsberg Plateau (Malz et al. 2019). Boreholes are ESS-101: Essavilly-101, HER-1: Hermrigen-1, HU-2: Humilly-2, RX-1: Risoux-1, SCH-1: Schafisheim-1 and TRE-1: Treykovagnes-1.

(1980). More recent studies such as Madritsch (2008), Ustaszewski (2004) and Madritsch and Deplazes (2014) moved the front of the JFTB northwards, adding para-autochthonous zones of Chauve and Perriax (1974) and Trümpy (1980) to the JFTB (i.e. eastern part of Avant-Monts, Ferrette Zone and Vorfaltenzone, see Fig. 2.1). An updated, homogeneous and sufficiently detailed tectonic

map covering the whole of the Jura was not available and therefore, a new map was compiled for this study (Enclosure 01, extracts in Fig. 2.1, Fig. 2.2, Fig. 2.3 and Fig. 2.4).

2.2.2 New structural maps

The subdivision of *faisceaux* and plateaus made for this study is given in Fig. 2.2. An overview of important fault systems is shown in Fig. 2.3. A 1:500'000 structural map of the study area in PDF-format is provided in Enclosure 01 and the corresponding GIS shapefiles are available in the Supplementary Material A.01 and A.02 (revised traces of folds, thrusts, normal faults, strike-slip faults, basement connected faults and revised subdivision of tectonic domains).

The naming and separation of structural domains in Fig. 2.2 is based on Bichet and Campy (2016), Chauve and Perriaux (1974), Philippe (1995), Sommaruga (1997) and Trümpy (1980). However, boundaries of the structural domains of the JFTB are revised. In particular, the subdivision of the External Jura is refined based on a structural analysis of digital elevation models (IGN-F 2018; NASA 2014; Swisstopo 2011), geological maps at a scale of 1:50'000 in France (BRGM 2004) and 1:25'000 in Switzerland (Swisstopo 2012) and own local field data. The new tectonic map (Fig. 2.2) includes recent re-definitions at the front of the JFTB, such as the Avant-Monts (Madritsch 2008), the Ferrette Zone (Ustaszewski 2004) and the Vorfaltenzone (e.g. Madritsch and Deplazes 2014).

2.2.3 Eastern, Central and Southern Jura

In this study, the JFTB is laterally distinguished into a Southern, Central and Eastern Jura structural domain according to different regional orientations of fold axes (see limits in Fig. 2.2 and Fig. 2.3).

Eastern Jura

The Eastern Jura (Fig. 2.2, 2.3) contains the eastern tip of the Internal Jura, as well as the Ferrette Zone and the Vorfaltenzone, both allocated to the External Jura. The latter two zones are designated as frontal *faisceaux*, as they are in connection with downward steps in the Pre-Mesozoic basement, similar to the frontal *Faisceau lédonien* (No. 4, 9 in Fig. 2.2) in the west. The Eastern Jura contains the majority of the Jura Molasse outcrops (Fig. 2.2). Fold axes and thrusts (structural trends) roughly strike west-east (Fig. 2.3). NNE–SSW oriented lineaments indicate a connection to southwards prolonged Rhenish structures from the Upper Rhine Graben (Laubscher 1970, 1972). Cretaceous sediments are widely absent in the Eastern Jura (Beres 2005; Swisstopo 2012).

Central Jura

The Central Jura reveals rough NE–SW structural trends (Fig. 2.3) and the presence of large sinistral strike-slip fault zones such as the Vuache, St-Claude, Septmoncel, Morez-St-Cergue and Pontarlier fault zones (Fig. 2.3, no. 3;5-9). The Central Jura comprises the highly deformed Internal Jura in its south-eastern portion, as well as the External Jura that is separated into several *faisceaux* and plateaus. Kilometric plateaus surrounded by *faisceaux* are

a unique feature of the external Central Jura, not occurring in the Southern and Eastern Jura (Fig. 2.2).

Southern Jura

Structural trends of folds and thrusts in the Southern Jura are roughly SSE–NNW (Fig. 2.3). The re-orientation of structural trends is in connection with a thinning out of the Triassic series towards the south and increased friction on the basal décollement (Philippe 1994). The southern anticlines (Mont Chat, Parves, Gros Foug Anticlines, Fig. 2.3) peek out from the Molasse Basin and have a more N–S orientation. Note that the Salève Anticline south of Lake Geneva (Fig. 2.3) is allocated to the Subalpine Chains in this study due to a proposed connection of its basal thrust to the basement (Beck et al. 1998). Similarly, NNE–SSW oriented anticlines between Voreppe and Chambéry (Ratz Anticline and Echelles Anticline, Fig. 2.1a) are allocated to the Subalpine Chains in this study. In contrast to this, Philippe (1995) and Sommaruga (1997) allocate the Salève, Ratz and Echelles Anticlines to the Jura Mountains. The External Jura consists of the *Faisceau de Bugey* (no. 1 in Fig. 2.2) and the southern part of the *Faisceau d'Ambérieu* (no. 2 in Fig. 2.2).

2.2.4 Southern and northern Plateau Jura

The external part of the Central Jura is additionally subdivided in this study. The plateaus including their surrounding *faisceaux* (i.e. no. 3 to 35, Fig. 2.2) are referenced as Plateau Jura. The southern and northern Plateau Jura are separated along the southern limits of the *Faisceau salinois* and *Faisceau de Quingey* (no. 17 and 20, see Fig. 2.2).

2.2.5 Tabular Jura

The Tabular Jura (TJ) is the autochthonous Mesozoic part of the European platform and therefore, it is not part of the JFTB. The TJ is vertically displaced by normal faults that root in the basement (see Fig. 2.3). In the study area, the TJ is represented by the autochthonous Mesozoic cover south of the Black Forest and Vosges basement (Sommaruga 1997), which includes the Rhine–Bresse Transfer Zone (Fig. 2.2). Note that also the Ile Crémieu belongs to the TJ as well as the Haute-Saône Plateau lying north of the Bresse Graben (Fig. 2.2). Previously the Avant-Monts s.l., Ferrette Zone (FZ, no. 36 in Fig. 2.2) and Vorfaltenzone (VZ, 37 and 38 in Fig. 2.2) were attributed to the para-autochthonous or autochthonous Tabular Jura (TJ, see Sommaruga 1997; Trümpy 1980). Within this study, the *Faisceau des Avant-Monts* (27, 28, eastern part of the Avant-Monts s.l.), Ferrette Zone (36) and Vorfaltenzone (37, 38) are regarded as integral part of the JFTB, allocated to the *Faisceau Jura* (Fig. 2.2).

Rhine–Bresse Transfer Zone

The Rhine–Bresse Transfer Zone (RBTZ, Fig. 2.2) is also called the Burgundy Transfer Zone (e.g. Schumacher

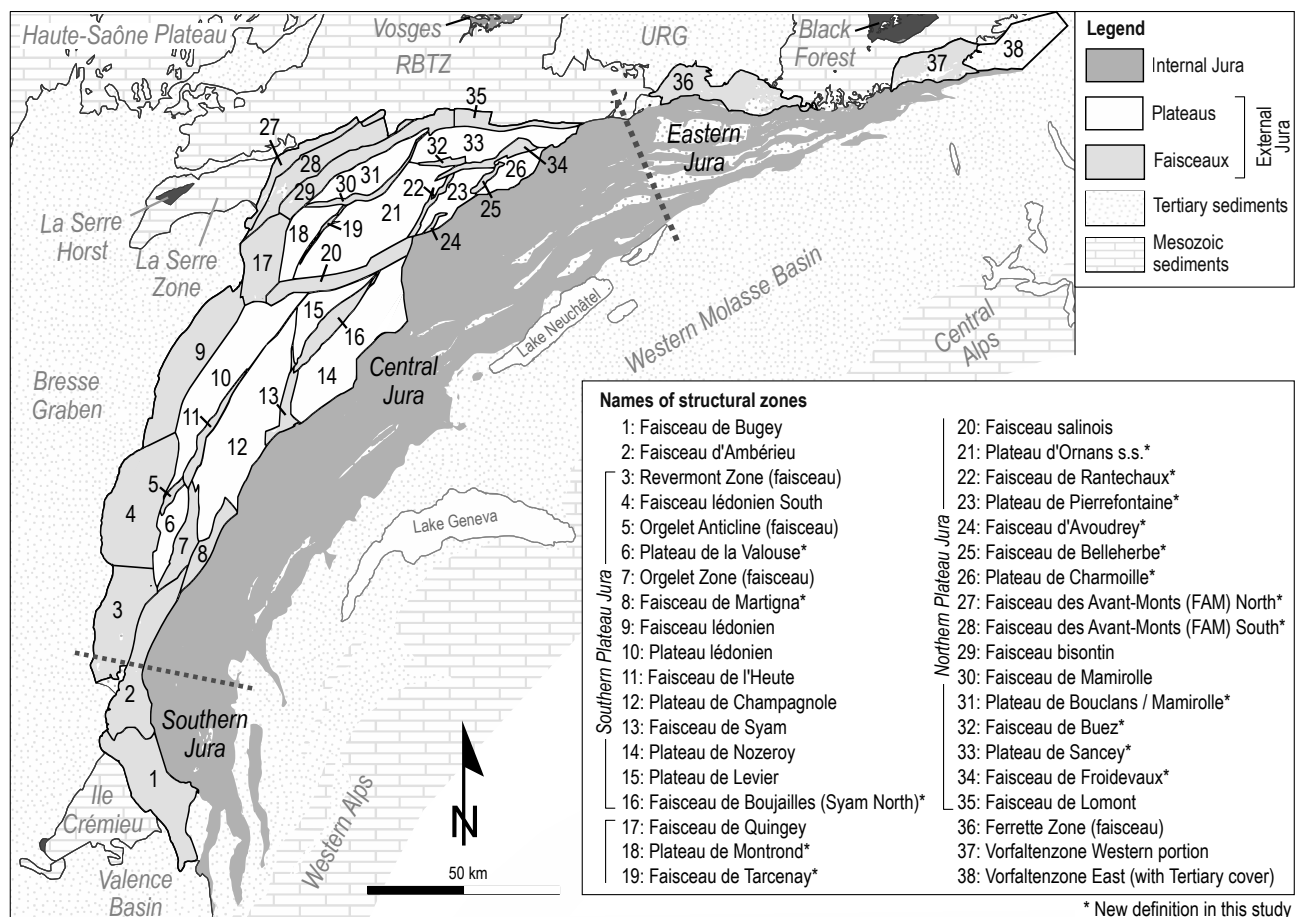


Fig. 2.2 – Subdivision of faisceaux and plateaus of the Jura fold-and-thrust belt. Names and subdivisions are based on Chauve and Perriaux (1974), Philippe (1995), Sommaruga (1997) and Trümpy (1980). The asterisk (*) marks structural zones for which new names were defined in this study, due to new structural subdivisions or reallocations.

2002; Ziegler and Dèzes 2005). The RBTZ shows Eo-Oligocene reactivation of pre-Mesozoic faults (Illies 1972; Madritsch et al. 2009) and sits on the northern margin of the Late Palaeozoic and Triassic Burgundy Trough (Boigk and Schöneich 1974).

2.2.6 Faisceaux and plateaus

The naming of structural domains in Fig. 2.2 generally follows Chauve (1975), Philippe (1995), Sommaruga (1997) and Trümpy (1980). The faisceaux and plateaus distinguished in this study are commonly named after villages they enclose (with some historical exceptions). The re-worked geological map of this study (Enclosure 01) reveals some deformed zones that were not designated as individual structural zones by previous authors (Chauve and Perriaux 1974; Philippe 1995; Sommaruga 1997; Trümpy 1980). The presence of unattributed deformation zones in the External Jura suggested the definition of some new faisceaux. They are (see Fig. 2.2 for locations) the «Faisceau de Martigna» (8), «Faisceau de Boujailles» (16), «Faisceau de Tarcenay» (19), «Faisceau de Rantechaux» (22), «Faisceau d'Avoudrey» (24), «Faisceau de Belleherbe» (25), «Faisceau des Avant-Monts» (27, 28), «Faisceau de Buez» (32) and «Faisceau de Froidevaux» (34). Due to the distinction of new faisceaux, the Plateau de Champagnole and Plateau d'Ornans s.l. of previous

studies (Chauve 1975; Philippe 1995; Sommaruga 1997; Trümpy 1980) are subdivided into smaller plateaus. They are the «Plateau de Valouse» (6), «Plateau de Montrond» (18), «Plateau d'Ornans s.s.» (21), «Plateau de Pierrefontaine» (23), «Plateau de Charmoille» (26), «Plateau de Bouclans / Mamirolle» (31) and «Plateau de Sancey» (33), see Fig. 2.2.

Subsequently, selected structural zones that deserve special attention are briefly described (see locations in Fig. 2.2):

Faisceau de Bugey (1)

The Faisceau de Bugey (1) shows NW–SE structural trends of anticlines and thrusts, which are notably oblique to the Faisceau d'Ambérieu (2). Philippe (1994) points out the imbrication style of the structures and attributes the structural style to the pinch out of the Keuper Group, which constitutes the décollement in this area. The Faisceau de Bugey is separated from the Faisceau d'Ambérieu along the «Gorges d'Albarine».

Faisceau de l'Heute (11)

The Faisceau de l'Heute is also called «Faisceau de l'Euthe» in Chauve and Perriaux (1974) or Homberg et al. (2002). The Faisceau de l'Heute overprints a pre-

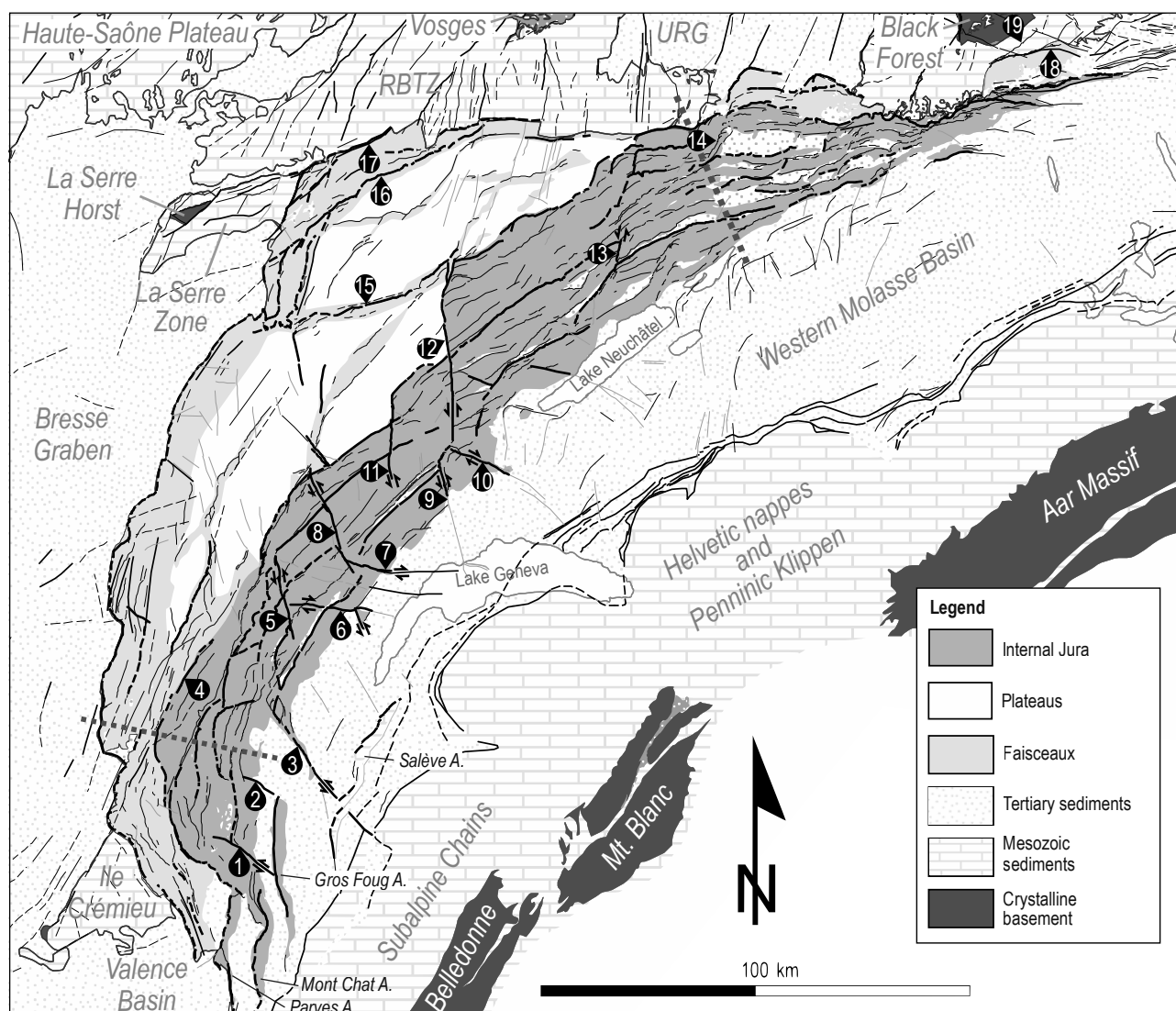


Fig. 2.3 – Structural map illustrating important fault systems. Thick black faults constitute main strike-slip faults and thrusts. Within the Internal Jura, these faults constitute the limits of tectonic nappes. 1: Culoz Fault Zone (sinistral), 2: Droisy Fault (sinistral), 3: Vuache Fault Zone (sinistral), 4: Oyonnax Thrust, 5: St-Claude Fault Zone (sinistral), 6: Septmoncel Fault Zone (dextral), 7: St-Cergue Fault Zone (dextral), 8: Morez Fault Zone (sinistral), 9: Pontarlier Fault Zone southern segment (sinistral), 10: La Sarraz Fault Zone (dextral), 11: Mouthe Fault Zone (sinistral), 12: Pontarlier Fault Zone northern segment (sinistral), 13: La Ferrière Fault (sinistral), 14: Caquerelle structure, 15: Salinois thrust system, 16: Doubs Thrust, 17: Chailluz Thrust, 18: Mandach Thrust, 19: Mettau Thrust.

existing normal fault system (called «pincée», see definition in Glangeaud 1944). Normal faults of the «Pincée de l'Heute» continue to the north-east of the Faisceau de l'Heute (Fig. 2.4), without being overprinted by thrusts during the formation of the JFTB.

Faisceau de Boujailles (Syam North, 16)

The Faisceau de Boujailles (16) is a deformed zone north of the Faisceau de Syam. Structural orientations are roughly NE–SW in the Faisceau de Boujailles, whereas orientations are more NNE–SSW in the Faisceau de Syam (13). The Faisceau de Boujailles is not distinguished in Chauve and Periaux (1974) or Trümpy (1980) and is therefore a new definition of this study. Note that this faisceau separates the Plateau de Levier (15) to the north from the Plateau de Nozeroy (14) to the south.

Faisceau lédonien (4, 9)

The northern portion of the Faisceau lédonien (9, Fig. 2.2) reveals virtually no compressional structures but abundant normal faults (Fig. 2.4). Nevertheless, boreholes show that the area is detached in Triassic evaporites (Lienhardt 1962; Michel et al. 1953). Due to the unique structural style, Mugnier and Vialon (1984, 1986) suggested that the Faisceau lédonien (and Plateau lédonien) is not connected with the basal décollement of the Jura Mountains and rather constitutes an area of Mio-Pliocene gravity sliding, in connection with the Eo-Oligocene formation of the Bresse Graben. This view is opposed in Chauve et al. (1988) who assign the detachment of the Faisceau lédonien to the basal décollement of the JFTB. In this study, the more established view of Chauve et al. (1988) is followed.

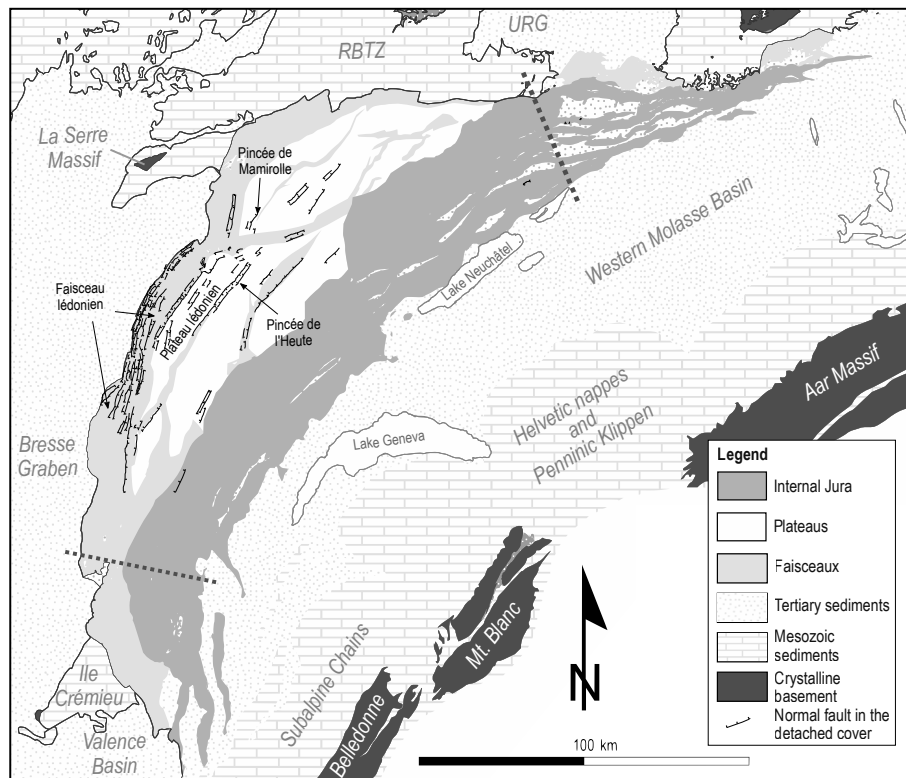


Fig. 2.4 – Structural map illustrating normal faults in the Mesozoic cover of the JFTB. Normal fault systems are called «pincée» and supposed to originate from Eo-Oligocene extensional tectonics (Glangeaud 1944). Most normal fault systems are identified at the front of the southern Plateau Jura (Plateau lédonien and Faisceau lédonien).

Faisceau de Tarcenay (19)

The Faisceau de Tarcenay (19, Fig. 2.2) is a new definition of this study. There are curved anticlines and suspected thrusts, which are interpreted as thin-skinned compressional structures. Due to the compressional character of the zone, a faisceau is distinguished in this study. This zone is also known as «Pincée de Mamirolle» (Glangeaud 1944; Homberg et al. 2002), because extensional structures (Oligocene normal faults) occur (Fig. 2.4). Note that the town of Mamirolle lies to the north of this zone, in the Plateau de Bouclans / Mamirolle (31, Fig. 2.2) proper. Therefore, the village Tarcenay is preferred in here to designate the faisceau.

Faisceau bisontin (29)

The Faisceau bisontin lies south of Besançon and is in connection with the Doubs Normal Fault (DNF). It is a main normal fault zone seen on seismic lines (Madritsch 2008) within the basement that dips to the north-west. The normal fault is not visible at the surface, where it is hidden beneath the compressional structures of the Faisceau bisontin. The western part of the Faisceau bisontin is also called «Faisceau de Besançon» in Bichet and Campy (2016).

Orgelet Anticline (5)

The Orgelet Anticline (5) is a small faisceau in the south-western prolongation of the Faisceau de l'Heute (11). The name is also used in Bichet and Campy (2016).

Orgelet Zone (7)

The Orgelet Zone (7) belongs to the Faisceau Jura. It is also called «Faisceau d'Orgelet» in Trümpy (1980) and Wildi and Huggenberger (1993). However, the village of Orgelet lies in the domain of the Orgelet Anticline (5) and the name is therefore misleading. This study prefers to follow Philippe (1995), who introduced the term Orgelet Zone, thereby implying the loose usage of the village name.

Ferrette Zone (36)

Ustaszewski (2004) showed that the Ferrette Zone was properly detached in Triassic evaporites and therefore constitutes part of the JFTB. Downward steps in the Pre-Mesozoic basement were mirrored during folding and thrusting of the Jura Mountains. Since the Ferrette Zone is connected to downward basement steps similar to frontal faisceaux such as the Faisceau lédonien (4, 9) and the Faisceau de Quingey (17), the Ferrette Zone is allocated to the Faisceau Jura in this study. Note that the Ferrette Zone is allocated to the Internal Jura in the Tectonic map of Switzerland, 1:500'000 (Beres 2005).

Vorfaltenzone (37, 38)

The Vorfaltenzone was not attributed to the JFTB by previous authors (Chauve and Perriau 1974; Trümpy 1980). According to investigations carried out by Nagra in past years, this zone is detached in Triassic evaporites (Madritsch and Deplazes 2014) and constitutes a mildly de-

formed frontal part of the Jura Mountains. The front of the Vorfaltenzone terminates at the Mandach Thrust (no. 18 in Fig. 2.3), as suggested in cross-sections in Madritsch and Deplazes (2014). The Mettau Thrust to the north of the Vorfaltenzone (no. 19 in Fig. 2.3) was speculated to be a result of an Oligocene gravity landslide induced by the uplift of the Black Forest Massif (Laubscher 1982). Nevertheless, Laubscher (1982) also points out that the NW verging Mandach and SE verging Mettau Thrust are probably linked due to their geographic connection and possibly both linked to the JFTB. Therefore, the area between the Mandach and the Mettau Thrust is possibly detached as well. The front of the Vorfaltenzone is defined as «front of the detached foreland which is mappable on seismic lines» in Madritsch and Deplazes (2014). In this study, the Vorfaltenzone is considered a faisceau.

Avant-Monts, Besançon Zone and La Serre Zone

The expression Avant-Monts s.l. was classically used for the slightly deformed area to the north and west of Besançon, which includes the La Serre Zone (comprising the La Serre Massif), as well as faisceaux 27 and 28 in Fig. 2.2 (Bersier 1932; Chauve and Perriaux 1974; Philippe 1995; Sommaruga 1997; Trümpy 1980). This area was not counted to the JFTB and specified as para-autochthonous Tabular Jura (Chauve and Perriaux 1974; Trümpy 1980). Investigations by Madritsch (2008) suggest a subdivision of the Avant-Monts s.l. into a thin-skinned eastern and a thick-skinned western zone. Madritsch (2008) introduced the term Besançon Zone (BZ) for the thin-skinned area north of Besançon and allocated it as a faisceau to the JFTB. Accepting this structural distinction, Bichet and Campy (2016) provide a geological map where the thin-skinned BZ is called «Faisceau des Avant-Monts» (FAM, 27 and 28 in Fig. 2.2). In this study, a new name is introduced for the western part of the Avant-Monts s.l., called the La Serre Zone (LSZ), see Fig. 2.2. The zone includes exposed crystalline rocks (mainly granites and ignimbrites) of the La Serre Horst (LSH, Coromina and Fabbri 2004) and autochthonous Mesozoic sediments (Fig. 2.2). On behalf of seismic lines, Madritsch (2008) showed that the LSZ is probably not detached in Triassic evaporites and that this zone represents a horst structure between the Bresse Graben in the south and the RBTZ to the north (Fig. 2.2). The front of the eastern part of the LSZ is suspected to be in connection with a recent thick-skinned inversion of the Avant-Monts Normal Fault (see Madritsch et al. 2008, line 4). Bichet and Campy (2016) additionally distinguish the «Plateau de Besançon» within the FAM, which defines the somewhat less deformed southern portion. However, there are abundant folds present, which rather discourages from the separation of a plateau. In this study, this less deformed portion of the FAM is referred to as the southern Faisceau des Avant-Monts (28, Fig. 2.2).

2.2.7 Normal faults in the cover of the Jura Mountains

Normal faults given in the structural map in Fig. 2.4 are according to previous publications (Bersier 1932; Bichet and

Campy 2016; Chauve et al. 1988; Homberg et al. 2002; Lienhardt 1962; Michel et al. 1953; Trümpy 1980; Wildi and Huggenberger 1993) and partially according to new interpretations of French geological maps (BRGM 2004). In the Faisceau lédonien (4, 9), many normal faults are inferred from Mesozoic layers that show vertical offsets but virtually no folding (Fig. 2.4). In the Plateau d'Ornans s.s. (21), Faisceau de Quingey (17), Faisceau de Tarcenay (19), north of the Faisceau de l'Heute (11), the Faisceau de Syam (14) and Faisceau de Boujailles (16), narrow grabens (pincées, Glangeaud 1944) are inferred from the French geological maps (BRGM 2004).

2.3 DÉCOLLEMENT DYNAMICS OF THE NORTHERN ALPINE FORELAND

The Jura Mountains and the Molasse Basin lie on a SE dipping lithosphere, which is mainly due to down-flexing of the European plate during its subduction beneath the Adriatic plate (Burkhard and Sommaruga 1998; Laubscher 1992). Therefore, the dip of the basement beneath the Molasse Basin and the JFTB increases towards the Alps. In transects across the SMB, the Tertiary sequence forms a triangular wedge with a maximum thickness of 5 to 6 km in the SE, below the penninic and helvetic frontal thrusts and the main body of the Alps (Sommaruga et al. 2012, see Fig. 2.1b). When the western Molasse Basin detached in Mio-Pliocene times, it became part of the Alps forming as a wedge-top basin (Willett and Schlunegger 2010). In the sense of the critical wedge theory (Fig. 2.5, Dahlen 1990; Davis et al. 1983), the basal tilt (β) of the Molasse Basin was already equal to the critical taper (Philippe et al. 1996) and continuous sedimentation into the wedge-top basin maintained a constant surface slope α (Willett and Schlunegger 2010). Therefore, the detached Molasse

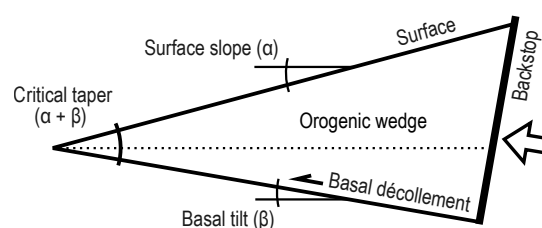


Fig. 2.5 – Illustration of geometrical parameters in the critical taper model of accretionary wedges (Dahlen 1990; Davis et al. 1983).

Basin remained remarkably intact as it was pushed north-westwards by the Alps and transferred most of the deformation to the area of the Jura Mountains (Buxtorf 1907; Laubscher 1961; Philippe et al. 1996; Willett and Schlunegger 2010). The basal detachment of the foreland was likely connected with the Alpine sole thrust to the south-east, that roots beneath the Crystalline Massifs of the External Alps (Boyer and Elliott 1982; Burkhard 1990, Fig. 2.1b). Therefore, the Mio-Pliocene evolution of the detached NAF (Becker 2000; Laubscher 1986) and the exhumation of the Aar, Gotthard, Aiguilles Rouges, Mont Blanc and Belledonne Massifs (Fig. 2.1a) were coupled and synchronous (Boyer and Elliott 1982; Burkhard 1990;

Buxtorf 1907).

2.4 BASAL DÉCOLLEMENT IN TRIASSIC EVAPORITES

The Triassic evaporite series, wherein the basal décollement of the detached NAF happened, is a very inhomogeneous interval with a thickness of several hundreds of metres. It contains alternating anhydrite-clay-limestone-dolomite systems and salt-rich layers wherein deformation mainly concentrated. These incompetent systems occur at different stratigraphic levels within Upper and Middle Triassic units, varying strongly depending on the geographic location. Furthermore, the burial depth of evaporites certainly has influence on rock mechanics, and consequently on the internal friction angle of the basal décollement. The JFTB décollement rather concentrates in salt-bearing systems (Deville 2021; Sommaruga et al. 2017), whereas the décollement of the Molasse Basin also reveals deformation structures in anhydrite systems, even in the presence of salt systems (Jordan 1994; Jordan and Nuesch 1989). In the following chapter, physical and mechanical conditions of the Triassic décollement are specified and further mechanical reflections are addressed.

Localisation of deformation in halite and anhydrites

Based on the assumption that the basal décollement of the JFTB was active at least from 12 Ma to 4 Ma (Becker 2000), with a shortening up to about 30 km (Affolter and Gratier 2004; Laubscher 1961; Philippe et al. 1996), an average propagation speed of the hanging wall of 3.75 mm/y is calculated (corresponding to a strain rate of $3.96 \cdot 10^{-15} \text{ s}^{-1}$). In the borehole Schafisheim-1 (Fig. 2.1a), in the eastern Swiss Molasse Basin and south of the JFTB, the basal décollement took place in Muschelkalk Group anhydrites, even though weaker halite is present at deeper levels (Jordan and Nuesch 1989). In western Switzerland, however, the basal décollement rather localised in Keuper Group evaporites (Gruber 2017; Jordan 1992).

In the Jura Mountains, Mid- and Late Triassic evaporites are commonly buried beneath at least about 0.8 km to 2.5 km Mesozoic sediments and in the SE of the Molasse Basin, up to 6 km siliciclastic Cenozoic sediments lie on top of that. Recent clumped isotope measurements in Schafisheim-1 (Looser et al. 2020) revealed vein calcite that precipitated between temperatures of 53° to 104° at the depth of the décollement (the Muschelkalk Group interval lies at a borehole depth of 1224 m to 1478 m, Weber et al. 1986). The geothermal gradient is expected between 25–40° C (Sommaruga et al. 2017), from which an initial burial depth of about 2.5 km of Mid-Triassic evaporites at Schafisheim-1 can be deduced.

Müller et al. (1981) show that grain size in anhydrite has important effects on the mineral strength. Experiments showed that grain-boundary migration is facilitated in fine-grained anhydrite and fine-grained anhydrite weakens at relatively low temperatures between 100–200 °C, dropping below the strength of halite (Müller et al. 1981). Anhydrite as main décollement level in presence of halite is thus

rather expected in the Molasse basin, where higher temperatures occur. Yet, in the Jura Mountains, where overburden was significantly lower, the critical 100 °C (or 2.5 km burial depth assuming a geothermal gradient of 40 °C) were commonly not reached at the décollement level.

Upper detachments

Several mechanically weak horizons of marls and clay occur in the Jurassic and Cretaceous series, providing possible local upper detachments in addition to the basal décollement in Triassic evaporites. For example, the Risoux-1 borehole (Fig. 2.1a, Winnock 1961), drilled in the Internal Jura, penetrated an important upper detachment in Lower Jurassic marls. In the Internal Jura, upper detachments were responsible for the staircase geometries of faults during the evolution of fault-bend folds (Nussbaum et al. 2017; Philippe et al. 1996; Rime et al. 2019; Schori et al. 2015; Sommaruga 1997). In the Vorfaltenzone (Fig. 2.1a), lying in front of the easternmost Internal Jura, triangle zones (fish-tails) resulted as a consequence of Middle and Upper Jurassic detachments (Malz et al. 2016).

2.5 TECTONIC EVOLUTION OF CENTRAL AND WESTERN EUROPE

In order to follow subsequent descriptions, references to ages, relative plate motion directions and resulting tectonic events are illustrated in the overview chart of Fig. 2.6. Complementary to this, stress fields during the Cenozoic evolution of the study area are shown in Fig. 2.7.

2.5.1 Variscan orogeny and post-Variscan collapse

During Late Carboniferous times (Westphalian), the study area in central and western Europe (Fig. 2.1a) was under the influence of the Variscan orogeny (Raumer 1998; Ziegler and Dèzes 2005), with a stress field that resulted from the collision between Laurussia and Gondwana (Fig. 2.6). Large shear zones in the Palaeozoic basement formed across the study area, with sinistral shear zones having a NNE–SSW (Rhenish) orientation (Illies 1962; Schumacher 2002, see Fig. 2.6 and Fig. 2.8). These sinistral shear zones were the structural seeds for later Eocene-Oligocene grabens in western Europe, e.g. the URG, BG, Valence Graben, the Roanne Graben and the Limagne Graben (Fig. 2.9). In addition to that, NW–SE to WNW–ESE (Hercynian) trending dextral shear zones formed (Edel et al. 2013; Schumacher 2002), named after the Harz Mountains in Germany. Note that in here, the term “Hercynian” is used as a reference to Late Palaeozoic NW-orientations (roughly parallel to the long-axis of the Harz Mountains, Fig. 2.9) whereas “Variscan” refers more broadly to the Late Palaeozoic orogeny. Dextral NW–SE striking shear zones were the structural seeds for the Lower Rhine Graben (LRG, Fig. 2.9) or the Freiburg-Bonnndorf-Bodensee graben system, which extends from the Black Forest to north-eastern Switzerland (Egli et al.

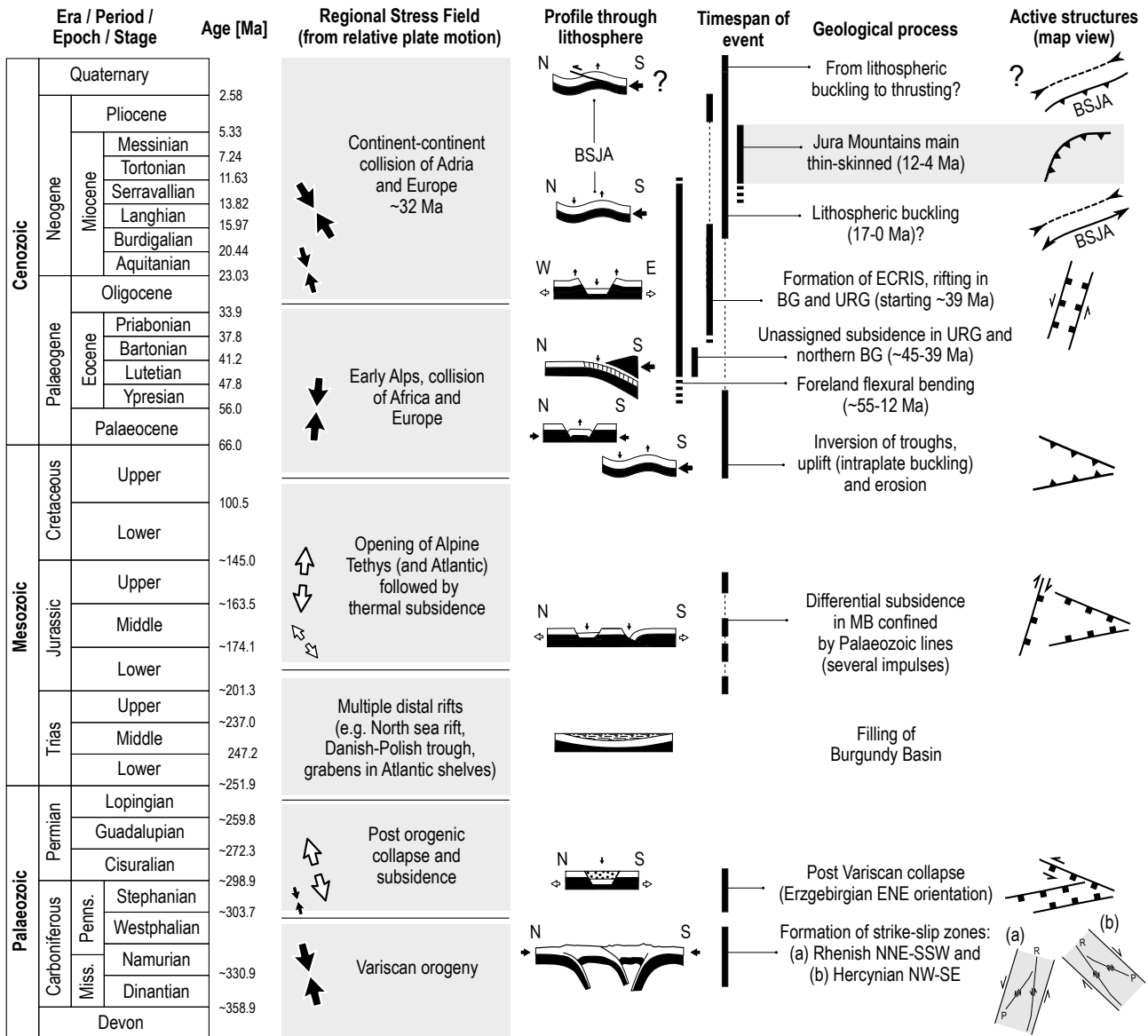


Fig. 2.6 – Tectonic events affecting the study area (Fig. 2.1). Note that the thin-skinned formation of the JFTB temporally overlaps with lithospheric deformation. Ages are according to the International Chronostratigraphic Chart (Cohen et al. 2020). Stages for the Carboniferous era are after the regional stratigraphy of north-west Europe. Indicated Cenozoic regional stress fields are from Bergerat (1987), Bourgeois et al. (2007), Schumacher (2002), Sissingh (1998) and Ziegler and Dèzes (2005). Mesozoic and Palaeozoic stress fields are according to Blés et al. (1989) and Schumacher (2002). BG: Bresse Graben, BSJA: Burgundy-Swabian Jura Anticline, ECRIS: European Cenozoic Rift System, MB: Molasse Basin, URG: Upper Rhine Graben.

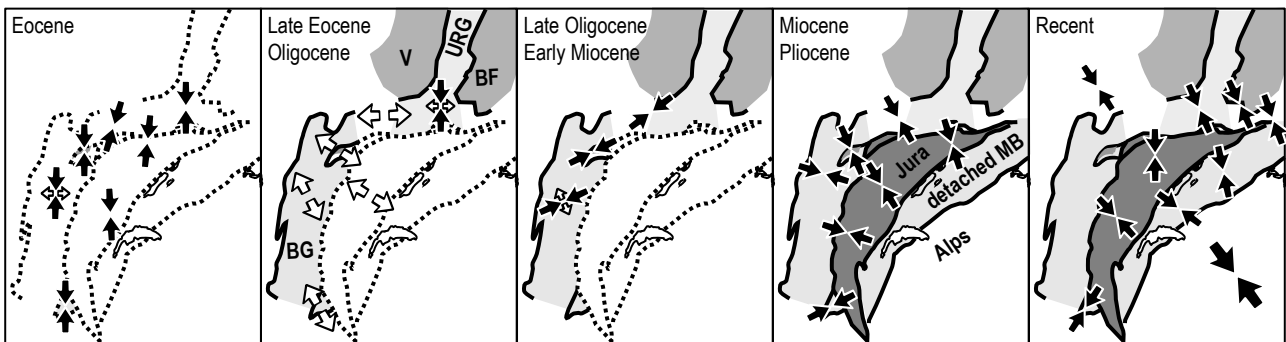


Fig. 2.7 – Cenozoic stress evolution in the Northern Alpine Foreland compiled from palaeostress studies in Larroque and Laurent (1988), Madritsch et al. (2009), Rocher et al. (2003), Rocher et al. (2004), Homberg et al. (2002) and the world stress map of Heidbach et al. (2016). V: Vosges Massif, URG: Upper Rhine Graben, BF: Black Forest Massif, BG: Bresse Graben, MB: Molasse Basin.

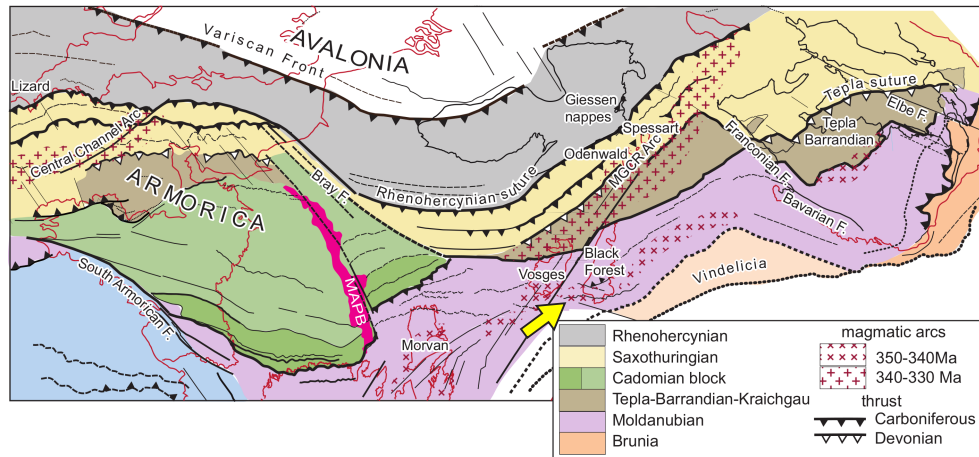


Fig. 2.8 – Map of the European Variscides according to Edel et al. (2013). The study area (arrow) lies in the Moldanubian tectonic zone south of the Vosges and Black Forest and is under the influence of Variscan sinistral (NNE–SSW) and dextral shear zones (WNW–ENE). MAPB: magnetic anomaly of the Paris Basin, MGCR: Mid-German Crystalline Rise.

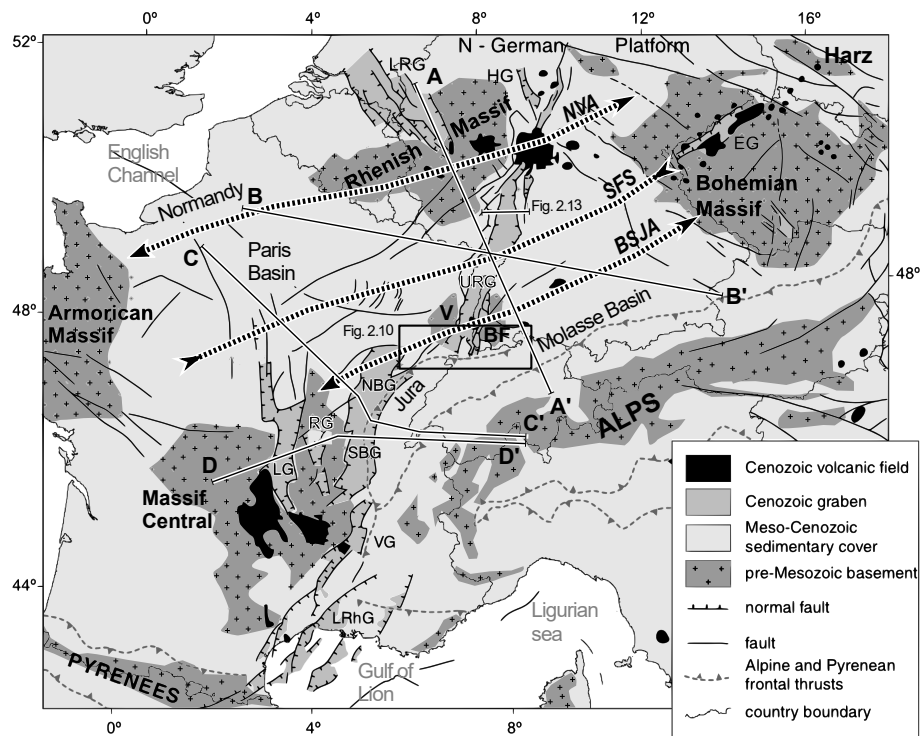


Fig. 2.9 – Structural overview map of western Europe modified from Dèzes et al. (2004) and Bourgeois et al. (2007). Indicated cross-sections are to be found in Fig. 2.15a and b. BF: Black forest, EG: Eger Graben, FP: Franconian Platform, HG: Hessian Grabens, LG: Limagne Graben, LRG: Lower Rhine Graben, LRhG: Lower Rhône Grabens, NBG: Northern Bresse Graben, RG: Roanne Graben, SBG: Southern Bresse Graben, URG: Upper Rhine Graben, V: Valence Graben. Lithospheric buckle folds (dashed lines) after Bourgeois et al. (2007) are BSJA: Burgundy-Swabian Jura Anticline, SFS: Sologne-Franconian Basin Syncline, NVA: Normandy-Vogelsberg Anticline.

2016, see Fig. 2.8). Within these mega shear zones, strike variations of individual faults can partly be explained by Riedel shear structures (Schumacher 2002). In Late Carboniferous (Stephanian) and Early Permian, the post Variscan collapse led to wrench tectonics, where transtensional Permo-Carboniferous (PC) troughs formed with a NE–SW to ENE–WSW (Erzgebirgian) orientation (Boigk and Schöneich 1970, 1974; Dèzes et al. 2004; Schumacher 2002). The orientation of PC-troughs was partially inherited from suture zones of the Variscan orogeny. With this last tectonic event (Fig. 2.6), some important Palaeozoic orientations were imprinted within the basement of the study area (Illies 1962; Reisdorf and Wetzel 2018; Schu-

macher 2002): 1) NNE-Rhenish, 2) NW-Hercynian and 3) ENE-Erzgebirgian. They remained mechanically weak zones that were reactivated during subsequent deformation of the basement.

Permo-Carboniferous troughs reveal complex internal structures, with border faults that are partially inherited from the Variscan orogeny (Egli et al. 2016; Madritsch et al. 2018; Schumacher 2002). They show polyphase transtension and transpression tectonics (Diebold et al. 1991). Permo-Carboniferous troughs were drilled in many places across the study area (Fig. 2.1a), including the Molasse Basin, the Jura Mountains, the Tabular Jura as well as in the BG and URG. They are furthermore exposed within

the Black Forest, Vosges, the French Massif Central and in the ECM (Fig. 2.1). Their distribution in the study area is documented on seismic lines, by boreholes or traceable on gravity maps (Laubscher 1986; Leu 2008; Madritsch et al. 2018; Philippe et al. 1996; Sommaruga et al. 2012; Truffert et al. 1990; Ziegler 1992b), but underneath the Jura Mountains, the knowledge of their extent is still comparably fragmentary. The ENE–WSW to NE–SW strike of Permo–Carboniferous troughs is maybe best visible in the Massif Central, where they are exposed and retraceable on geological maps (e.g. Blanzky Basin, Autun Basin).

2.5.2 Overview of Palaeozoic trends

In Fig. 2.10, I compiled traces of major faults documented in the crystalline basement and autochthonous Mesozoic and Cenozoic sediments north of the Jura Mountains (Egli et al. 2016; Faber et al. 1994; Hauber 1993; Larroque and Laurent 1988; Laubscher 1986; Madritsch and Deplazes 2014; Madritsch et al. 2018, 2008; Malz et al. 2016; Philippe 1995; Rotstein and Schaming 2011; Rotstein et al. 2005; Swisstopo 2012; Ustaszewski 2004). The area comprises the northern BG and southern URG, the autochthonous Tabular Jura including the RBTZ as well as the southern extents of the exposed Vosges and Black Forest crystalline massifs (Fig. 2.10). Numerous studies on seismic lines, boreholes and gravity maps provide a well constrained insight into the faults within this area (Egli et al. 2016; Hauber 1993; Larroque and Laurent 1988; Laubscher 1982; Madritsch and Deplazes 2014; Madritsch et al. 2009, 2018, 2008; Philippe 1995; Rat 1974; Rotstein et al. 2005; Ustaszewski 2004). Many structural orientations of faults are associated with the Variscan orogeny and post-Variscan collapse (Illies 1962, see Fig. 2.6) and faults are grouped according to their orientations, into three Palaeozoic trends following Illies (1962), Reisdorf and Wetzel (2018) and Schumacher (2002): (1) NNE–SSW Rhenish, (2) NW–SE Hercynian and (3) NE–SW to ENE–WSW Erzgebirgian. Some Palaeozoic fault zones with these structural trends were reactivated during Mesozoic and Cenozoic times (Laubscher 1986; Meier 2010). Since this caused offset of Mesozoic layers, Palaeozoic structural trends were mirrored by the sedimentary cover during the formation of the JFTB.

Rhenish trends

The dominant trend of Rhenish NNE–SSW faults (Fig. 2.10b) is ca. N020°, roughly parallel to the large-scale orientation of the URG. This orientation is attributed to faulting of Late Carboniferous age, originating from sinistral strike-slip zones during the Variscan orogeny (Boigk and Schöneich 1974; Metz 1970; Schumacher 2002; Wetzel et al. 2003). Faults with a more northward strike (compare Fig. 2.10b) presumably formed as R-shear Riedel faults within the larger strike-slip zone (Schumacher 2002). A second set of faults with a dominant ~N035° trend was furthermore extracted, which shows abutting relationships with N020° faults. In the URG and Vosges, N030°–N040° trends are thought to originate from Variscan sinistral strike-slip faults (Edel and Fluck 1989; Rotstein et

al. 2006). Their orientation would fit P-shear faults within the sinistral shear zone (Fig. 2.10b). Faults with Rhenish trends are abundantly documented within the detached cover of the External Jura and Eastern Jura. In the southern Plateau Jura near Lons-le-Saunier for example, they have been active as BG border faults during Eocene to Early Miocene (Chauve et al. 1988; Michel et al. 1953). In the northern Plateau Jura (Plateau d’Ornans s.l.), normal faults in the cover with a NNE–SSW Rhenish orientation were partially reactivated during thin-skinned deformation as sinistral strike-slip faults, providing tear faults that separate fold segments (Laubscher 1981; Philippe et al. 1996; Tschanz 1990).

Hercynian trends

Faults showing a NW–SE Hercynian orientation mainly occur in the east of the study area (Fig. 2.10a, c) and can be followed from the Constance-Frick Trough (CFT, Fig. 2.10a) through the crystalline basement of the Black Forest into the URG (Fig. 2.10a). We observe abutting relationships between some of the NW trending faults and therefore, we distinguished two fault sets with dominant N295° and N313° trends (Fig. 2.10c). The very high spread of orientations (compare Fig. 2.10) hints the presence of even more fault sets, with more NNW–SSE orientations, which we did not distinguish furthermore. Since the main Hercynian orientation is NW–SE and originates from Variscan dextral shear-zones, faults with a N295° trend might correspond to P-shear faults within the shear zone. The N295° trending faults are parallel to the Vorwald fault in the south of the BF (Fig. 2.10) and N313° faults correspond to the orientation of the Hegau Graben (Fig. 2.10a, e). The Hegau and Bonndorf grabens (Fig. 2.10a, e) belong to a larger system which connects to Lake Constance in NE Switzerland (Egli et al. 2016), that lies east of the study area. Normal faults with a similar trend as the Vorwald fault constitute the CFT (Fig. 2.10a), together with ENE Erzgebirgian faults (Madritsch et al. 2018).

Erzgebirgian trends

ENE–WSW Erzgebirgian faults trending N075° on average (Fig. 2.10d) constitute the CFT together with normal faults showing NW–SE Hercynian orientations (Fig. 2.10a). To the west of the study area, we estimate a slightly rotated dominant N064° trend for Erzgebirgian faults (Fig. 2.10d). This orientation can be followed over large distances into the Massif Central lying to the west of the Jura Mountains (Madritsch et al. 2009; Rocher et al. 2003).

2.5.3 Triassic basin and opening of Alpine Tethys in Jurassic

The Variscan orogen suffered a widespread erosion and was tectonically exhumed during Late Carboniferous (Stephanian) and Early Permian (Ziegler and Dèzes 2005, Fig. 2.6). The Mesozoic platform sediments were deposited on the regularly peneplated pre-Mesozoic basement, discordantly on Permo–Carboniferous troughs (Ziegler and

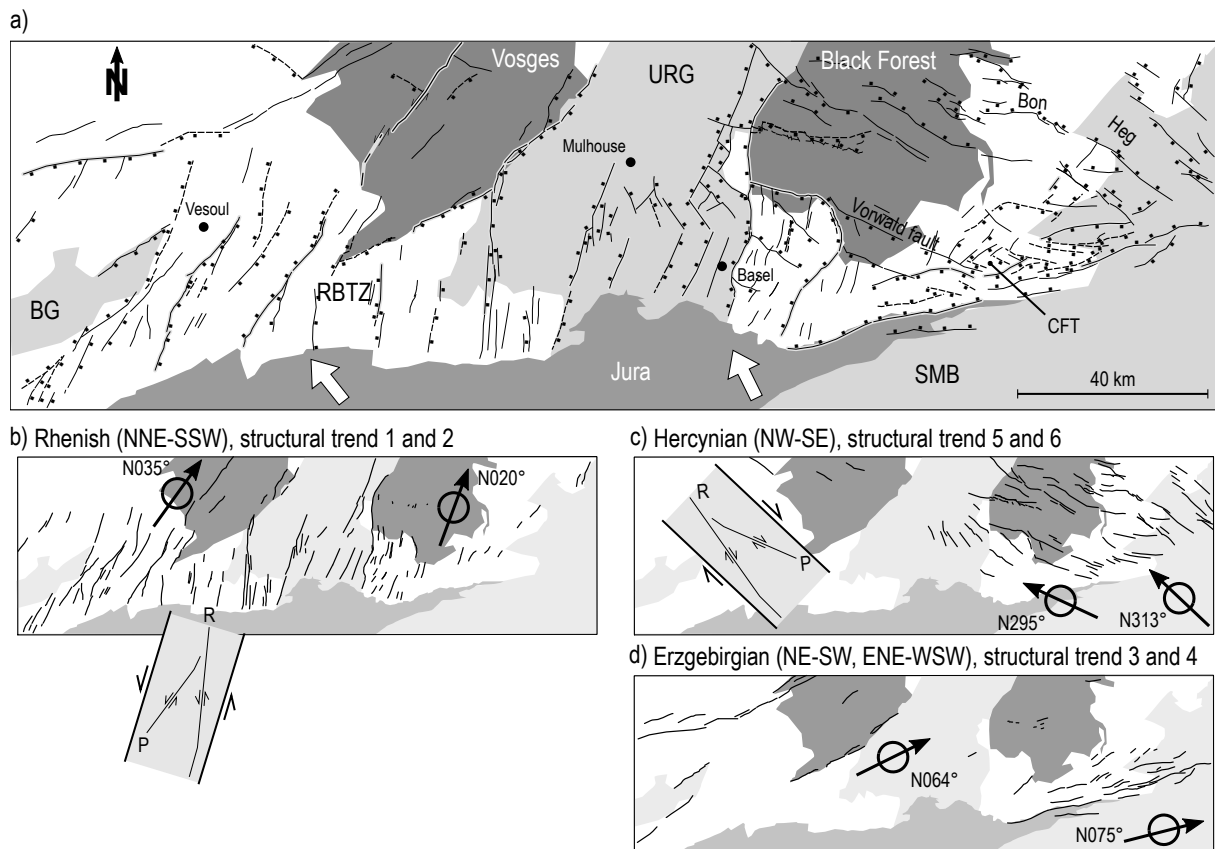


Fig. 2.10 – Overview of faults north of the Jura Mountains (location indicated in Fig. 2.9). Local transport directions during JFTB evolution (Philippe et al. 1996) are indicated in white arrows. a) Tectonic overview map showing faults with vertical displacements (see references in Chapter 2.5.2). Faults are separated into groups according to their orientation: b) faults with a NNE–SSW Rhenish orientation - dominant trends are indicated in black arrows. The Riedel scheme suggests that the different trends originate from a sinistral strike-slip zone. c) NW–SE Hercynian faults show trends that fit into the Riedel scheme for dextral shear zones. d) NE–SW to ENE–WSW Erzgebirgian faults are documented within the CFT, BG and Vosges. BG: Bresse Graben, Bon: Bonndorf Graben, CFT: Constance-Frick Trough, Heg: Hegau Graben, RBTZ: Rhine-Bresse Transfer Zone, SMB: Swiss Molasse Basin, URG: Upper Rhine Graben.

Dèzes 2005). In the study area (Fig. 2.1), Triassic sandstones, carbonates and evaporites of the Germanic facies (Buntsandstein, Muschelkalk, Keuper) were deposited into a shallow epicontinental basin (Boigk and Schöneich 1974). The basin was separated from the Tethyan realm to the south by the Vindelician land (Fig. 2.11). The shallow Triassic basin in the study area is known as Burgundy Trough and inherited from Early Permian extension (Boigk and Schöneich 1974; Ziegler 1982). Contemporaneously, multiple rifts with different orientations developed around the Burgundy Basin in Western and Central Europe (e.g. North sea rift, North Danish-Polish Trough, graben systems of the Atlantic shelves and Bay of Biscay rift, Ziegler and Dèzes 2005).

This was followed in Early to Middle Jurassic (Fig. 2.6) by the opening of the Alpine Tethys system (to which the Ligurian, Piemont and Valais Ocean belong) as a subsidiary of the Atlantic rift (Stampfli et al. 2001; Ziegler 1988b; Ziegler and Dèzes 2005) and the Burgundy Trough became a distant (rim basin) part of the Atlantic and Alpine Tethys rift system (Philippe et al. 1996; Stampfli et al. 1998; Ziegler and Dèzes 2005). Within the study area, differential subsidence associated with far-field N–S directed opening of the Alpine Tethys occurred, evidenced by hydrothermal veins (Allenbach and Wetzel 2006; Pietsch et al. 2016; Reisdorf and Wetzel 2018; Wetzel et al. 2003,

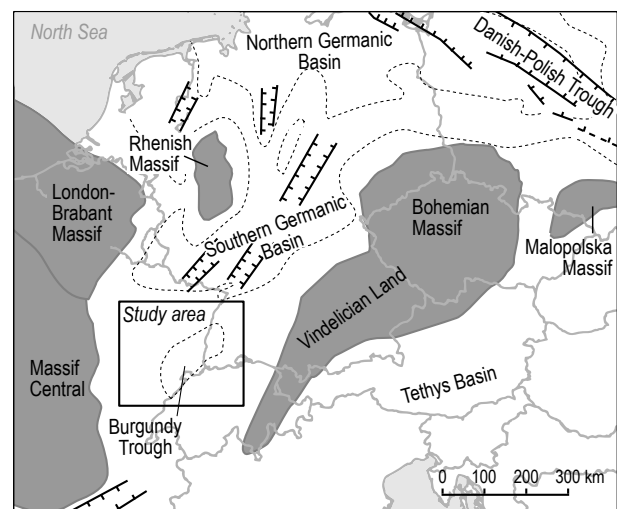


Fig. 2.11 – Palaeogeography of Central and Western Europe in Middle Triassic modified from Ziegler (1982, 1988a). The Burgundy Trough within the study area lies south of the Germanic Basin and is separated from the Tethyan realm by the Vindelician Land.

see Fig. 2.6). Tectonic subsidence patterns of boreholes in the SMB reveal at least four subsidence impulses during Mesozoic, namely in Upper Triassic, Aalenian, Bajocian and Oxfordian (according to subsidence curves in Wetzel et al. 2003). During these subsidence movements, ENE–

WSW (Erzgebirgian) and NW (Hercynian) striking border faults of Permo-Carboniferous troughs were partly reactivated as well as the NNE–SSW trending Rhenish Lineament, which follows the eastern border fault of the URG and prolongs beneath the Eastern Jura (Allenbach and Wetzel 2006; Wetzel et al. 2003; Ziegler and Dèzes 2005).

2.5.4 Cretaceous plate collision and lithospheric folding

N to NNE directed intraplate compression started during Upper Cretaceous in Turonian-Santonian (Stampfli et al. 1998; Ziegler and Dèzes 2005), resulting from the collision between Europe and Africa, which led to the progressive closure of the Alpine Tethys (Fig. 2.6). The study area including the area of the Massif Central, the future Haute-Saône Plateau, the BG, Jura and URG (Fig. 2.1) was uplifted, causing a partial erosion of Cretaceous and Upper Jurassic sediments (Bourgeois et al. 2007; Ziegler and Dèzes 2005) and some grabens were inverted (e.g. inversion of NNE–SSW Palaeozoic lines in the BG such as the Cormoz high, Debrand-Passard et al. 1984). Upper Cretaceous uplift of the future NAF has been proposed to be in connection with long-wavelength flexural folding of the lithosphere, since the Paris Basin and the lower Rhône valley to the north (Fig. 2.9) show increased subsidence rates at the same time (Bourgeois et al. 2007; Dèzes et al. 2004).

2.5.5 Evolution of the Alpine flexural basin system

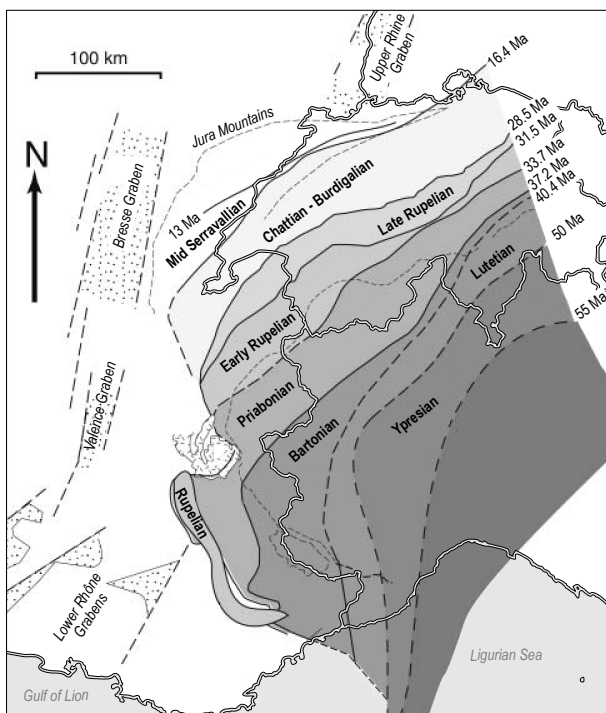


Fig. 2.12 – Map showing the migration of the Alpine foreland basin (foredeep) in Eocene to Miocene times (modified from Ford et al. 2006). Country boundaries are indicated with light grey lines. Dashed foredeep limits are not well constrained. The foreland basin reaches the domain of the future Jura Mountains in Burdigalian times (~20 to 16 Ma).

The early Alpine flexural foreland basin is not well constrained. However, some early Eocene sediments (~55 Ma) in northern Corsica supposedly represent the first subsidence (Ford et al. 2006). Beginning in Lutetian (~45 Ma), the migration of the flexural basin is more confidently constrained (Ford et al. 2006). Flexural subsidence of the Helvetic shelf started sometime in late Eocene (Burkhard and Sommaruga 1998; Guellec et al. 1990; Ziegler and Dèzes 2005), see Fig. 2.12. At about 28.5 Ma in early Oligocene, Alpine foredeep deposits arrived in the Molasse Basin (Ford et al. 2006) and by 20 Ma in Early Miocene, foredeep deposits reached the domain of the future Jura Mountains (Burkhard and Sommaruga 1998; Ford et al. 2006; Ziegler and Dèzes 2007). Finally, around Mid-Serravalian (13 Ma), the foredeep arrived at the front of the future Internal Jura (Burkhard and Sommaruga 1998; Ford et al. 2006; Pfiffner et al. 2002). The forebulge depozone (containing Eocene karst and siderolithic deposits) reached the domain of the future Jura already in Bartonian (Late Eocene, 37.8 to 33.9 Ma), which is for example indicated by siderolithic mammal deposits in the Mormont area (Hooker and Weidmann 2000; Hooker and Weidmann 2007). This shows that the forebulge preceded the foredeep by 18 to 21 My. The evolution of the foredeep is not constrained after about 12 Ma (due to a lack of sediments) and Burkhard and Sommaruga (1998) suggest that flexural bending became inactive.

Flexural bending was presumably accompanied by faulting. Within the Vorfaltenzone in the Eastern Jura for example (Fig. 2.1), NW–SE lithospheric extension due to flexural subsidence probably reactivated border faults of the Permo-Carboniferous Constance-Frick Trough (Diebold and Noack 1997; Malz et al. 2019).

2.5.6 Cenozoic rifting

Starting in Eocene, the ECRIS opened, with the BG, southern URG and RBTZ as the rift segments lying closest to the future Jura Mountains (Sissingh 1998; Ziegler and Dèzes 2005). Main rifting in these segments happened in Eo-Oligocene (~39 to 28 Ma, Madritsch et al. 2008; Ring and Gerdes 2016; Sissingh 1998) still under N–S to NNE–SSW directed plate convergence (Fig. 2.6). Sissingh (1998) also suggests an early initial phase of rifting that started in middle Eocene based on shallow lacustrine sediments in the BG and URG (Lutetian to Bartonian age), occurring in some restricted locations. However, such moderate subsidence might as well be connected to the backbulge syncline that forms in response to flexural bending of the Alpine foreland or be in connection with Upper Cretaceous to Eocene buckling of the lithosphere (compare tectonic events chart in Fig. 2.6). The regional compression changed to a more NW orientation when the Valais Ocean was finally subducted and Adria collided with Europe (see Fig. 2.6, Bourgeois et al. 2007; Sissingh 1998). The opening of the ECRIS followed inherited Variscan and post-Variscan faults, which were extensionally and transtensionally reactivated (Dèzes et al. 2004; Illies 1962). Rifting in the southern URG and BG ceased in Chattian (~28 Ma, Ring and Gerdes 2016; Sissingh 1998) but prevailed until Mid-Miocene in the northern URG (Sissingh 1998, see Fig.

2.6). Sinistral shear rifting in the northern URG continuous until today (Sissingh 1998) and a second short rifting event in the BG is distinguished in Pliocene (Sissingh 1998).

2.5.7 Formation of the Jura Mountains

It is classically proposed that the western NAF was detached in Triassic evaporites (Buxtorf 1907; Laubscher 1961) during Middle Miocene (Serravallian, ~14 to 12 Ma) to Pliocene times, which caused the translation of the Molasse Basin and its Mesozoic substratum to the NW and the formation of the JFTB. Based on Tertiary sediments, main thin-skinned deformation in the JFTB is presumed to have ceased at around 4 Ma (Becker 2000, see more details in Chapter 7.1.2).

2.5.8 Recent basement tectonics

Beneath the Jura Mountains and the Molasse Basin, basement faults were possibly reactivated locally causing inversion of PC-troughs after the formation of the JFTB (Guellec et al. 1990; Madritsch et al. 2008; Ustaszewski and Schmid 2007). At the northern front of the Jura Mountains, post-JFTB inversion of basement faults was proposed based on interpretations of seismic lines (Madritsch et al. 2008; Ustaszewski and Schmid 2006) and structural relations to the "Sundgau Gravels", which were deposited between 4.2 and 2.7 Ma (Ustaszewski and Schmid 2007). Recently, Egli et al. (2017) showed that thick-skinned compressional tectonics was active at 7.3 ± 1.3 Ma, deduced from U-Pb calcite dating of slickenfibres (indicating right lateral movement) on the NW (Hercynian) oriented Randen Fault, roughly 25 km to the NE of the Eastern Jura. This indicates that thick-skinned basement tectonics was ongoing north-east of the JFTB (and underneath the JFTB by implication) even during the main thin-skinned JFTB formation stage.

Northwest directed compressional basement tectonics prevailed until today, as evidenced by intense seismic activity of the Alpine foreland and in-situ stress measurements in boreholes (see Becker 2000; Mosar 1999 and references therein). Pliocene to Quaternary tectonic uplift of the peripheral Alpine foreland is for example evidenced by subsidence diagrams of boreholes across the Molasse Basin (Lemcke 1974). In the autochthonous Molasse Basin in Austria and Germany, the Pliocene to Quaternary basement uplift is in the range of 480 to 870 m (Lemcke 1974). The origin of recent uplift is still discussed:

i) Andeweg and Cloetingh (1998) proposed «unflexing» of the Alpine Foreland Basin in response to breaking up parts of the plate (slab break-off). However, slab breakoff beneath the Central Alps happened much earlier at 32–30 Ma (Schlunegger and Castellort 2016; Schlunegger and Kissling 2015). ii) Mosar (1999) suggests present-day tectonic underplating of the European crust to explain the uplift of the peripheral Alpine foreland basin. iii) Complementary to this, Lefort and Agarwal (1996, 2002) and Bourgeois et al. (2007) suggest that NE–SW trending lithospheric buckle folds with a large wavelength of 250 to 300 km and an amplitude of ~1.5 km developed in response to north-west directed shortening between Europe

and Adria, starting in Burdigalian and lasting until today (17–0 Ma). In the study area, the formation of a lithospheric anticline (the Burgundy-Swabian Jura Anticline, see definition in Bourgeois et al. 2007, Fig. 2.9) would explain documented tectonic uplift of the Black Forest, URG, the Vosges, the Haute-Saône Plateau and the northern Massif Central (Fig. 2.1a). Below the Vosges and Black Forest massifs, the distribution of earthquakes suggests that the NE-striking Burgundy-Swabian Jura anticline (Fig. 2.9) started to thrust northwards recently (Bourgeois et al. 2007; Edel et al. 2006).

2.6 LITHOSPHERIC DEFORMATION IN THE ALPINE FORELAND: PROCESSES / MECHANISMS

2.6.1 Intraplate lithospheric folding

Based on gravity maps, lithospheric buckling has been proposed for Western Europe including the study area by Lefort and Agarwal (1996, 2002). The collision of Africa and Europe starting in Lower Cretaceous caused lithospheric deformation far into the European continent, resulting in long-wavelength elastic folding of several hundreds of kilometres. Bourgeois et al. (2007) suggest the formation of new lithospheric folds between 17–0 Ma, shortly after rifting of the ECRIS came to an end. This is proposed because 1000 m of post-rift uplift is required to explain structural elevations in boreholes in the southern URG (Staffelfelden boreholes, north of the study area) whilst at the same time, sediments were accumulated in the northern URG. Bourgeois et al. (2007) identify three north-east striking lithospheric folds, which are from SE to NW the Burgundy-Swabian Jura Anticline (), the Sologne-Franconian Basin Syncline (SFS) and the Normandy-Vogelsberg Anticline (NVA, see Fig. 2.9 and Fig. 2.15a). This system of lithospheric buckle folds, has a wavelength of 270 km and an amplitude of 1.5 km (Fig. 2.15a).

2.6.2 European Cenozoic rifting

The ECRIS consists of multiple rift segments (Fig. 2.9) showing variable spreading widths. Extension in the Limagne Graben (Fig. 2.9) is estimated to 2–3 km, 1–2 km across the Roanne Graben (Fig. 2.9) and 2 km across the BG (Michon 2000). More localised deformation happened in the URG, where roughly 7 km stretching was derived from upper crustal faulting (Bourgeois et al. 2007). Rifting of the ECRIS started in Late Eocene with transtensional kinematics and a main extension followed in Oligocene (Michon 2000; Ring and Gerdes 2016; Sissingh 1998).

Subsidence movements within the European Cenozoic rift system were accompanied by uplift of rift shoulders, suggested to be the result of the flexural cantilever effect (Fig. 2.13, Kusznir et al. 1991) and up-flowing mantle material (Illies 1972; Michon 2000), leading to the exposed crystalline massifs of the Vosges and the Black Forest among others. Uplift of rift shoulders and subsidence of graben segments are estimated to have a ratio of 1/2 in

the URG (Bourgeois et al. 2007). Based on this proportion, Bourgeois et al. (2007) modelled synthetic uplift and subsidence profiles for the BG (see Fig. 2.15). The URG shows 1500 m uplift of rift shoulders (corresponding to the Black Forest and Vosges) and a graben depth of about 3000 m, filled with Tertiary sediments (Bourgeois et al. 2007). The eastern BG shoulder, which is hidden beneath the JFTB, is suggested to have uplifted 900 m with a corresponding subsidence of 1800 m (Fig. 2.15b) next to Lons-le-Saunier (see Fig. 2.1). The width of the BG rift shoulders is proposed to be up to 150 km (Bourgeois et al. 2007, compare Fig. 2.15b) and therefore, the whole of the JFTB is presumably affected by ECRIS uplifts and not only the External Jura.

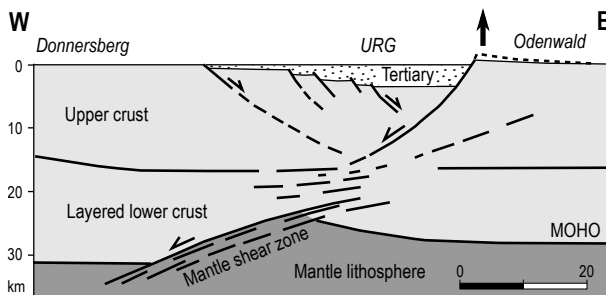


Fig. 2.13 – Cross-section through the northern Upper Rhine Graben interpreted from a reflection seismic line, based on Brun et al. (1992). The trace is indicated in Fig. 2.9. The cross-section illustrates a base-lithosphere detachment and the eastern rift shoulder shows structural uplift, which can be explained by footwall uplift according to the flexural cantilever model Kuszniir et al. (1991).

2.6.3 Foreland basin systems

Flexural bending and depozones

The process of foreland flexural bending leads to basin systems, which commonly show four discrete depozones, referred to as wedge-top, foredeep, forebulge and back-bulge (DeCelles and Giles 1996, see Fig. 2.14a and b). The evolution of a foreland basin system can be reconstructed by analysing the migration of these depocentres (DeCelles and Giles 1996). Typical foredeep depozones show flexural subsidence causing 2 to 8 km deep wedge-shaped basins, filled with a sequence of deep-marine flysch sediments which pass into non-marine and shallow-marine Molasse sediments (DeCelles and Giles 1996). In contrast to this, the forebulge depozone is characterised by flexural uplift (Fig. 2.14a), which may prevent the deposition of sediments. The horizontal width of foredeeps of broken plates is calculated using the formula $\pi\alpha/2$ and the forebulge is two times wider, corresponding to $2\pi\alpha$ (Decelles 2012). The position of the forebulge crest is given at $3\pi\alpha/4$ (Allen and Allen 2013). The parameter α is the flexural parameter, which mainly depends on the flexural rigidity of the lithosphere (D) and the density difference between the mantle and basin fill (DeCelles and Giles 1996). Foredeeps of broken plates are typically between 110-350 km wide, whereas continuous plates show wider foredeeps of about 170-515 km (Decelles 2012). Moreover, the amplitude of the forebulge (uplift) is ~4-7% of the negative deflection (subsidence) of the foredeep (Decelles 2012).

Therefore, typical forebulge crests are between 200 to 400 m high and can be followed by a shallow back-bulge syncline, which is typically 10-50 m deep (Allen and Allen 2013; Bourgeois et al. 2007; Decelles 2012; Sinclair et al. 1991). Flexural forebulging may interfere with lithospheric buckling and effects of both processes must be distinguished (Allen and Allen 2013). The forebulge of a flexural foreland basin owes its formation to the load of the approaching wedge (vertical forces) whereas lithospheric buckling is the result of horizontal plate compression, spreading far into an affected plate yielding decisively more uplift than flexural bending.

The foredeep of the northern Alpine foreland reveals an up to 5.5 km thick Cenozoic sequence close to the Alpine front (Sommaruga et al. 2012) in Switzerland and up to 6 km further east in Germany. Accordingly, flexural uplifts of the Alpine forebulge are calculated to be about 370-400 m, partially coinciding with uplifts of a lithospheric buckle anticline (Bourgeois et al. 2007, see BSJA in Fig. 2.15a). The Alpine foredeep is rather narrow, varying between 80 to 140 km (Burkhard and Sommaruga 1998; Laubscher 1992) from west to east, which suggests that the flexural basin must be calculated assuming a broken plate (DeCelles and Giles 1996). The precise signature of the flexural Alpine foreland basin in the area of the JFTB however is under discussion since the forebulge interferes with the ECRIS and is lost within the stronger signatures of the BG, RBTZ and URG (Burkhard and Sommaruga 1998; Laubscher 1992). The preceding weakening of the lithosphere, caused by the European rift system, might have significantly affected the geometry of the western part of the Alpine flexural basin system (Laubscher 1992). Therefore, different geometries of the western Alpine foreland basin system were suggested in the past (Burkhard and

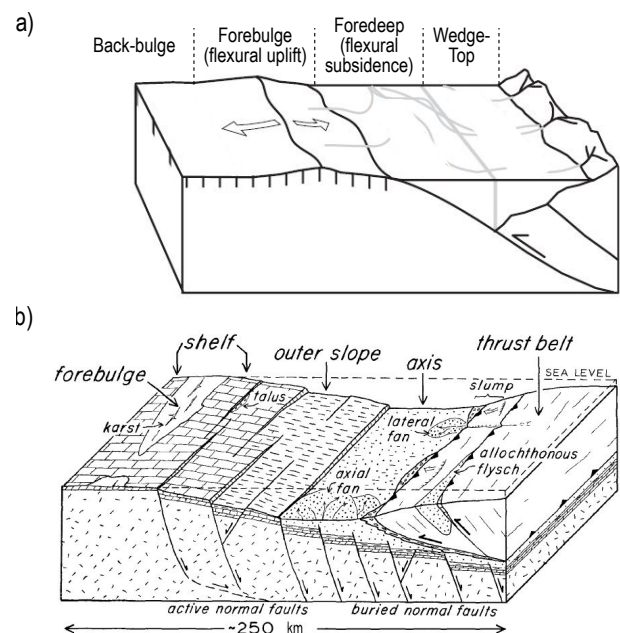


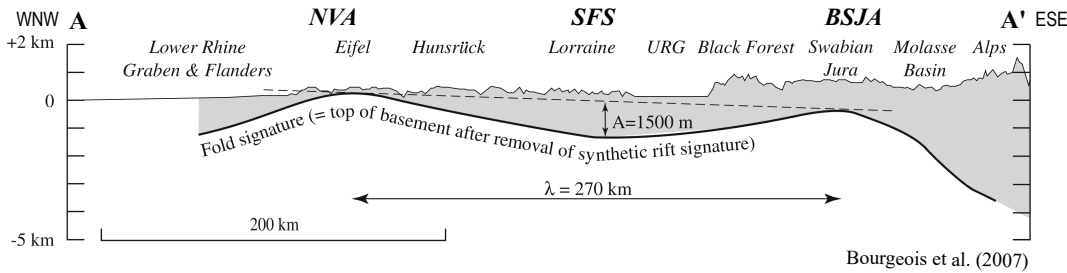
Fig. 2.14 – a) Sketch showing depozones in connection with flexural bulging (Decelles 2012). The forebulge is exposed and eroded, developing an unconformity. b) Illustration of depozones and crustal scale faults according to Bradley and Kidd (1991). The exposed forebulge shows extensional fractures affected by karst. Normal faults causing notable vertical offsets are formed on the outer slope, in the distal foredeep.

Sommaruga 1998; Gutscher 1995; Laubscher 1992, see Fig. 2.15c).

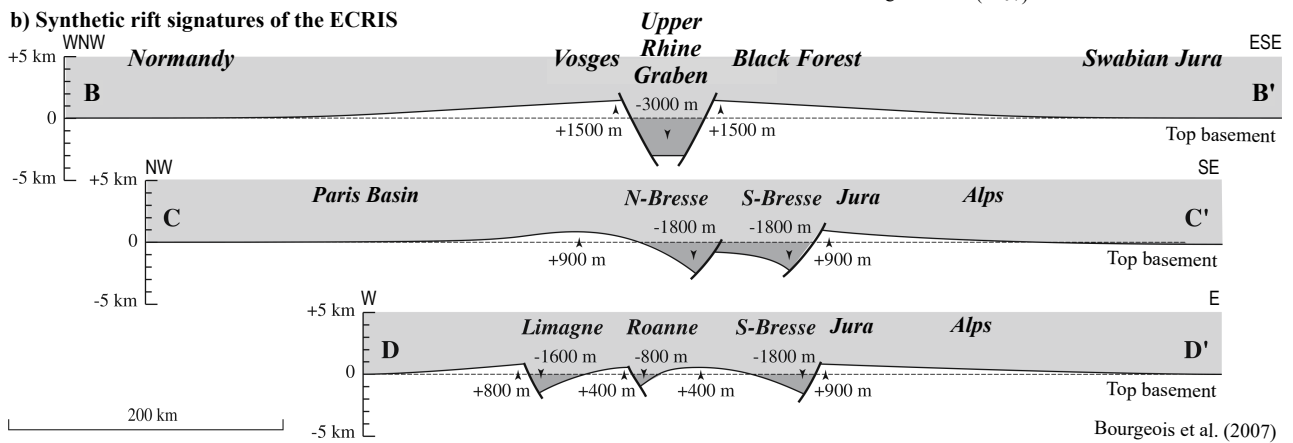
Flexural extension

As the lithosphere is bent down and loaded with an accretionary prism, the upper part of the lithosphere suffers extension whereas the lower part is compressed (Bradley and Kidd 1991). Extensional deformation therefore commonly leads to extensional fractures in the forebulge, whereas extensional faults with notable offsets are seen on seismic images across foredeeps (Bradley and Kidd 1991; Doglioni 1995; Granado et al. 2016; Lorenzo et al. 1998; Ranero et al. 2003; Sabbatino et al. 2020; Tavani et al. 2015). Extensional structures either form as new crustal features or also quite commonly, reactivate inherited faults (Bradley and Kidd 1991; DeCelles and Giles 1996). It appears that throws on extensional faults are relatively constant through the foredeep and remain inactive until they reach the orogenic front (Bradley and Kidd 1991). In the foreland of the Appalachian Mountains, the Mohawk foredeep for example is roughly 120 km long and extensional faults form only in the first 35 km behind the forebulge depozone (Bradley and Kidd 1991). Bradley and Kidd (1991) proposed a lithospheric model with toppled blocks, separated by normal faults that end in a common detachment level, supposedly at the brittle-ductile transition level between 15-20 km (Eastern N-America, see Fig. 2.15d). Therefore, the upper crust is typically stretched a few kilometres (Bradley and Kidd 1991) whereas compressional earthquakes at depth (> 15-20 km) predominate. As a consequence of the tilted domino-geometry model, normal faults are commonly verging to the foreland and only few hinterland verging (antithetic) normal faults occur (Fig. 2.14b, Fig. 2.15d). From seismic lines of oceanic trenches and collisional foredeeps on continental lithosphere, Bradley and Kidd (1991) estimated throws of up to 380 m in front of the orogen, whereas antithetic normal faults show rather smaller throws. Displacements on normal faults become significantly larger underneath the orogen, showing throws up to 1 km.

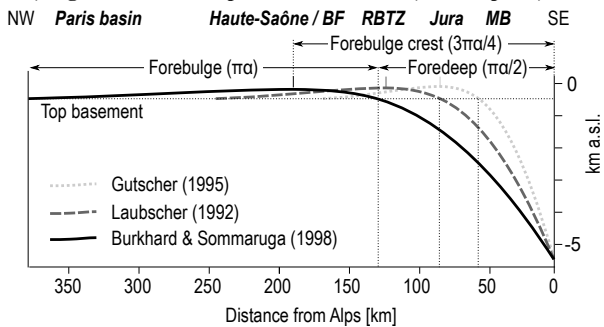
a) Signature of intraplate buckle folds in Western Europe



b) Synthetic rift signatures of the ECRIS



c) Signature of the Alpine flexural basin (broken plate)



d) Model of normal faults in response to flexural extension

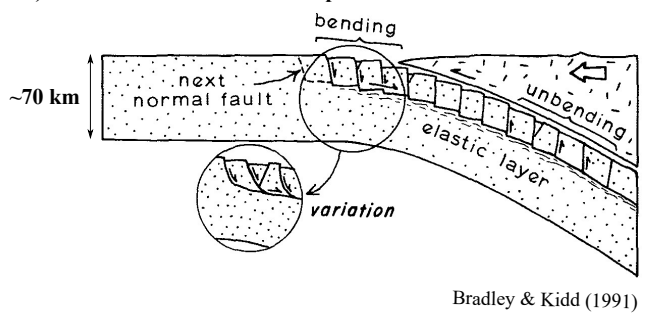


Fig. 2.15 – Lithospheric deformation signatures in the Northern Alpine Foreland. Traces of cross-sections are illustrated in Fig. 2.9. a) Intraplate buckling as present today and b) synthetic rift signatures in the URG and BG (Bourgeois et al. 2007). c) Signature of the Alpine flexural basin through the Jura and Switzerland, based on calculations in Burkhard and Sommaruga (1998) assuming a broken plate. Additional signatures are indicated derived from given forebulge crest-lines in Gutscher (1995) and Laubscher (1992). Curves are calculated using Eq. 6.1 on page 82 according to Turcotte and Schubert (2002). d) Generic model of flexural bending illustrating fault kinematics proposed by Bradley and Kidd (1991). BSJA: Burgundy-Swabian Jura Anticline, SFS: Sologne-Franconian Basin Syncline, NVA: Normandy-Vogelsberg Anticline, MB: Molasse Basin.

2.7 STRATIGRAPHY

The subdivision of stratigraphic units is based on lithostratigraphic groups according to the Western European stratigraphy, following classifications of borehole logs and seismic models (Gruber 2017; Landesgeologie 2017; Sommaruga et al. 2012) that are partially integrated subsequently. In Fig. 2.16, a representative stratigraphy for the Central Jura is illustrated. A correlation between the lithostratigraphic groups of Western Europe and the International chronostratigraphy is shown in Fig. 2.17. I am using older lithostratigraphic units for the Triassic and Jurassic periods in order to keep consistency with most publications and data available for the JFTB, which was collected since more than 100 years in France and Switzerland. The correlation of facies between the French and Swiss stratigraphy contains slight imprecisions (see specifications in Chapter 3.3.3), especially the limits between the Lower and Upper Malm group, as well as between the Lias and Dogger group. The Triassic series in the area of the Jura Mountains and surrounding shows Germanic Triassic facies, which was classically subdivided into siliciclastic rocks of the Buntsandstein Group, as well as marine limestones and mixed evaporite-carbonate deposits of the Muschelkalk and Keuper Groups. The Triassic stratigraphy was reworked recently for Switzerland (Jordan et al. 2016; Pietsch et al. 2016) and notably, the Lettenkohle unit was reallocated to the Asp-Member (Pietsch et al. 2016), therefore belonging to the Muschelkalk Group in Swiss stratigraphy today (Fig. 2.17), whereas it belonged to the Keuper Group previously. Note that the Lettenkohle unit is therefore attributed to the Keuper Group in Swiss studies and bore-logs before 2016 (e.g. Sommaruga 1997; Sommaruga et al. 2012). This study follows Pietsch et al. (2016).

The stratigraphy in Fig. 2.17 also indicates the French and Swiss codes, which are used in geological maps.

2.7.1 Basement, basal décollement and cover

Mechanically, the stratigraphy of the JFTB is subdivided into the detached cover (the hanging wall), the basal décollement zone that is up to several hundreds of metres thick and the mechanical basement (the footwall), see Fig. 2.16. The mechanical basement includes the pre-Mesozoic basement (composed of the crystalline basement and Permo-Carboniferous clastic sediments) as well as the Triassic sequence beneath the basal décollement of the JFTB (Fig. 2.16). Note that the basal décollement zone concentrates in Upper Triassic evaporites in the Central and Southern Jura, whereas it concentrates in Middle Triassic evaporites in the Eastern Jura (Laubscher 1961; Philippe et al. 1996). Therefore, depending on the location in the JFTB, the limits of the mechanical subdivision are slightly different, yet always within the Middle and/or Upper Triassic sequence.

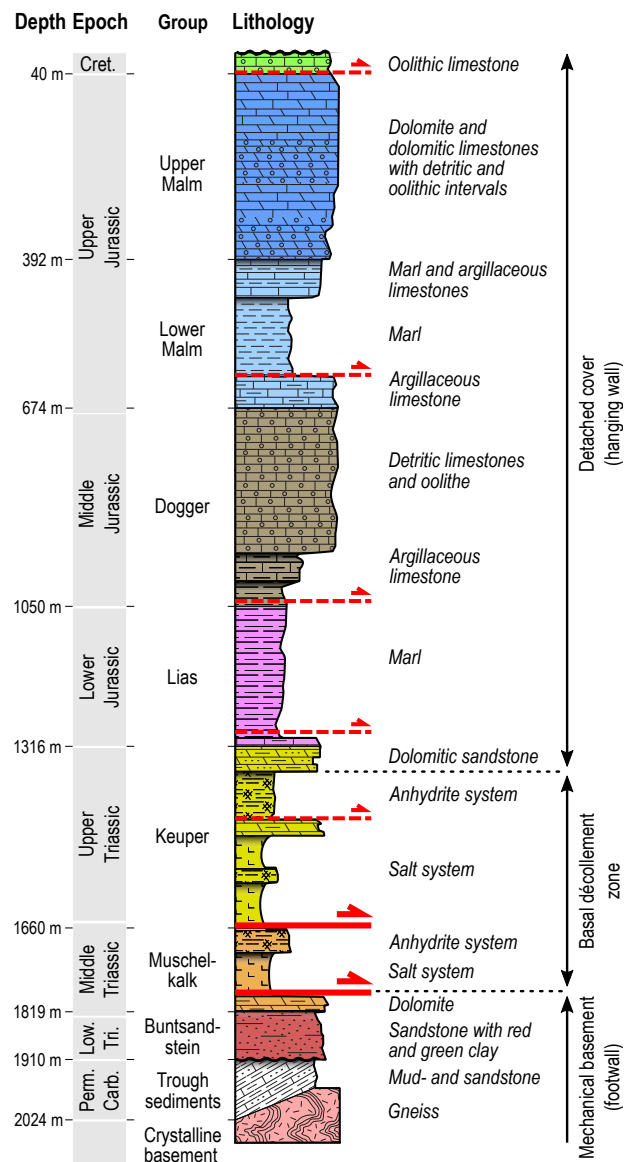


Fig. 2.16 – Representative stratigraphy of the Jura Mountains, based on borehole Essavilly-101 (Delmas 1965) lying in the central External Jura, Plateau de Nozeroy. Typical detachment horizons of the JFTB are indicated (dashed, red lines), which are hosted by incompetent clay, marl, sulphate and salt-bearing layers. The basal décollement in the Eastern Jura is predominantly in salt-bearing layers of the Muschelkalk Group, whereas the basal décollement of the Central and Southern Jura concentrates in salt-bearing layers of the Keuper Group.

2.7.2 Mesozoic sediments of the Jura

The Mesozoic sequence of the JFTB sets in with the Buntsandstein Group (Fig. 2.16), which is a sandstone that indicates a transgression. This is followed by the Muschelkalk and Keuper groups, which contain important sulphate and salt systems that hosted the basal décollement of the JFTB (Buxtorf 1907, 1916; Laubscher 1961, see Fig. 2.16). The Jurassic sequence contains different intervals of clay, marls, limestones and dolomites (Fig. 2.16). It starts with the clay-rich Lias Group, followed by the Dogger Group that commonly contains more limestones and during upper Jurassic, massive, commonly bright limestones (often micrites and dolomites) were deposited. The youngest Cretaceous deposits in the Jura are of Coniacian age (~90 to 86 Ma), belonging to the Narlay-

ICS 2020

ICS 2020			This study					Abb.	TQu / TCen		
Era	Period / Epoch	French litho-stratigraphy	Swiss litho-stratigraphy	Lithostratigraphic group	French code	Swiss code	Colour code				
~2.6 Ma	Cenozoic	Quaternary	Undifferentiated	Glacial, fluvial, lacustrine	Quaternary			#FFFFFF	Qu		
		Neogene	Pliocene	Hiatus						BQu	
			Miocene	Rift sediments (URG, BG)	OSM	Tertiary	e, g, m, p	m, o, e	#FFFFBE	Ter	
		Oligocene	OMM								
		Eocene	USM								
		Palaeocene	UMM								
			Siderolithic								
~23 Ma											
~34 Ma											
~56 Ma											
66 Ma											
100.5 Ma	Mesozoic	Cretaceous	Upper	Hiatus						BCen	
Lower			Crétacé	Narlay-Fm. to Goldberg-Fm.	Cretaceous	j _p , n, c	i _{8b} , c	#95FF5C	Cr		
Jurassic		Upper	Portlandien Kimméridgien Séquanien	Twannbach-Fm. to Vellerat-Mbr.	Upper Malm	j ₆₋₉	i ₆₋₈	#65A0FF	UMa	TMa	
			Rauracien Argovien Oxfordien	Günsberg-Fm. to Bärschwil-Fm.	Lower Malm	j ₅	i ₄₋₅	#A1D2FF	LMa	TLMa	
			Dogger Aalénien	Ifenthal-Fm. to Opalinus-Ton	Dogger	l ₉ , j ₁₋₄	a ₁ , i ₁₋₃	#AA9D7B	Do	TDo	
			Lower	Lias	Staffelegg-Fm.	Lias	l	l	#F290FF	Li	TLi
			Upper	Rhétien Keuper	Klettgau-Fm. Bänkerjoch-Fm.	Keuper	t ₆₋₇	t _{III} , r	#E0E000	Ke	TKe
Triassic		Middle	Lettenkohle	Schinznach-Fm. Zeglingen-Fm. Kaiseraugst-Fm.	Muschelkalk	t ₃₋₅ , 6a	t _{II}	#EEB055	Mk	TMk	
			Muschelkalk								
			Lower	Grès bigarrés / Buntsandstein	Dinkelberg-Fm.	Buntsandstein	t ₁₋₂	t _I	#D35C5C	Bss	TBss
~247 Ma											
~252 Ma		Palaeozoic	Permian Carboniferous	Hiatus							BMes
Permian Carboniferous				Permian Stephanian Westphalian	Wiesental-Fm. Weitenau-Fm. Weiach-Fm.	Permo-Carboniferous sediments	h, r	p	#FFFFFF	PC	
				Socle cristallin	Crystalline Variscan basement	Crystalline basement			#FFAAAA	Bas	TBas

Fig. 2.17 – Stratigraphic units used in this study. Ages are according to the International Chronostratigraphic Chart (Cohen et al. 2020). The French Cenozoic stratigraphy is based on Sissingh (1998), the Mesozoic and Palaeozoic stratigraphy reflects the lithologic divisions commonly used in French boreholes. The Cenozoic Swiss lithostratigraphy is according to Sommaruga et al. (2012). Mesozoic and Palaeozoic lithostratigraphy is according to the Swiss Committee on Stratigraphy (S.C.S. 2020), based on «Lithostratigraphie des Jura-gebirges, 2018» (www.strati.ch). Definitions of stratigraphic units in this study follow previous studies (Gruber 2017; Landesgeologie 2017; Sommaruga et al. 2012). French and Swiss lithologic codes used in geological maps (BRGM 2004; Swisstopo 2012), and their allocation in this study are indicated.

Formation (Strasser et al. 2016). Cretaceous deposits are widely eroded but are preserved in synclines, mostly in the Internal Jura. Across the Jurassic and Cretaceous series, incompetent clay and marl layers are known to host upper detachments (Caër et al. 2018; Malz et al. 2016; Noack 1995; Philippe et al. 1996; Rime 2017; Schori et al. 2015, see Fig. 2.16).

2.7.3 Cenozoic sedimentation

The French and Swiss Palaeogene and Neogene (Tertiary Group) lithostratigraphy in Fig. 2.17 reflect different tectonic domains, with French units reflecting rift deposits within the BG and URG and Swiss units showing the Molasse cycles of the NAFB. In the strict sense, Tertiary units cannot be separated by countries. However, the BG and the vast majority of the URG lies in France and Ger-

many, whereas the largest portion of the Molasse Basin in the study area belongs to Switzerland.

I added a detailed tectono-lithostratigraphy of Cenozoic sediments that correlates the different Cenozoic deposits of the MB, BG, URG and the External Alps with Alpine tectonic impulses (Fig. 2.18). The URG and BG reveal several rift impulses documented by accelerated sediment deposition and in the case of the BG, several longer hiatus (Fig. 2.18). I also added overview maps (Piquerez et al. 2012, Fig. 2.19) showing the Oligocene to Pliocene deposits in the Swiss Jura Mountains. Early UMM deposits of the Jura Molasse are rather in connection with rift sediments of the URG (Fig. 2.19a). Note that most outcrops of Jura Molasse lie on Swiss territory, whereas Palaeogene and Neogene sediments in the French Jura mostly occur NW of the first and highest chains or towards the front of the JFTB. The Palaeogene and Neogene map-view sketches

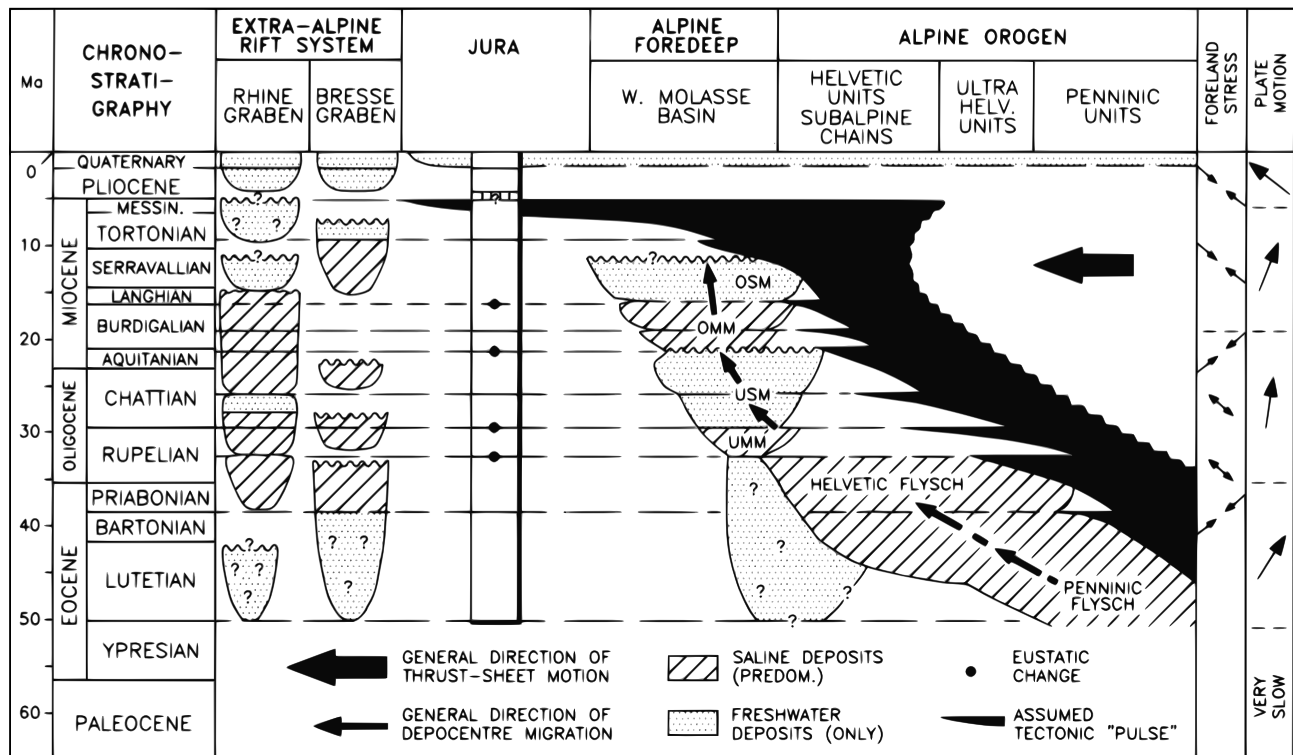
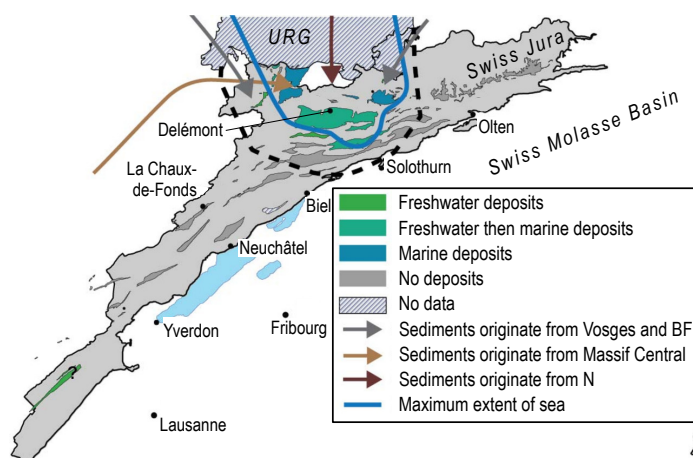


Fig. 2.18 – Cenozoic tectonostratigraphic diagram modified from Sissingh (1998), correlating Cenozoic deposits in the ECRIS, Molasse Basin and the Alps. Tectonic «pulses» are presumed to be responsible for changes in sedimentation.

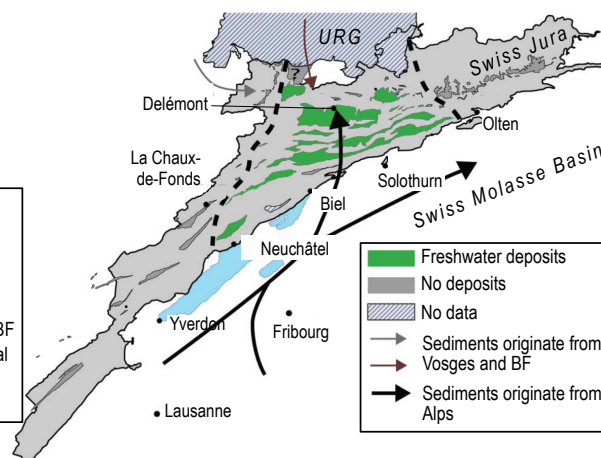
in Fig. 2.19 reveal some interesting structural developments of the JFTB, standing in a broad context with the development of the NAFB in Oligo-Miocene times. The first Cenozoic sediments in the Eastern Jura date to Middle to Late Priabonian (part of Late Eocene, Mojon et al. 2018). These sediments (mainly karst and fracture filling, Becker 2003) belong to the Siderolithic and constitute pre-Molasse deposits. Subsequently, Oligocene UMM deposits in the Delémont Basin and north of it occurred in a prolongation of the URG (Fig. 2.19a), with sediments transported from the Vosges, Black Forest and the Massif Central (Piquerez et al. 2012). The timing corresponds with the overall formation of the ECRIS during Eo-Oligocene (Dèzes et al. 2004; Sissingh 1998). The UMM of the Plateau Molasse was yet deposited far away from the JFTB, in front of the Alps (Piquerez et al. 2012). During Oligocene, the prolongation of the URG extended even further to the south (Fig. 2.19b) but progressively, USM deposition in the area of Delémont ceased and the connection to the URG was lost (Fig. 2.19c). By about 20 Ma, OMM deposits originating from the Alpine domain reached the south of the future Jura Mountains (Fig. 2.19d) and transgressed north-westwards subsequently. This is in a larger context with flexural subsidence of the NAFB, induced by the Alpine orogenic load flexing the European lithosphere (Burkhard and Sommaruga 1998; DeCelles and Giles 1996; Ford et al. 2006; Laubscher 1992; Sinclair et al. 1991). Note that the Ferrette Zone and the Internal Jura around Solothurn and Olten do not reveal Burdigalian deposits, indicating topographic highs at the time (Fig. 2.19d). The sketch in Fig. 2.19e shows absence of OSM deposits in the region of the first Jura chains, which indicates an early topography between 16 to 11.6 Ma. Sedimentation after about

11.6 Ma in the JFTB is poorly constrained and largely absent, which indicates that the JFTB was in a state of uplift (Becker 2000 and references therein). Only to the north of the JFTB, infill from the BF and the Vosges occur, as for example the Sundgau gravels deposited between 4.2 and 2.9 Ma (Petit et al. 1996), which provide evidence for late Pliocene to recent thick-skinned deformation (Madritsch et al. 2010; Ustaszewski and Schmid 2006).

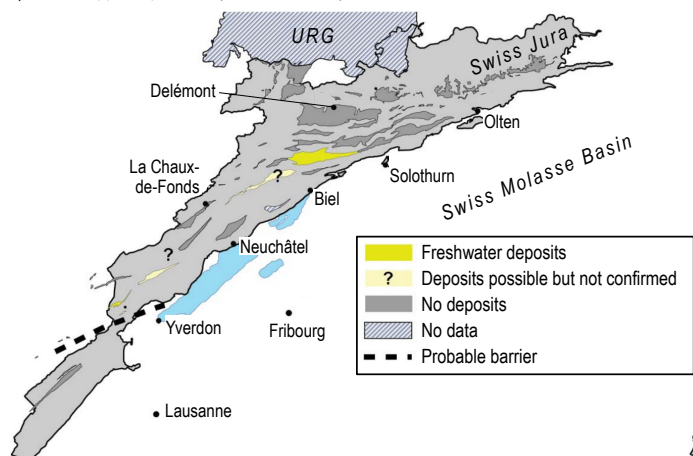
a) UMM, ~Rupelian (33.9 to 28.4 Ma)



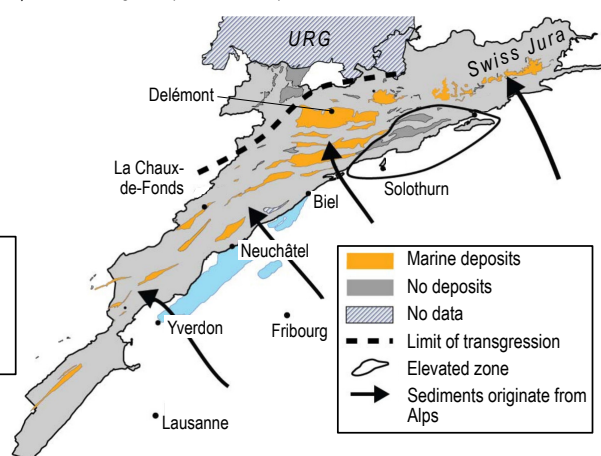
b) USM, ~Chattian to Lower Aquitanian (28.4 to 21.5 Ma)



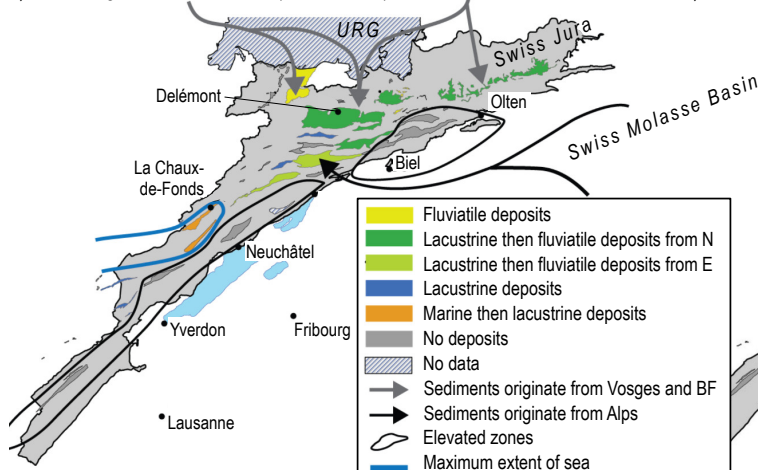
c) USM, ~Upper Aquitanian (21.5 to 20.4 Ma)



d) OMM, Burdigalian (20.4 to 16 Ma)



e) OSM, Langhian and Serravallian (16 to 11.6 Ma)



f) Tortonian to Pliocene (11.6 to 2.6 Ma)

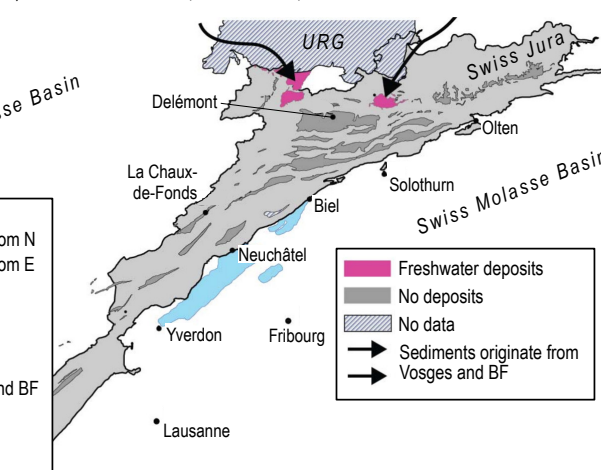


Fig. 2.19 – Source areas and age of Tertiary sediments within the Swiss Jura (comprising the Internal and Tabular Jura on Swiss territory) modified from Piquerez et al. (2012). a) The oldest Oligocene sediments occur in the wider area of Delémont and originate from the Massif Central, the Vosges and the Black Forest. b) During Chattian and Lower Aquitanian, sediments are deposited in a prolongation of the Rhine Graben and deposits originating from the Alps occur for the first time. c) Only few deposits with an Upper Aquitanian age are documented. d) The «Molasse sea» reaches the Jura Mountains in Burdigalian times, with sediments originating from the Alps. e) OSM deposits in the Jura Mountains are complex, mostly containing fluvialite or lacustrine sediments. f) The deposition of Molasse ceases at the end of Tortonian but some younger freshwater deposits originating from the Vosges and BF are documented north of Delémont. BF: Black Forest Massif, URG: Upper Rhine Graben.

3 - BOREHOLE INVENTORY

3.1 AIM OF INVENTORY

At the beginning of this study, I had limited access to borehole documentations. In 2016, the French Office of Exploration and Production of Hydrocarbons (BEPH) provided a fee-based database that was later replaced by the online « Banque de sous sol », a free borehole database of France, provided by the geological service of France BRGM (Bureau Recherche Géologiques et Minières, <http://infoterre.brgm.fr>). Deep wells from Switzerland can be found in the archives of the corresponding cantons, which are partially online. In addition, wells are recapitulated in recent seismic studies, such as in the SMB 3D modelling studies of Gruber (2017), Landesgeologie (2017) and Sommaruga et al. (2012). Also, the Swiss Federal Office for Topography (swisstopo) provides access to data from deep wells through the map layer « Wells deeper than 500 m » on <https://map.geo.admin.ch>. Most deep wells of eastern Switzerland can be found in reports of the National Cooperative for the Disposal of Radioactive Waste (Nagra). In summary, there is a wealth of excellent sources that are freely available today.

Since boreholes in the JFTB and surroundings were drilled for more than 100 years across two countries, different terminologies were applied. I harmonised the data using the stratigraphy presented in Fig. 2.17, in order to create a digital borehole database dockable to a Geographic Information System (GIS). The borehole database serves as a basis for further applications in this study, in particular the creation of elevation and thickness models. A PDF document is also provided with Supplementary Material C, where comments and notes to boreholes can be scrutinised. A complete list of boreholes included in the borehole database is available in the Appendix A.1 and locations of boreholes are indicated in the overview map of Fig. 3.1.

The subsequent documentation of the borehole database focuses on the technical setup and the assignment of lithostratigraphic groups. It is not the aim of this study to make a new facies correlation in the study area. The borehole inventory rather unifies the various terminologies and documents mechanically weak layers in the JFTB. The

definition of lithostratigraphic groups is based on common divisions in bore-logs. Lithological descriptions are only checked in more detail when limits of geological units are undefined in bore-logs.

3.2 HISTORICAL BACKGROUND

Subsurface knowledge and geophysical studies in the Jura Mountains were mainly acquired by oil companies in the 20th century, up to the late 80ies. The External Jura is the most intensely explored part of the JFTB where the French oil industry acquired numerous seismic lines and exploratory wells, mainly between 1960 to 1980. The exploration fields around Lons-le-Saunier (in the Faisceau lédonien) shows the highest concentration of boreholes and the precursory studies of Lienhardt (1962) and Michel et al. (1953) gave important clues on the contact zone between the Jura Mountains and the Eo-Oligocene Bresse Graben. Note that many drilling locations were chosen to penetrate anticlines since oil traps were targeted. Therefore, depth maps deduced from boreholes tend to underestimate the regional depth of Mesozoic horizons.

The first gas fields in the French Jura were discovered in 1906 and intensified investigations followed in the 50ies lasting up to the 80ies. Gas was for example extracted in Ambérieu (1906 to 1941, see Heritier 1994), Vaux-en-Bugey (1922 to 1959, see Philippe 1994) and Revigny (1942, 1946–1958), oil in Briod (1954), Lons-le-Saunier (1957, Michel et al. 1953) and Valempoulières (1961, Heritier 1994). However, most occurrences of hydrocarbons were rather disappointing with only little exploitable gas or oil. Typical targeted horizons lay in the Triassic sediments, such as the Buntsandstein Group, Lettenkohle or Rhetian beds. Exploration was rather restricted to the External Jura, probably due to very practical reasons such as less complex deformation favouring the quality of seismic lines, easier accessibility and certainly also due to a regional erosion of the Mesozoic series which facilitates the access to the targeted Triassic units.

In comparison to the French Jura, the Swiss Jura has

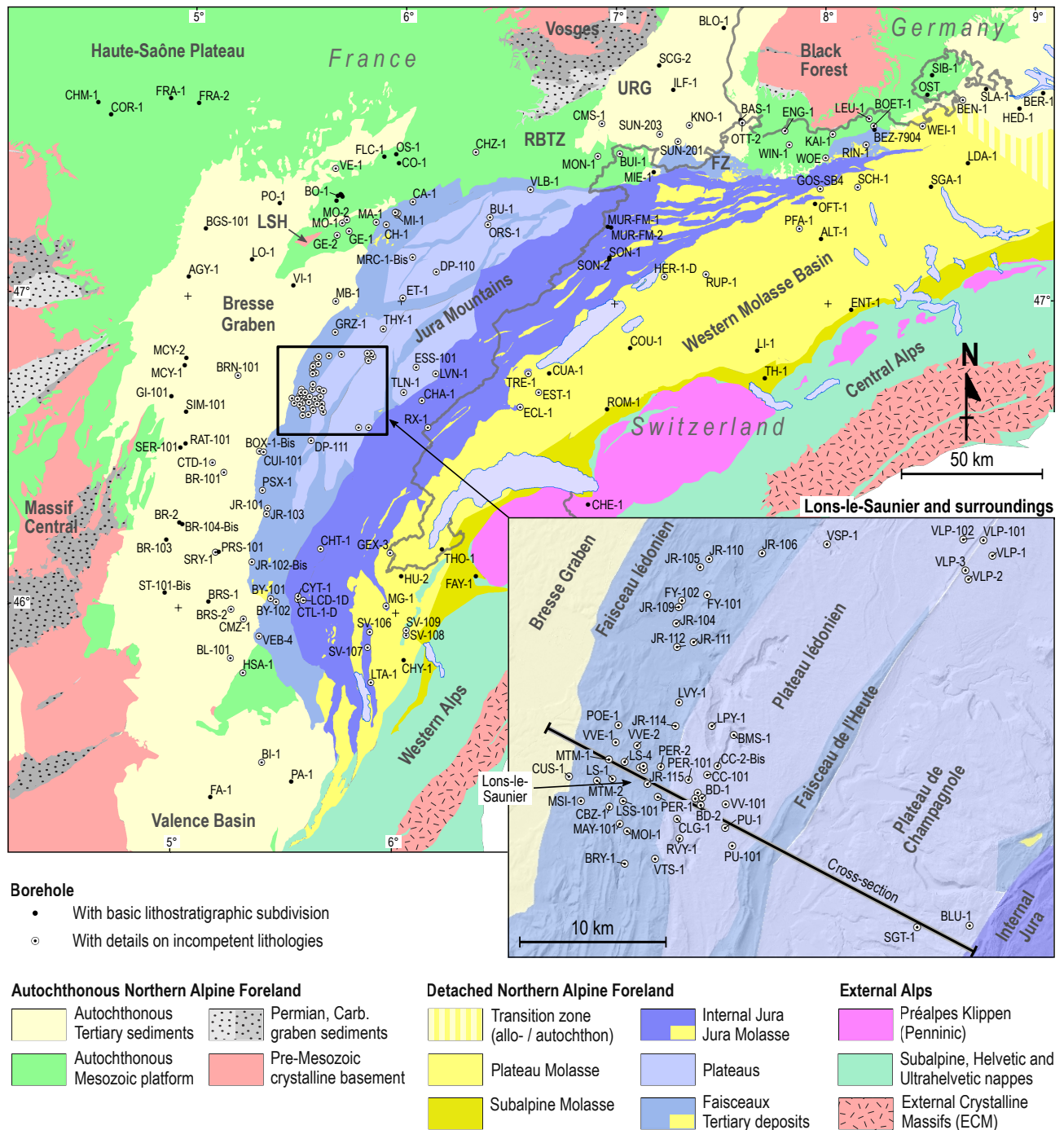


Fig. 3.1 – Locations of boreholes in the data inventory of this study. Detailed descriptions for all boreholes are provided in Supplementary Material C. The list of boreholes is furthermore given in the Appendix A.1, where abbreviations are attributed to full names. The cross-section trace shows the position of Fig. 3.2b. BG: Bresse Graben, FZ: Ferrette Zone, LSH: La Serre Horst, RBTZ: Rhine–Bresse Transfer Zone, URG: Upper Rhine Graben.

been considerably less explored by the oil industry. The borehole at Risoux (RX-1, 1960-1961, Winnock 1961) was the only deep well (> 500 m) drilled in the Swiss Jura proper and did not even penetrate into Triassic rocks but instead, a repetition of roughly 1230 m of the Upper and Middle Jurassic series was observed along the borehole. Only 5 more deep boreholes have been drilled in the Internal Jura west of Risoux, in France. In comparison to that, more than 80 deep wells were drilled in the External Jura that reached Triassic or pre-Mesozoic rocks. There are seismic studies in the central Internal Jura (Guellec et al. 1990; Sommaruga 1997) that are based on seis-

mic lines from the oil industry. In the Eastern Jura, Nagra accomplishes exhaustive geophysical studies since more than 30 years (see Nagra reports on www.nagra.ch).

3.3 METHODS, LOGGING AND DEFINITIONS

3.3.1 General

Boreholes are compiled in a file-based relational database (Microsoft Access Database, see borehole list in Ap-

pendix A.1). Geographical coordinates are transformed from national coordinate systems (French boreholes commonly use France II, EPSG: 27582, Swiss boreholes are in CH1903, EPSG: 21781) into the World Geodetic System WGS 84 (EPSG: 4326). Coordinate transformations are done using the open-source library «pyproj» of the Python 2.7 programming language (<http://www.python.org>). Lithostratigraphic groups are defined according to the stratigraphy in Fig. 2.17. Another Python 2.7 based script suite provides automated exports of the database content to a PDF-file, including graphical representations for each borehole. Individual tables of the Microsoft Access Database can be linked to a GIS. A complete documentation of boreholes in the database is provided in Supplementary Material C. The database contains more than 200 boreholes for which coordinates are reviewed, lithostratigraphic groups attributed and depth as well as elevation of horizons defined.

In the JFTB and close surrounding, I furthermore digitised the occurrence of incompetent lithologies (clay, marl, evaporite) as well as bedding dips and deviation charts if available. Subdivisions are made for the salt and anhydrite systems of the Keuper and Muschelkalk Groups, in order to have a clue on possible stratigraphic levels of the basal décollement (the basal décollement is usually not indicated in bore-logs). Documented faults are digitised and thrusts distinguished from normal faults, if indicated in bore-logs. I added suspected thrusts or detachments in bore-logs of this study, if breccias or «tectonised» zones are documented in lithological descriptions of boreholes. Suspected faults are denoted accordingly (see detailed logs in Supplementary Material C). True vertical depths are calculated if deviation charts are available but deviations smaller than 3° are considered negligible for the purpose of this study and therefore, they are omitted (at a deviation of 3° and a drilling distance of 1 km, the true vertical depth is reduced a mere 1.4 m).

3.3.2 Thickness used for isopach maps

The Microsoft Access based borehole database contains a parameter for each geological unit, which is called «Undisturbed Depositional Thickness» (UDT). This parameter is checked (value is true), when the thickness of a given lithostratigraphic group is evaluated to be representative for the true vertical thickness. The unit has to fulfil following conditions: i) tectonic disturbances are absent, i.e. no evident duplications or normal faulting are documented, ii) the top and bottom of a Mesozoic unit are conformable contacts. Note that a non-conformable top, covered by Tertiary sediments is allowed as well as the non-conformable contact at the base of the Buntsandstein Group. The Tertiary unit is excluded from this unconformity. iii) The bedding of the geological unit is generally not significantly inclined (average bedding less than about 10°).

Graphical exports of boreholes indicate the checked UDT-flag with an asterisk (*) next to the thickness value of the corresponding unit (see boreholes in Fig. 3.2). Note that isopach models in Chapter 4 only include thickness values of boreholes if the UDT-flag is checked in the borehole database for the corresponding lithostratigraphic

group.

3.3.3 Ambiguous limits of lithostratigraphic groups

Commonly, limits of lithostratigraphic groups are attributed according to the stratigraphy in Fig. 2.17 and a brief lithologic characterisation for these limits is given in Table 3.1. Occasionally, limits of lithostratigraphic groups cannot be unambiguously derived with given subdivisions in bore-logs. Subsequently, I specify ambiguous limits that require additional definitions.

Top Lower Malm Group (TLMa)

The Sequanian series, which is an outdated terminology formerly used in Swiss and French bore-logs, comprises the Upper Oxfordian and the beginning of the Kimmeridgian stages. The TLMa is set at the base of the Sequanian series. In French bore-logs, the Oxfordian stage is occasionally subdivided into an upper calcareous and a lower argillaceous interval and TLMa is then set at the limit between these two lithologies. If the Oxfordian stage was not subdivided, TLMa is defined where argillaceous limestones and clay or alternatively, pyrite-bearing limestones set in. If distinguished, the top of the «Rauracian» unit is used as TLMa limit.

Top Lias Group (TLi)

The Aalenian-Toarcian boundary is not defined in all bore-logs, as for example in Thésy-1 (THY-1), all Valem-poulières wells, Bois-des-Chaux-1bis (BOX-1-Bis) and Cuiseaux-101 (CUI-101). In the latter two, the boundary is set using the rather distinct «schistes cartons», which is a black or grey, slaty clay belonging to the Lias Group. Also belonging to the Lias Group is an interval of grey and black clay present above the «schistes cartons». The end of the Dogger Group is frequently marked by a sandy limestone («calcaire gréseux») followed by clay and argillaceous limestones. However, at La Chandelière-1d, the sandy limestone is allocated to the Upper Toarcian according to the bore-log (ESSO REP 1989), which lies directly above the «schistes cartons». In contrast to that, at Châtelblanc-1, Montbouton-1 and Knoeringue-1, the Upper Toarcian boundary is set directly above the «schistes cartons» in bore-logs. Note, the argillaceous Aalenian series are also attributed to the Lias Group (see Ornans-1, Delmas and Iriarte 1965). Note that the Opalinus-Ton mainly belongs to the Lower Aalenian but already starts in the Upper Toarcian stage with the «Pleydellienbank» (Wetzel et al. 2003), belonging to the Aalensis zone of the Toarcian stage proper.

Top Muschelkalk Group (TMk)

The Lettenkohle constitutes the top of the Muschelkalk Group in this study (Fig. 2.17). The Lettenkohle are sandy, coal bearing layers, which are distinguished in French boreholes as separate interval, between Keuper and Muschelkalk. In Swiss stratigraphy, the Lettenkohle is

Table 3.1 – Limits of lithostratigraphic groups assigned in the borehole inventory. Their position in the stratigraphy is indicated in Fig. 2.17.

Abb.	Full name	Common lithological attributes
TQu	Top Quaternary	Unconsolidated sediments, always top of well
BQu	Base Quaternary (i.e. top Tertiary)	Can coincide with BCen
TCen	Top Cenozoic	Siliceous sediments, often top of well
BCen	Base Cenozoic (= top Mesozoic)	Boundary between silicates / carbonates
TMa	Top Malm Group (= top Jurassic)	Boundary clay / micritic limestones
TLMa	Top Lower Malm Group	Boundary limestones / marls
TDo	Top Dogger Group	Boundary micritic / detritic limestone
TLi	Top Lias Group	Boundary clay / marl
TKe	Top Keuper Group	Boundary limestone (calcite) / clay, marl, dolomite
TMk	Top Muschelkalk Group	Boundary evaporites, clay / dolomite
TBss	Top Buntsandstein Group	Boundary marl / sandstone
BMes	Base Mesozoic	Boundary sandstone / red sandstone
NBMes	Near Base Mesozoic	Used when BMes is estimated
TBas	Top Basement (crystalline basement)	Boundary sediments / crystalline rocks
<i>Subdivisions of the Keuper and Muschelkalk Group</i>		
TKeEv	Top Keuper Group evaporites (i.e. sulphate system)	Boundary carbonates / sulphate system
BKeEv	Base Keuper Group evaporites (i.e. sulphate system)	Boundary sulphate system / carbonates
TKeSa	Top Keuper Group salt system	Set in of salt system, can contain sulphates
BKeSa	Base Keuper Group salt system	End of salt occurrence
TMkEv	Top Muschelkalk Group evaporites (i.e. sulphate system)	Boundary carbonates / sulphate system
BMkEv	Base Muschelkalk Group evaporites (i.e. sulphate system)	Boundary sulphate system / carbonates
TMkSa	Top Muschelkalk Group salt system	Set in of salt system, can contain sulphates
BMkSa	Base Muschelkalk Group salt system	End of salt occurrence

at the top of the Schinznach-Formation in the Asp-Member (Pietsch et al. 2016). As the Lettenkohle interval was previously attributed to the Keuper Group, the limit between the Muschelkalk and Keuper Groups of this study slightly deviates from previous Swiss studies, such as Sommaruga (1997), Sommaruga et al. (2012) and Thury and Amman (1990) and Nagra reports before 2016.

There are several wells in the Valence basin and BG where the Triassic series is not subdivided. The TMk is defined at the top of the first dolomite layer in the Valence Basin and at the top of the second dolomite layer (underneath salts) in the BG.

Buntsandstein Group (Bss)

The Buntsandstein Group (Bss) corresponds to the Dinkelberg-Formation in Swiss stratigraphy and to the «Grès bigarrés» in French terminology (Fig. 2.17). It constitutes a sandstone interval at the base of the Triassic sequence. The Dinkelberg-Formation encompasses siliciclastic, mainly fluvial to coastal marine sediments, corresponding to the combined Rötton-Fm., Plattensandstein-Fm. and Vogesensandstein-Fm. of southern Germany (Jordan et al. 2016). In the Jura Mountains, the Buntsandstein Group is often a white, grey and green more or less coarse sandstone with intercalation of red, sandy clay and conglomerates can occur (see example in the borehole Laveron-1, PREPA 1960). In the URG at Montbouton-1 (Ramaut 1958), the Buntsandstein Group starts with red argillaceous marls and an argillaceous sandstone with mica, followed by a coarse pink sandstone and red clay. At

the base, a red, clay-rich conglomerate with quartz grains is documented.

In the eastern SMB, the sand interval at the base of the Triassic sequence is called «Basissand». In this study, the «Basissand» is allocated to the Buntsandstein Group following Heidbach and Reinecker (2013). The list in Table 3.2 denotes boreholes containing sandstone intervals at the base of the Triassic sequence that are similar to the description above and allocated to the Buntsandstein Group in this study. However, these intervals are not explicitly assigned to the Buntsandstein Group in original borehole descriptions.

3.3.4 Triassic evaporites

Triassic sulphate and salt systems are allocated to separate containers in the database, which are «Muschelkalk Group salt», «Muschelkalk Group sulphates», «Keuper Group salt» and «Keuper Group sulphates». Sulphates that occur in the Lettenkohle are not added to the «Muschelkalk Group sulphates» container. The thickness of the Lettenkohle interval is commonly a few metres, but reaches up to about 40 m in some boreholes. Salt systems are allocated to «Muschelkalk Group salt» or «Keuper Group salt», even in the presence of sulphates. The same goes for sulphate intervals containing dissolved salt (e.g. Briod-2, Courbouzon-1, Domblans-1, Gendrey-1, Lons-1 to Lons-4, Moiron-1, Montmorot-1, Otterbach-2, Perry-1, Vernantais-1). Sulphate and salt systems commonly contain various amounts of clay or intercalations of clay and limestone. Subsequently, I briefly describe typical terms

Table 3.2 – Examples of boreholes, where sandstones at the base of the Triassic series are not explicitly designated as Buntsandstein or « grès bigarrés » in bore-logs, but allocated to the Buntsandstein Group in the borehole inventory of this study (see Supplementary Material C).

Borehole	Country	Interval description	Reference
Argilly-1	FR	White sandstone	Ramaut and Warthmann (1957)
Berlingen-1	CH	«Basissand»	Büchi et al. (1965)
Bizonnes-1	FR	Brown, sandy dolomite	SPV (1958)
Bresse-104bis	FR	Sst and conglomerates	Caillon and Michel (1955)
Bresse-2	FR	Grey-green sst with feldspar	Bugnicourt and Michel (1953)
Chapéry-1	FR	Grey and orange sandstone	Sadoux (1970)
Chazelot-1	FR	Vosges sandstone	Fournier (1922)
Faucigny-1	FR	« Trias gréseux »	ESSO REP (1970)
Gigny-101	FR	Grey, greenish sandstone	Marti (1963)
Herdern-1	CH	«Basissand»	Heidbach and Reinecker (2013)
Humilly-2	FR	Green greywacke	Marti (1969)
Lindau-1	CH	«Basissand»	Büchi et al. (1965)
Meersburg-1	DE	«Basissand»	Heidbach and Reinecker (2013)
Montoisson-1	FR	Sst, local conglomerates	Pochitaloff (1963)
Paladru-1	FR	Green sandstone	SPV (1959)
Pfaffnau-1	CH	«Basissand»	Büchi et al. (1965)
Simandre-101	FR	Grey, coarse sandstone	Carrel (1969)

and the rough appearance of these evaporite systems.

Keuper Group sulphates (TKeEv - BKeEv)

Keuper anhydrite systems normally lie within the upper Keuper Group and are often covered with a clay series. Anhydrite occurs together with colourful clay or marl (« marne bariolée » or « argile bariolée » in French bore-logs). A thin dolomite bank sometimes separates red marls from colourful marls (e.g. Bornay-1, Lienhardt 1962). Polyhalite ($K_2Ca_2Mg[SO_4]_4 \cdot H_2O$) sometimes occurs within the Keuper sulphate zone. The Gipskeuper of Swiss boreholes (e.g. Riniken-1, Nagra 1990) is attributed to the «Keuper sulphates» container. Several sulphate systems can occur within the Keuper Group, though commonly one sulphate system is deposited on top of an older salt system.

Keuper Group salt (TKeSa - BKeSa)

The Keuper salt system typically contains pinkish salt, colourful clay (« marne bariolée »), anhydrite and gypsum. The clay can contain grey-green colours. Nodules with polyhalite can occur. The salt sometimes shows yellow stains (e.g. Bois de Chaux-1). Several hundreds of metres thick salt intervals are indicative for tectonically induced thickening along the basal décollement (Sommaruga et al. 2017). Note that salt breccias are distinguished in some boreholes, as for example Briod-104 (BRGM 1955) and Bornay-1 (Lienhardt 1962). They might be sedimentary and/or diagenetic in nature and without further description, salt breccias cannot implicitly be attributed to décollement tectonics. Keuper Group salt is absent in the RBTZ, URG, Eastern Jura and the SMB east of the borehole Courtion-1 and therefore, no German terminology exists.

Muschelkalk Group sulphates (TMkEv - BMkEv)

Muschelkalk Group sulphates contain anhydrite and gypsum mixed with clay. The « couches grises » and « couches rouges » in Lienhardt (1962) refer to intervals containing Muschelkalk sulphates. The « obere Sulfatschichten » and « untere Sulfatschichten » of Swiss boreholes are both encompassed in the «Muschelkalk sulphates» container. However, the «Sulfatschichten» do not encompass all sulphate systems of the Muschelkalk Group and in this study, all sulphate bearing layers are attributed to the Muschelkalk Group sulphates (e.g. Riniken-1 Nagra 1990, Böttstein-1 Peters et al. 1986).

Muschelkalk Group salt (TMkSa - BMkSa)

The rock salt of the Muschelkalk Group is typically white or pink. Anhydrite and intercalations of grey and green clay layers can occur (e.g. Laveron-1, PREPA 1960). Muschelkalk Group salt is absent in western Switzerland and in the south-western JFTB. In the eastern SMB, the salt system separates the « obere Sulfatschichten » and « untere Sulfatschichten » (e.g. Riniken-1).

3.4 BOREHOLE OVERVIEW

A complete overview of boreholes that I integrated in the database is compiled in Supplementary Material C (see borehole list in Appendix A.1 on page 164). The overview map of digitised boreholes is given in Fig. 3.1. Incompetent lithologies are described for boreholes within the JFTB and in the near surrounding, whereas boreholes in the MB, BG or URG generally only show lithostratigraphic groups (Fig. 3.1). In order to illustrate the borehole inventory in a broader context, I created isopach models of the study area, which additionally include structural inform-

ation and additional constraint points of previous studies (see descriptions in Chapter 4).

3.5 BOREHOLE BASED SECTION ACROSS LONS-LE-SAUNIER, EXTERNAL JURA

In the area of Lons-le-Saunier, which lies in the structural domain of the Faisceau lédonien (Fig. 3.1), the basement is relatively high and the pre-Mesozoic basement was partially reached after a depth of 450 m (Fig. 3.2). The French oil industry drilled many exploratory wells in this area and the dense network allows to prospect the deep geology quite well (Lienhardt 1962; Michel et al. 1953). As for example, along a NW–SE striking section trace across the External Jura (see trace in Fig. 3.1), altitude differences of the mechanical, pre-Mesozoic and crystalline basement can be associated with three tectonic fault generations (Fig. 3.2b). This includes Palaeozoic normal faults, which only affect the crystalline basement. This first set of faults is rather hypothetical, as smaller altitude differences of the crystalline basement may alternatively be attributed to an uneven erosive surface (palaeotopography). A second generation of faults are Eo-Oligocene normal faults in connection with the formation of the Bresse Graben, which affect both the detached Mesozoic cover and the mechanical basement. These normal faults are cut off by a third generation of faults, which are Mio-Pliocene thrusts and the basal décollement that are restricted to the cover. The reconstruction in Fig. 3.2b illustrates that throws of Eo-Oligocene faults are in the range of about 50 to 200 m along the trace in the External Jura whereas towards the front of the JFTB, the Bresse Graben border faults show notably higher throws (up to several kilometres, see Blanc et al. 1991; Guellec et al. 1990; Michel et al. 1953).

The residual Bouguer gravity curve (see gravity model in Fig. B.1) shows a positive anomaly with a peak in the Faisceau lédonien (Fig. 3.2b). The Bouguer anomaly correlates roughly with the top of the crystalline basement (Fig. 3.2).

3.6 DIFFERENTIAL SUBSIDENCE IN THE BRESSE GRABEN

3.6.1 Structural context

In the Bresse Graben, the two boreholes Bresse-104bis (BR-104-Bis) and Bresse-2 (BR-2, see Fig. 3.1) are only 1.1 km apart and both boreholes were drilled into the pre-Mesozoic basement. Despite the proximity of these boreholes, the thickness of lithological units varies considerably. A seismic study of the area, conducted by the Régie Autonome des Pétroles (RAP) for the borehole BR-2 (Bugnicourt and Michel 1953), reveals a NNE–SSW striking fault in between the two boreholes, explaining the thickness variations. BR-104-Bis is situated on a horst called Limonest Sill (Fig. 3.3). This unique borehole setting doc-

uments differential subsidence movements along the fault during Mesozoic and Cenozoic times.

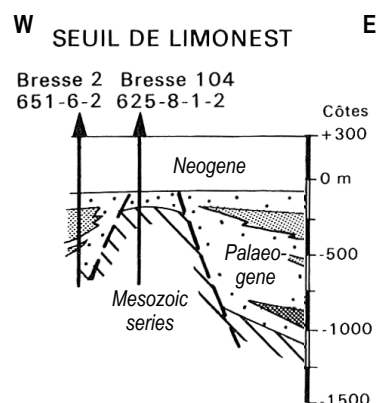


Fig. 3.3 – Sketch of the Limonest Sill according to Debrand-Passard et al. (1984).

3.6.2 Methodology

The borehole logs that are displayed in Fig. 3.4 are based on Bugnicourt and Michel (1953) and Caillon and Michel (1955). The thickness of units in Bresse-2 are depth-corrected according to the deviation chart given in Bugnicourt and Michel (1953). The stratigraphy of Bresse-104bis is assembled from the deviation corrected log of Bresse-104 (Malm and Dogger Group) and the log of Bresse-104bis (Caillon and Michel 1955), which constitutes the prolongation of Bresse-104 after a drilling incident. The subsidence rate for each lithostratigraphic group is calculated using an estimated timespan of deposition (Table 3.3) and the thickness of groups documented in the borehole logs of Bugnicourt and Michel (1953) and Caillon and Michel (1955).

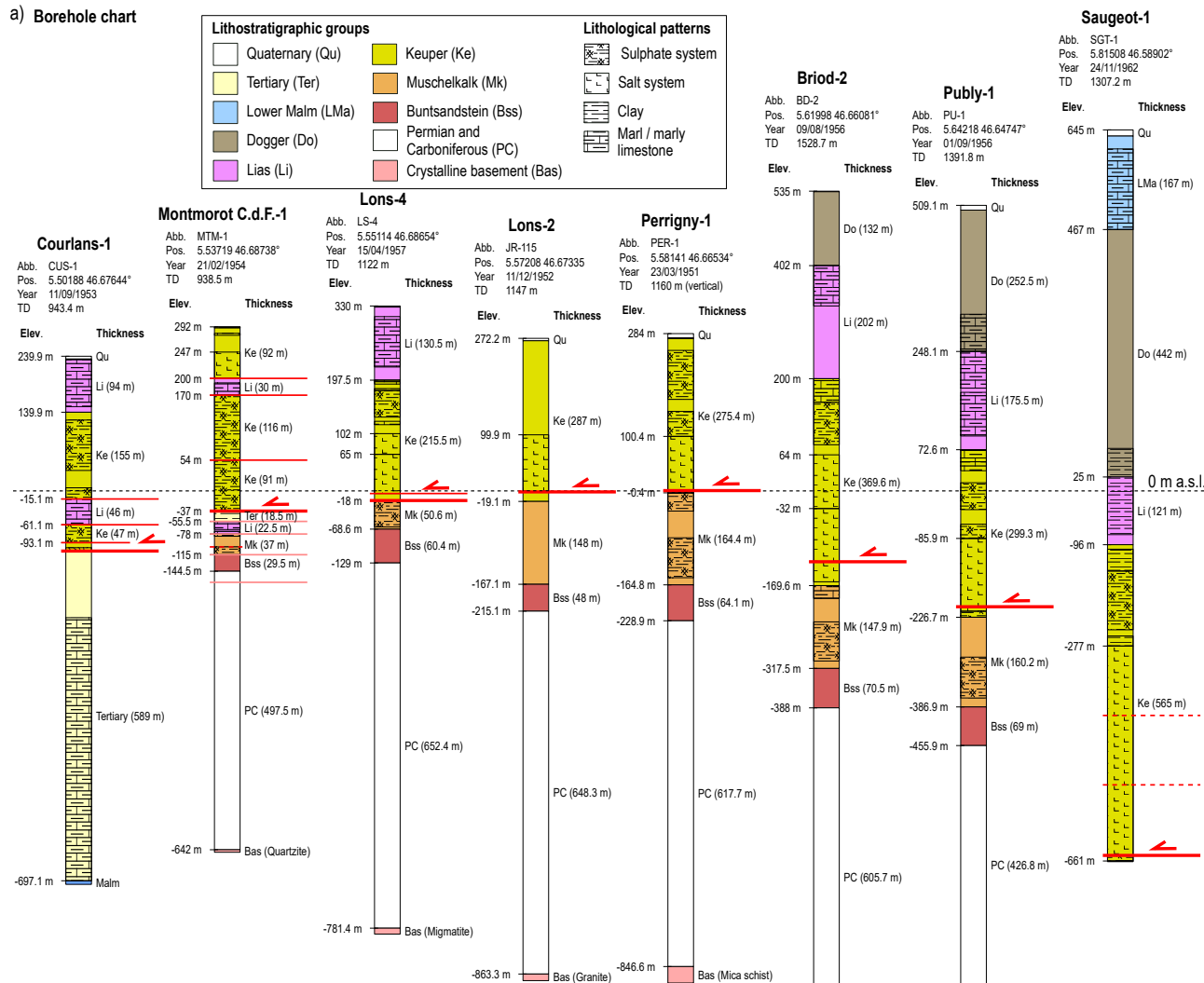
Table 3.3 – List of estimated timespan of deposition for lithostratigraphic groups. Absolute ages are according to Cohen et al. (2020), see Fig. C. Δ : timespan

Unit	Series / Stage	From [Ma]	To [Ma]	Δ [Myr]
Bss	Lower Triassic	252	247	5
Mk	Middle Triassic	247	237	10
Ke	Upper Triassic	237	201	36
Li	Lower Jurassic	201	174	27
Do	Middle Jurassic	174	164	10
LMa	Oxfordian	164	157.3	6.7
UMa	Kimmeridgian, Tithonian	157.3	145	12.3
Cr	Lower Cretaceous	145	100.5	44.5
Ter	Oligo-Pliocene	34	2.6	31.4

3.6.3 Observations

The comparison between the boreholes Bresse-2 and Bresse-104-Bis (Fig. 3.4a to i) shows an overall slow absolute subsidence during Triassic and Lower Jurassic times, with subsidence rates between 1.5 to 7.7 m/Ma (Fig. 3.4a to d). Notably fast subsidence occurs in Middle Jurassic, with subsidence rates of about 19.2 m/Ma in Bresse-2

a) Borehole chart



b) Cross-section

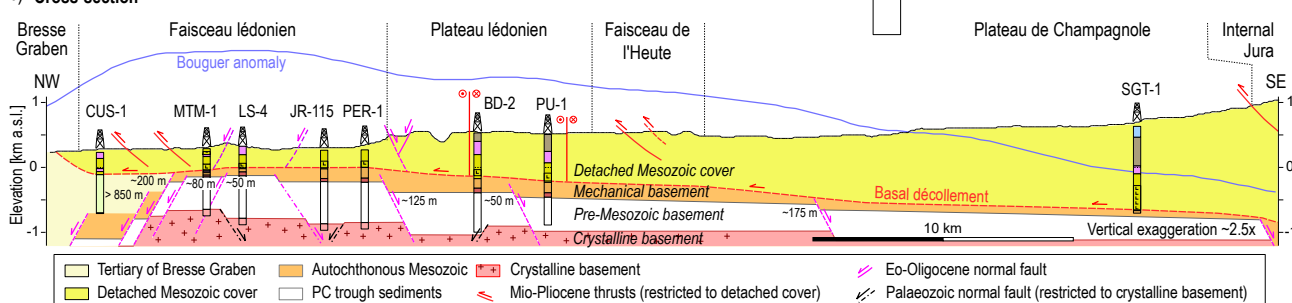


Fig. 3.2 – Borehole overview along a cross-section in the area of Lons-le-Saunier (the cross-section trace is shown in Fig. 3.1). a) Borehole chart illustrating the décollement zone in the Keuper Group and duplication along thrusts in Courlans-1 and Montmorot C.d.F.-1. b) Cross-section illustrating steps in the crystalline, pre-Mesozoic and mechanical basement, interpreted from boreholes. Fault-throws of the top of the Pre-Mesozoic basement are indicated next to normal faults. The Bouguer gravity anomaly (extracted from the gravity model in App. B.1) seems to correlate with structures in the crystalline basement. Three generations of faults are distinguished, which are normal faults restricted to the crystalline basement, normal faults that are presumably in connection with the Eo-Oligocene formation of the Bresse Graben and finally, Mio-Pliocene thrusts.

and 32.5 m/Ma in Bresse-104-Bis (Fig. 3.4e). Fast subsidence rates prevail during Upper Jurassic (Fig. 3.4j, g). Sedimentation is drastically decreased in Lower Cretaceous in Bresse-2, and no Cretaceous deposits occur at all in Bresse-104-Bis in (Fig. 3.4h). It is possible, that the location of Bresse-104-Bis was inverted and uplifted during Late Cretaceous or Palaeocene times, which led to erosion of previously deposited Cretaceous sediments, but an inversion cannot be finally assessed. However, in Cretaceous times, a change in the differential subsidence

of the two borehole locations sets in. During Mesozoic times, Bresse-104-Bis shows notably higher subsidence rates whereas during the Cenozoic formation of the Bresse Graben, Bresse-2 suddenly shows the higher subsidence rates (Fig. 3.4h).

3.6.4 Discussion

As differential subsidence is visible in Triassic and Lower Jurassic times, it is concluded that the boreholes BR-2 and

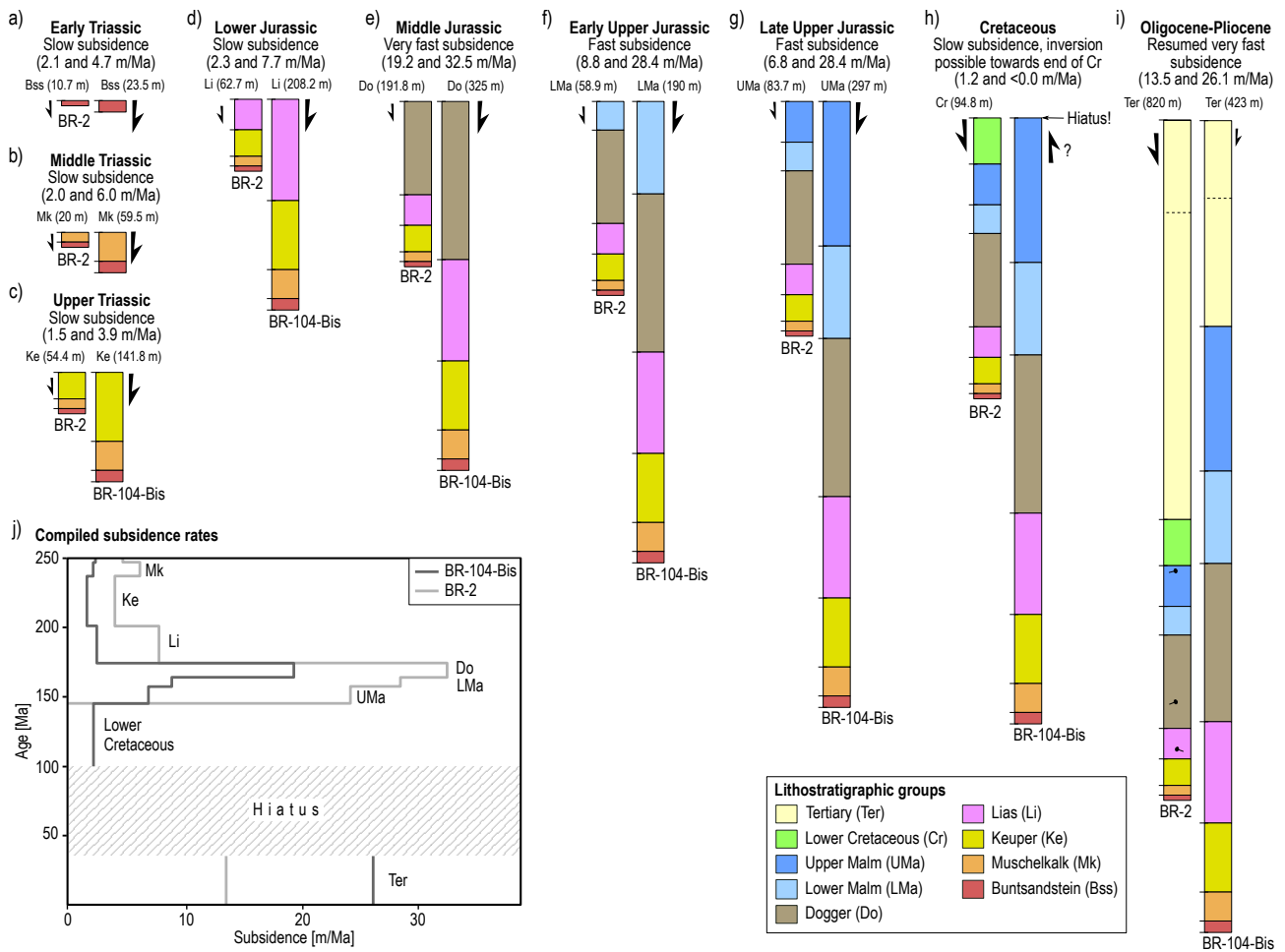


Fig. 3.4 – Comparison between boreholes BR-2 and BR-104-Bis, lying in the Bresse Graben. The boreholes show substantial stratigraphic differences due to an important fault in between the two boreholes, the thickness of individual lithostratigraphic groups is specified above the graphical log. a–d) Relatively slow subsidence rates prevail during Triassic and Early Jurassic. e–g) Subsidence accelerates during Middle and Upper Jurassic. h) Slow subsidence is calculated in Lower Cretaceous. The Cretaceous to Oligocene hiatus in BR-104-Bis is interpreted as inversion of the location, resulting in an erosion of the Lower Cretaceous series. i) During Cenozoic graben formation, the relative subsidence switches and BR-2 shows a higher subsidence rate. j) Overview chart for subsidence rates in BR-2 and BR-104-Bis.

BR-104-Bis were mechanically separated by a fault. Increased subsidence rates during Middle and Upper Jurassic are presumably in connection with the breakup of Pangaea (opening of the Tethys to the south and the North Atlantic Ocean to the west, Reisdorf and Wetzel 2018). The suspected inversion of BR-104-Bis during Upper Cretaceous or Palaeocene fits with beginning plate collision of Europe and Africa, which led to the emersion of the NAF that caused the hiatus spanning from Lower Cretaceous to Oligocene. In conclusion, the Limonest Sill is rather a Tertiary structure, which formed during Oligocene rifting of the Bresse Graben according to ages of Tertiary sediments in BR-2 and BR-104-Bis. The transition from relative eastward subsidence in Mesozoic to relative westward subsidence in Tertiary would need different geometries of the normal fault plane. How exactly this transition happened is not explored in here.

4 - THICKNESS MODELS OF STRATIGRAPHIC GROUPS

4.1 INTRODUCTION

Defining the thickness of Mesozoic units is challenging for large parts of the JFTB. Boreholes reaching the basement are relatively scarce, except for the exceptionally thoroughly explored area around Lons-le-Saunier (Fig. 3.1). Commonly, the geologist bases thickness estimates on the closest borehole, which in the Internal Jura may be far apart from the chosen section trace (possibly several tens of kilometres). The thickness of geological units exposed in the area (commonly Cretaceous to Jurassic units in the Internal Jura) can be verified in the field or estimated from geological maps, if bedding inclinations are known. Therefore, the thickness of surface near layers is commonly confidently constrained, but the local thickness of Triassic and Lower Jurassic sediments is mostly not verifiable since these geological units are hardly exposed. Relying on the thickness of boreholes projected from great distance is delicate, due to the fact that boreholes are often drilled into anticlines, which means that Triassic evaporites probably show local, tectonic thickening, if the structure evolved above the Triassic basal décollement (and not above an upper detachment in the Jurassic or Cretaceous series). Another problem is the fact that the sedimentary thickness of geological units varies spatially (up to several hundreds of metres for the UMa and Cr), which is a problem that gets more important for long cross-sections (e.g. transects across the whole JFTB).

Aiming to build a framework that facilitates the construction of cross-sections in the Jura Mountains, I compiled thickness maps of the Mesozoic sequence across the JFTB and surroundings. These maps are based on interpolation models that incorporate complementary data to boreholes. Boreholes constitute pin-points for the thickness of stratigraphic units. There are existing different thickness models for the surroundings of the Jura Mountains, which I included to complement the borehole dataset (specification follows in the method chapter below).

For the Buntsandstein, Muschelkalk, Keuper and Lias Groups, the thickness models reflect the initial depositional thickness, partially including tectonic thickening (which is specified subsequently). The Dogger, Lower Malm, Upper Malm and Cretaceous Groups are intensely eroded in some locations across the study area and the regional, average remaining thickness was estimated. Erosion is partially due to the formation of the JFTB, involving regional exhumation and erosion due to maximum 30 km (Affolter and Gratier 2004; Burkhard 1990; Laubscher 1965; Philippe et al. 1996) north-westward transport of the cover on the moderately SE-inclined basement and more localised erosion of anticlines. Furthermore, the Upper Mesozoic series is also eroded due to Eocene-Oligocene uplift of graben shoulders of the ECRIS (Bourgeois et al. 2007; Illies 1972), flexural bulging of the NAF (Burkhard and Sommaruga 1998; Laubscher 1992) and finally, due to lithospheric long-wavelength lithospheric buckling resulting from plate conversion in Upper Cretaceous and Palaeogene (Bourgeois et al. 2007; Lefort and Agarwal 1996, 2002), as well as resumed buckling from Middle Miocene onwards (Bourgeois et al. 2007). For the area of the JFTB, I tried to represent the thickness of units shortly before the formation of the JFTB, as this is the relevant thickness for constructing cross-section.

4.2 METHODOLOGY

4.2.1 General procedure

I aimed to remove the effect of tectonic thickening in the thickness models, at least in the JFTB. For one thing, I removed documented repetitions of geological units within boreholes. Also, I did not include thicknesses of boreholes where a geological unit is notably tectonically disturbed (e.g. internal repetitions or large faults noted in borelogs). Incompetent clay-rich or evaporite units, especially in the Dogger, Lias, Keuper and Muschelkalk Groups that

host detachments, are certainly prone to tectonic thickening (Sommaruga et al. 2017), i.e. due to internal faulting (duplexing) or possibly because of salt flow. However, with the available information in some boreholes and existing seismic models (e.g. Landesgeologie 2017; Sommaruga et al. 2012), it was not always possible to estimate internal tectonic thickening of geological units. Therefore, the thickness models of this study still include a signature of some tectonic thickening, in particular in the Molasse Basin, where thickness data is predominantly based on seismic models (Landesgeologie 2017; Sommaruga et al. 2017). However, for the JFTB, BG and URG, I aimed to constrict or remove local thickening (e.g. thickening of evaporites at the centre of anticlines, local thickening of evaporites along basement faults) and to represent regional thickness values.

Finally, the thickness maps presented in here are not palinspastically restored in respect to the Miocene-Pliocene thin-skinned displacement of the detached NAF. The thickness models therefore reflect the spatial situation after about 4 Ma in the detached MB and the JFTB. This is fine for cross-section construction, but it would be wrong to use these thickness models without retro-deformation for the unfolded state of forward models (it must be kept in mind that the JFTB is displaced up to 30 km to the north-west in its central segment). In conclusion, the subsequently presented thickness models do not reflect the state at one specific point in time. Around the JFTB, they reflect the present day thickness of units but in the JFTB, thickness models indicate an average thickness shortly before the formation of the JFTB (removing local tectonic thickening and local erosion), optimised for cross-section construction.

4.2.2 Tools and technique

Thickness models are interpolated from boreholes in the borehole database (chapter 3) and additional data points of previous studies (Table 4.1). For the JFTB, I included field-based stratigraphies, which are occasionally available with geological maps 1:25'000 of Switzerland, published by swisstopo. The erosive limit of geological units next to the Massif Central, Vosges and Black Forest are defined according to geological maps (BRGM 2004; Swisstopo 2012). Additionally, I tried to respect important faults along which sudden thickness changes of units occur. Thickness changes along faults are for example observed in seismic studies in the Molasse Basin (Gruber 2017; Landesgeologie 2017; Sommaruga et al. 2012), towards the front of the JFTB (Lienhardt 1962; Madritsch 2008; Michel et al. 1953; Ustaszewski 2004) and in the Bresse Graben (Bergerat et al. 1989) in connection with normal faults. Incompetent marl, clay and evaporites tend to fill gaps created by basement offsets which leads to tectonic thickness changes that are spatially confined to the fault (e.g. Fig. 4.1). Note that the Alps are excluded from interpolations.

The interpolation between data-points is done using the algorithm «Spline with barriers» of the ESRI ArcGIS 10.6 suite, applied using the Python programming library «arcpy». Faults for each Mesozoic unit are specified as «barrier» in the interpolation algorithm. Resulting models are

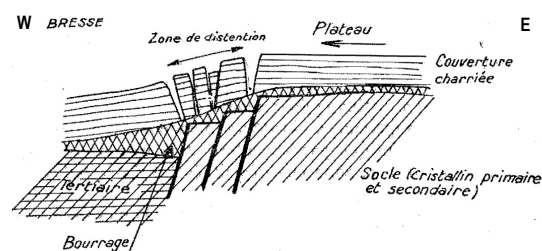


Fig. 4.1 – Scheme illustrating the eastern BG border faults at the front of the Faisceau lédonien according to Michel et al. (1953). Basement blocks subside into the BG and Triassic evaporites fill spaces and therefore show substantial thickness variation close to basement faults.

in the form of geo-referenced surface grids (available in Supplementary Material B.01) and are used to create colour coded contour maps for each Mesozoic unit (available in Supplementary Material A.05). I also created summed up grids, i.e. total Triassic thickness model (Bss + Mk + Ke), total Malm Group thickness model (UMa + LMa) and a total Mesozoic thickness model (all models summed up), available through the Supplementary Material B.01 of this study.

4.3 TRIASSIC SERIES

Thickness maps of the Triassic series in the study area were previously published in Boigk and Schöneich (1974) and Sommaruga et al. (2017). Boigk and Schöneich (1974) based isopach maps on a compilation of boreholes and contemporary French and Swiss studies. These maps reflected the palaeographic thickness of Triassic deposits, which means that the original Mesozoic overburden in the area of the Vosges and BF was reconstructed. However, the Mio-Pliocene displacements of the detached NAF were not considered, and the positions of boreholes were apparently not palinspastically restored. In Boigk and Schöneich (1974), geological data for the Molasse Basin was scarce but today, the SMB is well known due to several area covering seismic studies (Landesgeologie 2017; Sommaruga et al. 2012). In Sommaruga et al. (2017), we compiled existing maps and models for the MB to present updated Triassic thickness maps. However, a «.. detailed revision and integration of all existing well data was beyond the scope of... » Sommaruga et al. (2017). In the present study, I proceeded to a re-evaluation of boreholes, which was particularly made possible by the recent policy of BRGM to freely publish French borehole data. The thickness maps presented subsequently are based on re-evaluated boreholes (see chapter 3), combined with new interpretations that are described in the following. The full documentation of boreholes, containing more detailed descriptions and graphical boreholes, is available in Supplementary Material C. Positions of boreholes and abbreviations are indicated in Fig. 3.1.

Table 4.1 – Sources of additional data points, next to boreholes, used to create thickness models of the Mesozoic stratigraphic units. VZ: Vorfaltenzone, RBTZ: Rhine–Bresse Transfer Zone. : Geological Atlas of Switzerland 1:25000, map sheets published by swisstopo.

Domain	Source	Ter	Cr	UMa	LMa	Do	Li	Ke	Mk	Bss
Additional data points										
Molasse Basin	Landesgeologie (2017)	-	●	●	●	●	●	●	●	-
	Sommaruga et al. (2012)	●	●	●	-	-	●	-	-	-
	Gruber (2017)	●	●	●	●	●	●	●	●	-
	Boigk and Schöneich (1974)	-	-	-	-	-	-	-	-	●
Jura Mountains	GA25 (swisstopo)	-	●	●	●	●	●	-	-	-
	Schori (2014)	-	-	-	●	-	-	-	-	-
	Ustaszewski (2004)	-	-	-	-	-	-	-	●	-
Bresse Graben	Boigk and Schöneich (1974)	-	-	-	-	-	-	-	●	●
	Alabouvette et al. (1984)	●	-	-	-	-	-	-	-	-
Valence Basin	Boigk and Schöneich (1974)	-	-	-	-	-	-	●	-	●
Upper Rhine Graben	Rupf and Nitsch (2008)	-	-	-	-	-	-	●	●	●
	Rotstein et al. (2006)	●	-	-	-	-	-	-	-	-
Haute-Saône Plateau	Boigk and Schöneich (1974)	-	-	-	-	-	-	●	●	-
VZ / Tabular Jura	Rupf and Nitsch (2008)	-	-	-	-	-	-	●	●	●
	Jordan (2016)	-	-	-	-	-	-	-	-	●
Faults										
Molasse Basin	Gruber (2017)	●	●	●	●	●	●	●	●	-
	Landesgeologie (2017)	●	●	●	●	●	●	●	-	-
	Sommaruga et al. (2012)	●	-	-	-	-	-	-	-	-
Ile Crémieu	Rocher et al. (2004)	●	●	●	●	-	-	-	-	-
Bresse-Jura	Guellec et al. (1990)	-	●	●	●	●	-	●	●	-
	Alabouvette et al. (1984)	●	-	-	-	-	-	-	-	-
RBTZ	BRGM (2004)	-	●	●	●	●	●	-	-	-
URG	Ustaszewski (2004)	●	-	●	-	-	-	●	-	-
	Laubscher (1961)	-	-	●	●	●	●	●	●	-

4.3.1 Buntsandstein Group

Data processing

At the Poisoux-1 borehole (PSX-1, Fig. 3.1), the Keuper Group lies on top of the pre-Mesozoic basement and the Buntsandstein and Muschelkalk Group are absent. Guellec et al. (1990) show that the absence of the Lower and Middle Triassic interval in PSX-1 is a local feature, owed to a normal fault at the base of the Mesozoic series. Middle and Lower Triassic sediments are present in boreholes close by (e.g. BOX-1-Bis or DP-111). Therefore, I exclude PSX-1 from interpolations in the Buntsandstein Group and Muschelkalk-Group thickness models. Similarly, Vaux-en-Bugey-4 (VEB-4) is ignored as I interpret the absence of Lower and Middle Triassic sediments to normal faulting, analogous to PSX-1.

The borehole Bois-des-Chaux-1bis (BOX-1-Bis, Fig. 3.1) lies in the BG, just in front of the JFTB. It contains a 255 m thick interval of Buntsandstein Group siliciclastic sediments according to the fundamental log (Shell 1980). This is an unusually high value and might be an overestimate, since the limit to Permian sandstones is possibly misplaced (Sommaruga et al. 2017 mentions that the discrimination between the Permian and Lower Triassic red sandstones is very difficult and therefore, overestimations probably occur). A re-evaluation of the limit between Per-

mian and Lower Triassic sediments is not possible with the available information. Due to this ambiguity, the Buntsandstein Group thickness value of BOX-1-Bis is excluded from interpolations to avoid an over-estimation. Note that based on this borehole, previous studies (Otto 1994; Sommaruga et al. 2017) placed the deepest part of the Early Triassic Buntsandstein-Group basin east of Cormoz (Fig. 4.2). Furthermore, the wells Pontallier-1 (PO-1) and Frasn-le-Château-1 (FLC-1) in the RBTZ north of the La Serre Horst are excluded from interpolations as they are suspected to underestimate the thickness of the Buntsandstein Group – logs do not include the conglomerate-rich sandstone at the base of the Triassic series.

Resulting model

The Buntsandstein-Group thickness model (Fig. 4.2) indicates an Early Triassic, shallow, siliciclastic basin, with a depositional centre south of Ornans, roughly coinciding with the centre of the today's Jura Mountains (Fig. 4.2). The maximum thickness of the depo-centre is 106 m (borehole Éternoz-1, ET-1). More centres are identified in the URG west of Basel (borehole Knoeringue-1, KNO-1, 122 m) and in the Dinkelberg Graben east of Basel (Jordan 2016, see Fig. 4.2). The centres around Basel and south of Ornans might be connected (suggested in Boigk and Schöneich 1974), but there are no boreholes between Porrentruy and

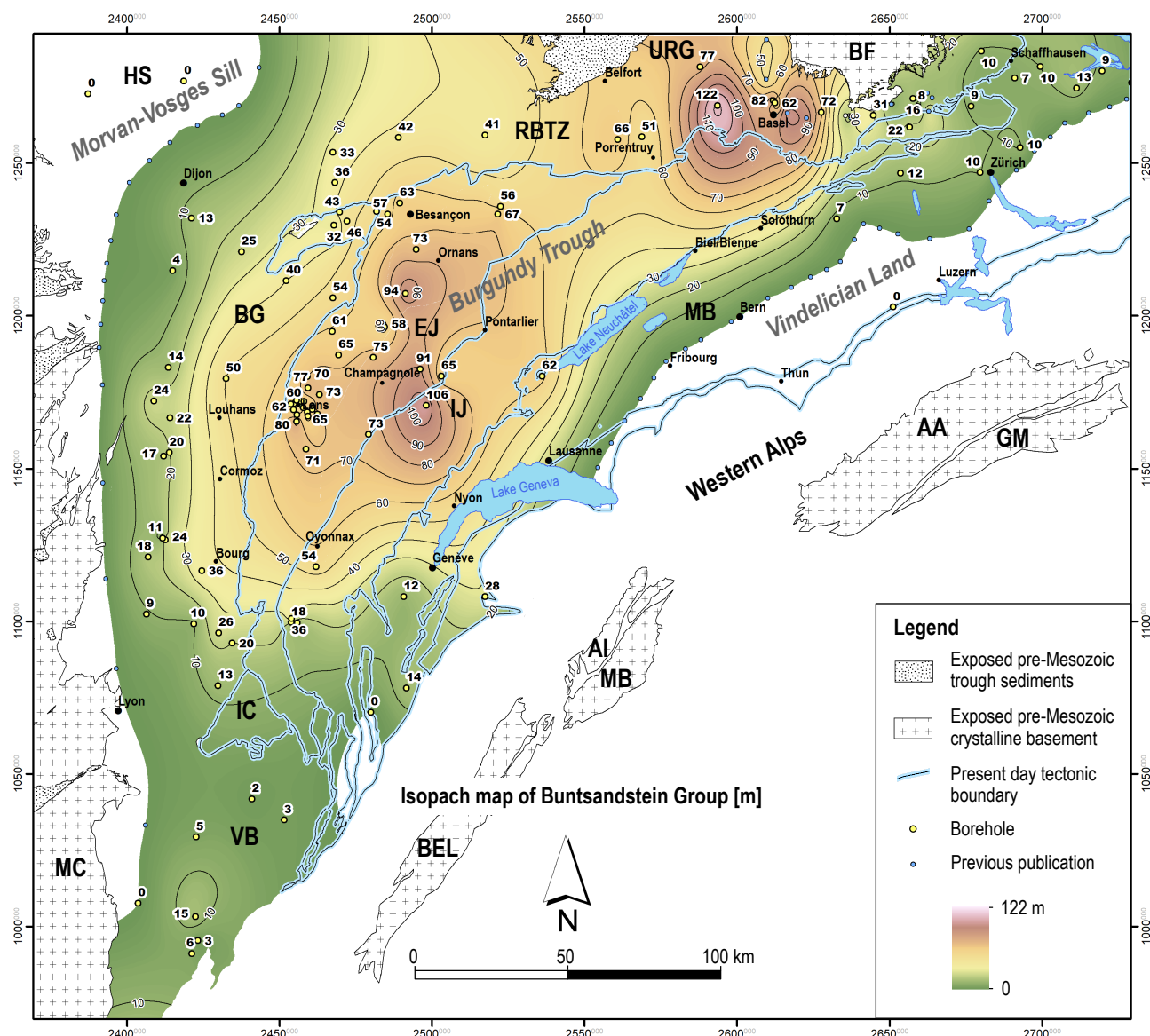


Fig. 4.2 – Isopach map of the Buntsandstein Group. The definition of Palaeogeographic environments is according to Boigk and Schöneich (1974), comprising the *Morvan-Vosges Sill*, *Burgundy Trough* and *Vindelician Land*. Present day tectonic domains are MC: Massif Central, VB: Valence Basin, IC: Ile Crémieu, BG: Bresse Graben, HS: Haute-Saône Plateau, EJ: External Jura, IJ: Internal Jura, MB: Molasse Basin, URG: Upper Rhine Graben, BF: Black Forest, RBTZ: Rhine-Bresse Transfer Zone. BEL: Belledonne Massif, AI: Aiguilles-Rouges Massif, MB: Mont Blanc Massif, AA: Aar Massif, GM: Gotthard Massif.

Pontarlier that give evidence (Fig. 4.2).

I used Boigk and Schöneich (1974) and Jordan et al. (2016) to define the limits of the Buntsandstein Group to the south, where the topographically high Vindelician Land prevented a deposition of sediments (Boigk and Schöneich 1974). To the north-west of the study area, on the Haute-Saône Plateau, Early Triassic deposits are absent due to the Morvan-Vosges Sill (Boigk and Schöneich 1974) that connects the Morvan and Vosges Massifs. In the south-west of the study area, in the area of the Valence Basin, only a few metres of the Buntsandstein-Group facies are deposited. This area constitutes a sill that separates the Early Triassic Buntsandstein-Group basin in the area of the JFTB from the Rhodanian Basin south of the study area (Boigk and Schöneich 1974).

Interpretation

The shallow Early Triassic basin in Fig. 4.2 is referred to as Burgundy Trough in Boigk and Schöneich (1974), which is inherited from Early Permian extension and therefore also visible in isopach maps of the «Rotliegend» lithostratigraphic group (Boigk and Schöneich 1974).

At the beginning of the Triassic period, the study area is a peneplain and slow subsidence prevails. Across the region of the future Jura Mountains, no more than about 100 m sediments are deposited until the end of the Early Triassic period. According to Boigk and Schöneich (1974), the depo-centres close to Basel indicate activity of a roughly N-S (Rhenish) oriented system. The Morvan-Vosges Sill and the Vindelician Land (Fig. 4.2) have a rough ENE-WSW orientation, similar to the overall orientation of the Burgundy Trough in Early Permian times, owing to their Variscan inheritance (Boigk and Schöneich 1974).

4.3.2 Muschelkalk Group

Data processing: faults and interpolation barriers

In the area of the present day Molasse Basin, Landesgeologie (2017) provide additional data points for the Muschelkalk-Group thickness model of the present study. As Landesgeologie (2017) only provides a combined Muschelkalk and Buntsandstein-Group isopach map, the thickness of the Buntsandstein-Group model (Fig. 4.2) is subtracted from probing points of Landesgeologie (2017) to receive a more accurate estimate for the Muschelkalk Group.

A notably increased thickness of the Muschelkalk Group is documented locally in the URG north of Basel (Allschwil Graben), in the borehole Otterbach-2 (thickness in OTT-2 is ~358 m) and in the BG east of Cormoz, in the borehole Bois-des-Chaux-1bis (thickness in BOX-1-Bis is ~311 m). Both boreholes are close to large graben border-faults of the URG and the BG, respectively. High thickness values of the Muschelkalk Group in these boreholes are therefore suspected to represent local tectonic thickening, restricted to graben border faults, analogous to the sketch in Fig. 4.1. Accordingly, I introduced normal faults next to these boreholes (following Guellec et al. 1990; Laubscher 1961) along which sudden thickness changes occur (Fig. 4.3).

In the External Jura, the borehole Laveron-1 (LVN-1) lying east of Champagnole, is drilled into an anticline and an enormously thick sequence of 464 m Muschelkalk Group is documented (Fig. 4.3). This increased thickness can be attributed to an evaporite cored pillow (Sommaruga 1997, also see seismic line CM16S in Fig. 5.2d on page 75). Thickening in Laveron-1 is restricted to the evaporite pillow and therefore, an interpolation barrier is defined around the NE–SW striking Laveron pillow in order to avoid a regional influence of this thick value.

Resulting model

The Muschelkalk-Group thickness model (Fig. 4.3) shows a centre in the Swiss Molasse Basin, roughly between Lausanne–Lake Neuchâtel–Solothurn–Thun, which is well explored and documented (Gruber 2017; Landesgeologie 2017; Sommaruga et al. 2012). In this centre, the Muschelkalk Group thickness notably exceeds values of 250 m, whereas in the rest of the study area, this limit is only locally reached close to fault systems or evaporite pillows (e.g. BOX-1-Bis, LVN-1, OTT-2) and therefore likely connected to tectonic processes. East of Fribourg, Gruber (2017) interprets more than 700 m of Muschelkalk Group on seismic lines, locally restricted in a NNE–SSW striking fault system (Fribourg fault zone, Fig. 4.3).

The regional thickness of the Muschelkalk Group in the Internal Jura is largely based on interpolation and only constrained locally by four boreholes south of Oyonnax (Fig. 4.3). East of Lake Neuchâtel, the basal décollement of the detached NAF is mainly hosted in evaporites of the Muschelkalk Group (Deville 2021; Gruber 2017; Jordan 1994; Sommaruga 1999; Sommaruga et al. 2017). From this it follows that the Muschelkalk Group shows tectonic thickening (e.g. duplexing, low-angle thrusting) east

of Lake Neuchâtel (Sommaruga et al. 2017). Accordingly, an interpolation barrier is introduced following the northern front of the Central and Eastern Jura, which restrains high values of the Muschelkalk Group within the detached foreland (Fig. 4.3).

According to Boigk and Schöneich (1974), Middle Triassic sediments were not deposited in the French Massif Central. The Morvan–Vosges Sill constitutes the north-western limit of the Middle Triassic Burgundy Trough and the topographically high Vindelician Land retreats southwards into the area of the future Western Alps (Boigk and Schöneich 1974).

Interpretation

In the thickness model of the Muschelkalk Group (Fig. 4.3), exceptionally high thickness values in BOX-1-Bis and OTT-2 are interpreted to be of tectonic origin resulting during Eo-Oligocene graben formation. It is interpreted that incompetent evaporites within the Muschelkalk Group filled up space created by normal faults (Fig. 4.1).

In boreholes across the Molasse Basin, it is observed that the basal décollement of the detached NAF is mainly hosted in the Keuper Group west of Lake Neuchâtel, whereas it is hosted in the Muschelkalk Group east of Lake Neuchâtel (Deville 2021; Gruber 2017; Jordan 1994; Sommaruga 1999). This transition seems to correlate with the presence of salt systems within the lithostratigraphic group that hosts the basal décollement (compare the limits of salt systems in Fig. 4.3 and Fig. 4.4). Furthermore, Sommaruga et al. (2017) point out that the transition of the basal-décollement host correlates with an increased thickness of the hosting lithostratigraphic group, which is attributed to tectonic thickening (e.g. duplexing and low-angle thrusting). Based on observed thickness values in the Molasse Basin and in the transition zone, Sommaruga et al. (2017) propose that a thickness of the Muschelkalk Group of more than about 200 m (yellow and red colours in isopach map Fig. 4.3) is preferentially owed to tectonic duplication within the basal décollement of the detached NAF. Following this, values between 200–250 m in the area of Ornans and Besançon (Fig. 4.3) imply a minor Muschelkalk-Group décollement activity, next to the main décollement in the Keuper Group (which is for example documented in Buez-1, BU-1). Tectonic thickening in central parts of the External Jura (e.g. Laveron-1) suggests that the Muschelkalk Group is still locally involved in the basal décollement around Champagnole (Fig. 4.3). In the borehole Valempoulières-1 (VLP-1, NW of Champagnole) for example, the Muschelkalk Group is thrusts onto the Keuper salt system (see structural interpretation in Philippe et al. 1996).

At the eastern tip of the JFTB, the Muschelkalk Group thickness is between 150–200 m, which correlates with the eastern limit of the basal décollement in the Muschelkalk Group. Interestingly, thickness values of more than 250 m are documented to the south of Zurich (Fig. 4.3), suggesting that the basal décollement jumps southwards, from the Eastern Jura to the southern Molasse Basin.

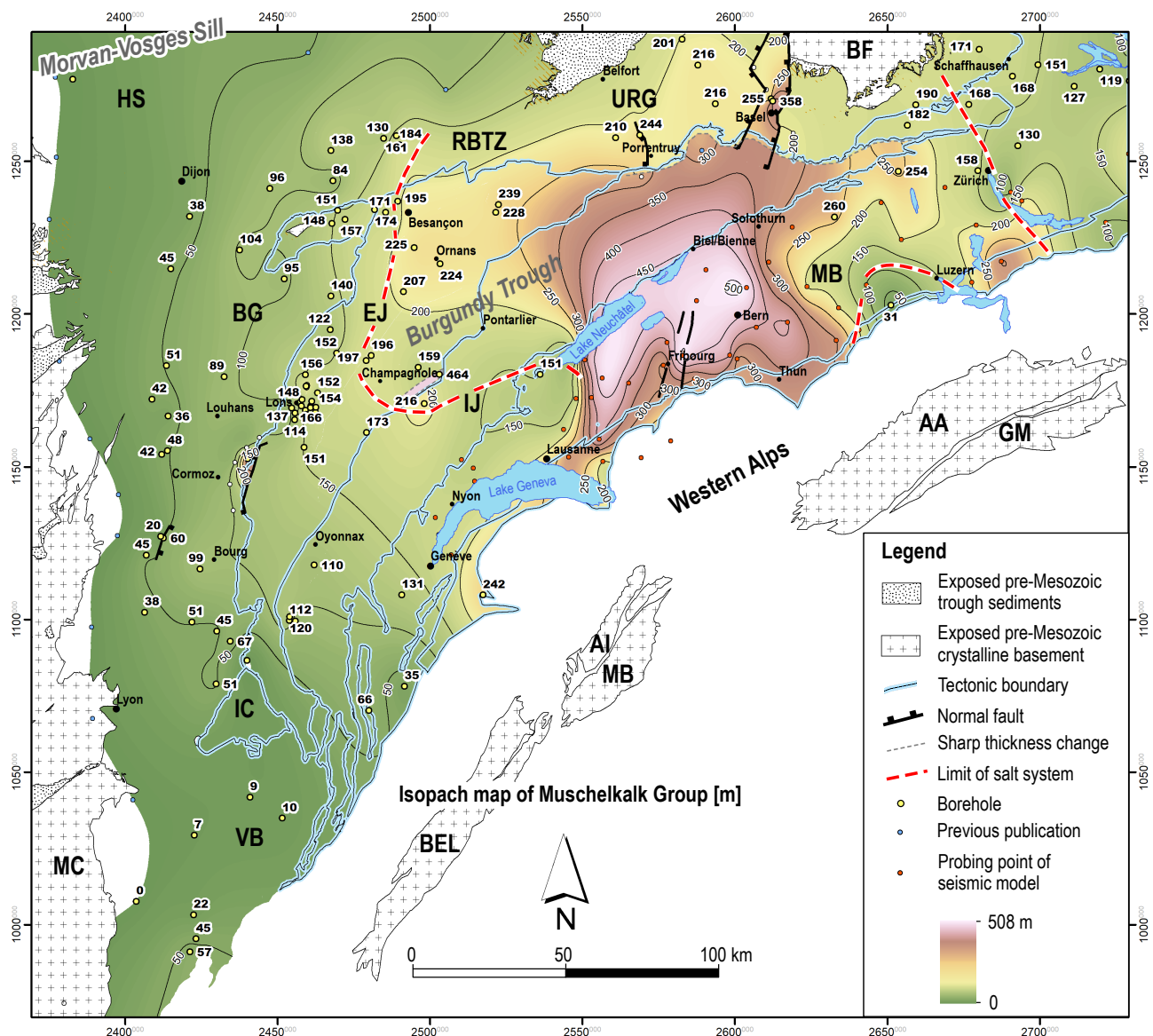


Fig. 4.3 – Isopach map of Muschelkalk Group. The definition of Palaeogeographic environments is according to Boigk and Schöneich (1974), comprising the Morvan–Vosges Sill and the Burgundy Trough. The western and eastern limit of salt-bearing systems within the Muschelkalk Group (red dashed line) is interpreted from the description of boreholes. Present day tectonic domains are MC: Massif Central, VB: Valence Basin, IC: Ile Crémieu, BG: Bresse Graben, HS: Haute-Saône Plateau, EJ: External Jura, IJ: Internal Jura, MB: Molasse Basin, URG: Upper Rhine Graben, BF: Black Forest, RBTZ: Rhine–Bresse Transfer Zone. BEL: Belledonne Massif, AI: Aiguilles-Rouges Massif, MB: Mont Blanc Massif, AA: Aar Massif, GM: Gotthard Massif.

4.3.3 Keuper Group

Data processing: faults and interpolation barriers

There are several normal faults that I propose, either deduced from abrupt thickness changes between closely spaced boreholes or due to exceptionally thick Keuper Group evaporites close to known graben border-faults. West of Bourg in the BG, an eastward dipping normal fault is proposed, deduced from comparison between BR-2¹ and BR-104-Bis² (Fig. 4.4, see borehole comparison in Fig. 3.4). In the Jura Mountains, normal faults affecting the Keuper Group are furthermore proposed east of Cormoz (due to thick Ke at BOX-1-Bis³), south of Ornans in the Faisceau salinois (due to thick Ke at ET-1⁴) and at Valem-

poulières (VLP-102⁵ versus VLP-101⁶). Furthermore, normal faults are proposed close to Basel, along which the thickness of the Keuper Group changes abruptly. Faults in the Molasse Basin are either according to Landesgeologie (2017) or Gruber (2017), who show that the Keuper Group thickness abruptly changes several hundreds of metres along some faults.

Finally, in front of the Internal Jura, I introduced interpolation barriers for the SGT-1⁷ and TLN-1⁸ boreholes that are both drilled into evaporite cored pillows (e.g. Sommaruga 1997). High thickness values in these boreholes do not show the regional thickness of the Keuper Group but reflect local structures.

According to Boigk and Schöneich (1974), the bound-

¹Bresse-2, vertical thickness Ke = 54 m

²Bresse-104bis, vertical thickness Ke = 142 m

³Bois-des-Chaux-1bis, vertical thickness Ke = 365 m

⁴Eternoz-1, vertical thickness Ke = 476 m

⁵Valempoulières-102, vertical thickness Ke = 491 m

⁶Valempoulières-101, vertical thickness Ke = 339 m

⁷Saugeot-1, vertical thickness Ke = 565 m

⁸Toillon-1, vertical thickness Ke = 882 m

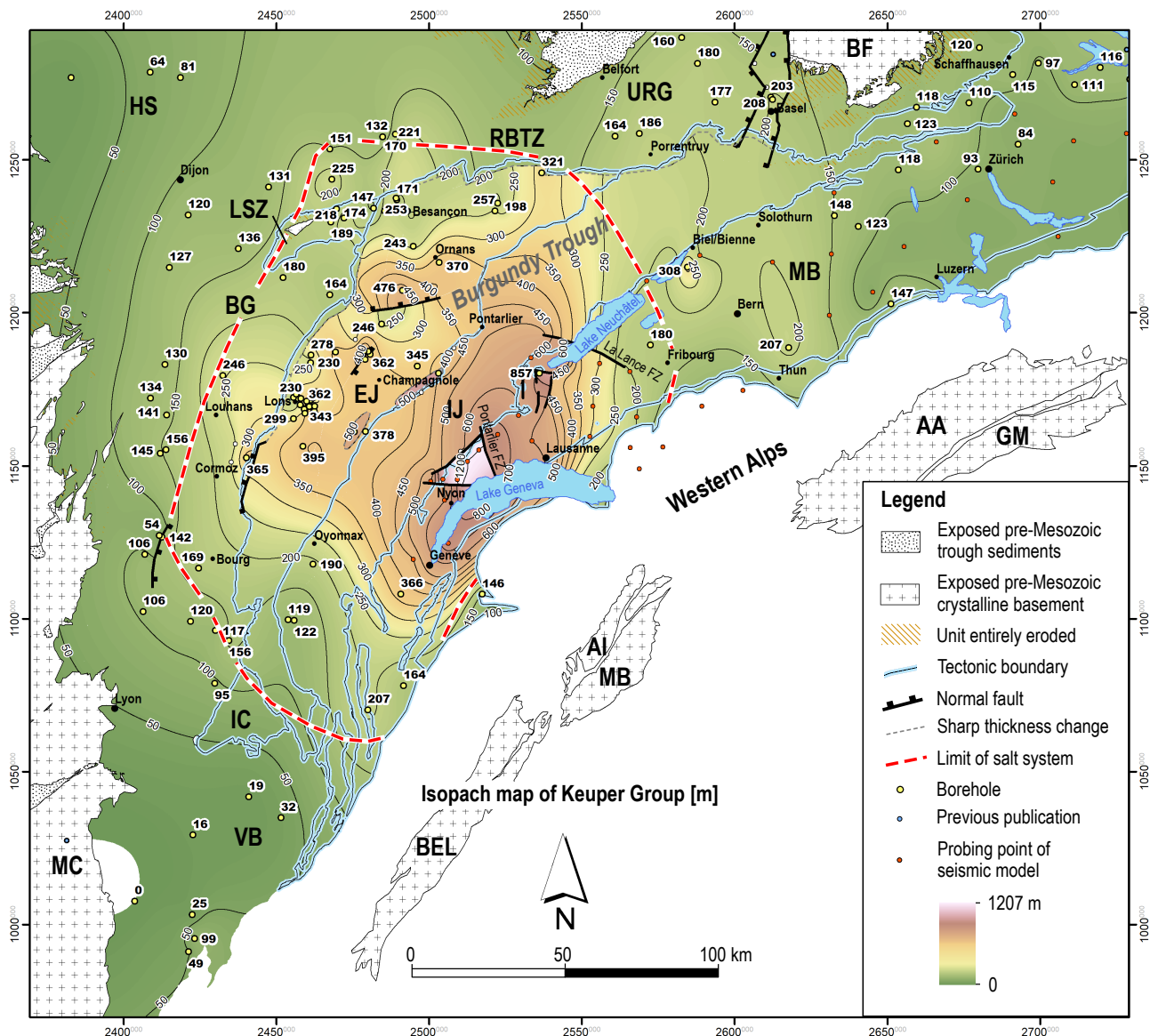


Fig. 4.4 – Isopach map of the Keuper Group. The limit of salt systems within the Keuper Group (red dashed line) is interpreted from the description of boreholes. Present day tectonic domains are MC: Massif Central, VB: Valence Basin, IC: Ile Crémieu, BG: Bresse Graben, LSZ: La Serre Zone, HS: Haute-Saône Plateau, EJ: External Jura, IJ: Internal Jura, MB: Molasse Basin, URG: Upper Rhine Graben, BF: Black Forest, RBTZ: Rhine–Bresse Transfer Zone. BEL: Belledonne Massif, AI: Aiguilles-Rouges Massif, MB: Mont Blanc Massif, AA: Aar Massif, GM: Gotthard Massif.

ary of the Keuper Group basin lies in the Massif Central, therefore the thickness decreases towards the west (Fig. 4.4).

Resulting model

The thickness model of the Keuper Group (Fig. 4.4) shows a thickness centre north of Nyon, confined by faults (Gruber 2017; Landesgeologie 2017). Within the MB, the thickness model (Fig. 4.4) is constrained by probing points of seismic models (Gruber 2017; Landesgeologie 2017) but in the Internal Jura, only three boreholes south of Oyonnax constrain the Keuper Group thickness locally. The thickness in the Internal Jura is widely deduced from interpolation between the MB and the External Jura. In the External Jura, the evaporite cored pillow at Saugeot-1 (SGT-1) shows thickening of the Keuper Group. The borehole Laveron-1, drilled into another evaporite pillow, was deep enough to reveal thickening of both, the Keuper and

Muschelkalk Group (Fig. 4.4). In the Tabular Jura in the region of the RBTZ and south of the BF, the Keuper Group is partially completely eroded (Fig. 4.4).

Note that the Keuper thickness model shows considerable tectonic thickness changes along Mio-Pliocene strike-slip faults such as the Pontarlier and La Lance fault zones (Fig. 4.4), which is not the case in the Muschelkalk Group model (Fig. 4.3).

Interpretation

Analogously to the interpretation of increased thickness values of the Muschelkalk Group (section 4.3.2), Sommaruga et al. (2017) suggests that a Keuper Group thickness of more than 250 m is indicative for tectonic thickening within the basal décollement. The thickness model in Fig. 4.4 indicates values greater than 250 m in yellow to red to white colours, which occur at the centre of the JFTB. The Keuper Group model (Fig. 4.4) shows that

large parts of the JFTB have a thickness greater than 250 m (Fig. 4.4). Note that even though the Keuper Group thickness south of Oyonnax is below 250 m, the basal décollement of the JFTB is hosted within the Keuper Group (Philippe 1994). The thinning out of the Keuper Group correlates with an increased friction on the basal décollement and SSE–NNW structural trends in the Southern Jura (Philippe 1994). The centre of the original Keuper Group basin and the centre of tectonic thickening are mechanically linked, as the initial evaporite thickness controls the degree of later tectonic activity (Sommaruga et al. 2017). The overall Keuper-Group thickness map (Fig. 4.4) reflects the extent of the Burgundy Trough during Late Triassic (Boigk and Schöneich 1974). The trough was limited to the north-west by the Morvan–Vosges Sill, in the west by the MC and to the south by the Vindelician Land, roughly in the area of the present day Western Alps (Boigk and Schöneich 1974).

The Keuper Group tapers off in the Southern Jura (Fig. 4.4). Thinning out of the basal-décollement host is the main reason for increased basal friction and a regional change of fold-axis orientation in the Southern Jura (Philippe 1994). The thickness model (Fig. 4.4) furthermore suggests that the basal décollement is rather hosted in the Muschelkalk Group east of Lake Neuchâtel (compare 4.3), coinciding with the Keuper-Muschelkalk Group transition of the basal décollement in the SMB (Gruber 2017). Therefore, the Plateau Jura is rather detached in evaporites of the Keuper Group. Note that in the northern Plateau Jura, the Muschelkalk Group reveals thickness values of more than 200 m and salt-bearing layers (4.3). Therefore, a subordinate tectonic activity in the Muschelkalk Group is suspected in the northern Plateau Jura.

The La Serre Zone shows thicknesses clearly below the limit of 250 m (4.4), which corroborates the interpretation of Madritsch et al. (2008) that this zone is not detached in Upper Triassic units.

The URG shows constant thickness values of the Keuper Group with no outliers close to border faults. In contrast to this, the Muschelkalk-Group thickness model shows significant variations in this region (4.3), which indicates that it was rather the Muschelkalk-Group evaporite series filling gaps when the URG formed in Cenozoic times and evaporites of the Keuper Group were hardly involved.

4.4 JURASSIC SERIES

4.4.1 Lias Group

Data processing: faults and additional locations

The thickness model of the Lias Group (Fig. 4.5) is based on seismic models in the area of the Molasse Basin (Gruber 2017; Landesgeologie 2017; Sommaruga et al. 2012). Faults are according to Gruber (2017) and Landesgeologie (2017). In the eastern Jura, the Triassic series is partially exposed and the thickness of the Lias Group is therefore locally documented by outcrops. I added two locations from Geological Atlas Sheets 1:25'000 (map sheet Delémont and map sheet Hauenstein, Bläsi et al.

2018; Keller and Liniger 1930, indicated in Fig. 4.5 with blue dots), representing the mean thickness for each map-sheet. In the BG west of Bourg, a roughly N–S striking normal fault is introduced due to a notable thickness difference between closely spaced boreholes (BR-104-Bis⁹ and BR-2¹⁰, see Fig. 3.4).

Resulting model

The overall thickness model of the Lias Group shows a basin with two thickness centres. To the east of the study area (Fig. 4.5), the overall thickness is below 50 m. In the area of the future Valence Basin, a sill separates the Dauphiné Basin in the south from depo-centres to the north (Boigk and Schöneich 1974). To the north-west, the Morvan–Vosges Sill lying north of the Haute-Saône Plateau, separates the Lower Jurassic (Lias Group) basin of the study area from the Paris Basin to the north (Boigk and Schöneich 1974, see location of Paris basin in Fig. 2.9).

A roughly N–S (Rhenish) oriented depo-centre of maximum 300 m depth is visible in the area of Bourg and Louhans, constituting the first predisposition for the Cenozoic BG (Boigk and Schöneich 1974). A normal fault was active east of Bourg (see Chapter 3.6). A second centre lies in between Pontarlier-Oyonnax-Geneva-Fribourg. Notable thickness changes of the Lias Group are documented along Mio-Pliocene strike-slip faults such as the Vuache, Pontarlier and La Lance fault zones (Gruber 2017; Landesgeologie 2017). This suggests that the thickness values up to 661 m in the Molasse Basin do not represent the sedimentary thickness of the Lias Group but rather tectonic duplications.

In some areas, the Lias Group is exposed or entirely eroded, as for example at the front of the JFTB in the area north of Lons-le-Saunier and the Eastern Jura, in the La Serre Zone, as well as in the Tabular Jura south of the Black Forest and Vosges Massifs (Fig. 4.5).

Interpretation

The Lias Group consists mainly of incompetent clay and marls, which are at least partially the locus of upper detachments in the Central Jura (RX-1, Aubert 1971; Winnock 1961). The Lias Group thickness model (Fig. 4.5) implies substantial tectonic thickening in the Molasse Basin, between the La Lance fault system (Lake Neuchâtel) and the Vuache fault system (Geneva Basin). Based on Fig. 4.5, I propose values greater than 250 m to be indicative for tectonic thickening. The thickness centre in the region of the future Molasse Basin roughly coincides with the centre of the Keuper Group (Fig. 4.4). Boreholes in the eastern study area, in between Lucerne, Basel and Schaffhausen show thicknesses below 50 m. Marls of the Lias Group therefore have few potential to host upper detachments in the Eastern Jura.

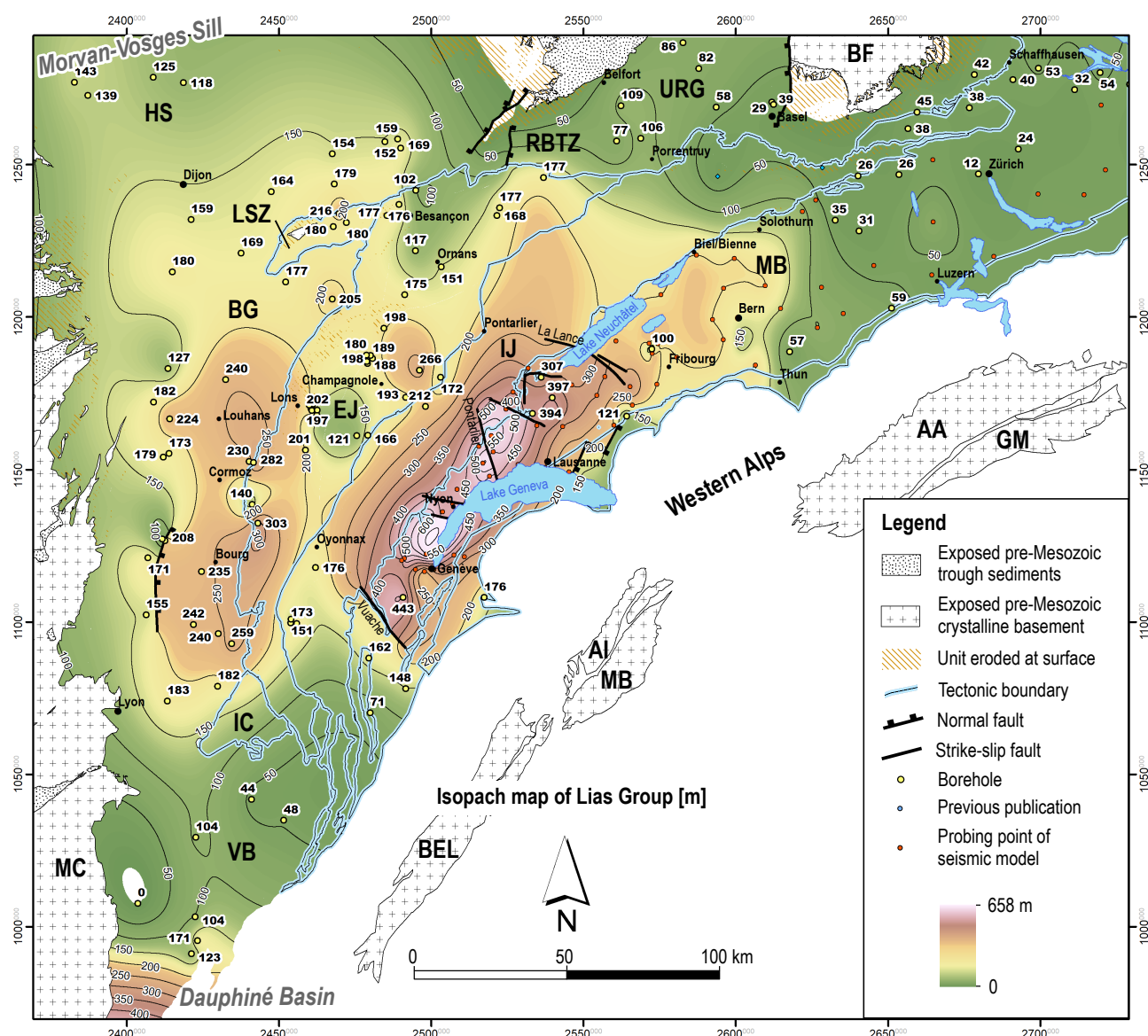


Fig. 4.5 – Isopach map of Lias Group. Present day tectonic domains are MC: Massif Central, VB: Valence Basin, IC: Ile Crémieu, BG: Bresse Graben, LSZ: La Serre Zone, HS: Haute-Saône Plateau, EJ: External Jura, IJ: Internal Jura, MB: Molasse Basin, URG: Upper Rhine Graben, BF: Black Forest, RBTZ: Rhine-Bresse Transfer Zone. BEL: Belledonne Massif, AI: Aiguilles-Rouges Massif, MB: Mont Blanc Massif, AA: Aar Massif, GM: Gotthard Massif.

4.4.2 Dogger Group

Data processing: additions from map sheets and faults

Additional data points in the Molasse Basin are according to seismic models of Gruber (2017) and Landesgeologie (2017). In the eastern Jura, the Dogger Group is partially fully exposed and the thickness locally documented by outcrops. Two locations from the geological Atlas 1:25000 of Switzerland (map sheets Delémont and Hauenstein, Bläsi et al. 2018; Keller and Liniger 1930) represent the mean thickness of each map-sheet. Strike-slip faults in the Molasse Basin are according to Gruber (2017) and Landesgeologie (2017). In the Bresse Graben, I interpreted a roughly NNE–SSW striking normal fault west of Bourg (Fig. 4.6), deduced from thickness differences in the boreholes BR-2 (Bresse-2 vertical thickness Do = 192 m) and BR-104-Bis (Bresse-104bis vertical thickness Do

= 325, also see Fig. 3.4). Furthermore, I added interpolation barriers for high values at SGT-1 and TLN-1, as these boreholes are drilled into known evaporite cored pillow structures (Sommaruga 1997) and I interpreted exceptionally thick Dogger Group values to be spatially linked to NE–SW striking pillows.

Resulting model

The thickness model of the Dogger Group illustrates an overall NE–SW striking basin with several depo-centres, concretely the Dauphiné Basin (name according to Boigk and Schöneich 1974) to the south (in the area of the future Valence Basin), the southern BG, the Central Jura, the western Swiss Molasse Basin and in the Upper Rhine Graben (Fig. 4.6).

The thickest Dogger Group series is documented on seismic lines in the Western Swiss Molasse Basin, between Nyon-Fribourg-Pontarlier in the Central Jura (Gruber 2017; Landesgeologie 2017). Abrupt thickness

⁹Bresse-104bis, vertical thickness Li = 208m

¹⁰Bresse-2, vertical thickness Li = 63m

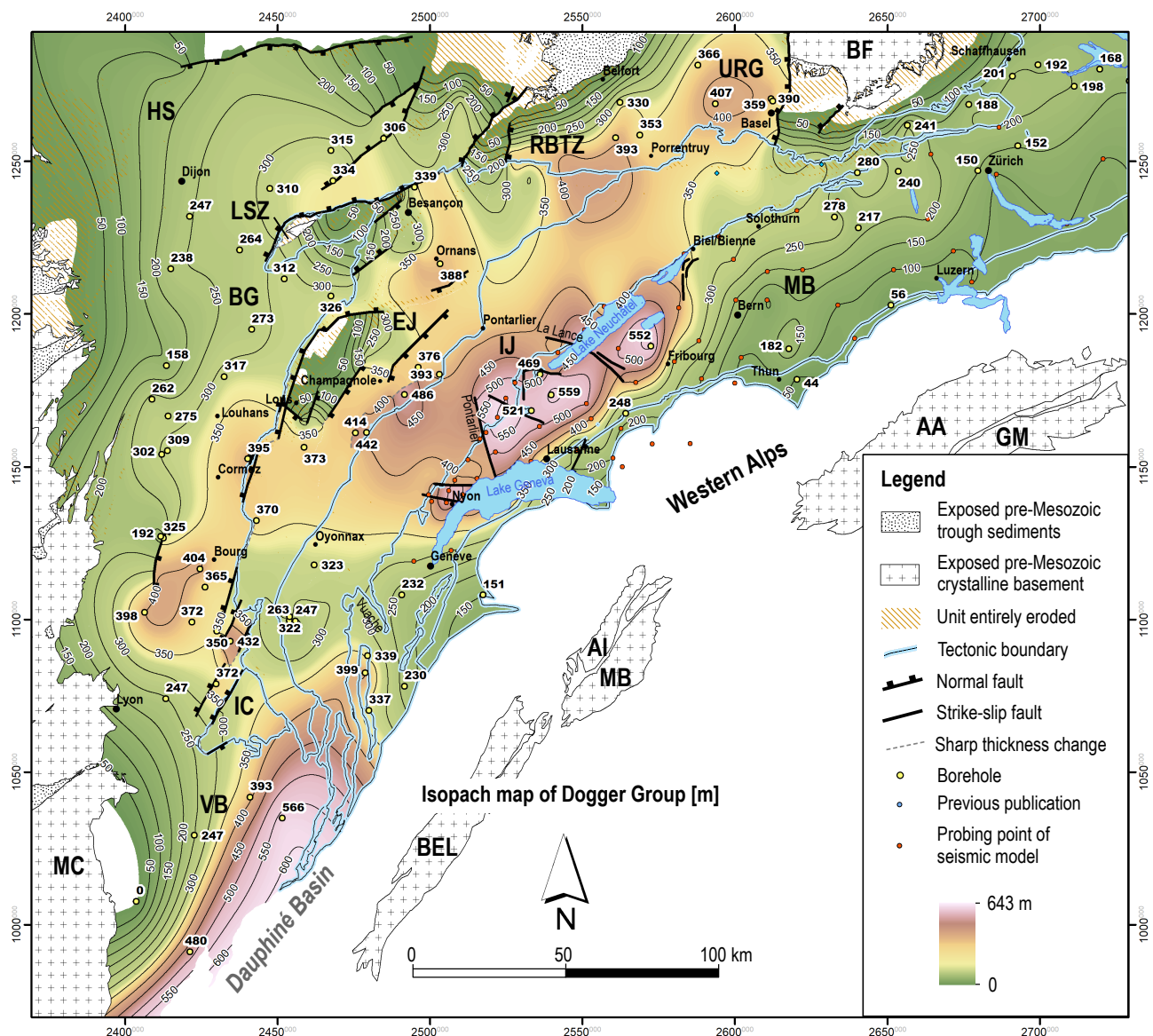


Fig. 4.6 – Isopach map of the Dogger Group. Present day tectonic domains are MC: Massif Central, VB: Valence Basin, IC: Ile Crémieu, BG: Bresse Graben, LSZ: La Serre Zone, HS: Haute-Saône Plateau, EJ: External Jura, IJ: Internal Jura, MB: Molasse Basin, URG: Upper Rhine Graben, BF: Black Forest, RBTZ: Rhine-Bresse Transfer Zone. BEL: Belledonne Massif, AI: Aiguilles-Rouges Massif, MB: Mont Blanc Massif, AA: Aar Massif, GM: Gotthard Massif.

changes are documented along strike-slip faults in connection with the Miocene-Pliocene detachment of the NAF (Gruber 2017; Landesgeologie 2017), which suggests that the Dogger Group is tectonically thickened due to thin-skinned deformation. A thickness change along a normal fault to the east of Lausanne documents syn-sedimentary normal faulting brought into connection with Middle Jurassic extension and the opening of the Alpine Tethys (Gruber 2017). The thickness centre of the Dogger Group lies more to the east than the thickness centre in the Lias Group model (compare Fig. 4.6 with Fig. 4.5).

The Dogger Group is entirely eroded in some parts of the study area, namely towards the front of the JFTB between Lons-le-Saunier and Besançon, the La Serre Zone and in the Tabular Jura south of the Vosges and Black Forest massifs. Eroded areas follow faults that are in connection with the formation of the ECRIS, such as the Ognon fault in the RBTZ (Madrtsch et al. 2008; Ruhland 1959) and the eastern border fault of the BG (Lienhardt

1962; Michel et al. 1953).

Interpretation

Eocene to Oligocene uplifts accompanied ECRIS rifting (e.g. see ECRIS uplifts Bourgeois et al. 2007) leading to erosion that follows main faults active during rifting. Whether the Dogger Group in the area of Lons-le-Saunier at the front of the Jura Mountains was eroded before the formation of the JFTB is debatable. At least nowadays, no Dogger Group outcrops are documented at Lons-le-Saunier or north of it. Also, no boreholes in the thoroughly explored Lons-le-Saunier area revealed hidden Dogger Group sediments underneath thrusts (see boreholes in Fig. 3.2), suggesting that the Dogger Group series was truly not involved during folding and thrusting.

The different thickness centres of the overall Dogger Group basin indicates differential subsidence during Middle Jurassic, within several sub-basins. Syn-

sedimentary normal faults in the Molasse Basin and the Bresse Graben document Middle Jurassic, fault-related subsidence. In the western Swiss Molasse Basin, the Dogger Group is tectonically thickened due to Mio-Pliocene thin-skinned tectonics. The thickness model (Fig. 4.6) interpolates thickening from the SMB into the Central Jura, supporting tectonic thickening in the JFTB and the existence of upper detachments in the JFTB such as proposed by Noack (1995), Nussbaum et al. (2017) and Schori et al. (2015). Note that west of the Pontarlier fault zone, it is more probable that the Lias Group hosted upper detachments as the thickness model in there (Fig. 4.5) contains a notable signature of tectonic thickening.

4.4.3 Lower Malm Group

Data processing: additions from map sheets and faults

In Fig. 4.7, abrupt thickness changes occur along faults in the Molasse Basin, drawn according to Gruber (2017) and Landesgeologie (2017). In addition to this, a normal fault north of the Ile Crémieu is according to Rocher et al. (2004) and the Limonest fault west of Bourg is deduced from height and thickness differences between boreholes BR-2 and BR-104-Bis (see Fig. 3.4). Additional data-points in the Swiss Molasse Basin are according to seismic models of Gruber (2017) and Landesgeologie (2017). In the Internal Jura, additional constraint points are from Swiss Geological Atlas 1:250000 map sheets (Orbe, Chasseral, Saignelégier, Travers, Les Verrières and Delémont, Aubert and Dreyfuss 1963; Aufranc and Burkhalter 2017; Aufranc et al. 2016; Keller and Liniger 1930; Muhlethaler 1930; Pasquier et al. 2013), representing mean thickness values for each map sheet and local stratigraphic sections.

Resulting model

The Lower Malm Group is exposed in many parts of the Jura Mountains. In the Internal JFTB, the marls of the Lower Malm Group tend to form high valleys along the Dogger Group core of anticlines. Towards the front of the External Jura and in the Tabular Jura, the Lower Malm Group is partially completely eroded due to Eocene-Oligocene uplifts of graben shoulders of the BG and URG (Bourgeois et al. 2007; Ziegler and Dèzes 2007). Furthermore, the Lower Malm Group is not present in the area of the Haute-Saône Plateau.

The overall shape of the Lower Malm Group model (Fig. 4.7) shows a basin with a rough NE–SW oriented long axis, and the thickest LMa-sequence occurs near Lausanne (Fig. 4.7). The LMa-sequence is only about 100 m thick in the RBTZ and even less at the tips of the JFTB.

In the Molasse Basin, thickness changes of the Lower Malm Group occur along the Pontarlier and La Lance fault systems, which suggests that the LMa thickness is partially tectonically altered due to Miocene-Pliocene thin-skinned deformation. Consequently, the thickest sequences at Lausanne and Nyon are likely owed to tectonic thickening. Similarly, in the Jura Mountains south of Champagnole, Bonlieu-1 (BLU-1) shows an uncharacteristically

thick LMa-sequence of 351 m. I interpret this high thickness at BLU-1 as tectonic thickening and added an interpolation barrier parallel to the front of the Internal Jura.

In the Bresse Graben, ongoing syn-sedimentary differential subsidence is deduced from boreholes BR-2 and BR-104-Bis (Fig. 4.7). In comparison to this, the Ile Crémieu is exhumed in Cenozoic times (Rocher et al. 2004) leading to subsequent erosion of the LMa above the Ile Crémieu (Fig. 4.7).

To the north-west of the thickness model (Fig. 4.7) in the area of the Haute-Saône Plateau, the interpolated sedimentary thickness of the LMa is reduced (Fig. 4.7). Note that the LMa is eroded in the Haute-Saône Plateau and values of the thickness model are a rough interpolation (Fig. 4.7).

Interpretation

The reduced LMa-thickness in the area of the Haute-Saône Plateau (Fig. 4.7) suggests the continuous existence of the Morvan–Vosges Sill (name after Boigk and Schöneich 1974), which constitutes a topographic high at least since Triassic times (Boigk and Schöneich 1974, see Fig. 4.2). The nowadays complete erosion of the Lower Malm Group in the Haute-Saône Plateau is suggested to be in connection with Upper Cretaceous to Neogene uplifts due to long wavelength buckling of the lithosphere (i.e. Burgundy-Swabian Jura Anticline, Bourgeois et al. 2007, Fig. 2.9 on page 30). In contrast to this, erosion of the LMa in the External Jura and the Tabular Jura is rather connected to Eo-Oligocene uplift of rift graben shoulders (Bourgeois et al. 2007; Dèzes et al. 2004).

Two boreholes in the BG show that the LMa was eroded before Oligocene, as Mesozoic sediments are covered by Oligocene graben sediments and the LMa is missing. This is the case in Blyes-101 (BL-101) and Bresse-103 (BR-103). In the case of Blyes-101, erosion of Upper Jurassic sediments is likely in connection with Eocene uplift of the Ile Crémieu (Rocher et al. 2004), followed by block subsidence in Oligocene times.

Locations with a LMa-thickness of 350 m can be connected to tectonic disturbances close to faults. Therefore, I suggest that thickness values greater than about 300 m of the LMa are due to tectonic thickening.

4.4.4 Upper Malm Group

Data processing: additions from map sheets and faults

In the URG, I added two normal faults (Illfurth and Ferrette fault according to Ustaszewski 2004), which are used to explain sudden thickness changes between boreholes. Due to similar reasons, normal faults are added in the southern Bresse Graben and close to the Ile Crémieu. Additional data points from seismic models across the Molasse Basin are from Gruber (2017), Sommaruga et al. (2012) and Landesgeologie (2017). I added mean thicknesses of geological maps sheets 1:25'000 of swisstopo (Saignelégier, Chasseral, Val-de-Ruz, Travers, Les Verrières, le Sentier, Aubert 1941; Aufranc and Burkhalter 2017; Aufranc et al. 2016; Muhlethaler 1930; Pasquier et

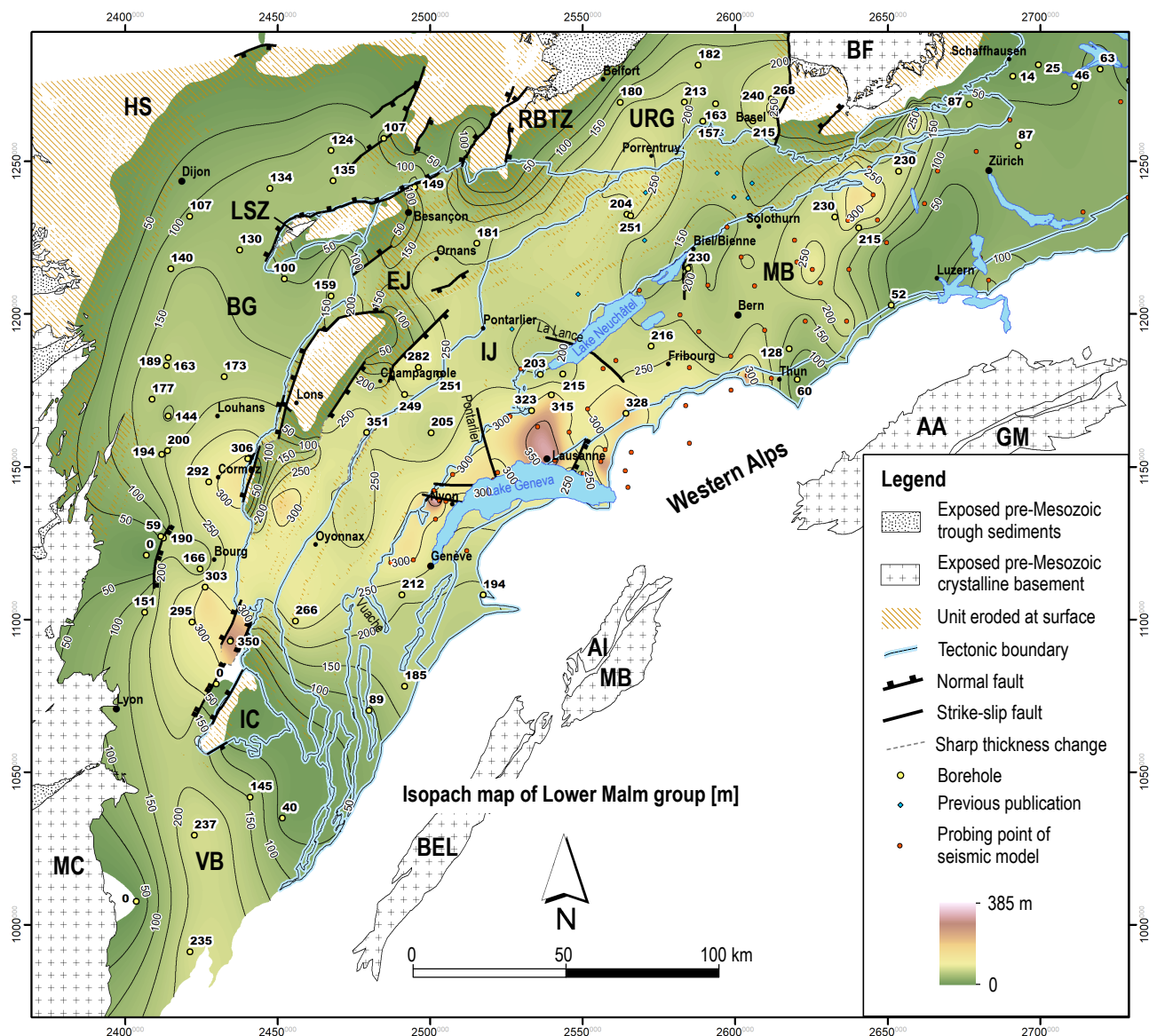


Fig. 4.7 – Isopach map of Lower Malm Group. Present day tectonic domains are MC: Massif Central, VB: Valence Basin, IC: Ile Crémieu, BG: Bresse Graben, LSZ: La Serre Zone, HS: Haute-Saône Plateau, EJ: External Jura, IJ: Internal Jura, MB: Molasse Basin, URG: Upper Rhine Graben, BF: Black Forest, RBTZ: Rhine-Bresse Transfer Zone. BEL: Belledonne Massif, AL: Aiguilles-Rouges Massif, MB: Mont Blanc Massif, AA: Aar Massif, GM: Gotthard Massif.

al. 2013; Suter and Lüthi 1969) to constrain the thickness within some locations in the Internal Jura.

Resulting model

The Upper Malm thickness model (Fig. 4.8) reflects a several hundred metres deep basin, becoming deeper towards the south-east, in the area of the Molasse Basin. An exceptionally thick series of up to 900 m of limestone and dolomite was deposited in a depo-centre south of Geneva. The basin centre prolongs southwards and into the Alpine domain, which is not any more depicted on the UMA isopach map (Fig. 4.8). Thrusts within the UMA are hardly documented in boreholes (e.g. HU-2, FAY-1), illustrating that high thickness values are entirely sedimentary. Some minor thickness changes of the UMA along Mio-Pliocene strike-slip faults such as the Pontarlier fault and the La Serre fault are distinguished on seismic models (Gruber 2017).

In the area of the Jura Mountains, only a hand full of boreholes document the full stratigraphy through the Upper Malm, as the top of the UMA is commonly eroded in the Internal Jura and in the central External Jura, UMA is completely eroded. The thickness of the UMA limestones is interpolated to be rather constant between 300 and 350 m in the Central Jura and increases drastically in the southern Jura. In contrast to that, the thickness is reduced to partially less than 50 m in the Eastern Jura (Fig. 4.8). The UMA thickness model (Fig. 4.8) shows a NW-SE striking high zone existing during Upper Late Jurassic, roughly along a line Zurich-Basel-Belfort.

Continued development of basins at Louhans and Bourg precede the deepest locations of the future Cenozoic Bresse Graben (Fig. 4.8).

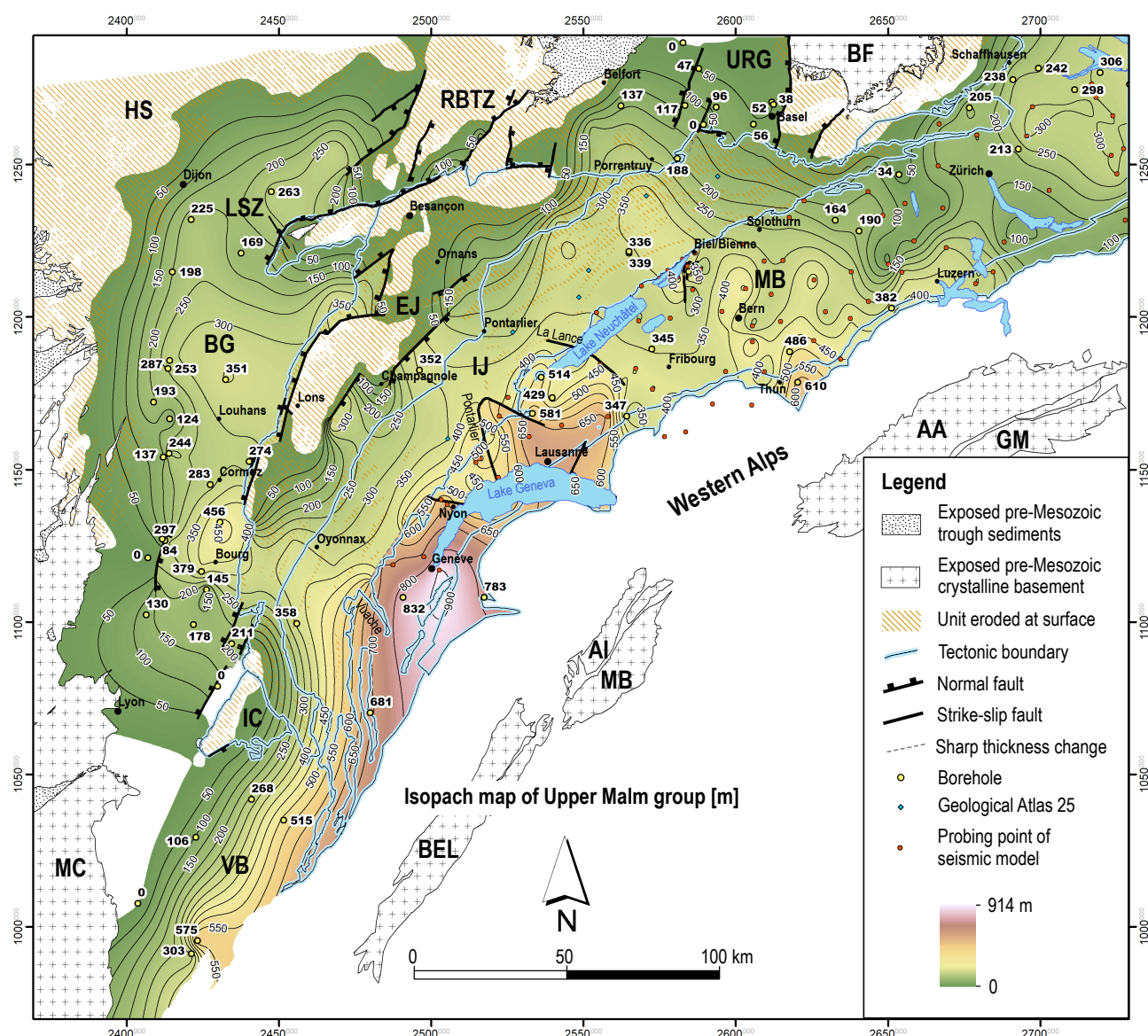


Fig. 4.8 – Isopach map of Upper Malm Group. Present day tectonic domains are MC: Massif Central, VB: Valence Basin, IC: Ile Crémieu, BG: Bresse Graben, LSZ: La Serre Zone, HS: Haute-Saône Plateau, EJ: External Jura, IJ: Internal Jura, MB: Molasse Basin, URG: Upper Rhine Graben, BF: Black Forest, RBTZ: Rhine-Bresse Transfer Zone. BEL: Belledonne Massif, AI: Aiguilles-Rouges Massif, MB: Mont Blanc Massif, AA: Aar Massif, GM: Gotthard Massif.

Interpretation

The UMa thickness model (Fig. 4.8) shows that UMa does not exist in the URG north of Belfort. As for example, in the boreholes SCG-2 and BLO-1, UMa is absent and Lower Malm is covered by Eocene sediments. This suggests that the area north of Belfort was either already exposed at the end of Jurassic or alternatively, that the area experienced uplift and high erosion before Eocene. Bourgeois et al. (2007) suggests long-wavelength lithospheric buckling leading to fast uplifts in the URG north of Belfort (Fig. 4.8) during Upper Cretaceous and Paleocene to explain the absence of Cretaceous sediments. Note that the location coincides with a Moho peak in the Moho depth map (published in Ziegler and Dèzes 2006 after Dèzes and Ziegler 2002), which prolongs WSW into the Massif Central. Therefore, I speculate that lithospheric buckling (as suggested by Bourgeois et al. 2007) extended west-south-westwards across the former Morvan-Vosges Sill. If this is

the case, then the erosion of UMa and LMa in the Haute-Saône Plateau started before Eocene, too. This presumption is reflected in the UMa and LMa thickness models, where the Haute-Saône Plateau is shown as limit of deposits, as I intend to represent the thickness of sediments in Middle Miocene.

Erosion of Upper Malm sediments in the area of the Jura Mountains are rather in connection with uplifts induced by the formation of the ECRIS in Eocene and Oligocene. Therefore, UMa was at least partially eroded in the External Jura before the formation of the JFTB happened. This is confirmed in boreholes Blyes-101 (BL-101) or Courlans-1 (CUS-1), which lie at the eastern periphery of the BG. These boreholes contain Tertiary graben sediments that overlie the Dogger Group and Sequanian unit, respectively. Additionally, uplifts induced by forebulging of the peripheral Alpine flexural basin presumably overlap in the area of the RBTZ or north of it (Burkhard and Sommaruga 1998; Laubscher 1992). However, uplifts

due to forebulging are not expected to be more than 300 m at the forebulge crest (Decelles 2012; DeCelles and Giles 1996), whereas uplifts induced by ECRIS rifting has probably reached up to 1500 m in the area of the Jura Mountains (Bourgeois et al. 2007).

4.5 CRETACEOUS SERIES

Data processing: choice of source, faults

The Cretaceous series is widely eroded within the area of the JFTB (Fig. 4.9) but preserved within synclines of the Internal Jura. I added several NNE–SSW and ENE–WSW striking normal faults in the JFTB along which the thickness of Cretaceous sediments changes rapidly. These normal faults are all in connection with the formation of the Eocene to Oligocene ECRIS, comprising the eastern BG border faults that are partially hidden underneath the detached JFTB cover and the normal fault system constituting the northern limit of the La Serre Zone (Fig. 4.9). Two faults in the BG are added due to abrupt changes of the Cretaceous thickness between boreholes. Additional data points in the Molasse Basin are from seismic models of Gruber (2017) and Landesgeologie (2017).

Resulting model

The Cretaceous Group is missing widely within the study area. It is not documented within the Upper Rhine Graben or east of Biel (Fig. 4.9). In the Cretaceous thickness map (Fig. 4.9), Cretaceous outcrops in the JFTB are indicated, which mainly lie within synclines.

The eastern limit of Cretaceous deposits follows a roughly NNW–SSE striking line Thun–Bern–Biel (Fig. 4.9). Therefore, Cretaceous deposits are absent in the eastern SMB, the eastern Jura and the URG. In the eastern SMB, the Eocene Bohnert-Formation is commonly followed by USM deposits starting in Chattian (Oligocene) times. In some boreholes, UMM starting in Rupelian (Eocene) was also deposited. In summary, Cenozoic sediments are deposited onto an eroded surface of carbonates or marls of the Malm Group within the Molasse Basin (e.g. Rupoldsried-1, Linden-1, Altshofen-1, Oftringen-1, Schlattigen-1). In the area of the URG, the Malm Group is covered by Cenozoic graben sediments setting in Eocene.

Cretaceous sediments are also missing on the Ile Crémieu and partially in the eastern Bourg Basin. East of Bourg, Upper Malm sediments are overlain by Oligocene sediments (see boreholes Bresse-104-bis and Bresse Sud-1 in Supplementary Material C) showing that Cretaceous was partially absent when the main rifting phase of the Bresse Graben initiated. Similarly, west of Lons-le-Saunier in the borehole Courlans-1 (CUS-1), a subsided block underneath the detached Jura cover reveals Upper Malm directly superposed by Oligocene deposits, suggesting that Cretaceous deposits were eroded during Eocene to Early Oligocene, on uplifted graben shoulders. Differential subsidence can be thus concluded in the Bresse Graben, where the Cretaceous Group is

partly missing, partly present. From borehole comparison between BR104-bis and BR-2 (Fig. 3.4), I also propose inversion of a former normal fault during Upper Cretaceous or Palaeocene, west of Bourg.

Youngest ascertained Cretaceous sediments in boreholes across the study area are from Upper Cretaceous. Confirmed Turonian sediments occur in boreholes Montcoy-1 and Montcoy-2 (MCY-1, MCY-2), which lie in the BG to the north-west of Louhans. Debrand-Passard et al. (1984) interprets slightly younger Cretaceous ages in these boreholes, dating to Coniacian (i.e. Lower Senonian). The youngest Cretaceous deposits exposed in the Jura Mountains are from Coniacian times and belong to the Narlay-Formation (Strasser et al. 2016, the type locality of the formation lies south of Champagnole, see Fig. 4.9). Consequently, the Cretaceous (Coniacian) to Eocene (Lutetian) hiatus (Fig. 2.17) in the detached NAF, BG and URG spans at least about 38 Ma, from about 86 Ma to 48 Ma (using absolute ages according to the International Chronostratigraphic Chart, Cohen et al. 2020, see Fig. C on page 197).

The Cretaceous thickness model (Fig. 4.9) represents the thickness after Eocene to Early Oligocene erosion. Note that in the JFTB, the remaining Cretaceous thickness of sediments is reconstructed that was involved during Mio-Pliocene folding and thrusting. Although Cretaceous carbonates are mostly exposed in synclines today, more Cretaceous sediments are hidden underneath main thrusts in the Internal Jura, having a rough thickness as proposed in the Cretaceous thickness model (Fig. 4.9). The thickness in the Molasse Basin reflects the present day situation, which likely contains some local thickening signatures in connection with Mio-Pliocene thin-skinned tectonics.

Interpretation

During Lower Cretaceous, the area of the Bresse Graben was a shallow carbonate platform and differential subsidence led to several depo-centres. The thickest deposits are less than ~300 m thick and the extent of these basins is small, only a few tens of kilometres (Fig. 4.9). According to Strasser et al. 2016 and references therein, the area of the Jura Mountains belonged to the northern passive margin of the Tethys Ocean. The southern Molasse Basin (south of Geneva) belonged to the deeper parts of the platform, lying on the Helvetic shelf.

During Upper Cretaceous and Palaeocene, the whole study area was exposed as commonly no sediments younger than Coniacian are documented (sedimentation might have continued in Santonian in some restricted locations). Locally, structures were inverted (i.e. inversion of Limonest fault west of Bourg, section §3.6), supposedly in connection with the beginning collision of Africa and Europe (Ziegler and Dèzes 2005). The regional absence of Cretaceous deposits in the east of the study area is likely connected to an elevated lithosphere, which either completely prevented sedimentation already during Lower Cretaceous or alternatively, led to erosion of Cretaceous sediments during Upper Cretaceous and Palaeocene times. The elevated lithosphere signature has a

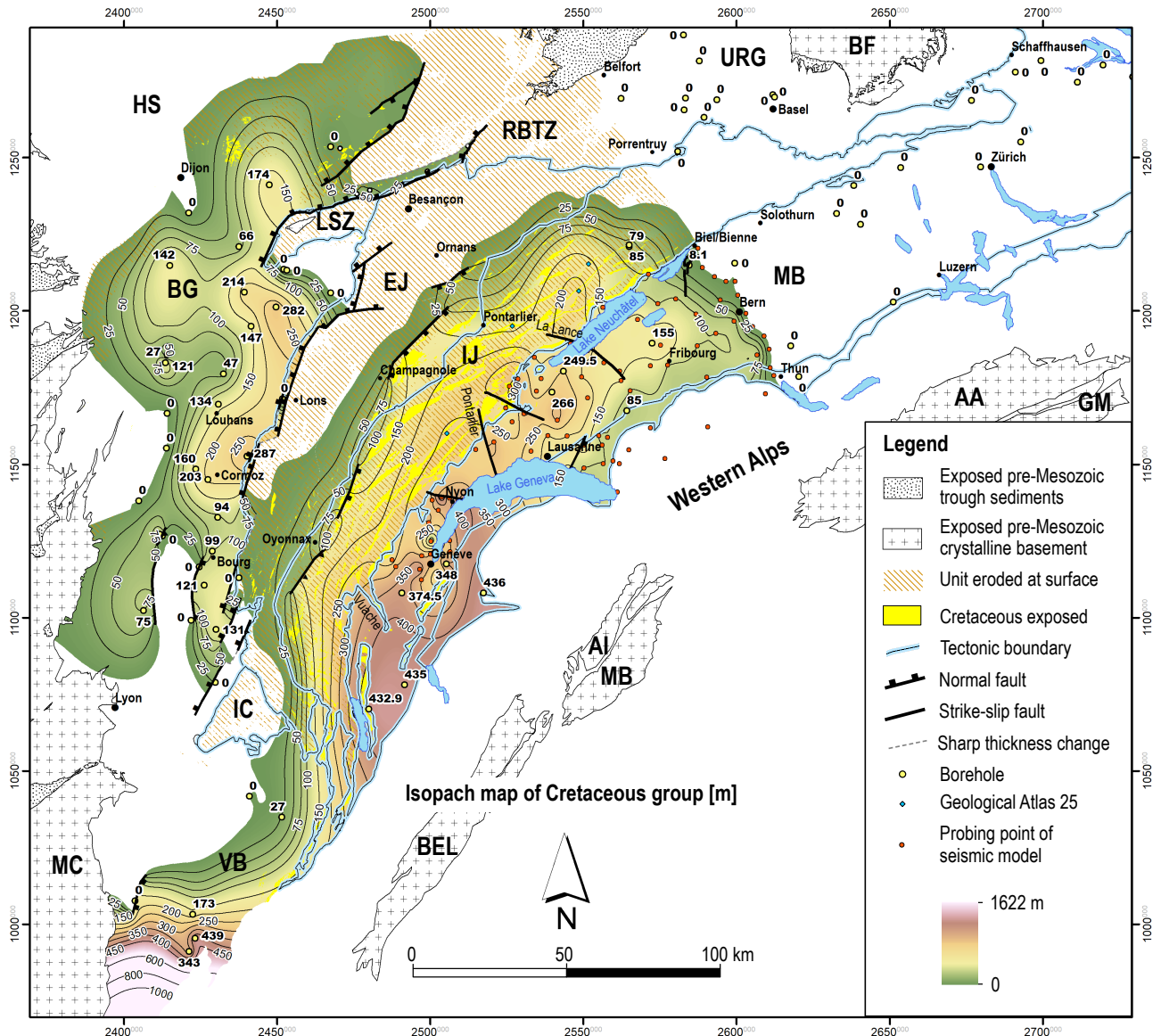


Fig. 4.9 – Isopach map of Cretaceous Group, showing remaining thickness after Eocene-Oligocene erosion in the External Jura, IC and RBTZ. Present day tectonic domains are MC: Massif Central, VB: Valence Basin, IC: Ile Crémieu, BG: Bresse Graben, LSZ: La Serre Zone, HS: Haute-Saône Plateau, EJ: External Jura, IJ: Internal Jura, MB: Molasse Basin, URG: Upper Rhine Graben, BF: Black Forest, RBTZ: Rhine-Bresse Transfer Zone. BEL: Belledonne Massif, AI: Aiguilles-Rouges Massif, MB: Mont Blanc Massif, AA: Aar Massif, GM: Gotthard Massif.

NNW–SSE trend, parallel to the well documented eastern limit of Cretaceous sediments in the SMB.

The erosion of Cretaceous towards the front of the Jura and in the External Jura undoubtedly follows faults that were active during Eocene and Oligocene rifting. It suggests that the erosion of the Jura cover is mainly due to the ECRIS rifting phase (Bourgeois et al. 2007; Dèzes et al. 2004; Illies 1962). A weaker signature of flexural forebulging is suspected to be hidden within the dominant ECRIS uplifting signature (Burkhard and Sommaruga 1998; Laubscher 1992).

The thickness of Cretaceous sediments in the Internal Jura is at maximum 250 to 300 m and about 290 m in the thickest depo-centres in the area of the Bresse Graben (Fig. 4.9). Therefore, it can be speculated that before Eocene-Oligocene rifting and connected erosion in the External Jura, the thickness of Cretaceous sediments in the External Jura was similar, at maximum 300 m.

4.6 TOTAL MESOZOIC THICKNESS

The map Fig. 4.10 shows the summed up thickness of all previously described Mesozoic thickness models. In the Internal JFTB, a maximum Mesozoic thickness of about 2600 m occurs at the centre (Fig. 4.10), whereas at the southern and eastern tips of the JFTB, the Mesozoic cover is only a few hundred metres thick. Towards the front of the External Jura, north of Lons-le-Saunier and at Besançon, the Mesozoic cover is thoroughly eroded, which is connected to Eocene-Oligocene uplifts of graben shoulders during rifting of the ECRIS. Therefore, towards the front of the JFTB, the Mesozoic cover was already reduced before the JFTB has formed in Mio-Pliocene. The thickness centre north of Lake Geneva is in connection with tectonic thickening (e.g. duplexing) of incompetent evaporites or clay-rich sediments in the Ke, Do and Li.

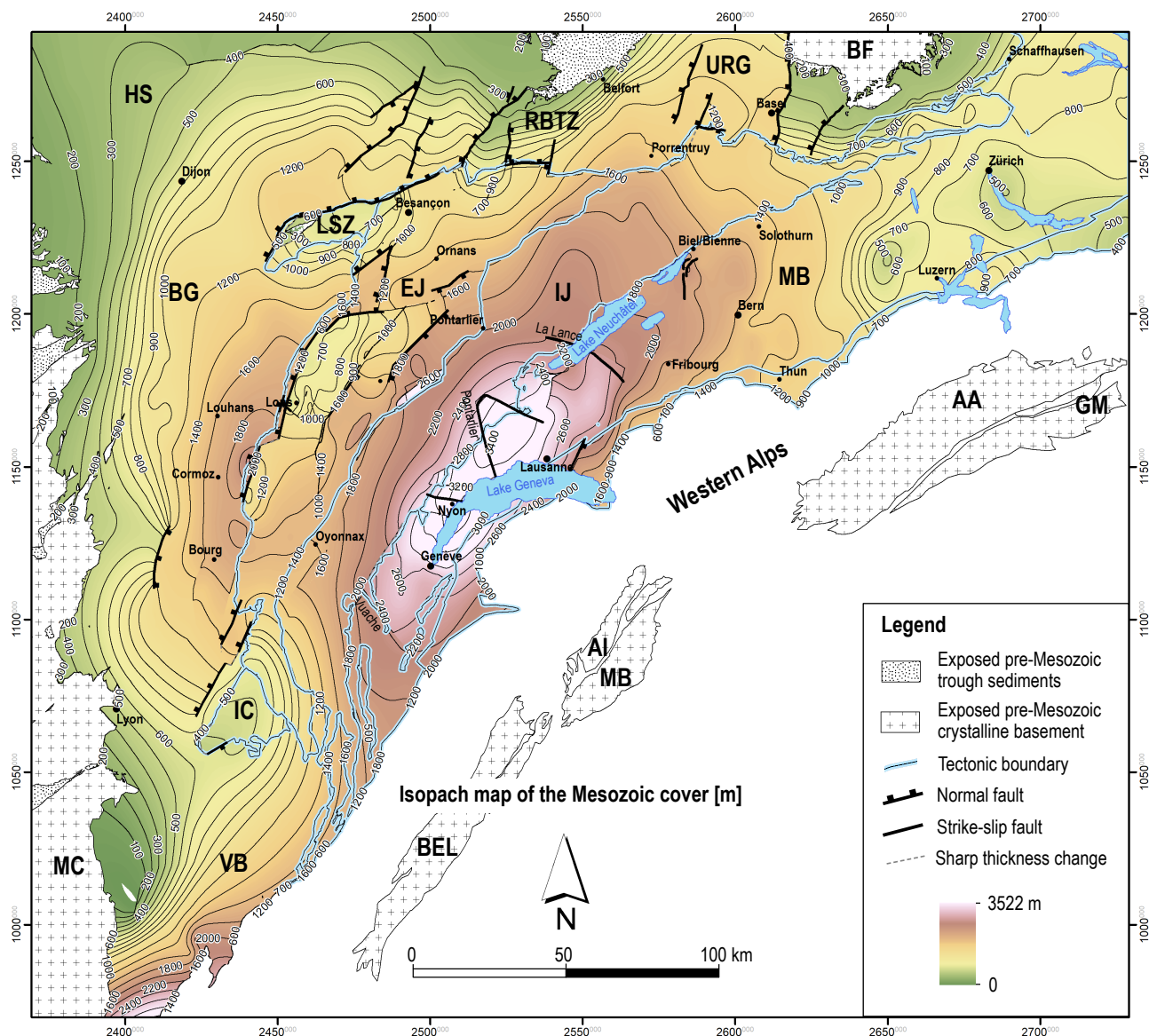


Fig. 4.10 – Total Mesozoic thickness. Towards the front of the JFTB, the exposed Mesozoic cover is eroded following faults that were active during ECRIS graben formation. The remaining thickness of the Mesozoic cover is a few hundred metres. Present day tectonic domains are MC: Massif Central, VB: Valence Basin, IC: Ile Crémieu, BG: Bresse Graben, LSZ: La Serre Zone, HS: Haute-Saône Plateau, EJ: External Jura, IJ: Internal Jura, MB: Molasse Basin, URG: Upper Rhine Graben, BF: Black Forest, RBTZ: Rhine-Bresse Transfer Zone. BEL: Belledonne Massif, AI: Aiguilles-Rouges Massif, MB: Mont Blanc Massif, AA: Aar Massif, GM: Gotthard Massif.

4.7 TERTIARY GROUP

Data processing

The MB is additionally constrained by data points of seismic models (Gruber 2017; Landesgeologie 2017; Sommaruga et al. 2012). In the BG and Valence Basin, additional thickness values are calculated from the Tertiary depth map of Alabouvette et al. (1984). Faults in the BG are based on Debrand-Passard et al. (1984) and Alabouvette et al. (1984). Additional thickness values in the URG are according to Rotstein et al. (2006), who follow Doebl and Olbrecht (1974). The thickness of the Jura Molasse is locally constrained in map sheets of the Swiss geological Atlas 1:25'000 (Aubert 1941; Muhlethaler 1930; Suter and Lüthi 1969). East of Louhans, the maximum depth of the Louhans Basin is constrained on a seismic line in Blanc et al. (1991).

Resulting model

The Tertiary thickness model (Fig. 4.11) shows an increase of Tertiary sediments in the SMB towards the Alps, with a maximum thickness of about 5800 m. The MB is notably thinner to the south of Lausanne, where a maximum thickness of about 1260 m is reached close to Geneva. The thickening of the Tertiary Molasse sequences towards the Alps is commonly attributed to flexural bending of the Northern Alpine Foreland, with the Molasse sequence constituting the foredeep depo-zone (Decelles 2012; DeCelles and Giles 1996). The Molasse sequence reaches into the Internal Jura, where Tertiary sediments are preserved in synclines. The north-west limit of Tertiary sediments in the JFTB (Fig. 4.11) follows outcrops documented in geological maps. The Bresse Graben shows three main depocentres, which are the Bourg Basin, the Louhans Basin and the Chalon Basin, lying south of Dijon. The thick-

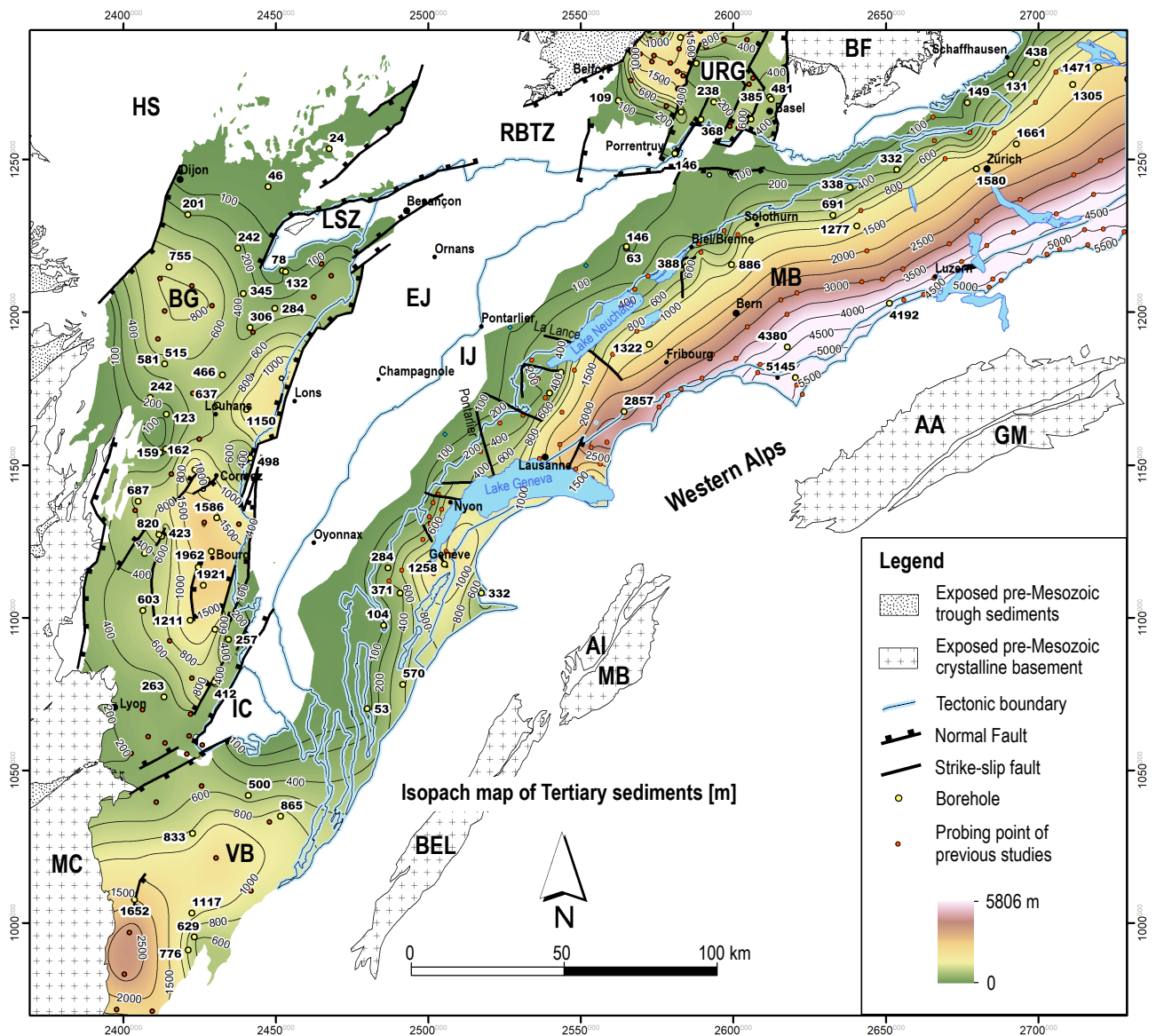


Fig. 4.11 – Tertiary thickness map. Present day tectonic domains are MC: Massif Central, VB: Valence Basin, IC: Ile Crémieu, BG: Bresse Graben, LSZ: La Serre Zone, HS: Haute-Saône Plateau, EJ: External Jura, IJ: Internal Jura, MB: Molasse Basin, URG: Upper Rhine Graben, BF: Black Forest, RBTZ: Rhine-Bresse Transfer Zone. BEL: Belledonne Massif, AI: Aiguilles-Rouges Massif, MB: Mont Blanc Massif, AA: Aar Massif, GM: Gotthard Massif.

est values in the Bourg Basin are at about 2000 m, in the Louhans Basin at about 1400 m, whereas the Chalon Basin shows a maximum Tertiary thickness of about 830 m (Fig. 4.11). The BG is separated from the Valence Basin to the south by a horst in between the Ile Crémieu and the Massif Central, which is called the Vienne–Chamagnieu Sill (Laubscher 1985) or alternatively, Lyon Sill (Sissingh 1998). The thickest Tertiary sequence in the URG is about 1600 m thick and is deposited in the Dannemarie Basin, lying east of Belfort (Fig. 4.11). As the top of Tertiary sediments in the study area is relatively flat, the thickness model (Fig. 4.11) reflects the relative depth of the various basins.

Interpretation

Molasse deposits in the Molasse Basin and the JFTB constitute the foredeep depo-zone (Decelles 2012; DeCelles and Giles 1996). Note that the JFTB is displaced up to 30 km north-westwards at its centre (Affolter and Gratier

2004; Philippe et al. 1996) and therefore, the original maximum extent of the Molasse basin (the foredeep) was further SE. Tertiary deposits in the Eastern Jura, north of Biel and Solothurn, were partially deposited in a prolongation of the Rhine Graben (Piquerez et al. 2012, also see Fig. 2.19) and therefore, they do not indicate the foredeep depo-zone. The flexural uplift of the forebulge can be calculated from the negative deflection of the lithosphere (Allen and Allen 2013). The deflection of the lithosphere is represented by the depth of the foreland flexural basin. At the given maximum depth of the flexural foreland basin of 5800 m east of Lucerne (Fig. 4.11), the calculated flexural uplift of the Alpine forebulge (formula for broken plates according Allen and Allen 2013) is in the range of about 390 m.

4.8 CONCLUSION

4.8.1 Tectonic signatures in the Mesozoic and Cenozoic cover

The Mesozoic sedimentary record in the study area, visualised in interpreted thickness maps that base on seismic models and boreholes, reveals different tectonic signatures imprinted during the Mesozoic and Cenozoic evolution, before the JFTB formed in Mio-Pliocene. These signatures comprise the following events:

- The continued evolution of the Burgundy Trough in Triassic Times, which initiated in Permian along inherited ENE–WSW striking Variscan structures (Boigk and Schöneich 1974). A depo-centre of the Early Triassic Burgundy Trough is roughly at the centre of the present day JFTB and the southern and eastern limits of the present day JFTB lie on the rim of the Early Triassic basin (Fig. 4.2). The Morvan–Vosges Sill constitutes the northern rim of the Triassic basin.
- Lower and Middle Jurassic sediments indicate fast differential subsidence during the opening of the Tethys. Some basins constitute the first pre-dispositions of the URG and BG, seemingly following inherited NNE–SSW striking Variscan structures.
- Upper Cretaceous to Early Eocene lithospheric uplift and erosion is interpreted from the Cretaceous to Eocene hiatus. A rough ENE–WSW uplift signature proceeds across the URG north of Belfort and continuous in the Haute-Saône Plateau north of Dijon, roughly coinciding with the Triassic Morvan–Vosges Sill. Authors such as Bourgeois et al. (2007) and Dèzes et al. (2004) suggest a model of lithospheric long-wavelength folding in response to beginning collision of Africa and Europe in Upper Cretaceous times.
- A lithospheric uplift signature with a NW–SE orientation is distinguished, indicated by a thinned UMa sequence roughly along a line between Zurich–Basel and the absence of the Cretaceous sequence east of a NW–SE striking line Thun–Bern–Biel. The eroded top of the UMa is covered by Eocene deposits, suggesting that NW–SE striking lithospheric uplift happened contemporaneously to long-wavelength lithospheric buckling (Bourgeois et al. 2007; Lefort and Agarwal 1996, 2002) between Upper Cretaceous and Early Eocene. The NW–SE lithospheric signature is roughly perpendicular to lithospheric buckle folds.
- Erosion of ECRIS rift shoulders is documented by a base Oligocene unconformity, close to main border faults of the BG and URG rift segments. Some tilted blocks that subsided in Oligocene document that several hundreds of metres of the Mesozoic cover were eroded during initial Eocene rifting. Therefore, the Cr, UMa, LMa and Do are notably eroded in the External Jura, and the erosion is parallel to ECRIS border faults. Erosion in connection with rifting happened above uplifted rift-shoulders of the eastern BG, comprising the Ile Crémieu, the front of the External Jura, as well as the rift shoulders of the URG, i.e. the BF and Vosges

massifs.

Flexural bending of the Alpine foreland cannot be extracted from the Mesozoic sedimentary record. However, the transgression of the Oligocene to Miocene Molasse sediments in the MB documents the evolution of the Alpine flexural foreland basin (e.g. Ford et al. 2006). In addition, Eocene siderolithic sediments in the MB supposedly document the evolution of the Alpine forebulge, which migrated north-westwards in front of the flexural Alpine basin (Burkhard and Sommaruga 1998; Laubscher 1992).

4.8.2 Tectonic thickening of Mesozoic units in Cenozoic times

Tectonic thickening predominantly occurs within lithostratigraphic groups containing incompetent evaporites, marl or clay. Especially the Mk, Ke, Li and Do are proposed to contain strong signatures of tectonic thickening. The thickest locations of the Ke, Mk, Li and Do within the detached MB and the JFTB are attributed to Mio-Pliocene tectonic thickening, and such thickness centres therefore do not necessarily show the original depo-centres. However, strong tectonic thickening is controlled by the original depo-centres, as deformation preferably concentrates in the thickest anhydrite and marl series. Therefore, thickness peaks of the Mk and Ke in the area of the Molasse Basin reflect the activity of the basal décollement during Mio-Pliocene, indicating displacement peaks within individual lithostratigraphic groups. Thickness peaks in the Do and Li are interpreted as tectonic thickening due to upper detachments (oblique reflectors are observed in seismic lines).

Eocene-Oligocene rifting led to the formation of normal faults in the study area, e.g. the eastern BG border faults that are hidden underneath the thrust front of the JFTB and the border faults of the URG. The Ke and Mk are interpreted to be tectonically thickened close to some ECRIS border faults, as a result of evaporites that filled gaps during rifting.

4.8.3 Cenozoic erosion and consequences on the formation of the JFTB

Boreholes CUS-1, JR-102bis and BL-101, penetrating subsided blocks close to the eastern BG border fault, show that the Cretaceous Group was entirely eroded before Oligocene. In the case of BL-101 (at the western border of the Ile Crémieu), the Malm Group is also missing and the Dogger Group is overlain by Oligocene rift sediments. This shows that several hundreds of metres (at least 600 m, e.g. BL-101) of Mesozoic sediments were eroded during initial rifting (starting in Lutetian according to Sissingh 1998) and connected graben shoulder uplift in the area of the future External Jura (see erosion model in Fig. B.3). Consequently, exposures of the Dogger Group and even some Triassic units in the External Jura are predominantly due to pre-JFTB erosion. An erosion and thinning out of the Mesozoic cover towards the NW has important consequences on the JFTB formation:

- The ratio between the thickness of the décollement

zone and the thickness of the detached cover (hanging wall) increases towards the front of the detached JFTB.

- The reduced thickness of the cover towards the JFTB front invariably leads to smaller folds in the External Jura than in the Internal Jura, as a result of geometric relations between layer thickness and fault angles (Allemand and Brun 1991).
- A reduced lithostatic pressure on the décollement towards the front changes the mechanical conditions within the décollement.
- Due to the thin cover towards the front, infiltration of meteoric water into the décollement towards the front is more likely, reducing the friction of the evaporite décollement.

The JFTB formation led to an additional regional uplift of the Jura platform, due to NW displacement of up to ~30 km (Affolter and Gratier 2004; Philippe et al. 1996) on the moderately inclined basement. As a sample calculation, on a 3° south-eastward inclined basement (Sommaruga 1997), 30 km north-westward displacement of the JFTB leads to ~1.6 km uplift. This has certainly led to an additional regional erosion in the detached NAF, next to locally high incision rates along the centre of anticlines.

5 - GEOLOGICAL CROSS-SECTIONS

5.1 INTRODUCTION

The oil industry has diligently explored the External Jura for gas and oil in the past, whereas the subsurface of the Internal Jura is comparatively little investigated. There is good geological reason to concentrate exploration on the External Jura. The Triassic units that were commonly targeted (see Sommaruga 1999 for a compilation of oil occurrences) are not deeply buried and the relatively flat topography of the External Jura (especially the plateaus) facilitate the access and logistics of surveys. Therefore, boreholes as well as seismic lines are much more frequent in the External Jura than in the Internal Jura. Less complex deformation and the reduced thickness of the Mesozoic cover improve the visibility of near basement structures in seismic lines. Also quite importantly, the External Jura does not feature kilometeric duplications of the Mesozoic sequence, which could be mistaken for highs of the pre-Mesozoic basement. Owing to all these geological factors and available data, it is possible to assess the basement topography in the External Jura with high confidence, unlike in the Internal Jura. Many previous studies in the External Jura confirmed faults in the mechanical basement and unmistakably revealed that *faisceaux* often correlate with faults in the pre-Mesozoic basement (Bièvre and Mercier 2010; Chauve et al. 1988; Madritsch 2008; Martin and Mercier 1996; Michel et al. 1953; Mugnier and Vialon 1984; Wildi and Huggenberger 1993). In comparison to this, basement faults underneath the Internal Jura remain predominantly hypothetical or simply unrecognised.

In this chapter, I present five cross-sections across the External Jura (one section also includes the Internal Jura) that illustrate the principal structural situation. Notable features of these cross-sections are extensional systems in the detached cover and an inferred topography of the pre-Mesozoic basement. I paid special attention to infer and quantify steps in the pre-Mesozoic basement, in order to discuss possible basement-controlled structures in the detached Mesozoic cover. Note that the subsequent cross-sections are constructions from surface data and boreholes, only locally constrained by a seismic line. I did not

conduct kinematic modelling on these sections in order to test structures and instead, I discuss alternate models for particular structures in question.

5.2 METHODS

Cross-sections across the External Jura are constructed based on geological maps 1:50'000 provided by the French Geological Service (BRGM 2004). The principal subdivision of lithostratigraphic units is based on the stratigraphic description in Fig. 2.17. Folds and faults are re-evaluated by a combined analysis of digital elevation models (IGN-F 2018; NASA 2014, see Fig. C), aerial photographs and previously mentioned geological maps (including geological units, interpreted faults and dip-data). An extract of the structural map created for this study is shown in Fig. 5.1. The depth and thickness of lithological horizons are locally constrained by boreholes that are projected perpendicular into the sections. Steps in the pre-Mesozoic basement of the JFTB are inferred from the surface geology. The thickness of the Keuper Group (Upper Triassic unit) varies drastically as it comprises halite-bearing layers wherein the Mio-Pliocene basal décollement of the JFTB predominantly concentrates. Evaporites of the Muschelkalk Group (Middle Triassic unit) were possibly involved to a minor degree in the basal décollement, too (halite-bearing Middle Triassic layers are documented in boreholes of the External Jura, north of Champagnole, see Fig. 4.3 on page 56). However, except for restricted locations such as the Valempoulières gas-field north of the *Faisceau de l'Heute* (Deville 2021; Philippe et al. 1996, see location in Fig. 2.2), no major tectonic activity in Middle Triassic layers is documented in boreholes of the Plateau Jura. Therefore, I resolved illustrating the Muschelkalk Group in the following sections as part of the autochthonous mechanical basement.

Section A reaches into the Molasse Basin (Fig. 5.2a) and in addition to boreholes, I used vertical depth grids of Sommaruga et al. (2012) to constrain the depth of horizons in the ESE. The complex structural style at depth of

the south-eastern segment of Section B (Fig. 5.2b) is in agreement with the seismic line CM16S (Fig. 5.2d, courtesy of Celtique Energie Petroleum Ltd., 1971, processed by REXIMseis Ltd.).

Indicated throws of basement-steps in the External Jura (Fig. 5.2 and 5.3) contain an uncertainty of about ± 100 m.

Smaller graben structures and normal faults identified in the detached Mesozoic cover (hanging wall of the JFTB) are not prolonged into the basement as they are considered pre-JFTB extensional structures in connection with Eocene to Oligocene rifting or possibly with Cenozoic flexural bending of the Alpine foreland. Therefore, normal faults are detached and transported towards the foreland. Consequently, extensional structures are conceptually drawn to be sheared off and displaced north-westwards above the basal décollement of the JFTB. I indicate Miocene to Pliocene displacements from block restoration models of Philippe et al. 1996 and Affolter and Gratier (2004) at the bottom of sections A to E (Fig. 5.2 and 5.3), which allows backtracing the original position of cover structures in order to evaluate possible triggers in the mechanical basement (i.e. basement faults). The designation of structural zones follows the structural map in Fig. 2.2.

5.3 SECTION A: CUISEAUX – PLATEAU DE CHAMPAGNOLE – INTERNAL JURA

Section A (Fig. 5.2a) is a transect across the entire JFTB, starting in the Bresse Graben, crossing the southern plateaus and faisceaux of the External Jura, the Internal Jura and ending in the French Molasse Basin NW of Geneva. The depth of lithological units at the NW front of the Section A in the Bresse Graben (Fig. 5.2a, between along-strike position km 0 and 2) is constrained by the boreholes Cuiseaux-1 (CUI-1) and Bois-des-Chaux-1bis (BOX-1-Bis). I interpret tilted blocks in order to fit structural altitudes of lithological units in these boreholes. At CUI-101, the Cretaceous series is missing and Oligocene graben sediments are deposited on the Upper Malm Group. Note that in contrast to CUI-101, the Cretaceous Group at BOX-1-Bis is preserved. The basement is substantially offset underneath the front of the JFTB (between km 3 to 5, underneath the frontal Faisceau lédonien). The total vertical offset of the basement is about 1.6 km between BOX-1-Bis and the front of the JFTB. The basement beneath the frontal Faisceau lédonien (roughly between position 3 to 7 km) is reconstructed by interpolation of surface information alone and therefore not well constrained at depth. An interpreted seismic line of Guellec et al. (1990), which is parallel to Section A (Fig. 5.2a) and about 11 km to the south, reveals a frontal horst (Poisoux horst, see location in overview map Fig. 5.2) that is separated by a roughly 4 km wide and 1.5 km deep graben from the high basement beneath the JFTB, yet it is not possible to confirm the presence of this small graben in Section A (Fig. 5.2a) with the currently available geological data. Generally, the basement is highest beneath the frontal Faisceau lédonien

and deepens towards the ESE. Discrete important basement steps that are interpreted in Section A (Fig. 5.2a) show heights between 150 to 450 m and constitute upward steps in respect to the transport direction of the JFTB. Consequently, the basal décollement has to ramp upwards in order to overcome these basement steps.

The External Jura between positions 16 km and 31.5 km shows two plateaus revealing different structural altitudes. The Plateau de Valouse is about 150 m higher than the Plateau de Champagnole to the ESE (Fig. 5.2a). The mechanical basement of the Internal Jura dips about 3° to the ESE (between positions km 31.5 to 57.5) and lies at about -2 km a.s.l. in the French Molasse Basin (Fig. 5.2a). In the Internal Jura, between km 42 and 57 (Fig. 5.2a), I interpret substantial kilometric duplication of the detached Mesozoic cover in order to comply with the basement depth, which is inferred from seismic depth maps of Sommaruga et al. (2012). The interpreted structures at depth are hypothetical and a reliable pinning down of basement faults is impossible with the available geological information.

5.4 SECTION B: FAISCEAU LÉDONIEN – PLATEAU DE NOZEROT

Cross-section B (Fig. 5.2b) starts in the Bresse Graben, proceeds across faisceaux and plateaus of the External Jura and ends in the Internal Jura. The basement in the Bresse Graben is about 1400 m deeper than the basement at Grozon-1 (GRZ-1). There are surprisingly little compressive structures in the External Jura along the trace of section B and instead, abundant normal faults are identified, which are cut off by the basal décollement of the JFTB (Fig. 5.2b). The basement is highest at GRZ-1 and deepens towards the south-east of the section.

The Plateau lédonien, Plateau de Champagnole and Plateau de Nozeroy reveal different structural altitudes, which are constrained by boreholes (VSP-1, VLP-2, TLN-1). At Vallengpoulières, several oil-exploratory boreholes document that the Muschelkalk Group thrusts the Keuper Group salt system (see boreholes VLP-1, VLP-2 and VLP-101, Fig. 5.2b). This is interpreted in Section B as a Middle Triassic sliver that is sheared off due to a shortcut associated with a basement step. The Middle Triassic sliver is thus incorporated in the hanging wall (Fig. 5.2b, along-strike position km 21 to 24), similar to an interpretation in Philippe et al. (1996).

The l'Heute structure (Fig. 5.2b, position km 21) is shown as a roughly 200 m wide graben restricted to the detached Mesozoic cover. Such extensional structures in the Jura Mountains are classically known as «pincée» (Glangeaud 1944) and they are commonly given an Oligocene age (see Homberg et al. 2002 and references). Structural interpretation suggests that the «Pincée de l'Heute» is inverted above the basal décollement of the JFTB south of Section B, where the structure is distinguished as a faisceau featuring folds and thrusts (see location in overview map of Fig. 5.2). Note that the Pincée de l'Heute in Section B (Fig. 5.2b) lies above a normal

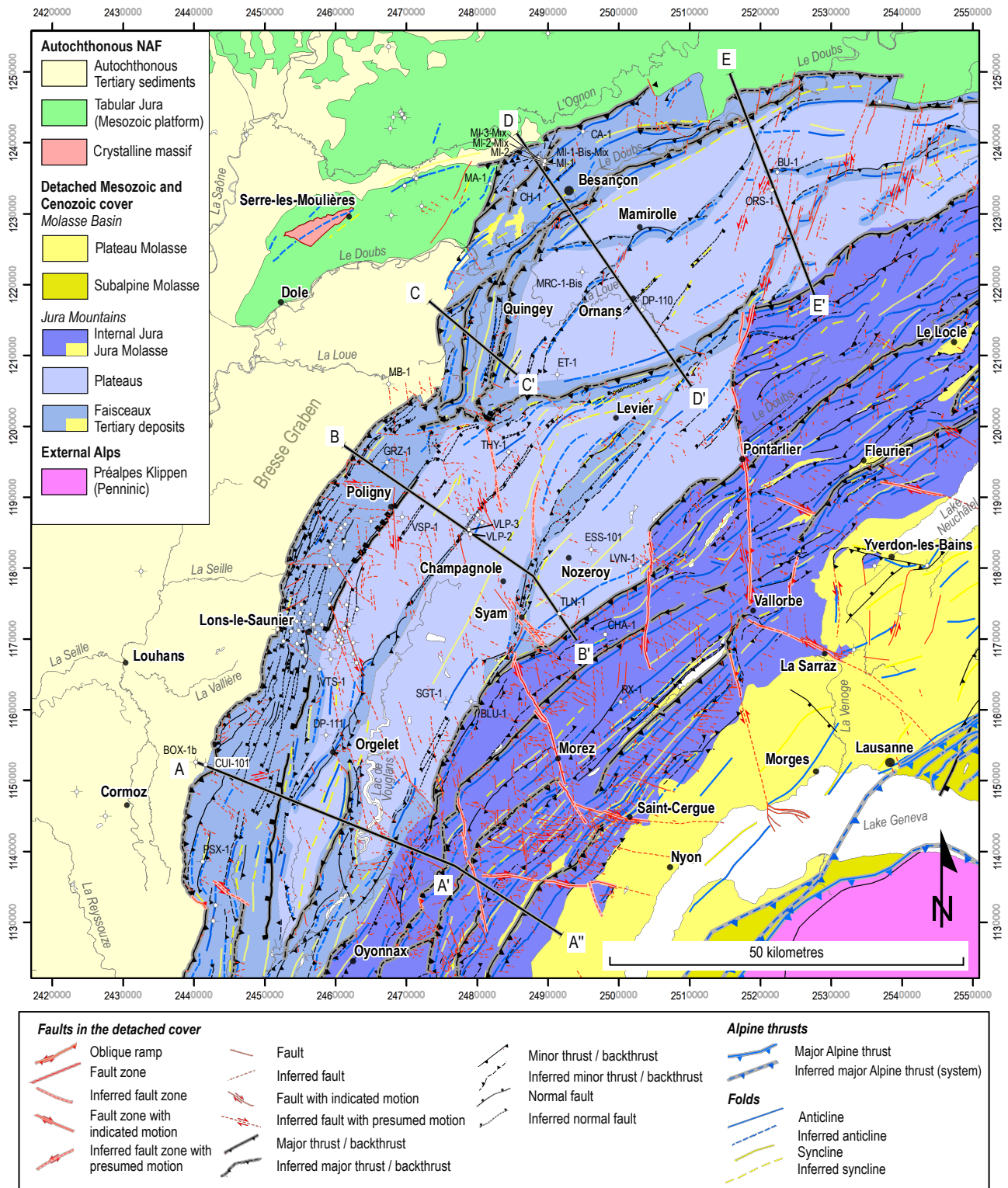


Fig. 5.1 – Structural map of the Jura Mountains of this study with traces of cross-sections in this chapter (Fig. 5.2 and Fig. 5.3).

fault in the mechanical basement with roughly 320 m vertical offset, yet the two structures do not share a mutual tectonic history. The Pincée de l'Heute is interpreted to be sheared off its basement and transported about 9.5 km north-westward (displacement estimated in Philippe et al. 1996) during the formation of the JFTB.

An exceptionally high basement step of ~600 m at the Faisceau de Syam is deduced from combined borehole comparison and seismic line interpretation (Fig. 5.2b, po-

sition km 31). The precise geometry at depth of this structure is not well constrained and therefore, two structural interpretations are proposed (Fig. 5.2b and c) requiring different basement-cover interactions (see discussion in Chapter 5.8). A kinematic analysis of structures in this section, between positions 19 to 38 km, is presented in Chapter 9.4.

The Plateau de Nozeroy constitutes a roughly 9 km wide, open anticline above an evaporite cored pillow (Fig.

5.2b between km 35 and 43, also addressed in Sommaruga 1997). The evaporite core of the Plateau de Nozeroy is penetrated by the borehole Toillon-1 (TLN-1) that reveals an exceptionally thick Keuper Group series of more than 465 m (TLN-1 ends in the Lower Keuper Group series) featuring a 224 m thick salt system (Warthmann 1959). The evaporite pillow is also depicted on the seismic line CM16S, which reveals discontinuous reflectors in the Triassic series indicative for tectonic thickening by duplexing or low-angle thrusting (Fig. 5.2d). A distinct seismic reflector at the base of the evaporite pillow (Fig. 5.2d) is interpreted as the south-east plunging basal-décollement above a series of subsided basement blocks (Fig. 5.2b, position km 38 to 43). Note that the top of the basement is not visible on the seismic line CM16S (Fig. 5.2d) and the proposed basement faults are rather hypothetical.

5.5 SECTION C: FAISCEAU DE QUINGEY

The trace of the Section C (Fig. 5.3a) has a length of 16 km illustrating structures of the Faisceau de Quingey. This faisceau reveals three consecutive anticlines striking NNE–SSW to N–S with an orientation oblique to the principal NW–SE palaeostress direction (Homberg et al. 2002; Laubscher 1972; Philippe et al. 1996). A previous geometrical study (Martin and Mercier 1996) demonstrated that inherited Cenozoic normal faults controlled the localisation and orientation of folds in the Faisceau de Quingey. For this faisceau, Mio-Pliocene displacement vectors of Philippe et al. (1996) suggest a rough N–S directed transport that is almost parallel to anticlines and consequently, I consider the suggested vectors for the area as kinematically questionable. I prefer to indicate Mio-Pliocene displacement vectors of Affolter and Gratier (2004) at the base of Section C (Fig. 5.3a), which have a more favourable orientation parallel to principal palaeostress orientations (Homberg et al. 2002; Laubscher 1972).

The depth of the basement in Section C (Fig. 5.3a) is constrained by two boreholes, which are Montbouton-1 (MB-1, Ramaut 1958) lying in the Bresse Graben and Eternoz-1 (ET-1, COPEFA 1960) drilled in the Plateau d'Ornans about 5.7 km east of the south-eastern tip of Section C. The total height difference between the basement of the Bresse Graben and the basement in the External Jura (Plateau de Montrond) is therefore only about 425 m (two basement steps with a 150 m and 275 m throw), which is considerably less than in the previous sections A and B (Fig. 5.2). The overall vertical basement offset localises on two discrete basement steps (Fig. 5.3a, along-strike positions km 4.8 and 15), which form downward steps in respect to Mio-Pliocene transport directions. Note that the Pagnoz–Grange Anticline towards the centre of Fig. 5.3a lies above a flat basement. A tectonic graben is identified between along-strike positions km 11 and 12. According to the displacement model of Affolter and Gratier (2004), the Mio-Pliocene transport distance was about 4.4 km parallel to the trace, which suggests that the graben has formed in connection with the

275 m high basement step (Fig. 5.3a, position km 15). The basal décollement of the JFTB ramps downwards at the south-eastern basement step, whereas no downward ramping is attested at the north-western step that is 150 m high.

It is noteworthy that at MB-1 (Fig. 5.3a, position km 0.2), the Cretaceous series is not present and the Upper Malm Group is overlain by 72 m Plio-Pleistocene gravel (SAFREP 1959). Since Eocene and Oligocene graben sediments are absent, MB-1 lies not in the tectonic Bresse Graben proper, but rather on the rim of the graben.

5.6 SECTION D: FAISCEAU DES AVANT-MONTS – PLATEAU D'ORNANS WEST

Section D (Fig. 5.3b) shows a roughly 43 km long transect starting to the north-west in the RBTZ and ending in the Plateau de Nozeroy. Boreholes penetrating the Triassic series reveal that salt systems are present in both, the Middle and Upper Triassic units, but tectonic duplications are only ascertained in the Upper Triassic unit (boreholes BU-1 and MRC-1). However, due to the presence of Middle Triassic salt systems, a subordinate involvement of the Middle Triassic unit in the basal décollement is possible.

Cross-section D reveals upward and downward steps in the basement with throws between 60 to 330 m within the JFTB, higher throws occur at the front of the JFTB. Sediments of the Cretaceous and Upper Malm groups are widely eroded in Section D, but Cretaceous sediments are exposed in the Ognon valley (position km 2) and in the thrust syncline of the Faisceau salinois at the SE of the section (position km 39). The basement in the RBTZ lies about 1175 m lower than in Miserey-1 (MI-1) at the front of the JFTB (Fig. 5.3b, compare position km 3 and 6). The vertical offset is exceedingly high and the basal décollement of the JFTB does not ramp downwards, but thrusts upwards onto the subsided Mesozoic sequence of the Ognon valley (Fig. 5.3b). The basement along the section trace shows two kilometric horsts, one to the north-west of the city of Besançon (Fig. 5.3b, between along-strike position km 3 and 8) and a second horst in the area of the slightly elevated Plateau de Montrond (Fig. 5.3b, position km 18 to 26). Besançon lies in a basement trough that has a rough NE–SW orientation, parallel to the Doubs river. The anticline south of Besançon shows kilometric, thrust-related duplication (between km 13 and 16) presumably induced by downward steps in the basement (Fig. 5.3b, position km 16 and 18). A similar downward-step related structure is interpreted at the Faisceau salinois in the SE (Fig. 5.3b, position km 43).

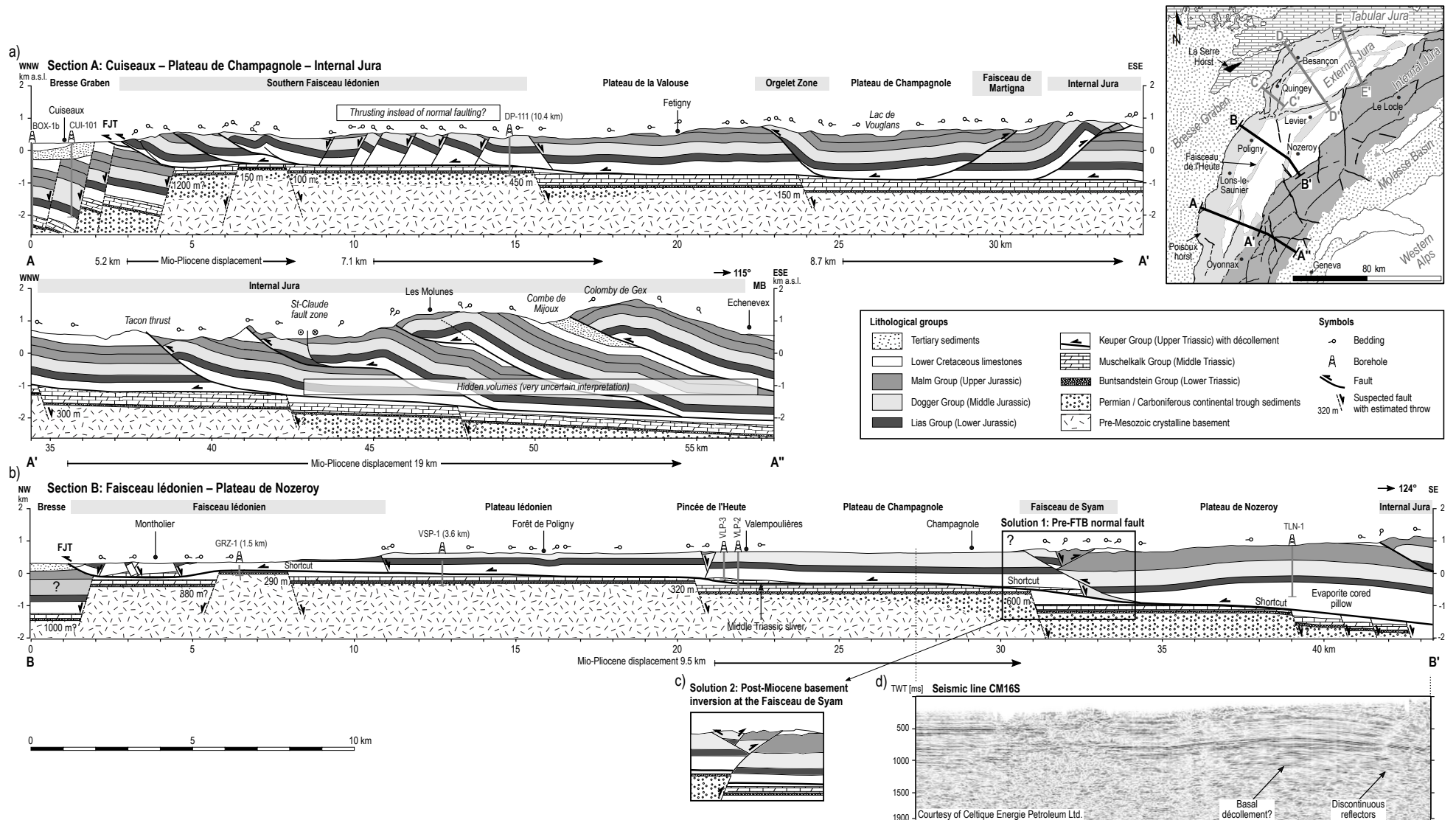


Fig. 5.2 – Cross-sections across the southern Plateau Jura, interpreted from surface data, boreholes and locally from a seismic line (see locations of cross-sections in Fig. 5.1). Note that individual plateaus have different structural altitudes. Throws at suspected basement steps are indicated in metres. Mio-Pliocene displacements along the basal décollement of the JFTB are according to Philippe et al. (1996), illustrated at the bottom of cross-sections. The segment between 17 to 39 km of Section B is kinematically modelled in Chapter 9.4 (Fig. 9.3 on page 139). Boreholes are BOX-1b: Bois-des-Chaux-1 bis, CUI-101: Cuiseaux-101, DP-111: Présilly-1, GRZ-1: Grozon-1, VSP-1: Vaux-sur-Poligny-1, VLP: Valempoulières (several boreholes), TLN-1: Toillon-1. The projection distance is indicated in brackets for boreholes more than 0.3 km away from the section trace. MB: Molasse Basin, RBTZ: Rhine–Bresse Transfer Zone. FJT: Frontmost Jura Thrust.

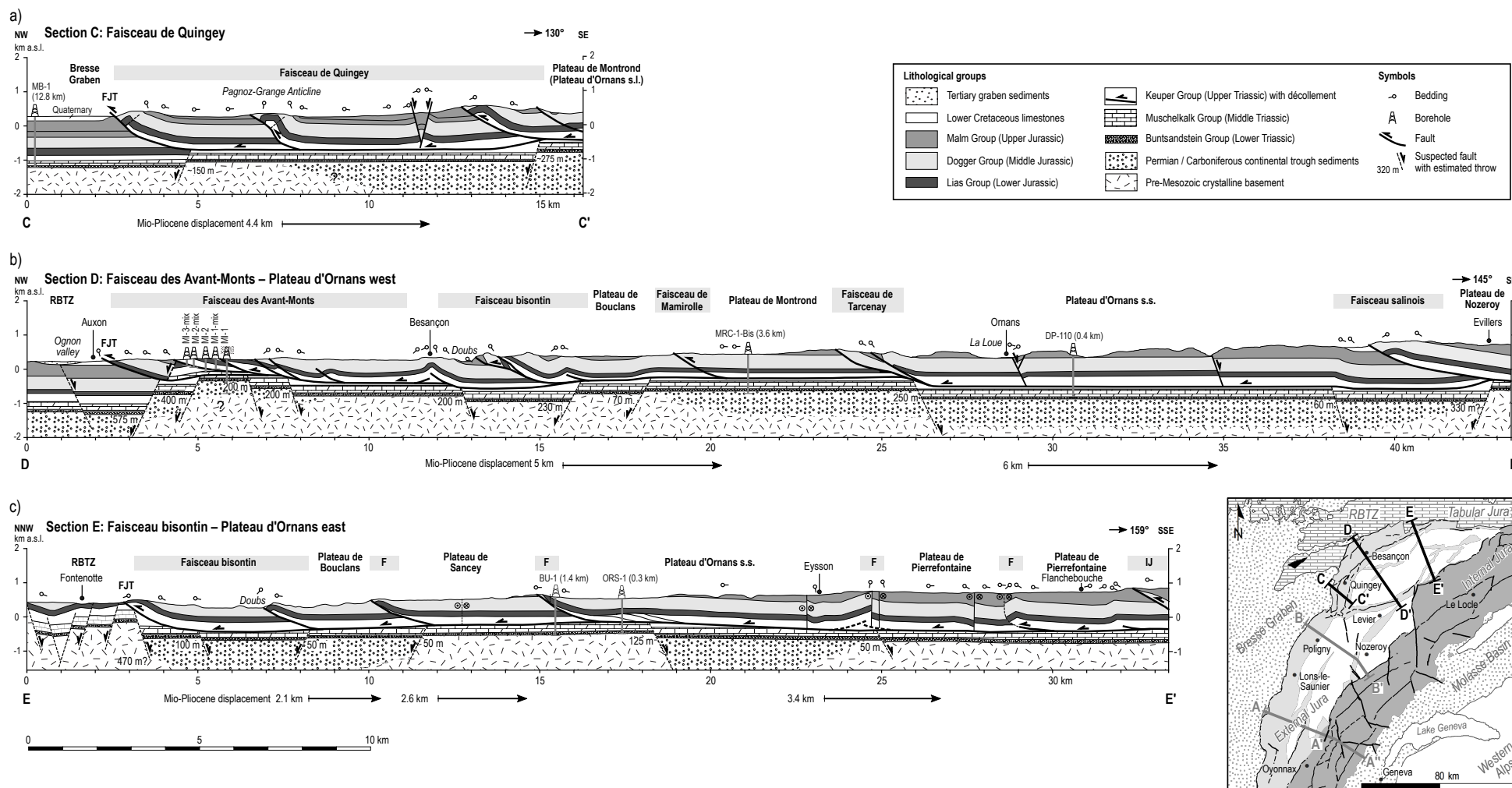


Fig. 5.3 – Cross-sections across the northern Plateau Jura (see locations of cross-sections in Fig. 5.1). The Mio-Pliocene displacement in a) is according to Affolter and Gratier (2004), whereas in b) and c), displacements are according to Philippe et al. (1996). Boreholes are MB-1: Montbarrey-1, MI: Miserey, MRC-1-Bis: Montrond-le-Château-1 bis, DP-110: Ornans-1, BU-1: Buez-1, ORS-1: Orsans-1. The projection distance is indicated in brackets for boreholes more than 0.3 km away from the section trace. Abbreviations for tectonic domains are IJ: Internal Jura, F: Faisceau, RBZ: Rhine–Bresse Transfer Zone. FJT: Frontmost Jura Thrust.

5.7 SECTION E: FAISCEAU BISONTIN – PLATEAU D'ORNANS EAST

To the NNW, Section E (Fig. 5.3c) starts in the RBTZ forming parts of the Tabular Jura, where the autochthonous Mesozoic cover is exposed. The section proceeds south-south-eastwards across several smaller faisceaux and kilometric plateaus including the eastern Plateau d'Ornans s.s., and prolongs into the Internal Jura. The section trace is parallel to principal stress directions according to Laubscher (1972) and Homberg et al. (2002). Mio-Pliocene displacement vectors of Philippe et al. (1996) are sub-parallel to the section trace and they are indicated at the base of Section E (Fig. 5.3c).

The RBTZ contains NNE–SSW striking basement faults with a vertical offset of a few hundred metres at maximum (Fig. 5.3c). Note that faults of the autochthonous RBTZ are interpreted to prolong from the cover into the basement. Section E indicates that the RBTZ is structurally slightly higher than the front of the External Jura, in particular the frontal Faisceau bisontin (Fig. 5.3c). Note that compared to previous Section D (Fig. 5.3b), the frontal Faisceau des Avant-Monts is missing. The Doubs valley lies in a basement depression with a ENE–WSW orientation. Anticlines between along-strike positions km 7 and 12 (Fig. 5.3c) seem to be connected to downward steps in the basement, which show rather small throws of about 50 m. The two boreholes Buez-1 (BU-1) and Orsans-1 (ORS-1) penetrate a basement horst that is about 7 km wide along the section trace. The SSE of Section E, comprising the Plateau d'Ornans s.s. and the Plateau de Pierrefontaine, features several sinistral strike-slip faults with a NNE–SSW orientation. These faults are conceptually drawn to end in the basal décollement of the JFTB, assuming that they were active during Mio-Pliocene thin-skinned deformation. Supporting this assumption, two of the strike-slip faults are interpreted as oblique ramps (Fig. 5.3c, position km 25 and 29), above which small scale anticlines form that I distinguish from plateaus by denoting them as thin NE–SW striking faisceaux. Note that the basement beneath the Plateau d'Ornans and the Plateau de Pierrefontaine is rather flat and faisceaux do not necessarily superpose basement offsets. The estimated shortening of individual anticlines between position km 3 and 17 (Fig. 5.3c) is in the range of some 500 metres.

5.8 DISCUSSION

Section A: imbricate stacks or tilted blocks

Cross-section A (Fig. 5.2a) shows an imbricate stack between km 3 and 7, whereas the Southern Faisceau lédonien between km 9 and 15 is interpreted as a series of consecutive tilted blocks. This structural solution for the latter segment is not well constrained, but is justified by the fact that beds are mostly inclined to the ESE and that folds seem to be largely absent (no attested compressive structures). In agreement with previous studies of this structural zone (Trümpy 1980; Wildi and Huggenberger

1993), I interpreted this case as a series of tilted blocks. It appears reasonable that such extensional structures pre-date the JFTB, presumably forming due to Eo-Oligocene rifting. Subsequently, the tilted blocks are passively transported to the WNW along the basal décollement of the JFTB during Mio-Pliocene. Alternatively, instead of tilted blocks, an imbricate stack similar to the front of the Southern Faisceau lédonien can be interpreted (Fig. 5.2a). Note that with the geological data available for this study, it is not possible to unambiguously define the structural model for the eastern segment of the Southern Faisceau lédonien (Fig. 5.2a).

Section B: the Middle Triassic sliver of Valempoulières

The Middle Triassic sliver of Valempoulières (Fig. 5.2b, position km 21 to 24) is suggested to originate from a décollement shortcut at a basement step (Philippe et al. 1996). The north-westward Mio-Pliocene displacement at Valempoulières is about 9.5 km according to Philippe et al. (1996). Therefore, a décollement shortcut is indicated at the Faisceau de Syam (Fig. 5.2b, position km 30 to 31), which constitutes the presumed origin of the Middle Triassic sliver of Valempoulières. This structural concept has two important consequences: 1) The sliver of Middle Triassic sediments, incorporated within the regional décollement in Upper Triassic evaporites, indicates a pre-JFTB basement step. 2) The vertical offset of the pre-JFTB basement step exceeds the thickness of the basal décollement zone in Upper Triassic evaporites (the total thickness of the evaporite zone of the Keuper Group is about 220 m to 280 m in VLP-3 and VSP-1, respectively).

In Chapter 9, a kinematic forward model is presented that shows the formation of the sliver of Middle Triassic sediments within the basal décollement.

Section B: structural implications of the Faisceau de Syam

I propose two structural models for the internal construction of the Faisceau de Syam: 1) in Fig. 5.2b (between positions km 30 and 34), a pre-JFTB hinterland-dipping normal fault is dissected by thrusts and the basal décollement of the JFTB. In this case, the Faisceau de Syam is controlled by a basement step lying about 9.5 km SE of the faisceau, considering the JFTB displacements of Philippe et al. (1996). It is a mere coincidence that the Faisceau de Syam lies above a 600 m high basement step (Fig. 5.2b, position km 31). 2) Alternatively, a post-Miocene inversion of the basement that dissects the formerly continuous JFTB décollement is proposed in Fig. 5.2c.

It should be pointed out that the Middle Triassic sliver at Valempoulières (Fig. 5.2b, position km 21 to 24) is suggested to be in connection with a pre-JFTB basement step at the Faisceau de Syam (see kinematic model in Chapter 9). Furthermore, Oligocene conglomerates with a local source were documented in the Faisceau de Syam (Mugnier and Vialon 1986 referring to Aubert 1975; Duplaix and Guillaume 1962; Weber 1960), which supports that Cenozoic

Table 5.1 – Overview of interpreted basement steps in Sections A to E (Fig. 5.2 and Fig. 5.3), sorted by step type (down / up) and throw. The second column specifies the along-strike position of the basement step (indicated at the bottom of the sections). In column three, upward and downward-type steps (up / down) are defined in respect to the general NW transport direction of the JFTB. The vertical throw of basement steps is given in column four. The quality-indicator (column five) indicates the assuredness of inferred basement steps (1: confident, 2: likely, 3: possibly). The Ramp-column shows whether the basal décollement of the JFTB ramps upwards or downwards to compensate the vertical offset at the basement step.

Sec.	Position	Type	Throw	Qual.	Ramp
E	8.2 km	Down	50 m	2	Yes
E	11.6 km	Down	50 m	2	Yes
D	18.1 km	Down	70 m	2	Yes
A	6.1 km	Down	150 m	3	(No)
C	4.8 km	Down	150 m	2	No
D	16.1 km	Down	230 m	2	Yes
C	15.0 km	Down	275 m	2	Yes
D	42.9 km	Down	330 m	3	Yes
B	5.8 km	Down	380 m	3	(No)
D	5.0 km	Down	400 m	3	(No)
D	3.8 km	Down	575 m	2	No
B	1.9 km	Down	1000 m	3	No
A	4.1 km	Down	1200 m	3	No
E	24.9 km	Up	50 m	3	Yes
D	38.1 km	Up	60 m	3	Yes
A	8.0 km	Up	100 m	2	Yes
E	5.0 km	Up	100 m	3	Yes
E	18.2 km	Up	125 m	2	Yes
A	23.8 km	Up	150 m	1	Yes
D	6.5 km	Up	200 m	2	Yes
D	7.8 km	Up	200 m	2	Yes
D	12.8 km	Up	200 m	1	Yes
D	26.0 km	Up	250 m	1	Yes
B	8.0 km	Up	290 m	1	Yes
A	34.3 km	Up	300 m	1	Yes
B	20.5 km	Up	320 m	1	Yes
A	15.5 km	Up	450 m	1	Yes
E	3.2 km	Up	470 m	3	No
B	31.0 km	Up	600 m	2	(Yes)

extensional structures are overprinted by the formation of the JFTB. These observations rather point to solution 1. A kinematic analysis of the Faisceau de Syam, showing the interplay of Eo-Oligocene extension and Mio-Pliocene compression, is presented in Fig. 9.3.

Ramps in the regional basal décollement

Heights of upward basement-steps, accommodated by ramps in the décollement, are estimated between 50-450 m (Table 5.1) within sections A to E (Fig. 5.2 and Fig. 5.3). In one case in Section B (Fig. 5.2b), an exceptionally high décollement ramp of maximum 600 m is suspected. Downward steps where the basal décollement forms downward ramps show vertical offsets between 50 m and 330 m (Table 5.1). Higher downward basement-steps only

occur at the front of the JFTB and they seem not to be accommodated by décollement ramps. It appears that downward steps higher than about 400 m blocked the downward propagation of the basal décollement, forcing the décollement to ramp upwards. Normal faults at the front of Sections A and B (Fig. 5.2a and b) correspond to NNE–SSW striking border faults of the BG (Lienhardt 1962; Michel et al. 1953), and to ENE–WSW striking faults of the RBTZ (Fig. 5.3) in Sections D and E (Fig. 5.3c and d). The frontal limits of the JFTB in Sections A to E are therefore pre-conditioned by Eocene-Oligocene extensional faults in connection with the formation of the ECRIS.

Large anticlines with several kilometres shortening are observed at downward steps, such as in Fig. 5.3b at the Faisceau salinois (downward step ca. 330 m) and south-east of Besançon (downward step 230 m). Compared to this, upward steps seem to trigger considerable smaller structures if any at all (Fig. 5.3b).

5.9 CONCLUSIONS

Cross-sections constructed from boreholes and surface information (aided locally by a seismic line) permit to reliably identify and illustrate the variation of structural altitudes in the External Jura. Abrupt differences in structural altitudes emerge at distinct locations. Discrete vertical basement offsets of 50 m and more are inferable across most parts of the central External Jura. In conclusion, Sections A to E (Fig. 5.2 and 5.3) across plateaus and faisceaux reveal several important structural observations in connection with basement topography:

- The northern Plateau Jura (Sections C, D and E, Fig. 5.3) reveals few extensional structures in the cover. The basement at the front of the JFTB is partially only little offset (e.g. Fig. 5.3a). The overall basement topography underneath the JFTB indicates several moderately high horsts and grabens. The basal décollement of the JFTB accommodates abrupt basement offsets by ramping upwards and downwards (Fig. 5.3). In comparison, the southern Plateau Jura (Sections A, B) shows high frontal basement offsets, abundant extensional structures in the cover (normal faults and grabens) and a simpler basement topography (Fig. 5.2). In the southern Plateau Jura, the basement is highest underneath the frontal faisceaux and deepens constantly to the ESE. Since only upward basement steps (in the direction of tectonic transport) occur within the southern Plateau Jura (except at the front), the basal décollement exclusively forms upward ramps (Fig. 5.3).
- Faisceaux partially overlie basement faults with considerable throws (up to several hundred metres), which is particularly the case for frontal faisceaux (e.g. Faisceau lédonien, Faisceau des Avant-Monts). However, inner faisceaux do not necessarily overlie basement faults (e.g. Faisceau de Mamirolle, Faisceau salinois), as they are transported several kilometres north-westwards and away from triggers in the pre-JFTB basement.

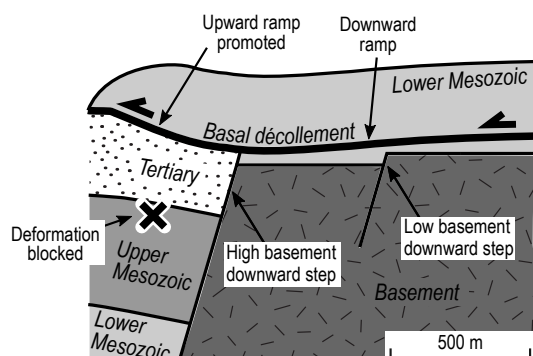


Fig. 5.4 – Sketch illustrating the front of the JFTB above a high downward basement step. The high downward step prevents down-ramping of the basal décollement and instead, the basal décollement ramps upwards.

- Beds in most plateaus are sub-horizontal. Individual plateaus reveal different structural altitudes. Altitude changes of plateaus coincide with regional changes of the exposed lithostratigraphic unit (e.g. Dogger Group is exposed in the Plateau de Champagnole whereas the Malm Group is exposed in the Plateau de Nozeroy, Fig. 5.2b).
- Within Sections A to E across the Plateau Jura, vertical basement offsets commonly do not exceed 450 m. One uncharacteristically high upward basement step of about 600 m is suspected in front of the Internal Jura (Fig. 5.2b, Faisceau de Syam). Underneath the front of the JFTB, basement normal faults are hidden that constitute downward steps in the direction of tectonic transport. These basement normal faults formed in connection with Eo-Oligocene rifting (border faults of the BG and faults of the RBTZ). High downward basement-steps of several hundred metres blocked the propagation of the JFTB basal décollement and pre-conditioned the front of JFTB (Fig. 5.4).

6 - TOPOGRAPHY OF THE PRE-MESOZOIC BASEMENT

6.1 INTRODUCTION

This chapter is dedicated to the topography of the pre-Mesozoic basement and the signatures of lithospheric tectonic events that are contained therein, in particular the signature of the Northern Alpine flexural basin system. In the previous chapters, it is shown that substantial offsets of the pre-Mesozoic basement can occur, which are commonly in connection with normal faults, or partially supposedly with an inverted basement (Guellec et al. 1990; Madritsch et al. 2008; Ustaszewski and Schmid 2007). There are four main events that affected the lithosphere in Upper Cretaceous to Cenozoic times, possibly leading to observed basement offsets (see Fig. 2.6 on page 29):

1. Strike-slip faulting (Homberg et al. 2002) and intra-plate lithospheric buckling (Lefort and Agarwal 1996, 2002) due to N-S directed collision between Africa and Europe in Upper Cretaceous to Oligocene
2. Flexural bending of the Northern Alpine Foreland in Eocene to Middle Miocene (Burkhard and Sommaruga 1998; Ford et al. 2006; Laubscher 1992)
3. Eo-Oligocene rifting in connection with the formation of the ECRIS (Illies 1962; Illies 1972; Michon 2000)
4. Recent lithospheric buckling in Neogene and Quaternary (Bourgeois et al. 2007) due to NW–SE directed collision of Adria and Europe

An attempt to distinguish these lithospheric signatures in the geometry of the pre-Mesozoic basement is conducted in Bourgeois et al. (2007). This study focuses on Central and Western Europe and particularly describes the uplift of graben shoulders of the ECRIS and the effects of recent lithospheric buckling beginning at about 17 Ma.

The current chapter follows a similar approach, but focuses on a smaller study area in the southern URG, BG, Tabular Jura, JFTB and detached MB. The top of the pre-Mesozoic basement is modelled in more detail, taking care to include abrupt changes in elevation due to major fault

systems. The top pre-Mesozoic basement map allows to explore structural domains of the JFTB in function of basement geometry. Thereafter, the signature of the flexural Alpine foreland basin within the pre-Mesozoic basement model is discussed. This is still not very well known in the area of the detached NAF, mainly due to interference with the ECRIS (see discussions in Burkhard and Sommaruga 1998; Laubscher 1992; Sinclair et al. 1991; Stampfli et al. 1998). The migration of the flexural foreland since its initiation at about 55 Ma (Ford et al. 2006, Fig. 2.12 on page 33) is illustrated on large scale maps. This helps to deduce the occurrence of extensional fractures and faults in connection with flexural bulging in the area of the JFTB, which depends on assumptions concerning formation of flexural faults within the foredeep and forebulge (Bradley and Kidd 1991; Decelles 2012; DeCelles and Giles 1996).

Note that the introduction chapter of this thesis contains a brief description of lithospheric deformation concepts (Chapter 2.6 on page 34), which are discussed subsequently. It may be helpful to polish up these concepts before continuing with the current chapter.

6.2 METHODS

6.2.1 Faults in the pre-Mesozoic basement

Faults that offset the pre-Mesozoic basement in the autochthonous Alpine foreland are compiled from geological maps of France (1:50'000, BRGM 2004), Germany (1:200'000, BGR 2015) and Switzerland (1:25'000, Swisstopo 2012), published studies and PhD theses (Table 6.1). Within the autochthonous Mesozoic platform (Fig. 2.1), surface traces of faults are adjusted to structures visible on the digital terrain model SRTM1 (NASA 2014). Basement faults in the detached NAF are hidden beneath the displaced Mesozoic cover and cannot be verified by means of surface structures. In the detached External Jura (Fig. 2.1), vertical offsets of the pre-Mesozoic basement

Table 6.1 – Studies used to complement borehole data in order to render an elevation model of the top of the pre-Mesozoic basement. BF: Black Forest, LSZ: La Serre Zone, RBTZ: Rhine–Bresse Transfer Zone.

Location	Basement faults	Top basement
Valence Basin	Otto (1994)	Debrand-Passard et al. (1984)
Bresse Graben	Bergerat et al. (1989); Debrand-Passard et al. (1984); Laubscher (1986); Rat (1974); Rocher et al. (2004)	Bergerat et al. (1989); Blanc et al. (1991); Debrand-Passard et al. (1984); Guellec et al. (1990)
LSZ and RBTZ	Madritsch (2008); Madritsch et al. (2009)	Debrand-Passard et al. (1984); Guellec et al. (1990)
URG	Faber et al. (1994); Hauber (1993); Larroque and Laurent (1988); Laubscher (1982); Philippe (1995); Rotstein et al. (2005); Ustaszewski (2004)	Caër (2016); Hauber (1993); Philippe (1995); Ustaszewski (2004)
BF and surrounding	Egli et al. (2016); Madritsch et al. (2018); Madritsch and Deplazes (2014)	Egli et al. (2016); Madritsch et al. (2018); Sommaruga et al. (2012)
External Jura	Bergerat et al. (1990); Laubscher (1986); Philippe (1995); Ustaszewski and Schmid (2006); Chauve et al. (1980); Chauve et al. (1988); Diebold and Noack (1997); Wildi and Huggenberger (1993); Madritsch et al. (2008); Madritsch et al. (2009); Martin and Mercier (1996); Philippe et al. (1996)	Blanc et al. (1991); Guellec et al. (1990); Madritsch et al. (2008); Philippe (1995); Ustaszewski and Schmid (2006, 2007)
Molasse Basin	Landesgeologie (2017); Meier (2010); Sommaruga et al. (2012)	Debrand-Passard et al. (1984); Gruber (2017); Sommaruga et al. (2012)

are identified by cross-section construction and comparison of boreholes (Chapter 5). Across the northern front of the JFTB, basement faults known from the autochthonous foreland can be extended. Traces of faults in the Base Mesozoic model indicate interpreted main fault zones (Fig. 6.2, Supplementary Material A.01). An uninterpreted illustration of identified basement faults is given in the geological map in Enclosure 01 and Shapefiles to this project in Supplementary Material A.01.

In the URG and RBTZ, numerous geophysical reconnaissance has been conducted and studies are abundant (EUCOR-URGENT project, Behrmann et al. 2005), providing a solid understanding of the subsurface (Table 6.1). The BG was investigated by oil-companies, mainly between the 50ies and 80ies and structures are known from boreholes, seismic lines and gravimetry (Debrand-Passard et al. 1984). The Internal Jura is too extensively deformed (e.g. duplication of the Mesozoic series) to confidently evaluate offsets in the pre-Mesozoic basement. The thick Triassic sequence hosting the décollement of the detached NAF, accommodates gaps and obscures faults in the pre-Mesozoic basement. Unfortunately, the resolution at depth of available seismic lines is not sufficient to unambiguously identify faults in the pre-Mesozoic basement beneath the Internal Jura (Guellec et al. 1990; Sommaruga 1997)..

6.2.2 Base Mesozoic model

An elevation map of the base Mesozoic horizon (BMes) is created using 118 boreholes penetrating the pre-Mesozoic basement and 25 published geological cross-sections (Table 6.1). New cross-sections within the External Jura (Fig. 5.2 and Fig. 5.3, partially based on seismic lines), complete depth constraints furthermore. Additional elevation estimates based on boreholes that do not reach the basement are added, using previously created thickness

grids of the Mesozoic cover (chapter 4) to estimate the depth of the BMes-horizon. Published studies containing models, cross-sections and depth maps are integrated according to Table 6.1. Exposures of the BMes-horizon (crystalline basement or Permian-Carboniferous continental sediments contrasting with Mesozoic sediments) constitute the boundary of the interpolated model. Since exposed crystalline massifs (Massif Central, Vosges, Black Forest and La Serre Massifs) are excluded from interpolations, the base Mesozoic model is equivalent to the top of the pre-Mesozoic basement. Altitudes of the exposed BMes-horizon are taken from the SRTM topographic model (NASA 2014) at locations given in geological maps. The elevation grid is modelled from compiled data-points using a minimum curvature algorithm that allows modelling abrupt elevation changes along faults. The integrated algorithm “spline with barriers” (Zoraster 2003) of the geo-software ESRI ArcMap 10.6 is used to render the elevation grid (Fig. 6.2).

6.2.3 Calculation of flexural foreland basin

In order to distinguish lithospheric signatures within the geometry of the BMes-model, a synthetic flexural foreland basin signature is calculated (Allen and Allen 2013; Angevine et al. 1990; Turcotte and Schubert 2002). Flexural basin systems are well studied and their geometry predictable by an Euler-exponential function (Eq. 6.1). The geometry of a flexural basin system in connection with a broken lithosphere (Turcotte and Schubert 2002) is calculated with the formula (Allen and Allen 2013; Turcotte and Schubert 2002)

$$w(x) = w_d \exp(-x/\alpha) \cos(x/\alpha) \quad (6.1)$$

Where w is the vertical deflection of the plate and x the horizontal distance from the front of the wedge (Fig.

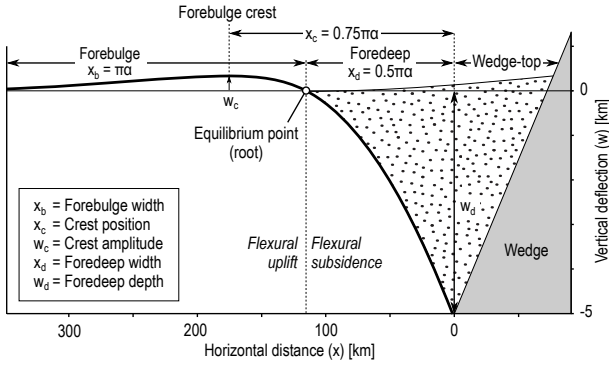


Fig. 6.1 – Geometry of a flexural basin system modified from DeCelles and Giles (1996) and Turcotte and Schubert (2002).

6.1). The parameter w_d gives the maximum negative deflection of the foredeep (depth of foredeep) and α is the flexural parameter. The flexural parameter is a function of the flexural rigidity (D) and the density contrast between the mantle and the basin infill ($\Delta\rho$):

$$\alpha = \sqrt[4]{\frac{4D}{\Delta\rho g}}$$

or

$$D = \frac{1}{4}\alpha^4 \Delta\rho g$$

An average mantle density (ρ_m) of 3300 kg/m³ is assumed and the basin infill (ρ_b) of the Molasse is about 2500 kg/m³, so that $\Delta\rho$ equals 800 kg/m³. The flexural parameter α can be deduced from the width of the foredeep (x_d), which is defined by the equation $x_d = 0.5\pi\alpha$ for broken plates. The forebulge is twice as long as the foredeep $x_b = \pi\alpha$ and the position of the forebulge crest, following from equation (6.1), is given by the formula $x_c = 0.75\pi\alpha$ (Fig. 6.1).

The effective elastic thickness (T_e) of a plate, is a function of the flexural rigidity

$$T_e = \sqrt[3]{\frac{12D(1-\nu^2)}{E}}$$

where E is the Young's Modulus and ν the Poisson's ratio. All values for the elastic thickness given subsequently are calculated assuming $E = 7^{10} \text{ Pa}$ and $\nu = 0.3$ (Angewine et al. 1990). The elastic thickness is commonly used to express the flexural rigidity of a plate (Burkhard and Sommaruga 1998; Karner and Watts 1983; Stampfli et al. 1998), although the significance for continental plates is enigmatic, poorly corresponding to geological or physical boundaries (Burov and Diamant 1995).

6.3 RESULTS

6.3.1 Top basement model

Fig. 6.2 is a map showing the elevation model of the surface of the pre-Mesozoic basement (corresponding to the base Mesozoic horizon) in the study area. The model illustrates ascertained fault zones, but their geometry is not

modelled and the elevation model merely indicates a vertical plane. Vertical offsets are mostly due to Eocene to Miocene normal faults (formation of the ECRIS and evolution of the Alpine flexural basin system) but in some few cases, basement faults are proposed to be inverted as for example the fault segment SE of Oyonnax (Guellec et al. 1990), the frontal fault of the Ferrette Zone (Ustaszewski and Schmid 2007) and a segment of the Avant-Monts fault zone (Madritsch et al. 2008, see positions in Fig. 6.2). For all of these basement faults, the authors proposed a post-JFTB (recent) inversion.

Model limitations

In order to detect a basement fault beneath the detached Mesozoic cover in seismic lines or by means of cross-section constructions, throws must be sufficiently high, at least 50 m, and displacements on these faults preferably happened during Mesozoic and Cenozoic times (i.e. the cover is vertically offset). Therefore, the model shows the largest fault zones active during Mesozoic and Cenozoic times. Furthermore, basement faults in the Internal Jura and the Molasse Basin are not shown because the depth resolution of seismic lines is commonly insufficient to reveal basement offsets underneath the thick Mesozoic and Cenozoic sequence confidently. Note that important basement faults beneath the Internal Jura certainly exist since basement controlled lineaments in the detached cover are quite abundant (Laubscher 2008b; Laubscher 1961; Meier 2010; Philippe 1995; Steinmann 1902).

Southern Jura and southern Plateau Jura, Bresse Graben

NNE–SSW to NE–SW striking (Rhenish) orientations are dominant in the BG and Jura, south of the 1'200'000 Y-coordinate (Fig. 6.2). The basins at Bourg and NE of Louhans (Fig. 6.2) show the deepest parts of the BG (ca. –3000 m a.s.l.), with Eocene to Pliocene sediment infill (Blanc et al. 1991; Sissingh 1998). In contrast to this, the basement is relatively high at Lons-le-Saunier (ca. –200 m a.s.l., Fig. 6.2). The NNE–SSW striking fault zone in between corresponds to the eastern BG border fault system. Presuming a graben shoulder uplift to graben subsidence ratio of 1/2 (Bourgeois et al. 2007) for both the URG and BG, the top basement model supports an uplift of 930 m of the BG shoulder close to Lons-le-Saunier and a subsidence of 1860 m to the east of Louhans in the BG. This substantial throw is not accomplished by one discrete fault but by a toppled block system as shown on a cross-section based on seismic data and boreholes (Blanc et al. 1991, see Fig. 6.5).

The BG border fault-zone can be followed underneath the western front of the Jura Mountains, along a distance of about 120 km. To the south, the fault zone fades out south of Bourg (Fig. 6.2) and overlaps with the border fault of the uplifted autochthonous plateau of the Île Crémieu (Rocher et al. 2004), which results in a relay ramp. Consequently, the Île Crémieu is considered the southern part of the eastern BG shoulder. The border fault of the Île Crémieu seems to prolong along the front of the Internal Jura and might connect with the basement fault east of

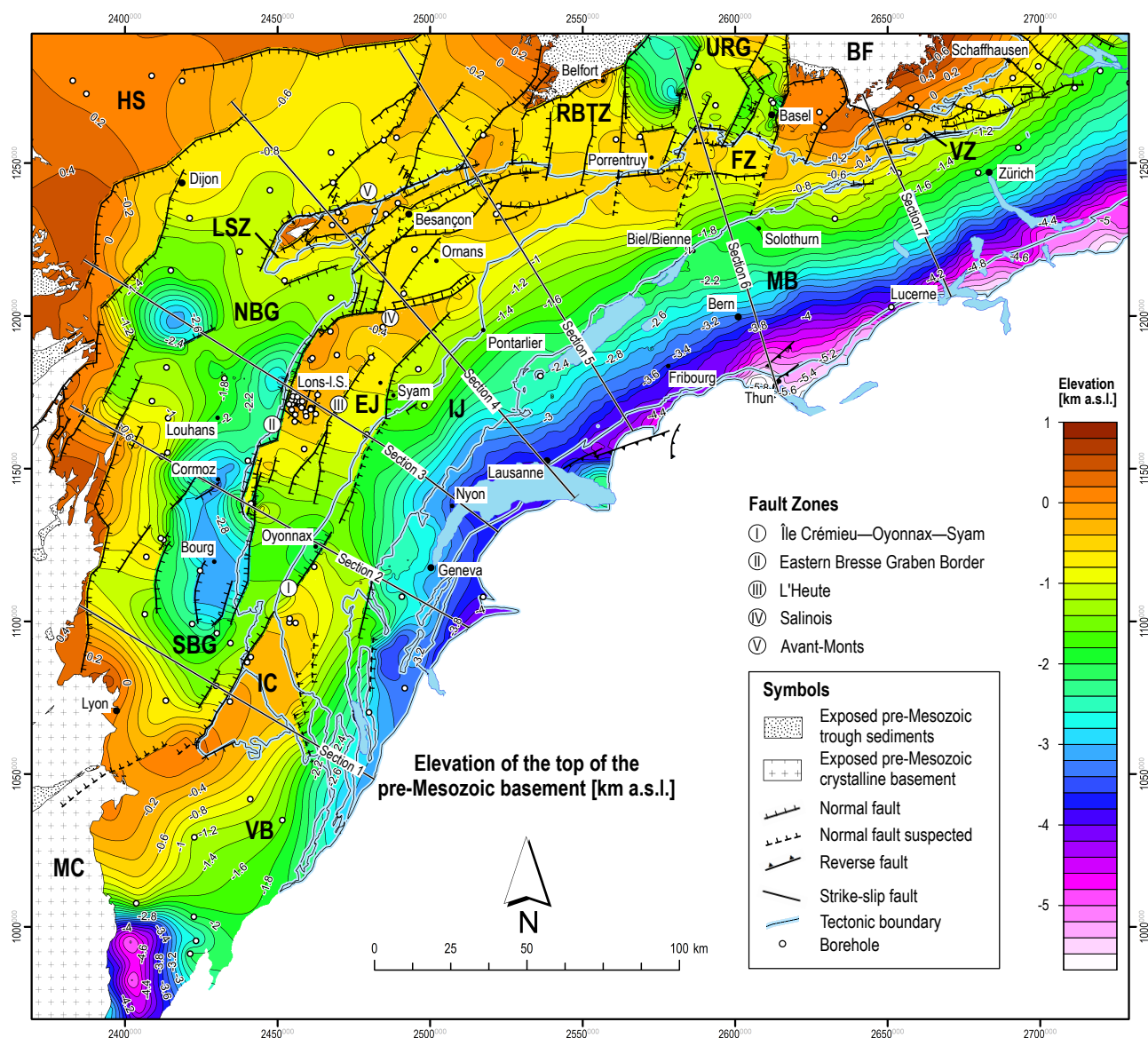


Fig. 6.2 – Elevation model of the top of the pre-Mesozoic basement (corresponding to the base Mesozoic horizon). BF: Black Forest, EJ: External Jura, FZ: Ferrette Zone, HS: Haute-Saône Plateau, IC: Île Crémieu, IJ: Internal Jura, LSZ: La Serre Zone, MB: Molasse Basin, MC: Massif Central, NBG: Northern Bresse Graben, RBTZ: Rhine-Bresse Transfer Zone, SBG: Southern Bresse Graben, URG: Upper Rhine Graben, VB: Valence Basin, VZ: Vorfaltenzone.

Oyonnax, which is possibly inverted (Guellec et al. 1990). This NNE–SSW (Rhenish) line prolongs further into the External Jura, where it is documented in the Faisceau de Syam (Fig. 6.2).

Northern Jura front, BG, RBTZ and URG

In the area of the La Serre Zone, RBTZ, URG and Black Forest (Fig. 6.2), ENE–WSW (Erzgebirgian) trending faults occur in addition to NNE–SSW (Rhenish) orientations. ENE–WSW striking normal faults are present in the La Serre Zone, constitute the front of the northern Central Jura, the front of the Ferrette zone and the Eastern Internal Jura. Additionally, within the External Jura, an important ENE–WSW striking graben between Pontarlier and Ornans (Salinois Fault Zone, Fig. 6.2) separates the southwestern and north-eastern Jura plateaus. At the surface, this fault zone corresponds to the Faisceau salinois. Besançon lies in an ENE–WSW striking (Erzgebirgian) graben,

enclosed to the north and south by faisceaux and plateaus that lie structurally higher (Fig. 6.2). NNE–SSW striking (Rhenish) faults are dominant in the RBTZ and URG. NW–SE striking (Hercynian) basement faults occur rather locally in the autochthonous Jura south of the Black Forest Massif, in the area of Schaffhausen (Fig. 6.2).

Basement throws at the northern front of the JFTB are considerably smaller than at the western front (Fig. 6.2). Compared to the cumulative vertical offset at Lons-le-Saunier of about 2800 m, less than 200 m vertical throw is estimated north of Besançon and in the Ferrette Zone (FZ, Fig. 6.2), a maximum of about 800 m is documented (Ustaszewski and Schmid 2006).

Linkage of basement faults and Jura extent

The top basement model (Fig. 6.2) outlines the shape of the detached Jura Mountains. This supports Laubscher (1961) who suggested a connection between basement

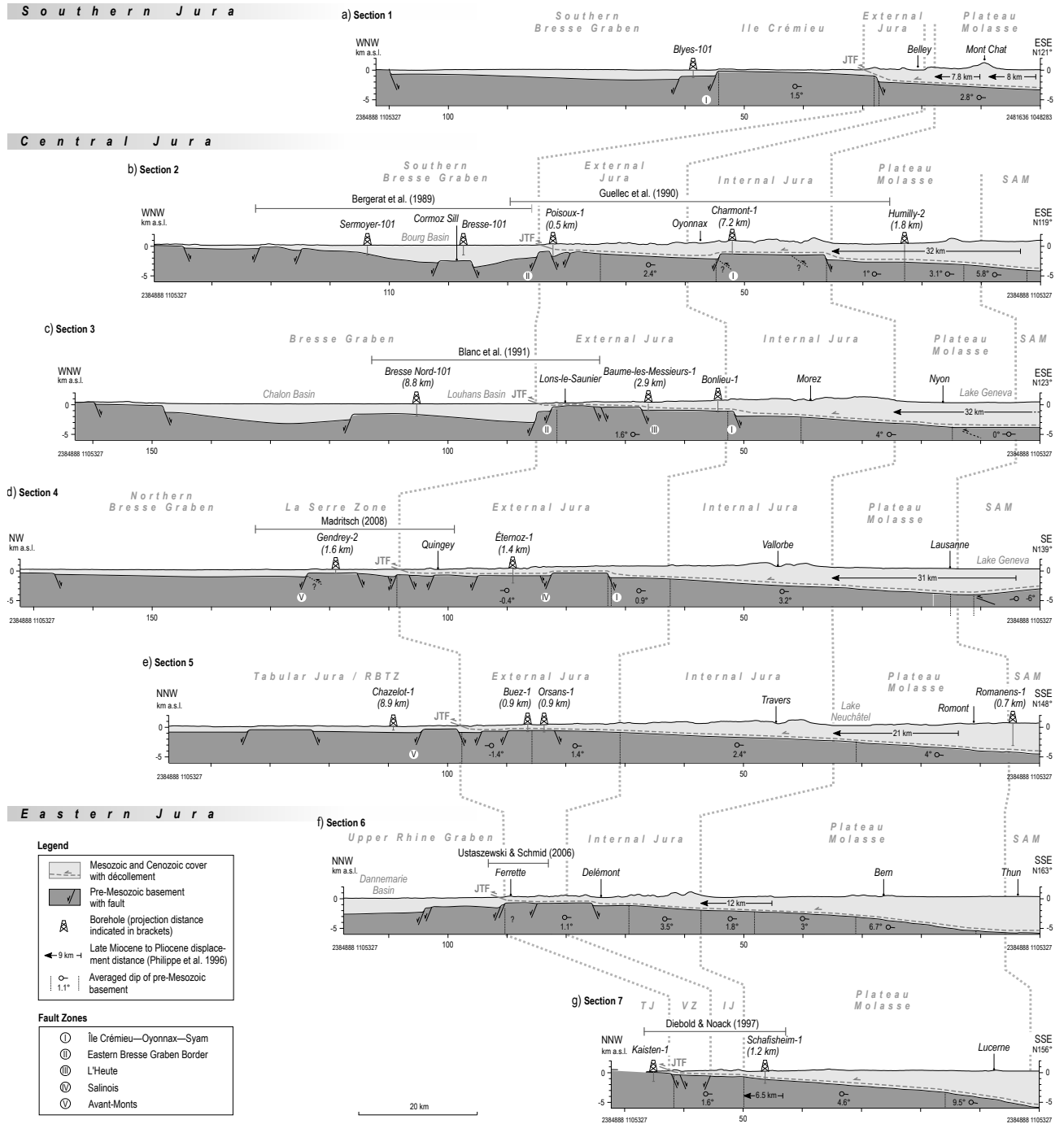


Fig. 6.3 – Transects across the study area illustrating structures in the pre-Mesozoic basement, extracted from the BMes-model in Fig. 6.2. Cross-sections of previous studies, used to constrain the basement topography along transects, are indicated with author reference. BG: Bresse Graben, EJ: External Jura, IJ: Internal Jura, JTF: Jura Thrust Front, RBTZ: Rhine–Bresse Transfer Zone, SAM: Subalpine Molasse, VZ: Vorfaltenzone.

topography and the extent of the Jura Mountains. The western front of the Jura Mountains follows the NNE–SSW (Rhenish) striking BG border faults whereas to the north, the front of the Jura Mountains partly coincides with ENE–WSW (Erzgebirgian) striking normal faults. Both systems correspond to pre-Mesozoic, Variscan and post-Variscan faults which were reactivated during the formation of the ECRIS (e.g. Lienhardt 1962; Madritsch et al. 2009). In conclusion, the front of the JFTB was essentially pre-determined by downward steps (with respect to the tectonic transport direction of the JFTB), which have formed during Eocene-Oligocene reactivation of Palaeozoic faults.

6.3.2 Top basement cross-sections

Fig. 6.3 shows transects across the BMes-model, with traces more or less perpendicular to contour lines in the Molasse Basin and Internal Jura. Traces start at the south-eastern limit of the Molasse Basin (Fig. 6.2) and therefore include the Subalpine Molasse. Table 6.2 lists the tectonic uplift of ECRIS rift-shoulders, which is estimated for transects in Fig. 6.3. Estimations are based on an uplift to subsidence ratio of $\frac{1}{2}$, as proposed by Bourgeois et al. (2007) for the URG and BG (Fig. 6.4).

Table 6.2 – Estimated tectonic uplift of ECRIS rift-shoulders for transects in Fig. 6.3. A rift-shoulder uplift to graben subsidence ratio of $\frac{1}{2}$ is assumed, as suggested in Bourgeois et al. (2007) for the URG and BG (see sketch in Fig. 6.4). Δh_{tot} : Total vertical height difference between rift-shoulder and graben. Uplift: Tectonic uplift of rift-shoulder.

Section	Transition zone	Δh_{tot}	Uplift
Section 1	SBG–Île Crémieu	1375 m	458 m
Section 2	SBG–Poisoux	2645 m	882 m
Section 3	BG–Lons-le-Saunier	2780 m	927 m
Section 5	RBTZ–Jura	610 m	203 m
Section 6	URG–Ferrette Zone	840 m	280 m

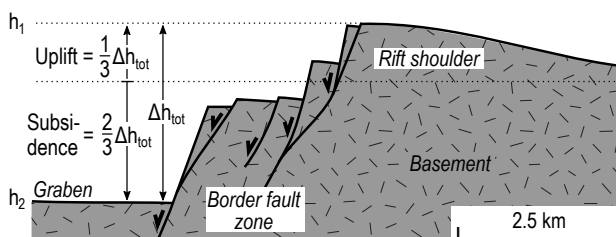


Fig. 6.4 – Scheme illustrating the uplift to subsidence ratio between rift-shoulder and graben, respectively. According to Bourgeois et al. (2007), the uplift to subsidence ratio in the URG and BG is 1 to 2. The maximum height difference (Δh_{tot}) is the difference between the highest location on the rift shoulder (h_1) and deepest location in the graben (h_2). Note that Δh_{tot} is the cumulative vertical offset (throw) of subsided blocks in the border fault zone.

Section 1 (Fig. 6.3a)

The detached NAF lies on a basement which is 2.8° moderately inclined to the ESE. The autochthonous Île Crémieu (Fig. 6.3a) lies structurally higher than the JFTB and the BG. The Île Crémieu is classically seen as an uplifted plateau, which was not affected by thin-skinned deformation in Late Miocene and Pliocene times (Rocher et

al. 2004). Its uplift was likely the counter movement to subsidence in the adjacent BG and therefore, it is suggested to constitute the rift-shoulder of the southern BG. The Triassic series along this section is very thin in comparison to the rest of the JFTB, which coincides with a notable increase of the friction on the décollement and a regional NW–SE orientation of folds in the Southern Jura (Philippe 1994).

Section 2 (Fig. 6.3b)

The trace of this section is parallel to an ECORS seismic line across the Central Jura (Bergerat et al. 1989; Guellec et al. 1990). It shows a basement high SE of Oyonnax (Fig. 6.3b) beneath the Internal Jura, which was proposed to be inverted after the formation of the JFTB or alternatively, to constitute a pre-JFTB basement horst (Guellec et al. 1990). The External Jura in this section is notably deformed and attributed to the Faisceau Jura. At the front of the Jura, the ECORS seismic line reveals the presence of a small basement horst (Poisoux horst) which was thrust by the Mesozoic cover in Late Miocene (Fig. 6.3b). Another basement horst close to Cormoz ("Cormoz Sill", Debrand-Passard et al. 1984) is revealed beneath a thick Cenozoic sequence (about 900 m in borehole Bresse-101) in the Bourg Basin, lying within the Bresse Graben (Bergerat et al. 1989).

Section 3 (Fig. 6.3c)

The Internal Jura and northern Plateau Molasse reveal a basement dip of roughly 4° to the ESE. The plateaus and faisceaux of the External Jura lie above a significantly flatter basement, dipping about 1.6° in average (Fig. 6.3c). The horst beneath the front of the Jura at Lons-le-Saunier was thoroughly investigated by the oil industry and numerous boreholes were drilled (Lienhardt 1962; Michel et al. 1953). A seismic line (Blanc et al. 1991, see Fig. 6.5 and location in Fig. 6.3c) is parallel to the section trace showing the transition from the Jura into the Bresse Graben. The interpretation of the seismic line reveals onlap structures of Eocene and Early Oligocene sediments in the Louhans Basin (Fig. 6.3c), documenting its formation age. The seismic line (Fig. 6.5) also reveals that the Miocene infill of the Louhans Basin is thrust by the detached cover of the JFTB along a distance of about 8 km.

Section 4 (Fig. 6.3d)

The Internal Jura and Plateau Molasse reveal a basement dip of 3.2° to the SE. In contrast to that, the basement beneath the External Jura reveals considerable lower basement dips of no more than 0.9° to the SE. Since the External Jura lies above a horst of roughly 30 km transect length, the frontal part of the External Jura dips to the NW. A series of low downward steps were identified around the townlet of Quingey (Madritsch et al. 2009; Martin and Mercier 1996). These steps were sufficiently small for the JFTB décollement to ramp down, with throws of about 200 m. To the NW of the JFTB lies the La Serre Horst, which

is a basement block that was exposed during Eocene-Oligocene, when the RBTZ formed (Coromina and Fabbri 2004; Madritsch et al. 2009). Section 4 shows the eastward prolongation of the La Serre Horst, which is covered by Mesozoic sediments. The section trace crosses the relatively shallow northern BG in the NW and ends in the Haute-Saône Plateau (Fig. 6.3d).

Section 5 (Fig. 6.3e)

The Plateau Molasse reveals an average dip of 4° to the SSE whereas the Internal Jura is less steep with a dip of about 2.4° to the SSE. The External Jura lies on a horst structure, which is roughly 20 km wide. Averaged basement dips are about 1.4° to the SSE and NNW (Fig. 6.3e). A basement horst lies north of the detached Jura, which is a prolongation of to the La Serre Horst (the La Serre Massif is exposed roughly 55 km to the WSW).

Section 6 (Fig. 6.3f)

Beneath the Plateau Molasse, the basement reveals dips between 1.8° and 6.7° . The Internal Jura partially lies above a 3.5° SSE dipping basement and the External Jura lies above a flatter basement of 1.1° . Delémont lies structurally on a smaller plateau in the Internal Jura. At the front of the Jura, the basement subsides into the Danemarie Basin, which belongs to the URG. The detached Jura cover does not ramp down the large downward step of about 840 m (Fig. 6.3f). The basement beneath the front of the Jura is documented on seismic lines and interpreted in Ustaszewski and Schmid (2006).

Section 7 (Fig. 6.3g)

The basement beneath the Molasse Basin is rather steep showing a SSE dip of about 4.6° (Fig. 6.3g). From a structural point of view, the Vorfaltenzone is a detached frontal plateau with only little displacement, probably less than a few hundred metres at the front. It lies above a moderately dipping basement of 1.6° . The northern and southern boundaries of the Vorfaltenzone seem to be controlled by the border faults of a Permo-Carboniferous Trough (Constance-Frick Trough, Malz et al. 2019, 2016). In comparison to previous sections (Fig. 6.3b-f), the basement north of the JFTB does not subside but keeps rising towards the Black Forest Massif, which constitutes the eastern rift-shoulder of the URG. The basement along Section 7 is partially constrained by a seismic line, interpreted in Diebold and Noack (1997).

6.3.3 Basement dips of structural domains

Averaged basement inclinations are indicated for all transects in Fig. 6.3 and an overview is compiled in Table 6.3. Dips are separated according to structural domains, which are External Jura, Internal Jura, Plateau Molasse and Subalpine Molasse. Additional histogram plots are created for each structural domain (Fig. 6.6a), showing the distribution of non-averaged basement dips for probing points across the top basement model (Fig. 6.2). Plots in Fig. 6.6b

illustrate the shift to slightly steeper basement dips after a palinspastic restoration of (thin-skinned) structural domains. The palinspastic restoration is done using the displacement model in Appendix B.3 on page 182.

External Jura

Underneath the External Jura, basement dips of max. 2.8° (Fig. 6.3a) to the SE and max. 1.4° to the NW (Fig. 6.3e) are observed. Plateaus of the External Jura lie above scarcely inclined basement blocks, with dips mostly below 1.5° (Fig. 6.3c to e, Fig. 6.6). Strikingly, the front most plateaus lie above basement horsts that show a transect length of about 10 km (Fig. 6.3b to e). Faisceaux tend to lie above steps in the pre-Mesozoic basement. The large frontal faisceaux are commonly associated with border faults of the ECRIS that dip to the NW or WNW and therefore, the décollement of the JFTB partly formed downward ramps (e.g. Faisceau de Quingey in Martin and Mercier 1996). In contrast to that, inner smaller faisceaux are more likely associated with upward steps in the pre-Mesozoic basement and the décollement must form upward stepping ramps to compensate throws. Note that inner faisceaux are transported several kilometres away from the basement step that controlled their deformation and therefore, inner faisceaux might not overlie a basement structure anymore (e.g. Fig. 5.3c and d on page 76).

Internal Jura

The basement beneath the Internal Jura commonly dips between 2.4 to 4° to the SE except in the Eastern Jura, where notably lower dips of 1.6° are observed (Fig. 6.3f and g). Since the JFTB is detached from its pre-Mesozoic basement, the structural domains of the Jura Mountains have initiated several kilometres (up to some 30 km according Affolter and Gratier 2004; Laubscher 1961; Philippe et al. 1996) to the south-east of the present-day position. Considering the restored position of structural domains (Fig. 6.6b), structures in the Internal Jura have initiated above a pre-Mesozoic basement with most abundant dips between 2 to 3° to the SE.

Molasse Basin

Basement inclinations beneath the Internal Jura and the northern Molasse Basin are quite similar. Beneath the central and north-western Plateau Molasse, dips between about 1° to 4.6° are observed (Fig. 6.3a to e). At the restored positions of the Plateau Molasse, the most frequent basement dips are between 3.5° and 4° to the SE (Fig. 6.6b). Neither the present day nor the restored Molasse Basin – Jura limit coincide with abrupt changes in the basement (compare transects in Fig. 6.3). Underneath the eastern Plateau Molasse, the basement shows exceptionally high dips of 6.7° to 9.5° (beneath Bern and Lucerne, see Fig. 6.3f and g). The inclination of the pre-Mesozoic basement underneath the Subalpine Molasse shows high variation, because the basement is partially inverted (e.g. Fig. 6.3c and d), featuring basement dips towards the foreland.

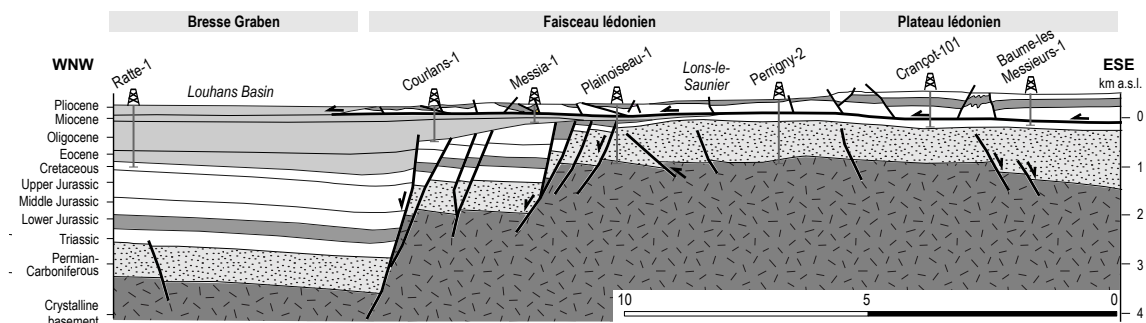


Fig. 6.5 – ESE segment of cross-section modified from Blanc et al. (1991), based on a seismic line and boreholes across the front of the Jura Mountains into the Bresse Graben (see location in Section 3, Fig. 6.3). The JFTB thrusts the eastern border fault zone of the Bresse Graben, which reveals several subsiding blocks. The Bresse Graben shows Eo-Oligocene sediments with onlap structures.

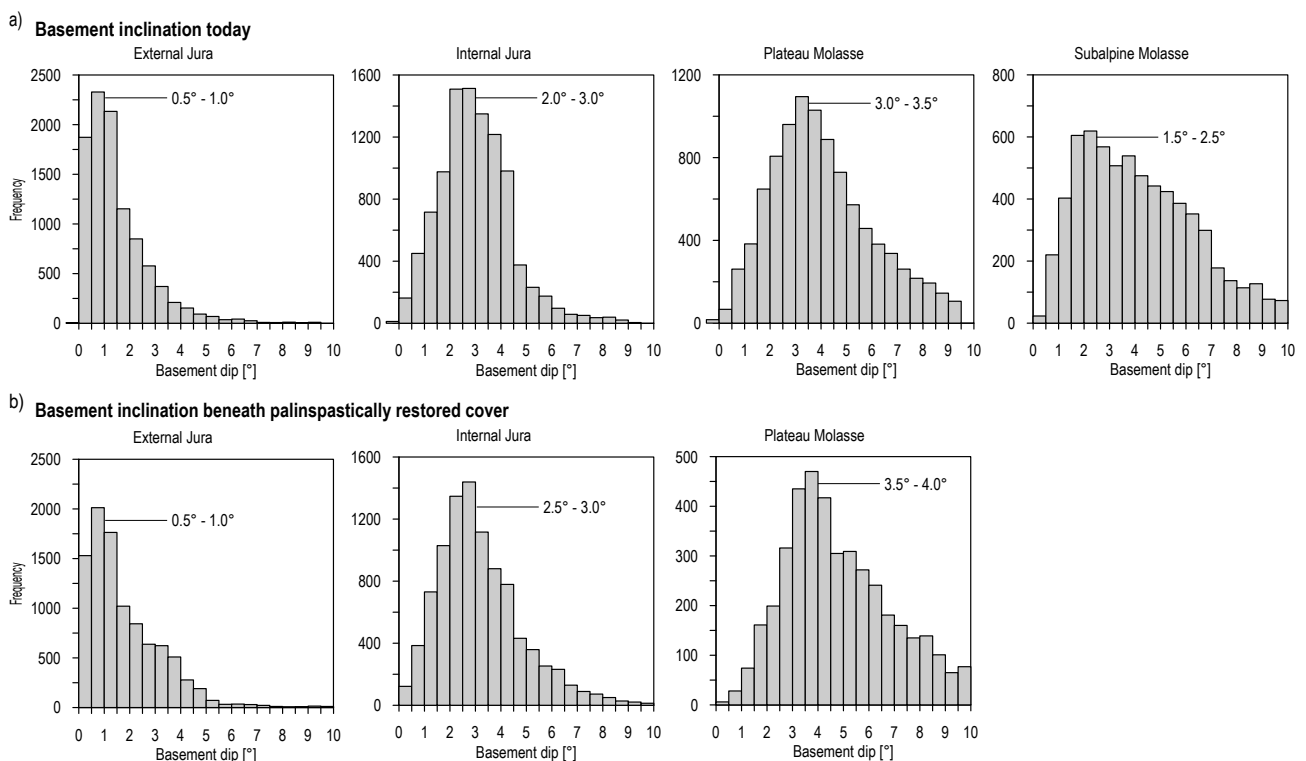


Fig. 6.6 – Distribution of basement inclinations (not averaged) within structural domains in the Molasse Basin and the JFTB. Each histogram contains 10'000 random probing points across the top basement model (Fig. 6.2). Steep dips occurring close to faults are excluded. a) The upper plots illustrate the present-day basement inclinations underneath tectonic domains. b) The lower plots reveal the basement inclination after palinspastic restoration of the cover and its tectonic domains, using the Mio-Pliocene displacement model in Appendix B.3 on page 182. A general shift to slightly steeper dips is observed in comparison to upper plots, but the most frequent dips remain constant except for the Molasse Basin. Basement dips beneath the restored Subalpine Molasse are not shown since restored positions are outside of the range of the top basement model.

Structural domain	Observed basement dip	
	Min.	Max.
External Jura	1.4° NW	2.8° SE
Internal Jura	1.6° SE	4.0° SE
Plateau Molasse	1.0° SE	4.6° SE
Subalpine Molasse	6.0° NW	9.5° SE

Table 6.3 – Averaged basement dips underneath structural domains in the detached Northern Alpine Foreland, observed in cross-sections (Fig. 6.3).

6.3.4 Signature of the flexural basin system

Derivation from top basement model

In order to define an average geometry of the flexural basin system in the study area, profiles from the top basement

model (Fig. 6.2) are extracted and superposed, and a best-fit curve is added (Fig. 6.7a). Uplift and subsidence outliers are highlighted and attributed to the corresponding tectonic system. The most obvious outliers are clearly connected to the formation of the European rift-system (Fig. 6.7a).

Two synthetic curves of flexural basin systems are calculated following different proposals of the foredeep width and forebulge crest positions, based on Burkhard and Sommaruga (1998), Laubscher (1992) and Sinclair et al. (1991). The rather short foredeeps of <120 km that are proposed by these authors, suggest using the formula equation (6.1) for broken plates (DeCelles and Giles 1996). The best-fit curve in Fig. 6.7 indicates a negative deflection of the foredeep (w_d) of -5000 m at the SE rim of the Molasse Basin.

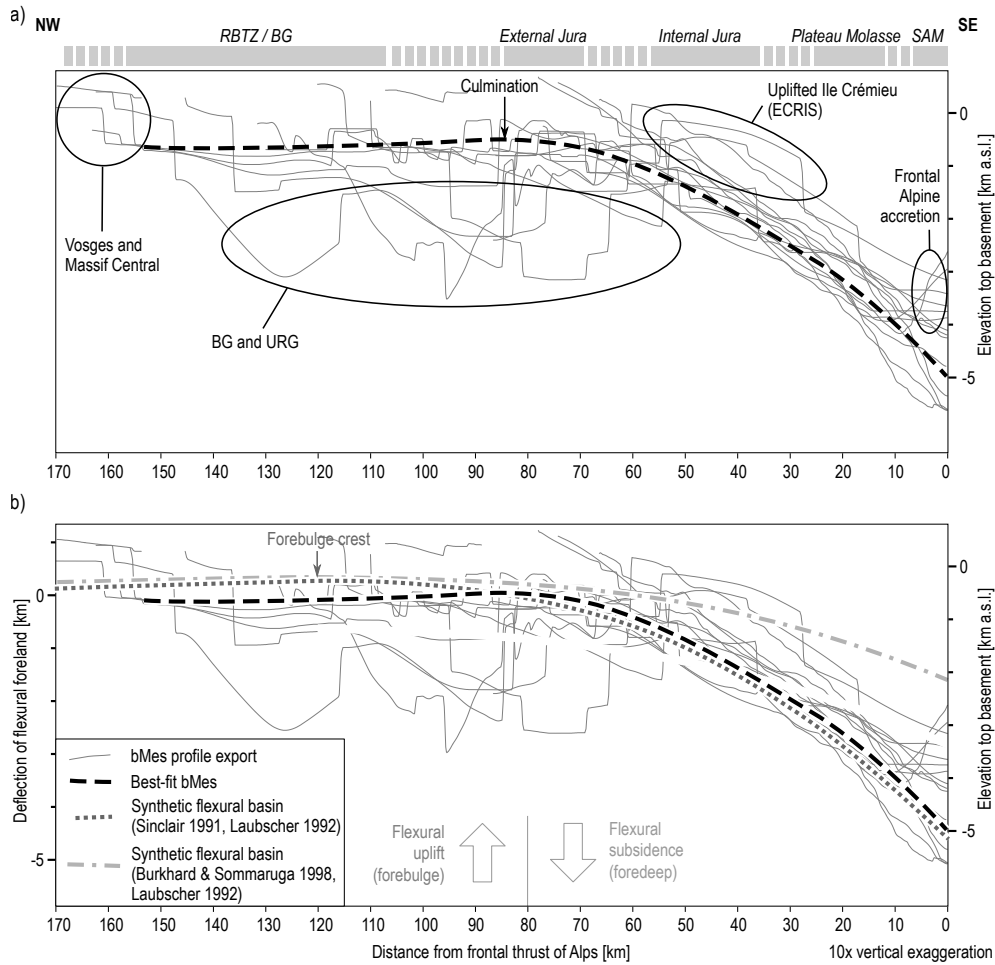


Fig. 6.7 – Geometry of the basement in the study area. a) Averaged best-fit geometry of the basement, deduced from super-position of profiles, extracted from the top basement model (Fig. 6.2). The bold dashed line indicates the best fitting curve for an average basement profile. Outliers are marked, denoting the tectonic system they belong to. Tectonic domains of the Central Jura and Swiss Molasse Basin are given at the top of the diagram, with stippled areas specifying the overlap of domains. b) Comparison of synthetic flexural basin signatures (based on Burkhard and Sommaruga 1998; Laubscher 1992; Sinclair et al. 1991) with the best-fit geometry of the basement (this study). The position of the forebulge crest is set according to Laubscher (1992). Domains of flexural uplift and subsidence for the synthetic curve of Laubscher (1992) and Sinclair et al. (1991) are indicated with arrows at the bottom of the diagram. BG: Bresse Graben, RBTZ: Rhine–Bresse Transfer Zone, SAM: Subalpine Molasse and URG: Upper Rhine Graben.

Comparison of the two synthetic curves with the best-fit curve of the base Mesozoic geometry illustrates that the combined suggestion of Sinclair et al. (1991) and Laubscher (1992) explains the today's basement topography in the area of the JFTB and detached Western Molasse Basin quite well (Fig. 6.7a and b). The flexural uplift at the calculated forebulge crest is 335 m (given the negative deflection w_d of -5000 m). The culmination in the best-fit curve at about 84 km (Fig. 6.7a) is rather owed to interference with the ECRIS and therefore, does not indicate the forebulge crest (roughly at 120 km according to Laubscher 1992, see Fig. 6.7b).

The synthetic flexural forebulge, inferred from the base Mesozoic model of the detached foreland, suggests that the today's foredeep is about 80 km wide (x_d). Therefore, the distal parts of the central External Jura lie in the forebulge, although the forebulge crest lies north of the JFTB. Accordingly, the internal part of the External Jura, the Internal Jura and Molasse Basin lie in the today's foredeep proper (Fig. 6.7).

Flexural Basin across Central and Western Europe

The averaged geometry of the top basement model suggests that the foredeep in the study area is about 80 km wide (Fig. 6.7b). However, the eastern Germanic Molasse Basin is up to 120 km wide and therefore, the foredeep is decidedly larger. In order to understand the regional context of the flexural Alpine foreland, the deflection signature (relative uplift and subsidence) of the present day flexural foreland basin in Central and Western Europe is calculated and presented in maps (Fig. 6.8a and b).

Several profile traces are defined across Central and Western Europe (see Fig. 6.8a), with traces roughly perpendicular to contour lines of the Moho-depth map of Ziegler and Dèzes (2006), close to the Alpine front. The foredeep width (x_d) and negative deflection (w_d) are determined for each profile based on previous works (Table 6.4), and used to calculate the curve of the flexural basin system with equation (6.1). In the Austrian-Germanic Molasse Basin, the calculated deflection signature is based on the foredeep width (x_d) extracted on geological maps (BGR 2015; Pawlewicz et al. 1997) and the thickness of Tertiary deposits (w_d) based on the European GeoMol pro-

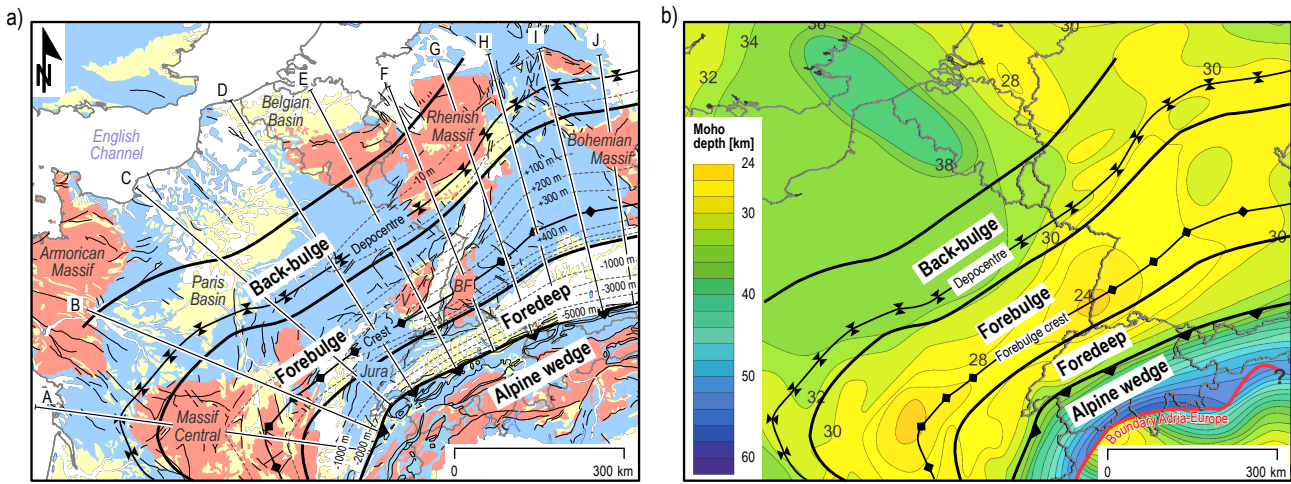


Fig. 6.8 – Calculated flexural basin signature in the Northern Alpine Foreland. Bold dark lines mark the limit between depo-zones (equilibrium lines). a) Depozones of the flexural foreland above the geological map of Central and Western Europe (Pawlewicz et al. 1997). The foredeep corresponds to the Molasse Basin in front of the Alpine wedge. Note that the foredeep is smaller towards the JFTB and broader in the German-Austrian Molasse basin. Profiles A-J are specified in Table 6.4. b) Foreland basin signature above the Moho depth map of Ziegler and Dèzes (2006). The forebulge crest coincides with highs of the mantle, in particular beneath the Massif Central and the Upper Rhine Graben. V: Vosges Massif, BF: Black Forest Massif.

Table 6.4 – Specifications on calculated profiles of the Northern Alpine flexure. Profiles C to F adopt a foredeep geometry as suggested by the geometry of the BMes-model. This involves a shortening of the foredeep in comparison to the foredeep of the German-Austrian foredeep and consequently, a reduced effective elastic thickness. w_d : Negative deflection of the foredeep, x_d : width of the foredeep, T_e : effective elastic thickness, w_c : uplift at the forebulge crest, max. dip: maximum dip of calculated profile, vt_Cen: Vertical thickness of Cenozoic sediments.

Profile	Comment	w_d [km]	x_d [km]	T_e [km]	w_c [m]	Max. dip
J	w_d according LGRB (2019), x_d from Cenozoic deposits	-5.2	115	20.6	349	4.1°
I	Mean of profile H and J	-5.6	118	21.4	375	4.3°
H	w_d according LGRB (2019), x_d from Cenozoic deposits	-6.1	110	19.5	409	5.0°
G	w_d roughly according LGRB (2019), x_d from Cenozoic deposits	-5.4	93	15.6	362	5.2°
F	w_d according vt_Cen of Sommaruga et al. (2012)	-5.2	82.3	13.2	362	5.9°
E	w_d according to Sommaruga et al. (2012) plus rift-signature	-5.0	78	12.3	335	5.7°
D	w_d according vt_Cen of Sommaruga et al. (2012)	-3.6	74.3	11.5	241	4.4°
C	w_d according according Bourgeois et al. (2007)	-2.9	77	12.1	194	3.4°
B	w_d according LGRB (2019), x_d similar profile H	-2.4	108	19.0	161	2.0°
A	w_d roughly according LGRB (2019), x_d from Laubscher (1992)	-2.5	128	23.8	168	1.8°

ject (LGRB 2019, Table 6.4 Profiles G to J). In the area of the Swiss Molasse Basin, the negative deflections of the foredeep (x_d) are according to Bourgeois et al. (2007) and Sommaruga et al. (2012) (Table 6.4, Profiles C to F). The modelled flexural basin signature for the French Molasse Basin is poorly constrained and roughly follows the proposition of Laubscher (1992), see Table 6.4, Profiles A and B.

The calculated flexural basin signature (Fig. 6.8a) illustrates that the foredeep and forebulge depo-zones in the study area and to the north (Fig. 6.8a, sections C to E) are shorter than to the east, in the German-Austrian Molasse Basin. The foredeep width in the German Molasse Basin is up to about 120 km, corresponding to an elastic thickness (T_e) of maximum 22 km. In contrast to this, the foredeep is as short as ~74.3 km in section D (Table 6.4), corresponding to an elastic thickness (T_e) of 11.5 km. The negative deflection of the flexural foredeep (w_d) is significantly smaller in the south-west, where only ~2.5 km Cenozoic sediments are documented (Table 6.4, sections A and B). In contrast to this, the German Molasse Basin shows a thick Cenozoic sequence of up to ~6 km (Table 6.4, sec-

tion H).

Note that maximum uplift of the forebulge is in the range of about 400 m (in Germany) and up to 350 m north of the JFTB (Fig. 6.8a). The calculated signature of the flexural forebulge coincides with peaks of the Moho, underneath the Massif Central and the exposed Vosges and Black Forest Massifs (Fig. 6.8b).

6.3.5 Migration of the flexural basin system

In the previous chapter, the present-day signature of the flexural foreland basin is calculated and shown on maps (Fig. 6.8). However, the flexural basin system migrated across the European (and Briançonnais) plate during Cenozoic times. Associated to this, extensional fractures in the forebulge and extensional faulting in the distal foredeep (Bradley and Kidd 1991) migrated along (the concept of flexural extension is explained in Chapter 2.6.3 on page 35). Note that the foreland flexural basin system evolved during Eocene and Miocene and therefore, faults and fractures due to flexural extension affect the basement as well as the Mesozoic and Tertiary layers. In order to un-

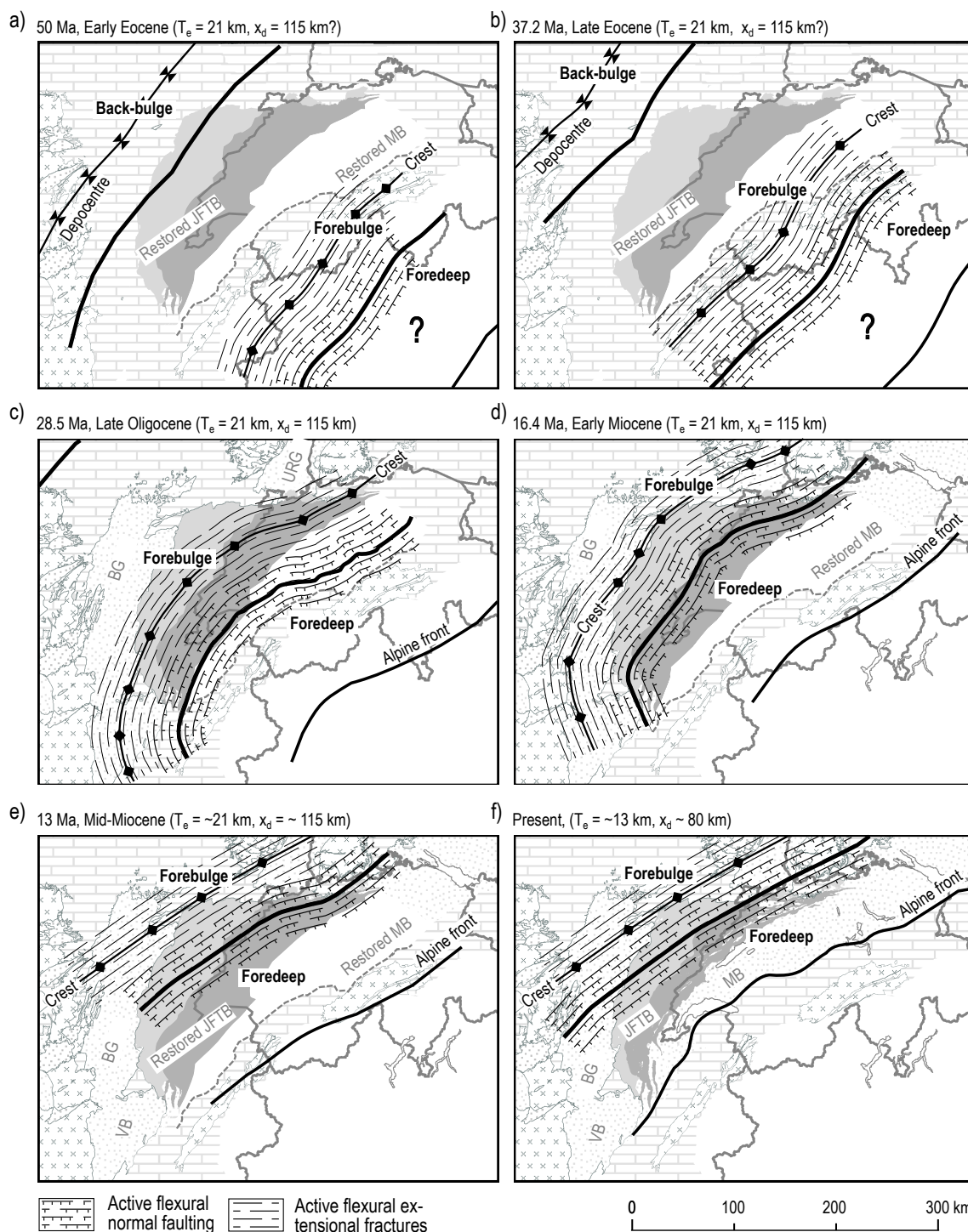


Fig. 6.9 – Sketches of the study area illustrating depo-zones of the flexural Alpine foreland between Eocene and present (see Fig. 6.1 on page 83 for an illustration of depo-zones). The frontal limits of the foredeep are according to Ford et al. (2006), whereas the forebulge, back-bulge and elastic thickness (T_e) of the lithosphere are calculated based on an estimated foredeep width (x_d). Zones of active flexural fracturing and flexural faulting are indicated following observations of Bradley and Kidd (1991) in the Mohawk fold-and-thrust belt (see introduction of concept in Chapter 2.6.3 on page 35). Note that the JFTB is palinspastically restored for Eocene to Mid-Miocene sketches, using the displacement model in Appendix B.3. a, b) The Eocene position of the foredeep is not well constrained (Ford et al. 2006) and the geometry of the flexural forebulge uncertain, since the Briançonnais Plate is still subducting. c) In Late Oligocene, the European plate is subducting. The forebulge crest reaches the domain of the future JFTB and extensional fractures are expected close to the forebulge crest. Active flexural normal faults are expected in the area of the future Molasse Basin. d) Flexural normal faults start to affect the area of the future External Jura and the Internal Jura in Early Miocene. e) The forebulge crest reaches the crustal weakening provided by the northern Bresse Graben, RBTZ and the URG. f) The forebulge crest remains in the area of the RBTZ but the foredeep possibly still propagates. The elastic thickness of the lithosphere is reduced allowing a narrower forebulge. BG: Bresse Graben, JFTB: Jura fold-and-thrust belt, MB: Molasse Basin, URG: Upper Rhine Graben, VB: Valence Basin.

derstand the arrival of depo-zones and flexural extension fractures in the study area, the migration of the flexural basin system during Cenozoic is modelled and presented on maps (Fig. 6.9a to f). The limits of Tertiary sediments of Ford et al. (2006) are used to constrain the foredeep position through Cenozoic times and the geometry of the flexural basin is based on previously established parameters (Fig. 6.7 and Fig. 6.8).

Derivation of parameters and limitations

The Eastern Molasse Basin shows a maximum foredeep width (x_d) of about 115–130 km corresponding to an elastic thickness of 21 to 24 km (see Table 6.4). This is assumed to represent the flexural parameters of the European plate, unaffected by a pre-existing weakening of the ECRIS. The present day geometry of the detached foreland basin, extracted from the top basement model (Fig. 6.7), supports a short foredeep in the area of the Western Molasse Basin and indicates a foredeep width of about 80 km (corresponding to an elastic thickness of ~13 km). Laubscher (1992) justifies a short width of the western foredeep by suggesting that the forebulge is locked on the lithospheric mechanical weakness provided by the ECRIS, in particular the northern BG, RBTZ and URG. Therefore, a reduced foredeep width is supposed to only occur close to the ECRIS and rather late in the evolution of the flexural basin. Note that Burkhard and Sommaruga (1998) point out that the foredeep width (x_d , as well as the elastic thickness of the lithosphere T_e) is possibly not reduced after all, since the Penninic and Helvetic nappes of the Alps are thrust over the south-eastern part of the Molasse Basin and hide several kilometres of Tertiary deposits (up to about 40 km).

The evolution of the forebulge and associated flexural parameters from Eocene to present day involve large insecurities (Stampfli et al. 1998). At the end of Eocene (about 34 Ma), the European slab break-off occurs (Schlunegger and Kissling 2015) together with beginning continent-continent collision of Adria and Europe. Before this major dynamic change, the Briançonnais Plate was still subducting and it is unclear, how far the European plate was deflected as well. Therefore, the representation of the flexural foreland basin in Eocene (Fig. 6.9a and b) is fraught with high uncertainty. The Oligocene to present day geometry of the foredeep is better constrained and the foredeep width is estimated roughly between 100 to 150 km (Burkhard and Sommaruga 1998; Stampfli et al. 1998).

Eocene

Inferred from the Eocene limits of the foredeep (Ford et al. 2006), the forebulge crest would lie in the area of the present day position of the External Crystalline Massifs (Belledonne, Aiguilles-Rouges, Mont-Blanc, Aar and Gotthard Massif) by 37.2 Ma (Fig. 6.9b) and at the end of Eocene (~34 Ma), the forebulge crest arrives in the area of the future Internal Jura. First flexural extensional fracturing is therefore expected in the Internal Jura by Late Eocene, no earlier than Priabonian (Fig. 6.9b). Furthermore, the Eocene unconformity in the Molasse Basin and

Internal Jura is likely associated with the migration of the forebulge.

Late Oligocene

By Late Oligocene, the forebulge crest migrated north-westwards into the domain of the future External Jura (Fig. 6.9c). Following this, the western External Jura and the Eastern Jura are affected by flexural extensional fractures whereas the southern Internal Jura, as well as the Mesozoic sediments and Oligocene Molasse deposits (UMM and USM) within the future Molasse Basin are affected by flexural normal faulting.

Early Miocene

The forebulge crest arrives at the front of the JFTB in Early Miocene (Fig. 6.9d). The foredeep is still about 120 km wide but the forebulge crest reaches the URG, where it remains stationary during the future evolution of the flexural basin. Mesozoic sediments of the future Internal Jura lie within the zone of flexural normal faulting and first flexural normal faults affect the most internal part of the future External Jura as well (Fig. 6.9d).

Mid-Miocene

Shortly before the main formation stage of the JFTB, the forebulge crest reaches its final position, which follows the lithospheric weakening of the ECRIS across the Northern Bresse Graben, the RBTZ and the southern URG (Fig. 6.9d).

Present

The Molasse Basin is transported up to about 30 km north-westwards in Mio-Pliocene (Affolter and Gratier 2004; Laubscher 1961; Philippe et al. 1996) and the JFTB forms at the same time. Former flexural fractures and faults are therefore transported north-westwards above the basal décollement of the detached NAF. Between Mid-Miocene and the present day, the forebulge crest seems not to have migrated any more (Burkhard and Sommaruga 1998). However, due to continuous Alpine growth and lithospheric subduction, the foredeep might have migrated yet, which needs a reduced elastic thickness of the European plate (Fig. 6.9f). Associated to ongoing evolution of the northern Alpine foredeep, recent flexural normal faulting would still affect the Central and Eastern Jura (Fig. 6.9f).

6.4 DISCUSSION

6.4.1 Inherited Palaeozoic structures controlling deformation in the Jura

Of the three Palaeozoic structural trends (Chapter 2.5.2 on page 31), which are inherited from the Variscan orogeny and post-orogenic collapse, NNE–SSW (Rhenish) and ENE–WSW (Erzgebirgian) lines within the basement

of the Jura Mountains are clearly identified. NW–SE (Hercynian) orientations are not completely represented in the top basement model of the JFTB (Fig. 6.2). Nevertheless, NW–SE striking basement faults are suspected in the Southern Jura towards the limit to the île Crémieu and they were also documented in the Vorfaltenzone and the Tabular Jura south of Schaffhausen (Fig. 6.2). Their localisation underneath the highly deformed Mesozoic cover of the Internal Jura is complex and a constraint from boreholes was not possible.

NW–SE Hercynian faults

NW–SE striking Hercynian faults constituted smaller trigger lines for the deformation of the detached cover in the Vorfaltenzone, which lies on the outermost tip of the Eastern Jura south of the Black Forest Massif (Madritsch et al. 2018). Similarly, Chauve et al. (1988) proposed NW–SE striking basement faults in the External Jura close to Lons-le-Saunier (Fig. 6.2), derived from boreholes, yet these basement faults seem not to have localised deformation of the detached Mesozoic cover. In the central Internal Jura, east of the Pontarlier fault zone, Philippe (1995) proposed NW–SE striking lineaments in the detached cover, which are presumably controlled by basement structures. Furthermore, the NW–SE striking Vuache and Pontarlier lines of the Internal Jura are also suspected to reflect a basement structure with a similar orientation (Laubscher 1961). From analogue modelling in this study (Chapter 8 on page 107), it is furthermore suspected that triangular nappes between Oyonnax and Vuache were controlled by a NW–SE striking basement fault.

An attempt to specify the origin of basement faults that controlled lineaments in the JFTB is presented in Appendix B.4 on page 192. By means of palinspastic restoration based on the displacement model in Appendix B.3 on page 182, lineaments are palinspastically restored. NW–SE to NNW–SSE striking basement faults are suspected underneath the Southern Jura and the Central Internal Jura, partially continuing underneath the Molasse Basin (Fig. B.10 on page 193).

NNE–SSW Rhenish faults

Structures with a NNE–SSW (Rhenish) orientation are abundantly documented within the detached cover of the External Jura (Madritsch et al. 2009; Ustaszewski and Schmid 2006) and Eastern Jura (Laubscher 2008a,b; Steinmann 1902). In the western External Jura around Lons-le-Saunier, basement rooting, NNE–SSW striking BG border faults were active during Eocene to Early Miocene (Chauve et al. 1988; Michel et al. 1953; Sissingh 1998). The western front of the Jura was pre-determined by border faults of the eastern BG, showing high vertical offsets of up to 2.8 km (see Fig. 6.3, Table 6.2). These border faults exceeded a critical throw (threshold offset) and the basal décollement of the Jura does not ramp downwards, but rather propagates horizontally and up-section, thrusting the Tertiary infill of the BG. In the northern plateaus of the External Jura, however, NNE–SSW (Rhenish) trending normal faults within the cover were partially react-

ivated during thin-skinned deformation as sinistral strike-slip faults, that dissect and offset folds (Laubscher 1981; Philippe et al. 1996; Tschanz 1990).

ENE–WSW Erzgebirgian faults

ENE–WSW Erzgebirgian striking normal faults occur along the northern and eastern front of the JFTB and seem to have defined the frontal limit of the Jura in the area around Besançon, the Ferrette Zone lying in between Porrentruy and Basel and the Eastern Internal Jura (Fig. 6.2). Additionally, a rather important ENE–WSW striking normal fault system beneath the Faisceau salinois separates the southern Plateau Jura from the northern Plateau Jura (Salinois fault zone, no. IV, Fig. 6.2). Identified ENE–WSW (Erzgebirgian) striking normal faults commonly constitute downward steps in the direction of transport during the formation of the JFTB. These ENE–WSW fault systems are oblique to the general NW direction of transport of the JFTB and therefore, oblique structures with downward ramps are triggered at ENE–WSW (Erzgebirgian) striking basement steps. An exception occurs north of Besançon, where an ENE–WSW striking normal fault system provides an upward step for the Late Miocene direction of transport (Fig. 6.2 on page 84 and Sections 4 and 5 in Fig. 6.3 on page 85).

6.4.2 Eo-Oligocene rifting

Towards the front of the Jura Mountains, the uplift of rift-shoulders associated with ECRIS rifting led to a moderate initial basement inclination towards the ESE and SSE, of no more than 1.5° to 2° . Given the maximum tectonic uplift of about 930 m at Lons-le-Saunier (Table 6.2) and an estimated basement inclination of $\sim 1.5^{\circ}$ in the External Jura (e.g. Section 3, Fig. 6.3), it is estimated that the main effects of rift-shoulder uplift affected the basement at least up to 35 km away from ECRIS border faults. It is suggested that rift-shoulder uplift led to a reactivation of pre-existing Variscan basement faults in the area of the External Jura, such as the L'Heute Fault Zone, Salinois Fault Zone or the normal fault at Syam (Fig. 6.2). Faults that were active during uplift of rift shoulders formed between Late Eocene and Early Oligocene (about 39 to about 28 Ma, Madritsch et al. 2009; Ring and Gerdes 2016; Sissingh 1998).

Rift-shoulder uplift also induced a thorough erosion of the Mesozoic cover towards the front of the future JFTB and certainly prevented sedimentary deposits after Late Eocene times above rift-shoulders. The Eocene unconformity at the front of the JFTB and parts of the External Jura is therefore owed to rift-shoulder uplift.

6.4.3 Oligo-Miocene foredeep evolution

Modelling of the migration of the flexural basin system shows that the forebulge crest reached the Mesozoic sediments beneath the future Molasse Basin by Late Eocene and the crest did not reach the Mesozoic sediments of the future JFTB before Priabonian (Fig. 6.9b and c). The model therefore confirms that the base Eocene unconformity in the Molasse Basin is in connection with the fore-

bulge. The crest migrated to the front of the JFTB by Early Miocene (in about 15–20 My).

The present-day forebulge crest presumably remained in the area of the RBTZ since Miocene (Fig. 6.9d to f). Only the northern External Jura (e.g. Plateau d'Ornans s.l., Faisceau de Quingey, Besançon zone) is therefore presently affected by the present day forebulge, which is superposed on uplift of the ECRIS rift shoulders. Calculated uplift owed to the forebulge in the northern External Jura are below 250 m, whereas uplift owed to rift shoulder uplift is estimated at ~200 m in the Plateau d'Ornans (Table 6.2 on page 86, section 5).

The main vertical movements occur in the foredeep, which enters the domain of the future JFTB by Late Oligocene (Fig. 6.9c). Connected to subsidence movements is normal faulting in the distal foredeep and the proximal forebulge depozone, with offset distances along individual faults of several hundred metres, similar to observations in the Mohawk thrust-belt (Bradley and Kidd 1991). It is proposed that mainly pre-existing faults are reactivated, which are inherited from the Variscan orogeny. Reactivations of faults in connection with the foredeep in the JFTB are presumed to be younger than about 28 Ma (Fig. 6.9c), therefore post-dating normal faulting owed to rifting of the BG and URG. Note that faults active during Eo-Oligocene rifting were possibly reactivated again during the evolution of the flexural foredeep. This situation applies in particular to the External Jura that is strongly affected by the effects of Eo-Oligocene rifting (see Chapter 9.4 on page 138 for a more detailed study). The pre-existing L'Heute Fault Zone and Syam Fault Zone (Fig. 6.2) for example show ideal NNE–SSW strikes to be reactivated during WNW–ESE and NW–SE extension occurring due to the inflection of the European lithosphere.

6.4.4 Basement dip and structural domains

In the sense of the critical wedge theory (Dahlen 1990; Davis et al. 1983), the dip of the basement in the detached NAF corresponds to the basal taper (β) of the foreland wedge. Generally, a steeper basal taper leads to more internal deformation of a wedge and connected to this, a steeper surface taper α (Davis et al. 1983). Measured dips in the top basement model suggest that a decrease of the basal angle (taper β) below about 2° was favourable for the formation of kilometric plateaus in the External Jura. Basement dips in the Internal Jura are rather steeper. Therefore, it is concluded that the basal taper pre-determined the limit between the Internal and the External Jura. Note that a basement inclination of more than about 2° is rather owed to the evolution of the flexural foredeep.

In contrast to this, the limit between the Molasse Basin and the Jura Mountains is decidedly not in connection with a change of the basal taper β . The most frequent basement dips in the Internal Jura (2.5°–3°, Fig. 6.6) are slightly lower than in the Molasse Basin (3°–3.5°, Fig. 6.6), which would even contradict a more intensive deformation of the Internal Jura. It follows that the extent of Tertiary deposits within the Alpine foredeep maintaining a sufficient surface taper α prevented intense internal deformation of the Molasse Basin, which supports findings of Philippe (1995)

and Philippe et al. (1996).

6.5 CONCLUSIONS

Fault zones in the basement

Faults in the pre-Mesozoic basement of the JFTB, active during Cenozoic times, are proposed to follow inherited Variscan orientations revealing Rhenish, Erzgebirgian and Hercynian orientations (see Chapter 2.5.2 on page 31):

- In the Southern Jura and the southern Plateau Jura, NE–SW to NNE–SSW striking (Rhenish) basement faults are dominant. The northern Plateau Jura (north of the Salinois Fault Zone) and Eastern Jura reveal abundant ENE–WSW (Erzgebirgian) basement faults next to Rhenish basement fault.
- NW–SE (Hercynian) basement faults are proposed beneath the Internal Jura, on behalf of lineaments in the JFTB as for example the Vuache lineament (Laubscher 1961). However, such basement faults would lie several kilometres south-east of lineaments that are imprinted in the detached cover.
- The eastern border fault zone of the Bresse Graben follows a NNE–SSW Rhenish trend. The fault zone shows frontal horsts (e.g. Poisoux horst) and subsiding blocks. The Île Crémieu constitutes the uplifted rift shoulder of the southern Bresse Graben.
- The border fault of the Ile Crémieu lies on a NNE–SSW (Rhenish) striking line with the possibly inverted Oyonnax fault and the normal fault beneath the Faisceau de Syam. Between the Ile Crémieu and the Faisceau de Syam, this fault system coincides with the front of the Internal Jura. The Ile Crémieu–Oyonnax segment shows subsidence to the NW whereas the Syam segment shows subsidence of the south-eastern block.

Inclination of the basement

Frontal faisceaux (e.g. Revermont, Faisceau lédonien, Faisceau de Quingey, Faisceau des Avant-Monts) lie above downward steps in the basement, whereas inner faisceaux (e.g. Faisceau de Syam, Faisceau de l'Heute) tend to be in connection with upward basement steps. The External Jura reveals a pre-Mesozoic basement with most frequent inclinations smaller than about 1.5°, both to the NW and SE. Most frequent basement dips in the Internal Jura are between 2° to 3°, whereas in the Plateau Molasse, most frequent dips are slightly steeper, between 3° and 3.5°. The proximal Plateau Molasse in eastern Switzerland shows considerably steeper basement inclinations of up to 9.5°. The Subalpine Molasse reveals a basement with high dip variation in the range of 6° NW to 9.5° SE. Dips to the NW are owed to a partial inversion of the basement.

Cenozoic uplift and erosion

The uplift of ECRIS rift-shoulders resulted in an increased erosion of the Mesozoic cover towards the front of the fu-

ture Jura Mountains, prevailing since Late Eocene (about 39 Ma). Substantial tectonic uplift in connection with rifting is estimated along the eastern BG border fault zone (Fig. 6.2), with uplifts of up to ~930 m in the area of Lons-le-Saunier. In comparison to this, the highest calculated flexural uplift of the Northern Alpine forebulge crest is in the range of 350 m. Therefore, the erosion of about 1200 m sediments at the front of the Jura (see Fig. B.3 on page 180), is mainly linked to rift shoulder uplift and only subordinately to flexural bulging.

The crest of the present-day forebulge lies to the north of the JFTB and therefore, the majority of the Jura Mountains passed the stage of flexural uplifting. Only the northern External Jura (northern Plateau d'Ornans s.l., Besançon Zone) probably still lies in the recent forebulge proper, showing uplift of no more than 250 m. The majority of the JFTB lies in the present day foredeep. Subsidence of the flexural basin competed with uplifts of ECRIS graben shoulders and therefore, Molasse deposits are generally absent in the External Jura.

Migration of flexural depo-zones

A reconstruction of the migration of the flexural foreland basin system since Eocene reveals the arrival of depo-zones and flexural fracturing:

- In Early Eocene, the Mesozoic sediments of the future JFTB and MB lie within the distal forebulge. Flexural extensional fractures are not expected. The back-bulge lies in the area of the northern BG and northern URG during Eocene times, possibly causing shallow lacustrine deposits in the BG and URG of Lutetian age (Singh 1998), which are slightly older than main rifting.
- The Eocene unconformity in the Molasse Basin and Internal Jura is likely associated with the migration of the forebulge (Fig. 6.9a and b), whereas the Eocene unconformity in the External Jura is rather owed to the formation of the ECRIS.
- Flexural extensional fractures are not expected in the area of the JFTB before Oligocene. Flexural normal faults enter the domain of the JFTB by Late Oligocene, the External Jura by Early Miocene. They post-date normal faults of the ECRIS therefore. Flexural extensional fractures and normal faults at least partially manifest along inherited Rhenish (NNE–SSW) and Erzgebirgian (ENE–WSW) orientations.

Factors controlling deformation of the detached foreland

In summary, there are three main factors in connection with Cenozoic deformation, which effectively controlled the Miocene deformation of the Molasse Basin and in particular the JFTB:

- The basement is inclined (basal taper β) due to uplift of ECRIS graben shoulders and due to subsidence in the flexural foredeep. The main factor for the structural difference of Internal and External Jura is ascribed to a difference of the basal taper β .

- Deposition of Molasse (maintaining a constant surface taper α) in the flexural foredeep is considered the main factor for a concentration of deformation in the distal Internal Jura rather than in the proximal Molasse Basin.
- There are pre-existing Variscan basement discontinuities, reactivated during uplift of ECRIS graben shoulders in Eo-Oligocene and again by flexural faulting beginning no earlier than Late Oligocene. Such pre-JFTB normal faults with several hundred metres offset controlled deformation of the JFTB: i) The front of the JFTB was pre-conditioned by the eastern BG border fault zone and to the north, by ENE–WSW striking faults (e.g. Avant-Monts fault zone, frontal fault of Ferrette Zone). ii) The southern Plateau Jura is separated by the Salinois fault zone from the northern Plateau Jura. iii) Finally, the front of the Internal Jura is partially pre-conditioned by basement faults.

7 - DATING AND CHRONOLOGY OF TECTONIC EVENTS

7.1 INTRODUCTION

7.1.1 Aim of chapter

This chapter is dedicated to the structural understanding of dated locations in the JFTB. Only recently, in-situ U-Pb calcite dating was successfully used to date precipitated calcite in faults and it is now proven to be an efficient tool to date tectonic events in the relatively young JFTB (Looser et al. 2020; Ring and Gerdes 2016; Rittner 2012; Smeraglia et al. 2021). U-Pb dating has great potential to shed new light on the whole of the Jura arc, because it is not restricted to locations where Tertiary sediments occur.

Subsequently, an overview of currently discussed ages in the JFTB and surrounding is presented. Available data points of dated locations are illustrated on a structural map (Fig. 7.1) and chronologically listed in Table 7.2, which helps to visualise and understand the structural context of dated locations. Finally, an own sample of a thrust in the southern Plateau Jura is discussed, which contains interesting U-Pb calcite ages, dated and courtesy by Nathan Looser at ETH Zurich.

7.1.2 Dating of the Jura: an overview

For a long time, dating of tectonic ages in the JFTB was done by means of Tertiary sediments and their structural relations with folds and thrusts (Becker 2000 and references therein). Such dating ultimately concentrates on the Eastern Jura, parts of the Internal Jura and the front of the JFTB, where suitable Tertiary sediments predominantly occur. Subsequently, absolute age allocations follow Berger et al. (2005) for European Mammal Zones (MN-zonation, see Table 7.1). Only recently, U-Pb calcite dating of faults and veins is used to improve the resolution of structural ages within the JFTB and surrounding (Egli et al. 2017; Looser et al. 2020; Mazurek et al. 2018; Ring and Gerdes 2016; Rittner 2012; Smeraglia et al. 2021).

Beginning of thrust-belt tectonics

According to Becker (2000), the youngest OSM deposits within the Jura belong to MN8 (~13.6 to 11.2 Ma). These freshwater deposits are found in the Ajoie and at Laufen (Table 7.2) and originate from the Vosges and the Black Forest Massif (BF). It is supposed that tectonic uplift in connection with the thin-skinned detachment of the Jura Mountains prevented further deposition of siliciclastic sediments afterwards. Folding probably started slightly ahead of these OSM deposits, in Serravallian but no later than ~12 Ma. Note that the majority of the Jura Molasse is found in the Eastern and Central Internal Jura, and ages deduced from Tertiary deposits are assumed to be representative for the rest of the fold-and-thrust belt. In the Delémont basin, the fauna from the Bois de Raube Formation can be used to specify additional tectonic events. It is concluded that folding must be younger than MN7 (~13.6 Ma) with thrusting of the Vorbourg anticline after MN9 (11.2 to 9.5 Ma, Becker 2000 acc. Kälén 1997). It seems that these ages can be correlated to a dynamic change in the ongoing

MN-zone	Absolute Age
MN5	16.7 - 14.8 Ma
MN6	14.8 - 13.7 Ma
MN7	13.7 - 13.6 Ma
MN8	13.6 - 11.2 Ma
MN9	11.2 - 9.5 Ma
MN10	9.5 - 9.0 Ma
MN11	9.0 - 8.2 Ma
MN12	8.2 - 7.0 Ma
MN13	7.0 - 4.8 Ma
MN14	4.8 - 4.2 Ma
MN15	4.2 - 3.4 Ma

Table 7.1 – Absolute age allocation of Neogene European Mammal Zones (MN-zone) according to Berger et al. (2005).

Table 7.2 – List of dated locations in the JFTB and surroundings (see Fig. 7.1 for positions). The specification of absolute ages for stages is according to the International Chronostratigraphic Chart (Cohen et al. 2020). The «Pontian» age formerly used in French literature corresponds to the Messinian stage (Cohen et al. 2020). Absolute ages of Neogene Mammal Faunal Zones (MN-zones) are according to Berger et al. (2005) if not specified differently. Ages in the list are allocated to different tectonic events: AC = Alpine compression, FAC = basement involved, far-field Alpine compression, Flex = flexural extension and faulting of the peripheral Alpine foreland, Jura = thin-skinned deformation of the Jura Mountains, Rift = formation of the ECRIS.

No.	Age	Event	Description
1	2.2±6.4 Ma	Jura	This work, U-Pb calcite dating of slickenfibres in reverse fault
2	3.4 to 4.2 Ma	Jura	Becker (2000), MN15, karstic fissure filling from the «Vue des Alpes»
3	3.9±2.9 Ma	Jura	Smeraglia et al. (2021), Vue des Alpes tear fault, U-Pb calcite dating of extensional vein
4	4.5±1.5 Ma	Jura	Looser et al. (2020), Habsburg, U-Pb calcite dating of slickenfibres in gently dipping thrust
5	4.8±1.7 Ma	Jura	Smeraglia et al. (2021), Pratz tear fault, U-Pb calcite dating of slickenfibres
6	5 to 12 Ma	AC	Mock et al. (2019), activity of thrusts from low-temperature apatite thermochronometry
7	5.3 to 7.2 Ma	Jura	Michel et al. (1953), thrust «Pontian» sediments in Courlans-1
8	5.3 to 7.2 Ma	Jura	Chauve et al. (1988) referring to Lefavrais-Raymond (1962), stratigraphic age of tectonic breccia
9	5.3 to 7.2 Ma	Jura	Geological map 1:50K France (BRGM 2004), tectonic breccia (Late Miocene / «Pontian» age)
10	5.7±4.7 Ma	Jura	Smeraglia et al. (2021), Buron tear fault, U-Pb calcite dating of extensional vein
11	6.1±0.5 Ma	Jura	Looser et al. (2020), Aaretal-Auenstein, U-Pb calcite dating of sinistral slickenfibres
12	6.2±0.7 Ma	FAC	Egli et al. (2017), Randen Fault (sample 1), U-Pb dating of slickenfibres in dextral fault
13	7.3±1.3 Ma	FAC	Egli et al. (2017), Randen Fault (sample 2), U-Pb dating of slickenfibres in dextral fault
14	7.3±1.9 Ma	Jura	Smeraglia et al. (2021), Pratz tear fault, U-Pb calcite dating of extensional vein
15	7.5±1.1 Ma	Jura	Smeraglia et al. (2021), Arguel thrust, U-Pb calcite dating of extensional vein
16	9.1±6.5 Ma	Jura	Smeraglia et al. (2021), Pratz tear fault, U-Pb calcite dating of extensional vein
17	9.1±1.4 Ma	Jura	Looser et al. (2020), Schafisheim-1 (SCH-1), U-Pb calcite dating of veins (population VP4)
18	9.1±0.9 Ma	Jura	Rittner (2012), U-Pb calcite dating of slickenfibres in strike-slip fault, indicating maximum age of folding
19	9.3±1.1 Ma	Jura	Looser et al. (2020), Asperchus, U-Pb calcite dating of sinistral slickenfibres
20	9.6±0.2 Ma	Jura	Smeraglia et al. (2021), Fuans thrust, U-Pb calcite dating of slickenfibres
21	9.7±1.4 Ma	Jura	Smeraglia et al. (2021), Fuans thrust, U-Pb calcite dating of slickenfibres
22	9.9±0.6 Ma	Jura	Looser et al. (2020), Asp-Ueslimatt, U-Pb calcite dating of slickenfibres on gently dipping thrust
23	10.5±0.4 Ma	Jura	Smeraglia et al. (2021), Pratz tear fault, U-Pb calcite dating of extensional vein
24	10.6±0.5 Ma	Jura	Smeraglia et al. (2021), Buron thrust, U-Pb calcite dating of extensional vein
25	10.6±0.4 Ma	Jura	Looser et al. (2020), Habsburg, U-Pb calcite dating of slickenfibres on gently dipping thrust
26	10.8±1 Ma	Jura	Looser (2019, personal communication), U-Pb calcite dating of slickenfibres in dextral fault
27	~11 Ma	Jura	Becker (2000) according Kälén (1997), thrust Bois de Raube Formation (MN9)
28	11 to 15 Ma	Flex	Mazurek et al. (2018), Schlattigen-1 (SLA-1), U-Pb calcite age dating of veins in Dogger Group
29	11.2 to 13.6 Ma	Jura	Piquerez et al. (2012), Laufen, youngest OSM deposits (MN8) indicate initial folding
30	11.2 to 13.6 Ma	Jura	Piquerez et al. (2012), Ajoie, youngest OSM deposits (MN8) indicate initial folding
31	11.3±0.9 Ma	Jura	Looser et al. (2020), Asp-Ueslimatt, U-Pb calcite dating of slickenfibres on gently dipping thrust
32	11.4±1.3 Ma	Jura	Smeraglia et al. (2021), Montlebon thrust, U-Pb calcite dating of extensional vein
33	13.6 to 13.7 Ma	Jura	Becker (2000) according Kälén (1997), MN7
34	13.8 to 16.0 Ma	Jura	Deville et al. (1994), thrust Molasse deposits (Late Burdigalian-Langhian)
35	14.3±0.5 Ma	Jura	Looser et al. (2020), Schafisheim-1 (SCH-1), U-Pb calcite dating of veins (population VP1)
36	15 to 18 Ma	Flex	Mazurek et al. (2018), Oftringen-1 (OFT-1), U-Pb calcite age dating of veins
37	~16.7 Ma	Flex?	Rime (2017), gompholite (base MN5) indicating first topography
38	21.8±3.4 Ma	Rift	Ring and Gerdes (2016), U-Pb calcite dating on fibres on fault (sample H3)
39	22.3±4.6 Ma	Rift	Ring and Gerdes (2016), U-Pb calcite dating on fibres on fault (sample H6)
40	24±6.3 Ma	Rift	Ring and Gerdes (2016), U-Pb calcite dating on fibres on fault (sample H2)
41	25.3±5.6 Ma	Rift	Ring and Gerdes (2016), U-Pb calcite dating on fibres on fault (sample H4)
42	31 to 37 Ma	Rift	Mazurek et al. (2018), Schlattigen-1 (SLA-1), U-Pb calcite age dating of veins
43	32 to 38 Ma	Rift	Madritsch et al. (2009), fission track ages of La Serre horst border faults, indicating exhumation
44	39±3 Ma	Rift	Mazurek et al. (2018), Oftringen-1 (OFT-1), U-Pb calcite age dating of vein in Effingen Member
45	44.3±4 Ma	Rift?	This work, U-Pb calcite dating of vein
46	44.7±2.4 Ma	?	Smeraglia et al. (2021), Vue des Alpes tear fault, U-Pb calcite dating of shear vein (strike-slip)
47	48.4±1.2 Ma	?	Smeraglia et al. (2021), Vue des Alpes tear fault, U-Pb calcite dating of shear vein (strike-slip)

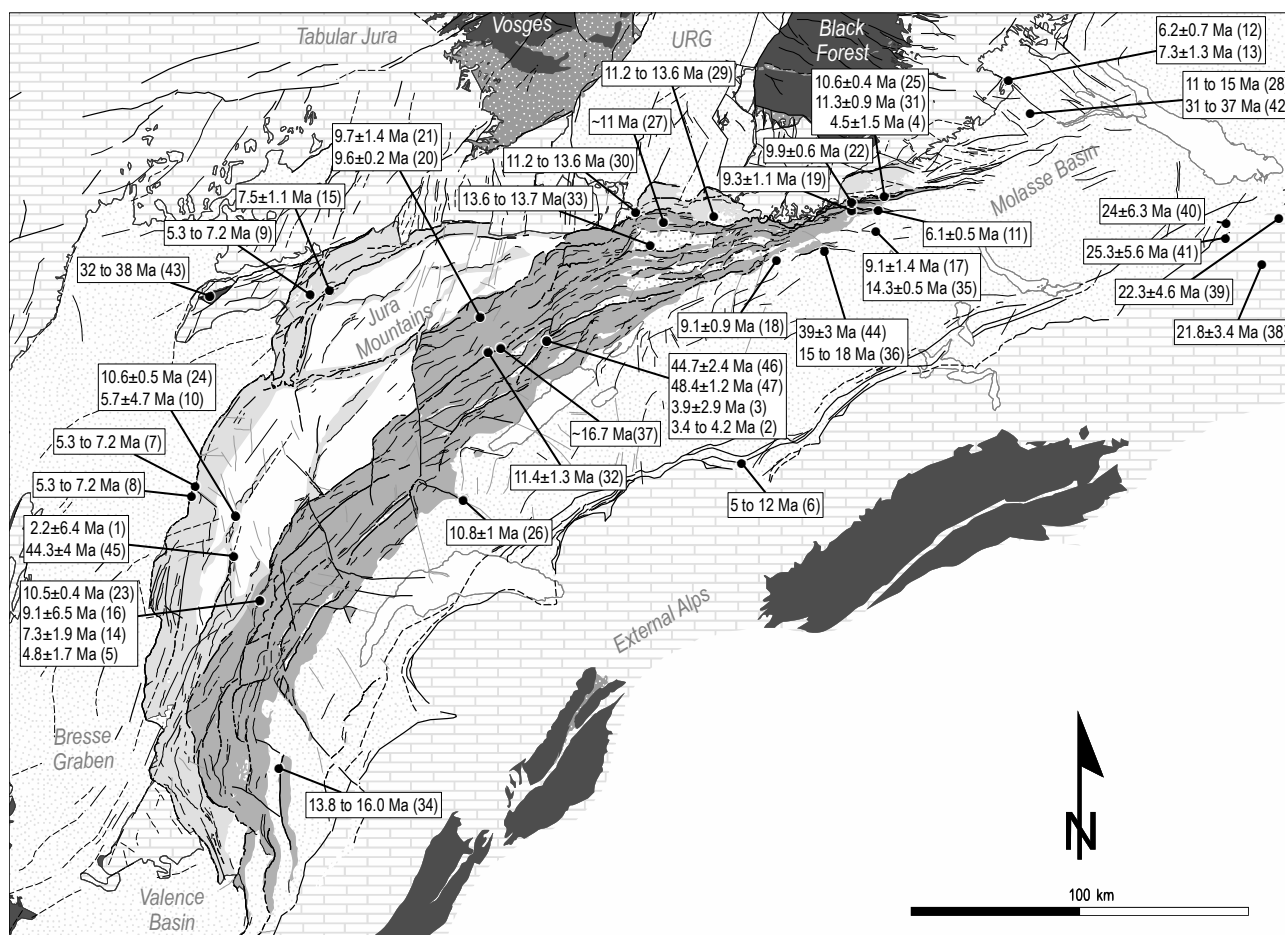


Fig. 7.1 – Overview map showing dated locations in the JFTB and surroundings, derived from Neogene Mammal Faunal Zones of Tertiary sediments and absolute age dating. See descriptions in Table 7.2.

ing uplift of the ECM. Also at ~12 Ma, relative vertical motion between the Mont Blanc and Aiguilles Rouges Massifs sets in, leading to the activation of the Mont Blanc shear zone (Leloup et al. 2005).

Absolute U-Pb age dating on a calcite fault surface in the south of the Jura has been accomplished by Rittner (2012), who received an age of 9.1 ± 0.9 Ma east of the Born–Engelberg anticline (no. 18, Fig. 7.1), constraining the maximum age of folding that deformed the fault plane. This age clearly shows out-of-sequence deformation of the JFTB given the older ages of the Delémont basin further north. Strike-slip motion on the La Sarraz fault is also dated by U-Pb calcite dating, showing activity at 10.8 ± 1.0 Ma (personal communication, Looser 2019, no. 26 in Fig. 7.1). The La Sarraz fault acted as conjugate fault system to the southern Pontarlier system, which reveals folds in connection with sinistral oblique ramps. Very recently, Looser et al. (2020) and Smeraglia et al. (2021) contributed even more U-Pb calcite ages, constraining the age of various faults, in various locations across the Internal and the External Jura. As a whole, the received ages confirm previous ages of the tectonic activity of the JFTB, with the youngest ages at the Vue-des-Alpes about 3.9 ± 2.9 Ma (no. 3 in Fig. 7.1) and oldest ages of about 11.4 ± 1.3 Ma (no. 32 in Fig. 7.1) on thrusts in the Eastern Jura (Smeraglia et al. 2021). Additionally, Smeraglia et al. (2021) found Eocene ages of about 44.7 and 48.4 Ma in

slickenfibres of a strike-slip fault at the Vue-des-Alpes (no. 46, 47 in Fig. 7.1).

Deformation preceding main Jura thrusting

There is evidence that the Alpine foreland was detached before Serravallian times: U-Pb calcite dating of veins in the footwall of the Muschelkalk décollement at the Schafisheim-1 borehole in the SMB reveal activity at ~14.3 Ma (Looser et al. 2020) and it can be assumed that the basal décollement of the detached NAF is even older towards the south-west. Within the Eastern Jura, Kälén and Engesser (2001) conclude ongoing synsedimentary tectonics between biozones MN5 to MN7 (Burdigalian to Serravallian ~16.7 to 13.6 Ma), since sedimentation occurred «...at different times in different areas, ... sometimes connected and at other times completely isolated from one another». And also within the south-western Molasse Basin south of Geneva, the beginning of the formation of the Gros Foug anticline is suggested to have started in Late Burdigalian to Langhian (~16.0 to 13.8 Ma, Deville et al. 1994), estimated from thrust Tertiary deposits in the footwall of the Gros Foug.

Connection between Alps and Jura

The basal décollement of the detached NAF is presumably connected to the sole thrust of the ECM (Burkhard and

Sommaruga 1998). Th-Pb dating of hydrothermal monazite veins in the Aar-Massif (Ricchi et al. 2019) document a compressional event between roughly 18 to 6 Ma. Leloup et al. (2005) used Ar/Ar geochronology to date the beginning of the exhumation of the Aiguilles-Rouges and Mont Blanc Massifs to 22 Ma and from structural relations, they conclude that the Alpine sole thrust prolonged into the Triassic evaporites of the foreland no later than ~15 Ma. Similarly, Boutoux et al. (2016) show that a thermal cooling event in the cover of the Mont Blanc and Aiguilles Rouges Massifs set in at 18 ± 1 Ma, which is interpreted to indicate beginning exhumation of the massifs. Stutenbecker et al. (2019) found grossular- and spessartine-rich garnet occurring abundantly in Miocene deposits (~14 Myr) of the foreland basin, which is proposed to show that the external massifs were exposed at this time already. Furthermore, much thrusting and folding of the Subalpine Molasse happened between 23 to 5 Ma (Burkhard 1990).

Recently, calcite fibres (slickenfibres) of the Randen fault in Northern Switzerland were dated using U-Pb calcite dating, revealing ages of 6.2 ± 0.7 Ma and 7.3 ± 1.3 Ma (Egli et al. 2017). The NW–SE trending Randen fault lies in the autochthonous Alpine foreland and movement on the fault was therefore connected to basement tectonics, with an oblique right-lateral and NE-down movement. The tectonic setting suggests that compressive far-field Alpine compression of the basement happened contemporary to thin-skinned deformation of the JFTB.

Ceasing of main thrust-belt tectonics

The frontal thrust of the JFTB is assumed to be amongst the youngest features of the JFTB. Michel et al. (1953) and Chauve et al. (1988) mention a «Pontian» age (obsolete stage roughly between 7.2 to 5.3 Ma) from fossil dating in thrustured Tertiary sediments of the eastern Bresse Graben, at the front of the Jura, in the Courlans-1 well (Michel et al. 1953, no. 7 in Fig. 7.1) and close to Frébuans (Chauve et al. 1988 according Lefavrais-Raymond 1962, no. 8 in Fig. 7.1). At the Vue-des-Alpes in the Internal Jura, the fauna MN15 (4.2 to 3.4 Ma) has been found in a karstic fissure filling (Becker 2000). Folding in there must be older than the filling, which lies in its original horizontal position and is apparently unaffected by folding. This location is frequently used as a marker for the end of the Jura folding. However, folding in there might have ended well before 4 Ma and additionally, it cannot be excluded that other parts of the fold-and-thrust belt were still active afterwards. Indications on the reason for the end of the Jura thrusting phase can be found in the ECM. With apatite fission track data, Leloup et al. (2005) could show that the Mont Blanc massif stopped thrusting the Aiguilles Rouges massif prior to ~4 Ma and instead, the backthrust of the Mont Blanc massif became active. This dynamic change within the ECM would coincide with the presumed end of the activity of the basal décollement in the detached NAF. However, seismotectonic data combined with GPS observations in the JFTB indicates that the cover in the Eastern JFTB is still detached from its basement (Rabin et al. 2018).

Summary

Considering the available age markers (Fig. 7.1, Table 7.2), it is concluded that main fold-and-thrust tectonics in the Jura Mountains ended around ~4 Ma (Early Pliocene). Present day tectonic activity still shows some basement-detached deformation, indicating that the basal décollement of the detached NAF is still at least partially active. Within the Eastern Jura, considerable uplift due to folding and thrusting is detectable at ~12 Ma (Serravallian). In this study, these upper and lower ages are used to refer to the main stage of the basement-detached formation of the fold-and-thrust belt. It can be debated whether earlier buckle folds or décollement activity in the Molasse Basin should be attributed to the main JFTB formation stage as well. In here, buckling is regarded as pre-JFTB stage marking the arrival of the basement-detached stress-field that eventually led to the formation of the Jura Mountains. There are implications that the Alpine sole thrust connected to the Molasse Basin by about 15 Ma at the latest (Leloup et al. 2005; Looser et al. 2020), potentially even by 16 Ma (Gros Foug anticline, Deville et al. 1994), slightly ahead of the main JFTB formation stage between ~12 to 4 Ma. Following Leloup et al. (2005), the main Jura folding stage coincides (and was possibly connected) to relative motion between the Mont-Blanc and Aiguilles Rouges Massifs. In addition, the different available ages across the JFTB clearly reveal that deformation of the JFTB was not in-sequence (Fig. 7.1). However, the Jura thrust front propagated NW-wards over a time-span of 2 to 5 Myr, reaching the External Plateaus by ~10.6 Ma at the latest (Fig. 7.1, see age of Buron thrust in Smeraglia et al. 2021) and the basal décollement arrived at the front of the JFTB in Late Tortonian–Early Messinian times.

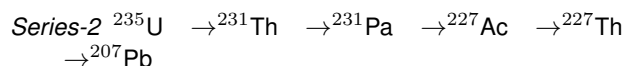
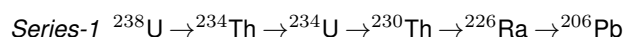
7.1.3 U-Pb calcite dating

Of particular interest in U-Pb calcite dating studies is the use of in-situ LA-ICP-MS (laser ablation inductively coupled plasma mass spectrometry), which can be used to pool data from multiple spot analyses and average the data. The in-situ LA method is fast, needs a minimum of preparation (no chemical preparation with risk of contamination) and a minimum of sample amount. A big issue in U-Pb dating is the contamination of the probe, therefore a high sample throughput with minimal preparation (handling errors and contamination) outweighs the disadvantages of lower-precision in individual measurements (Rittner 2012).

LA-MC-ICPMS (MC = Multi collector, high precision due to several collectors typically with Faraday detectors) can be used if thousands of ppm Pb are available in a sample (Woodhead et al. 2009) however, the observed Pb concentration in slickensides is commonly too low for the Faraday detectors of the MC-ICPMS (Rittner 2012). Isotopic analysis by LA-MC-ICPMS requires a two orders of magnitude larger sample volume than that required by LA-ICP-QMS instruments (QMS = quadrupole mass spectrometer, system with 4 magnets and one collector, Pickhardt et al. 2005). Alternatively to an ICP-QMS, an ICP-SFMS (SFMS = sector-field mass spectrometer with single ion detection) can be advantageous for studies with small amounts of

radiogenic Pb, providing high sensitivity at low-mass resolution (Pickhardt et al. 2005).

The calcite U-Pb dating method relies on two decay chains:



The two decay chains allow the identification of different signals, namely the initiation and a later opening of the system (if Pb is lost). There are following quality assurance steps that help to receive meaningful calcite ages (Rittner 2012):

1. Avoiding detrital clay particles contamination (e.g. by checking trace elements such as Al, Si)
2. Disturbance of the system (fractionation, e.g. due to weathering) is identified by discordant ages of the two decay series $^{238}\text{U}/^{206}\text{Pb}$ (Series 1) and $^{235}\text{U}/^{207}\text{Pb}$ (Series 2)

7.1.4 Veins and slickensides associated with faults

Brittle faulting is frequently associated with pressure solution leading to stylolites and slickolites (Fig. 7.2a) and synkinematic growth of minerals, resulting in slickenfibres (growth fibres) and mineral steps. Stylolites show characteristic peaks (or teeth) whereas slickolites (oblique stylolites) form incongruous mineral steps (pointed shape) on contractional fault facets, which is often accompanied by a concentration of clay particles since calcite is dissolved. Slickenfibres form congruous mineral steps (Twiss and Moores 2007) by precipitation of calcite on dilational fault facets (Fig. 7.2). A fault surface revealing shear sense indicators is called a slickenside (Fig. 7.2a).

U-Pb calcite dating of faults by LA-ICP-MS is commonly done on slickenfibres (Fig. 7.2a), as they precipitate during a tectonic shear event. Alternatively, veins can be dated that form in the fault core or in the damage zone of a fault (Fig. 7.2b).

7.1.5 Previous studies

Rittner (2012) successfully applied U-Pb dating by LA-ICP-MS on a fault surface in the Eastern Jura Mountains. Similarly, Egli et al. (2017) dated Late Miocene activity of a fault surface (Randen fault) in limestones of North-Eastern Switzerland. Calcite veins in boreholes in Eastern Switzerland (Schlattingen-1 and Oftringen-1) were successfully dated by LA-ICP-MS in Mazurek et al. (2018), revealing Middle Miocene and Late Eocene to Oligocene ages. Looser et al. (2020) dated calcite veins in the Schafisheim-1 borehole, documenting Middle to Late Miocene activity of the basal décollement of the SMB. Smeraglia et al. (2021) recently published absolute U-Pb ages for various faults in the JFTB, demonstrating that absolute age dating of faults is a powerful tool for dating individual structures and events across the JFTB.

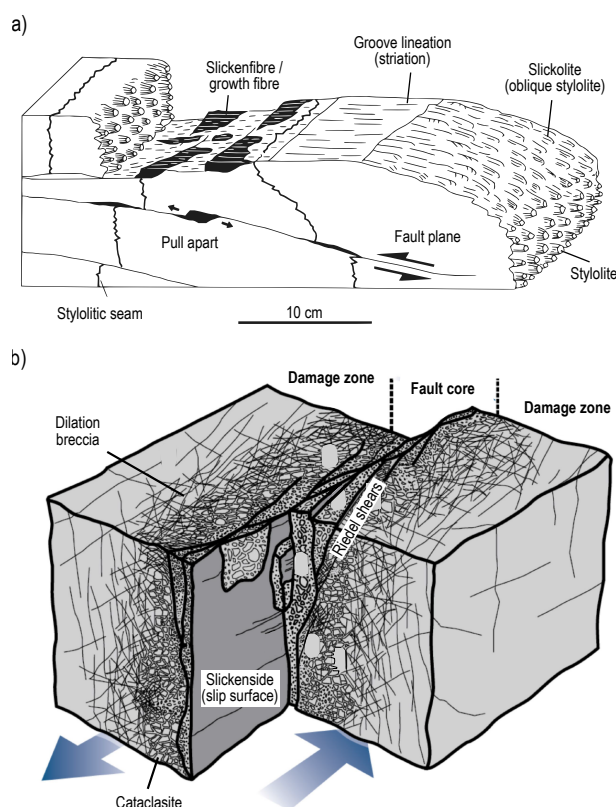


Fig. 7.2 – a) Scheme of a slickenside (slip surface) with shear sense indicators, stylolites and Riedel shear planes, occurring within a fault core (modified from NAB 12-41 and Meschede 1994). b) Sketch of a sinistral strike-slip fault zone, modified from Schröckenfuchs et al. (2015).

7.2 METHODOLOGY

A fault in the External Jura (Orgelet Zone) was sampled and in-situ U-Pb dating performed on the fault surface (slickenside) as well as on vein calcite in the brecciated damage zone. U-Pb dating was performed by Nathan Looser at ETH Zurich. Therefore, the analytical method corresponds to Looser et al. (2020) and Smeraglia et al. (2021). The following description of the analytical method is from Looser et al. (2020):

Calcite U-Pb dating was performed by laser ablation inductively coupled plasma mass spectrometry (LA-ICP-MS) on polished thick sections mounted in epoxy, using an ASI RESOLUTION S-155, excimer (ArF, 193 nm) laser ablation system coupled to a Thermo Element XR sector-field ICP-MS. The analytical method and correction procedure follow Roberts et al. (2017) using NIST 614 and WC-1 primary reference materials (Guillong et al. 2020). U-Pb ages were calculated from Tera-Wasserburg concordia lower intercepts using the IsoplotR software package (Vermeesch 2018). All uncertainties are reported at 95% confidence level. A long-term excess variance of 2.5% relative was propagated by quadratic addition to the uncertainty of the individual, lower intercept dates (Guillong et al. 2020). Prior to and after LA-ICP-MS measurements, cathodoluminescence microscopy was conducted in order to identify growth zonings and to identify misplaced ablation spots which then were excluded from the data. In addition to this, the lower intercept dates showing a MSWD value >

4.3 or an uncertainty > 2 Ma were not considered.

7.3 RESULT

7.3.1 Structural context of sampling location

The sampling location lies in the Orgelet Zone (Fig. 7.3a and b), which is a roughly N–S striking *faisceau* in the southern Plateau Jura. To the north, the N–S striking Orgelet Zone connects with the NNE–SSW striking *Faisceau de l'Heute* (Fig. 7.3b). The local direction of tectonic transport during JFTB formation was roughly NW–SE (Philippe et al. 1996). On the tectonic map (Fig. 7.3b), oblique thrusts with sinistral strike-slip components are visible, which are sub-parallel to the general N–S strike of the Orgelet Zone. Several fronts of thrust sheets are curved in the Orgelet Zone and the *Faisceau de l'Heute* (Fig. 7.3b), which suggests strong structural control of pre-existing structures during JFTB formation (see Chapter 8). On the 5 m digital terrain model of France (IGN-F 2018), several lineaments are visible striking between N100°–110° close to the sampling location, which are identified as dextral strike-slip faults in the field. NNE–SSW striking Oligocene normal faults are known from literature close to the area, such as the «Pincée de l'Heute» north of the *Faisceau de l'Heute* (Homberg et al. 2002) and a normal fault system SE of the Orgelet Anticline (Wildi and Huggenberger 1993, see Fig. 7.3b). These pre-JFTB structures presumably controlled the orientation of the *Faisceau de l'Heute* and the Orgelet Anticline during JFTB formation (Homberg et al. 2002). According to the geological map 1:50'000 of France (BRGM 2004), the exposed limestones at the sampling location belong to the Upper Malm Group.

7.3.2 Sample description

The sample contains a fault surface exposed in the External Jura, Orgelet Zone (WGS 1984 5.6568 46.4910°), taken at an outcrop that is exposed due to road constructions. Azimuth and dip of the fault surface is N109/72°E and the lineation on the fault is N096/65°E indicating an upward thrusting sense of shear. Intersecting slickensides have been recognised in the field, with strikes of about N100° showing dextral shear. The bedding at the sampling location was measured N054/33°E. The restored orientation of the fault surface in respect to bedding is N124/56°E and the lineation is N075/36°E (Fig. 7.4c). The sample is brecciated close to the slickenfibres, revealing a network of stylolitic seams (with concentration of brown clay) and calcite veins. The host rock is a micritic limestone with a light grey matrix that shows yellow stains, presumably due to limonite inclusions. Pyrite grains occasionally occur. Fossil fragments (bivalves) are recrystallised and appear dark grey in the brighter matrix. Veins are filled with calcite. Dendrites (of very thin manganese precipitations) are occasionally observed on fractures.

A thick section was prepared oriented parallel to fault slip indicators and perpendicular to the fault surface. The weathered slickenfibres have a millimetre thick brown seam

of clay. The slickenfibres reveal a maximum thickness of 7 mm and individual calcite crystals in the slickenfibres have a diameter of up to 2 mm (Fig. 7.4a). The limestone is brecciated beneath the slickenfibres and veins contain millimetre sized calcite crystals. Stylolitic seams are abundant showing various orientations (Fig. 7.4a). The slickenfibres and a vein are dated using U–Pb calcite dating.

7.3.3 U–Pb ages of sample

U–Pb calcite ages are retrieved for both, the slickenfibres and a vein beneath the slickenfibres. CL images of the two probing locations in the thick-section show notably different calcite luminosities of vein and slickenfibres calcite (Fig. 7.4b and c), confirming different compositions of the calcite. Probing points were kept within a constant calcite zoning in order to avoid mixed ages (Fig. 7.4b and c). The probed slickenfibres reveal an age of 2.2 ± 6.4 Ma (Fig. 7.5a) and the vein calcite shows an absolute age of 44.3 ± 4.0 Ma (Fig. 7.5b).

7.4 DISCUSSION

The overall N–S orientation of thrusts and folds at the sampling location (Fig. 7.4b) is oblique to the local NW transport direction of the JFTB (Philippe et al. 1996) and NW–SE principal palaeostress orientations deduced from folds and faults (Homberg et al. 2002; Laubscher 1972). This suggests structural control of pre-existing structures during the formation of the JFTB. Assuming that the NNE–SSW orientation of the sampled thrust plane is inherited and older than the JFTB, the fault is restored to its original orientation by correcting it to a flat bedding. The strike of the restored fault is N034° and therefore parallel to the orientations of the *Faisceau de l'Heute* (Homberg et al. 2002) and the normal fault south of the Orgelet Anticline (Wildi and Huggenberger 1993, see Fig. 7.3b), which are presumed to be inherited from Oligocene extensional tectonics (Homberg et al. 2002; Wildi and Huggenberger 1993). Unfortunately, no cross-cutting relationships of shear sense indicators on the fault plane (slickensides) are observed, which would confirm a multiple reactivation of the sampled fault plane. Nevertheless, the U–Pb age of the vein calcite in the breccia (belonging to the fault core) beneath the slickenfibres confirms a pre-JFTB inheritance, suggesting that the fault plane was already active during Lutetian times (Middle Eocene).

7.4.1 Interpretation of slickenfibres

The absolute calcite age obtained for the slickenfibres has a wide spread and includes the Quaternary period. The documented shear sense indicators on the fault plane indicate upward thrusting with a plunge of 65°, which is rather steep and mechanically not favourable for active thrusting. The restored plunge of 36° (Fig. 7.3c) is more favourable for thrusting, suggesting that the thrust plane rotated (due to folding) after its activity. The restored fault plane indicates an oblique-thrust with a dextral strike-slip component.

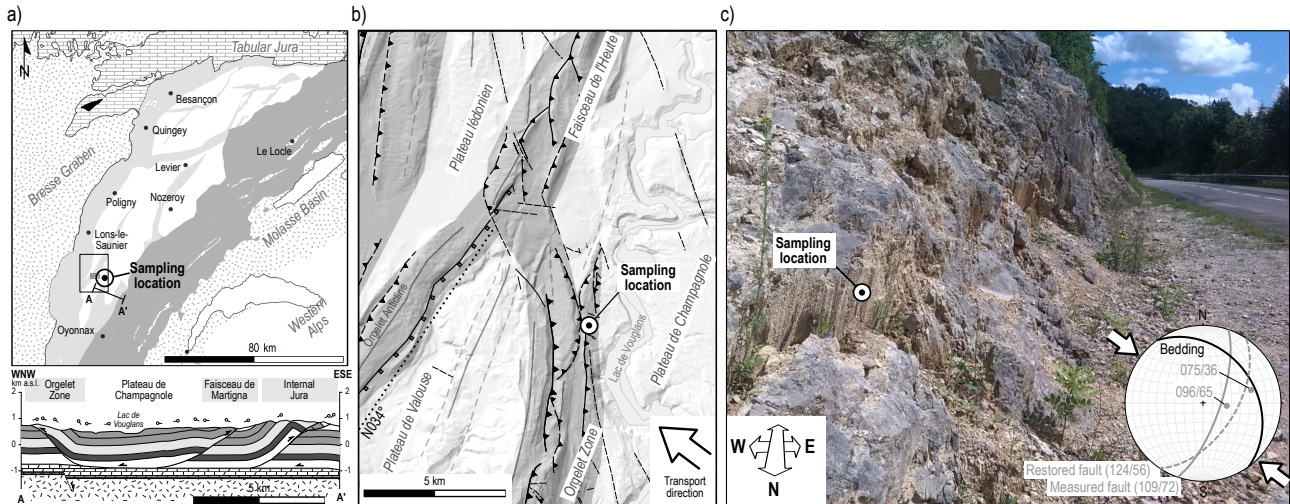


Fig. 7.3 – Overviews of the sampling location. a) Sampling location within the southern Plateau Jura and cross-section across the Orgelet Zone and Plateau Champagnole (from Fig. 5.2a on page 75). b) Structural overview map of the Orgelet Zone. c) Photograph of sampled fault surface along the roadside. A steep fault with vertical striation is visible. The stereonet shows the orientations of the fault and bedding measured in the outcrop. The restored fault plane in respect to bedding (dashed great circle) indicates that the fault plane rotated counter-clockwise during folding and originally had a more NE–SW orientation parallel to the Faisceau de l'Heute.

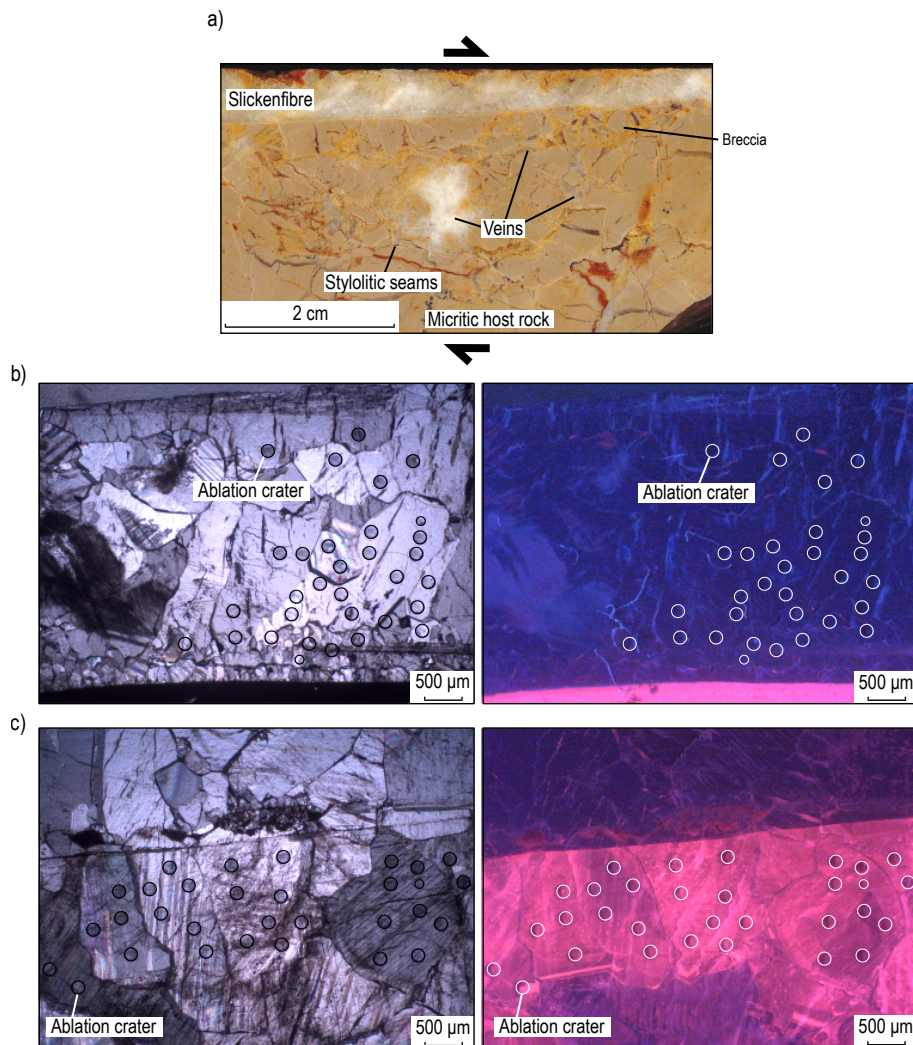


Fig. 7.4 – Photographs of sample. a) Photograph of cut surface, showing a maximum 6 mm thick slickenfibre with mm-sized calcite crystals. The micritic hostrock is brecciated more intensely close to the slickenfibre and calcite veins are abundant. b) Thick section photographs showing ablation craters in the slickenfibre under the microscope with crossed polarisers (left) and a cathodoluminescence photograph (right). The CL image shows that ablation craters are within a constant zonation. c) Crossed polarisers microscope photograph (left) and cathodoluminescence photograph (right) of ablation craters on the vein. Probing points are within a single calcite zoning, visualised by the CL-image.

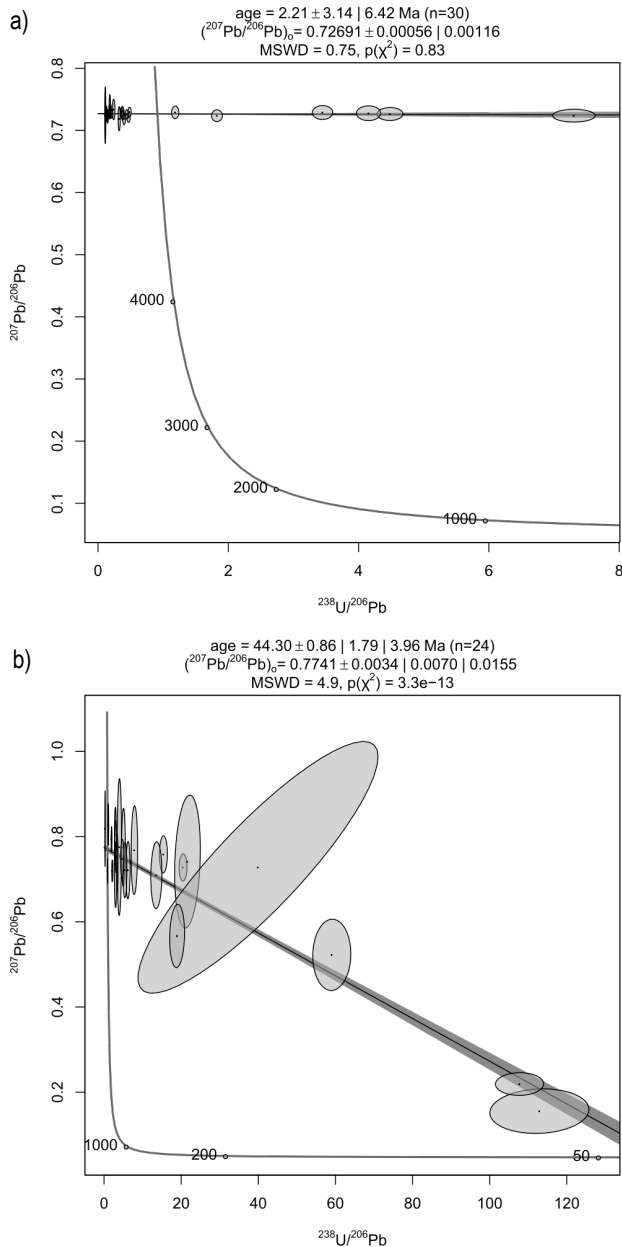


Fig. 7.5 – Tera-Wasserburg concordia diagrams, created with the IsoPlotR software package (Vermeesch 2018). a) Subset of slickenfibres samples and b) subset of vein samples.

The slickenfibres is relatively young and fits into the known formation age of the JFTB. It is concluded that the sampled thrust was active in a late stage of the main Jura thrust-and-fold activity. This is expected since the basal décollement of the JFTB had to propagate north-westwards and presumably arrived in the External Jura some time after the initiation of the first main thrusts at about 12 Ma in the Internal Jura. The obtained age of the slickenfibres does not constitute an upper or lower limit of thrust activity and merely represents a moment during ongoing activity of the thrust and associated folding (more measurements on different slickenfibres and fault surfaces are necessary to constrain the long-time activity of the fault).

7.4.2 Interpretation of vein calcite

The absolute age received for the vein calcite reveals a Lutetian age. This is distinctly before the JFTB and justifies that the fault plane is restored to bedding in order to receive the initial orientation of the fault plane. The orientation of the dated vein does not indicate an unambiguous palaeostress direction since the vein lies within a brecciated zone within the fault core (Fig. 7.4a). The restored fault plane shows an inclination of 56° , which is in the expected range of dips for normal faults. The received vein age of 44.3 ± 4 Ma rather precedes the main (Late-Eocene to Oligocene) rifting phase of the Bresse Graben, which started at about 39 Ma (see comparison of tectonic events Fig. 2.6). There are several tectonic events, which possibly led to the formation of the dated vein:

1. Based on fault-slip data, Homberg et al. (2002) suggest Eocene NNE–SSW strike-slip faults induced by the N–S directed collision of Africa and Europe, coinciding with the age of the dated vein. However, the restored inclination of the dated fault of 56° rather suggests a normal fault instead of a strike-slip fault.
2. Sissingh (1998) suggested an initial rifting phase beginning at about 45 Ma from the presence of local, shallow lacustrine sediments in the BG and URG, preceding main rifting in Late Eocene and Oligocene. However, this interpretation is debatable since most authors set the beginning formation of the BG and URG to Bartonian–Priabonian, no earlier than about 39 Ma (Madritsch et al. 2008; Ring and Gerdes 2016).
3. Bourgeois et al. (2007) and Lefort and Agarwal (1996, 2002) suggest lithospheric buckling of the European lithosphere, starting in Upper Cretaceous and prevailing in Eocene due to the collision of Africa and Europe. Lithospheric buckling may have induced strike-slip faults as well as extensional fractures or normal faults.

Flexural extension of the peripheral forebulge is excluded as deformation source, as the forebulge crest and the northern limit of the flexural foreland basin are still more than 200 km to the south-east of the sampling location in Lutetian times (see Fig. 6.9 on page 91). An unambiguous allocation of a tectonic event is not possible. In any case, it is probable that the Lutetian formation of the dated fault followed even older Variscan structural seeds (with NNE–SSW Rhenish orientation), analogous to the border faults of the BG and URG (Illies 1972).

7.5 CONCLUSION

Combining available ages across the JFTB and new U–Pb ages obtained on a sample in this study, the following conclusions are drawn:

- U–Pb dating of vein and slickenfibres calcite in exposed faults of the JFTB reveal ages between 2.2 ± 6.4 Ma (this study) and 11.4 ± 1.3 Ma (Smeraglia et al. 2021). The young age of this study has a very high uncertainty and

cannot be used to constrain the end of the JFTB formation. In summary, the currently available U-Pb calcite ages of faults in the JFTB are consistent with a main formation stage of the JFTB between 12 Ma to 4 Ma (as suggested by Becker 2000 and references therein). This is considered the main JFTB formation stage in this study. However, the basal detachment of the JFTB and in particular the Molasse Basin initiated earlier, at the latest at ~15 Ma, possibly even at 16 Ma. This is documented by calcite ages close to the detachment level in the SMB (Looser et al. 2020) and Tertiary sediments and their structural relations (Deville et al. 1994).

- The age of a measured slickenfibres in the External Jura reveals that the sampled thrust in the southern Plateau Jura was active in the second half of the main Jura fold-and-thrusting stage, after about 8.3 Ma. Together with additional U-Pb calcite ages in the External Jura (Smeraglia et al. 2021), this age supports that the basal décollement progressed north-westwards after its initiation in the Internal Jura, and arrived about 10.5 Ma in the Faisceau de l'Heute at the latest.
- The overall available ages across the JFTB (Fig. 7.1) clearly show that the deformation of the JFTB was not in-sequence, as relatively young ages of 4 Ma are attested on faults in the Internal Jura. This is in agreement with a mechanical wedge achieving internal equilibrium by oscillating thrusts (Dahlen 1990; Davis et al. 1983). The front of the JFTB seems to have propagated north-westwards during a time span of about 2 to 5 Myr.
- The Orgelet Zone, which is the southern continuation of the Faisceau de l'Heute (pincée de l'Heute to the north), reveals Eocene (44.3 ± 4.0 Ma) activity on a fault, which was reused during the formation of the JFTB.
- The NNE–SSW orientation of the sampled fault plane is parallel to BG border faults, which follow inherited Variscan orientations. The orientation is furthermore similar to the pincée de l'Heute and the northern Faisceau de Syam, also presumed to follow basement discontinuities following Variscan orientations (Homberg et al. 2002; Mugnier and Vialon 1986).
- The Eocene age of the dated vein is not unambiguously attributable to a tectonic event. The restored orientation of the fault reveals a dip that is typical for a normal fault. This suggests extensional tectonics either due to an initial rifting stage of the BG (Sissingh 1998) or due to lithospheric folding (Lefort and Agarwal 1996, 2002). Smeraglia et al. (2021) received a similar Lutetian age for a shear vein in a tear fault in the Vue-des-Alpes, lying in the Internal Jura south of the URG. The Vue-des-Alpes lies on a NNE–SSW striking strike-slip fault (La Ferrière fault zone), suspected to follow an inherited Rhenish trend from the Variscan orogeny (Laubscher 2008a; Meier 2010). Ypresian–Lutetian ages currently belong to the oldest tectonic event attested by U-Pb dating in Mesozoic sediments of the JFTB.

It is vital to factor in inherited systems when interpreting ages of fault planes in the External Jura. U-Pb calcite dating of faults has a great potential to resolve the tectonic

history of the JFTB. There are tectonic events that are yet unattested in the JFTB by absolute age dating of faults, such as the Eo-Oligocene rifting event of the ECRIS, and subsidence in connection with the opening of the Tethys during Jurassic and Cretaceous times (Wetzel et al. 2003).

8 - INSIGHT FROM ANALOGUE MODELS

PREFACE

Chapter 5 of this study shows that the pre-Mesozoic basement underneath the External Jura contains basement faults with substantial vertical components (throws) of up to 450 m (possibly more, see Fig. 5.2 on page 75 and Fig. 5.3 on page 76). In Chapter 6, basement faults are suggested to pre-date the JFTB, and to be mostly in connection with the formation of the ECRIS and the evolution of the northern Alpine flexural basin system. Some faults are suggested to follow inherited Variscan discontinuities. Orientations of main fault systems are shown in a map of the pre-Mesozoic basement (Fig. 6.2 on page 84). In the current chapter, the influence of pre-existing structures in the pre-Mesozoic basement on the development of structures in the Jura Mountains is tested, using brittle-viscous analogue sandbox models.

The current chapter was published in *Tectonophysics* on June 2021 (Schori et al. 2021) under the CC BY license. The supplementary material to the article is available online through Schori et al. (2020), providing top-view videos of performed models and cross-sections of CT-scans. Protocols of experiments are furthermore provided in Supplementary Material E. Schori et al. (2021) was financed by the University of Fribourg and is part of the PhD thesis of the first author (this study). It was edited by Prof. Philippe Agard (University of Sorbonne) and reviewed by Dr. Pauline Souloumiac (University of Cergy-Pontoise) and Dr. Alexander Malz (Friedrich Schiller University Jena).



Contents lists available at ScienceDirect

Tectonophysics

journal homepage: www.elsevier.com/locate/tecto

Pre-existing Basement Faults Controlling Deformation in the Jura Mountains Fold-and-Thrust Belt: Insights from Analogue Models

Marc Schori^{a,*}, Frank Zwaan^b, Guido Schreurs^b, Jon Mosar^a

^a Earth Sciences, University of Fribourg, Chemin du Musée 6, CH-1700 Fribourg, Switzerland

^b Institute of Geological Sciences, University of Bern, Baltzerstrasse 3, CH-3012 Bern, Switzerland

ARTICLE INFO

Keywords:

Jura Mountains fold-and-thrust belt
Analogue modelling
Lineament
Oblique ramp
Basement-cover interaction
Localization of deformation at basement fault

ABSTRACT

Pre-existing faults in the mechanical basement are believed to play an important role in controlling deformation of the thin-skinned Jura Mountains fold-and-thrust belt, which constitutes the northernmost extension of the European Alps. We use brittle-viscous analogue models to investigate the influence of frontal and oblique basement steps on the subsequent evolution of structures during thin-skinned shortening. Vertical offset between two rigid baseplates (simulating the mechanical basement) causes the formation of reverse faults and grabens in the overlying brittle layers that are not reactivated during subsequent thin-skinned shortening. However, baseplate steps localise deformation, causing a temporary frontward propagation of deformation in an early stage and inhibiting propagation afterwards. Downward baseplate steps induce very strong deformation localisation and foster the formation of fault-bend folds. Models featuring upward steps develop step-controlled pop-up structures with imbricated fronts and viscous ramps that shorten dynamically with progressive contraction. We find that deformation localisation increases both with higher step-throws and lower obliquity (α) of the strike of the step (e.g. frontal step $\alpha = 0^\circ$). With increasing step-throws, $\alpha = 30^\circ$ and $\alpha = 45^\circ$ oblique upward-steps lead to a characteristic imbrication of the brittle cover with laterally confined thrust-slices and step-parallel oblique-thrusts, which rotate up to 15° about a vertical axis over time. Step-controlled backthrusts preceding the formation of thrust-slices do not show notable rotation and hence constitute excellent indicators for the orientation of oblique upward-steps. The topographic patterns of oblique-step models resemble individual thin-skinned structures of the Internal Jura (i.e. Pontarlier and Vuache fault zones, the nappe system SE of Oyonnax and the Chasseral anticline), strongly suggesting that pre-existing NNE-SSW and NW-SE striking oblique upward-steps in the basement controlled deformation in the overlying cover. Our model results may be applied to other thin-skinned fold-and-thrust belts worldwide that formed above pre-existing basement structures.

1. Introduction

The Jura Mountains fold-and-thrust belt (JFTB) forms the outermost front of the Central and Western European Alps that became detached in Triassic evaporites during Middle Miocene (Serravallian) to Pliocene times (Buxtorf, 1907; Laubscher, 1961). The thin-skinned JFTB evolved above a pre-structured basement, which affected the deformation style of the Mesozoic and Cenozoic sedimentary cover (Homberg et al., 2002; Laubscher, 1986, 1961; Malz et al., 2019; Philippe et al., 1996; Tschanz, 1990). Pre-existing basement structures frequently controlled the formation of cover structures that are oblique to the JFTB transport directions (Laubscher, 1961). Although obscuring most underlying basement structures, the JFTB is full of inherited strike directions, which

highly motivated us to study the formation of complex fold and thrust arrangements.

The aim of this study is to understand the kinematic and mechanic conditions of basement-controlled structures in the detached cover of the JFTB. First, we present brittle-viscous sandbox analogue-models that explore the spatial and kinematic evolution of a brittle sand cover above a viscous detachment, migrating across oblique and frontal basement steps associated with the reactivation of inherited faults. Thereafter we compare structures observed in our analogue models with natural examples from the JFTB. Although we study the case of the thin-skinned JFTB in the first place, our model results may be applied to other fold-and-thrust belts worldwide that deformed above pre-existing basement structures. Some examples among others, where inherited structures are

* Corresponding author.

E-mail address: marc.schori@unifr.ch (M. Schori).

<https://doi.org/10.1016/j.tecto.2021.228980>

Received 17 November 2020; Received in revised form 28 May 2021; Accepted 19 June 2021

Available online 27 June 2021

0040-1951/© 2021 The Authors. Published by Elsevier B.V. This is an open access article under the CC BY license (<http://creativecommons.org/licenses/by/4.0/>).

proposed to have exerted an important structural control, are the Taiwan orogen (Yang et al., 2006, 1996), the Apennines (Coward et al., 1999; Tavarnelli, 1997), the Zagros Mountains (Berberian, 1995) and the Prebaetic System of the Baetic Cordillera in Spain (Peper and Cloetingh, 1992).

2. Regional setting

2.1. Jura Mountains fold-and-thrust belt

The Jura Mountains are an arc-shaped mountain range of ~300 km width and a transect length of ~75 km at its centre (Fig. 1a). The Mesozoic and Cenozoic cover of the Jura Mountains and the western Molasse Basin (Fig. 1a, b) was detached in Triassic evaporites and transported north-westwards, which was proposed by Buxtorf (1907, 1916) and Schardt (1908) based on observations in railway tunnels and because no rocks exposed in the JFTB pre-date a Triassic age. Several decades later, boreholes and seismic lines within the detached Molasse Basin and the Jura Mountains confirmed the existence of a regional basal décollement in Triassic evaporites (Burkhard, 1990; Jordan, 1992;

Jordan and Nuesch, 1989; Laubscher, 1961; Lienhardt, 1962; Michel et al., 1953; Sommaruga, 1997). The basal detachment of the JFTB is very probably connected with the Alpine sole thrust in the south-east, that roots beneath the External Crystalline Massifs (ECMs) of the Alps (Burkhard, 1990; Bellahsen et al., 2014, Fig. 1b), namely the Belledonne, Aiguilles-Rouges, Mont-Blanc, Aar and Gotthard Massifs (Fig. 1a). Therefore, the evolution of the JFTB and the exhumation of the ECMs were coupled and contemporaneous (Becker, 2000; Burkhard, 1990; Laubscher, 1986). From structural relations of Tertiary sediments across the Jura Mountains, the main folding and thrusting of the JFTB occurred between about 12 and 4 Ma (Becker, 2000 and references therein), which we consider the thin-skinned main formation stage of the JFTB. However, the basal décollement of the JFTB and Molasse Basin was active before (Deville et al., 1994; Leloup et al., 2005; Looser et al., 2020). From the thermal and structural evolution of the ECMs, Leloup et al. (2005) concludes that the Alpine sole thrust (see Fig. 1b) prolonged into the Triassic evaporites beneath the Molasse Basin by ~15 Ma at the latest. This is supported by recent U-Pb dating of calcite veins in the Schafisheim-1 borehole situated in the Molasse Basin west of Zürich (see position in Fig. 1a) that shows activity of the basal décollement at 14.3

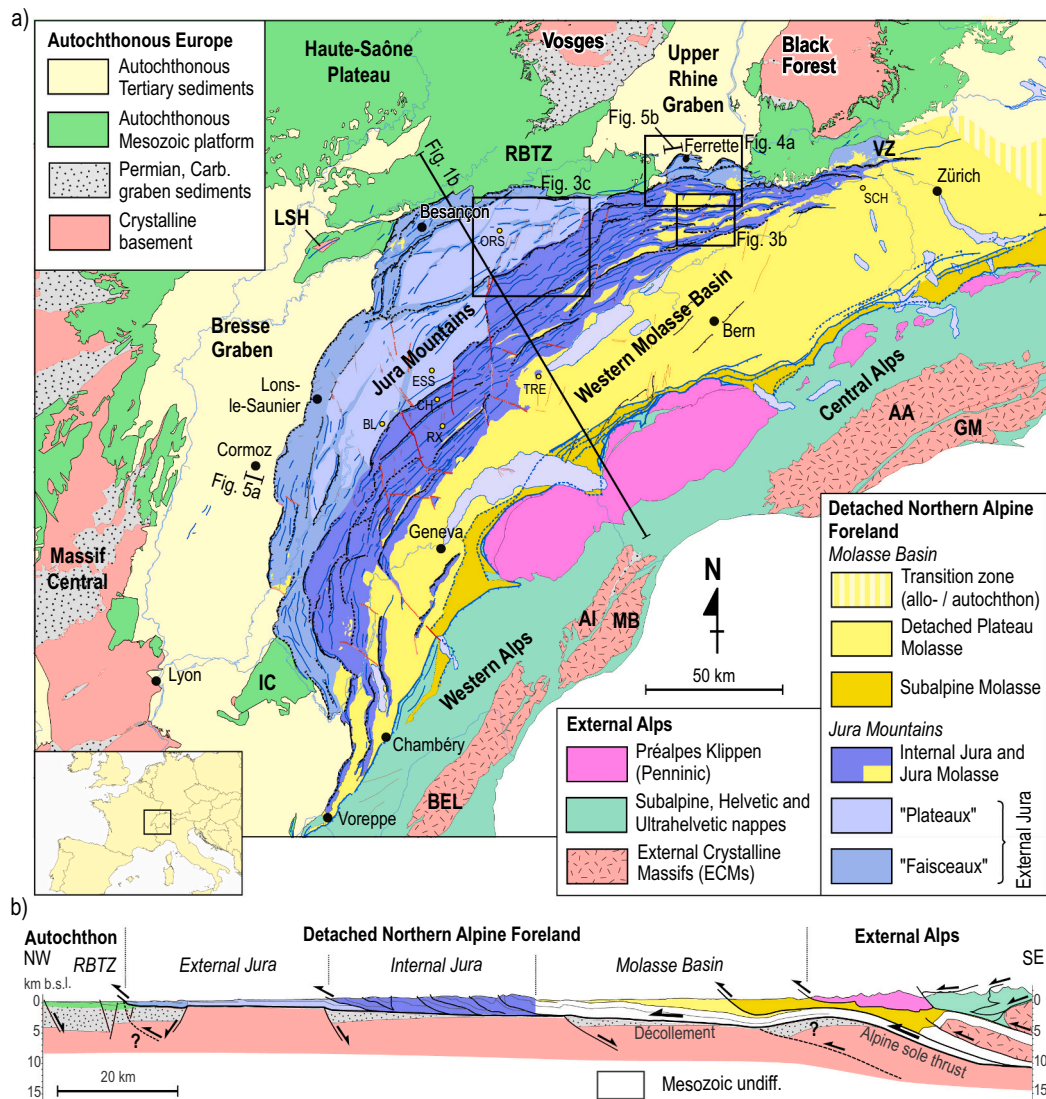


Fig. 1. a) Tectonic map of the Jura Mountains and surroundings, based on existing maps (Chauve and Perriaux, 1974; Sommaruga et al., 2017; Trümpy, 1980) and new observations. b) Regional cross-section modified from Sommaruga et al. (2017). AA: Aar Massif, AI: Aiguilles Rouges Massif, BEL: Belledonne Massif, GM: Gotthard Massif, IC: Ile Crémieu, LSH: La Serre Horst, MB: Mont Blanc Massif, RBTZ: Rhine-Bresse Transfer Zone, VZ: Vorfaltenzone. Indicated boreholes are BL: Bonlieu-1, CH: Châtelblanc-1, ESS: Essavilly-101, ORS: Orsans-1, RX: Risoux-1, SCH: Schafisheim-1 and TRE: Treykovagnes-1.

± 0.5 Ma (Looser et al., 2020).

The JFTB is classically divided into a highly deformed internal tectonic domain and a considerable less deformed external part (Chauve and Perriaux, 1974; Trümpy, 1980, Fig. 1a). The strongly deformed Internal Jura or High Jura (Fig. 1) shows maximum northwest displacements of about 30 km (Affolter, 2004; Laubscher, 1965; Philippe et al., 1996), featuring well-developed ramps and fault-propagation folds that partially led to kilometeric duplication of the Mesozoic cover (Fig. 1b, Winnock, 1961; Aubert, 1971; Sommaruga, 1997). The less deformed External Jura is subdivided into narrow zones of localised deformation called “faisceaux” (meaning “bundles” in English) and scarcely folded and intact plateaus (Fig. 1a). These plateaus are blocks of Mesozoic carbonates, each several hundred square kilometres large, embedded within the faisceaux (Fig. 1a).

The front of the JFTB is controlled by rift segments of the European Cenozoic Rift System (ECRIS, Dézes et al., 2004; Lacombe and Bellahsen, 2016; Madritsch et al., 2008; Malz et al., 2016; Ustaszewski and Schmid, 2006; Ziegler, 1992), i.e. the Bresse Graben (BG) to the west and the Upper Rhine Graben (URG) to the north, connected by the Rhine-Bresse Transfer Zone (RBTZ, Fig. 1a). Therefore, faisceaux at the front of the JFTB follow extensional structures of the ECRIS (Bièvre and Mercier, 2010; Chauve and Perriaux, 1974; Glangeaud, 1951; Lienhardt, 1962; Martin and Mercier, 1996; Michel et al., 1953; Philippe et al., 1996).

2.2. Mechanical stratigraphy

The mechanical basement of the JFTB (footwall) encompasses the geological units beneath the basal décollement in Triassic evaporites. Apart from the crystalline basement, this includes Permian and Carboniferous continental sediments deposited within troughs in the crystalline basement as well as the Triassic series beneath the basal décollement (Fig. 2). The evaporite décollement of the JFTB concentrated predominantly in halite-bearing layers (Deville, 2021; Sommaruga et al., 2017), deposited in shallow basins on an epicontinental platform (Lienhardt et al., 1984; Philippe et al., 1996). Salt occurs mainly in Upper Triassic evaporites (Keuper group) in the Central and Southern Jura and mostly in the Middle Triassic series (Muschelkalk group) in the Eastern Jura (Debrand-Passard et al., 1984; Guellec et al., 1990; Jordan, 1992; Laubscher, 1986, 1961; Philippe et al., 1996; Sommaruga et al., 2017).

The stratigraphy in Fig. 2 is representative of the Central Jura, where the décollement is predominantly localised in Upper Triassic evaporites (Laubscher, 1961; Philippe et al., 1996). We estimate a décollement/cover thickness ratio of about 1/8, assuming the Upper Triassic salt system to be the basal décollement (Fig. 2). However, anhydrite layers present throughout the Triassic series were at least partially involved in the décollement (Jordan, 1992; Müller et al., 1981), leading to a décollement/cover thickness ratio of ca. 1/5 (Fig. 2). This ratio increases even more towards the front of the JFTB, where the detached Mesozoic cover is extensively eroded due to Eocene to Oligocene rift-shoulder uplift associated with the formation of the ECRIS (Illies, 1972; Michon, 2000) and forebulging of the peripheral Alpine foreland basin (Burkhard and Sommaruga, 1998; Laubscher, 1992). Although detachments in the overlying Jurassic and Cretaceous series can occur locally (Malz et al., 2019; Noack, 1995; Nussbaum et al., 2017; Philippe et al., 1996; Schori et al., 2015, see Fig. 2), we focus on the role of the main basal Triassic décollement in this study.

2.3. Inherited basement faults

In the URG and Vorfaltenzone (Fig. 1a), numerous studies of seismic lines, boreholes and gravimetry provide well-constrained insights into faults affecting the basement, with structural orientations being frequently associated with the Variscan orogeny and post-Variscan collapse (Egli et al., 2016; Hauber, 1993; Illies, 1972; Larroque and Laurent, 1988; Laubscher, 1982; Madritsch et al., 2018; Madritsch et al.,

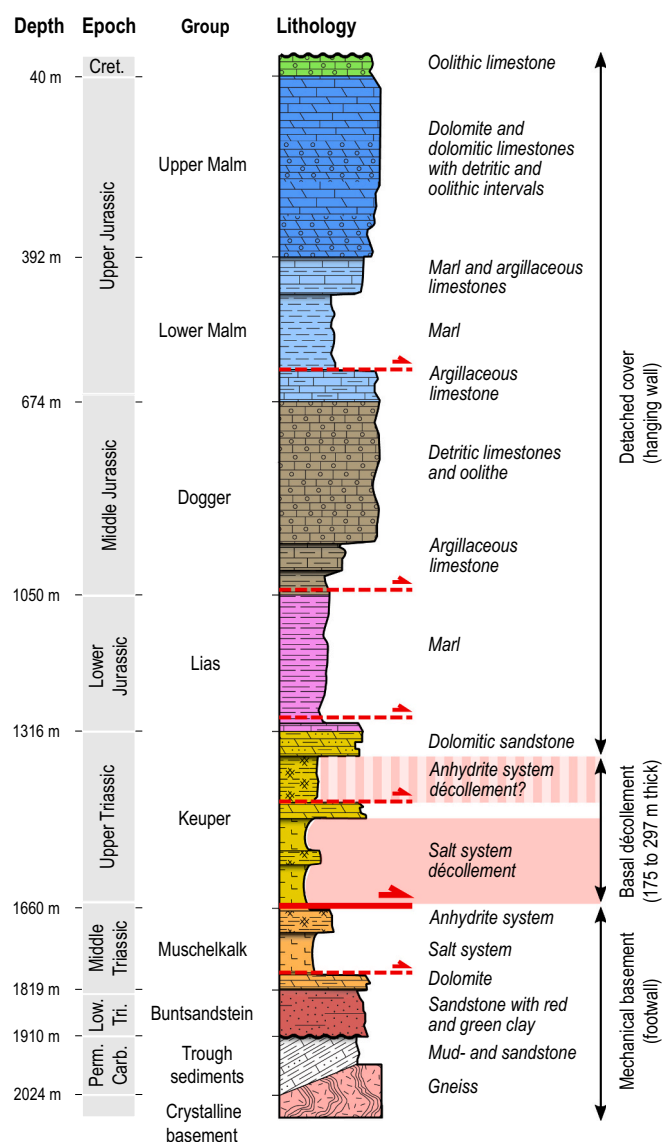


Fig. 2. Representative stratigraphy of the Central Jura Mountains based on borehole Essavilly-101 (Delmas, 1965). The top of the mechanical basement of the JFTB (footwall) lies near the bottom of the Upper Triassic series. The Upper Triassic anhydrite system at least partially contributed to the basal décollement zone, next to the Upper Triassic salt system. Note that local upper detachments occur in the Jurassic series.

2009, 2008; Madritsch and Deplazes, 2014; Philippe, 1995; Rat, 1974; Rotstein et al., 2005; Ustaszewski, 2004). There are three main Palaeozoic trends present (Illies, 1962; Reisdorf and Wetzel, 2018; Schumacher, 2002), which originate from NNE-SSW (“Rhenish”, N010°-N020°) striking Variscan sinistral shear zones, NW-SE (“Hercynian”, N120°-N130°) striking Variscan dextral shear zones and ENE-WSW (“Erzgebirgian”, N070°-N080°) striking Variscan dislocation zones (Fig. 3a). Some of these Palaeozoic fault zones were transpressively or transtensionally reactivated during the Mesozoic opening of the Alpine Tethys, as well as during the evolution of the ECRIS and the Alpine flexural foreland basin system in Cenozoic times (Illies, 1962; Laubscher, 1986; Madritsch et al., 2009; Meier, 2010; Reisdorf and Wetzel, 2018; Schumacher, 2002; Wetzel et al., 2003; Ziegler, 1988a; Ziegler and Dézes, 2007). This led to: (1) depositional differences of Mesozoic and Cenozoic sediments along fault zones, (2) mechanical heterogeneities in the deformed sedimentary cover and (3) substantial vertical offsets of the basement and the cover. In this paper, we test the

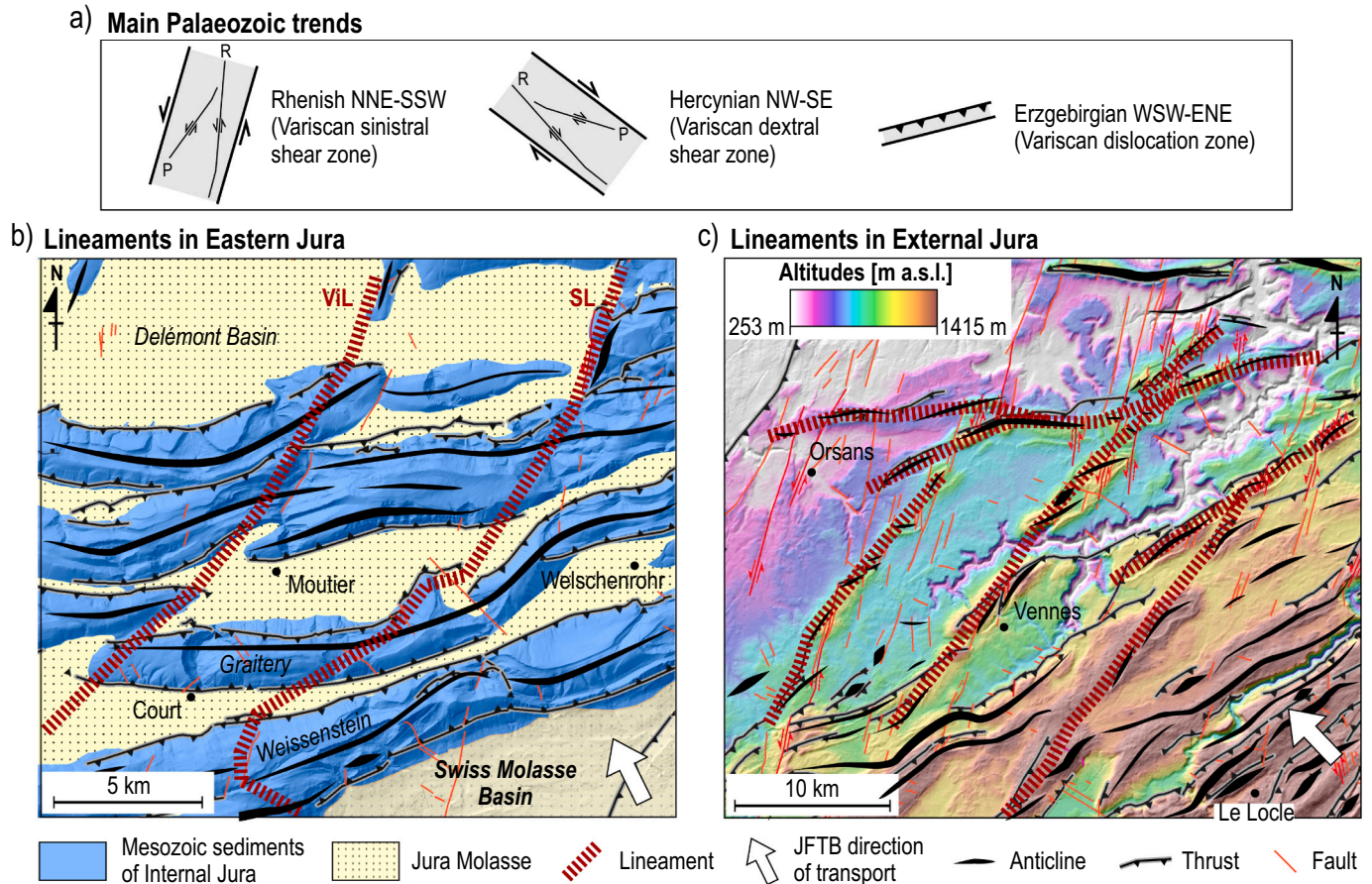


Fig. 3. Examples of lineaments in the JFTB. See overview map (Fig. 1a) for locations. a) Scheme of main Palaeozoic trends in the area of the URG, illustrating strike variations due to Riedel shear structures (R and P) for shear zones. b) Folds in the Eastern Jura tend to be bow-shaped, laterally confined or reveal a sigmoidal geometry (e.g. Graiterie Anticline). Lineaments with a NNE-SSW Rhenish orientation were proposed for this region (Allenbach and Wetzel, 2006; Laubscher, 2008b; Meier, 2010; Steinmann, 1902). The Schwarzwald Line (SL) and Vicques Line (ViL) are drawn according to Laubscher (2008b). c) Area in the External Jura showing lineaments composed of short, dissected folds that align along connected topographical elevations. JFTB transport directions are after Philippe et al. (1996). Note that lineaments are oblique to the local JFTB transport direction.

influence of the latter two predispositions on the evolution of the JFTB.

2.4. Lineaments in the Jura Mountains

In the Eastern Jura, folds frequently deviate from ideal cylindrical geometries, being bow-shaped, sigmoidal shaped or simply oblique to the transport direction of the JFTB in map view (Allenbach and Wetzel, 2006; Laubscher, 2008a; Meier, 2010). Such anomalous fold axes connect to lineaments with a rough NNE-SSW (Rhenish) orientation (Fig. 3a, b). The existence and implications of Rhenish lineaments in the Eastern Jura have been debated for more than a century (Laubscher, 2008a; Steinmann, 1892). Nowadays, anomalous fold orientations in the Eastern Jura are interpreted as thin-skinned structures pre-conditioned by NNE-SSW striking normal faults in the basement, that are southward continuations of Eo-Oligocene URG faults (Allenbach and Wetzel, 2006; Boigk and Schöneich, 1974; Laubscher, 2008a, 2008b; Meier, 2010; Steinmann, 1902), forming preferentially along Palaeozoic Rhenish structural trends.

Also in the central External Jura, the Mesozoic cover deformed along lineaments (see Fig. 3c), which are oblique to the general northwest-directed tectonic transport of the JFTB. In Fig. 3c, lineaments strike NE-SW, NNE-SSW (Rhenish) and ENE-WSW (Erzgebirgian). Along these lineaments, we observe alignments of short, dissected folds (Fig. 3c). Analogous to the situation in the Eastern Jura (Fig. 3b), we propose that lineaments in Fig. 3c are the consequence of aforementioned pre-

existing basement steps, which controlled deformation of the detached cover during formation of the JFTB.

3. Examples of basement-fault related structures

3.1. Basement-fault controlled frontal faisceau

The Ferrette Zone is a faisceau at the front of the Eastern Jura (see Fig. 1a for location). Thrusts at the front of the Ferrette Zone strike NNE-SSW and abruptly turn into a rough E-W direction (Fig. 4a). Structural analysis (Ustaszewski and Schmid, 2006 and references therein) reveals two intersecting fault systems in the basement, which are oriented NNE-SSW and E-W (Fig. 4a). Both systems formed during Eo-Oligocene rifting related to the formation of the URG and provided downward steps during formation of the JFTB, localising deformation in the Mesozoic cover (Fig. 4b). Note that downward steps in the Pre-Mesozoic basement controlled the formation of the two anticlines in Fig. 4b.

3.2. Basement-fault induced cover structures

To the west of the JFTB, in the autochthonous Bresse Graben close to Cormoz (Fig. 1a), Bergerat et al. (1989) interpreted an ECORS seismic line, showing a relatively steep normal fault of 75° in the crystalline basement, above which a reverse fault disrupts the Mesozoic cover (Fig. 5a). There is also a minor extensional collapse in the Jurassic series,

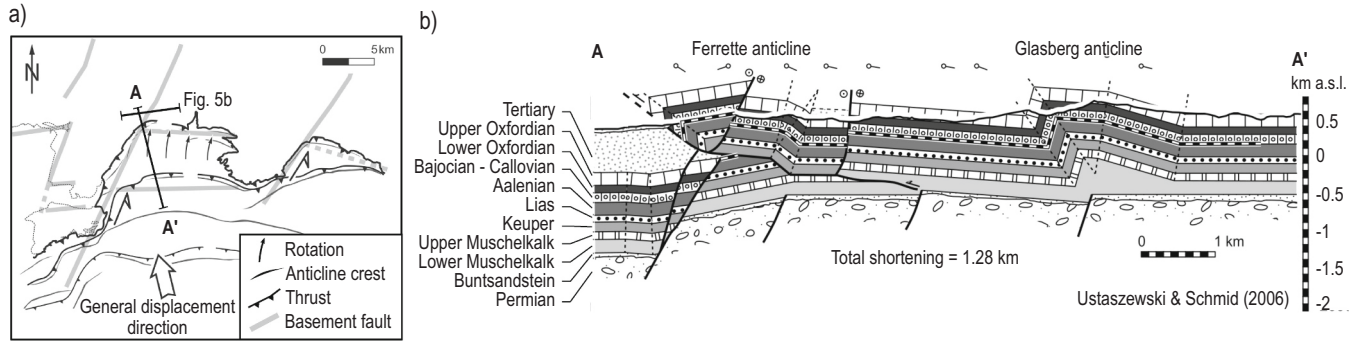


Fig. 4. Structural overview of the Ferrette Zone. a) Structural overview sketch, indicating the relation between NNE-SSW and E-W striking basement faults and thin-skinned structures (Ustaszewski and Schmid, 2006). See Fig. 1a for location. b) Cross-section across the Ferrette Zone (Ustaszewski and Schmid, 2006).

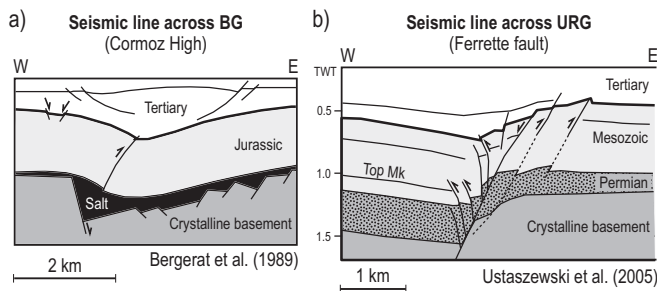


Fig. 5. Basement induced structures in the Bresse Graben (BG) and Upper Rhine Graben (URG). a) Seismic line interpretation across the Cormoz High in the BG, adapted from Bergerat et al. (1989). b) Seismic line interpretation across the URG, adapted from Ustaszewski et al. (2005). Profile traces are indicated in the tectonic overview map in Fig. 1a.

above the higher western basement block. The Triassic salt system accommodates offsets in the basement (Fig. 5a). Normal faults in the basement that induce reverse faults in the cover are also documented in the URG (Ustaszewski et al., 2005), north of Ferrette (Fig. 5b, for location see Fig. 1a). Note that the cross-sections in Fig. 5 show extensional systems in connection with graben formation of the ECRIS, but the dominant structures in the Mesozoic cover are reverse faults (Fig. 5). We also like to point out that basement faults in Fig. 5a do not continue as a single fault into the cover. The salts in Fig. 5a distribute basement

induced deformation, i.e. decoupling (e.g. Withjack and Callaway, 2000), causing different structures in the cover than in the basement.

4. Working hypothesis

Our working hypothesis states that during JFTB formation, deformation of the Mesozoic cover was influenced by offsets along pre-existing basement faults resulting in thrust ramps. Since basement faults were inherited, they were usually oblique to the JFTB transport direction and a variety of oblique, lateral and frontal ramps resulted from the interaction of the cover with basement faults (Fig. 6a). Furthermore, depending on the relative vertical offset of basement faults, the décollement had to ramp upwards (Fig. 6b) or downwards (Fig. 6c) to compensate for higher or lower basement positions respectively.

In order to test the influence of basement faults on the structures in the JFTB, we performed a series of analogue model experiments, in particular testing different throws and strikes of basement faults.

5. Material and methods

5.1. Material properties in analogue models

We apply a 1:20,000 model-to-nature scaling ratio for our brittle-viscous models, so that 70 mm thick dry quartz sand simulates ca. 1400 m of uniform brittle Mesozoic cover. One model tested a reduced cover of 40 mm (corresponding to 800 m in nature). The sand has a

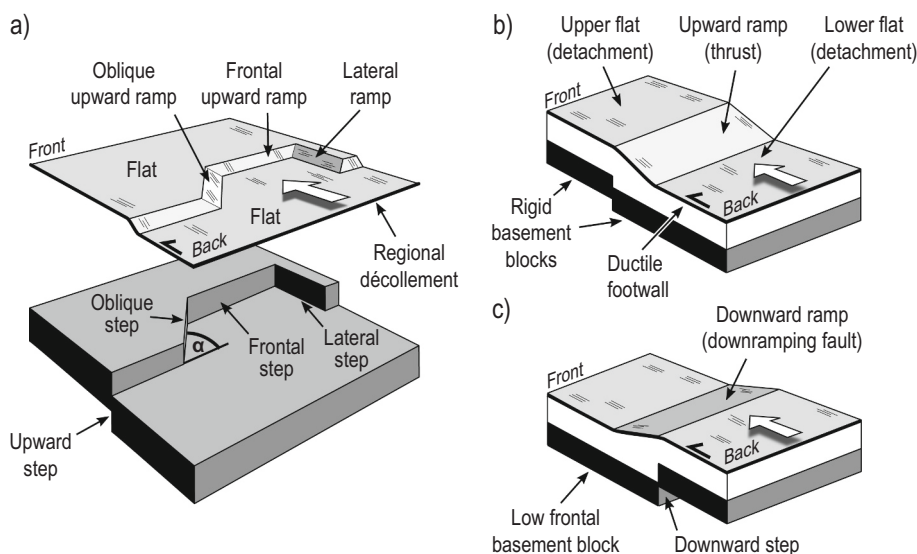


Fig. 6. Sketches illustrating different ramp types of a regional décollement above pre-existing vertical steps in the basement. a) Schematic drawing showing different types of upward ramps (after Apotria et al., 1992) above corresponding basement steps. The angle α specifies the angular deviation of an oblique step from a frontal step and therefore, the angle α is 0° for a frontal step and 90° for a lateral step. Transport directions are indicated with white arrows. b) A low-angle thrust-ramp accommodates a vertical upward step. c) A frontal downward ramp covers a vertical downward step in the basement.

homogeneous density (ρ) of ca. 1560 kg/m³ when sieved from 30 cm height (Klinkmüller et al., 2016), its grain size (ϕ) ranges between 60 and 250 μ m and its angle of internal friction is 36.1° (Zwaan et al., 2016, 2018a, see Table 1). The sand surface is flattened with a scraper at every centimetre during model preparation. One model is scanned using X-Ray Computed Tomography (CT), for which we create a layering visible on CT-imagery by adding a very thin corundum layer (< 1 mm) on top of the sand pack after each scraping. The corundum sand has a density (ρ) of 1890 kg/m³, grain sizes (ϕ) between 88 and 125 μ m and an angle of internal friction of 37° (Panien et al., 2006). A viscous layer of about 13 mm thickness represents a 260 m thick basal décollement zone of weak Triassic salt layers (Fig. 2). The viscous material consists of Polydimethylsiloxane (PDMS, type Dow Corning SGM-36) and corundum sand, mixed in a one-to-one weight ratio. The mixture density (ρ) is ca. 1600 kg/m³, close to the density of the quartz sand (Table 1), and has a near-Newtonian rheology with a viscosity (η) of 1.5·10⁵ Pa·s given our model strain rates (Zwaan et al., 2018b). This way, the density profiles of the models correspond to conditions in the Jura Mountains, where Upper Triassic salt systems are usually associated with various contents of clay, anhydrite and gypsum, and relatively dense compared to pure halite (Bergerat et al., 1990, see Table 2). The density profile of our models also prevents diapirism, taking account of the general absence of salt diapirs in the JFTB.

5.2. Model scaling

Analogue models are scaled with the equation $\sigma^* = \rho^* g^* L^*$ (Eq. 1, King Hubbert, 1937; Ramberg, 1981) where σ^* , ρ^* , g^* and L^* represent the ratios of stress, density, gravity and length between the model and the natural example. The gravity ratio is $g^* = 1$ and the density ratio ρ^* corresponds to ca. 0.6 (Table 2), so that $\sigma^* = 0.6L^*$, where L^* is set to 1/20,000. The viscometric function $\sigma^* = \eta^* \dot{\epsilon}^*$ (Eq. 2, Weijermars and Schmeling, 1986) is used to calculate the strain rate ratio ($\dot{\epsilon}^*$), where η^* is the viscosity ratio and the equation $\dot{\epsilon}^* = v^*/L^*$ (Eq. 3) provides the velocity ratio (v^*).

In nature, the viscosity of pure dry halite is around 10¹⁸ Pa·s, whereas the effective viscosity of halite with small grain sizes at high temperatures is 10¹⁷ Pa·s, ranging up to 10²⁰ Pa·s for large grain sizes at low temperatures (van Keken et al., 1993). Present-day maximum overburden of the basal décollement level in the Jura Mountains hardly exceeds 2.3 km (e.g. borehole Treycovagnes-1 in Sommaruga, 1997; Sommaruga et al., 2012), which at a temperature gradient of 35 °C/km calculates to relatively low maximum temperatures of about 80 °C. In addition, the Triassic salt systems of the Jura Mountains commonly contain various amounts of clay, anhydrite and gypsum, which further increases the viscosity of the salt. We therefore aim to simulate a rock salt décollement with an elevated viscosity (> 10¹⁸ Pa·s).

Table 1
Material properties after Panien et al. (2006) and Zwaan et al. (2016, 2018a, 2018b).

Granular materials	Quartz sand	Corundum sand
Grain size range (ϕ)	60–250 μ m	88–175 μ m
Bulk density (sieved, ρ)	1560 kg/m ³	1890 kg/m ³
Angle of internal friction	36.1°	37°
Angle of dynamic-stable friction	31.4°	32°
Cohesion (C)	9 ± 98 Pa	39 ± 10 Pa
Viscous material	PDMS/corundum-sand mixture	
Weight ratio PDMS/corundum	1/1	
Mixture density (ρ)	Ca. 1600 kg/m ³	
Viscosity (η) [*]	Ca. 1.5·10 ⁵ Pa·s	
Rheology (with sensitivity to strain)	Near-Newtonian ($n = 1.05$ to 1.10)	

^{*} Valid for model strain rates <10⁻⁴ s⁻¹.

Table 2

Parameters used for model scaling. Densities for the Jura Mountains are deduced from density logs of boreholes Bonlieu-1 and Châtelblanc-1 (Bergerat et al., 1990, see positions in Fig. 1a). The densities given for the décollement (ρ_d) and cover (ρ_c) in the Jura correspond to densities of the Upper Triassic salt system and Jurassic limestone-marl layers, respectively..

Parameter	Model	Jura Mountains	Ratio
Density of décollement (ρ_d)	1600 kg/m ³	2500 kg/m ³	0.6
Density of cover (ρ_c)	1560 kg/m ³	2530 kg/m ³	0.6
Gravitational acc. (g)	9.81 m/s ²	9.81 m/s ²	1
Length (L)	1 cm	200 m	5·10 ⁻⁵
Velocity (v)	10 cm/h	3.75 mm/yr	2.34·10 ⁵
Strain rate ($\dot{\epsilon}$)			4.67·10 ⁹
Stress (σ)			3·10 ⁻⁵
Viscosity (η)	ca. 1.5·10 ⁵ Pa·s	2.34·10 ¹⁹ Pa·s	6.42·10 ⁻¹⁵
Time (t)	1 h	533 kyr	2.14·10 ⁻¹⁰

The maximum displacement of the central Jura Mountains is about 30 km (Affolter, 2004; Laubscher, 1965; Philippe et al., 1996). Since the main Jura formation stage lasted roughly 8 Ma (Becker, 2000), we estimate an average natural displacement velocity of 3.75 mm per year. We adjust the model velocity accordingly to 10 cm/h to obtain a velocity ratio (v^*) of 2.34·10⁵ (Table 2). This translates to a strain rate ratio ($\dot{\epsilon}^*$, see Eq. 3) of 4.67·10⁹, which in turn yields an appropriately high viscosity (η) of 2.34·10¹⁹ Pa·s for the simulated salt system (Eq. 2). The time ratio is calculated with $t^* = 1/\dot{\epsilon}^*$ so that one model hour corresponds to 533 kyr in nature (Table 2).

5.3. Experimental set-up

The experimental apparatus is 117 cm long for frontal step experiments and 113 cm long for oblique steps and flat-base models, at a constant width of 50 cm (Fig. 7a). The sandbox frame consists of 2.1 cm thick rigid pine-plywood with two mobile parts: a horizontal mobile frontal baseplate and a vertical mobile backstop (Fig. 7b). The bottom of the apparatus includes two baseplates (Fig. 7a, b). The baseplate underneath the backstop remains fixed whereas the horizontal mobile baseplate to the front can be moved vertically with maximum offsets of 20 mm (400 m in nature) upwards or downwards. An upward offset of the frontal baseplate constitutes an upward step in the direction of transport, whereas a downward offset produces a downward step (Fig. 6b, c). By using different baseplate configurations, the orientation of the plate contact is varied, specified as angle α that gives the deviation from a frontal step (Fig. 7a). This allows the simulation of abrupt frontal steps ($\alpha = 0^\circ$) or oblique steps ($\alpha = 30^\circ$ and 45°), analogous to steps in the basement that pre-date JFTB tectonics (Fig. 6).

The mobile backstop can be moved horizontally towards the front of the apparatus, with a maximum displacement (D_{max}) of 39 cm (Fig. 7a, b), corresponding to a shortening of 7800 m in nature. Models featuring frontal steps (except model U10 with a 10 mm upward step, Table 3) are terminated at $D = 35$ cm. Note that we define the left and right hand side of the model apparatus with regard to the displacement direction of the backstop (Fig. 7a). The backstop is installed 1.3 cm above the fixed baseplate, so that only the sand is compressed without actively squeezing the PDMS/corundum-sand mixture (Fig. 7b).

The sidewalls, front wall, backstop and baseplates are covered with a PVC foil (formerly “Alkor” foil 120,010, now available as “Gekkofix 282 11325”, Klinkmüller et al., 2016) that reduces boundary friction. The angle of dynamic stable friction between sand and foil is about 16.5° ± 0.3° (Schreurs et al., 2006). Computer-steered motors ensure precise motion of the backstop and mobile plates. The velocity of the backstop and the mobile baseplate is 10 cm/h for all experiments.

With this experimental set-up, we focus on testing discrete oblique and frontal steps. It is beyond the scope of this study to model the evolution of the whole Jura arc above a fractured basement, or to test local variations of the cover and basal décollement (e.g. thickness or

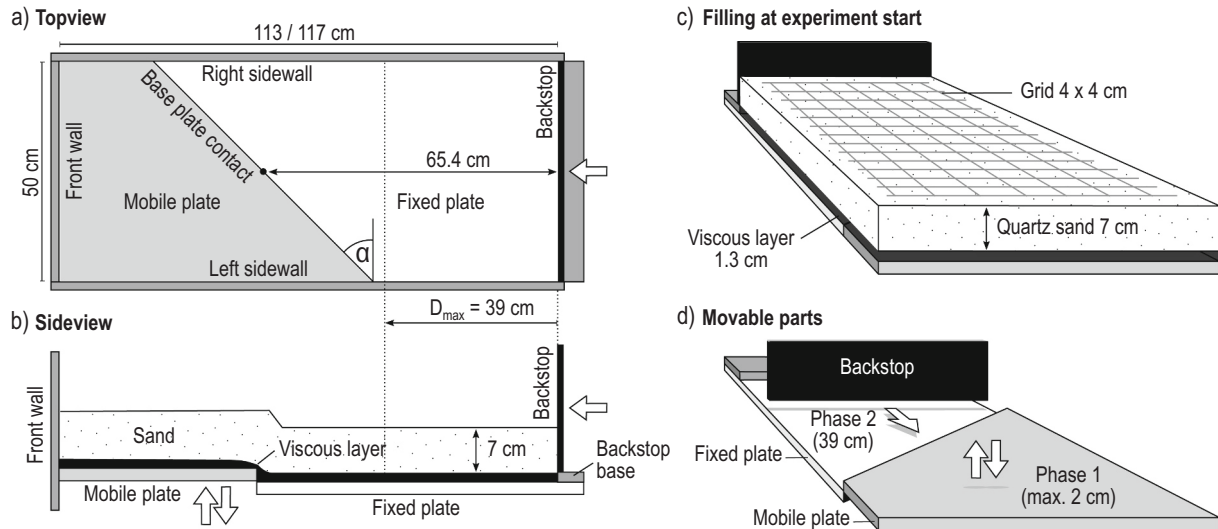


Fig. 7. Schematic representations of the model apparatus. a) Bird's-eye perspective illustrating the 45° oblique baseplate setting. b) Cross-section through the centre of the box, with viscous layer and quartz sand filling. The frontal mobile plate is illustrated with a 20 mm uplift. c) Perspective view without front and sidewalls, illustrating the filling at the start of an experiment and d) perspective view showing movable parts of the apparatus. α : angle of obliquity of the plate contact, with 0° perpendicular to the regional direction of transport (frontal step).

Table 3

List of experiments. A negative throw implies downward steps and a positive throw upward steps. The value α gives the obliquity of the strike of the step with respect to a frontal step ($\alpha = 0^\circ$). The thickness of the viscous and brittle layers are given in columns five and six respectively. Note that model names indicate the type of a step, specifying throw (for step models) and step obliquity angle α (for oblique steps). Model overviews are given in Fig. A.1 and Fig. A.2. Abbreviations in model names are D: downward step, F: flat base, U: upward step, CT: computed tomography, RC: reduced cover.

	Model name	Throw [mm]	α	Viscous [mm]	Brittle [mm]
1	D05	−5	0°	14	70
2	D10	−10	0°	13	70
3	D10–30°	−10	30°	13	70
4	D20	−20	0°	12	70
5	F1	0	–	14	70
6	F2	0	–	15	70
7	U05	5	0°	14	70
8	U05–30°	5	30°	13	70
9	U05–45°	5	45°	13	70
10	U10	10	0°	13	70
11	U10–30°	10	30°	13	70
12	U10–45°	10	45°	13	70
13	U15–30°	15	30°	15	70
14	U15–45°	15	45°	13	70
15*	U20	20	0°	13	70
16	U20–30°	20	30°	14	70
17	U20–45°	20	45°	13	70
18	U20–45°-CT	20	45°	13	70
19	U20–45°-RC	20	45°	13	40

reological changes). The granular material simulating the Mesozoic cover of the JFTB does not allow for modelling overturned forelimbs of anticlines, since the sand collapses at slopes higher than $\sim 35^\circ$. Our models do not include redistribution of granular material by erosion and sedimentation, which can affect the tectonic evolution of structures (e.g. Bonnet et al., 2008; Caër et al., 2018).

5.4. Modelling procedure

Every experimental run starts with a flat baseplate setting. The PDMS/corundum-sand mixture is filled in and a minimum of two days of resting time ensures an even distribution of the viscous layer. The sand layers are sieved in afterwards. A 4×4 cm grid of dark corundum sand

(Table 1) is added to the final sand surface, which allows tracking surface displacements and rotations (Fig. 7c).

Models that contain a step are conducted in two phases: first, the mobile plate is moved upwards or downwards (max. 20 mm, Fig. 7d). In the second phase (or first and only phase for models without a step), the backstop pushes the sand across the produced step (Fig. 7d). There was no resting time between the two phases. A total of 19 models were completed (Table 3). The models are classified into a downward-step (D), flat-base (F) and an upward-step (U) series (Table 3).

5.5. Model analysis

Bird's-eye perspective photographs of the model surface evolution are taken at 1-min intervals, which translates to a displacement of $1\frac{2}{3}$ mm between each image (about 33 m in nature). Videos of all models, except model U20–45°-CT, are provided in the supplementary materials (Schori et al., 2020). After every model run, the sand is removed and the surface of the viscous layer is photographed. Experiment U20–45°-CT is scanned at intervals of 15 min using a 64-slice Siemens Somatom Definition AS X-Ray CT scanner, located at the Institute of Forensic Medicine, University of Bern. The scanned cylindrical volume of 104.4 cm length with a diameter of 50 cm is digitised into 3480 circular slices, each with a diameter of 512 pixels. Slices are scanned at a tube setting of 211 mA and 140 kV and exported with an I30 and I70 filter that highlight different parts of the model. We use the software RadiAnt DICOM Viewer V.4.6.8 by Medixant to analyse scans and export cross-sections for illustrations. Note that the viscous layer is poorly distinguishable from the quartz sand in CT-scans and for intermediate model stages ($D < 39$ cm) of Model U20–45°-CT, the viscous layer is reconstructed based on structural observations after removal of the sand.

6. Analogue model results

6.1. Flat-base models

The flat-base models F1 and F2 serve as a reference for the other models that include a baseplate-step. The first structure in the flat-base models is an imbricate stack that forms in front of the backstop (referred to as backstop imbricate BI, see Fig. 8a-c). The subsequent thrust sheets T1 and T2 forming in front of the BI show leading pop-up structures (Fig. 8c). The BI and thrust sheet T1 are closely spaced and in an evolved

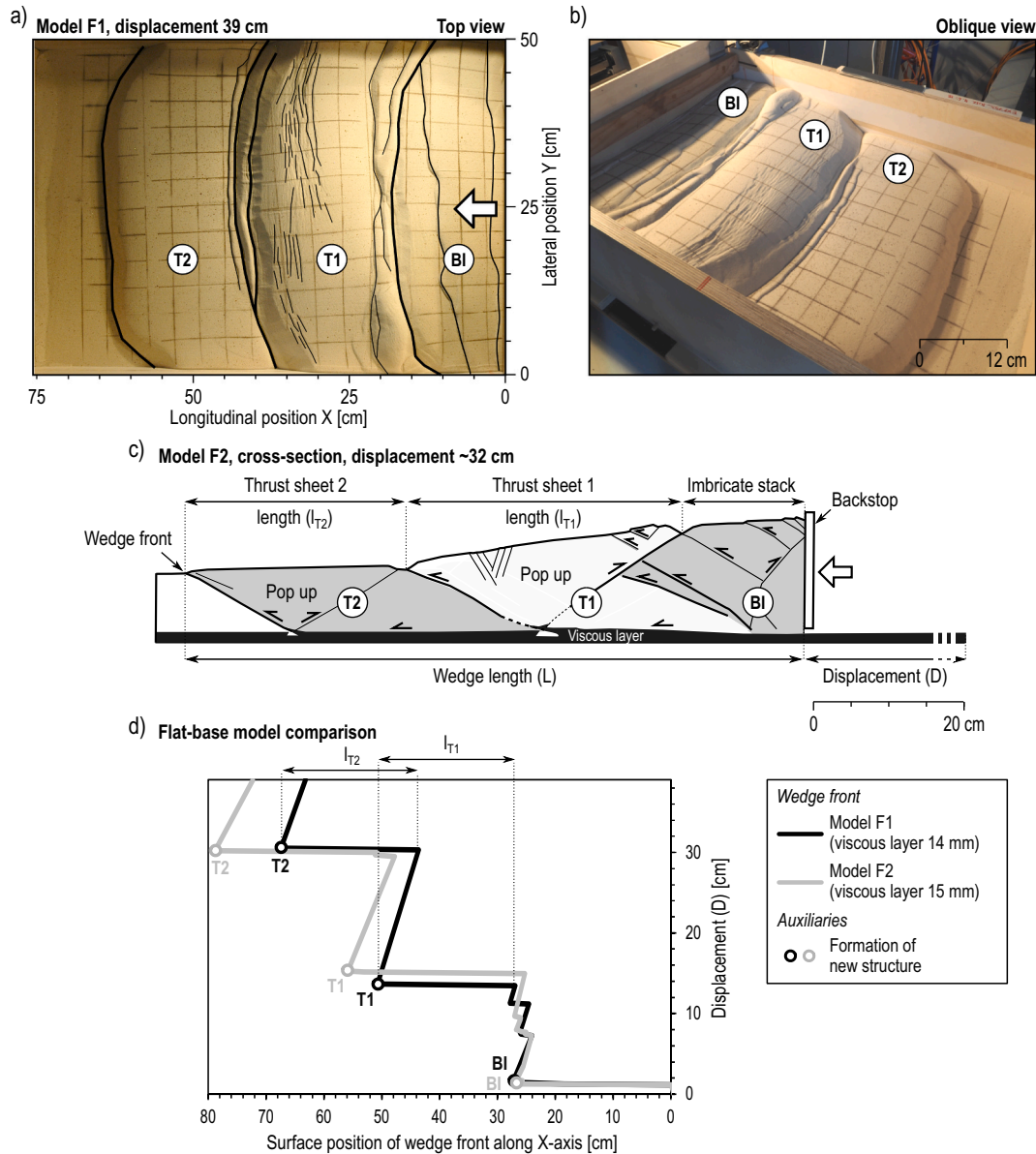


Fig. 8. Analysis of flat-base models. a) Top-view illustrating structures of model F1, which form in sequence from right to left. Two thrust sheets T1 and T2 follow the backstop imbricate stack (BI). The white arrow indicates the direction of compression. b) Oblique view photo of model F1. c) Interpreted cross-section sketch across flat-base model F2 at ~32 cm displacement, illustrating principal structures and parameters. Structural units BI, T1 and T2 are accentuated in different shades of grey. T1 is in an evolved stage, backthrusting the imbricate stack BI whereas T2 just emerges. Note that the wedge front and the length of structures are measured at the model surface. d) Wedge-propagation plot illustrating the difference between flat-base models F1 and F2, of which the latter has a thicker viscous layer that reduces the basal friction. A sudden increase of L is caused by the formation of new structures (BI, T1 and T2). Note that lengths of thrust sheets (l_{T1} and l_{T2}) between models differ. BI adds thrust-slices by frontal accretion, which leads to a jagged graph between $X = 24$ and 28 cm. BI: Backstop imbricate-stack, T1, T2: Thrust sheet 1 and 2, l_{T1} , l_{T2} : length of thrust sheets T1 and T2 at the surface.

stage of T1, its backthrust interferes with the previous structure (Fig. 8c). In each flat-base model, thrust sheets T1 and T2 are identical in their internal architecture and dimension.

In order to compare the structural wedge-development of models, wedge-propagation plots are used (Fig. 8d), which show the evolution of the wedge length L (corresponding to the distance between the backstop and the wedge front) with respect to the backstop displacement D (see Fig. 8c for an illustration of parameters). This representation of data was proposed in Strayer et al. (2001) and called G-grams in Mary et al. (2013). Flat-base models F1 and F2 had slightly different viscous layer thicknesses, which are 14 mm and 15 mm respectively (~280 m and ~300 m in nature). The comparison between flat-base models F1 and F2 (Fig. 8d) shows that the thicker viscous layer leads to longer thrust

sheets T1 and T2 (Fig. 8c, d), which in the whole reduces the surface angle of the wedge. This is analogous to critical wedge mechanics (Dahlen, 1990; Davis et al., 1983), where a lower basal friction (i.e. thicker viscous layer) leads to a smaller taper angle of the wedge. Note that thrust fronts of our flat-base models are generally convex to the foreland due to boundary friction at the sidewalls (Fig. 8a), which is characteristic of sandbox-analogue models using a mobile backstop (e.g. Schreurs et al., 2006).

6.2. Evolution of structures related to basement step formation

During vertical movement of the mobile base plate in phase 1, a major reverse fault rooting at the upper step-edge commonly forms in

the brittle sand cover. Sub-parallel to that, a minor reverse fault with less offset is seen on CT imagery of model U20–45°-CT, rooting at the lower step edge (Fig. 9a). At a step offset of roughly 10 mm (200 m in nature), the major reverse fault appears on the sand surface. Reverse faults are verging towards the lower baseplate and show inclinations between ca. 55° and 65°. At an offset of ca. 15 mm (300 m in nature), extensional collapse of the quartz sand occurs above the higher plate (Fig. 9a). Fig. 9a shows structures after 20 mm (400 m in nature) upward displacement of the mobile plate. In the case of a 20 mm downward displacement, structures are the same but mirror-inverted. Note that similar reverse faults and collapse structures induced by basement faults are known from seismic lines (Fig. 5).

Reactivation of phase 1 faults is not observed during subsequent thin-skinned deformation in phase 2 (Fig. 9b, c), which suggests a high friction angle of these pre-existing faults (Caër et al., 2015). Instead, new thrusts with shallower and mechanically favourable angles between ca. 20° and 33° are formed (Fig. 9b, c). In the case of upward steps with a vertical offset of at least 10 mm (200 m in nature), a backthrust temporarily leading the deformation front nucleates in the viscous layer above the upper step edge (Fig. 9b). Only afterwards, the pop-up structure at the front of thrust sheet T1 appears (Fig. 9c). Note that both the fore- and backthrust of the pop-up structure nucleate above the lower baseplate but the fore-thrust traverses the upper edge of the

baseplate step (Fig. 9c). Although genetically different, extensional and compressional structures of phase 1 and 2 are controlled by the same baseplate step and therefore, their position is ultimately linked. In the upward-step model in Fig. 9, structures of phase 1 (Fig. 9a) are embedded in the central and frontal part of the pop-up structure of T1 during phase 2 (Fig. 9b, c). The distinct extensional collapse structure of phase 1 remains in the frontal half of the evolving pop-up structure (Fig. 9c).

6.3. Frontal steps ($\alpha = 0^\circ$)

Fig. 10 shows wedge-propagation plots for frontal-step models ($\alpha = 0^\circ$). In all plots, we add the graph of flat-base model F1 as a reference, in order to infer the influence of baseplate steps. Furthermore, the calculated surface position of step-controlled fore-thrusts (Fig. 9c) and leading backthrusts (Fig. 9b) are plotted in wedge-propagation plots of Fig. 10 (dotted graphs). If abrupt slope changes of solid black graphs (wedge front) coincide with dotted graphs, the wedge front is likely controlled by the step. Nucleation centres of step-controlled thrusts are assumed according to observations in CT-scans (see fault nucleation lines in Fig. 9b, c).

6.3.1. Frontal downward-steps

Frontal downward-step models (Fig. 10a–c) illustrate that with increasing throw of downward steps, thrust sheet T1 forms at less displacement (D) of the backstop and additionally, T1 becomes increasingly larger. In comparison to flat-base model F1, our downward steps therefore lead to a notable forward advancement of the deformation front (Fig. 10a–c). In an evolved stage however, localisation of deformation at the step prevents downward ramping onto the lower baseplate and inhibits an overall propagation of deformation in comparison to flat-base models (Fig. 10b, c).

After the step-controlled front of T1 has formed in models D10 and D20, backthrusts appear in a backbreaking sequence (see videos in supplementary material, Schori et al., 2020). The overall structure at the front of T1 corresponds to a fault-bend fold with a single thrust-ramp, where backthrusts nucleate (Fig. 11a). The thrust-ramp at the front of T1 roots at the upper edge of the baseplate step and continuous upwards, over the sand of the lower baseplate (Fig. 11a).

6.3.2. Frontal upward-steps

The small upward step of 5 mm (100 m in nature) in model U05 does not trigger thrusts and the overall wedge propagation plot of model U05 is quite similar to flat-base model F1 (Fig. 10d). Upward steps of 10 and 20 mm height (corresponding to 200 and 400 m in nature) localise deformation (step-controlled thrusts), and the deformation front is attracted forwards leading to an enlarged thrust sheet T1 (Fig. 10e, f). In all our upward-step models, a long viscous ramp smoothens the abrupt step between the two baseplates (Fig. 11b) enabling a propagation of deformation onto the higher baseplate (Fig. 11b). Backthrusting becomes increasingly prominent with higher steps (Fig. 10e, f). For one thing, step-controlled leading backthrusts (Fig. 9b) precede the formation of thrust-sheet T1 in models U10 and U20 (Fig. 10e, f). For another thing, the backthrust of the pop-up structure shows concentrated displacement (Fig. 11b) and remains constantly active during shortening of T1. Wedge-propagation plots of models U10 and U20 (Fig. 10e, f) show jagged graphs at the front of thrust sheet T1. This is due to thrust slices that are added at the toe of T1, nucleating beyond the step above the higher frontal baseplate (Fig. 11b). The accretion of thrust-slices distributes deformation among several thrust planes so that individual fore-thrusts absorb notably less displacement than the long-time active backthrust (Fig. 11a). The overall structure at the front of thrust sheet T1 in model U10 is a pop-up with dominant backthrusting (Fig. 11b) and an imbricated front.

In contrast to downward steps (Fig. 10a–c), thrust sheet T1 in the upward step models forms at about the same displacement (D) of the

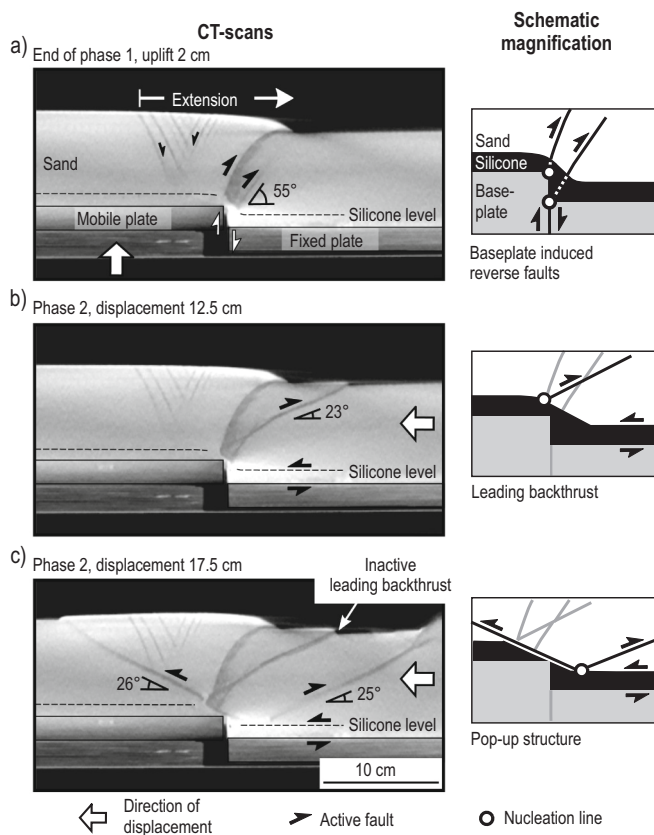


Fig. 9. Cross-sections of CT scans showing step induced structures of model U20–45°-CT, which are representative for the structures in the other models involving steps. a) After 20 mm vertical displacement of the mobile baseplate, an extensional collapse structure is visible in the sand layer. A reverse fault nucleates at the upper step edge and becomes sub-horizontal towards the surface and additionally, a blind reverse fault nucleates at the lower step edge. b) After 12.5 cm displacement (D) of the backstop in phase 2, a backthrust nucleating in the viscous layer above the upper step-edge is observed. c) After 17.5 cm displacement (D), structures that formed in phase 1 are embedded in the pop-up of thrust sheet T1. Note that pre-existing faults of phase 1 are not reactivated.

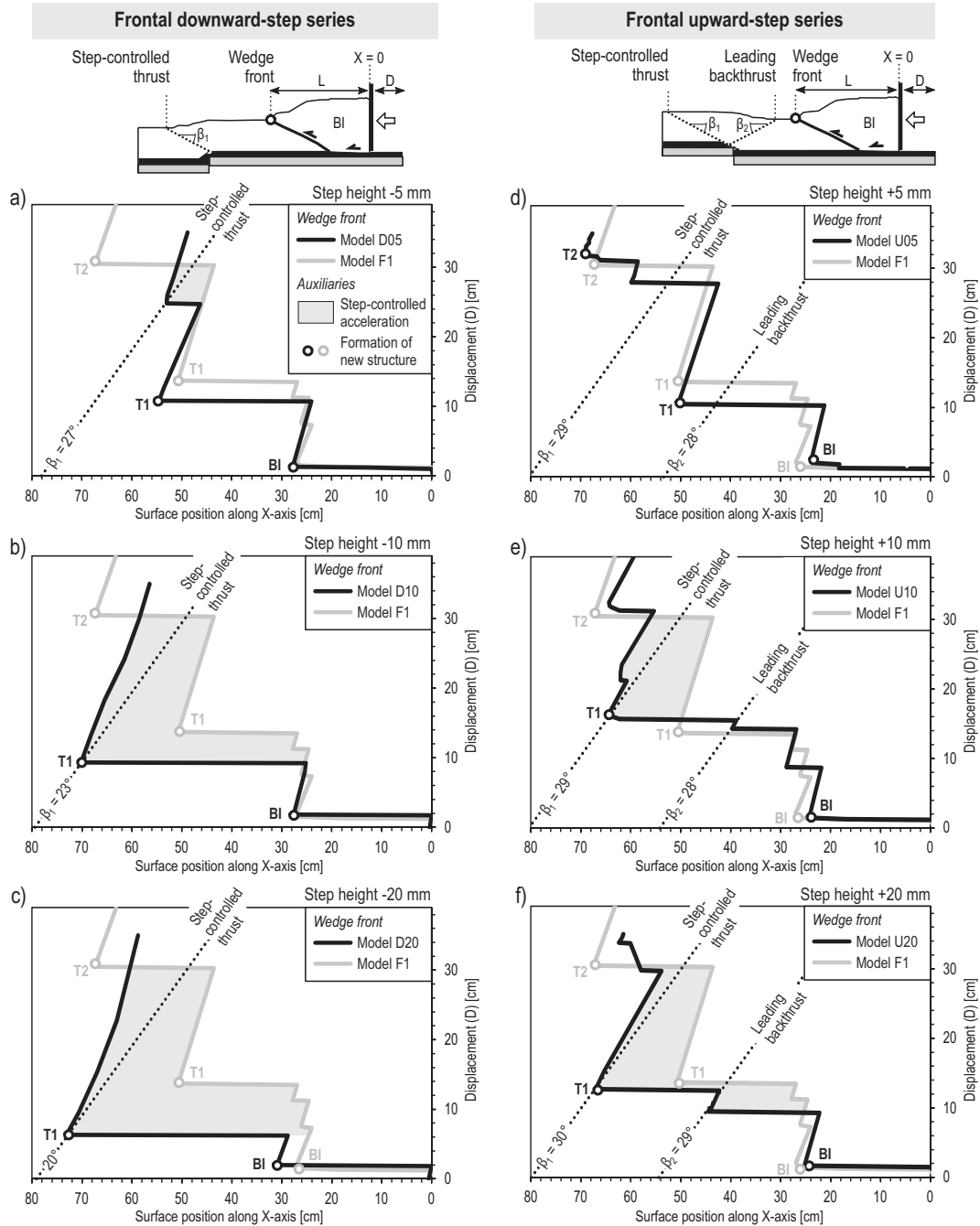


Fig. 10. Wedge-propagation plots of frontal-step models showing compressional phase 2. Cross-sections at the top illustrate parameters after formation of structure BI. The wedge front is the intersection of the foremost active thrust with the sand surface. The surface position along the X-axis indicates the distance to the backstop. Flat-base model F1 (grey graph) is given as reference to evaluate the influence of steps. Dotted graphs plot the calculated surface position of step-controlled thrusts and leading backthrusts for D between 0 and 39 cm. Dip angles of thrusts (β) used to plot the surface positions are indicated at the bottom of dotted graphs. a-c) The downward-step series reveals increasing localisation of the wedge front at higher steps and associated to this, a temporary forward movement of the wedge front. d) The 5 mm high upward step does not control the wedge front. e, f) By contrast, 10 and 20 mm upward steps trigger step-controlled and fore-thrusts and leading backthrusts. D: Displacement of backstop, L: Length of wedge at the surface.

backstop as observed in flat-base model F1 (Fig. 10d-f) and therefore, forward advancement of the deformation front is due to enlarged thrust sheets only. Note that frontal-step models do not form thrust sheet T2, except for model U05, where the low upward-step of 5 mm does not trigger thrusts (Fig. 10d).

6.4. Oblique downward-step model

Model D10-30° is the only experiment featuring an oblique

downward-step (10 mm, at $\alpha = 30^\circ$, Fig. 12). No downward ramp forms at the transition from the upper to the lower baseplate. Instead, a large fault-bend fold develops that thrusts the sand on the lower baseplate (Fig. 11a). Due to the oblique step, we observe important lateral variations. The deformation front sufficiently close to the oblique step is advanced forward between $Y = 0$ to 30 cm in Fig. 12a, attracted by the step. As the step controls the deformation front of this segment, the thrust is parallel to the step (Fig. 12a). In flat-base model F1, the position of the regular thrust-front of thrust-sheet T1, which is unaffected by

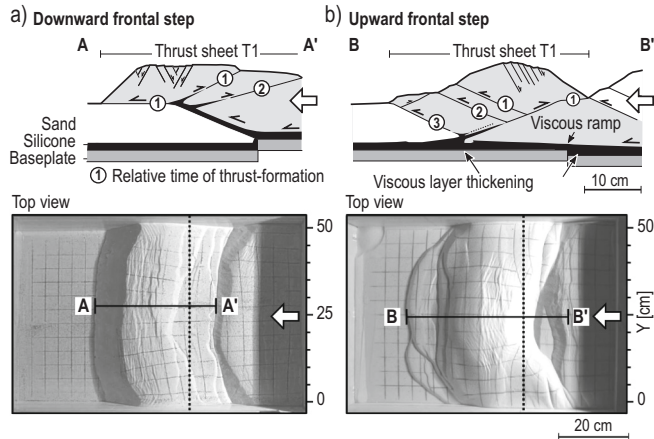


Fig. 11. Step-controlled structures of frontal-step models in phase 2, sketched based on surfaces of the sand and exhumed viscous layer (after removal of sand at the end of the experiment). a) Sketch of model D20, showing a 20 mm downward step. The overall step-controlled structure corresponds to a fault-bend fold that forms backthrusts in a backbreaking sequence, nucleating along the single, main thrust-ramp. b) Sketch of model U10, showing a 10 mm upward step. A pop-up structure nucleates at the step, moves forward and adds frontal thrust-slices subsequently. The step between baseplates is covered by a long viscous ramp with moderate inclination.

steps, is at $X = 50$ cm (Fig. 12a). The downward-step model forms a relay thrust that connects the regular thrust position and the forward promoted, step-controlled thrust front. This leads to an initial front of T1, which is a composite of two thrusts that are about 84° oblique to each other (Fig. 12a). We observe an overall angular deformation front that tapers in the direction of transport. Note that in model D10– 30° , no thrust is perpendicular to the direction of displacement (Fig. 12a–c).

In our experiment, deformation is step-controlled on the left side ($Y = 0$ to 30 cm) and afterwards, a thrust slice is added on the right-hand side (Fig. 12b, $Y = 25$ to 50 cm). The reverse fault remaining from baseplate-offset in phase 1 is passively transported forwards without significant rotation (see $Y = 0$ to 25 cm in Fig. 12a, b). In an evolved

stage of the experiment, a new graben structure forms due to extensional collapse roughly in the centre of the large oblique fault-bend fold (Fig. 12c). This graben is sub-parallel to the downward oblique step.

In summary, we observe three step-parallel structures, which are (1) a reverse fault related to vertical baseplate offset in phase 1, (2) an oblique thrust-front of T1 on the left (Fig. 12a, b) controlled by the oblique step during phase 2 and (3) a graben forming in response to localisation of deformation at the oblique step in phase 2 (Fig. 12c).

6.5. Oblique upward-step models

In the two oblique upward-step series with oblique angles (α) of 30° and 45° , we vary the step throw between 5 and 20 mm (Fig. 13). All oblique upward-step models form oblique viscous-ramps between the lower and higher baseplates (Fig. 11b). Above these continuous ramps, different oblique structures form in the brittle sand cover. These structures reveal step-controlled thrust segments that nucleate near the baseplate step and are therefore parallel or sub-parallel to the step. With increasing step throw, step-controlled thrusts on the sand surface are more numerous (Fig. 13).

6.5.1. 30° oblique-step series

At a low oblique upward-step height of 5 mm (100 m in nature), thrust sheet T1 remains a continuous structure with virtually no imbrication (Fig. 13a). The frontal thrust of T1 in Fig. 13a is step-controlled on the left, roughly between $Y = 0$ to 15 cm. In an evolved model stage, this leads to a continuous, *bow-shaped* front of thrust sheet T1 (Fig. 13a, late stage). Note that flat-base model F1 (Fig. 8a) is notably less bow-shaped than U05– 30° (Fig. 13a), illustrating that the bow shape is not a mere cause of boundary effects.

Model U10– 30° (Fig. 13b), with a 30° oblique-upward step and a throw of 10 mm (200 m in nature), develops thrust slices that pinch out laterally and reveal curved fronts, resulting in distinct *crescent-shaped* structures (Fig. 13b, late stage). These thrust-slices are added at the toe of the wedge, alternatingly on the left and right hand side. Crescent-shaped thrust-slices nucleate in the viscous layer on the upper plate, commonly beyond the step. With increasing throw of the oblique step, curved thrusts become less numerous in favour of angular thrusts (Fig. 13c, d). Therefore, at step throws of 15 and 20 mm (300 to 400 m in

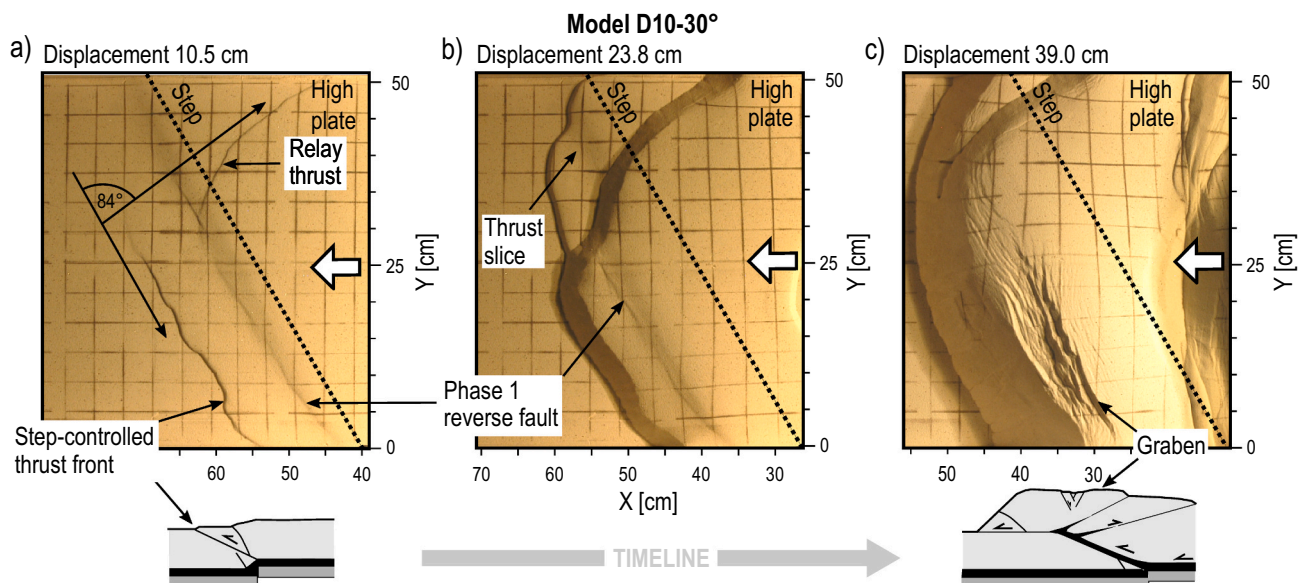


Fig. 12. Top-view photos showing the evolution of structures in model D10– 30° , which has a 30° oblique downward-step with a throw of 10 mm. a) The front of thrust sheet T1 nucleates at the step between $Y = 0$ to 30 cm and therefore, it is parallel to the step. b) A thrust slice is added on the right hand side of the model subsequently. c) Individual oblique thrusts connect to a single thrust front. Due to its large size, the fault-bend fold collapses at the centre forming a graben, parallel to the oblique step.

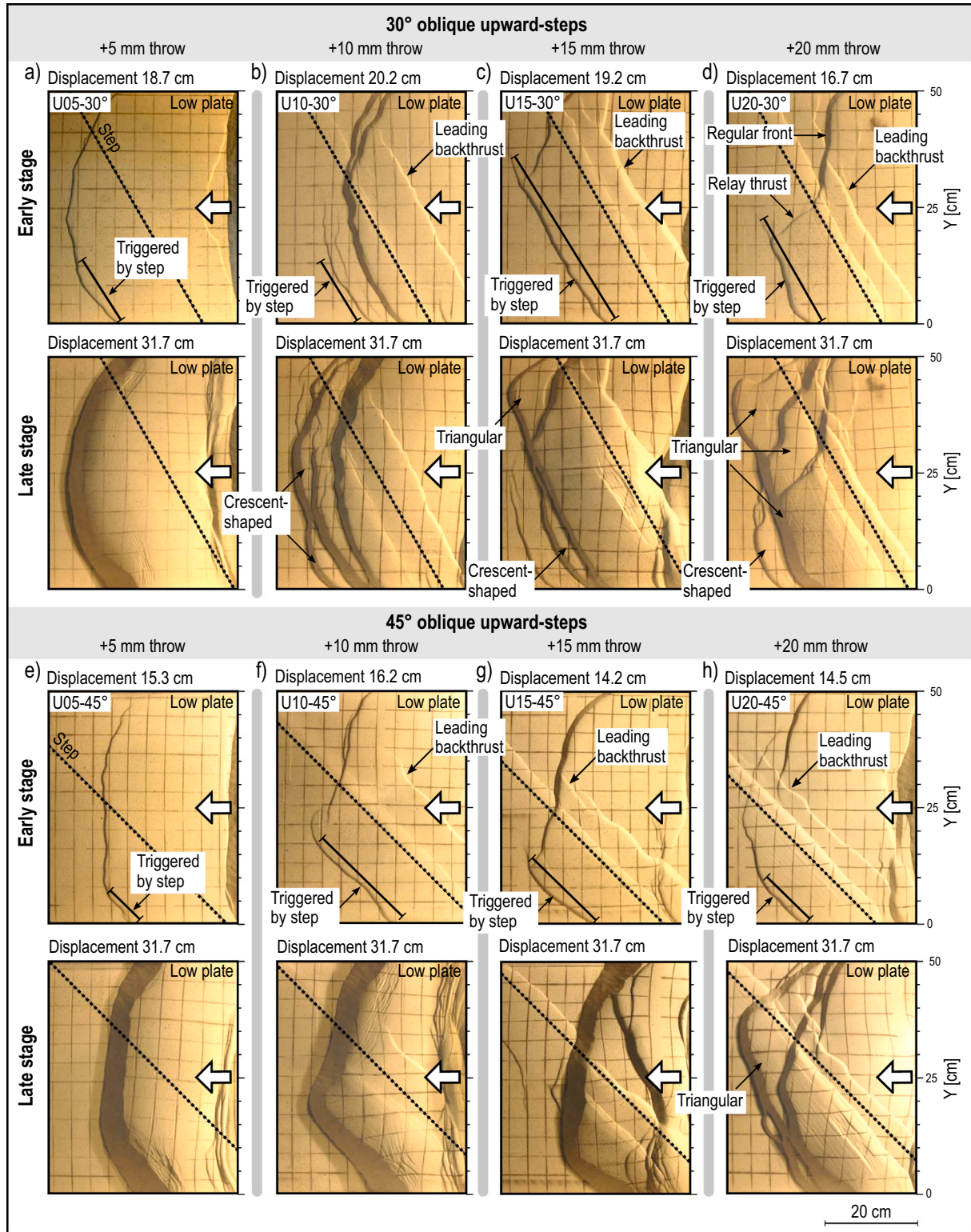


Fig. 13. Evolution of step-controlled structures with increasing throws for 30° (a-d) and 45° oblique upward-steps (e-h). a) A 30° oblique step with a low throw (5 mm) leads to a continuous structure which is step-controlled between $Y = 0$ to 15 cm. b) With increasing step throw, imbrication increases and thrusts are curved. c) Angular thrusts with step-controlled left sides are accompanied by curved thrusts. d) At a 30° oblique step and a high throw of 20 mm, the thrust front between $Y = 0$ to 20 cm is step-controlled, whereas on the right between $Y = 25$ to 50 cm, the regular thrust front lags behind. A relay oblique thrust connects both fronts. e-g) At 45° oblique upward-steps with throws of 5 to 15 mm, the front of T1 is continuous but asymmetric, being step-controlled on the left side. h) At a high 45° oblique step with a throw of 20 mm, imbrication of T1 occurs.

nature), individual thrust-slices are reminiscent of triangles (Fig. 13c,d). The left side of angular thrusts (left limb of triangle) mirrors the orientation of the step and nucleates at the upper step-edge, thus representing a step-controlled feature (Fig. 13c, d).

At the highest oblique upward-step of 20 mm (400 m in nature), step-controlled thrust segments are initially sub-parallel to the step (Fig. 13d, early stage), but rotate clockwise with progressive deformation (Fig. 13d, late stage). The thrust segment between $Y = 20$ to 25 cm in Fig. 13d (early stage), forms as a relay oblique-thrust that is ca. 80° oblique to the step and also distinctly oblique to the direction of transport (Fig. 13d). The relay thrust connects the step-controlled thrust front above the upper baseplate with the trailing regular thrust-front on the lower baseplate.

6.5.2. 45° oblique-step series

At step throws of 5 to 15 mm (100 to 300 m in nature) in 45° oblique-step models, the thrust front of T1 is continuous, but becomes increasingly asymmetric and angular with higher step throws (Fig. 13e-g). The left sides of these continuous thrusts nucleate above the upper step-edge and are step-controlled features (Fig. 13e-g, early stage). Only at a high step throw of 20 mm (400 m in nature), the 45° oblique-step model shows imbrication of thrust sheet T1 (Fig. 13h).

6.5.3. Difference between 30° and 45° oblique steps

We observe a fundamental difference between 30° and 45° oblique-step models at intermediate step heights of 10 and 15 mm (200 to 300 m in nature, Fig. 13b, c, f, g). The overall wedge-length evolution plots of 30° oblique-step models show a notable influence of the step (Fig. 14a, b), whereas the wedge-length plots of 45° oblique-step models resemble

flat-base model F1 (Fig. 14c, d). For one thing, this difference is because 30° oblique steps cause a strong frontal imbrication of thrust sheet T1 at a step height of 10 and 15 mm (Fig. 13b, c), which is not the case for 45° oblique steps with the same throws (Fig. 13f, g). For another thing, instead of adding thrust-slices to T1, deformation propagates forwards in the 45° models and a new thrust-sheet T2 forms similar to flat-base models (Fig. 14c, d).

6.5.4. Leading backthrusts

At 30° and 45° oblique upward-steps of 10 to 20 mm (200 to 400 m in nature), we observe step-controlled leading backthrusts (Fig. 13) that temporarily constitute the front of the wedge, preceding T1 (also see Fig. 9b, c). In bird's eye perspective, leading backthrusts are relatively long, stretching the entire width of 30° oblique-step models (e.g. Fig. 13c, d). They are distinctly step-parallel and become inactive after only 1 to 3 cm displacement and subsequently, they are dissected during imbrication of thrust sheet T1 (Fig. 13c, d, late stage). Since leading backthrusts are step-controlled features that hardly experience subsequent rotation (Fig. 13d, f), they constitute excellent indicators for the orientation of oblique steps, even in an evolved stage of models (Fig. 13).

6.5.5. Lineament rotation

Step-controlled thrusts start forming on the left side of our oblique-step models and append sequentially along the step (Fig. 15a). This is typically accompanied by crescent-shaped thrust slices that are added on the left wedge front (Fig. 15a, b), seemingly to compensate an asymmetric deformation front, and resulting in an overall thrust front that becomes more perpendicular to the direction of transport. When triangular thrust-slices append, their step-controlled left segments connect to

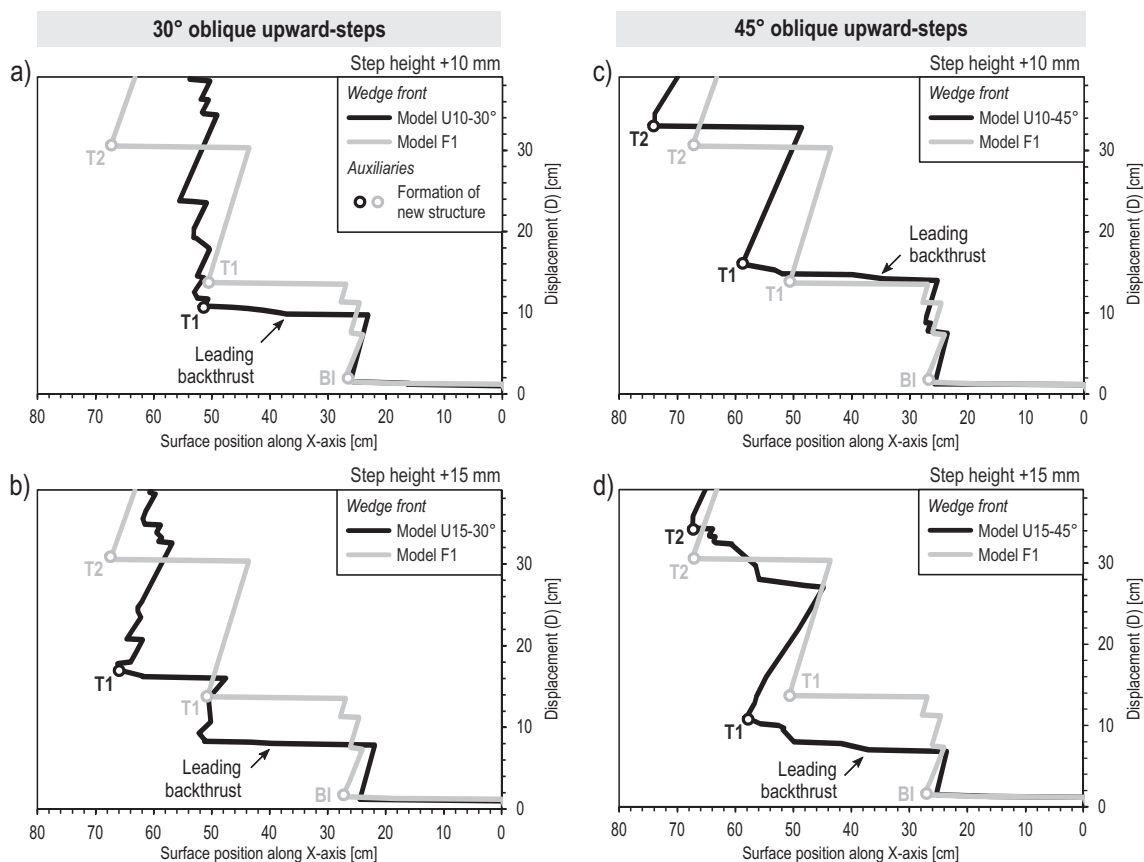


Fig. 14. Wedge-propagation plots for 10 and 15 mm high oblique upward-step models. Note that the wedge-length (L) is given with respect to the front-most thrust measured on the sand surface. a, b) Plots of 30° oblique upward-step models differ considerably from flat-base model F1, featuring strong imbrication of thrust sheet T1 and absence of thrust sheet T2. c, d) Plots of 45° oblique upward-steps resemble flat-base model F1, because both thrust sheets T1 and T2 form and imbrication is virtually absent.

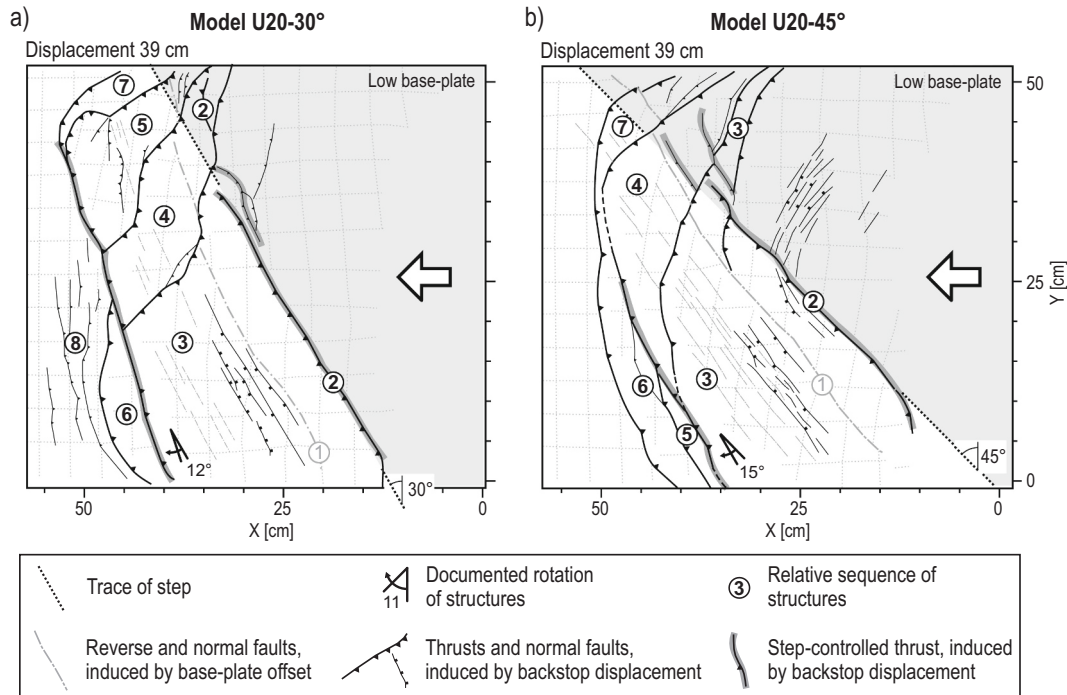


Fig. 15. Line drawings of top-views illustrating the relative sequence of structures in models U20–30° and U20–45°. Structures are (1) reverse faults forming in phase 1, (2) step-controlled leading backthrusts, (3) initial pop-up structures and (4) first triangular thrust-slices. Subsequent structures vary in between the two models. a) In the model U20–30° featuring a 30° oblique step, structure (5) is another triangular thrust-slice, (6) and (7) follow as crescent-shaped thrust-slices whereas structures (8) are thrusts associated with small buckle folds. b) In comparison to this, at the 45° oblique step of U20–45°, structures (5) to (7) are crescent-shaped thrust-slices.

a single lineament (Fig. 15a) that shows an overall clockwise rotation about a vertical axis over time. This rotation is strongest for high upward steps in models U20–30° and U20–45°, where we measure a rotation of 12° and 15°, respectively of step-controlled fore-thrusts (see Fig. 15a, b).

Table 4 shows observed rotations at different step throws. In contrast to step-controlled fore-thrusts, step-controlled leading backthrusts do not reveal any noticeable rotations (see Fig. 15a, b, sequence number 2).

6.6. CT-scanned oblique upward-step model

Model U20–45°-CT is a CT-scanned rerun of model U20–45°, featuring a 20 mm (400 m in nature) upward-step of 45° obliquity. The CT scans allow the reconstruction of cross-sections at different model stages (Fig. 16). Raw CT-scan sections interpreted for Fig. 16 are compiled in the supplementary material of this article (Schori et al., 2020).

Structures of phase 1 (Fig. 16a) are fragmented laterally and at depth during horizontal shortening, and transported forwards embedded in the front of thrust sheet T1 (compare to Fig. 16c and d). In contrast to this, late collapse structures due to sediment stacking are situated at the

back of thrust sheet T1 and not at the front (e.g. Fig. 16d, cross-section B4 and C4).

The front of thrust sheet T1 is step-controlled on the left side (Fig. 16b, cross-sections D2 and E2) whereas the right hand side is yet unimpeded by the step (Fig. 16b, cross-section A2). By comparison, pop-up structures in cross-sections D2 and E2 (Fig. 16b) lie slightly more frontwards, attracted by the upward oblique-step, which results in an overall curved thrust front, visible on the top view image in Fig. 16b.

The thrust-slice added in cross-sections B3 to E3 (Fig. 16c) corresponds to a triangular thrust-slice in top-view images of Fig. 16c, d. Cross-sections C3 and D3 (Fig. 16c) illustrate that on the left side, the triangular thrust-slice nucleates near the step, whereas in C4 to D4 (Fig. 16d), the subsequent crescent-shaped thrust-slice nucleates beyond the step. The backthrust of pop-up structure T1 is permanently active whereas fore-thrusts become inactive when new thrust-slices are added to the front of the wedge (e.g. compare cross-sections A2 to A4, Fig. 16).

6.6.1. Formation of viscous ramps

In all models, viscous material thins out underneath the backstop imbricate fan BI (Fig. 16d), which is the structure showing most sand stacking and therefore, the vertical load exerted on the PDMS/corundum-mixture by the overburden is highest. Consequently, viscous material flows forward with no material escaping backwards through the gap between the backstop and the baseplate (Fig. 16d). In upward-step models, the forward flowing viscous material accumulates in two locations. First, thickening occurs underneath the front of the pop-up structure of T1 (Fig. 16d, section A4). Secondly, upward steps cause an accumulation of viscous material on the lower baseplate, between the step and the roots of BI, thereby forming a long viscous ramp with moderate inclination (Fig. 16d, C4 to E4). Since the length of the ramp depends on the spacing between the step and BI, the length of the viscous ramp varies laterally (Fig. 16d, C4 to E4) and furthermore, over time with ongoing displacement of the backstop (Fig. 16a to d). Note that if the step-throw exceeds the thickness of the viscous layer (e.g. step

Table 4
Overview of observed clockwise rotations of step-controlled fore-thrusts over time. A negative throw denotes a downward step whereas positive throws indicate upward steps. α : Obliquity of step.

Step throw	Rotation of thrust	
	$\alpha = 30^\circ$	$\alpha = 45^\circ$
–10 mm	<1°	–
5 mm	4°	13°
10 mm	8°	6°
15 mm	10°	3°
20 mm	12°	15°

^a No imbrication of thrust sheet T1.

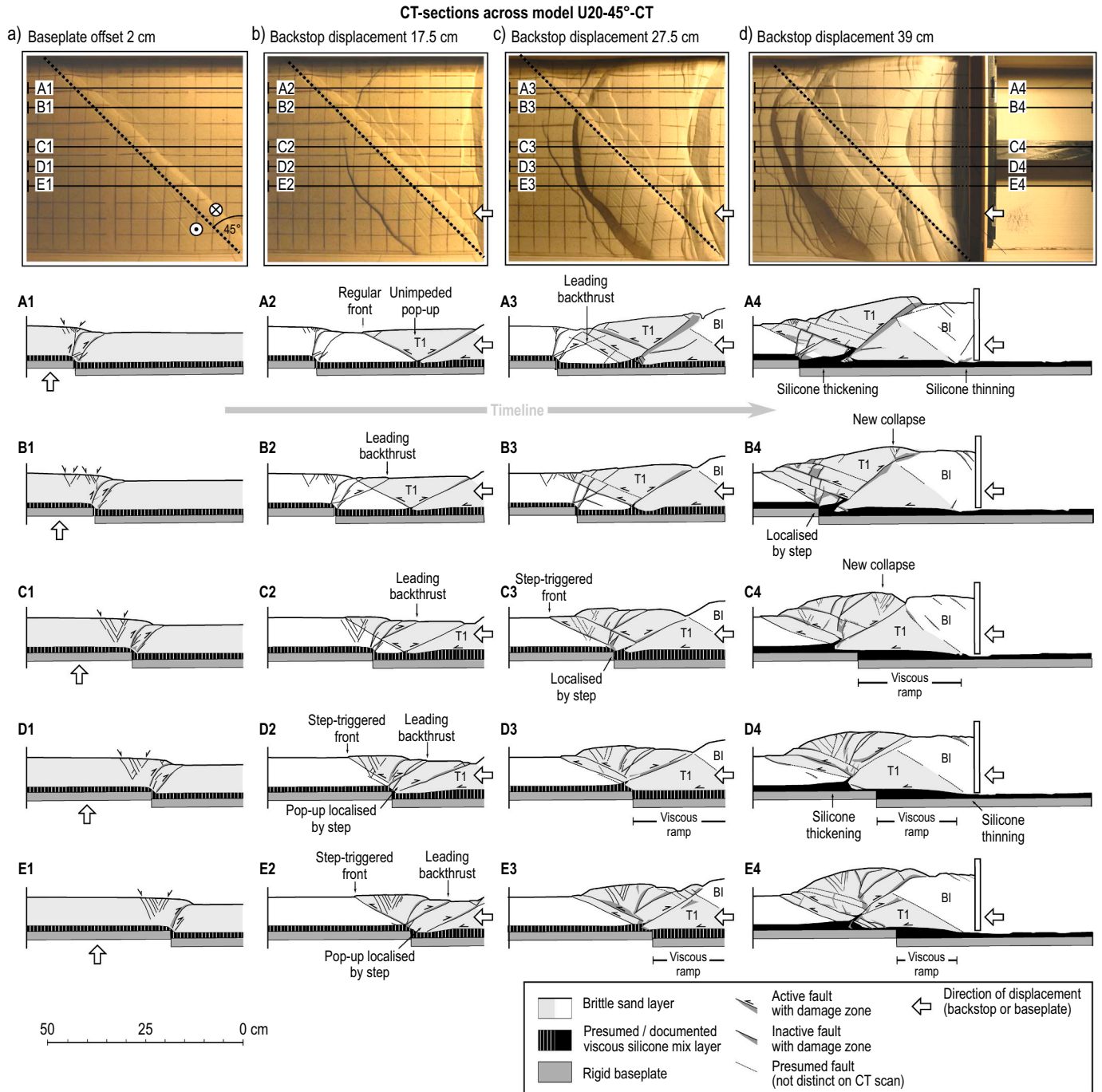


Fig. 16. Interpreted CT-sections across model U20-45°-CT, showing five sections at different model stages. a) The first stage shows the model after baseplate-offset phase 1. An extensional collapse structure and two reverse faults form in the sand cover in response to vertical offset of the baseplates. b) The front of thrust sheet T1 reveals a pop-up, which is localised by the step in cross-sections D2 and E2. c) Thrust-slices are added to the front of T1. d) The final stage gives detailed insight into structures of the viscous layer. A viscous ramp is documented in cross-sections C4, D4 and E4. The along-strike length of the ramp varies laterally. BI: Backstop imbricate stack, T1: Thrust sheet 1.

height 15 or 20 mm, 300 or 400 m in nature), the formation of the viscous ramp ultimately leads to in-situ uplift of a few millimetres. Above the edge of the upper baseplate, the viscous layer thins out down to a few millimetres (Fig. 16d, C4 to E4).

6.7. Oblique upward-step model with reduced cover

Model U20-45°-RC tests a 20 mm (400 m in nature) oblique upward-step with a reduced sand cover of 40 mm instead of 70 mm (Fig. 17a, b). The thinner sand cover leads to shorter and more numerous thrust sheets

and generally smaller thrust-slices in comparison to a cover thickness of 70 mm (Fig. 17c), which is directly related to the geometric relationship between layer thickness and thrust-fault dip-angle (Allemand and Brun, 1991). However, similar step-controlled features as observed in models with a high oblique upward-step and a sand thickness of 70 mm are present, such as triangular thrust-slices and a step-controlled leading backthrust (Fig. 17a). In the model, an overall sigmoidal structure is the result of triangular thrust-slices of variable size that grow sequentially (Fig. 17a, b). The overall step-controlled front of connected triangular thrust-slices rotates by about 15° clockwise (Fig. 17b).

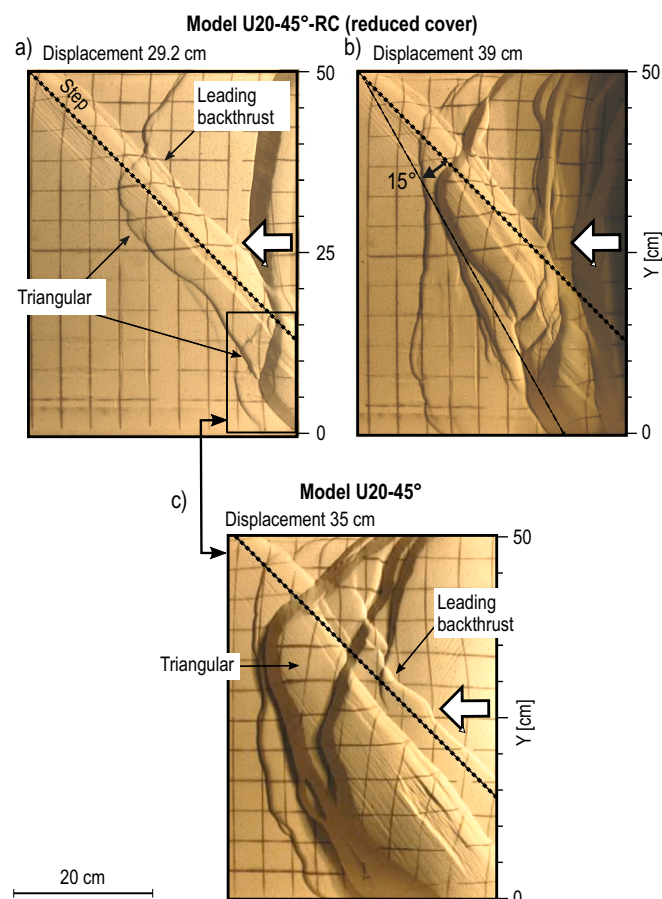


Fig. 17. Top view photographs of model U20–45°-RC, featuring a 45° oblique ramp, 20 mm step-throw and a reduced sand thickness of 40 mm. a) The left side of the large triangular thrust slice is initially parallel to the step. b) In the final stage, an overall sigmoidal shape results from connected triangular thrust-slices. c) Top view of model U20–45°, featuring a 70 mm thick sand cover and therefore showing larger but similar structures as model U20–45°-RC.

7. Discussion

7.1. Summary of model results

An overview of experiments and the first order influence of upward and downward steps is summarised in (Fig. 18). Flat-base models (Fig. 18a, b) develop two similar thrust sheets (T1 and T2) with notable less stacking of granular material than observed in step models and there is no imbrication of thrust sheets. Vertical offset of baseplates (Fig. 18c) induces graben structures and reverse faults in the brittle sand cover. During subsequent thin-skinned compression, both downward and upward steps attract and localise deformation, which stimulates a fast forward propagation of deformation in an early stage, but retains the overall deformation in a late stage. Downward steps (Fig. 18d) show exceedingly strong localisation of deformation preventing the formation of viscous downward ramps and overall propagation of deformation onto the lower baseplate. Instead, fault-bend folds nucleating above the upper edge of the downward step form at the front of thrust sheet T1 (Fig. 18d). An oblique downward-step (Fig. 18e) controls the formation of fault-bend folds with oblique frontal thrusts. Numerical and analogue downward-step models of Caër et al. (2018) show that with sufficient shortening at step-controlled thrusts under the right mechanical conditions (high friction angle of cover sediments and low friction angle of décollement layers), deformation can propagate onto the lower baseplate.

The localisation of deformation at upward steps is less efficient than for downward steps. In comparison to downward steps, upward steps (Fig. 18f) feature smooth viscous ramps that enable a propagation of deformation onto the higher baseplate. Therefore, thickening and thinning of viscous material is observed close to upward steps. The brittle cover shows dominant backthrusts and frontal imbrication (Fig. 18f). Oblique upward-step models (Fig. 18g) reveal a more complex imbrication of brittle structures, featuring asymmetric thrust slices and step-controlled thrust segments that rotate up to 15° about a vertical axis. In contrast to this, oblique viscous ramps remain continuous structures.

Higher oblique steps increase deformation localisation and step-controlled thrust segments become more important, overall leading to angular structures (Fig. 18g, U20–30° and U20–45°). 45° oblique steps cause less localisation of deformation (less imbrication and faster wedge-propagation) than 30° oblique steps. Consequently, the efficiency of deformation-localisation does not depend on step height alone, but also on the angle of obliquity (α) of the upward-step.

In summary, the effect of deformation localisation at steps is (i) stronger at high steps than at low steps, (ii) stronger at downward steps than at upward steps and (iii) stronger at frontal steps than at oblique steps.

7.2. Comparison to previous oblique-ramp models

Previous models on oblique ramps in the Jura Mountains were carried out by Philippe (1995), see Fig. 19a. In contrast to our models, the baseplate geometry in Philippe (1995) provides an enforced, rigid ramp with an inclination of 30° (Fig. 19b). The brittle cover is thinner above the higher basal wooden plate (Fig. 19b) and no precursory baseplate-offset phase is simulated. Furthermore, the basal décollement is modelled using a thin layer of microbeads (Fig. 19b) and therefore, no viscous flow occurs. However, the top-view pattern of the early stages of the 45° oblique-ramp model of Philippe (1995) is very similar to the pattern forming in the 45° oblique-step model with reduced brittle cover U20–45°-RC of this paper (Fig. 19c). In addition to 45°-oblique rigid ramps, Philippe (1995) tested 60° oblique ramps as well as lateral ramps (Fig. 19a), showing that with increasing obliquity, triangular thrust-slices disappear in favour of thrust-sheets with a rather straight front perpendicular to the transport direction.

Our experiments demonstrate that deformation localisation at oblique steps is the reason for triangular structures. Therefore, the absence of such triangles in 60° oblique-step models (Fig. 19a) suggests reduced deformation localisation with increasing step-obliquity (α). Extrapolated, this suggests that lateral steps show the least localisation of deformation and frontal upward-steps the most.

7.3. Local and regional rotations of structures

Step-controlled fore-thrusts in our models reveal local rotations about a vertical axis of up to 15° over time (e.g. Fig. 17, Fig. 15), related to localisation of deformation at individual baseplate steps. The sketch in Fig. 20 shows a schematic overview of rotations of step-controlled thrusts deduced from observations in our models, with a transport direction and basement-step orientations matching typical cases in the JFTB. Note that step-controlled oblique structures are local anomalies within a regional trend of structures. The Central and Eastern Jura show a regional clockwise rotation of 7° to 8° (Laubscher, 1965, 1961), whereas regional counter-clockwise rotation is proposed for the Southern Jura (Affolter, 2004; Philippe, 1994). These regional rotations are more broadly linked to lateral displacement gradients across the Jura arc (Affolter, 2004). Regional and local rotations in the JFTB have a different origin; they were competing and have to be distinguished.

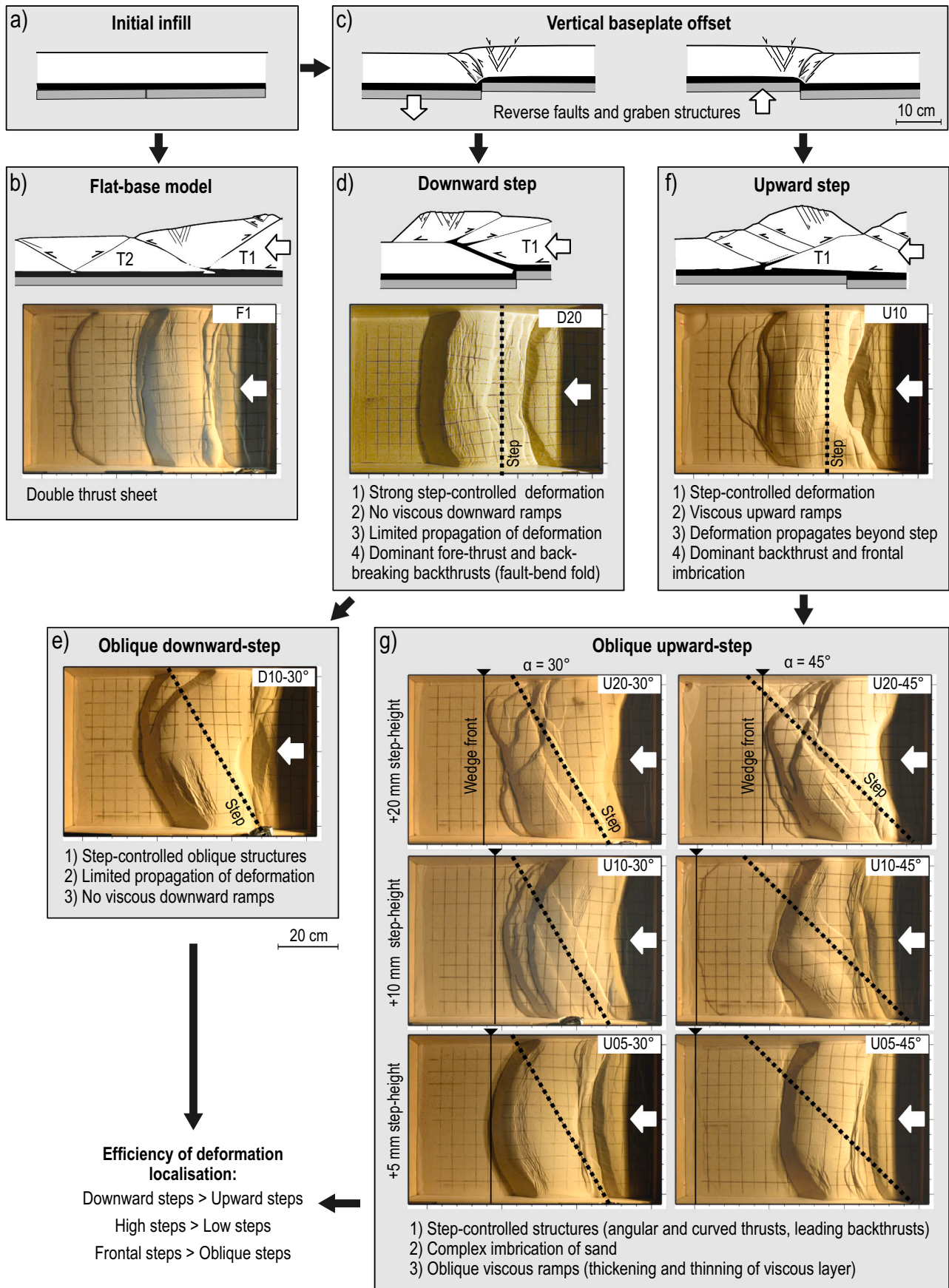


Fig. 18. Summary of experiments and first-order step-controlled structures. An overview of the final surface structures of the different model set-ups is presented in the Appendix (Fig. A.1 and Fig. A.2), and the original data are compiled in the supplementary material (Schori et al., 2020).

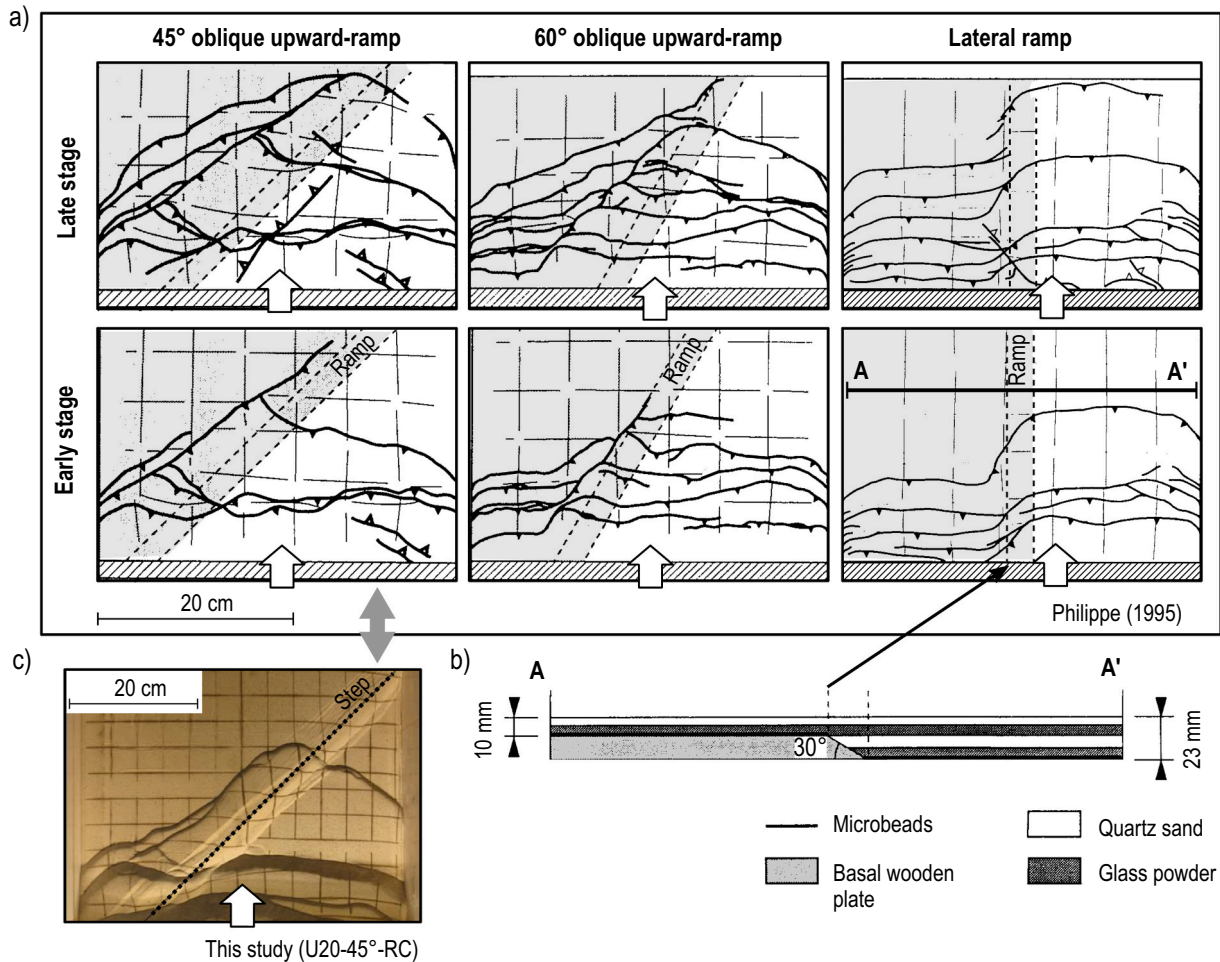


Fig. 19. a) Oblique and lateral-ramp analogue sandbox-models of [Philippe \(1995\)](#). b) Cross-section through the lateral ramp model illustrating a basal wooden plate that enforces a rigid ramp of 30°. A thin layer of microbeads provides the basal décollement. c) Model U20-45°-RC featuring a thin brittle layer shows remarkably similar structures as the 45° oblique upward-step model of [Philippe \(1995\)](#) in an early stage.

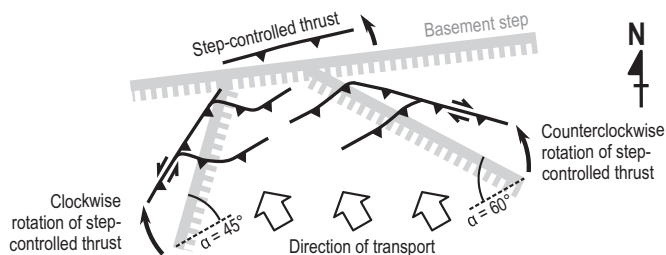


Fig. 20. Rotation scheme for thin-skinned thrusts that are controlled by pre-existing oblique upward-steps, derived from observations of our analogue models and those by [Philippe \(1995\)](#). The sketch fits typical directions that may occur in the JFTB, with basement faults striking NNE-SSW, ENE-WSW and NW-SE, and a transport direction to the NW.

7.4. Natural examples of step-controlled structures

Our analogue models show that sufficiently high oblique steps ultimately lead to step-controlled oblique structures, such as sigmoidal, curved or angular thrusts viewed from above (e.g. [Fig. 17b](#), [Fig. 18g](#)). In the tectonic map of [Fig. 21a](#), we point out exemplary zones in the JFTB, where we propose oblique structures, associated with pre-existing basement faults that acted as structural controls. These zones are described with sketches ([Fig. 21b](#)) outlining the proposed tectonic

linkage between basement faults and corresponding thin-skinned structures in the cover. Note that sketches in [Fig. 21b](#) illustrate thin-skinned structures of the JFTB, which formed during Mio-Pliocene times above a basal décollement in Triassic evaporites. Therefore, oblique structures were also transported several kilometres north-westwards after their formation, at least in the Internal Jura (see displacements indicated in [Fig. 21a](#)).

7.4.1. Zones I and II – Pontarlier fault zone and Internal Jura north of La Chaux-de-Fonds

Zone I in [Fig. 21a](#) marks the northern termination of the Pontarlier fault zone. Angular thrusts are observed and folds parallel to NNE-SSW trending sinistral strike-slip faults reveal the thrusting component of oblique ramps. We interpret this system as a connection of oblique and lateral ramps that constituted the western lateral limits of thrust-sheets of the Internal Jura ([Fig. 21b](#), zone I). It follows that the Pontarlier sinistral fault zone was contemporaneously active to folding and thrusting, and does not represent a late structural feature of the Jura Mountains. This agrees with previous suggestions by [Laubscher \(1961\)](#).

Zone II to the north of the town of La Chaux-de-Fonds ([Fig. 21a](#)) shows angular and overlapping thrusts. Therefore, similar to zone I, we propose NNE-SSW striking oblique basement-steps that triggered the observed structures in the Mesozoic cover ([Fig. 21b](#)). The sketch for zones I and II in [Fig. 21b](#) correlates with structures of analogue models of [Philippe \(1995\)](#) featuring 60° oblique upward-steps, where laterally confined triangular thrust-slices are absent ([Fig. 19a](#)).

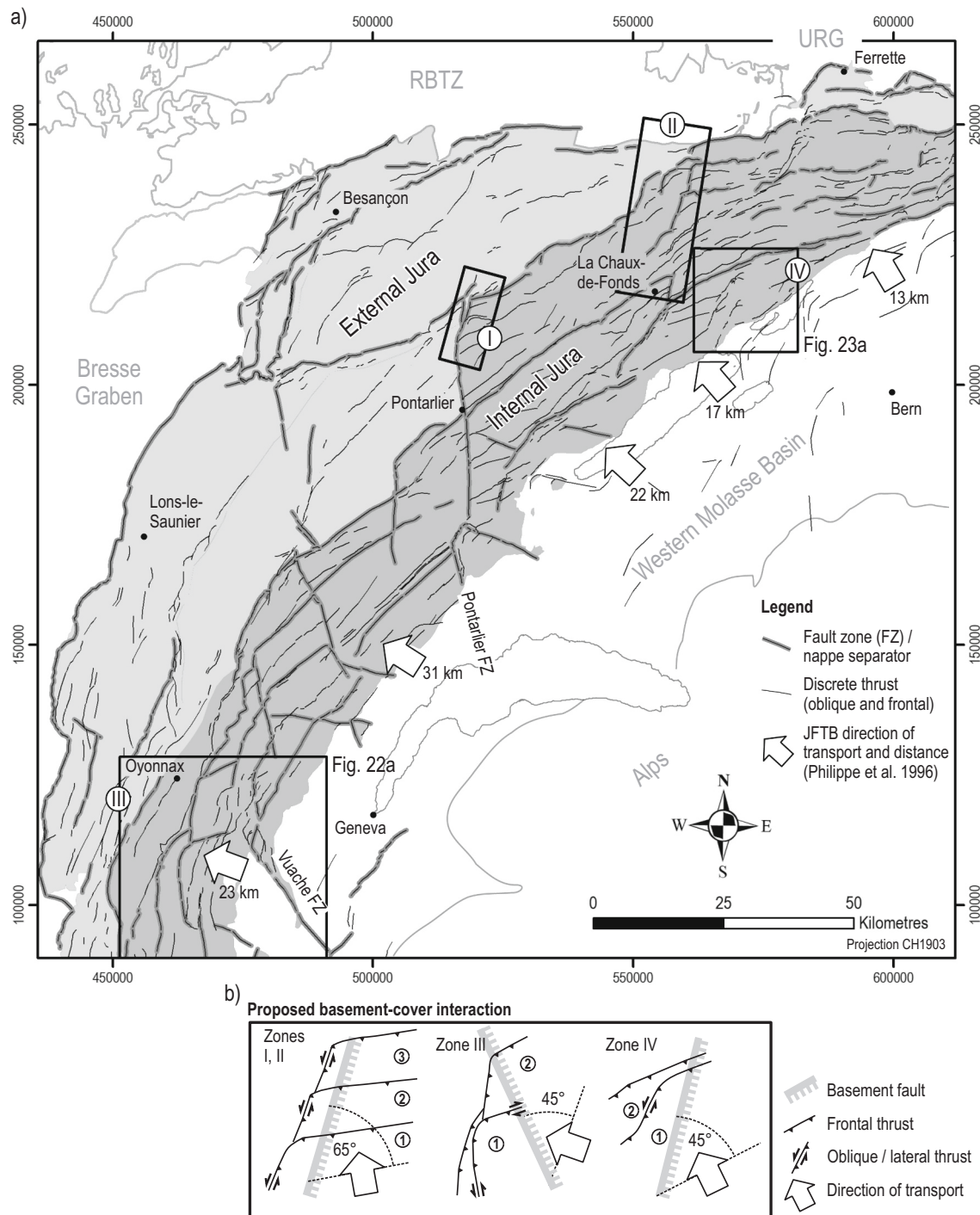


Fig. 21. a) Overview of faults in the Mesozoic cover across the JFTB. Zones in the Internal Jura with notable occurrences of oblique-thrust systems are marked with black rectangles. The tectonic map contains an updated structural interpretation, using available geological vector maps of France (BRGM, 2020) and Switzerland (Swisstopo, 2012) as well as high-resolution digital elevation models (IGN-F, 2018; Swisstopo, 2011). b) Structural interpretations illustrating pre-existing basement steps (thick, grey normal faults) that trigger thrusts in the Mesozoic cover (black thrusts). Numbers indicate the relative sequence of structures. RBTZ: Rhine-Bresse Transfer Zone, URG: Upper Rhine Graben.

7.4.2. Zone III - Oyonnax-Vuache

Zone III (Fig. 21a) lies in the Southern Jura Mountains and an enlargement is depicted in Fig. 22a. The Vuache fault zone in the southern part of Fig. 22a reveals oblique ramps that are indicative of step-controlled structures and a NW-SE trending basement step. A connection to pre-JFTB tectonic features has also been proposed in previous studies (Laubscher, 1981; Philippe et al., 1996).

A distinct triple-nappe system south of Oyonnax comprises two

triangular nappes and a more crescent-shaped nappe (Fig. 22a), which bears resemblance to our analogue model U20–45°, featuring a 20 mm (400 m in nature) 45° oblique upward-step (Fig. 22b). In analogy to model U20–45°, we propose a NW-SE trending basement fault for the structures that formed in zone III (Fig. 21b). Within the 45° oblique-step series, triangular thrust-slices occur at the highest throw of 20 mm only (Fig. 13h) and accordingly, we infer a basement step for the natural example of at least 400 m. This is in agreement with a seismic line

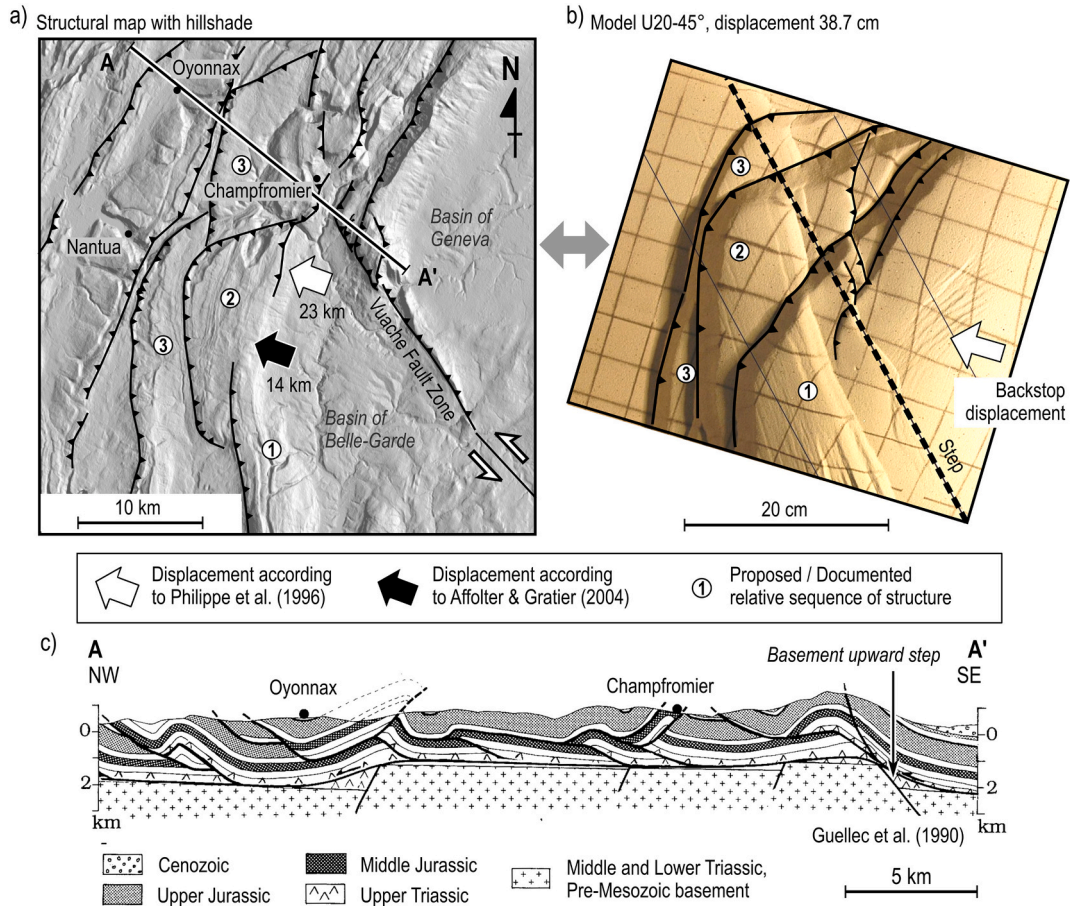


Fig. 22. Natural example in the Internal Jura, Zone III - Oyonnax-Vuache (location in Fig. 21a). a) Hillshade model derived from NASA (2014) in the area of Oyonnax with highlighted main thrusts. b) Model U20-45° shows similar triangular structures as the natural example in the area of Oyonnax. c) Cross-section from Guellec et al. (1990) based on a seismic survey, showing a basement high underneath Champfromier.

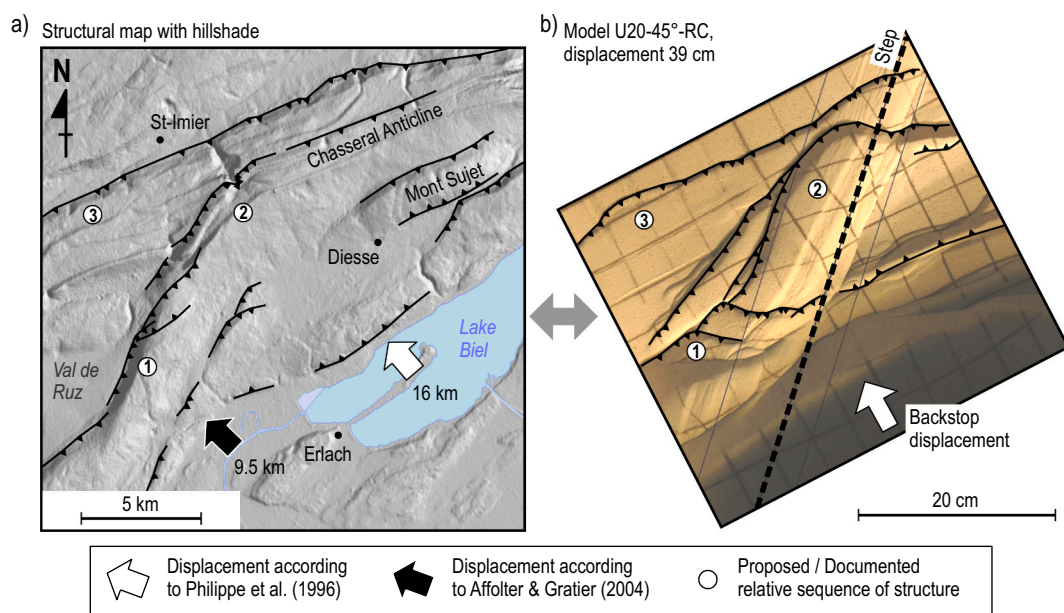


Fig. 23. Natural example in the Internal Jura, Zone IV - Chasseral anticline (location in Fig. 21a). a) Hillshade model derived from NASA (2014) in the area of St-Imier and Lake Biel with highlighted main thrusts. b) Model U20-45°-RC shows similar structures as the natural example.

interpretation across Oyonnax-Champfromier (Guellec et al., 1990), which reveals a basement high with a throw of several hundreds of metres, SE of Oyonnax (Fig. 22c). Whether this basement high formed by post-Jura inversion or rather represents a horst that predates the Jura Mountains (see tectonic solutions addressed in Guellec et al., 1990), remains debated. However, as thrust geometries in Fig. 22a are strongly suggestive of a pre-existing oblique-step in the basement, our study supports the latter solution. In addition, a direct comparison between the natural example and our analogue model (Fig. 22a, b) suggests a probable structural evolution as depicted in Fig. 22a. Note that a pre-JFTB normal fault in the basement does not rule out a subsequent inversion of the basement in recent times.

7.4.3. Zone IV - Chasseral Anticline

Zone IV (Fig. 21a) lies in the Internal Jura and comprises the Chasseral anticline, which contains an oblique fold-segment in respect to JFTB transport directions (see magnification in Fig. 23a). The overall structure in Fig. 23a is remarkably similar to our 45° oblique upward-step model with a reduced cover U20–45°-RC (Fig. 23b). The comparison between the model (Fig. 23b) and the natural example (Fig. 23a) suggests that the curved shape of the Chasseral anticline is connected to a NNE-SSW trending basement fault. This supports previous suggestions by Lüthi (1954), Laubscher (2008b) and Meier (2010). We furthermore deduce a high basement step of about 400 m for the natural example, as the best-fit model U20–45°-RC features a 20 mm upward step. Based on our model (Fig. 23b), we also deduce a rough relative sequence of structures for the natural example (Fig. 23a). Note that the basement structure that controlled the oblique Chasseral anticline lies between 9.5 and 16 km to the southeast, according to different displacement models of Affolter (2004) and Philippe et al. (1996), respectively.

7.5. Summary of natural structures

We propose the presence of pre-JFTB normal faults in the basement with NW-SE (Hercynian) and NNE-SSW (Rhenish) orientations that provided trigger lines for thin-skinned structures in the Internal Jura (Fig. 22, Fig. 23). The orientations of these basement faults suggest Palaeozoic Variscan fault systems, which were reactivated during Mesozoic and Cenozoic times. This led to important basement offsets that controlled the thin-skinned deformation in Miocene and Pliocene times. The tectonic events that come into question for fault reactivations are the opening of the Alpine Tethys rift system in Jurassic times (Stampfli et al., 1998; Ziegler, 1988b), Eo-Oligocene graben formation in connection with the ECRIS (Illies, 1972; Michon, 2000) and Eocene to Miocene evolution of the Alpine flexural foreland basin (Burkhard and Sommaruga, 1998; Laubscher, 1992).

Our models suggest that basement offsets in the examples in the Internal Jura (Fig. 22, Fig. 23) must reach at least 400 m in order to control the formation of triangular nappes or thrust-slices during Mio-Pliocene thin-skinned formation of the JFTB. Smaller basement throws rather led to continuous but curved or angular anticlines with few imbrication (e.g. Fig. 13a, e, f, g), such as for example the Graitery anticline in the Eastern Jura (Fig. 3b). Step-controlled structures were displaced up to about 30 km north-westwards during JFTB formation (Affolter, 2004; Philippe et al., 1996). Therefore, graben structures and reverse faults in the Mesozoic cover, which formed due to pre-JFTB basement extension, are allochthonous and do not overlie their original basement fault.

Basement structures were undoubtedly present before the formation of the JFTB and controlled thin-skinned structures. In addition, seismic surveys and earthquakes show that the area of the Jura Mountains and surrounding was under the influence of thick-skinned compression after the main thin-skinned JFTB stage until today, which caused local basement inversion (Caër, 2016; Edel et al., 2006; Lacombe and Belahsen, 2016; Madritsch et al., 2008; Ustaszewski and Schmid, 2007). Recent inversion may be related to tectonic underplating in connection

with an equilibration of the Alpine wedge (Mosar, 1999) and/or lithospheric long-wavelength buckling (Bourgeois et al., 2007; Lefort and Agarwal, 1996).

8. Conclusions

Thin-skinned deformation of the JFTB during Mio-Pliocene was locally pre-conditioned by steps (faults) in the pre-Mesozoic basement (Laubscher, 1961). By means of brittle-viscous analogue sandbox-models, we study the formation of step-controlled structures. Our models involve the formation of steps between rigid baseplates, overlain by a viscous layer at the base of a brittle sand layer. The brittle sand layer is subsequently pushed horizontally across the step. The following important observations characterise the deformation style:

- Initial vertical baseplate offset induces reverse faults and extensional collapse structures in the brittle cover that nucleate at the step and above the higher plate. A reactivation of these initial structures is not observed during subsequent horizontal compression.
- During subsequent horizontal compression, pre-existing steps in the rigid footwall trigger step-controlled thrusts, because they localise deformation in a different position due to stress perturbations. Localisation of deformation results in a fast forward propagation of deformation in an early stage but inhibits propagation later.
- Downward steps lead to the formation of fault-bend folds with considerable duplication of the brittle cover. In contrast, upward steps control pop-up structures with imbricated fronts, dominant backthrusts and long viscous ramps with moderate inclinations.
- The effect of deformation localisation at baseplate steps is stronger at high steps than at low steps, stronger at downward steps than at upward steps and stronger at frontal steps than at oblique steps.
- 30° and 45° oblique upward-steps lead to imbrication with laterally confined thrust-slices. Imbrication and angular thrusts, pointing into the direction of transport, are more abundant with increasing step-height. Angular thrusts are composed of two oblique-thrust segments, with one side that is step-controlled and the other side forming a relay thrust that connects to the regular trailing thrust front. Laterally confined, triangular thrust-slices are characteristic for 30° and 45° oblique steps (this study), but they are absent at oblique steps of 60° and more (Philippe, 1995).
- Upward oblique-step models with high step throws of 20 mm (400 m in nature) reveal vertical rotations of up to 15° of step-controlled fore-thrusts. Step-controlled leading backthrusts hardly rotate and provide excellent indicators for the orientation of oblique steps.
- Frontward flow of viscous material during thin-skinned deformation has important consequences for upward-step dynamics. In particular, viscous ramps form in front of upward-steps, assisting deformation to propagate onto the upper plate. Subsequently, the viscous ramp ensures the transition of more material onto the upper baseplate without forming new step-controlled structures in the cover. Viscous ramps are dynamic structures, adapting their length laterally (in the case of oblique upward-steps) and over time. Accumulation of viscous material occurs in front of upward steps and towards the front of the wedge. Oblique viscous ramps are large continuous structures whereas the overlying brittle layer may show strong imbrication.

We find good correlations of model structures with oblique structures in the Internal Jura (Fig. 22 and Fig. 23). Correlations allow inferring the rough orientation and throw of pre-existing basement steps in nature that controlled thin-skinned deformation. In particular, our models support a NNE-SSW striking oblique upward-step with a throw of 400 m that controls the Chasseral anticline and a NW-SE striking oblique upward-step with a throw of 400 m controlling the Oyonnax-Vuache nappe system. Step-controlled structures of the Internal Jura are transported several kilometres north-westwards, away from the basement

step that induced deformation. Therefore, step-controlled structures need a palinspastic restoration to identify the position of a corresponding basement step. Model-to-nature comparison of step-controlled oblique structures can also be a powerful tool to assess the relative age of basement structures. An important basement high was for example documented on a seismic line across the Internal Jura (Guellec et al., 1990), but interpretations did not unambiguously reveal whether the basement high formed before or after the JFTB. Correlations with our models strongly support that the basement high predates the JFTB and controlled characteristic oblique structures in the cover. Examples from the JFTB highlight the importance of analysing structures of fold-and-thrust belts in all three dimensions, and our model results may be of use for interpreting fold-and-thrust belts from around the globe.

Funding

This work was supported by the University of Fribourg, Department of Geosciences, Earth Sciences, Switzerland; and the University of Bern, Institute of Geological Sciences, Switzerland.

Credit author statement

Marc Schori: Conceptualization, Methodology, Validation, Formal analysis, Investigation, Data Curation, Writing – Original Draft, Writing

- Review & Editing, Visualization; **Frank Zwaan:** Conceptualization, Methodology, Writing - Review & Editing; **Guido Schreurs:** Resources, Writing - Review & Editing, Supervision; **Jon Mosar:** Resources, Writing - Review & Editing, Supervision, Funding acquisition.

Declaration of Competing Interest

The authors declare that they have no known competing financial interests or personal relationships that could have appeared to influence the work reported in this paper.

Acknowledgements

This study was financed by the University of Fribourg, Switzerland as part of the PhD research project of the first author. We express our gratitude to Nicole Schwenderer of the Institute of Forensic Medicine (University of Bern) for assisting us with the CT scanner. Furthermore, we are indebted to Anna Sommaruga for sharing her expertise on the Jura Mountains. Sandra Borderie is thanked for critically scrutinising our modelling parameters and for discussions on the effect of pre-existing basement faults. We would also like to thank the reviewers, Pauline Souloumiac and Alexander Malz, as well as the editor Philippe Agard for their helpful and constructive comments.

Appendix A. Appendix

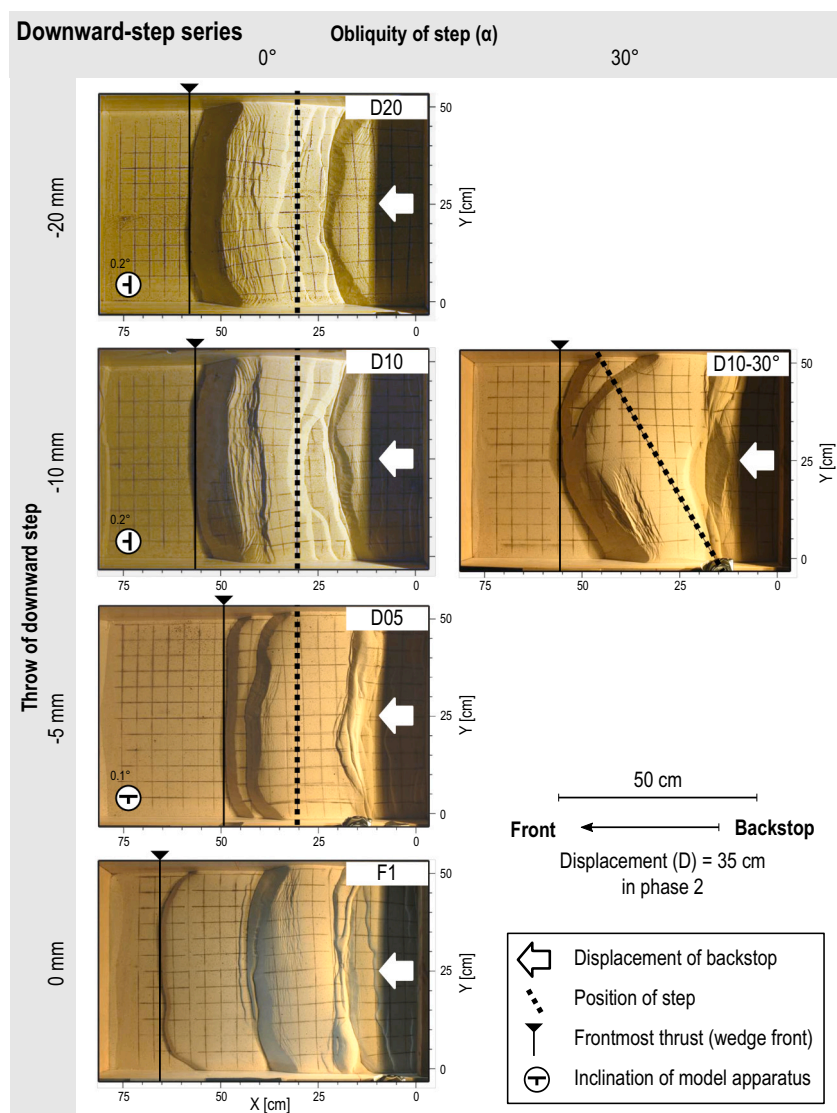


Fig. A.1. Overview of downward-step models showing top-view photos at a displacement $D = 35$ cm. Slight inclinations of the model apparatus have no detectable influence. Even the small downward step of 5 mm already controls deformation exceedingly and outweighs uneven distributions of viscous material.

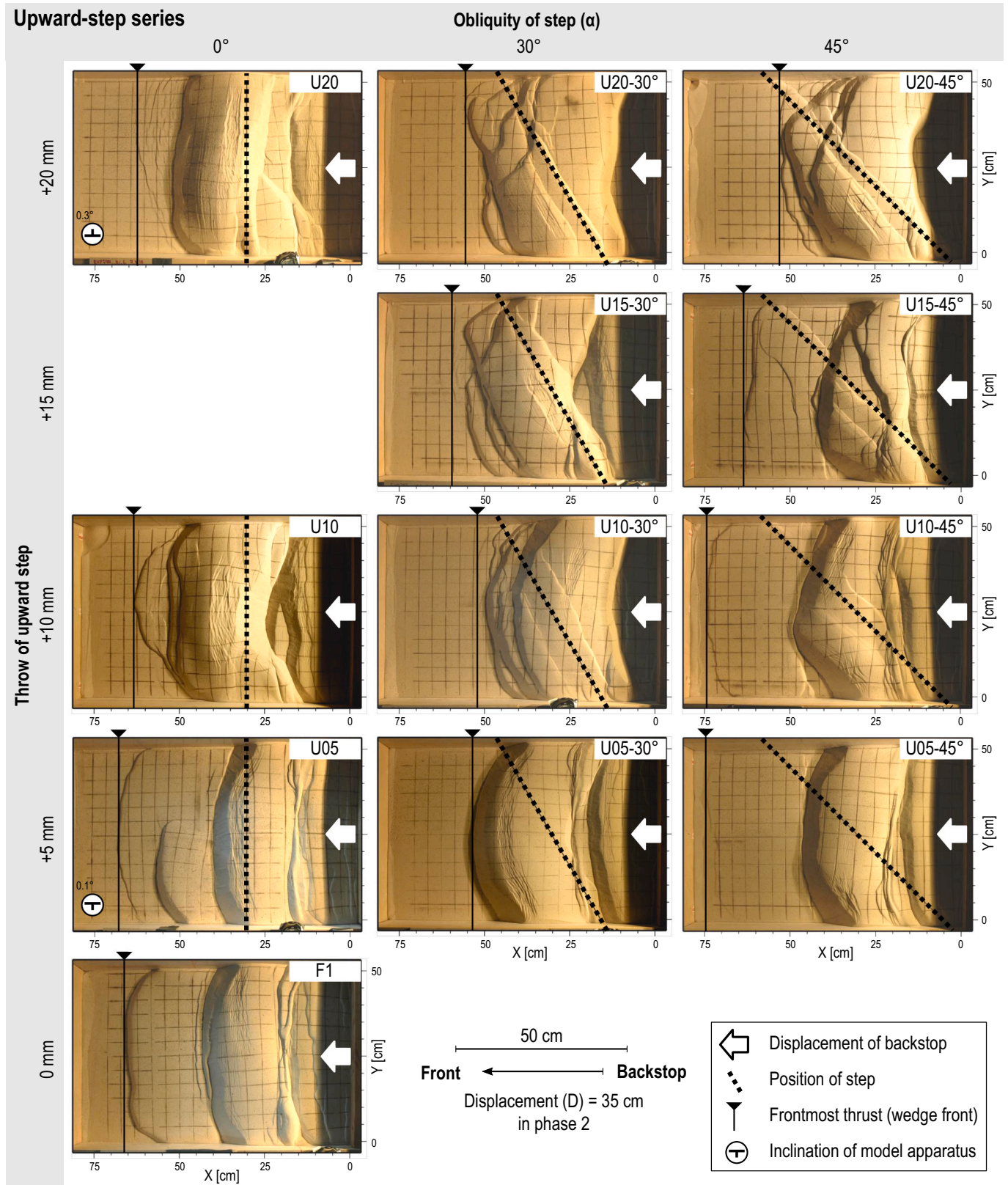


Fig. A.2. Overview of upward-step models showing top-view photos at a displacement $D = 35$ cm. In experiments U05 and U20, the model apparatus is slightly tilted along the long axis. This causes an asymmetric distribution of viscous material, which is slightly thicker (less friction) on the plunging side. Models U05 and U20 consequently develop asymmetric structures.

References

- Affolter, T., 2004. Map view retrodeformation of an arcuate fold-and-thrust belt: The Jura case. *J. Geophys. Res.* 109, B03404 <https://doi.org/10.1029/2002JB002270>.
- Allemand, P., Brun, J.P., 1991. Width of continental rifts and rheological layering of the lithosphere. *Tectonophysics* 188, 63–69. [https://doi.org/10.1016/0040-1951\(91\)90314-1](https://doi.org/10.1016/0040-1951(91)90314-1).
- Allenbach, R.P., Wetzell, A., 2006. Spatial patterns of Mesozoic facies relationships and the age of the Rhenish Lineament: a compilation. *Int. J. Earth Sci.* 95, 803–813. <https://doi.org/10.1007/s00531-006-0071-0>.
- Apotria, T.G., Snedden, W.T., Spang, J.H., Wiltshko, D.V., 1992. Kinematic models of deformation at an oblique ramp. In: *Thrust Tectonics*. Springer, pp. 141–154. https://doi.org/10.1007/978-94-011-3066-0_12.
- Aubert, D., 1971. Le Risoux, un charriage jurassien de grandes dimensions. *Eclogae Geol. Helv.* 64, 152–156. <https://doi.org/10.5169/seals-163975>.
- Becker, A., 2000. The Jura Mountains - an active foreland fold-and-thrust belt? *Tectonophysics* 321, 381–406. [https://doi.org/10.1016/S0040-1951\(00\)00089-5](https://doi.org/10.1016/S0040-1951(00)00089-5).
- Bellahsen, N., Mouthereau, F., Boutoux, A., Bellanger, M., Lacombe, O., Jolivet, L., Rolland, Y., 2014. Collision kinematics in the Western external Alps. *Tectonics* 33, 1055–1088. <https://doi.org/10.1002/2013TC003453>.
- Berberian, M., 1995. Master 'blind' thrust faults hidden under the Zagros folds: active basement tectonics and surface morphotectonics. *Tectonophysics* 241, 193–224. [https://doi.org/10.1016/0040-1951\(94\)00185-C](https://doi.org/10.1016/0040-1951(94)00185-C).
- Bergerat, F., Cazes, M., Damotte, B., Guellec, S., Mugnier, J.-L., Roure, F., Truffert, C., 1989. Les structures distensives en Bresse d'après les données du profil sismique Jura-Bresse (programme ECORS). *Comptes rendus l'Académie des Sci. Série 2, Mécanique. Phys. Chim. Sci. l'univers, Sci. la Terre* 309, 325–332.
- Bergerat, F., Mugnier, J.-L., Guellec, S., Truffert, C., Cazes, M., Damotte, B., Roure, F., 1990. Extensional tectonics and subsidence of the Bresse basin: An interpretation from ECORS data. In: Roure, F., Heitzmann, P., Polino, R. (Eds.), *Deep Structures of the Alps*. *Mém. Soc. géol. suisse*, pp. 145–156.
- Bièvre, G., Mercier, E., 2010. The 'Bois du Peu' thrust sheets (external French Jura mountains): re-examining the concept of 'Fault-Fold'. *HAL-INSU Arch. Ouvert. Insu-00442*.
- Boigk, H., Schöneich, H., 1974. Perm, Trias und älterer Jura im Bereich der südlichen Mittelmeer-Mjösen-Zone und des Rheingraben. In: Illies, J.H., Fuchs, K. (Eds.), *Approaches to Taphrogenesis: Proceedings of an International Rift Symposium Held in Karlsruhe, April 13–15, 1972 - Inter-Union Commission on Geodynamics*. Scientific Report. Schweizerbart, Stuttgart, Germany, pp. 60–71.
- Bonnet, C., Malavielle, J., Mosar, J., 2008. Surface processes versus kinematics of thrust belts: impact on rates of erosion, sedimentation, and exhumation - Insights from analogue models. *Bull. la Société Géologique Fr.* 179, 297–314. <https://doi.org/10.2113/gssgfbull.179.3.297>.
- Bourgeois, O., Ford, M., Diraison, M., Le Carlier de Veslud, C., Gerbault, M., Pik, R., Ruby, N., Bonnet, S., 2007. Separation of rifting and lithospheric folding signatures in the NW-Alpine foreland. *Int. J. Earth Sci.* 96, 1003–1031. <https://doi.org/10.1007/s00531-007-0202-2>.
- BRGM, 2020. Cartes géologiques à 1/50000 format 'vecteurs'. Bureau de recherches géologiques et minières (BRGM).
- Burkhard, M., 1990. Aspects of the large-scale Miocene deformation in the most external part of the Swiss Alps (Subalpine Molasse to Jura fold belt). *Eclogae Geol. Helv.* 83, 559–583. <https://doi.org/10.5169/seals-166602>.
- Burkhard, M., Sommaruga, A., 1998. Evolution of the western Swiss Molasse basin: Structural relations with the Alps and the Jura belt. In: Puigdefabregas, A., Luterbacher, H.P., Fernandez, M. (Eds.), *Masclé, A. Geological Society Special Publication, Geological Society Special Publications*, pp. 279–298. <https://doi.org/10.1144/GSL.SP.1998.134.01.13>.
- Buxtorf, A., 1907. Zur Tektonik des Kettenjura. *Bericht der Versammlung des Oberrheinischen Geol. Vereins* 40, 29–38.
- Buxtorf, A., 1916. Prognosen und Befunde beim Hauensteinbasis- und Grenchenbergtunnel und die Bedeutung der Letzteren für die Geologie des Jura gebirges. *Verh. Naturforsch. Ges. Basel* 27, 184–254.
- Caër, T., 2016. Interprétation structurale et équilibre mécanique: Le calcul à la rupture appliqué aux chaînes d'avant-pays. Université de Cergy-Pontoise, Dr. thesis.
- Caër, T., Maillot, B., Souloumiac, P., Leturmy, P., de Lamotte, D.F., Nussbaum, C., 2015. Mechanical validation of balanced cross-sections: the case of the Mont Terri anticline at the Jura front (NW Switzerland). *J. Struct. Geol.* 75, 32–48. <https://doi.org/10.1016/j.jsg.2015.03.009>.
- Caër, T., Souloumiac, P., Maillot, B., Leturmy, P., Nussbaum, C., 2018. Propagation of a fold-and-thrust belt over a basement graben. *J. Struct. Geol.* 115, 121–131. <https://doi.org/10.1016/j.jsg.2018.07.007>.
- Chauve, P., Perriaux, J., 1974. Le jura. In: Debelmas, J. (Ed.), *Géologie de La France: Les Chaînes Plissées Du Cycle Alpin et Leur Avant-Pays*. Doin, Paris, pp. 443–464.
- Coward, M.P., De Donatis, M., Mazzoli, S., Paltrinieri, W., Wezel, F.C., 1999. Frontal part of the northern Apennines fold and thrust belt in the Romagna-Marche area (Italy): Shallow and deep structural styles. *Tectonics* 18, 559–574. <https://doi.org/10.1029/1999TC000003>.
- Dahlen, F.A., 1990. Critical taper model of fold-and-thrust belts and accretionary wedges. *Annu. Rev. Earth Planet. Sci.* 18, 55–99. <https://doi.org/10.1146/annurev. ea.18.050190.000415>.
- Davis, D., Suppe, J., Dahlen, F.A., 1983. Mechanics of fold-and-thrust belts and accretionary wedges. *J. Geophys. Res. Solid Earth* 88, 1153–1172. <https://doi.org/10.1029/JB088iB02p01153>.
- Debrand-Passard, S., Courbouleix, S., Lienhardt, M.-J., 1984. Synthèse géologique du Sud-Est de la France. *Mémoire BRGM France n° 125*, 69–78.
- Delmas, M., 1965. Rapport de fin de sondage H.J. Essavilly 101. Société Nationale Pétrologique d'Aquitaine (S. N. P.A.).
- Deville, E., 2021. Structure of the tectonic front of the Western Alps: Control of fluid pressure and halite occurrence on the decollement processes. *Tectonics* 1–21. <https://doi.org/10.1029/2020TC006591>.
- Deville, E., Blanc, E., Tardy, M., Beck, C., Cousin, M., Ménard, G., 1994. Thrust Propagation and Syntectonic Sedimentation in the Savoy Tertiary Molasse Basin (Alpine Foreland). In: *Hydrocarbon and Petroleum Geology of France*. Springer, pp. 269–280. https://doi.org/10.1007/978-3-642-78849-9_19.
- Dèzes, P., Schmid, S.M., Ziegler, P.A., 2004. Evolution of the European Cenozoic Rift System: interaction of the Alpine and Pyrenean orogens with their foreland lithosphere. *Tectonophysics* 389, 1–33. <https://doi.org/10.1016/j.tecto.2004.06.011>.
- Edel, J.B., Whitechurch, H., Diraison, M., 2006. Seismicity wedge beneath the Upper Rhine Graben due to backwards Alpine push? *Tectonophysics* 428, 49–64. <https://doi.org/10.1016/j.tecto.2006.08.009>.
- Egli, D., Mosar, J., Ibele, T., Madritsch, H., 2016. The role of precursory structures on Tertiary deformation in the Black Forest-Hegau region. *Int. J. Earth Sci.* 1–22. <https://doi.org/10.1007/s00531-016-1427-8>.
- Glangeaud, L., 1951. Interprétation tectono-physique des caractères structuraux et paléogéographiques de la Méditerranée occidentale. *Bull. la Société Géologique Fr.* 6, 735–762. <https://doi.org/10.2113/gssgfbull.S6-1.8.735>.
- Guellec, S., Mugnier, J.-L., Tardy, M., Roure, F., 1990. Neogene evolution of the western Alpine foreland in the light of ECORS data and balanced cross sections. In: Roure, F., Heitzmann, P., Polino, R. (Eds.), *Deep Structures of the Alps*. *Mém. Soc. géol. suisse*, pp. 165–185.
- Hauber, L., 1993. Der südliche Rheingraben und seine geothermische Situation. *Bull. der Vereinigung Schweizerischer Pet. und Ingenieure* 60, 53–69. <https://doi.org/10.5169/seals-216879>.
- Hombert, C., Bergerat, F., Philippe, Y., Lacombe, O., Angelier, J., 2002. Structural inheritance and cenozoic stress fields in the Jura fold-and-thrust belt (France). *Tectonophysics* 357, 137–158. [https://doi.org/10.1016/S0040-1951\(02\)00366-9](https://doi.org/10.1016/S0040-1951(02)00366-9).
- IGN-F, 2018. MNT RGE ALTI 5m, Digital Elevation Models. Institut national de l'information géographique et forestière (IGN-F).
- Illies, H., 1962. Oberrheinisches Grundgebirge und Rheingraben. *Geol. Rundsch.* 52, 317–332. <https://doi.org/10.1007/BF01840083>.
- Illies, J.H., 1972. The Rhine graben rift system-plate tectonics and transform faulting. *Geophys. Surv.* 1, 27–60. <https://doi.org/10.1007/BF01449550>.
- Jordan, P., 1992. Evidence for large-scale decoupling in the Triassic evaporites of northern Switzerland: an overview. *Eclogae Geol. Helv.* 85, 677–693. <https://doi.org/10.5169/seals-167025>.
- Jordan, P., Nuesch, R., 1989. Deformation Structures in the Muschelkalk Anhydrites of the Schaffsheim well (Jura Overthrust, Northern Switzerland). *Eclogae Geol. Helv.* 82, 429–454. <https://doi.org/10.5169/seals-166384>.
- King Hubbert, M., 1937. Theory of scale models as applied to the study of geologic structures. *Bull. Geol. Soc. Am.* 48, 1459–1520. <https://doi.org/10.1130/GSAB-48-1459>.
- Klinkmüller, M., Schreurs, G., Rosenau, M., Kemnitz, H., 2016. Properties of granular analogue model materials: a community wide survey. *Tectonophysics* 684, 23–38. <https://doi.org/10.1016/j.tecto.2016.01.017>.
- Lacombe, O., Bellahsen, N., 2016. Thick-skinned tectonics and basement-involved fold-thrust belts: insights from selected Cenozoic orogens. *Geol. Mag.* 153, 763–810. <https://doi.org/10.1017/S0016756816000078>.
- Larrouque, J.M., Laurent, P., 1988. Evolution of the stress field pattern in the south of the Rhine Graben from the Eocene to the present. *Tectonophysics* 148, 41–58. [https://doi.org/10.1016/0040-1951\(88\)90159-X](https://doi.org/10.1016/0040-1951(88)90159-X).
- Laubscher, H.P., 1961. Die Fernschubhypothese der Jura faltung. *Eclogae Geol. Helv.* 54, 222–282. <https://doi.org/10.5169/seals-162820>.
- Laubscher, H.P., 1965. Ein kinematisches Modell der Jura faltung. *Eclogae Geol. Helv.* 58, 232–318. <https://doi.org/10.5169/seals-163266>.
- Laubscher, H.P., 1981. The 3D propagation of décollement in the Jura. *Geol. Soc. Spec. Publ.* 9, 311–318. <https://doi.org/10.1144/GSL.SP.1981.009.01.27>.
- Laubscher, H.P., 1982. Die Südostecke des Rheingrabens - ein kinematisches und dynamisches Problem. *Eclogae Geol. Helv.* 75, 101–116. <https://doi.org/10.5169/seals-165219>.
- Laubscher, H.P., 1986. The eastern Jura: Relations between thin-skinned and basement tectonics, local and regional. *Geol. Rundsch.* 75, 535–553. <https://doi.org/10.1007/BF01820630>.
- Laubscher, H.P., 1992. Jura kinematics and the Molasse Basin. *Eclogae Geol. Helv.* 85, 653–675. <https://doi.org/10.5169/seals-167024>.
- Laubscher, H., 2008a. 100 years Jura décollement hypothesis: how it affects Steinmann's (1892) 'Schwarzwaldlinie'. *Int. J. Earth Sci.* 97, 1231–1245. <https://doi.org/10.1007/s00531-007-0224-9>.
- Laubscher, H., 2008b. The Grenchenberg conundrum in the Swiss Jura: a case for the centenary of the thin-skin décollement nappe model (Buxtorf 1907). *Swiss J. Geosci.* 101, 41–60. <https://doi.org/10.1007/s00015-008-1248-2>.
- Lefort, J.P., Agarwal, B.N.P., 1996. Gravity evidence for an Alpine buckling of the crust beneath the Paris Basin. *Tectonophysics* 258, 1–14. [https://doi.org/10.1016/0040-1951\(95\)00148-4](https://doi.org/10.1016/0040-1951(95)00148-4).
- Leloup, P.H., Arnaud, N., Sobel, E.R., Lacassin, R., 2005. Alpine thermal and structural evolution of the highest external crystalline massif: the Mont Blanc. *Tectonics* 24, 1–26. <https://doi.org/10.1029/2004TC001676>.
- Lienhardt, G., 1962. Géologie du bassin houiller stéphanois du Jura et de ses morts-terrains. *Mémoires du Bur. Rech. Géologiques Minières N°9*, 231–261.
- Lienhardt, M.-J., Aubague, M., Barféty, J.-C., Courel, L., Durand, M., Glintzboeckel, C., Mégard-Galli, J., 1984. Trias - Puissance et faciès de la partie supérieure, planche T2,

- in: Debrand-Passard, S., Courbouleix, S., Lienhardt, M.-J. (Eds.), *Synthèse Géologique Du Sud-Est de La France, Mémoire Du BRGM N°126*. BRGM France, p. T2.
- Looser, N., Madritsch, H., Guillon, M., Laurent, O., Wohlwend, S., Bernasconi, S.M., 2020. Absolute Age and Temperature Constraints on Faulting along the Basal Décollement of the Jura Fold-and-thrust Belt from carbonate U-Pb Dating and Clumped Isotopes. *Tectonics*. <https://doi.org/10.1002/Essoar.10503905.1>.
- Lüthi, E., 1954. *Geologische Untersuchungen im Gebiete zwischen Tessenberg und St. Immertal* (Bernier Jura). Promotionsarbeit Eidgenössische technische Hochschule Zürich 9–37.
- Madritsch, H., Deplazes, G., 2014. NTB 14-02, SGT Etappe 2: Vorschlag weiter zu untersuchender geologischer Standortgebiete mit zugehörigen Standortarealen für die Oberflächenanlage - Geologische Grundlagen - Dossier IV Geomechanische Unterlagen. In: *Nationale Genossenschaft für die Lagerung radioaktiver Abfälle (Nagra)*. Switzerland, Wettingen.
- Madritsch, H., Schmid, S.M., Fabbri, O., 2008. Interactions between thin- and thick-skinned tectonics at the northwestern front of the Jura fold-and-thrust belt (eastern France). *Tectonics* 27. <https://doi.org/10.1029/2008TC002282>.
- Madritsch, H., Kounov, A., Schmid, S.M., Fabbri, O., 2009. Multiple fault reactivations within the intra-continental Rhine-Bresse transfer Zone (La Serre Horst, eastern France). *Tectonophysics* 471, 297–318. <https://doi.org/10.1016/j.tecto.2009.02.044>.
- Madritsch, H., Naef, H., Meier, B., Franzke, H.J., Schreurs, G., 2018. Architecture and Kinematics of the Constance-Frick Trough (Northern Switzerland): Implications for the Formation of Post-Variscan Basins in the Foreland of the Alps and scenarios of their Neogene Reactivation. *Tectonics* 37, 2197–2220. <https://doi.org/10.1029/2017TC004945>.
- Malz, A., Madritsch, H., Meier, B., Kley, J., 2016. An unusual triangle zone in the external northern Alpine foreland (Switzerland): Structural inheritance, kinematics and implications for the development of the adjacent Jura fold-and-thrust belt. *Tectonophysics* 670, 127–143. <https://doi.org/10.1016/j.tecto.2015.12.025>.
- Malz, A., Madritsch, H., Jordan, P., Meier, B., Kley, J., 2019. Along-strike variations in thin-skinned thrusting style controlled by pre-existing basement structure in the easternmost Jura Mountains (Northern Switzerland). In: *Society, Geological (Ed.)*, London. Special Publications, Geological Society of London, pp. 199–220. <https://doi.org/10.1144/SP490-2019-090>.
- Martin, J., Mercier, E., 1996. Héritage distensif et structuration chevauchante dans une chaîne de couverture: apport de l'équilibre par modélisation géométrique dans le Jura nord-occidental. *Bull. Soc. Geol. Fr.* 167, 101–110.
- Mary, B.C.L., Maillot, B., Leroy, Y.M., 2013. Deterministic chaos in frictional wedges revealed by convergence analysis. *Int. J. Numer. Anal. Methods Geomech.* 37, 3036–3051. <https://doi.org/10.1002/nag.2177>.
- Meier, B., 2010. NAB 10-40, Ergänzung Interpretation reflexionsseismischer Linien zwischen dem östlichen und westlichen Molassebecken: Gebiete Waadtland Nord, Fribourg, Berner Seeland und Jura Südfuss zwischen Biel und Oensingen (Text und Beilage). In: *Nationale Genossenschaft für die Lagerung radioaktiver Abfälle (Nagra)*. Switzerland, Wettingen.
- Michel, P., Appert, G., Lavigne, J., Lefavrais, A., Bonte, A., Liénhardt, G., Ricour, J., 1953. Le contact Jura-Bresse dans la région de Lons-le-Saunier. *Bull. la Société géologique Fr.* 6, 593–611. <https://doi.org/10.2113/gssgfbull.s6-iii.7-8.593>.
- Michon, L., 2000. *Dynamique de l'extension continentale - Application au Rift Ouest-Européen par l'étude de la province du Massif Central*. Université Blaise Pascal, Dr. thesis.
- Mosar, J., 1999. Present-day and future tectonic underplating in the western Swiss Alps: reconciliation of basement/wrench-faulting and décollement folding of the Jura and Molasse basin in the Alpine foreland. *Earth Planet. Sci. Lett.* 173, 143–155. [https://doi.org/10.1016/S0012-821X\(99\)00238-1](https://doi.org/10.1016/S0012-821X(99)00238-1).
- Müller, W.H., Schmid, S.M., Briegel, U., 1981. Deformation experiments on anhydrite rocks of different grain sizes: Rheology and microfabric. *Tectonophysics* 78, 527–543. [https://doi.org/10.1016/0040-1951\(81\)90027-5](https://doi.org/10.1016/0040-1951(81)90027-5).
- NASA, 2014. Shuttle Radar Topography Mission, 1-Arc Second Scene. United States Geological Survey (USGS), College Park, Maryland.
- Noack, T., 1995. Thrust development in the eastern Jura Mountains related to pre-existing extensional structures. *Tectonophysics* 252, 419–431. [https://doi.org/10.1016/0040-1951\(95\)00089-5](https://doi.org/10.1016/0040-1951(95)00089-5).
- Nussbaum, C., Kloppenburg, A., Caër, T., Bossart, P., 2017. Tectonic evolution around the Mont Terri rock laboratory, northwestern Swiss Jura: constraints from kinematic forward modelling. *Swiss J. Geosci.* 110, 39–66. <https://doi.org/10.1007/s00015-016-0248-x>.
- Panien, M., Schreurs, G., Pfiffner, A., 2006. Mechanical behaviour of granular materials used in analogue modelling: insights from grain characterisation, ring-shear tests and analogue experiments. *J. Struct. Geol.* 28, 1710–1724. <https://doi.org/10.1016/j.jsg.2006.05.004>.
- Peper, T., Cloetingh, S., 1992. Lithosphere dynamics and tectono-stratigraphic evolution of the Mesozoic Betic rifted margin (southeastern Spain). *Tectonophysics* 203, 345–361. [https://doi.org/10.1016/0040-1951\(92\)90231-T](https://doi.org/10.1016/0040-1951(92)90231-T).
- Philippe, Y., 1994. Transfer Zone in the Southern Jura Thrust Belt (Eastern France): Geometry, Development, and Comparison with Analogue Modeling experiments. In: *Masclé, A. (Ed.), Hydrocarbon and Petroleum Geology of France. Special Publication of the European Association of Petroleum Geoscientists*. Springer, Berlin Heidelberg, Berlin, Heidelberg, pp. 327–346. https://doi.org/10.1007/978-3-642-78849-9_23.
- Philippe, Y., 1995. Rampes latérales et zones de transfert dans les chaînes plissées: géométrie, conditions de formation et pièges structuraux associés. Université de Savoie tel-00755680.
- Philippe, Y., Colletta, B., Deville, E., Masclé, A., 1996. The Jura fold-and-thrust belt: a kinematic model based on map-balancing. In: *Ziegler, P.A., Horvath, F. (Eds.), Peri-*
- Tethys Memoir 2: Structure and prospects of Alpine Basins and Forelands*. Editions du Muséum Paris, pp. 235–261.
- Ramberg, H., 1981. Gravity, Deformation and the Earth's Crust: In *Theory, Experiments and Geological Applications*. Academic Press, London.
- Rat, P., 1974. Le système Bourgogne-Morvan-Bresse (articulation entre le bassin parisien et le domaine péri-alpin). In: *Debelmas, J. (Ed.), Géologie de La France: Les Chaînes Plissées Du Cycle Alpin et Leur Avant-Pays*. Doin, Paris, pp. 480–500.
- Reisdorf, A.G., Wetzel, A., 2018. Evidence for synsedimentary differential tectonic movements in a low-subsidence setting: early Jurassic in northwestern Switzerland. *Swiss J. Geosci.* 111, 417–444. <https://doi.org/10.1007/s00015-018-0318-3>.
- Rotstein, Y., Schaming, M., Rousse, S., 2005. Structure and Tertiary tectonic history of the Mulhouse High, Upper Rhine Graben: Block faulting modified by changes in the Alpine stress regime. *Tectonics* 24, 1–15. <https://doi.org/10.1029/2004TC001654>.
- Schardt, H., 1908. Les causes du plissement et des chevauchements dans le Jura. *Eclogae Geol. Helv.* 10, 484–488.
- Schori, M., Mosar, J., Schreurs, G., 2015. Multiple detachments during thin-skinned deformation of the Swiss Central Jura: a kinematic model across the Chasseral. *Swiss J. Geosci.* 108, 327–343. <https://doi.org/10.1007/s00015-015-0196-x>.
- Schori, M., Zwaan, F., Schreurs, G., Mosar, J., 2020. Supplementary material - Pre-existing basement faults controlling deformation in the Jura Mountains fold-and-thrust belt: insights from analogue models. Mendeley Data V2. [10.17632/6pm5zwjv9w.2](https://doi.org/10.17632/6pm5zwjv9w.2).
- Schreurs, G., Buitert, S.J.H., Boutelier, D., Corti, G., Costa, E., Cruden, A.R., Daniel, J.-M., Hoth, S., Koyi, H.A., Kukowski, N., Lohrmann, J., Ravaglia, A., Schlische, R.W., Withjack, M.O., Yamada, Y., Cavozi, C., Del Ventisette, C., Brady, J.A.E., Hoffmann-Rothe, A., Mengus, J.-M., Montanari, D., Nilforoushan, F., 2006. Analogue benchmarks of shortening and extension experiments. *Geol. Soc. London. Spec. Publ.* 253, 1–27. <https://doi.org/10.1144/GSL.SP.2006.253.01.01>.
- Schumacher, M.E., 2002. Upper Rhine Graben: Role of preexisting structures during rift evolution. *Tectonics* 21, 6–17. <https://doi.org/10.1029/2001TC900022>.
- Sommeruga, A., 1997. *Geology of the Central Jura and the Molasse Basin: new insight into an evaporite-based foreland fold and thrust belt*. Mémoire la Société neuchâteloise des Sci. Nat. 12, 1–176.
- Sommeruga, A., Eichenberger, U., Marillier, F., 2012. Seismic Atlas of the Swiss Molasse Basin. In: *Kissling, E. (Ed.), Matériaux Pour La Géologie de La Suisse - Géophysique*. Federal Office of Topography (swisstopo), p. 90.
- Sommeruga, A., Mosar, J., Schori, M., Gruber, M., 2017. The Role of the Triassic Evaporites underneath the North Alpine Foreland. In: *Soto, J.I., Flinch, J., Tari, G. (Eds.), Permo-Triassic Salt Provinces of Europe, North Africa and the Atlantic Margins*. Elsevier, pp. 447–466. <https://doi.org/10.1016/b978-0-12-809417-4.00021-5>.
- Stampfli, G.M., Mosar, J., Marquer, D., Marchant, R., Baudin, T., Borel, G., 1998. Subduction and obduction processes in the Swiss Alps. *Tectonophysics* 296, 159–204. [https://doi.org/10.1016/S0040-1951\(98\)00142-5](https://doi.org/10.1016/S0040-1951(98)00142-5).
- Steinmann, G., 1892. Bemerkungen über die tektonischen Beziehungen der oberrheinischen Tiefebene zu dem nordschweizerischen Kettenjura. *Berichte der naturforschenden Gesellschaft zu Freiburg im Breisgau* 6, 150–159.
- Steinmann, G., 1902. Zur Tektonik des nordschweizerischen Kettenjura. *Cent. für Mineral. Geol. und Paläontologie Stuttgart* 488–492.
- Strayer, L.M., Hudleston, P.J., Lorig, L.J., 2001. A numerical model of deformation and fluid-flow in an evolving thrust wedge. *Tectonophysics* 335, 121–145. [https://doi.org/10.1016/S0040-1951\(01\)00052-X](https://doi.org/10.1016/S0040-1951(01)00052-X).
- Swisstopo, 2011. Digital elevation model swissALTI3D. In: *Federal Office of Topography (swisstopo)*, Wabern, Switzerland.
- Swisstopo, 2012. GeoCover geological vector data. In: *Federal Office of Topography (swisstopo)*, Wabern, Switzerland.
- Tavarnelli, E., 1997. Structural evolution of a foreland fold-and-thrust belt: the Umbria-Marche Apennines. *Italy. J. Struct. Geol.* 19, 523–534. [https://doi.org/10.1016/S0191-8141\(96\)00093-4](https://doi.org/10.1016/S0191-8141(96)00093-4).
- Trümpy, R., 1980. *Geology of Switzerland a guide-book: An Outline of the Geology of Switzerland*. In: *Wepf & co. Publishers*, Basel - New York.
- Tschanz, X., 1990. Analyse de la déformation du Jura central entre Neuchâtel (Suisse) et Besançon (France). *Eclogae Geol. Helv.* 83, 543–558. <https://doi.org/10.5169/seals-166601>.
- Ustaszewski, K., 2004. *Reactivation of Pre-Existing Crustal Discontinuities: The Southern Upper Rhine Graben and the Northern Jura Mountains - a Natural Laboratory*. University of Basel, Dr. thesis.
- Ustaszewski, K., Schmid, S.M., 2006. Control of preexisting faults on geometry and kinematics in the northernmost part of the Jura fold-and-thrust belt. *Tectonics* 25, 1–26. <https://doi.org/10.1029/2005TC001915>.
- Ustaszewski, K., Schmid, S.M., 2007. Latest Pliocene to recent thick-skinned tectonics at the Upper Rhine Graben - Jura Mountains junction. *Swiss J. Geosci.* 100, 293–312. <https://doi.org/10.1007/s00015-007-1226-0>.
- Ustaszewski, K., Schumacher, M.E., Schmid, S.M., 2005. Simultaneous normal faulting and extensional flexuring during rifting: an example from the southernmost Upper Rhine Graben. *Int. J. Earth Sci.* 94, 680–696. <https://doi.org/10.1007/s00531-004-0454-z>.
- van Keken, P.E., Spiers, C.J., van den Berg, A.P., Muysert, E.J., 1993. The effective viscosity of rocksalt: implementation of steady-state creep laws in numerical models of salt diapirism. *Tectonophysics* 225, 457–476. [https://doi.org/10.1016/0040-1951\(93\)90310-G](https://doi.org/10.1016/0040-1951(93)90310-G).
- Weijermars, R., Schmeling, H., 1986. Scaling of Newtonian and non-Newtonian fluid dynamics without inertia for quantitative modelling of rock flow due to gravity (including the concept of rheological similarity). *Phys. Earth Planet. Inter.* 43, 316–330. [https://doi.org/10.1016/0031-9201\(86\)90021-X](https://doi.org/10.1016/0031-9201(86)90021-X).

- Wetzel, A., Allenbach, R., Allia, V., 2003. Reactivated basement structures affecting the sedimentary facies in a tectonically 'quiescent' epicontinental basin: an example from NW Switzerland. *Sediment. Geol.* 157, 153–172. [https://doi.org/10.1016/S0037-0738\(02\)00230-0](https://doi.org/10.1016/S0037-0738(02)00230-0).
- Winnock, E., 1961. Résultats géologiques du forage Risoux 1. *Bull. der Vereinigung Schweizerischer Pet. und Ingenieure* 28, 17–26. <https://doi.org/10.5169/seals-191403>.
- Withjack, M.O., Callaway, S., 2000. Active normal faulting beneath a salt layer: an experimental study of deformation patterns in the cover sequence. *Am. Assoc. Pet. Geol. Bull.* 84, 627–651. <https://doi.org/10.1306/c9ebce73-1735-11d7-8645000102c1865d>.
- Yang, K.M., Wu, J.C., Wickham, J.S., Ting, H.H., Wang, J.B., Chi, W.R., 1996. Transverse structures in Hsinchu and Miaoli areas: Structural mode and evolution in foothills belt, northwestern Taiwan. *Pet. Geol. Taiwan* 30, 111–150.
- Yang, K.M., Huang, S.T., Wu, J.C., Ting, H.H., Mei, W.W., 2006. Review and new insights on foreland tectonics in western Taiwan. *Int. Geol. Rev.* 48, 910–941. <https://doi.org/10.2747/0020-6814.48.10.910>.
- Ziegler, P.A., 1988a. Evolution of the Arctic - North Atlantic and the Western Tethys - a Visual Presentation of a series of Paleogeographic-paleotectonic maps. *AAPG Mem.* 43, 164–196.
- Ziegler, P.A., 1988b. Late Jurassic-Early Cretaceous Central Atlantic Sea-Floor Spreading, Closure of Neo-Tethys, and Opening of Canada Basin. *AAPG Mem. In: Evol. Arctic-North Atl. West. Tethys*, Vol. 43, pp. 63–82. <https://doi.org/10.1306/M43478C6>.
- Ziegler, P.A., 1992. European Cenozoic rift system. *Tectonophysics* 208, 91–111. [https://doi.org/10.1016/0040-1951\(92\)90338-7](https://doi.org/10.1016/0040-1951(92)90338-7).
- Ziegler, P.A., Dèzes, P., 2007. Cenozoic uplift of Variscan Massifs in the Alpine foreland: timing and controlling mechanisms. *Glob. Planet. Chang.* 58, 237–269. <https://doi.org/10.1016/j.gloplacha.2006.12.004>.
- Zwaan, F., Schreurs, G., Naliboff, J., Buitter, S.J.H., 2016. Insights into the effects of oblique extension on continental rift interaction from 3D analogue and numerical models. *Tectonophysics* 693, 239–260. <https://doi.org/10.1016/j.tecto.2016.02.036>.
- Zwaan, F., Schreurs, G., Gentzmann, R., Warsitzka, M., Rosenau, M., 2018a. Ring-shear test data of quartz sand from the Tectonic Modelling Lab of the University of Bern (CH). *GFZ Data Serv* 1–9. <https://doi.org/10.5880/ridgeo.2018.028>.
- Zwaan, F., Schreurs, G., Ritter, M., Santimano, T., Rosenau, M., Naliboff, J., Buitter, S.J.H., 2018b. Rheology of PDMS-corundum sand mixtures from the Tectonic Modelling Lab of the University of Bern (CH). *GFZ Data Serv.* <https://doi.org/10.5880/ridgeo.2018.023>.

9 - KINEMATIC MODELLING

9.1 INTRODUCTION

The JFTB formed above a previously deformed carbonate platform (Laubscher 1961). Most notably, extensional deformation phases affect the brittle platform preceding the JFTB, including the formation of the ECRIS or flexural bulging of the peripheral northern Alpine foreland. Preceding extensional tectonics ultimately led to notable extensional structures in the brittle cover, well known in certain areas at the front of the JFTB (e.g. Lienhardt 1962; Michel et al. 1953). In the analogue model chapter of this study (Chapter 8), it is shown that extensional cover structures are not necessarily localised above basement faults, if a viscous layer is present between the brittle cover and the rigid basement.

This chapter is dedicated to a more detailed comprehension of extensional structures and the mechanical parameters that control them. First, various examples of extensional structures in models and nature are compiled from literature. Thereafter, a step-by-step kinematic forward model is presented illustrating the evolution of extensional structures during the formation of the JFTB, on behalf of a cross-section across the External Jura.

9.2 METHODS

Models are produced using the software MOVE 2019.1, kindly provided by Petroleum Experts (Petex). MOVE contains a move-on-fault module, which allows kinematic modelling, supporting classical geometrical fold models such as fault-bend folds (Suppe 1983), detachment folds, fault-propagation folds (Suppe and Medwedeff 1990) as well as a more dynamical algorithm for modelling trishear folds (Allmendinger 1998; Erslev 1991). These fold models are particularly suited for modelling the compressive structures occurring during the JFTB formation (e.g. Caër et al. 2018; Rime 2017; Schori et al. 2015). The complex Eo-Oligocene extensional structures that occur in the study area are not modelled in MOVE. Instead, observed extensional structures from analogue models or seismic lines

are used as structural templates to create realistic initial stage structures, which are forward modelled afterwards.

9.3 COMPILATION OF EXTENSIONAL STRUCTURES FROM MODELS AND NATURE

Analogue model studies show that basement offsets along discrete faults lead to a system of normal faults and reverse faults in an overlying brittle cover (Naylor et al. 1994; Richard and Krantz 1991). With the presence of a sufficiently thick viscous layer above the basement, the cover additionally reveals extensional collapse structures (normal faults growing from the surface downwards) not directly overlying the basement step that induces deformation. It is an oversimplification to prolong normal faults from the pre-Mesozoic basement across incompetent layers of the Triassic series into the Mesozoic cover of the JFTB. Fig. 9.1 shows subsidence structures from analogue modelling studies and documented structures from seismic lines in the study area. The compilation illustrates how different mechanical basement parameters control the resulting cover structures and it helps to understand observed extensional cover structures in the JFTB.

Fig. 9.1a shows a classical clay experiment (Laubscher 1982 according to an experiment conducted by Ernst Cloos in 1936). Based on boreholes in the Faisceau lédonien that revealed Tertiary sediments in the footwall that are thrust by the Mesozoic cover of the JFTB, Michel et al. (1953) developed a similar but conceptual model (Fig. 9.1b). The same borehole data was interpreted differently by Mugnier and Vialon (1986) who suggested Miocene collapsing of the Mesozoic cover that leads to gravity sliding (Fig. 9.1c). In this case, the Faisceau lédonien does not need to be connected to the basal décollement of the JFTB. However, Chauve et al. (1988) disproves this model arguing that it is mechanically invalid and that surface data is not properly respected.

Fig. 9.1d and Fig. 9.1e show analogue model series of

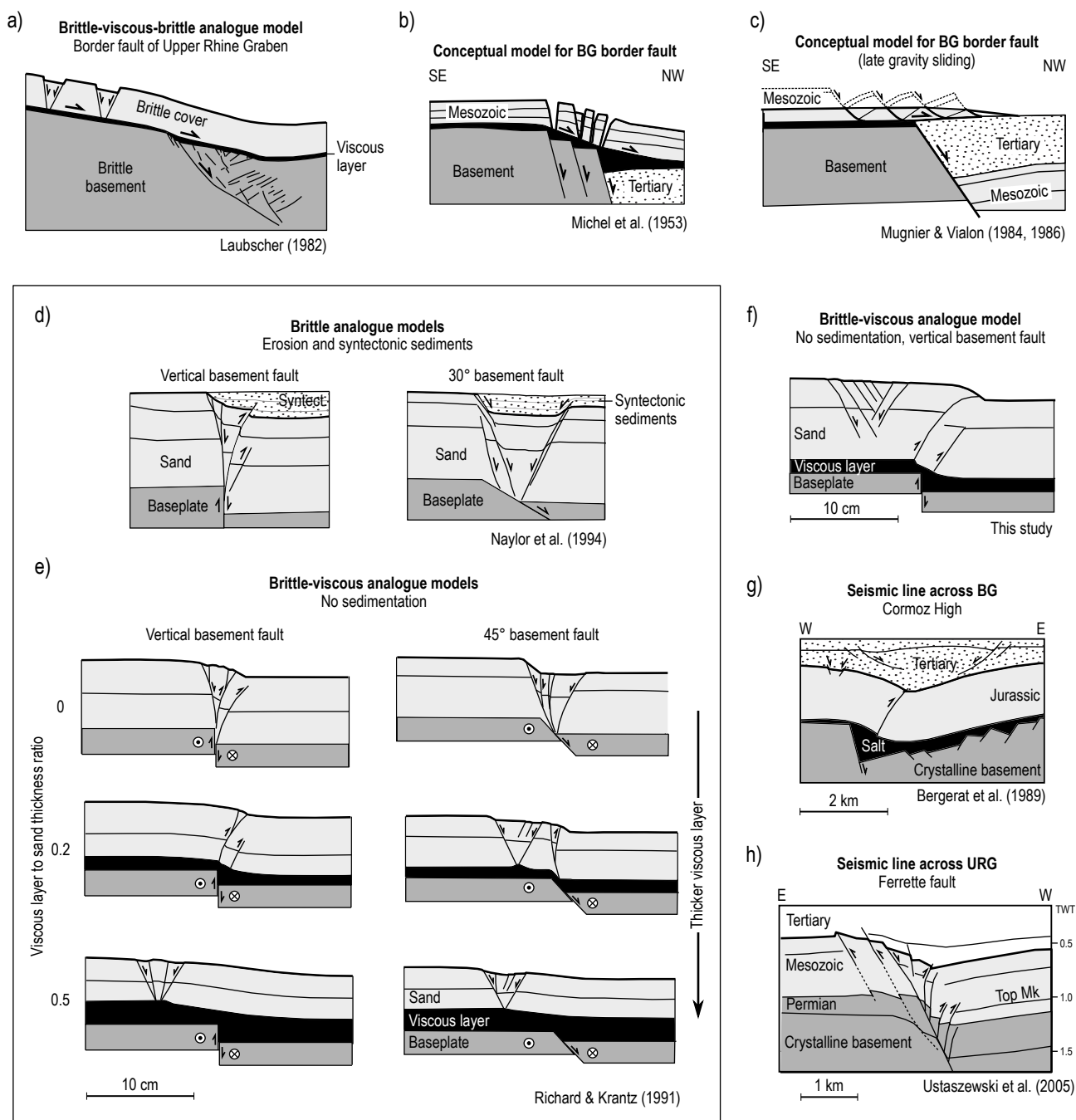


Fig. 9.1 – Compilation of cross-sections showing structures in a brittle cover induced by a relative basement offset. Some of these structures are subsequently used as starting situation for a kinematic analysis of present day structures. a) Brittle-viscous-brittle experiment modelling border faults of the URG (sketch after Laubscher 1982). b) Conceptual model sketching the BG border fault zone in Oligocene (west of Lons-le-Saunier, see overview map in Fig. 9.3 for location), after Michel et al. (1953). This concept was developed on behalf of implications in boreholes. c) Conceptual model sketching the BG border fault zone, modified from Guellec et al. (1990) based on Mugnier and Vialon (1984, 1986). The brittle cover forms tilted blocks with pronounced listric normal faults that end in Triassic evaporites. This model suggests delayed Miocene to Pliocene gravity sliding of the Mesozoic cover due to the formation of the Eo-Oligocene Bresse Graben proposed by Mugnier and Vialon (1984, 1986). d) Brittle analogue model experiments of Naylor et al. (1994), e) Brittle-viscous analogue model series testing varying décollement-cover thickness ratios and inclinations of basement faults, after Richard and Krantz (1991). An additional horizontal strike-slip movement of the base-plates was conducted after initial vertical offset and therefore, some of the initial grabens in the cover are moderately inverted. f) Brittle-viscous analogue model of this study. g) Seismic line interpretation across the Cormoz High in the Bresse Graben, after Bergerat et al. (1989). h) Seismic line interpretation across the Ferrette fault in the Upper Rhine Graben after Ustaszewski et al. (2005). Triassic evaporites are not specifically highlighted, but they occur at least above the subsided block within the Muschelkalk Group (Mk).

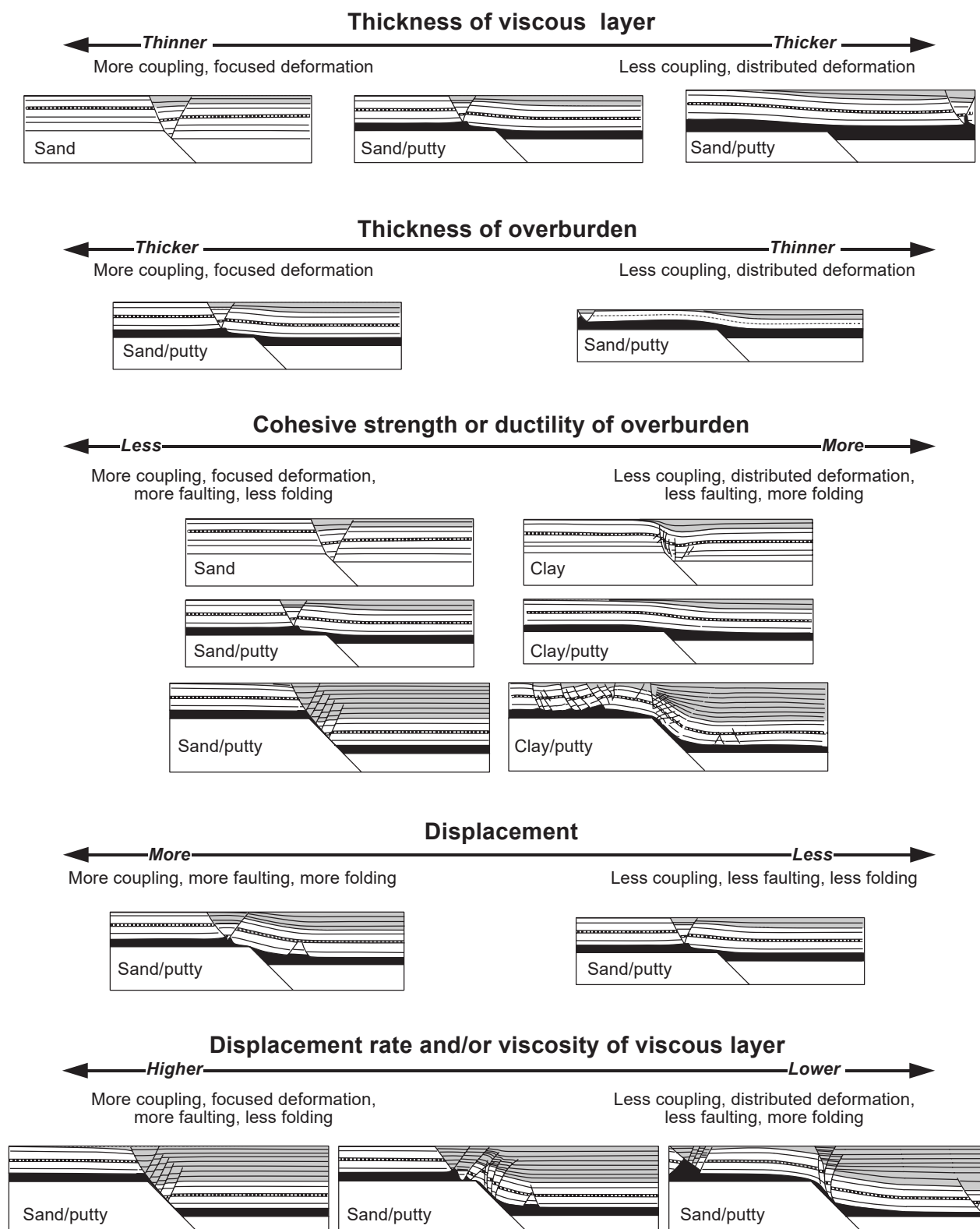


Fig. 9.2 – Analogue model series of Withjack and Callaway (2000), showing extensional structures in function of varying viscous layer (black layer) thickness, overburden thickness (white layers), cohesive strength of overburden, displacement and viscosity of the viscous layer. White base-plates are made of metal, the black layer represents silicone putty and the white layered cover is either made of sand or clay (indicated for each model). Grey layers represent growth layers of homogeneous sand or clay.

Naylor et al. (1994) and Richard and Krantz (1991). Note that in comparison to Richard and Krantz (1991), Naylor et al. (1994) involves syn-tectonic erosion and sedimentation (Fig. 9.1d and e). In Fig. 9.1e, a viscous layer between a brittle cover and a rigid basement acts as a mechanical strain separator. A thick viscous layer above a single basement fault causes de-localised structures in the cover (Fig. 9.1e). Therefore, the thickness of the viscous layer is an important parameter that controls the evolution of structures (Fig. 9.1e). Secondly, the inclination of a basement fault is tested (Fig. 9.1d and e). A vertical basement fault leads to different structures than an inclined basement fault, which induces horizontal stretching (Fig. 9.1d and e).

Fig. 9.1f is from brittle-viscous analogue modelling in this study, which shows similar structures as viscous models with vertical basement steps in (Fig. 9.1e). Note that the analogue model of this study (Fig. 9.1f) is remarkably similar to structures interpreted in a seismic line across the Bresse Graben (Fig. 9.1g, Bergerat et al. 1989). Fig. 9.1h illustrates a normal fault in the URG, which shows a single basement fault that induces a large normal fault and several smaller reverse faults in the Mesozoic cover. Note that this interpretation is similar to structures in brittle analogue models with a vertical basement step without viscous layer in Fig. 9.1d and e.

Withjack and Callaway (2000) tested the influence of several parameters on extensional structures in a brittle sand/clay cover above a layer of silicone putty (Fig. 9.2). The tested parameters include viscous layer thickness, overburden thickness, cohesive strength of the overburden, displacement and viscosity of the viscous layer. In summary, increasing coupling (more «friction») between cover and base-plates with more focused deformation is observed with a thinner viscous layer, a thicker overburden, decreasing cohesive strength of the cover and higher viscosity (higher displacement rate) of the ductile silicone layer (Fig. 9.2).

9.4 A KINEMATIC MODEL OF THE SOUTHERN PLATEAU JURA

9.4.1 Context

The transition from the Internal Jura to the southern Plateau Jura is analysed on behalf of Section B (Fig. 5.2b), presented previously in Chapter 5. This cross-section features important extensional structures in the Mesozoic cover and substantial vertical basement offsets of several hundred metres. Some of the extensional structures are brought into connection with Oligocene rifting that re-activated pre-existing structures (see discussions in Homberg et al. 2002; Mugnier and Vialon 1986; Philippe et al. 1996). In particular, Homberg et al. (2002) mentions that the «Pincée de l'Heute» (also called «Euthe Pincée») and the southern Faisceau de Syam contain abundant normal faults that are connected to Oligocene rifting. The Oligocene age of normal faults in the Faisceau de Syam is constrained by Oligocene conglomerates with a local source (Mugnier and Vialon 1986 according to Aubert

1975; Duplaix and Guillaume 1962; Weber 1960). Mugnier and Vialon (1986) and Philippe et al. (1996) both present balanced cross-sections across the Pincée de l'Heute and the Faisceau de Syam, and speculate about the origin of these extensional systems.

In order to establish a more detailed structural framework, a kinematic analysis is conducted, integrating the effects of Cenozoic rifting, Cenozoic flexural bending of the NAF and Mio-Pliocene JFTB formation. In a step-by-step forward analysis, tectonic signatures are quantified and their effects discussed.

9.4.2 Model results

The resulting kinematic model in Fig. 9.3 shows following steps in the development of the External Jura:

1. Early Cenozoic sediment thickness of the Mesozoic cover and the position of inherited basement discontinuities (Fig. 9.3a)
2. Eocene-Oligocene uplift of plateaus due to the formation of the Bresse Graben shoulder, re-activation of pre-existing basement discontinuities and the formation of proto-structures in the Mesozoic cover. The tectonic uplift induces erosion of uplifted plateaus (Fig. 9.3b).
3. Oligocene flexural subsidence to the SE (foredeep evolution) and connected flexural normal faulting, aggravating previous grabens and activating new basement faults (Fig. 9.3c)
4. Miocene-Pliocene deformation of the JFTB, propagating from SE to NW (Fig. 9.3d and e)
5. Erosion of tectonically uplifted domains since beginning JFTB formation (Fig. 9.3f)

9.4.3 Discussion

Stage 1: Pre-Lutetian Mesozoic platform

The kinematic forward model in Fig. 9.3 presumes a flat lying, tectonically undisturbed but exposed Mesozoic platform before Middle Eocene times (Lutetian). The total thickness of the Mesozoic sequence is estimated at roughly 2 km, based on documented unit thickness in the boreholes Valempoulières-2 (VLP-2) and Toillon-1 (TLN-1). The Mesozoic sediments that are involved have an age between Early Triassic and Early Cretaceous. The Upper Triassic Keuper Group contains a roughly 200 m thick salt system and additional sulphate layers, thereby constituting a very weak layer towards the base of the Mesozoic sequence. In Fig. 9.3a, three discontinuities in the pre-Mesozoic basement are suggested. They have a NNE–SSW to NE–SW orientation, roughly parallel to the eastern Bresse Graben border faults. As the opening of Bresse Graben and the ECRIS in general followed inherited Variscan basement faults (Dèzes et al. 2004; Illies 1962), it is suggested that the three basement discontinuities in the model (Fig. 9.3) are likewise inherited from Palaeozoic times. Along the illustrated section trace, no notable syn-sedimentary thickness changes of Mesozoic units

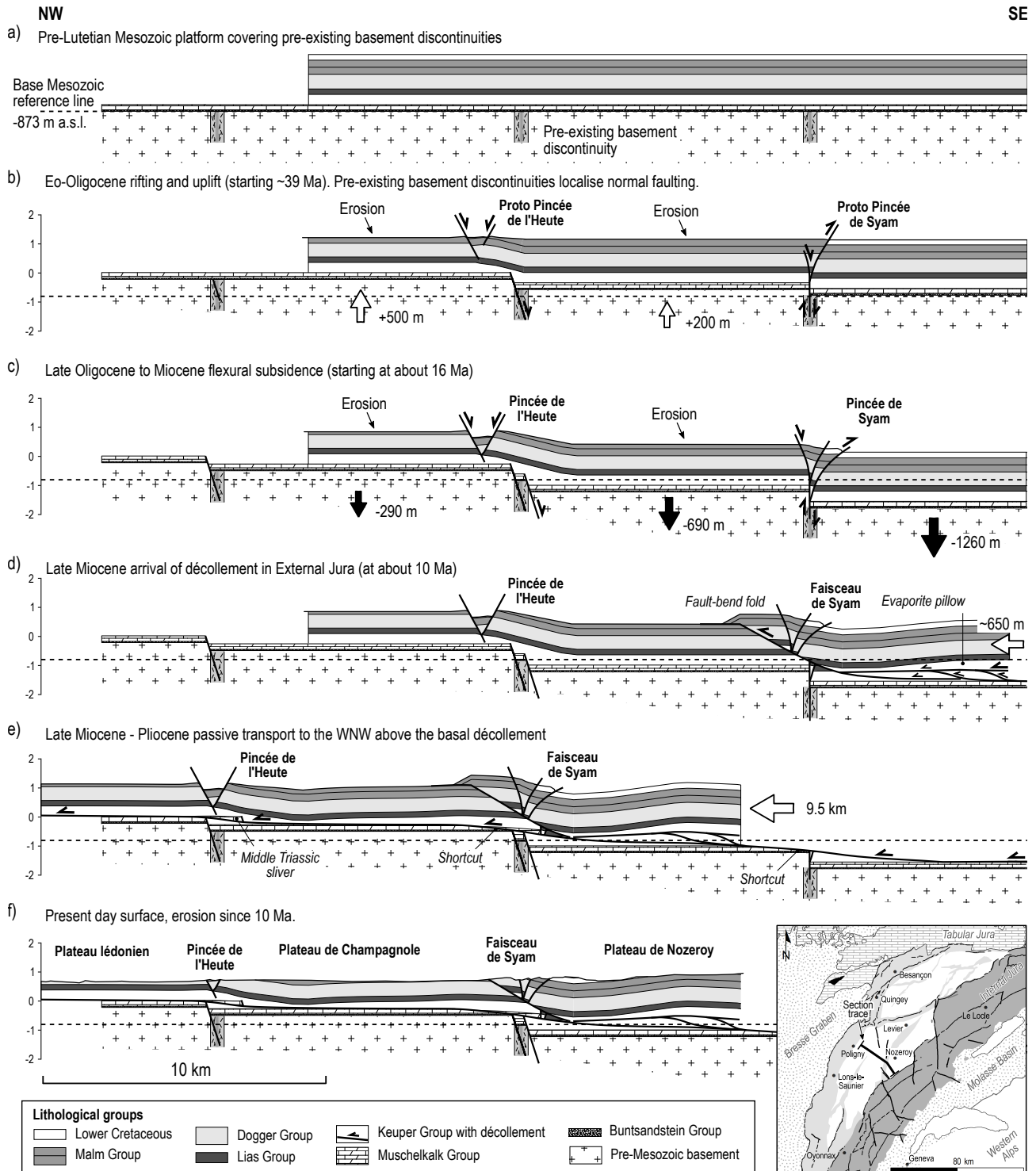


Fig. 9.3 – Kinematic forward model across the External Jura. The model is based on Section B in Fig. 5.2b on page 75. a) An undisturbed Mesozoic sequence is presumed before Middle Eocene (Lutetian) times. Pre-existing basement discontinuities do not affect the Mesozoic cover yet. The base Mesozoic reference line indicates the initial structural height of the pre-Mesozoic basement. b) Eo-Oligocene rifting in the Bresse Graben to the west of the section (Sissingh 1998) leads to several hundred meters of uplift in the area of the External Jura (Bourgeois et al. 2007). Basement blocks separated by pre-existing discontinuities are uplifted and different structures form in the Mesozoic cover. Erosion concentrates on uplifted domains. c) In Late Oligocene and Miocene, flexural subsidence connected with flexural faulting leads to subsidence of existing basement blocks and additional pre-existing basement discontinuities are reactivated. d) The basal décollement of the JFTB arrives in Tortonian times in the External Jura. The Toillon evaporite pillow is illustrated as a consequence of duplex structures within the Keuper Group. The future Faisceau de Syam forms as a fault-bend fold controlled by a roughly 600 m high basement step. e) The basal décollement progresses to the front of the JFTB and the plateaus and faisceaux are transported roughly 9500 m to the WNW during Late Miocene-Pliocene times. f) The tectonic topography forming during Mio-Pliocene stimulates further erosion that is intensified above higher basement block.

are recognised, which suggests that these three basement discontinuities were not notably active during Jurassic rifting in connection with the opening of the Alpine Tethys. The base Mesozoic reference line marks the altitude of the pre-Mesozoic basement in the initial phase Fig. 9.3a at -873 m a.s.l. This line helps to visually identify uplift or subsidence of basement blocks in the subsequent states of the kinematic forward model (Fig. 9.3b to d).

Stage 2: Eo-Oligocene rifting and uplift

The Bresse Graben opened in several discriminable phases according to Sissingh (1998), with main, regional rifting in Late Eocene to Oligocene (~39 Ma to 28 Ma). Bourgeois et al. (2007) estimate a maximum of about 900 m uplift of graben shoulders in response to subsidence movements in the Bresse Graben. This uplift affects the External Jura and possibly even the Internal Jura (Bourgeois et al. 2007), which is illustrated in Fig. 9.3b. Note that from the 900 m total uplift, only max. 500 m affect the basement along the modelled section trace, which is already some kilometres away from the Bresse Graben border faults. Erosion affects the uplifted blocks and the cover is therefore roughly 300 m thinner towards the NW (Fig. 9.3b).

Stage 3: Late Oligocene to Miocene flexural subsidence

The Section B (Fig. 5.2b on page 75) that is forward modelled in here reveals a total altitude difference of the basement of 1210 m between the borehole Grozon-1 (GRZ-1) at the front of the JFTB and the Plateau de Nozeroy. Since the maximum estimated uplift of the BG rift shoulder underneath the Faisceau lédonien is in the range of ~900 m (Bourgeois et al. 2007, also see Table 6.2 on page 86), not all the vertical offset along Section B (Fig. 5.2b) can be attributed to uplift of the rift shoulder. Consequently, I propose that parts of the vertical basement offset was achieved during flexural subsidence of the NAF, which results in a renewed re-activation of pre-existing basement discontinuities. Based on seismic surveys in the foreland of the Appalachian Mountains, Bradley and Kidd (1991) suggested that flexural normal faults only actively develop behind the forebulge (in the foredeep). According to reconstruction maps of Molasse sediments in Ford et al. (2006), the Alpine flexural foreland basin reached the Faisceau de Syam (the SE of the model) roughly in Late Oligocene (~16 Ma), which presumably coincides with beginning flexural normal faulting.

The modelled flexural subsidence is quite substantial and in Fig. 9.3c, 1260 m vertical offset is needed to match the constraints of the initial Section B (Fig. 5.2b). Normal faults in the basement that initiated in the previous stage are re-activated and throws are aggravated (Fig. 9.3c). In addition, some inherited basement discontinuities not active in the previous stage are re-activated. The basement induced structures in the Mesozoic cover (proto Pincée de l'Heute and proto Pincée de Syam, Fig. 9.3c) continue evolving. The Pincée de l'Heute (Fig. 9.3c) becomes a graben that lies in an uplifted position. Analogue models in Richard and Krantz (1991) show that the ratio between

the basal viscous layer (i.e. Keuper Group evaporites in the model) and the brittle cover and the inclination of the basement step control the type of structure that forms in the cover in response to basement offset (see Fig. 9.1e). Analogously, a varying ratio of Keuper Group evaporites and the brittle carbonate cover is a possible parameter that explains the structural difference of the Pincée de l'Heute (high décollement to cover ratio) and the Pincée de Syam (low décollement to cover ratio, Fig. 9.3c).

At the end of this stage, the pre-Mesozoic basement has its final geometry, featuring three basement steps with several hundred of metres vertical offset. Erosion on uplifted blocks continuous until the next stage in Late Miocene times. The Cretaceous sediments to the SE are preserved on a subsided block.

Stage 4: Late Miocene-Pliocene deformation

Recent U-Pb absolute age dating on calcite veins and slickensides in the region suggests that the Mio-Pliocene deformation arrived at about 10 Ma at the latest in the External Jura (Smeraglia et al. 2021). In the model (Fig. 9.3d), this is interpreted to lead to the formation of an evaporite pillow (Fig. 9.3d) and a fault-bend fold (Faisceau de Syam) that is controlled by the basement step. Subsequently, the décollement propagates relatively fast to the eastern border of the Bresse Graben, without forming notable anticlines (Fig. 9.3e). Relatively high steps of several hundred metres do not seem to control notable thrusts in the cover, possibly because the Keuper Group evaporites remained more or less connected during Eocene-Miocene basement tectonics. However, at high basement steps, the basal décollement shortcuts across the Middle Triassic Muschelkalk Group, which normally remains in the foot-wall. In this way, slivers of the Muschelkalk Group are incorporated in the hanging wall and passively transported to the NW (Fig. 9.3e). The thin-skinned JFTB formation leads to tectonically induced topography that is constantly eroded (Fig. 9.3f).

9.4.4 Conclusions

A kinematic forward model is conducted showing the evolution of a cross-section across the southern Plateau Jura. It integrates several observations such as (1) the formation of varying extensional structures in the Mesozoic cover in response to basement offset, (2) the formation of Middle Triassic slivers incorporated in the Upper Triassic décollement zone, (3) the localisation of extensional and compressional structures at basement steps, (4) erosion of tectonically induced topography, (5) recent age dating, (6) the influence of pre-existing Variscan basement discontinuities and (6) the local signature of Cenozoic tectonic processes. The kinematic model demonstrates important aspects of the timing of the involved Cenozoic tectonic processes, as well as their consequences on observed structures:

- Complex, partially reactivated structures documented in the Faisceau de Syam and the «pincée de L'Heute» are satisfactorily explained with two extensional phases

between Middle Eocene and Miocene and a subsequent thin-skinned JFTB formation. A recent inversion of the basement is non-essential, though not explicitly excluded.

- Both uplift and subsidence movements of the basement are needed to comply with the erosion pattern, generally showing high erosion of sediments towards the NW but an almost entire preservation of the Mesozoic cover to the SE. Eo-Oligocene rift shoulder uplift accentuates erosion whereas flexural subsidence of the peripheral Alpine flexural basin reduces erosion rates.
- In the External Jura, extensional faulting connected to rifting probably preceded extensional faulting connected to flexural subsidence.
- Eo-Oligocene erosion of the Mesozoic cover towards the front of the JFTB possibly controls the type of extensional structures formed in the Mesozoic cover, since erosion increases the thickness ratio between the décollement layer and the brittle carbonate cover on top (e.g. extensional collapse vs. normal faults accompanied by reverse faults).
- The spacing of main basement faults in the External Jura is about 10 km, similar to the Mio-Pliocene displacement distance (in this part of the JFTB). Therefore, present day extensional systems documented in the cover (e.g. «pincée de L'Heute») superpose basement structures by coincidence.
- It is precluded that normal faults in the basement are exclusively formed during Cenozoic rifting. The cumulative offsets of basement faults decidedly exceeds the estimated 900 m (Bourgeois et al. 2007) that can be attributed to rift shoulder uplift. Several hundred metres of additional basement offset is attributed to flexural subsidence of the peripheral Alpine foreland basin.

The interplay of Cenozoic rifting and forebulging is hardly addressed in connection with the Faisceau de Syam or the «pincée de l'Heute» in previous publications (e.g. Homberg et al. 2002; Mugnier and Vialon 1986). However, the kinematic model in here points out that both tectonic processes need to be integrated to fully understand extensional systems in the External Jura. Due to the prolonged north-west propagation of the flexural foredeep, the difference in age of these two extensional processes varies for each location and needs to be revised. However, especially in the wake of U-Pb calcite dating on faults (see Chapter 7 of this study), the concept of interplaying Cenozoic extension processes needs to be understood in order to correctly interpret Eo-Oligocene calcite ages.

10 - CONCLUSIONS

The aim of this study was to constrain and characterise the topography and structures in the pre-Mesozoic basement beneath the Jura Mountains and to assess the influence of the basement on the formation of the Jura Mountains. Furthermore, the tectonic processes that led to the present day basement configuration were evaluated and assessed. In realisation of this study, the following datasets were acquired:

- A new homogenised structural map of the whole Jura Mountains fold-and-thrust belt (JFTB, Enclosure 01). The map integrates geological information (dips, lithological units) of existing geological maps 1:25'000 maps of Switzerland and 1:50'000 maps of France and fault systems of previous studies. Folds and faults of existing maps and previous studies were revised using 5 m resolution digital surface models, dip data, lithological limits and new local field data. Additionally, folds and basement faults in the External Jura (Champagnole-Mouthe area) were locally constrained on seismic lines. Faults in the pre-Mesozoic basement beneath the External Jura were inferred from geological surface data (integrating cross-section construction). The new structural map follows classical subdivisions of the External Jura, recently re-defined areas at the front of the JFTB (Faisceau des Avant-Monts, Ferrette Zone and Vorfaltenzone) and proposes some additional sub-divisions.
- A database with 209 documented deep boreholes in the JFTB and surroundings was compiled (Supplementary Material C). For each borehole, depth and elevation of faults and horizons of 11 lithostratigraphic groups are digitised and observations from bore-logs are partially described. The lithostratigraphic groups are Tertiary (Ter), Cretaceous (Cr), Upper Malm (UMa), Lower Malm (LMa), Dogger (Do), Lias (Li), Keuper (Ke), Muschelkalk (Mk), Buntsandstein (Bss), Permo-Carboniferous (PC) and pre-Mesozoic crystalline basement (Bas). Digitised boreholes are geo-referenced and dockable to a Geographical Information System (e.g. QGIS or ArcGIS).
- Thickness models of Mesozoic units (Cr, UMa, LMa,

Do, Li, Ke, Mk, Bss) and Tertiary sediments across the JFTB and surroundings were created. These models integrate the borehole database, cross-sections of previous studies and thickness models of previous studies (in the surroundings of the JFTB). Sudden thickness changes along faults are integrated. The new models are provided as digital grids (Supplementary Material A.05, B.01) and edited maps.

- Five new geological cross-sections across plateaus and faisceaux of the central External Jura were constructed. One cross-section additionally includes the Internal Jura. The cross-sections are based on boreholes and geological surface data (including the new structural map) and in one location, a seismic line was used to validate the deep structures of a section segment. In the External Jura, offsets of the pre-Mesozoic basement are identified (basement faults).
- A model of the topography of the pre-Mesozoic basement, respecting main faults in the External Jura, Bresse Graben and Upper Rhine Graben was created. The model is based on top basement elevations of the borehole database (Supplementary Material C), interpreted basement fault systems deduced from the new structural map (Enclosure 01, Supplementary Material A.01), new geological cross-sections of this study, as well as additional models and cross-sections (based on seismic lines) from previous studies. The top basement model is provided as digital grid (Supplementary Material A.05, B.03) and as an edited map.
- U-Pb calcite dating of a slickenfibres and a vein in connection with a fault in a location in the External Jura (Orgelet Zone) was conducted. The received ages constrain the local deformation history, showing that an inherited fault (~Lutetian age) was reactivated during the formation of the JFTB.

In addition to the new datasets above, brittle-viscous analogue modelling was conducted in order to test the formation of oblique structures in the detached cover of the Jura Mountains in response to inherited faults in the basement. Based on insights of analogue models,

basement controlled structures of the JFTB are identified and palinspastically restored. Deduced from this, new basement faults are proposed beneath the Internal Jura and the Western Molasse Basin (preliminary study in Appendix B.4).

On the basis of these new datasets and models, the following conclusions are drawn in respect to structures in the basement beneath the JFTB:

- The pre-Mesozoic basement beneath the Jura Mountains was essentially pre-structured by the formation of the European Cenozoic Rift System (ECRIS) in Eo-Oligocene and flexural bending of the Northern Alpine foreland. The two processes produce offsets of several hundred metres along normal faults that controlled the formation of the younger JFTB locally. Uplift of ECRIS graben shoulders (up to ~930 m) led to erosion of the Mesozoic cover towards the front of the present day JFTB, whereas subsidence of the foredeep (~5000 m in front of the Alps) preserved the Mesozoic cover from being eroded towards the SE of the JFTB. Basement faults in the pre-Mesozoic basement beneath the External Jura are identified showing throws between 50 to 600 m (cross-section construction). Beneath the front of the JFTB, considerably higher basement offsets (up to several kilometres) in connection with the formation of the ECRIS occur locally. The presence of basement faults beneath the Internal Jura and Molasse Basin (at least up to 400 m) are strongly suggested from analogue modelling results (interpretation of oblique ramp systems in the JFTB). In the Internal Jura and Molasse Basin, flexural faulting is proposed to be the main responsible process for Cenozoic basement faults. The orientations of basement faults were likely inherited from the Variscan orogeny, according to structural orientations that are NW–SE (Hercynian), NNE–SSW (Rhenish) and ENE–WNW (Erzgebirgian).
- Flexural extensional fractures and normal faults in connection with the north-west migration of the flexural foreland basin system affected the Mesozoic cover of the JFTB by Early Oligocene (Rupelian, ~34 Ma) in the Internal Jura. By Late Oligocene (Chattian, ~28 Ma), flexural extension reached the front of the future JFTB. The northern Faisceau lédonien and northern Plateau Jura (Plateau d'Ornans s.l. and surrounding faisceaux) are presumably in the present day forebulge, whereas the rest of the JFTB (southern Plateau Jura, Southern Jura, Internal Jura, Ferrette Zone, Eastern Jura) lie in the present day foredeep.
- The Eocene unconformity in the Molasse Basin and Internal Jura (siderolithic deposits) is likely associated with the migration of the forebulge. The Eocene unconformity in the External Jura is rather owed to the formation of the ECRIS.
- The geometry of the top of the pre-Mesozoic basement in the JFTB and surrounding supports that the present day forebulge crest lies in the RBTZ to the north of the JFTB as proposed by Laubscher (1992). The maximum uplift at the forebulge crest is in the range of 300

to 350 m. The foredeep is relatively short (~80 km) whereas to the east in the German Molasse Basin, the foredeep is up to about 120 km long. This supports a reduced elastic thickness of the lithosphere in the area of the JFTB and surroundings, supposedly due to pre-existing lithospheric weakening by the ECRIS (Laubscher 1992).

In conclusion, the basement controlled the formation of the JFTB in the following way:

- Structural domains of the JFTB are connected to the topography and faults in the pre-Mesozoic basement. Most frequent basement dips in the External Jura are smaller than 1.5° and beneath the Internal Jura, most frequent dips are between 2 to 3°. It is suggested that the small basement inclination in the External Jura has fostered the formation of kilometric plateaus (internally undeformed Mesozoic units). The basement beneath the inner External Jura rather steps upwards in the direction of tectonic transport (higher towards NW), whereas beneath the front of the Jura, the pre-Mesozoic basement rather steps downwards (lower towards the NW). Most faisceaux reveal extensional structures and seem to be controlled by basement steps (e.g. Faisceau de Syam, Faisceau de l'Heute, Faisceau de Quingey, Faisceau lédonien, Faisceau salinois). Inner faisceaux are transported several kilometres away from the basement fault that controlled deformation and therefore, they may lie above a flat basement today.
- The front of the JFTB is mainly controlled by basement downward steps of > 400 m vertical offset. The lateral limits of the JFTB are rather connected to increased friction of the décollement and a Triassic unit that is tapering out (Deville 2021; Philippe et al. 1996), spatially corresponding to the limits of the Burgundy trough during Triassic times.
- The front of the JFTB shows uplifts of up to 930 m due to rift-shoulder uplift of the ECRIS beginning in Eocene. Therefore, the Mesozoic cover at the front of the JFTB was thoroughly eroded before the formation of the JFTB. In contrast, the Mesozoic cover of the Internal Jura was preserved due to flexural subsidence beginning in Late Oligocene.
- The décollement of the JFTB is predominantly controlled by salt-bearing units of the Middle and Upper Triassic evaporites. The main décollement level in the Eastern Jura is within the Middle Triassic salt-bearing layers, whereas in the Central and Southern Jura, the main décollement happens in Upper Triassic salt-bearing layers (Philippe et al. 1996). This correlates with thickness peaks on isopach maps. Furthermore, isopach maps suggest that the Middle Jurassic Group (Dogger Group) predominantly hosts upper detachments in the Eastern Jura, whereas upper detachments in the Central and Southern Jura are rather in the Lower Jurassic Group (Lias Group).

In summary, this study confirms an important influence of basement topography and pre-existing basement faults on

the structural development of the thin-skinned JFTB (Laubscher 1961). Variscan basement faults, reactivated during Eocene to Miocene extension, are verified beneath the External Jura and strongly suggested beneath the Internal Jura and Western Molasse Basin. It was not possible to test a recent inversion of the basement with the applied methods. The basement high of Champfromier south-east of Oyonnax is the only basement structure within the JFTB that was proposed to be due to basement inversion (Guellec et al. 1990). In this study, it is strongly suggested that the basement high of Champfromier pre-dates the formation of the JFTB and to have controlled the formation of oblique structures in the Mesozoic cover. Therefore, the basement high beneath Champfromier constitutes a pre-JFTB horst in the pre-Mesozoic basement.

BIBLIOGRAPHY

- Affolter, T. (2003). Étude des déformations et restaurations 3D d'un bassin de front de chaîne: l'exemple du Jura et des massifs Subalpins français. PhD thesis. Université de Grenoble, pp. 28–92.
- Affolter, T. and J.-P. Gratier (2004). Map view retrodeformation of an arcuate fold-and-thrust belt: The Jura case. *Journal of Geophysical Research*, 109 (B3), B03404. ISSN: 0148-0227. DOI: 10.1029/2002JB002270.
- Alabouvette, B., C. Cavelier and N. Debégli (1984). Tertiaire - Structure du mir et âge des premiers dépôts. In: *Synthèse Géologique du Sud-Est de la France, Mémoire du BRGM n° 126*. Ed. by S. Debrand-Passard, S. Courbouleix and M.-J. Lienhardt. BRGM France, P1.
- Allemand, P. and J. P. Brun (1991). Width of continental rifts and rheological layering of the lithosphere. *Tectonophysics*, 188 (1-2), pp. 63–69. ISSN: 00401951. DOI: 10.1016/0040-1951(91)90314-I.
- Allen, P. A. and J. R. Allen (2013). *Basin Analysis: Principles and Application to Petroleum Play Assessment*. Vol. 53. 9. John Wiley & Sons, pp. 98–118. ISBN: 9788578110796. DOI: 10.1017/CBO9781107415324.004. arXiv: arXiv:1011.1669v3.
- Allenbach, R. P. and A. Wetzel (2006). Spatial patterns of Mesozoic facies relationships and the age of the Rhenish Lineament: A compilation. *International Journal of Earth Sciences*, 95 (5), pp. 803–813. ISSN: 14373254. DOI: 10.1007/s00531-006-0071-0.
- Allmendinger, R. W. (1998). Inverse and forward numerical modeling of trishear fault-propagation folds. *Tectonics*, 17 (4), pp. 640–656. ISSN: 02787407. DOI: 10.1029/98TC01907.
- Andeweg, B. and S. Cloetingh (1998). Flexure and 'unflexure' of the North Alpine German-Austrian Molasse Basin: constraints from forward tectonic modelling. *Geological Society Special Publication*, 134 (1), pp. 403–422. ISSN: 03058719. DOI: 10.1144/GSL.SP.1998.134.01.19.
- Angevine, C. L., P. L. Heller and C. Paola (1990). Flexure of the Lithosphere. In: *Quantitative Sedimentary Basin Modeling*. AAPG Special Volumes. Chap. Chapter 5, pp. 36–58.
- Aubert, D. (1941). Vallée de Joux (AS 288, 297 bis - 299, La Muratte - Les Mines - Le Lieu - Le Brassus - Le Sentier, CN 1221 Le Sentier), avec annexes des feuilles 291 Vallorbe et 300 Mont-la-Ville. In: *Geological Atlas of Switzerland 1:25000*. Federal Office of Topography (swisstopo). ISBN: 978-3-302-40032-7.
- Aubert, D. and M. Dreyfuss (1963). Orbe (CN 1202). In: *Geological Atlas of Switzerland 1:25000*. Vol. 42. Wabern, Switzerland: Federal Office of Topography (swisstopo).
- Aubert, D. (1971). Le Risoux, un charriage jurassien de grandes dimensions. *Eclogae Geologicae Helveticae*, 64 (1), pp. 152–156. DOI: 10.5169/seals-163975.
- (1975). L'évolution du relief jurassien. *Eclogae Geologicae Helveticae*, 68 (1), pp. 1–64.
- Aufranc, J. and R. Burkhalter (2017). Chasseral (LK 1125). In: *Geological Atlas of Switzerland 1:25000*. Vol. 155. Wabern, Switzerland: Federal Office of Topography (swisstopo). ISBN: 978-3-302-40081-5.
- Aufranc, J., P. Jordan, A. Picquerez, D. Kälin and R. Burkhalter (2016). Bellelay, avec partie de Saignelégier (CN 1105/1104), notice explicative. In: *Geological Atlas of Switzerland 1:25000*. Vol. 147. Wabern, Switzerland: Federal Office of Topography (swisstopo). ISBN: 978-3-302-40079-2.
- Beck, C., E. Deville, E. Blanc, Y. Philippe and M. Tardy (1998). Horizontal shortening control of Middle Miocene marine siliciclastic accumulation (Upper Marine Molasse) in the southern termination of the Savoy Molasse Basin (northwestern Alps/southern Jura). In:

- Cenozoic Foreland Basins of Western Europe*. Ed. by A. Mascle, C. Puigdefàbregas, H. Luterbacher and M. Fernández. Vol. 134. 1. Geological Society of London, pp. 263–278.
- Becker, A. (2000). The Jura Mountains - an active foreland fold-and-thrust belt? *Tectonophysics*, 321 (4), pp. 381–406. ISSN: 00401951. DOI: 10.1016/S0040-1951(00)00089-5.
- Becker, D. (2003). Paléoécologie et paléoclimats de la Molasse du Jura (Oligo-Miocène): apport des Rhinocerotidea (Mammalia) et des minéraux argileux. PhD thesis. Université de Fribourg, p. 329.
- Behrmann, J. H., P. A. Ziegler, S. M. Schmid, B. Heck and M. Granet (2005). The EUCOR-URGENT Project, Upper Rhine Graben: evolution and neotectonics. *International Journal of Earth Sciences (Geologische Rundschau)*, 94, pp. 505–506. DOI: 10.1007/s00531-005-0513-0.
- Beres, M. (2005). *Tektonische Karte der Schweiz 1:500000*. Wabern, Switzerland: Federal Office of Topography (swisstopo). ISBN: 3-906723-56-9.
- Berger, J. P., B. Reichenbacher, D. Becker, M. Grimm, K. Grimm, L. Picot, A. Storni, C. Pirkenseer and A. Schaefer (2005). Eocene-Pliocene time scale and stratigraphy of the Upper Rhine Graben (URG) and the Swiss Molasse Basin (SMB). *International Journal of Earth Sciences*, 94 (4), pp. 711–731. ISSN: 14373254. DOI: 10.1007/s00531-005-0479-y.
- Bergerat, F., M. Cazes, B. Damotte, S. Guellec, J.-L. Mugnier, F. Roure and C. Truffert (1989). Les structures distensives en Bresse d'après les données du profil sismique Jura-Bresse (programme ECORS). *Comptes rendus de l'Académie des sciences. Série 2, Mécanique, Physique, Chimie, Sciences de l'univers, Sciences de la Terre*, 309 (3), pp. 325–332.
- Bergerat, F. (1987). Stress fields in the European platform at the time of Africa-Eurasia collision. *Tectonics*, 6 (2), pp. 99–132. ISSN: 19449194. DOI: 10.1029/TC006i002p00099.
- Bergerat, F., J.-L. Mugnier, S. Guellec, C. Truffert, M. Cazes, B. Damotte and F. Roure (1990). Extensional tectonics and subsidence of the Bresse basin: an interpretation from ECORS data. *Deep structures of the Alps*, 1. Ed. by F. Roure, P. Heitzmann and R. Polino, pp. 145–156.
- Bersier, A. (1932). *Carte tectonique du Jura*. Vol. fasc. I. Wepf, Bâle, planche III.
- BGR (2015). *General Geological Map of the Federal Republic of Germany 1:200,000 (GÜK200) (WMS)*. Bundesanstalt für Geowissenschaften und Rohstoffe, Hannover. URL: <https://services.bgr.de/wms/geologie/guek200/?>.
- Bichet, V. and M. Campy (2016). *Montagnes du Jura, géologie et paysages*. 4th ed. Néo éditions, p. 303. ISBN: 978-2-914741-56-1.
- Bièvre, G. and E. Mercier (2010). The "Bois du Peu" thrust sheets (external French Jura mountains): re-examining the concept of "Fault-Fold". *HAL-INSU: Archives ouvertes*, insu-00442. URL: <https://hal-insu.archives-ouvertes.fr/insu-00442191v2>.
- Blanc, G., B. Doligez, D. Lajat and A. Mascle (1991). Evaluation du potentiel pétrolier des formations paléozoïques de la Bresse et de sa bordure jurassienne, France. *Bulletin de la Société Géologique de France*, 162 (2), pp. 409–422. ISSN: 1777-5817. DOI: 10.2113/gssgfbull.162.2.409.
- Bläsi, H.-R., P. Jordan, H. P. Laubscher, D. Reber and R. Burkhalter (2018). Hauenstein (LK 11088). In: *Geological Atlas of Switzerland 1:25000*. Vol. 158. Wabern, Switzerland: Federal Office of Topography (swisstopo). ISBN: 978-3-302-40096-9.
- Blés, J. L., D. Bonijoly, C. Castaing and Y. Gros (1989). Successive post-Variscan stress fields in the French Massif Central and its borders (Western European plate): comparison with geodynamic data. *Tectonophysics*, 169 (1-3), pp. 79–111. ISSN: 00401951. DOI: 10.1016/0040-1951(89)90185-6.
- Boigk, H. and H. Schöneich (1970). Tiefenlage der Perm-basis im nördlichen Teil des Oberrheingrabens. In: *Graben Problems*. Ed. by J. Illies and S. Mueller. Schweizerbart, Stuttgart, Germany, pp. 45–55.
- (1974). Perm, Trias und älterer Jura im Bereich der südlichen Mittelmeer-Mjösen-Zone und des Rheingrabens. In: *Approaches to Taphrogenesis: proceedings of an International Rift Symposium held in Karlsruhe, April 13-15, 1972 - Inter-Union Commission on Geodynamics, Scientific Report*. Ed. by J. H. Illies and K. Fuchs. Vol. 8. Schweizerbart, Stuttgart, Germany, pp. 60–71.
- Bourgeois, O., M. Ford, M. Diraison, C. Le Carlier de Veslud, M. Gerbault, R. Pik, N. Ruby and S. Bonnet (2007). Separation of rifting and lithospheric folding signatures in the NW-Alpine foreland. *International Journal of Earth Sciences*, 96 (6), pp. 1003–1031. ISSN: 14373254. DOI: 10.1007/s00531-007-0202-2.
- Boutoux, A., N. Bellahsen, U. Nanni, R. Pik, A. Verlaquet, Y. Rolland and O. Lacombe (2016). Thermal and structural evolution of the external Western Alps: Insights from (U-Th-Sm)/He thermochronology and RSCM thermometry in the Aiguilles Rouges/Mont Blanc massifs. *Tectonophysics*, 683, pp. 109–123. ISSN: 00401951. DOI: 10.1016/j.tecto.2016.06.010.
- Boyer, S. E. and D. Elliott (1982). Thrust systems. *American Association of Petroleum Geologists Bulletin*, 66 (9), pp. 1196–1230. ISSN: 01491423. DOI: 10.1306/03B5A77D-16D1-11D7-8645000102C1865D.
- Bradley, D. C. and W. Kidd (1991). Flexural extension of the upper continental crust in collisional foredeeps. *Geo-*

- logical Society of America Bulletin*, 103 (11), p. 1416. ISSN: 0016-7606. DOI: 10.1130 / 0016 - 7606(1991) 103<1416:FEOTUC>2.3.CO;2.
- BRGM (1955). *Briod1 coupe technique géologique, planche II 2939*. Tech. rep. Bureau de Recherches Géologiques et Minières (BRGM).
- (2004). *Cartes géologiques à 1/50000 format "vecteurs"*. Bureau de recherches géologiques et minières (BRGM). URL: infoterre.brgm.fr.
- Brun, J. P., M. A. Gutscher and DEKORP-ECORS-teams (1992). Deep crustal structure of the Rhine Graben from DEKORP-ECORS seismic reflection data: a summary. *Tectonophysics*, 208 (1-3), pp. 139–147. ISSN: 00401951. DOI: 10.1016/0040-1951(92)90340-C.
- Büchi, U., K. Lemcke, G. Wiener and J. Zimdras (1965). Geologische Ergebnisse der Erdölexploration auf das Mesozoikum im Untergrund des schweizerischen Molassebeckens. *Bulletin der Vereinigung Schweiz. Petroleum-Geologen und -Ingenieure*, 32, pp. 7–38.
- Bugnicourt, D. and P. Michel (1953). *Log fondamental de sondage Bresse 2 1/2000, 16-1017*. Tech. rep. Régie Autonome des Pétroles (RAP).
- Burkhard, M. (1990). Aspects of the large-scale Miocene deformation in the most external part of the Swiss Alps (Subalpine Molasse to Jura fold belt). *Eclogae Geologicae Helvetiae*, 83 (3), pp. 559–583. DOI: 10.5169/seals-166602.
- Burkhard, M. and A. Sommaruga (1998). Evolution of the western Swiss Molasse basin: structural relations with the Alps and the Jura belt. In: *Geological Society Special Publication*. Ed. by A. Mascle, A. Puigdefàbregas, H. Luterbacher and M. Fernandez. Vol. 134. Geological Society Special Publications. Chap. 134, pp. 279–298. DOI: 10.1144/GSL.SP.1998.134.01.13.
- Burov, E. B. and M. Diament (1995). The effective elastic thickness (T_e) of continental lithosphere: what does it really mean? *Journal of Geophysical Research*, 100 (B3), pp. 3905–3927. ISSN: 01480227. DOI: 10.1029/94JB02770.
- Buxtorf, A. (1907). Zur Tektonik des Kettenjura. *Bericht der Versammlung des Oberrheinischen Geologischen Vereins*, 40, pp. 29–38.
- (1916). Prognosen und Befunde beim Hauensteinbasis- und Grenchenbergtunnel und die Bedeutung der Letzteren für die Geologie des Juragebirges. *Verhandlungen der Naturforschenden Gesellschaft in Basel*, 27, pp. 184–254.
- Caër, T. (2016). Interprétation structurale et équilibre mécanique: Le calcul à la rupture appliqué aux chaînes d'avant-pays. PhD thesis. Université de Cergy-Pontoise, 258 p.
- Caër, T., P. Souloumiac, B. Maillot, P. Leturmy and C. Nussbaum (2018). Propagation of a fold-and-thrust belt over a basement graben. *Journal of Structural Geology*, 115, pp. 121–131. ISSN: 01918141. DOI: 10.1016/j.jsg.2018.07.007.
- Caillon, G. and P. Michel (1955). *Rapport de fin de sondage Bresse 104 (Br.104 bis) 1/2000, 16-1024A*. Tech. rep. Régie Autonome des Pétroles (RAP).
- Carrel, C. (1969). *Rapport de fin de sondage de Simandre 101 Ma. Sim. 101 1/500, coupe géologique later-log, Pl. N°1*. Tech. rep. Société Nationale des Pétroles d'Aquitaine (SNPA).
- Chauve, P. (1975). *Jura: guides géologiques régionaux*. Masson, Issy les Moulineaux, France.
- Chauve, P., R. Enay, P. Fluck, C. Sittler and J. B. Edel (1980). France, Introduction à la géologie de l'est: Vosges, Fossé Rhénan, Bresse, Jura. *26th International Geological Congress*, 4 (1), pp. 3–80.
- Chauve, P. and J. Perriaux (1974). Le jura. In: *Géologie de la France: les chaînes plissées du cycle alpin et leur avant-pays*. Ed. by J. Debelmas. Vol. 2. Doin, Paris. Chap. Le Jura, pp. 443–464.
- Chauve, P., J. Martin, E. Petitjean and F. Sequeiros (1988). Le chevauchement du Jura sur la Bresse. Données nouvelles et réinterprétation des sondages. *Bulletin de la Société Géologique de France*, IV (5), pp. 861–870. ISSN: 1777-5817. DOI: 10.2113/gssgfbull.IV.5.861.
- Cohen, K. M., D. A. T. Harper, P. L. Gibbard and J.-X. Fan (2020). The ICS International Chronostratigraphic Chart. *Episodes* 36, pp. 199–204. URL: <http://www.stratigraphy.org>.
- COPEFA (1960). *Log final du sondage Eternoz 1 "ET.1", 16-1127*. Tech. rep. Compagnie des Pétroles France-Afrique (COPEFA).
- Coromina, G. and O. Fabbri (2004). Late Palaeozoic NE-SW ductile-brittle extension in the La Serre horst, eastern France. *Comptes Rendus Geoscience*, 336 (1), pp. 75–84. ISSN: 16310713. DOI: 10.1016/j.crte.2003.09.019.
- Dahlen, F. A. (1990). Critical taper model of fold-and-thrust belts and accretionary wedges. *Annual Review of Earth & Planetary Sciences*, 18 (1), pp. 55–99. DOI: 10.1146/annurev.ea.18.050190.000415.
- Davis, D., J. Suppe and F. Dahlen (1983). Mechanics of fold-and-thrust belts and accretionary wedges. *Journal of Geophysical Research: Solid Earth*, 88 (B2), pp. 1153–1172. DOI: 10.1029/JB088iB02p01153.
- Debrand-Passard, S., S. Courbouleix and M.-J. Lienhardt (1984). *Synthèse géologique du Sud-Est de la France*. Mémoire BRGM France, n° 125, p. 615.
- Decelles, P. G. (2012). Foreland basin systems revisited: variations in Response to Tectonic Settings. In: *Tectonics of Sedimentary Basins: Recent Advances*. Ed. by C. Busby and A. A. Pérez. Blackwell Publishing Ltd.

- Chichester, UK, pp. 405–426. ISBN: 9781405194655. DOI: 10.1002/9781444347166.ch20.
- DeCelles, P. G. and K. A. Giles (1996). Foreland basin systems. *Basin Research*, 8 (2), pp. 105–123. ISSN: 0950091X. DOI: 10.1046/j.1365-2117.1996.01491.x.
- Delmas (1965). *Rapport de fin de sondage de H.J. Es-savilly 101, coupe géologique, 16-1178*. Tech. rep. Société Nationale des Pétroles d'Aquitaine (SNPA).
- Delmas, M. and R. Iriarte (1965). *Rapport de fin de sondage Ornans 1 DP 110, Coupe géologique, Pl. 1*. Tech. rep. Mines domaniales de potasse d'Alsace (MDPA) / Soc Nationale Petr d'Aquitaine (SNPA).
- Deville, E. (2021). Structure of the Tectonic Front of the Western Alps: Control of Fluid Pressure and Halite Occurrence on the Decollement Processes. *Tectonics*, pp. 1–21. ISSN: 0278-7407. DOI: 10.1029/2020TC006591.
- Deville, E., E. Blanc, M. Tardy, C. Beck, M. Cousin and G. Ménard (1994). Thrust Propagation and Syntectonic Sedimentation in the Savoy Tertiary Molasse Basin (Alpine Foreland). In: *Hydrocarbon and Petroleum Geology of France*. Springer, pp. 269–280. DOI: 10.1007/978-3-642-78849-9_19.
- Dèzes, P., S. M. Schmid and P. A. Ziegler (2004). Evolution of the European Cenozoic Rift System: interaction of the Alpine and Pyrenean orogens with their foreland lithosphere. *Tectonophysics*, 389 (1-2), pp. 1–33. ISSN: 00401951. DOI: 10.1016/j.tecto.2004.06.011.
- Dèzes, P. and P. A. Ziegler (2002). *EUCOR URGENT: Moho depth map of Western and Central Europe*. Tech. rep. University of Basel. URL: <http://www.unibas.ch/eucor-urgent>.
- Diebold, P., H. Naef and M. Ammann (1991). *NTB 90-04, Zur Tektonik der zentralen Nordschweiz: Interpretation aufgrund regionaler Seismik, Oberflächen-Geologie und Tiefbohrungen*. Tech. rep. Wettingen, Switzerland: Nationale Genossenschaft für die Lagerung radioaktiver Abfälle (Nagra). URL: <http://www.nagra.ch>.
- Diebold, P. and T. Noack (1997). Late Palaeozoic troughs and Tertiary Structures in the eastern Folded Jura. In: *Deep Structure of the Swiss Alps - Results of NRP 20*. Ed. by O. A. Pfiffner, P. Lehner, P. Heitzmann, S. Mueller and A. Steck. Vol. 20. Birkhäuser Verlag, Basel, pp. 59–63. ISBN: 3-7643-5254-X.
- Doebl, F. and W. Olbrecht (1974). An Isobath Map of the Tertiary Base in the Rhinegraben. In: *Approaches to Taphrogenesis, Inter-Union Commission on Geodynamics, Scientific report No. 8*. Ed. by J. H. Illies and K. Fuchs. Schweizerbart, Stuttgart, Germany, pp. 71–72.
- Doglionni, C. (1995). Geological remarks on the relationships between extension and convergent geodynamic settings. *Tectonophysics*, 252 (1-4), pp. 253–267. ISSN: 00401951. DOI: 10.1016/0040-1951(95)00087-9.
- Duplaix, S. and S. Guillaume (1962). Étude stratigraphique et minéralogique de formations Tertiaires du Jura. *Revue de Géographie Physique et de Géologie Dynamique*, 5 (1), pp. 37–54.
- Edel, J. B. and P. Fluck (1989). The upper Rhenish Shield basement (Vosges, Upper Rhinegraben and Schwarzwald): Main structural features deduced from magnetic, gravimetric and geological data. *Tectonophysics*, 169 (4), pp. 303–316. ISSN: 00401951. DOI: 10.1016/0040-1951(89)90093-0.
- Edel, J. B., K. Schulmann, E. Skrzypek and A. Cocherie (2013). Tectonic evolution of the European Variscan belt constrained by palaeomagnetic, structural and anisotropy of magnetic susceptibility data from the Northern Vosges magmatic arc (eastern France). *Journal of the Geological Society*, 170 (5), pp. 785–804. ISSN: 00167649. DOI: 10.1144/jgs2011-138.
- Edel, J. B., H. Whitechurch and M. Diraison (2006). Seismicity wedge beneath the Upper Rhine Graben due to backwards Alpine push? *Tectonophysics*, 428 (1-4), pp. 49–64. ISSN: 00401951. DOI: 10.1016/j.tecto.2006.08.009.
- Egli, D., H. Madritsch, J. Mosar and W. Müller (2017). *AN 17-751, U/Pb dating of synkinematic calcite fibres from the Randen fault (NE Switzerland): implications for geodynamics of the northwestern Alpine foreland*. Tech. rep. Wettingen, Switzerland (unpublished): Nationale Genossenschaft für die Lagerung radioaktiver Abfälle (Nagra), p. 9.
- Egli, D., J. Mosar, T. Ibele and H. Madritsch (2016). The role of precursory structures on Tertiary deformation in the Black Forest-Hegau region. *International Journal of Earth Sciences*, pp. 1–22. ISSN: 1437-3262. DOI: 10.1007/s00531-016-1427-8.
- Erslev, E. A. (1991). Trishear fault-propagation folding. *Geology*, 19 (6), pp. 617–620. ISSN: 0091-7613. DOI: 10.1130/0091-7613(1991)019<0617:TFPF>2.3.CO;2.
- ESSO REP (1970). *Log fondamental au 1/500 Faucigny 1, 16-1193*. Tech. rep. Société Esso Recherche et Exploit (ESSO REP).
- (1989). *Log fondamental au 1/500 La Chandelière 1d*. Tech. rep. Société Esso Recherche et Exploit (ESSO REP).
- Faber, S., K. -P. Bonjer, W. Brüstle and N. Deichmann (1994). Seismicity and structural complexity of the Dinkelberg block, southern Rhine Graben. *Geophysical Journal International*, 116 (2), pp. 393–408. ISSN: 1365246X. DOI: 10.1111/j.1365-246X.1994.tb01805.x.
- Ford, M., S. Duchêne, D. Gasquet and O. Vanderhaeghe (2006). Two-phase orogenic convergence in the external and internal SW Alps. *Journal of the Geological Society*, 163 (5), pp. 815–826. ISSN: 00167649. DOI: 10.1144/0016-76492005-034.

- Fournier, E. (1922). Sur la structure tectonique profonde des Avant-Monts du Jura. *Bulletin de la Société géologique France*, 4 (XXII), p. 225.
- Gehring, A., P. Keller and F. Heller (1991). Paleomagnetism and tectonics of the Jura arcuate mountain belt in France and Switzerland. *Tectonophysics*, 186, pp. 269–278.
- Glangeaud, L. (1944). Le rôle des failles dans la structure du jura externe (pincée, faille-plis et gouttières). *Bulletin de la société d'histoire naturelle du Doubs*, 51, pp. 17–33.
- Glangeaud, L. (1951). Interprétation tectono-physique des caractères structuraux et paléogéographiques de la Méditerranée occidentale. *Bulletin de la Société Géologique de France*, 6 (8), pp. 735–762. ISSN: 1777-5817. DOI: 10.2113/gssgfbull.S6-I.8.735.
- Grad, M., T. Tiira and E. S. C. W. Group (2009). The Moho depth map of the European Plate. *Geophysical Journal International*, 176 (1), pp. 279–292.
- Granado, P., W. Thöny, N. Carrera, O. Gratzer, P. Strauss and J. A. Muñoz (2016). Basement-involved reactivation in foreland fold-and-thrust belts: The Alpine-Carpathian Junction (Austria). *Geological Magazine*, 153 (5-6), pp. 1110–1135. ISSN: 14695081. DOI: 10.1017/S0016756816000066.
- Green, A. G., K. Merz, U. Marti and T. Spillmann (2013). *NAB 13-40, Gravity Data in Northern Switzerland and Southern Germany*. Tech. rep. Wettingen, Switzerland: Nationale Genossenschaft für die Lagerung radioaktiver Abfälle (Nagra). URL: <http://www.nagra.ch>.
- Gruber, M. (2017). Structural Investigations of the Western Swiss Molasse Basin - From 2D Seismic Interpretation to a 3D Geological Model. PhD thesis. Université de Fribourg, 190 pp.
- Guellec, S., J.-L. Mugnier, M. Tardy and F. Roure (1990). Neogene evolution of the western Alpine foreland in the light of ECORS data and balanced cross sections. In: *Deep structures of the Alps*. Ed. by F. Roure, P. Heitzmann and R. Polino. 1st ed. Mémoires de la Société géologique suisse, pp. 165–184.
- Guillong, M., J. Wotzlaw, N. Looser and O. Laurent (2020). Evaluating the reliability of U-Pb laser ablation inductively coupled plasma mass spectrometry (LA-ICP-MS) carbonate geochronology: matrix issues and a potential calcite validation reference material. *Geochronology*, 2 (1), pp. 155–167. DOI: 10.5194/gchron-2-155-2020.
- Gutscher, M.-A. -A. (1995). Crustal structure and dynamics in the Rhine Graben and the Alpine foreland. *Geophysical Journal International*, 122 (2), pp. 617–636. ISSN: 1365246X. DOI: 10.1111/j.1365-246X.1995.tb07016.x.
- Hauber, L. (1993). Der südliche Rheingraben und seine geothermische Situation. *Bulletin der Vereinigung Schweizerischer Petroleum-Geologen und Ingenieure*, 60 (137), pp. 53–69. DOI: 10.5169/seals-216879.
- Heidbach, O. and J. Reinecker (2013). *NAB 12-05, Analyse des rezenten Spannungsfelds der Nordschweiz*. Tech. rep. Wettingen, Switzerland: Nationale Genossenschaft für die Lagerung radioaktiver Abfälle (Nagra). URL: <http://www.nagra.ch>.
- Heidbach, O., M. Rajabi, K. Reiter, M. Ziegler and W. S. M. Team (2016). World Stress Map Database Release 2016. *GFZ Data Services*. DOI: 10.5880/WSM.2016.001.
- Heritier, F. (1994). A history of petroleum exploration in France. In: *Hydrocarbon and Petroleum Geology of France*. Springer, pp. 29–45.
- Hindle, D. and M. Burkhard (1999). Strain, displacement and rotation associated with the formation of curvature in fold belts; the example of the Jura arc. *Journal of Structural Geology*, 21 (8-9), pp. 1089–1101. ISSN: 01918141. DOI: 10.1016/S0191-8141(99)00021-8.
- Homberg, C., F. Bergerat, Y. Philippe, O. Lacombe and J. Angelier (2002). Structural inheritance and cenozoic stress fields in the Jura fold-and-thrust belt (France). *Tectonophysics*, 357 (1-4), pp. 137–158. ISSN: 00401951. DOI: 10.1016/S0040-1951(02)00366-9.
- Hooker, J. J. and M. Weidmann (2000). *The Eocene Mammal Faunas of Mormont, Switzerland: Systematic Revision and Resolutions of Dating Problems*. Vol. 120. Kommission der Schweizerischen Paläontologischen Abhandlungen, pp. 1–143.
- Hooker, J. J. and M. Weidmann (2007). A diverse rodent fauna from the middle Bartonian (Eocene) of les alleveys, Switzerland: Snapshot of the early theridomyid radiation. *Swiss Journal of Geosciences*, 100 (3), pp. 469–493. ISSN: 16618734. DOI: 10.1007/s00015-007-1241-1.
- IGN-F (2018). *MNT RGE ALTI 5m, Digital Elevation Models*. Institut national de l'information géographique et forestière (IGN-F). URL: <http://www.ign.fr>.
- Illies, H. (1962). Oberrheinisches Grundgebirge und Rheingraben. *Geologische Rundschau*, 52 (1), pp. 317–332. ISSN: 14373262. DOI: 10.1007/BF01840083.
- Illies, J. H. (1972). The Rhine graben rift system-plate tectonics and transform faulting. *Geophysical Surveys*, 1 (1), pp. 27–60. ISSN: 00465763. DOI: 10.1007/BF01449550.
- Jordan, P. (1992). Evidence for large-scale decoupling in the Triassic evaporites of northern Switzerland: an overview. *Eclogae Geologicae Helveticae*, 85 (3), pp. 677–693. DOI: 10.5169/seals-167025.
- (1994). *Evaporite als Abscheehorizonte*. Vol. 164. Schweizerische Geologische Kommission.
- (2016). Reorganisation of the Triassic stratigraphic nomenclature of northern Switzerland: overview and the

- new Dinkelberg, Kaiseraugst and Zeglingen formations. *Swiss Journal of Geosciences*, 109 (2), pp. 241–255. ISSN: 1661-8726. DOI: 10.1007/s00015-016-0209-4.
- Jordan, P. and R. Nuesch (1989). Deformation Structures in the Muschelkalk Anhydrites of the Schafisheim Well (Jura Overthrust, Northern Switzerland). *Eclogae Geologicae Helveticae*, 82 (2), pp. 429–454. ISSN: 0012-9402. DOI: 10.5169/seals-166384.
- Jordan, P., J. S. Pietsch, H. Bläsi, H. Furrer, N. Kündig, N. Looser, A. Wetzel and G. Deplazes (2016). The middle to late Triassic Bänkerjoch and Klettgau formations of northern Switzerland. *Swiss Journal of Geosciences*, 109 (2), pp. 257–284. ISSN: 1661-8726. DOI: 10.1007/s00015-016-0218-3.
- Kälin, D. (1997). Litho- und Biostratigraphie der mittel- bis obermiozänen Bois de Raube-Formation (Nordwestschweiz). *Eclogae Geologicae Helveticae*, 90 (1), pp. 97–114. ISSN: 00129402.
- Kälin, D. and B. Engesser (2001). Die jungmiozäne Säugetierfauna vom Nebelbergweg bei Nunningen (Kanton Solothurn, Schweiz). *Schweizerische Paläontologische Abhandlungen*, 121, pp. 1–61.
- Karner, G. D. and A. B. Watts (1983). Gravity anomalies and flexure of the lithosphere at mountain ranges. *Journal of Geophysical Research*, 88 (B12), pp. 10449–10477. ISSN: 01480227. DOI: 10.1029/JB088iB12p10449.
- Keller, W. and H. Liniger (1930). Movelier - Soyhières - Delémont - Courrendlin (SA 92 - 95). In: *Geological Atlas of Switzerland 1:25000*. Vol. 1. Wabern, Switzerland: Federal Office of Topography (swisstopo).
- Klingelé, E. and H. Schwendener (1984). *NTB 84-22, Geophysikalisches Untersuchungsprogramm Nordschweiz: Gravimetrische Messungen*. Tech. rep. Wettingen, Switzerland: Nationale Genossenschaft für die Lagerung radioaktiver Abfälle (Nagra). URL: <http://www.nagra.ch>.
- Kusznir, N. J., G. Marsden and S. S. Egan (1991). A flexural-cantilever simple-shear/pure-shear model of continental lithosphere extension: Applications to the Jeanne d'Arc Basin, Grand Banks and Viking Graben, North Sea. *Geological Society Special Publication*, 56 (1), pp. 41–60. ISSN: 03058719. DOI: 10.1144/GSL.SP.1991.056.01.04.
- Landesgeologie (2017). *GeoMol: Geologisches 3D-Modell des Schweizer Molassebeckens - Schlussbericht*. Vol. 10. Wabern, Switzerland: Federal Office of Topography (swisstopo), 128 pp. ISBN: 978-3-302-40109-6. URL: <https://viewer.geomol.ch>.
- Larroque, J. M. and P. Laurent (1988). Evolution of the stress field pattern in the south of the Rhine Graben from the Eocene to the present. *Tectonophysics*, 148 (1-2), pp. 41–58. ISSN: 00401951. DOI: 10.1016/0040-1951(88)90159-X.
- Laubscher, H. (2008a). 100 years Jura décollement hypothesis: How it affects Steinmann's (1892) "Schwarzwaldlinie". *International Journal of Earth Sciences*, 97 (6), pp. 1231–1245. ISSN: 14373254. DOI: 10.1007/s00531-007-0224-9.
- (2008b). The Grenchenberg conundrum in the Swiss Jura: a case for the centenary of the thin-skin décollement nappe model (Buxtorf 1907). *Swiss Journal of Geosciences*, 101 (1), pp. 41–60. ISSN: 1661-8726. DOI: 10.1007/s00015-008-1248-2.
- Laubscher, H. P. (1961). Die Fernschubhypothese der Jurafaltung. *Eclogae Geologicae Helveticae*, 54, pp. 222–282. DOI: 10.5169/seals-162820.
- (1965). Ein kinematisches Modell der Jurafaltung. *Eclogae Geologicae Helveticae*, 58, pp. 232–318. DOI: 10.5169/seals-163266.
- (1970). *Grundsätzliches zur Tektonik des Rheingrabens*.
- (1972). Some overall aspects of Jura dynamics. *American Journal of Science*, 272 (4), pp. 293–304. ISSN: 0002-9599. DOI: 10.2475/ajs.272.4.293.
- (1981). The 3D propagation of décollement in the Jura. *Geological Society Special Publication*, 9 (1), pp. 311–318. ISSN: 03058719. DOI: 10.1144/GSL.SP.1981.009.01.27.
- (1982). Die Südostecke des Rheingrabens - ein kinematisches und dynamisches Problem. *Eclogae Geologicae Helveticae*, 75 (1), pp. 101–116. DOI: 10.5169/seals-165219.
- (1985). Large-scale, thin-skinned thrusting in the southern Alps: Kinematic models. *Geological Society of America Bulletin*, 96, pp. 710–718.
- (1986). The eastern Jura: Relations between thin-skinned and basement tectonics, local and regional. *Geologische Rundschau*, 75 (3), pp. 535–553. ISSN: 0016-7853. DOI: 10.1007/BF01820630.
- (1992). Jura kinematics and the Molasse Basin. *Eclogae Geologicae Helveticae*, 85 (3), pp. 653–675. DOI: 10.5169/seals-167024.
- Lefavrais-Raymond, A. (1962). Contribution à l'étude géologique de la Bresse d'après les sondages profonds. *Mémoires du Bureau de Recherches Géologiques et Minières*, 16, 170 p.
- Lefort, J. P. and B. N. Agarwal (1996). Gravity evidence for an Alpine buckling of the crust beneath the Paris Basin. *Tectonophysics*, 258 (1-4), pp. 1–14. ISSN: 00401951. DOI: 10.1016/0040-1951(95)00148-4.
- (2002). Topography of the Moho undulations in France from gravity data: Their age and origin. *Tectonophysics*, 350 (3), pp. 193–213. ISSN: 00401951. DOI: 10.1016/S0040-1951(02)00114-2.
- Leloup, P. H., N. Arnaud, E. R. Sobel and R. Lacassin (2005). Alpine thermal and structural evolution of the highest external crystalline massif: The Mont Blanc. *Tectonics*, 24 (4), pp. 1–26. ISSN: 02787407. DOI: 10.1029/2004TC001676.

- Lemcke, K. (1974). Vertikalbewegungen des vormesozoischen Sockels im nördlichen Alpenvorland vom Perm bis zur Gegenwart. *Eclogae Geologicae Helvetiae*, 67 (1), pp. 121–133. DOI: 10.5169/seals-164283.
- Leu, W. (2008). *NAB 08-49, Permokarbon-Kartenskizze (Rohstoffe), Kompilation eines GIS-Datensatzes auf der Basis von bestehenden Unterlagen (Bereich Schweizer Mittelland)*. Tech. rep. Wettingen, Switzerland: Nationale Genossenschaft für die Lagerung radioaktiver Abfälle (Nagra). URL: <http://www.nagra.ch>.
- LGRB (2019). *GeoMol MapViewer*. Tech. rep. Landesamt für Geologie, Rohstoffe und Bergbau (LGRB). URL: <http://maps.geomol.eu>.
- Lienhardt, G. (1962). *Géologie du bassin houiller stéphanien du Jura et de ses morts-terrains*. Editions Technip, Paris, 449 pp.
- Looser, N., H. Madritsch, M. Guillon, O. Laurent, S. Wohlwend and S. M. Bernasconi (2020). Absolute Age and Temperature Constraints on Faulting along the Basal Décollement of the Jura Fold-and-thrust Belt from carbonate U-Pb Dating and Clumped Isotopes. *Tectonics*. DOI: 10.1002/Essoar.10503905.1.
- Lorenzo, J. M., G. W. O'Brien, J. Stewart and K. Tandon (1998). Inelastic yielding and forebulge shape across a modern foreland basin: North West Shelf of Australia, Timor Sea. *Geophysical Research Letters*, 25 (9), pp. 1455–1458. ISSN: 00948276. DOI: 10.1029/98GL01012.
- Madritsch, H. (2008). Structural evolution and neotectonics of the Rhine-Bresse transfer zone. PhD thesis. Universität Basel, 178 p. DOI: 10.5451/unibas-004648278.
- Madritsch, H. and G. Deplazes (2014). *NTB 14-02, SGT Etappe 2: Vorschlag weiter zu untersuchender geologischer Standortgebiete mit zugehörigen Standortarealen für die Oberflächenanlage - Geologische Grundlagen - Dossier II Sedimentologische und tektonische Verhältnisse*. Tech. rep. Wettingen, Switzerland: Nationale Genossenschaft für die Lagerung radioaktiver Abfälle (Nagra). URL: <http://www.nagra.ch>.
- Madritsch, H., O. Fabbri, E. M. Hagedorn, F. Preusser, S. M. Schmid and P. A. Ziegler (2010). Feedback between erosion and active deformation: geomorphic constraints from the frontal Jura fold-and-thrust belt (eastern France). *International Journal of Earth Sciences*, 99 (Suppl. 1), pp. 103–122. ISSN: 14373262. DOI: 10.1007/s00531-009-0468-7.
- Madritsch, H., A. Kounov, S. M. Schmid and O. Fabbri (2009). Multiple fault reactivations within the intra-continental Rhine-Bresse Transfer Zone (La Serre Horst, eastern France). *Tectonophysics*, 471 (3-4), pp. 297–318. ISSN: 0040-1951. DOI: 10.1016/j.tecto.2009.02.044.
- Madritsch, H., H. Naef, B. Meier, H. J. Franzke and G. Schreurs (2018). Architecture and Kinematics of the Constance-Frick Trough (Northern Switzerland): Implications for the Formation of Post-Variscan Basins in the Foreland of the Alps and Scenarios of Their Neogene Reactivation. *Tectonics*, 37 (7), pp. 2197–2220. ISSN: 19449194. DOI: 10.1029/2017TC004945.
- Madritsch, H., S. M. Schmid and O. Fabbri (2008). Interactions between thin- and thick-skinned tectonics at the northwestern front of the Jura fold-and-thrust belt (eastern France). *Tectonics*, 27. ISSN: 02787407. DOI: 10.1029/2008TC002282.
- Malz, A., H. Madritsch, P. Jordan, B. Meier and J. Kley (2019). Along-strike variations in thin-skinned thrusting style controlled by pre-existing basement structure in the easternmost Jura Mountains (Northern Switzerland). In: *Geological Society, London, Special Publications*. Vol. 490. 1. Geological Society of London, pp. 199–220. DOI: 10.1144/SP490-2019-090.
- Malz, A., H. Madritsch, B. Meier and J. Kley (2016). An unusual triangle zone in the external northern Alpine foreland (Switzerland): Structural inheritance, kinematics and implications for the development of the adjacent Jura fold-and-thrust belt. *Tectonophysics*, 670, pp. 127–143. ISSN: 00401951. DOI: 10.1016/j.tecto.2015.12.025.
- Martellet, G., M. Sarraillh and N. Debeglia (2007). *Gravity and positioning control for the revision of the French gravity map and network*. Tech. rep. Bureau de recherches géologiques et minières (BRGM), p. 6.
- Marti, J. (1963). *Rapport de fin de sondage de Gigny 101 (Ma. Gi. 101) 1/500, F. S. N°581*. Tech. rep. Société Nationale des Pétroles d'Aquitaine (SNPA).
- (1969). *Log habille Humilly 2, rapport de fin de sondage N773, 16-1185*. Société Nationale des Pétroles d'Aquitaine (SNPA).
- Martin, J. and É. Mercier (1996). Héritage distensif et structuration chevauchante dans une chaîne de couverture: apport de l'équilibrage par modélisation géométrique dans le Jura nord-occidental. *Bulletin de la Société géologique de France*, 167 (1), pp. 101–110. ISSN: 00379409.
- Mazurek, M., D. W. Davis, H. Madritsch, D. Rufer, I. M. Villa, C. N. Sutcliffe, A. De Haller and D. Traber (2018). Veins in clay-rich aquitards as records of deformation and fluid-flow events in northern Switzerland. *Applied Geochemistry*, 95, pp. 57–70. ISSN: 0883-2927. DOI: 10.1016/j.apgeochem.2018.05.010.
- Meier, B. (2010). *NAB 10-40, Ergänzende Interpretation reflexionsseismischer Linien zwischen dem östlichen und westlichen Molassebecken: Gebiete Waadtland Nord, Fribourg, Berner Seeland und Jurasüdfuss zwischen Biel und Oensingen (Text und Beilage)*. Tech. rep. Wettingen, Switzerland: Nationale Genossenschaft für die Lagerung radioaktiver Abfälle (Nagra). URL: <http://www.nagra.ch>.
- Meschede, M. (1994). *Methoden der Strukturgeologie: ein Leitfaden zur Aufnahme und Auswertung strukturgeo-*

- logischer Daten im Gelände und im Labor*. Enke, Stuttgart, p. 169. ISBN: 3432262914.
- Metz, R. (1970). Dehnungsstrukturen im Grundgebirge des Schwarzwalds vor Beginn der Grabentektonik. *Graben problems. Schweizerbart, Stuttgart*, pp. 79–86.
- Michel, P., G. Appert, J. Lavigne, A. Lefavrais, A. Bonte, G. Liénhardt and J. Ricour (1953). Le contact Jura-Bresse dans la région de Lons-le-Saunier. *Bulletin de la Société géologique de France*, 6 (7-8), pp. 593–611. ISSN: 0037-9409. DOI: 10.2113/gssgfbull.s6-iii.7-8.593.
- Michon, L. (2000). Dynamique de l'extension continentale - Application au Rift Ouest-Européen par l'étude de la province du Massif Central. PhD thesis. Université Blaise Pascal, p. 266.
- Mock, S., C. von Hagke, F. Schlunegger, I. Dunkl and M. Herwegh (2019). Late Miocene thrusting in the North Alpine foreland: Driven by a deep-seated process and shaped by the local mechanical stratigraphy. *Solid Earth Discussions*, pp. 1–32. ISSN: 1869-9510. DOI: 10.5194/se-2019-56.
- Mojon, P. O., E. De Kaenel, D. Kälin, D. Becker, C. M. Pirkenseer, G. Rauber, K. Ramseyer, B. Hostettler and M. Weidmann (2018). New data on the biostratigraphy (charophytes, nannofossils, mammals) and lithostratigraphy of the Late Eocene to Early Late Miocene deposits in the Swiss Molasse Basin and Jura Mountains. *Swiss Journal of Palaeontology*, 137 (1), pp. 1–48. ISSN: 16642384. DOI: 10.1007/s13358-017-0145-6.
- Mosar, J. (1999). Present-day and future tectonic underplating in the western Swiss Alps: reconciliation of basement/wrench-faulting and décollement folding of the Jura and Molasse basin in the Alpine foreland. *Earth and Planetary Science Letters*, 173 (3), pp. 143–155. ISSN: 0012821X. DOI: 10.1016/S0012-821X(99)00238-1.
- Mugnier, J. L. and P. Vialon (1984). The mechanisms of overlapping of the Bresse graben by the Jura formations in the Vignoble area (France). *Tectonophysics*, 106 (1-2), pp. 155–163. ISSN: 00401951. DOI: 10.1016/0040-1951(84)90226-9.
- (1986). Deformation and displacement of the Jura cover on its basement. *Journal of Structural Geology*, 8 (3-4), pp. 373–387. ISSN: 01918141. DOI: 10.1016/0191-8141(86)90056-8.
- Muhlethaler, C. (1930). La Chaux - Les Verrières (AS 276 - 277). In: *Geological Atlas of Switzerland 1:25000*. Vol. 2. Wabern, Switzerland: Federal Office of Topography (swisstopo).
- Müller, W. H., S. M. Schmid and U. Briegel (1981). Deformation experiments on anhydrite rocks of different grain sizes: Rheology and microfabric. *Tectonophysics*, 78 (1-4), pp. 527–543. ISSN: 00401951. DOI: 10.1016/0040-1951(81)90027-5.
- Nagra (1990). *NTB 88-09, Sondierbohrung Riniken Untersuchungsbericht, Beilagenband*. Tech. rep. Wettingen, Switzerland: Nationale Genossenschaft für die Lagerung radioaktiver Abfälle (Nagra). URL: <http://www.nagra.ch>.
- NASA (2014). *Shuttle Radar Topography Mission, 1-Arc Second scene*. College Park, Maryland: United States Geological Survey (USGS).
- Naylor, M. A., J. M. Larroque and B. D. M. Gauthier (1994). Understanding extensional tectonics: insights from sand-box models. In: *Geodynamic Evolution of Sedimentary Basins - International Symposium, Moscow, May 18-23, 1992*. Ed. by F. Roure, N. Ellouz, V. Shein and I. Skvortsov. Éditions Technip, pp. 69–83. ISBN: 9782710806929.
- Noack, T. (1995). Thrust development in the eastern Jura Mountains related to pre-existing extensional structures. *Tectonophysics*, 252 (1-4), pp. 419–431. ISSN: 00401951. DOI: 10.1016/0040-1951(95)00089-5.
- Nussbaum, C., A. Kloppenburg, T. Caër and P. Bossart (2017). Tectonic evolution around the Mont Terri rock laboratory, northwestern Swiss Jura: constraints from kinematic forward modelling. *Swiss Journal of Geosciences*, 110 (1), pp. 39–66. ISSN: 16618734. DOI: 10.1007/s00015-016-0248-x.
- Olivier, R., B. Dumont and E. Klingelé (2010). Atlas gravimétrique de la Suisse. *Beiträge zur Geologie der Schweiz, v. Geophysik*, 40, 62pp.
- Otto, S. (1994). *Bresse-Valence Basin & Jura Foldbelt*. Basin Monitor Group, Petroconsultants (UK).
- Pasquier, F., M. Burkhard, P.-O. Mojon and S. Gogniat (2013). Travers (LK1163), notice explicative. In: *Geological Atlas of Switzerland 1:25000*. Vol. 162. Wabern, Switzerland: Federal Office of Topography (swisstopo). ISBN: 978-3-302-40068-6.
- Pawlewicz, M. J., D. W. Steinshouer and D. L. Gautier (1997). *Map showing geology, Oil and Gas Fields, and Geologic Provinces of Europe including Turkey*. Tech. rep., p. 14. DOI: 10.3133/ofr97470I.
- Peters, T., A. Matter, H.-R. Bläsi and A. Gautschi (1986). *NTB 85-02, Sondierbohrung Böttstein, Beilagenband*. Tech. rep. Wettingen, Switzerland: Nationale Genossenschaft für die Lagerung radioaktiver Abfälle (Nagra). URL: <http://www.nagra.ch>.
- Petit, C., M. Campy, J. Chaline and J. Bonvalot (1996). Major palaeohydrographic changes in Alpine foreland during the Pliocene - Pleistocene. *Boreas*, 25 (2), pp. 131–143. ISSN: 03009483. DOI: 10.1111/j.1502-3885.1996.tb00841.x.
- Pfiffner, O.-A., F. Schlunegger and S. J. H. Buiter (2002). The Swiss Alps and their peripheral foreland basin: Stratigraphic response to deep crustal processes. *Tec-*

- tonics*, 21 (2), pp. 1–15. ISSN: 0278-7407. DOI: 10.1029/2000TC900039.
- Philippe, Y. (1994). Transfer Zone in the Southern Jura Thrust Belt (Eastern France): Geometry, Development, and Comparison with Analogue Modeling Experiments. In: *Hydrocarbon and Petroleum Geology of France*. Ed. by A. Mascle. Vol. 4. Special publication of the European Association of Petroleum Geoscientists. Berlin, Heidelberg: Springer Berlin Heidelberg, pp. 327–346. ISBN: 978-3-642-78851-2. DOI: 10.1007/978-3-642-78849-9_23.
- (1995). Rampes latérales et zones de transfert dans les chaînes plissées: géométrie, conditions de formation et pièges structuraux associés. PhD thesis. Université de Savoie, p. 272. URL: <https://tel.archives-ouvertes.fr/tel-00755680>.
- Philippe, Y., B. Colletta, E. Deville and A. Mascle (1996). The Jura fold-and-thrust belt: a kinematic model based on map-balancing. *Peri-Tethys Memoir 2: Structure and Prospects of Alpine Basins and Forelands*, 170. Ed. by P. A. Ziegler and F. Horvath, pp. 235–261. ISSN: 1243-4442.
- Pickhardt, C., H. J. Dietze and J. S. Becker (2005). Laser ablation inductively coupled plasma mass spectrometry for direct isotope ratio measurements on solid samples. *International Journal of Mass Spectrometry*, 242 (2-3), pp. 273–280. ISSN: 13873806. DOI: 10.1016/j.ijms.2004.12.014.
- Pietsch, J. S., A. Wetzel and P. Jordan (2016). A new lithostratigraphic scheme for the Schinznach Formation (upper part of the Muschelkalk Group of northern Switzerland). *Swiss Journal of Geosciences*, 109 (2), pp. 285–307. ISSN: 1661-8726. DOI: 10.1007/s00015-016-0214-7.
- Piquerez, A., B. Mennecart, J.-P. Berger and J. Mosar (2012). *Paléogéographie et altimétrie des bassins molassiques du Jura*. Tech. rep. Université de Fribourg, pp. 1–14.
- Pochitaloff, A. (1963). *Laterolog Montoisson 1 1/500, Pl. 1, 18-1250*. Tech. rep. Société Nationale des Pétroles d'Aquitaine (SNPA).
- Poujol, P. and P. Michel (1958). *Log fondamentale de sondage Lons le Saunier N° 101 1/500, 16-1037*. Tech. rep. Régie Autonome des Pétroles (RAP).
- PREPA (1960). *Log fondamentale de sondage Laveron 1, 16-1120*. Tech. rep. Société de Prospection et Exploitations Pétrolières en Alsace (PREPA).
- (1963). *Log fondamentale de sondage Valempoulières 2 Val. 2, 16-1145*. Tech. rep. Société de Prospection et Exploitations Pétrolières en Alsace (PREPA).
- Rabin, M., C. Sue, A. Walpersdorf, P. Sakic, J. Albaric and B. Fores (2018). Present-Day Deformations of the Jura Arc Inferred by GPS Surveying and Earthquake Focal Mechanisms. *Tectonics*, 37 (10), pp. 3782–3804. ISSN: 19449194. DOI: 10.1029/2018TC005047.
- Ramaut, M. (1958). *Log fondamentale de sondage Montbouton 1 1/1000, 11-1110*. Tech. rep. Société de Prospection et Exploitations Pétrolières en Alsace (PREPA).
- Ramaut, M. and A. Warthmann (1957). *Log fondamentale de sondage Argilly 1 1/1000, 16-1033*. Tech. rep. Société de Prospection et Exploitations Pétrolières en Alsace (PREPA).
- Ranero, C. R., J. Phipps Morgan, K. McIntosh and C. Relchert (2003). Bending-related faulting and mantle serpentinization at the Middle America trench. *Nature*, 425 (6956), pp. 367–373. ISSN: 00280836. DOI: 10.1038/nature01961.
- Rat, P. (1974). Le système Bourgogne-Morvan-Bresse (articulation entre le bassin parisien et le domaine péri-alpin). In: *Géologie de la France: les chaînes plissées du cycle alpin et leur avant-pays*. Ed. by J. Debeltmas. Vol. 2. Doin, Paris, pp. 480–500.
- Raumer, J. F. von (1998). The Palaeozoic evolution in the Alps: from Gondwana to Pangea. *Geologische Rundschau*, 87 (3), pp. 407–435. ISSN: 0016-7835. DOI: 10.1007/s005310050219.
- Reisdorf, A. G. and A. Wetzel (2018). Evidence for synsedimentary differential tectonic movements in a low-subsidence setting: Early Jurassic in northwestern Switzerland. *Swiss Journal of Geosciences*, 111 (3), pp. 417–444. ISSN: 16618734. DOI: 10.1007/s00015-018-0318-3.
- Ricchi, E., C. A. Bergemann, E. Gnoss, A. Berger, D. Rubatto and M. J. Whitehouse (2019). Constraining deformation phases in the Aar Massif and the Gotthard Nappe (Switzerland) using Th-Pb crystallization ages of fissure monazite-(Ce). *Lithos*, 342-343, pp. 223–238. ISSN: 18726143. DOI: 10.1016/j.lithos.2019.04.014.
- Richard, P. and R. W. Krantz (1991). Experiments on fault reactivation in strike-slip mode. *Tectonophysics*, 188 (1-2), pp. 117–131. ISSN: 00401951. DOI: 10.1016/0040-1951(91)90318-M.
- Rime, V. (2017). Tectonics of the Neuchâtel Jura Mountains: insights from mapping and forward modelling. Master thesis (unpublished). Fribourg, Switzerland: University of Fribourg.
- Rime, V., A. Sommaruga, M. Schori and J. Mosar (2019). Tectonics of the Neuchâtel Jura Mountains: insights from mapping and forward modelling. *Swiss Journal of Geosciences*, 112 (2-3), pp. 563–578. ISSN: 16618734. DOI: 10.1007/s00015-019-00349-y.
- Ring, U. and A. Gerdes (2016). Kinematics of the Alpenrhein-Bodensee graben system in the Central Alps: Oligocene/Miocene transtension due to formation of the Western Alps arc. *Tectonics*, 35 (6), pp. 1367–1391. ISSN: 1944-9194. DOI: 10.1002/2015TC004085.

- Rittner, K. M. (2012). U-Pb dating of brittle deformation. PhD thesis. Royal Holloway University of London.
- Roberts, N. M., E. T. Rasbury, R. R. Parrish, C. J. Smith, M. S. Horstwood and D. J. Condon (2017). A calcite reference material for LA-ICP-MS U-Pb geochronology. *Geochemistry, Geophysics, Geosystems*, 18 (7), pp. 2807–2814. ISSN: 15252027. DOI: 10.1002/2016GC006784.
- Rocher, M., F. Chevalier, C. Petit and M. Guiraud (2003). Tectonics of the Northern Bresse region (France) during the Alpine cycle. *Geodinamica Acta*, 16 (2-6), pp. 131–147. ISSN: 09853111. DOI: 10.1016/j.geoact.2003.05.001.
- Rocher, M., M. Cushing, F. Lemeille and S. Baize (2004). L'île Crémieu (Jura, France), un plateau calcaire épargné par la tectonique? *Comptes Rendus - Geoscience*, 336 (13), pp. 1209–1218. ISSN: 16310713. DOI: 10.1016/j.crte.2004.06.001.
- Rotstein, Y., J. B. Edel, G. Gabriel, D. Boulanger, M. Schaming and M. Munschy (2006). Insight into the structure of the Upper Rhine Graben and its basement from a new compilation of Bouguer Gravity. *Tectonophysics*, 425 (1-4), pp. 55–70. ISSN: 00401951. DOI: 10.1016/j.tecto.2006.07.002.
- Rotstein, Y. and M. Schaming (2011). The Upper Rhine Graben (URG) revisited: Miocene transtension and transpression account for the observed first-order structures. *Tectonics*, 30 (3). ISSN: 02787407. DOI: 10.1029/2010TC002767.
- Rotstein, Y., M. Schaming and S. Rousse (2005). Structure and Tertiary tectonic history of the Mulhouse High, Upper Rhine Graben: Block faulting modified by changes in the Alpine stress regime. *Tectonics*, 24 (1), pp. 1–15. ISSN: 02787407. DOI: 10.1029/2004TC001654.
- Ruhland, M. (1959). Une dislocation majeure du socle vosgien dans la haute vallée de l'Ognon. *Bulletin du Service de la carte géologique d'Alsace et de Lorraine*, 12 (2), pp. 61–64. ISSN: 0037-2560. DOI: 10.3406/sgeol.1959.1199.
- Rupf, I. and E. Nitsch (2008). *Das Geologische Landesmodell von Baden-Württemberg: Datengrundlagen, technische Umsetzung und erste geologische Ergebnisse*. Vol. 21. 10. Landesamt für Geologie, Rohstoffe und Bergbau Baden-Württemberg, p. 81.
- S.C.S. (2020). *Lithostratigraphic Units of Switzerland*. URL: <http://www.strati.ch> (visited on 03/08/2020).
- Sabbatino, M., S. Vitale, S. Tavani, L. Consorti, A. Corradetti, A. Cipriani, I. Arienzo and M. Parente (2020). Constraining the onset of flexural subsidence and peripheral bulge extension in the Miocene foreland of the southern Apennines (Italy) by Sr-isotope stratigraphy. *Sedimentary Geology*, 401, p. 105634. ISSN: 00370738. DOI: 10.1016/j.sedgeo.2020.105634.
- Sadoux, J. (1970). *Log fondamental au 1/5000 Chapery 1*. Tech. rep. Société Esso Recherche et Exploit (ESSO REP).
- SAFREP (1959). *Structure de Montbarrey Mb. 1, log tabulaire, rapport fin de sondage*. Tech. rep. Société Anonyme Française de Recherche et d'Exploitation de Pétrole (SAFREP).
- Schlunegger, F. and S. Castelltort (2016). Immediate and delayed signal of slab breakoff in Oligo/Miocene Molasse deposits from the European Alps. *Scientific Reports*, 6, pp. 1–11. ISSN: 20452322. DOI: 10.1038/srep31010.
- Schlunegger, F. and E. Kissling (2015). Slab rollback orogeny in the Alps and evolution of the Swiss Molasse basin. *Nature Communications*, 6, p. 8605. ISSN: 20411723. DOI: 10.1038/ncomms9605.
- Schoeffler, J. (1941). *Rapport fin de sondage Vaux-en-Bugey, tableau de coupe géologique interprétée*. Tech. rep. Syndicat d'études et de recherches pétrolières (SERP).
- Schori, M. (2014). Combined structural field investigations and remote sensing analysis of the Combe Grède area (Chasseral, Central Jura). *Masterarbeit*, Universität Bern, unveröffentlicht, 56–71.
- Schori, M., J. Mosar and G. Schreurs (2015). Multiple detachments during thin-skinned deformation of the Swiss Central Jura: a kinematic model across the Chasseral. *Swiss Journal of Geosciences*, 108 (2-3), pp. 327–343. ISSN: 1661-8726. DOI: 10.1007/s00015-015-0196-x.
- Schori, M., F. Zwaan, G. Schreurs and J. Mosar (2020). Supplementary material - Pre-existing basement faults controlling deformation in the Jura Mountains fold-and-thrust belt: insights from analogue models. *Mendeley Data*, V2. DOI: 10.17632/6pm5zjw9w.2.
- (2021). Pre-existing Basement Faults Controlling Deformation in the Jura Mountains Fold-and-Thrust Belt: Insights from Analogue Models. *Tectonophysics*, 814, pp. 1–25. ISSN: 00401951. DOI: 10.1016/j.tecto.2021.228980.
- Schröckenfuchs, T., H. Bauer, B. Grasemann and K. Decker (2015). Rock pulverization and localization of a strike-slip fault zone in dolomite rocks (Salzach-Ennstal-Mariazell-Puchberg fault, Austria). *Journal of Structural Geology*, 78, pp. 67–85. ISSN: 01918141. DOI: 10.1016/j.jsg.2015.06.009.
- Schumacher, M. E. (2002). Upper Rhine Graben: Role of preexisting structures during rift evolution. *Tectonics*, 21 (1), pp. 6–17. ISSN: 1944-9194. DOI: 10.1029/2001TC900022.
- Shell (1980). *Log final sondage d'exploration Bois des Chaux-1bis, 16-1207A*. Tech. rep. Shell Française.
- Sinclair, H. D., B. J. Coakley, P. A. Allen and A. B. Watts (1991). Simulation of Foreland Basin Stratigraphy using

- a diffusion model of mountain belt uplift and erosion: An example from the central Alps, Switzerland. *Tectonics*, 10 (3), pp. 599–620. ISSN: 19449194. DOI: 10.1029/90TC02507.
- Sissingh, W. (1998). Comparative Tertiary stratigraphy of the Rhine Graben, Bresse Graben and Molasse Basin: correlation of Alpine foreland events. *Tectonophysics*, 300 (1-4), pp. 249–284. ISSN: 00401951. DOI: 10.1016/S0040-1951(98)00243-1.
- Smeraglia, L., N. Looser, O. Fabbri, F. Choulet, M. Guilong and S. M. Bernasconi (2021). U-Pb dating of middle Eocene-middle Pleistocene multiple tectonic pulses in the Alpine foreland. *Solid Earth Discussions*, 2021, pp. 1–14. ISSN: 1869-9537. DOI: 10.5194/se-2021-2.
- Sommaruga, A. (1997). Geology of the Central Jura and the Molasse Basin: new insight into an evaporite-based foreland fold and thrust belt. *Mémoire de la Société neuchâteloise des Sciences Naturelles*, 12, pp. 1–176. URL: <https://core.ac.uk/download/pdf/20637837.pdf>.
- (1999). Décollement tectonics in the Jura foreland fold-and-thrust belt. *Marine and Petroleum Geology*, 16 (2), pp. 111–134. ISSN: 02648172. DOI: 10.1016/S0264-8172(98)00068-3.
- Sommaruga, A., J. Mosar, M. Schori and M. Gruber (2017). The Role of the Triassic Evaporites Underneath the North Alpine Foreland. In: *Permo-Triassic Salt Provinces of Europe, North Africa and the Atlantic Margins*. Ed. by J. I. Soto, J. Flinch and G. Tari. Elsevier. Chap. 22, pp. 447–466. DOI: 10.1016/b978-0-12-809417-4.00021-5.
- Sommaruga, A., U. Eichenberger and F. Marillier (2012). Seismic Atlas of the Swiss Molasse Basin. In: *Matériaux pour la Géologie de la Suisse - Géophysique*. Ed. by E. Kissling. Vol. 44. Wabern. Switzerland: Federal Office of Topography (swisstopo), p. 90. ISBN: 978-3-302-40064-8.
- SPV (1958). *Log fin de sondage Bi.1. Bizonnes 1/2000*. Tech. rep. Société des Pétroles de Valence (SPV).
- (1959). *Log fin de sondage PA.1. Paladru 1/2000, 18-1197*. Tech. rep. Société des Pétroles de Valence (SPV).
- Stampfli, G. M., J. Mosar, D. Marquer, R. Marchant, T. Baudin and G. Borel (1998). Subduction and obduction processes in the Swiss Alps. *Tectonophysics*, 296 (1-2), pp. 159–204. ISSN: 00401951. DOI: 10.1016/S0040-1951(98)00142-5.
- Stampfli, G. M., J. Mosar, P. Favre, A. Pilleveit and J.-C. Vannay (2001). Permo-Mesozoic evolution of the western Tethys realm: the Neo-Tethys East Mediterranean Basin connection. In: *Peri-Tethys Memoir 6: Peri-Tethyan Rift/Wrench Basins and Passive Margins*. Ed. by P. A. Ziegler, W. Cavazza, A. Robertson and S. Crasquin-Soleau. Vol. 186. January. Mémoires du Muséum national d'histoire naturelle, pp. 51–108. ISBN: 2-85653-528-3.
- Steinmann, G. (1892). Bemerkungen über die tektonischen Beziehungen der oberrheinischen Tiefebene zu dem nordschweizerischen Kettenjura. *Berichte der naturforschenden Gesellschaft zu Freiburg im Breisgau*, 6, pp. 150–159.
- (1902). Zur Tektonik des nordschweizerischen Kettenjura. *Centralblatt für Mineralogie, Geologie und Paläontologie Stuttgart*, pp. 488–492.
- Strasser, A., J. Charollais, M. A. Conrad, B. Clavel, A. Pictet and B. Mastrangelo (2016). The Cretaceous of the Swiss Jura Mountains: an improved lithostratigraphic scheme. *Swiss Journal of Geosciences*, 109 (2), pp. 201–220. ISSN: 1661-8726. DOI: 10.1007/s00015-016-0215-6.
- Stutenbecker, L., P. M. Tolan, A. Madella and P. Lanari (2019). Miocene basement exhumation in the Central Alps recorded by detrital garnet geochemistry in foreland basin deposits. *Solid Earth*, 10 (5), pp. 1581–1595. ISSN: 18699529. DOI: 10.5194/se-10-1581-2019.
- Suppe, J. (1983). Geometry and kinematics of fault-bend folding. *American Journal of Science*, 283 (7), pp. 684–721. ISSN: 0002-9599. DOI: 10.2475/ajs.283.7.684.
- Suppe, J. and D. A. Medwedeff (1990). Geometry and kinematics of fault-propagation folding. *Eclogae Geologicae Helvetiae*, 83 (3), pp. 409–454.
- Suter, H. and E. Lüthi (1969). Val de Ruz (CN 1144), Erläuterungen. In: *Geological Atlas of Switzerland 1:25000*. Federal Office of Topography (swisstopo).
- Swisstopo (2011). *Digital elevation model swissALTI3D*. Wabern, Switzerland: Federal Office of Topography (swisstopo). URL: <http://www.swisstopo.ch>.
- (2012). *GeoCover geological vector data*. Wabern, Switzerland: Federal Office of Topography (swisstopo).
- Tavani, S., F. Storti, O. Lacombe, A. Corradetti, J. A. Muñoz and S. Mazzoli (2015). A review of deformation pattern templates in foreland basin systems and fold-and-thrust belts: Implications for the state of stress in the frontal regions of thrust wedges. *Earth-Science Reviews*, 141, pp. 82–104. ISSN: 00128252. DOI: 10.1016/j.earscirev.2014.11.013.
- Thurru, M. and M. Amman (1990). Les sept forages de la Cédra dans le nord de la Suisse. *Cédra informe*, 2, pp. 7–15.
- Truffert, C., J.-P. Burg, M. Cazes, R. Bayer, B. Damotte and D. Rey (1990). Deep structure of the Alps. In: *Mémoires de la Société géologique de France*. Ed. by F. Roure, P. Heitzmann and R. Polino. Vol. 156. Société géologique de France. Chap. Structures, pp. 157–164.
- Trümpy, R. (1980). Geology of Switzerland a guide-book: An Outline of the Geology of Switzerland. In: ed. by R. Trümpy. Wepf & Co. Publishers, Basel - New York, p. 334.

- Tschanz, X. (1990). Analyse de la déformation du Jura central entre Neuchâtel (Suisse) et Besançon (France). *Eclogae Geologicae Helvetiae*, 83 (3), pp. 543–558. DOI: 10.5169/seals-166601.
- Turcotte, D. L. and G. Schubert (2002). *Geodynamics, Second Edition*. Cambridge university press, pp. 1–848. ISBN: 0521666244.
- Twiss, R. J. and E. M. Moores (2007). *Structural Geology*. Second. University of California at Davis, W. H. Freeman and Company, pp. 61–89.
- Ustaszewski, K. (2004). Reactivation of pre-existing crustal discontinuities: the southern Upper Rhine Graben and the northern Jura Mountains - a natural laboratory. PhD thesis. University of Basel.
- Ustaszewski, K. and S. M. Schmid (2006). Control of preexisting faults on geometry and kinematics in the northernmost part of the Jura fold-and-thrust belt. *Tectonics*, 25 (5), pp. 1–26. ISSN: 02787407. DOI: 10.1029/2005TC001915.
- (2007). Latest Pliocene to recent thick-skinned tectonics at the Upper Rhine Graben - Jura Mountains junction. *Swiss Journal of Geosciences*, 100 (2), pp. 293–312. ISSN: 1661-8726. DOI: 10.1007/s00015-007-1226-0.
- Ustaszewski, K., M. E. Schumacher and S. M. Schmid (2005). Simultaneous normal faulting and extensional flexuring during rifting: an example from the southernmost Upper Rhine Graben. *International Journal of Earth Sciences*, 94 (4), pp. 680–696. ISSN: 14373254. DOI: 10.1007/s00531-004-0454-z.
- Vermeesch, P. (2018). IsoplotR: A free and open toolbox for geochronology. *Geoscience Frontiers*, 9 (5), pp. 1479–1493. ISSN: 16749871. DOI: 10.1016/j.gsf.2018.04.001.
- Warthmann, A. (1959). *Log fondamental de sondage TAILLON 1 1/1000, 16-1089*. Tech. rep. Société de Prospection et Exploitations Pétrolières en Alsace (PREPA).
- Weber, C. (1960). Etude géologique de la partie septentrionale du faisceau de Syam (Jura): relations entre les plateaux de Champagnole et de Nozeroy. PhD thesis. University of Paris.
- Weber, H. P., G. Sattel and C. Sprecher (1986). *NTB 85-50, Sondierbohrungen Weiach, Riniken, Schafisheim, Kaisten, Leuggern, Geophysikalische Daten Beilagenband*. Tech. rep. Wettingen, Switzerland: Nationale Genossenschaft für die Lagerung radioaktiver Abfälle (Nagra). URL: <http://www.nagra.ch>.
- Wetzel, A., R. Allenbach and V. Allia (2003). Reactivated basement structures affecting the sedimentary facies in a tectonically "quiescent" epicontinental basin: an example from NW Switzerland. *Sedimentary Geology*, 157 (1), pp. 153–172. ISSN: 0037-0738. DOI: 10.1016/S0037-0738(02)00230-0.
- Wildi, W. and P. Huggenberger (1993). Reconstitution de la plate-forme européenne anté-orogénique de la Bresse aux Chaînes subalpines: éléments de cinématique alpine (France et Suisse occidentale). *Eclogae Geologicae Helvetiae*, 86 (1), pp. 47–64. ISSN: 1420-9128. DOI: 10.5169/seals-167235.
- Willett, S. D. and F. Schlunegger (2010). The last phase of deposition in the Swiss Molasse Basin: From fore-deep to negative-alpha basin. *Basin Research*, 22 (5), pp. 623–639. ISSN: 0950091X. DOI: 10.1111/j.1365-2117.2009.00435.x.
- Winnock, E. (1961). Résultats géologiques du forage Risoux 1. *Bulletin der Vereinigung Schweizerischer Petroleum-Geologen und Ingenieure*, 28 (74), pp. 17–26. DOI: 10.5169/seals-191403.
- Withjack, M. O. and S. Callaway (2000). Active normal faulting beneath a salt layer: An experimental study of deformation patterns in the cover sequence. *AAPG Bulletin*, 84 (5), pp. 627–651. ISSN: 01491423. DOI: 10.1306/c9ebce73-1735-11d7-8645000102c1865d.
- Woodhead, J., J. Hergt, S. Meffre, R. R. Large, L. Danyushevsky and S. Gilbert (2009). In situ Pb-isotope analysis of pyrite by laser ablation (multi-collector and quadrupole) ICPMS. *Chemical Geology*, 262 (3-4), pp. 380–390. ISSN: 00092541. DOI: 10.1016/j.chemgeo.2009.02.003.
- Ziegler, P. A. and P. Dèzes (2006). Crustal evolution of Western and Central Europe. *Geological Society Memoir*, 32 (1), pp. 43–56. ISSN: 04354052. DOI: 10.1144/GSL.MEM.2006.032.01.03.
- Ziegler, P. A. (1982). Triassic rifts and facies patterns in Western and Central Europe. *Geologische Rundschau*, 71 (3), pp. 747–772. ISSN: 00167835. DOI: 10.1007/BF01821101.
- (1988a). Evolution of the Arctic - North Atlantic and the Western Tethys - A Visual Presentation of a series of Paleogeographic-paleotectonic maps. *AAPG Memoir*, 43, pp. 164–196. ISSN: 0271-8529.
- (1988b). Late Jurassic-Early Cretaceous Central Atlantic Sea-Floor Spreading, Closure of Neo-Tethys, and Opening of Canada Basin. *AAPG Memoir Volume 43: Evolution of the Arctic-North Atlantic and the Western Tethys*, pp. 63–82. DOI: 10.1306/M43478C6.
- (1992a). European Cenozoic rift system. *Tectonophysics*, 208 (1-3), pp. 91–111. ISSN: 00401951. DOI: 10.1016/0040-1951(92)90338-7.
- (1992b). *Geological Atlas of Western and Central Europe (2nd Edition)*. Vol. 2. Geological Society of London, p. 256. ISBN: 9066441259.
- Ziegler, P. A. and P. Dèzes (2005). Evolution of the lithosphere in the area of the Rhine Rift System. *International Journal of Earth Sciences*, 94 (4), pp. 594–614. ISSN: 1437-3262. DOI: 10.1007/s00531-005-0474-3.
- (2007). Cenozoic uplift of Variscan Massifs in the Alpine foreland: Timing and controlling mechanisms. *Global*

and Planetary Change, 58 (1-4), pp. 237–269. ISSN: 09218181. DOI: 10.1016/j.gloplacha.2006.12.004.

Zoraster, S. (2003). A surface modeling algorithm designed for speed and ease of use with all petroleum industry data. *Computers and Geosciences*, 29 (9), pp. 1175–1182. ISSN: 00983004. DOI: 10.1016/S0098-3004(03)00139-0.

APPENDICES

A - DATA DESCRIPTION

A.1 LIST OF BOREHOLES

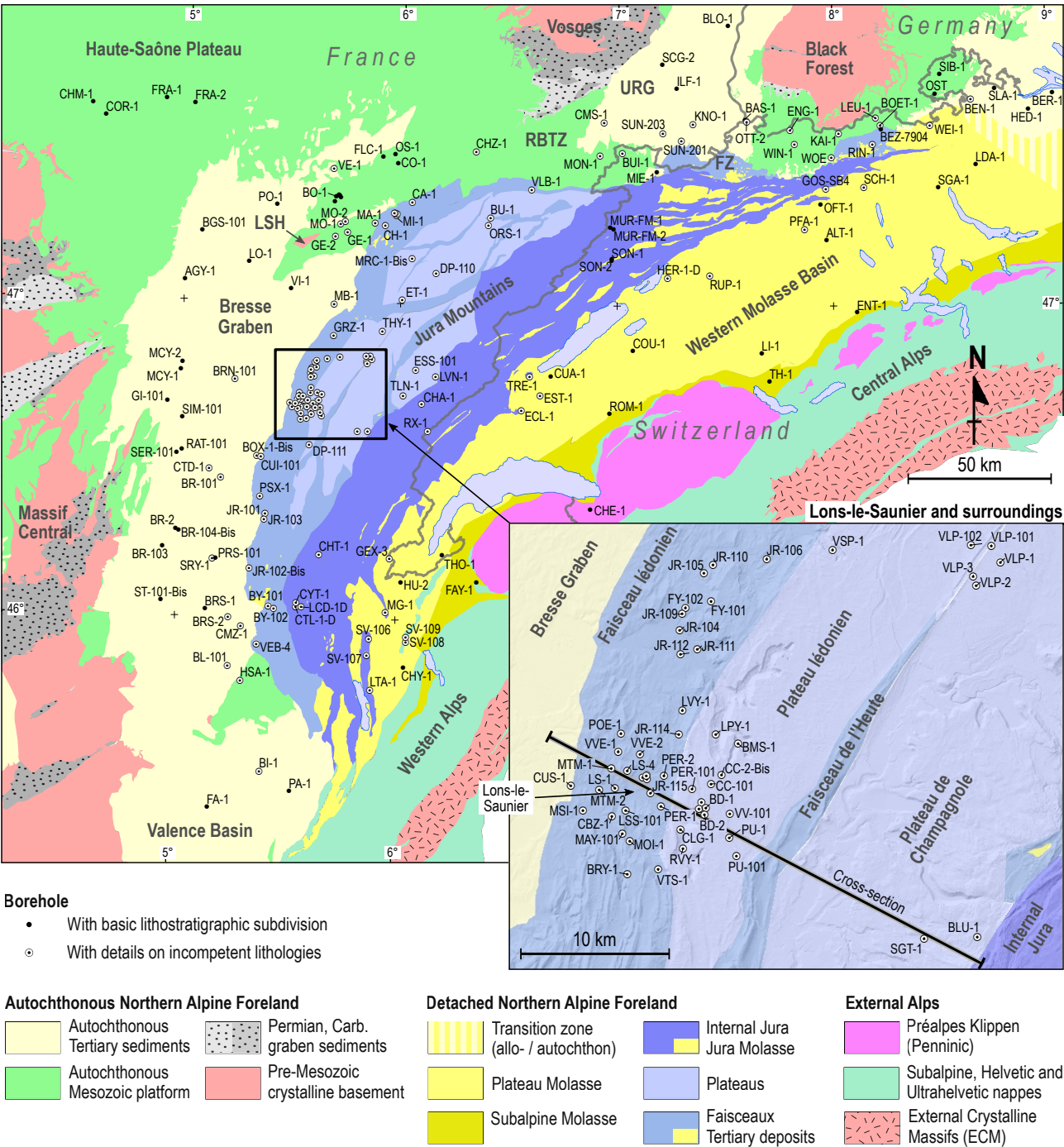


Fig. A.1 – Overview of boreholes in the borehole database of this study. Detailed descriptions for all boreholes are provided in Supplementary Material C. The cross-section trace shows the position of Fig. 3.2b on page 49. BG: Bresse Graben, FZ: Ferrette Zone, LSH: La Serre Horst, RBTZ: Rhine–Bresse Transfer Zone, URG: Upper Rhine Graben.

Table A.1 – List of boreholes available in the borehole data base. The last column gives the oldest unit, which was drilled (not the bottom most unit). TVD: Total vertical depth. An overview map is shown in Fig. A.1 on the current page.

	Abb.	Name	Long [°]	Lat [°]	Date end	TVD	Oldest unit
1	AGY-1	Argilly-1	5.0031	47.0586	22/08/1957	2222.0 m	Carboniferous
2	ALT-1	Altishofen-1	7.9725	47.2039	03/01/1953	2166.0 m	Lower Triassic
3	BAS-1	Basel-1	7.5956	47.5854	2006	5009.4 m	Paleozoic

	Abb.	Name	Long [°]	Lat [°]	Date end	TVD	Oldest unit
4	BD-1	Briod-1	5.6176	46.6647	15/05/1955	684.0 m	Middle Triassic
5	BD-103	Briod-103	5.6209	46.6652	20/08/1955	920.8 m	Permian
6	BD-104	Briod-104	5.6171	46.6685	12/10/1955	702.9 m	Middle Triassic
7	BD-105	Briod-105	5.6148	46.6646	27/11/1955	720.4 m	Middle Triassic
8	BD-2	Briod-2	5.62	46.6608	09/08/1956	1528.7 m	Carboniferous
9	BEN-1	Benken-1	8.6496	47.6449	1998	1007.0 m	Paleozoic Meta
10	BER-1	Berlingen-1	9.032	47.6615	19/09/1964	2310.7 m	Permian
11	BEZ-7904	Beznau-7904	8.229	47.5532	1980	321.8 m	Middle Triassic
12	BGS-101	Barges-101	5.0776	47.2148	22/07/1960	1151.8 m	Paleozoic Magm
13	BI-1	Bizonnes-1	5.4049	45.5087	20/12/1958	1427.5 m	Paleozoic Meta
14	BL-101	Blyes-101	5.2487	45.8396	04/11/1961	1281.5 m	Permian
15	BLO-1	Blodelsheim Hardt Nord-1	7.5168	47.8808	08/01/1954	2533.0 m	Lower Triassic
16	BLU-1	Bonlieu-1	5.8615	46.5905	06/07/1982	1862.3 m	Paleozoic Meta
17	BMS-1	Baume-les-Messieurs-1	5.648	46.7043	11/03/1941	1183.6 m	Permian
18	BMT-1	Montoisson-1	4.9669	44.7866	26/08/1962	3976.3 m	Paleozoic
19	BO-1	Bonboillon-1	5.6945	47.3299	25/12/1957	1132.0 m	Permian
20	BO-CD-3	Bonboillon Cd-3	5.7109	47.3341	03/07/1957	183.0 m	Malm
21	BO-CD-4	Bonboillon Cd-4	5.7159	47.3292	01/04/1957	351.0 m	Malm
22	BO-CD-5	Bonboillon Cd-5	5.7081	47.3367	17/03/1957	93.0 m	Malm
23	BO-CD-8	Bonboillon Cd-8	5.6894	47.3156	26/03/1957	77.2 m	Malm
24	BO-CD-9	Bonboillon Cd-9	5.7106	47.334	04/08/1957	207.0 m	Malm
25	BOET-1	Böttstein-1	8.2272	47.565	05/06/1983	1501.0 m	Paleozoic
26	BOX-1-Bis	Bois-des-Chaux-1bis	5.3572	46.5051	07/04/1980	3226.1 m	Permian
27	BR-101	Bresse-101	5.1941	46.4336	07/06/1953	1926.3 m	Dogger
28	BR-103	Bresse-103	4.937	46.2129	23/05/1954	1627.9 m	Carboniferous
29	BR-104-Bis	Bresse-104bis	5.0082	46.2647	02/04/1955	1735.5 m	Permian
30	BR-2	Bresse-2	4.9953	46.2695	13/03/1953	1538.9 m	Permian
31	BRN-101	Bresse Nord-101	5.2469	46.7456	09/06/1959	2147.3 m	Permian
32	BRS-1	Bresse Sud-1	5.1398	46.0197	18/08/1959	2599.8 m	Paleozoic Meta
33	BRS-2	Bresse Sud-2	5.2453	45.9948	05/03/1961	2416.5 m	Paleozoic
34	BRY-1	Bornay-1	5.5534	46.624	13/10/1955	1492.6 m	Carboniferous
35	BU-1	Buez-1	6.4134	47.2689	07/08/1961	1197.0 m	Paleozoic
36	BUI-1	Buix-1	7.0245	47.4776	03/05/1919	1052.8 m	Permian
37	BY-101	Bugey-101	5.4268	46.0322	17/04/1956	591.4 m	Upper Triassic
38	BY-102	Bugey-102	5.4518	46.0235	03/05/1956	275.1 m	Upper Triassic
39	CA-1	Chailluz-1	6.049	47.3166	26/08/1958	831.1 m	Upper Triassic
40	CBZ-1	Courbouzon-1	5.5388	46.6584	30/06/1954	1419.6 m	Paleozoic
41	CC-101	Crancot-101	5.6252	46.6798	16/06/1961	848.9 m	Lower Triassic
42	CC-2-Bis	Crancot-2bis	5.6342	46.6851	17/11/1986	708.0 m	Middle Triassic
43	CH-1	Champvans-1	5.9263	47.2403	09/11/1957	687.7 m	Permian
44	CHA-1	Châtelblanc-1	6.107	46.6787	07/06/1979	2664.3 m	Permian
45	CHE-1	Chessel-1001	6.8855	46.3516	24/06/1987	615.0 m	Upper Triassic
46	CHM-1	Chaume-1	4.5497	47.6076	10/10/1959	255.8 m	Paleozoic Magm
47	CHT-1	Charmont-1	5.6511	46.1975	05/11/1991	2285.4 m	Carboniferous
48	CHY-1	Chapery-1	6.0439	45.8453	08/08/1970	4162.3 m	Carboniferous
49	CHZ-1	Chazelot-1	6.3424	47.478	1922	700.0 m	Paleozoic Meta
50	CL-1	Claveyson-1	4.9409	45.1925	03/09/1959	1708.0 m	Paleozoic
51	CLG-1	Conliège-1	5.5993	46.6519	23/11/1948	1006.5 m	Paleozoic Meta
52	CMS-1	Charmois-1	6.938	47.5733	1914	1019.0 m	Upper Triassic
53	CMZ-1	Cormoz-1	5.3037	45.9666	23/09/1984	1806.0 m	Paleozoic Meta

	Abb.	Name	Long [°]	Lat [°]	Date end	TVD	Oldest unit
54	CO-1	Cordonnet-1	5.9806	47.4402	15/05/1958	909.7 m	Lower Triassic
55	COR-1	Corpoyer-1	4.611	47.5704	30/09/1959	275.0 m	Paleozoic Magm
56	COU-1	Courtion-1	7.0769	46.8553	22/11/1960	3083.8 m	Middle Triassic
57	CTD-1	Curciat-Dongalon-1	5.14	46.4635	30/04/1963	1546.7 m	Malm
58	CTL-1-D	Châtillon-1d	5.5508	46.0321	18/09/1991	1442.6 m	Carboniferous
59	CUA-1	Cuarny-1	6.6994	46.7715	26/02/1940	2228.0 m	Dogger
60	CUI-101	Cuiseaux-101	5.3759	46.5024	26/09/1965	2360.7 m	Upper Triassic
61	CUS-1	Courlans-1	5.5019	46.6764	11/09/1953	943.4 m	Triassic
62	CYT-1	Chaleyriat-1	5.5519	46.0435	15/06/1989	1361.9 m	Permian
63	DP-110	Ornans-1	6.1649	47.0915	14/10/1964	1160.5 m	Lower Triassic
64	DP-111	Présilly-1	5.5959	46.5437	21/01/1965	1270.2 m	Permian
65	ECL-1	Eclépens-1	6.5661	46.6633	06/11/1981	2150.0 m	Upper Triassic
66	ENG-1	Engerfeld-1	7.8059	47.5503	06/05/1983	600.0 m	Paleozoic Meta
67	ENT-1	Entlebuch-1	8.1116	46.9748	22/10/1980	5152.0 m	Carboniferous
68	ESS-101	Essavilly-101	6.0783	46.7861	17/12/1964	2067.4 m	Paleozoic Meta
69	EST-1	Essertines-1	6.651	46.7099	22/07/1963	2936.1 m	Upper Triassic
70	ET-1	Éternoz-1	6.0095	47.0075	24/06/1960	2497.0 m	Permian
71	FA-1	Faramans-1	5.1749	45.392	03/11/1957	1575.0 m	Paleozoic Meta
72	FAY-1	Faucigny-1	6.3696	46.118	10/03/1970	4951.3 m	Permian
73	FLC-1	Frasne-le-Château-1	5.9107	47.4582	29/05/1958	1078.7 m	Paleozoic Magm
74	FRA-1	Fraignot-1	4.8932	47.6301	21/09/1959	398.3 m	Paleozoic Magm
75	FRA-2	Fraignot-2	5.0268	47.6174	01/11/1959	378.0 m	Paleozoic Magm
76	FY-101	Frontenay-101	5.6214	46.7898	14/07/1964	441.0 m	Middle Triassic
77	FY-102	Frontenay-102	5.5991	46.7859	17/10/1982	356.0 m	Lower Triassic
78	GE-1	Gendrey-1	5.751	47.2178	06/02/1958	676.0 m	Permian
79	GE-2	Gendrey-2	5.695	47.2051	10/03/1958	583.1 m	Paleozoic Magm
80	GEX-3	Gex CD-3	5.9728	46.1883	21/12/1982	293.9 m	Cretaceous
81	GI-101	Gigny-101	4.9402	46.6725	19/11/1963	1278.2 m	Permian
82	GOS-SB4	Gösgen-SB4	7.9707	47.3658	31/09/2014	720.0 m	Upper Triassic
83	GRZ-1	Grozon-1	5.6971	46.8916	07/06/1939	328.1 m	Paleozoic Magm
84	HED-1	Herdern-1	8.9191	47.6126	22/02/1982	2155.0 m	Paleozoic
85	HER-1-D	Hermrigen-1d	7.2359	47.0848	24/09/1982	2173.2 m	Middle Triassic
86	HSA-1	Hières-sur-Amby-1	5.3082	45.7941	12/1919	694.0 m	Paleozoic Meta
87	HU-2	Humilly-2	6.0251	46.1148	30/01/1969	3051.0 m	Carboniferous
88	ILF-1	Illfurth-R1	7.2768	47.6839	23/04/1952	1353.8 m	Permian
89	JR-101	Jura-101	5.4013	46.3242	17/02/1951	1621.0 m	Upper Triassic
90	JR-102-Bis	Jura-102bis	5.3358	46.1488	25/05/1951	688.2 m	Lias
91	JR-103	Jura-103	5.3975	46.3041	27/11/1951	773.0 m	Cretaceous
92	JR-104	Jura-104	5.5944	46.7718	31/10/1951	273.0 m	Middle Triassic
93	JR-105	Jura-105	5.6144	46.8067	01/05/1952	513.5 m	Permian
94	JR-106	Jura-106	5.6696	46.8164	03/03/1952	369.2 m	Middle Triassic
95	JR-109	Jura-109	5.5962	46.7819	05/09/1952	331.9 m	Middle Triassic
96	JR-110	Saint-Lothain-1	5.6225	46.8118	05/10/1952	747.8 m	Paleozoic Meta
97	JR-111	Jura-111	5.6103	46.7606	01/07/1952	341.3 m	Middle Triassic
98	JR-112	Domblans-1	5.5955	46.7576	28/05/1953	1576.5 m	Paleozoic Meta
99	JR-114	Jura-114	5.5958	46.7091	19/10/1952	371.3 m	Middle Triassic
100	JR-115	Lons-2	5.5721	46.6733	02/05/1953	1147.3 m	Paleozoic Magm
101	KAI-1	Kaisten-1	8.0315	47.5398	27/06/1984	1303.0 m	Paleozoic Meta
102	KNO-1	Knoeringue-1	7.3531	47.5706	26/03/1959	2148.8 m	Paleozoic Magm
103	KRE-1	Kreuzlingen-1	9.1586	47.6244	14/10/1962	2550.0 m	Paleozoic Magm

	Abb.	Name	Long [°]	Lat [°]	Date end	TVD	Oldest unit
104	LCD-1D	La Chandelière-1d	5.5771	46.0309	30/11/1989	1426.1 m	Paleozoic Meta
105	LDA-1	Lindau-1	8.6691	47.4401	06/05/1964	2377.2 m	Paleozoic Magm
106	LEU-1	Leuggern-1	8.2048	47.589	10/02/1985	1650.5 m	Paleozoic Meta
107	LI-1	Linden-1	7.6712	46.848	31/05/1973	5447.5 m	Upper Triassic
108	LO-1	St-Jean-de-Losne-1	5.2979	47.1199	10/11/1958	1342.5 m	Permian
109	LPY-1	La Peyrouse-1	5.6283	46.7096	06/11/1985	366.0 m	Upper Triassic
110	LS-1	Lons-1	5.5408	46.6758	17/07/1952	831.1 m	Paleozoic Meta
111	LS-101	Lons-le-Saunier-101	5.5682	46.6839	26/08/1957	279.5 m	Middle Triassic
112	LS-102	Lons-le-Saunier-102	5.5686	46.6817	30/09/1957	340.9 m	Middle Triassic
113	LS-103	Lons-le-Saunier-103	5.5651	46.6828	09/11/1957	332.5 m	Middle Triassic
114	LS-3	Lons-3	5.5681	46.6839	09/04/1957	1129.3 m	Paleozoic Magm
115	LS-4	Lons-4	5.5511	46.6865	15/04/1957	1122.0 m	Paleozoic Meta
116	LSS-101	Lons-le-Saunier Sud-101	5.5507	46.6624	28/12/1964	374.4 m	Middle Triassic
117	LTA-1	La Tailla-1	5.8953	45.7724	16/11/1975	3346.3 m	Paleozoic
118	LVN-1	Laveron-1	6.1695	46.7663	23/01/1960	2485.2 m	Lower Triassic
119	LVY-1	Lavigny-1	5.5984	46.7237	26/01/1951	1353.1 m	Carboniferous
120	MA-1	Mazerolles-1	5.878	47.2481	26/12/1957	520.5 m	Permian
121	MAY-101	Macornay-101	5.5482	46.6485	02/08/1964	325.0 m	Middle Triassic
122	MB-1	Montbarrey-1	5.6965	46.991	24/10/1959	1454.3 m	Permian
123	MBG-1	Meersburg-1	9.2847	47.7013	1991	2540.0 m	Permian
124	MCY-1	Montcoy-1	4.9969	46.773	16/09/1958	2449.8 m	Permian
125	MCY-2	Montcoy-2	5.004	46.7966	10/10/1958	1098.0 m	Dogger
126	MG-1	Musiège-1	5.9581	46.019	24/05/1962	2036.4 m	Dogger
127	MI-1	Miserey-1	5.9767	47.2737	29/09/1957	1011.7 m	Permian
128	MI-1-Bis-Mix	Miserey-1bis (mix)	5.9791	47.2782	31/01/1957	277.0 m	Upper Triassic
129	MI-2	Miserey-2	5.9737	47.2788	16/04/1960	376.9 m	Middle Triassic
130	MI-2-Mix	Miserey-2 (mix)	5.9699	47.2809	08/02/1957	206.7 m	Upper Triassic
131	MI-3-Mix	Miserey-3 (mix)	5.9669	47.2816	12/02/1957	149.0 m	Lias
132	MIE-1	Miécourt-1	7.1849	47.4182	2008	462.8 m	Malm
133	MO-1	Moutherot-1	5.7184	47.2432	11/10/1957	1485.0 m	Paleozoic Meta
134	MO-2	Moutherot-2	5.7399	47.2529	22/02/1957	206.2 m	Lias
135	MO-CD-4	Moutherot Cd-4	5.7372	47.2543	25/02/1957	43.0 m	Dogger
136	MOI-1	Moiron-1	5.5549	46.6439	02/12/1954	1270.4 m	Paleozoic Meta
137	MON-1	Montbouton-1	6.92	47.469	23/02/1958	1130.5 m	Permian
138	MRC-1	Montrond-le-Château-1	6.0525	47.1381	14/01/1984	885.6 m	Middle Triassic
139	MRC-1-Bis	Montrond-le-Château-1bis	6.0525	47.1382	01/05/1985	1153.0 m	Permian
140	MSI-1	Messia-1	5.5131	46.6615	31/08/1953	945.7 m	Upper Triassic
141	MTM-1	Montmorot C.d.F.-1	5.5372	46.6874	21/02/1954	938.5 m	Paleozoic Meta
142	MTM-2	Montmorot C.d.F.-2	5.5271	46.6744	16/10/1958	1084.7 m	Paleozoic Meta
143	MUR-FM-1	Muriaux-FM-1	6.9695	47.2431	18/09/1999	615.0 m	Dogger
144	MUR-FM-2	Muriaux-FM-2	6.9854	47.2394	23/02/2000	635.0 m	Dogger
145	OFT-1	Oftringen-1	7.9457	47.3176	17/10/2007	719.0 m	Dogger
146	ORS-1	Orsans-1	6.4036	47.2461	13/09/1974	1032.3 m	Paleozoic Magm
147	OS-1	Oiselay-1	5.9662	47.4664	08/07/1958	837.2 m	Permian
148	OST	Osterfingen	8.4824	47.6619	18/01/2012	180.0 m	Upper Triassic
149	OTT-2	Otterbach-2	7.6038	47.5777	10/06/2001	2746.0 m	Paleozoic
150	PA-1	Paladru-1	5.5411	45.4493	15/05/1959	2119.5 m	Paleozoic Meta
151	PER-1	Perrigny-1	5.5814	46.6653	23/03/1951	1160.0 m	Paleozoic Meta
152	PER-101	Perrigny-101	5.6085	46.6761	06/02/1985	694.0 m	Middle Triassic
153	PER-2	Perrigny-2	5.5836	46.6838	15/03/1953	1144.2 m	Paleozoic Magm

	Abb.	Name	Long [°]	Lat [°]	Date end	TVD	Oldest unit
154	PFA-1	Pfaffnau-1	7.8706	47.2362	20/12/1963	1843.0 m	Paleozoic Magm
155	PO-1	Pontailier-1	5.4212	47.3029	30/08/1958	1356.4 m	Permian
156	POE-1	Plainoiseau-1	5.545	46.7086	18/10/1954	1223.7 m	Paleozoic Magm
157	PRS-101	Peronnas-101	5.1803	46.1781	28/01/1963	1531.9 m	Tertiary
158	PSX-1	Poisoux-1	5.3752	46.3791	28/05/1969	2516.7 m	Paleozoic Meta
159	PU-1	Publy-1	5.6422	46.6475	01/09/1956	1391.8 m	Carboniferous
160	PU-101	Publy-101	5.6489	46.6365	10/04/1961	954.8 m	Lower Triassic
161	RAT-101	Ratenelle-101	5.0128	46.522	05/06/1963	1349.3 m	Permian
162	RIN-1	Riniken-1	8.1899	47.5045	12/01/1984	1801.0 m	Permian
163	ROM-1	Romanens-1	6.9709	46.6569	22/11/1977	4022.0 m	Upper Triassic
164	RUP-1	Ruppoldsried-1	7.4314	47.0914	1977	986.0 m	Malm
165	RVY-1	Revigny-1	5.6017	46.6404	22/04/1943	896.3 m	Carboniferous
166	RX-1	Risoux-1	6.1378	46.5931	09/03/1961	1958.0 m	Dogger
167	SCG-2	Schweighouse-2	7.208	47.7601	30/04/1959	2414.8 m	Lower Triassic
168	SCH-1	Schafisheim-1	8.1487	47.3695	29/06/1984	2005.8 m	Paleozoic
169	SER-101	Sermoyer-101	4.989	46.5107	16/08/1964	1185.4 m	Permian
170	SGA-1	Sonnengarten-1	8.4934	47.368	14/02/2010	2708.0 m	Paleozoic Meta
171	SGT-1	Saugeot-1	5.8151	46.589	24/11/1962	1307.2 m	Middle Triassic
172	SIB-1	Siblingen-1	8.5061	47.7259	02/04/1989	1522.0 m	Paleozoic Magm
173	SIM-101	Simandre-101	5.0109	46.6241	11/10/1963	1112.5 m	Permian
174	SL-1	St-Lattier-1	5.1943	45.0873	30/06/1957	2790.0 m	Paleozoic Meta
175	SL-2	St-Lattier-2	5.1718	45.0484	18/07/1959	2425.2 m	Paleozoic
176	SLA-1	Schlattingen-1	8.7619	47.678	25/09/2011	1508.0 m	Paleozoic Meta
177	SON-1	Sonvillier-1	6.9761	47.1388	1996	666.6 m	Malm
178	SON-2	Sonvillier-2	6.9773	47.1432	1998	580.0 m	Malm
179	SRY-1	St-Rémy-1	5.1664	46.1773	03/04/1982	3589.7 m	Carboniferous
180	ST-101-Bis	St-Trivier-101bis	4.9379	46.0442	06/06/1963	1796.0 m	Carboniferous
181	SUN-201	Sundgau-201	7.2986	47.5185	22/09/1954	582.0 m	Dogger
182	SUN-203	Sundgau-203	7.2123	47.54	16/10/1954	446.0 m	Jurassic
183	SV-106	Savoie-106	5.8857	45.9334	29/01/1954	2107.7 m	Upper Triassic
184	SV-107	Savoie-107	5.8768	45.883	09/11/1954	2089.9 m	Dogger
185	SV-108	Savoie-108	6.0534	45.9257	01/08/1956	1260.3 m	Tertiary
186	SV-109	Savoie-109	6.0534	45.9405	29/10/1959	1203.6 m	Cretaceous
187	TH-1	Thun-1	7.7051	46.7579	01/08/1989	5914.0 m	Lias
188	THO-1	Thônex-1	6.2113	46.2018	15/09/1993	2530.0 m	Malm
189	THY-1	Thésy-1	5.9218	46.9078	02/07/1972	1107.5 m	Paleozoic Magm
190	TLN-1	Toillon-1	6.0217	46.7044	07/11/1958	1573.0 m	Upper Triassic
191	TRE-1	Treycovagnes-1	6.6025	46.7706	26/08/1978	3208.1 m	Permian
192	VE-1	Velesmes-1	5.6826	47.4189	01/08/1959	1250.1 m	Permian
193	VEB-4	Vaux-en-Bugey-4	5.3767	45.9115	17/09/1925	602.9 m	Permian
194	VI-1	Villette-lès-Dole-1	5.4947	47.0384	04/04/1958	1531.0 m	Paleozoic Meta
195	VLB-1	Vellerot-les-Belvoir-1	6.6028	47.3596	26/07/1961	949.6 m	Middle Triassic
196	VLP-1	Valempoulières-1	5.8753	46.8175	05/06/1961	1411.9 m	Paleozoic Meta
197	VLP-101	Valempoulières-101	5.8671	46.827	15/10/1964	1075.7 m	Middle Triassic
198	VLP-102	Valempoulières-102	5.8492	46.8275	07/12/1964	970.0 m	Middle Triassic
199	VLP-2	Valempoulières-2	5.8543	46.8029	07/02/1963	1252.0 m	Lower Triassic
200	VLP-3	Valempoulières-3	5.8517	46.8085	25/06/1964	805.1 m	Middle Triassic
201	VMO-2	Montmiral-2	5.1822	45.1577	28/11/1961	2480.2 m	Paleozoic Meta
202	VSP-1	Vaux-sur-Poligny-1	5.7273	46.8227	11/09/1946	763.8 m	Paleozoic Meta
203	VTS-1	Vernantois-1	5.5806	46.6272	26/09/1946	545.2 m	Middle Triassic

	Abb.	Name	Long [°]	Lat [°]	Date end	TVD	Oldest unit
204	VV-101	Vevy-101	5.6423	46.662	15/05/1961	918.0 m	Lower Triassic
205	VVE-1	Villeneuve-1	5.5429	46.6979	03/02/1957	1189.4 m	Paleozoic Magm
206	VVE-2	Villeneuve-2	5.562	46.6967	30/04/1957	1203.5 m	Paleozoic Meta
207	WEI-1	Weiach-1	8.4584	47.5638	12/11/1983	2477.4 m	Paleozoic Meta
208	WIN-1	Wintersingen-1	7.8261	47.5058	23/09/1939	440.0 m	Paleozoic Magm
209	WOE	Wölflinswil-1	7.9979	47.463	11/05/2012	260.0 m	Dogger

A.2 AERIAL MAPS AND ELEVATION MODELS

This chapter describes the available geospatial datasets that were used during the course of this study. Currently available digital Elevation Models (DEM) have different advantages and disadvantages, depending on their application. Such recent datasets constitute the backbone of the structural analysis that was conducted in this study, especially of structural interpretations of the geomorphology for the new structural map compiled for this study (Enclosure 01). Naturally, there will be more accurate models with higher resolution in the future, which will doubtlessly improve the accuracy of geological maps and models.

A.2.1 Satellite and aerial photography

There are several models of aerial photography that are accessible in public. Photographs of earth surface are provided in high-resolution allowing to identify individual trees, boulders or cars for example. They are a good possibility to evaluate artificial structures in DEMs, allowing to see whether a lineament represents a street for example and they are very useful to control the accuracy of GPS points.

World Imagery

A very convenient model is the «World Imagery» base-map that is available from the ArcGIS (GIS software by Environmental Systems Research Institute, ESRI) MapServer (Open source web mapping server, <http://mapserver.org>). It is a collection of satellite and aerial imagery covering the world. A resolution of up to 0.3 m in continental United States and parts of Western Europe is available, although not in all areas.

Google satellite imagery

The Google satellite imagery can be accessed through QGIS. This imagery shows an even better resolution in some parts of Switzerland than the World Imagery model. Images are basically a collection of the NASA and the United States Geological Survey (USGS) Landsat 7 and Landsat 8 observation satellites in combination with aerial photographs.

A.2.2 Terrain models

GDEM

The ASTER Global Digital Elevation Model (GDEM) is a product of METI and NASA. The ASTER GDEM is a popular and well known model and descriptions are extensive. The GDEM has a vertical accuracy of 20 m for 95%. The GDEM was downloaded and the tiles merged into a single raster (using «Mosaic to new raster» in ArcMap 10 without compression). The cell size of the model is 1 arc-second which is $0.000278 \times 0.000278^\circ$. This corresponds to 30.92×45.27 m in the projected coordinate system of Switzerland, CH1903. The GDEM is a good model to represent true elevations, including streets and trees, although surfaces on hillshade models look coarse. The ASTER GDEM shows more details of the surface than the two other models (SRTM DEM or EuroDEM), yet it may have a wider error range of vertical accuracy.

SRTM DEM

The Shuttle Radar Topography Mission (SRTM) DEM is a product of NASA and published in 2014 for the whole world (NASA 2014). The previous version SRTM3 (3 arc-seconds) had a resolution of ~90 m outside America, the current version provides a resolution of 1-arc-second (~30 x 45 m in the Jura area). The ASTER GDEM was used to fill no-data areas. Artificial structures are partially removed (e.g. rivers and roads) and the surface of hillshade models looks smoother

Table A.3 – Overview of available elevation models.

	GDEM	SRTM	EuroDEM	Swiss ALTI^{3D}	RGE ALTI[®]
Manufacturer	METI, NASA	NASA	EuroGeographics	swisstopo	IGN
Source	Satellite	Satellite	National maps	Aerial / LiDAR	Aerial / LiDAR
Resolution	1 arc-sec.	1 arc-sec.	2 arc-sec.	2 m	5 m
Model type	DEM	DEM	DTM	DTM	DTM
Vert. accuracy	20 m abs.	16 m	8–10 m.	0.5 m	~1.5 m
Coordinates	WGS 1984	WGS 1984	ETRS 1989	CH1903	RGF93
Artificial struct.	Yes	Partly	No	No	No
Year	2011	2014	2008		2018
Data depth	16 Bit	16 Bit	16 Bit	32 Bit	32 Bit

than the GDEM, allowing a better recognition of geological structures. According specifications on the USGS website, the vertical datum is EGM96 (Earth Gravitational Model 1996). Above 50°N and below 50°S the SRTM DEM has a resolution of 2 by 1 arc-seconds. NASA specifies an absolute height accuracy of ± 16 m and a relative height accuracy of ± 10 m (for 90% of data points) in the mission statistics.

EuroDEM

The EuroDEM is available in a 2 arc-second (~60 m) resolution model and shows a vertical accuracy of 8-10 m. It is a true Digital Terrain Model (DTM), with artificial structures completely removed. Comparisons between the SRTM DEM and EuroDEM show similar detection levels of structures. The EuroDEM is a compilation of various national maps that are mostly from 1990–2007. Therefore in Switzerland, the EuroDEM corresponds to the «digitales Höhenmodell 25» (DHM25), which is a DTM based on national topographical maps 1:25000, provided by swisstopo. Licenses are free, available from EuroGraphics in Belgium, but need to be prolonged every year.

Swiss ALTI^{3D}

The SwissALTI^{3D} is a DTM provided by the Swiss Federal Office of Topography (swisstopo) covering Swiss area only (Swisstopo 2011). The SwissALTI^{3D} is available in a 2 m resolution model with a precision of ± 50 cm (all axes) below 2000 m a.s.l. and ± 1 –3 m above. The model is mainly produced using digital photogrammetry and laser scanning (LiDAR) below 2000 m.

RGE ALTI[®]

The RGE ALTI[®] version 2 is a DTM provided by the French « Institut national de l'information géographique et forestière » (IGN) and covers French departments (IGN-F 2018). The model was available in a resolution of 5 m in the national coordinate system of France RGF93. The model is created with a combination of LiDAR and aerial photographs. Depending on the applied method, the altitude precision is between ± 0.2 m (laser topography) to ± 1.5 m (photogrammetry).

A.3 CONTENTS OF SUPPLEMENTARY MATERIAL

The supplementary material to this study is provided as a collection of files, including digital grids of models, GIS Shapefiles and others. The following list describes the contents of folders available through the supplementary material.

- A GIS packages:** This folder contains a compilation of GIS files, provided as ArcMap layer packages. A layer package is a 7zip compressed archive, readable by ArcGIS or alternatively, the free 7-Zip program.
- A.01 Structural lines of this study (Enclosure 01, Fig. 2.3, Fig. 2.4)
 - A.02 Tectonic division of this study (Fig. 2.2 on page 24)
 - A.03 Miscellaneous layers, such as names of geological structures, topographic crest, palaeostress trends of previous studies, interpreted occurrence of Permo-Carboniferous troughs (from boreholes in this study) and a line layer documenting anomaly ridges of the gravity model JGM v1.10.
 - A.04 Borehole / Well layers containing list of all boreholes documented in this study (Chapter 3 on page 43), formation tops and thickness of individual lithostratigraphic units in boreholes as well as a layer with compiled boreholes of the «Banque de Sous Sol» provided by BRGM.
 - A.05 Thickness maps (Chapter 4 on page 51), top basement map (Chapter 6 on page 81) and erosion model (Appendix B.2 on page 180)
 - A.06 Flexural-basin-system model (Fig. 6.8 on page 90)
 - A.07 Provisional lineaments and restored positions including interpreted basement fault map from lineament restoration (Appendix B.4 on page 192).
 - A.08 Compiled ages across the JFTB (Chapter 7 on page 97)
 - A.09 Palinspastic restoration model (Appendix B.3 on page 182)
 - A.10 Gravity model (Appendix B.1 on page 175)
 - A.11 Traces of cross-sections from previous studies and this study, as well as traces of seismic lines in the JFTB and surrounding
 - A.12 Compiled and geo-referenced geological maps of previous studies
- B Grids:** Folder containing uncompressed grids of models (all grids are referenced in EPSG:21781, CH1903 / LV03). Model grids are also provided as a layer package in Supplementary Material A. Sub-folders contain:
- B.01 Vertical thickness models, pre-Eocene (Cenozoic erosion removed) and post-Oligocene (models presented in Chapter 4 on page 51).
 - B.02 Mesozoic erosion model (Appendix B.2 on page 180) calculated from pre-Eocene thickness models
 - B.03 Top basement model (Chapter 6 on page 81)
 - B.04 Flexural-basin-system model (Fig. 6.8 on page 90) containing grids and an Excel calculation sheet
 - B.05 Gravity model (JGM v.1.10, Appendix B.1 on page 175)
- C Borehole inventory:** Database containing deep wells (MS Access database) of Chapter 3 on page 43. Graphical well logs are provided at a scale of 1:10'000 in PNG, PDF and SVG file formats. The complete borehole inventory is furthermore provided as a separate PDF document, provided in an A3 page format, containing unit descriptions and graphical logs at a scale of 1:10'000.
- D Cross-section collection:** Cross-sections from literature and this study (Chapter 5 on page 71) with an ArcGIS Shapefile containing traces with links to section figures. The Shapefile is also included in Supplementary Material A.11.
- E Analogue models:** This folder contains documentations to analogue model experiments in Chapter 8 on page 107, published in Schori et al. 2021. Additional videos of experiments and cross-sections extracted from CT-scans are available through the Mendeley Data Repository, Schori et al. (2020).
- E.01 Move (Petroleum Experts) projects for U10-30° (experiment 750) and U10 (experiment 762), containing 3D surfaces of analogue model end-states. Sand, silicone and base-plate 3D surfaces were created using Agisoft (software for photogrammetry).
 - E.02 Protocols of experiments and overview charts
- F Palinspastic restoration:** Python 2.7 based scripts for palinspastic restoration of maps (Appendix B.3 on page 182). Please read the header of Python scripts for more information on how to use the scripts correctly. There are three scripts allowing palinspastic restoration or forward modelling of i) geo-referenced maps in TIF-format (use the CH1903 coordinate system and add a world file), ii) point Shapefiles and iii) line Shapefiles. The Arcpy-extension of ESRI ArcMap is a prerequisite for the Shapefile restoration scripts.
- G Jura hillshade:** High quality hillshade figure of the study area (Fig. C on page 196).

A.4 DATA INTEGRATION FLOW-CHART

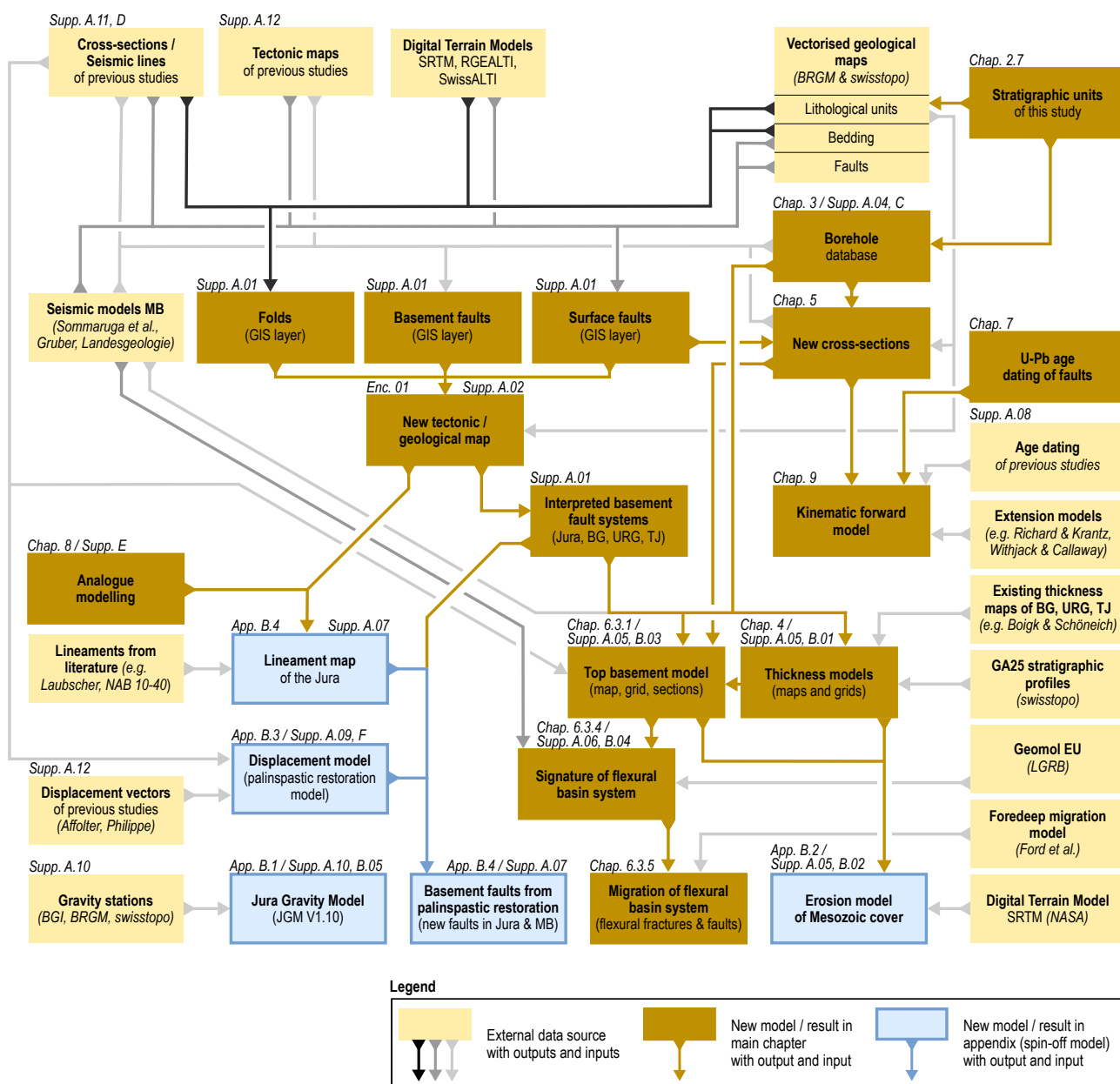


Fig. A.2 – Flow chart illustrating the connection and dependencies of models in this study. Abbreviations are App.: Appendix, Chap.: Chapter, Enc.: Enclosure, Supp.: Supplementary Materials. The Supplementary Material is described in Appendix A.3. Abbreviations of tectonic domains are BG: Bresse Graben, MB: Molasse Basin, TJ: Tabular Jura, URG: Upper Rhine Graben.

B - ADDITIONAL MODELS

B.1 GRAVITY MODEL

B.1.1 Methods

Data source

Available gravity data was compiled in and around the Jura Mountains and a Jura Gravity Model (JGM) was created. Gravity stations originate from three providers, namely the «Bureau de recherches géologiques et minières» (BRGM), swisstopo and the «Bureau gravimétrique international» (BGI). For all available data points, coordinates are provided in WGS 1984 (geographic). Altitude and absolute gravity values are given as well. Absolute gravity values are compatible with the International Gravity Standardization Net 1971 (IGSN71). Provided gravity stations were treated in a Microsoft Access database. There are 84672 stations in total which are partially overlapping (Table B.2), distributed between 4.4°–8.1°E and 45°–48.2°N (WGS 84), which includes the Bresse and southern Upper Rhine Graben, the Jura Mountains and Swiss and French Molasse Basin as well as a part of the Northern Alps. I mainly relied on gravity stations of BRGM and swisstopo. Locations with few stations were complemented with tiles from BGI. Only few stations were available for the Southern Jura.

The swisstopo data points correspond to those used in the «Atlas gravimétrique de la Suisse» (Olivier et al. 2010). They were collected between 1986–2000 and apart from absolute gravity values, complete Bouguer anomalies are provided with the ellipsoid 1967 (IGF1967), a density of 2670 kg/m³ and a topographical correction to 166.6 km around the stations in 4 zones. Data points from BRGM correspond to stations of the «Banque Gravimétrique de la France» (BGF), downloaded on January 25 in 2017. Most stations were collected between 1945–1975. The Terrain correction to each station was given in a separate column. The station dataset of BGI was downloaded on February 9 in 2017. The BGI database is a collection of various providers, including BRGM, the German Geodetic Commission between 1960–1987 and BGI. Terrain corrections are not provided within this data set.

Evaluation and filtering of stations

Overlapping data points of BGI and BRGM reveal a shift of position. All gravity points from the «Banque Gravimétrique de la France» (BGF) were corrected for a gravity map project in 2008 (personal communication Guillaume Martelet, 2017). The French dataset was largely collected between 1945 and 1975 by several operators. Hence, errors were introduced historically, due to changes of the gravity positioning system or during digitalisation of maps for example. Since many gravity measurements were taken along streets, past reworks of the database rectified the positioning of surveys (CM number) in respect to roads (Martelet et al. 2007). An automated minimisation of the altitude difference between given station altitude and DEMs was additionally performed to correct horizontal positions (Martelet et al. 2007). I cross-checked gravity measurement positions from BRGM with World Imagery maps and I can confirm that stations align correctly on roads where present, whereas corresponding BGI stations are often 40–80 m off (systematic shifts apply per survey). Apparently, the BGI database includes uncorrected gravity positions and thus the more recent BRGM data-points were used in overlapping areas. BGI stations were excluded that have a neighbour in a vicinity of 200 m («Find Identical» tool in ArcMap) to counteract distortion by wrongly geo-referenced points. However, BGI data is still used for locations with sparse data to improve the resolution. Less than 30 data points provided by BRGM showed different altitude and / or g_{obs} values at the same position, which may be attributed to historical errors as well. In such cases, stations with altitudes that

correspond closer to DEM values were kept. If filtering by altitude was not possible, an average of the corresponding two stations was used for the JGM. Bouguer anomaly differences between averaged stations are normally not more than 1 mGal and only in one case, a higher difference of 1.8 mGal was noted. The swisstopo dataset was given in WGS 1984 as well as CH 1903 coordinates.

The given altitude of stations was compared to values of two global DEMs, both available in a resolution of 1 arc-second spacing (~30 m). It is seen that the GDEM and SRTM DEM values can deviate substantially from given altitudes of stations (up to 2 km!), but also differences in between the DEMs of more than 300 m may occur. A station filtering was applied assuming averaging accuracies of ± 60 m (absolute height accuracy of SRTM DEM ± 16 m + max. cell inaccuracy at 45° inclination ± 40 m). The vast majority of station altitudes (~98.4%) lie within a range of ± 30 m compared to DEMs. Stations deviating more than the defined averaging accuracies from DEM values (SRTM DEM and GDEM) were excluded, assuming incorrect coordinates or altitude values. This removed about 0.45% stations (compare Table B.2) in the Alps, Black Forest, Vosges, Massif Central and the Jura Mountains, where high topographical changes occur. More than 99.5% of given measurements lie within a range of 60 m of the given DEMs. Note that only very few gravity stations were received for the Southern Jura, roughly between 5.4° – 5.9° E and 46.4° – 45.9° N. This area has a mean point distance of about 0.17° (~19 km) and cannot be interpreted for structures smaller than 20 km.

Calculation of the Bouguer anomaly

Absolute gravity values are reduced with the International Gravity Formula 1967 (IGF1967) at a density of 2670 kg/m^3 . Bouguer anomaly calculations were done for all stations. The following formulas were used:

Bouguer gravity anomaly

$$\Delta g_B = BA = g_{obs} - g_\phi + \delta g_F - \delta g_B (+\delta g_{ter})$$

Latitude correction formula IGF 1967¹ (Source NOAA)

$$g_\phi = 978031.846(1 + 0.005278895 \sin^2 \phi + 0.000023462 \sin^4 \phi)$$

Free-air correction

$$\delta g_F = FAC = 0.308596h$$

¹The International Gravity Formula 1967 (IGF 1967). The International Gravity Standardization Net 1971 (IGSN71), which is a reference frame for absolute gravity measurements, is compatible with IGF 1967.

Table B.1 – Sediment densities from boreholes (Bergerat et al. 1990). Weiach-1 are densities based on Nagra NTB 85-50 (Beilagen 4.8).

Sediment	Density [g/cm ³]
<i>Bresse Basin</i>	
Mio-Pliocene marl	2.4
Stampian marl and limestone	2.5
Late Eocene - Oligocene salt	2.5
Cretaceous and Malm limestone	2.65
Dogger and Lias limestone and marl	2.54
Keuper salt and Muschelkalk dolomite	2.53
Permo-Carboniferous formation	2.55
<i>Jura Mountains</i>	
Jurassic limestone and marl	2.53
Keuper salt	2.5
Permo-Carboniferous formation	2.55
<i>Molasse Basin</i>	
Post-Jurassic marl	2.4
Jurassic limestone	2.6
<i>Weiach-1</i>	
Cenozoic	2.46
Mesozoic	2.66
Permo-Carboniferous	2.56
Crystalline basement	2.71

Table B.2 – Overview of gravity stations sorted by provider. Note that the covered area of BGI, BRGM and swisstopo data overlaps partially. The last column shows the amount of stations that were excluded because the given station altitude does not lie within a range of ± 60 m in both the SRTM DEM and the GDEM elevation models. Final and total values as they account for the final Bouguer Jura Gravity Model (Bouguer JGM) are given in the last row.

	Stations	Area [km ²]	Stations / km ²	Excluded
BGI	11'699	11'103	1.05	82
BRGM	49'765	70'812	0.70	293
swisstopo	23'208	31'424	0.74	4
Total	84'672	113'339		379
- Excluded by altitude	379			
- Area overlap		15'568		
- BRGM duplicates	34			
- BGI duplicates	8990			
- Averaged stations	14			
Final model	75'255	97'771	0.77	

Bouguer mass effect correction

$$\delta g_B = BC = 0.0419008 \rho h$$

Δg_B : Bouguer gravity anomaly

g_{obs} : Measured gravity [mGal]

g_ϕ : Theoretical gravity at given latitude [mGal]

δg_F : Free-air correction [mGal]

δg_B : Bouguer mass effect correction [mGal]

δg_{ter} : Terrain effect correction [mGal]

ϕ : geographic latitude [°]

h : Height above mean sea level [m]

ρ : Mean crustal density [kg/m³]

Treatment of gravity stations

The data stations were treated as follows:

1. Drift correction, included in g_{obs} (swisstopo, BGI and BRGM)
2. Calibration, by provider (swisstopo, BGI and BRGM)
3. Latitude correction is done according to the formula IGF1967
4. Elevation (Free air) using height of given measurement station
5. Bouguer mass effect correction using height of given measurement station and a density of 2.67 g/cm³
6. Terrain correction, delivered by provider for swisstopo and BRGM data points (no Terrain correction was available for BGI stations).
7. Tidal correction, included in g_{obs}
8. Eotvös correction was not applied (no information)
9. Error correction was done manually by removing improbable measurements by comparing altitudes from DEMs and given values in stations.

Terrain correction

The swisstopo dataset included a column with complete Bouguer anomalies (Bouguer anomaly including Terrain correction). BRGM provides the Terrain correction as a separate column (CT167), respecting topographical effects up to 167 km around stations. This is the same perimeter as used for calculating the Terrain correction of swisstopo gravity stations (Olivier et al. 2010). Note that the BGI dataset does not comprise Terrain corrections. A mean rock density (ρ) of 2670 kg/m³ was assumed for calculations.

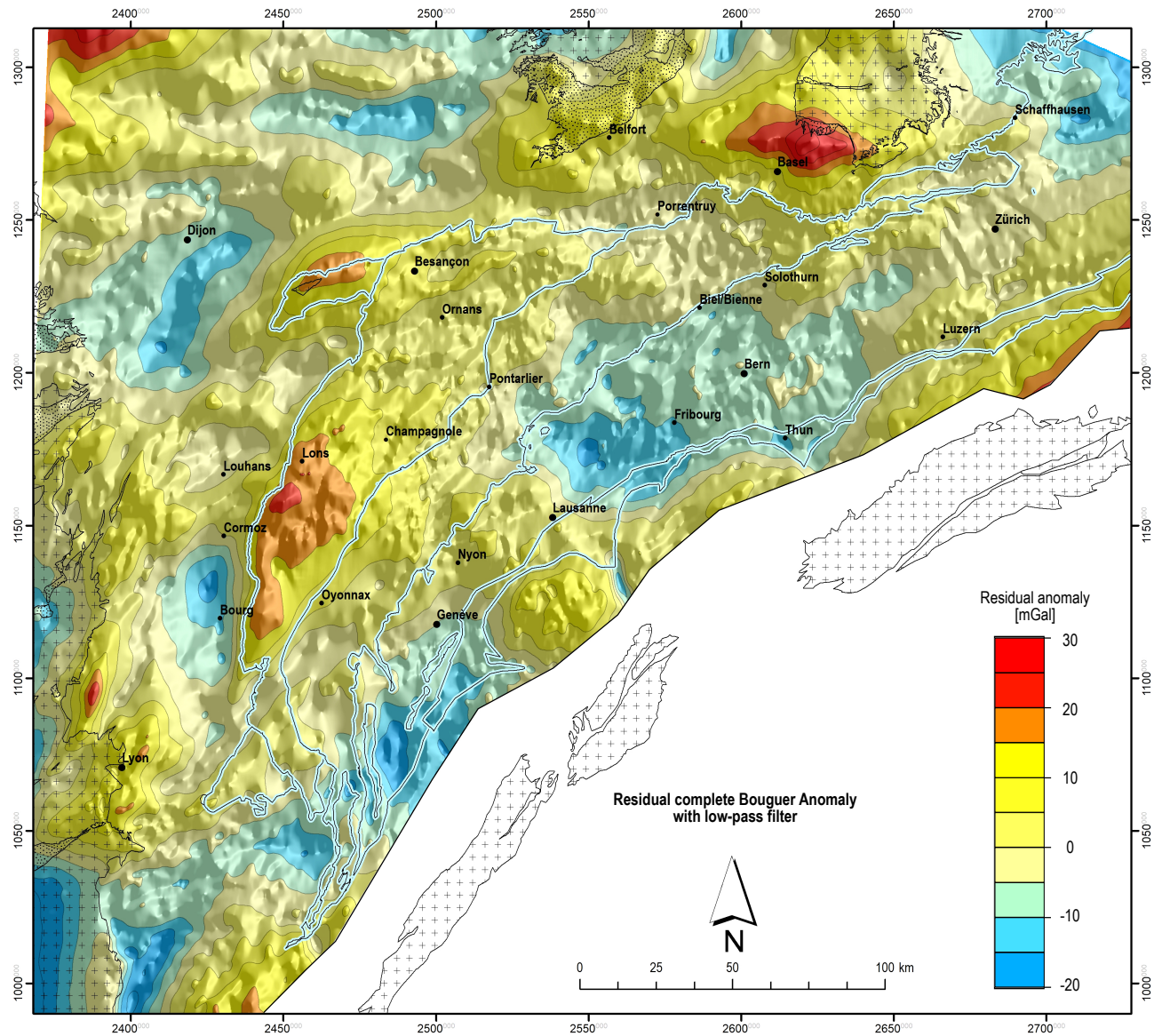


Fig. B.1 – Residual Complete Bouguer anomaly map with low-pass filtering of the Jura Mountains and surroundings. Anomalies are shaded to improve the visibility of peaks and troughs. Structural domains and locations are overlain.

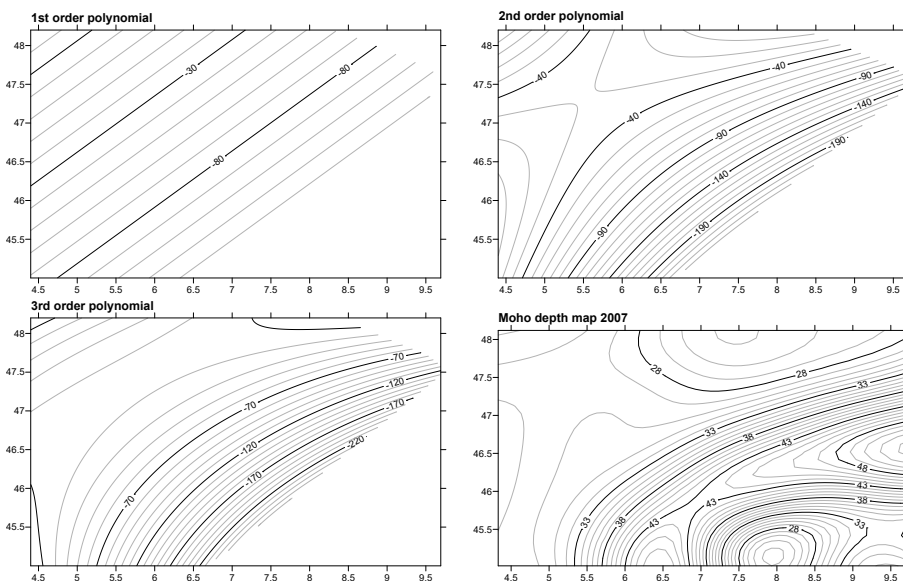


Fig. B.2 – Polynomial regressions on Bouguer data with values representing mGal. The Moho depth map (Grad et al. 2009) is showed in the lower right corner for comparison, values indicate depth in km.

B.1.2 Results

Bouguer and complete Bouguer anomaly grids

Linear Kriging was used on gravity data points to produce the Bouguer and the complete Bouguer map (grid names are JGM110_BA254 and JGM_cBA, see Supplementary Material A.10, B.05). At locations with dense measurements, e.g. along streets in the Bresse Graben, station spacing is in the range of ~200 m, yet a much lower mean spacing of 0.77 stations / km² (=1.3 km mean distance between 2 stations) is received for the whole covered area. Grids were interpolated at a cell size of 0.003° (~ 333 m). The Bouguer map contains regional (long wavelength, e.g. plunging slab) and residual (short wavelength, local features such as basement faults or lithological contrasts) anomalies.

Low-pass filtered, residual complete Bouguer anomaly grid

The complete Bouguer anomaly grid was sent through a low-pass (LP) filter and afterwards, a residual Bouguer anomaly grid was produced by first calculating a 3rd polynomial regression grid for stations (presumed to represent the plunging lithosphere, Green et al. 2013), which was then subtracted from the complete Bouguer anomaly low-pass filtered grid. The result is shown in Fig. B.1.

Low-pass filtering removes or minimises shallow effects (short wavelength) or noise. A moving average on 9 columns and rows (0.027° ~ 2.997 km) was applied on the complete Bouguer model (grid name JGM110_cBA_LP). Past gravity works in Switzerland used the least-square fitting 3rd-order polynomial to the Bouguer gravity data (Green et al. 2013; Klingelé and Schwendener 1984), which is considered the best representation of the regional gravity field in Northern Switzerland. In agreement with this, isolines of the 3rd-order polynomial grid of the JGM show an acceptable, curved shape across the Jura Mountains and surroundings, with a culmination close to Dijon (see comparison Fig. B.2). The contour pattern of the 3rd-order polynomial map (Fig. B.2) resembles the contour pattern extracted from the Moho depth map 2007 (Grad et al. 2009, see Fig. B.2), illustrating the connection between Moho depth and the regional gravity field.

B.2 EROSION MODEL OF THE MESOZOIC COVER

B.2.1 Method

Combining the previously created base Mesozoic (bMes) elevation model (Chapter 6) and thickness models (Supplementary Material B.01, pre-Eocene grids showing palaeo-thickness of lithological groups), a model showing the amount of eroded Mesozoic sediments is created. The total Mesozoic palaeo-thickness model and the BMes-elevation model are summed up in order to obtain the today's synthetic topography as it would be without Cenozoic erosion and thin-skinned deformation features. Thereafter the today's topography is subtracted using the SRTM1 digital elevation model (NASA 2014). The final map is smoothed to remove short wavelength signals caused by river incisions or thin-skinned folds, in order to obtain a regional signature of erosion. In function of the used thickness model, the resulting erosion model indicates the amount of Mesozoic sediments in metres that has been eroded roughly since Mid- to Late Eocene (Fig. B.3).

The resulting model (Fig. B.3) reveals regional erosion where Mesozoic sediments remained exposed during Cenozoic times. Note that Fig. B.3 does not show erosion of Cenozoic sediments. The model can be used as an indicator for tectonic uplift. The amount of erosion does not exactly equal tectonic uplift, since different factors such as climate (e.g. precipitation), fractures, lithology and duration of exposure affect the amount of erosion. The Mesozoic cover is tectonically duplicated in the Internal Jura and due to the applied calculation procedure, the erosion model cannot reveal erosion in this area, even though Mesozoic carbonates are exposed today.

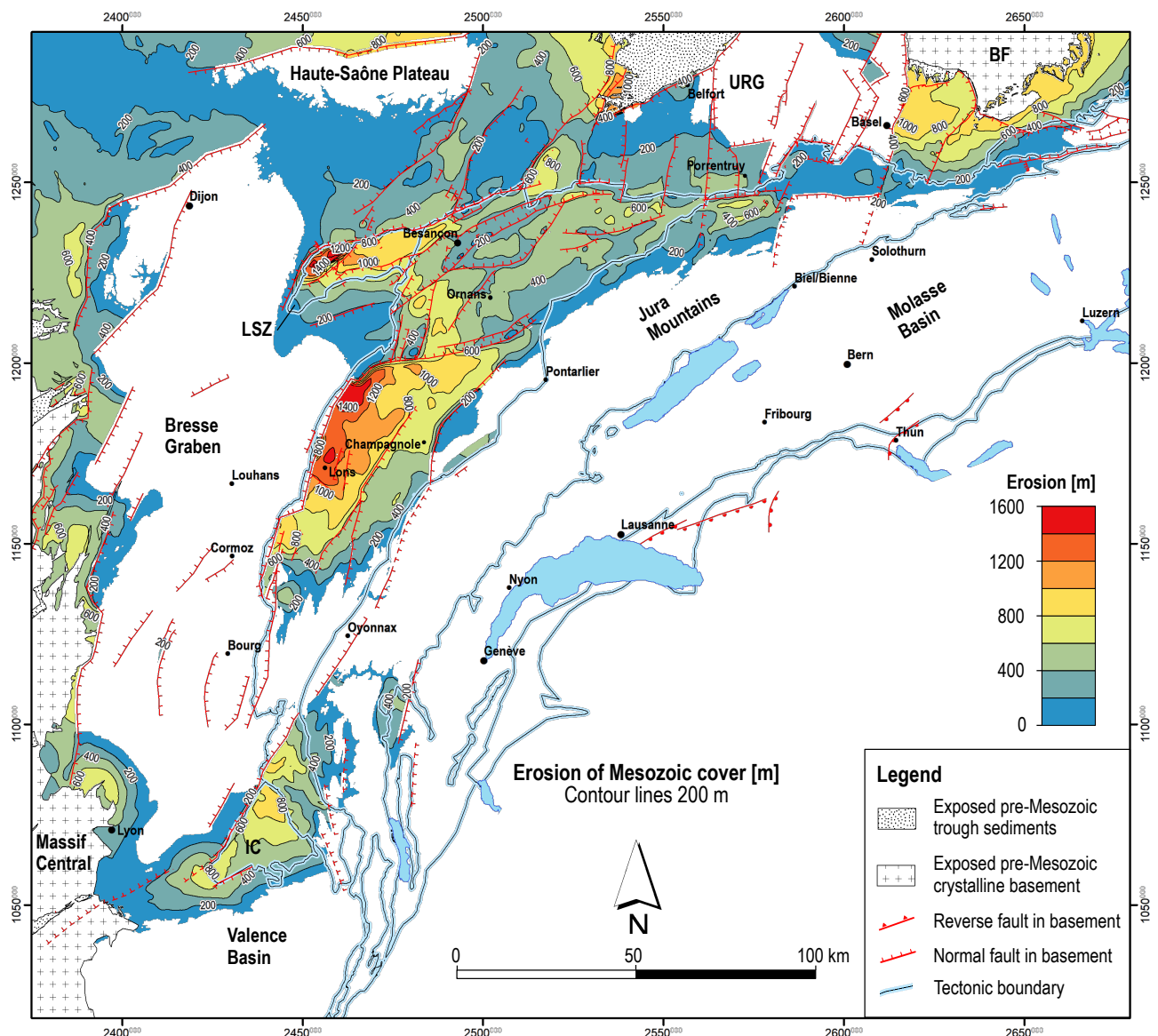


Fig. B.3 – Model illustrating the estimated regional erosion of Mesozoic sediments in the study area (roughly since Upper Cretaceous), before the formation of the JFTB. BF: Black Forest, IC: Île Crémieu, LSZ: La Serre Zone, URG: Upper Rhine Graben, .

B.2.2 Result

In the surroundings of the Jura Mountains, we denote high erosion of Mesozoic sediments at the toe of the Massif Central (> 700 m erosion), the Vosges (> 1000 m erosion) and Black Forest (> 1000 m erosion, Fig. B.3). In the area north of Dijon, at the Haute-Saône Plateau (Fig. B.3), moderate regional erosion of a few hundreds of metres (< 200 m) are identified (Fig. B.3). Within the Jura Mountains, highest erosions are identified in the Faisceau lédonien, north of Lons-le-Saunier (> 1400 m erosion, Fig. B.3), which lies above the eastern Bresse Graben shoulder. Two additionally significant zones are visible on the map (Fig. B.3), which lie in the autochthonous La Serre Zone to the west of Besançon (> 1400 m erosion) and in the Île Crémieu (> 800 m erosion, Fig. B.3). In both of these zones, outcrops of crystalline basement occur. Note that the SE boundary of the erosion in the Jura Mountains lies on a rough NE–SW line that strikes through the cities of Bourg and Basel and is oblique to NNE–SSW striking normal faults.

Note that the erosion model in Fig. B.3 includes cumulated uplift signatures, that is to say erosion as a result of uplift due to flexural bulging, lithospheric buckling and uplift of rift-shoulders. In contrast to this, uplift estimates from the BMes-model (Table 6.2 on page 86) indicate uplifts of rift-shoulders in respect to basin subsidence exclusively.

B.3 MIO-PLIOCENE DISPLACEMENT MODEL

B.3.1 Evaluation of previous displacement models

There are three notable Mio-Pliocene displacement models for the JFTB, which are from Affolter and Gratier (2004), Hindle and Burkhard (1999), Philippe (1995) and Philippe et al. (1996). In the model of Philippe (1995) and Philippe et al. (1996), displacements are based on cross-section and «block mosaic» restoration and displacement directions are based on palaeostress. The model covers the whole of the JFTB. Hindle and Burkhard (1999) present a much simplified displacement model assuming parallel displacement vectors all over the Jura. Due to shorter displacement magnitudes towards the tips of the Jura, a fan-shaped stress pattern is calculated, matching well with palaeostress data from fold-axes orientation and stylolite peaks. Affolter (2003) and Affolter and Gratier (2004) provide a «block mosaic» displacement model, which covers the Central and Southern Jura (the Eastern Jura is not modelled). Displacement magnitudes and directions are based on best-fit 3D block restoration. Forward displacement directions are relatively constant across the Internal Jura area but divergent in the External Jura. This model features rotations fitting well with palaeomagnetic data (Affolter and Gratier 2004).

The two block-restoration models of Philippe et al. (1996) and Affolter and Gratier (2004) were evaluated in terms of consistency with available data. For this, the two models were referenced in a GIS system and the given vectors were digitised. Own cross-section reconstructions and restoration indicate that displacement magnitudes in the model of Affolter and Gratier (2004) are rather underestimated and the magnitudes provided by Philippe (1995) match the reconstructions better, in the central and southern Internal Jura as well as for the Plateau de Champagnole and Plateau lédonien. There are areas in the Internal Jura where Affolter and Gratier (2004) estimates 50% less displacement than Philippe (1995). The Plateau de Champagnole rotated clockwise since its front is thrust in the south (Faisceau de l'Heute) but not in the north (Pincée de l'Heute). In here, the model of Affolter and Gratier (2004) fails to explain a rotation whereas the model of Philippe (1995) shows a differential displacement, which explains a rotation. Displacement directions given by both models within the Internal Jura are similar. However, in the central External Jura (Plateau d'Ornans s.l. and Champagnole as well as the Plateau and Faisceau lédonien), substantial differences are noted.

The model of Philippe (1995) fails to explain anticlines in the Faisceaux de Quingey because displacement vectors are sub-parallel to the traces of anticlines there. In comparison to that, the displacement directions in the model of Affolter and Gratier (2004) work better with own structural observations. In the southern part of the External Jura, vector directions of Affolter and Gratier (2004) are similar to palaeostress orientations from fault-slip data and fold-axis orientations (Homberg et al. 2002; Laubscher 1972), whereas directions of Philippe (1995) are rotated clockwise. Considering strike-slip systems that are documented on DEMs (IGN-F 2018), directions of displacement vectors in Affolter and Gratier (2004) at the Plateau lédonien are almost sub-parallel to sinistral strike-slip systems and thus rather improbable.

It is concluded that the displacement model of Philippe (1995) is a good representation for displacements in the Internal Jura and the southern External Jura (Plateau de Champagnole, Plateau de Levier, Plateau de Nozeroy, Faisceau lédonien, Plateau lédonien, etc.), whereas the model of Affolter and Gratier (2004) performs better in the central External Jura (Plateau d'Ornans s.l., Faisceau de Quingey and Faisceau des Avant-Monts).

B.3.2 Documentation of new displacement model

An own displacement model was created, incorporating evaluations of previous models (Affolter and Gratier 2004; Philippe et al. 1996), tectonic limits evaluated on a new tectonic map (Enclosure 01), structural observations as well as own cross-section restorations. The model covers the whole of the JFTB (e.g. including the Vorfaltenzone and the Faisceau des Avant-Monts, which were not included in Philippe et al. 1996) and the majority of the detached Plateau Molasse. The new displacement model can be used to restore or forward model any given digitised map, referenced in the coordinate system CH1903 / LV03. Referenced maps of the displacement model are provided in Supplementary Material A.09.

The model features «dynamic blocks» that allow shortening within individual blocks, geologically corresponding to moderate internal deformations (e.g. folding in the Molasse Basin or individual plateaus). A Python 2.7 based script suite is written (Supplementary Material F), based on the free PIL library of Python 2.7. The scripts allow a palinspastic restoration or forward-deformation of geo-referenced raster layers (TIF-files with world-file). Maps have to be projected in the Swiss coordinate system CH1903. In this way, evaluated lineaments of the JFTB can be restored to their pre-JFTB location. A script adaption for point and line shape-files was also developed, based on the Arcpy Python library (included in ESRI ArcGIS 10.6).

Block limits are defined using structural limits of an early version of the tectonic map created for this study (Enclosure 01). Small faisceaux in between the Jura plateaus are not modelled as independent blocks, but as transition zones between plateaus. The Internal Jura is distinguished into imbricates and nappes, following large tear faults (lateral thrusts) and thrust fronts (often showing kilometric displacements). The displacement of blocks is evaluated from south-east to north-west, first using estimates from literature for the Internal Jura (Philippe et al. 1996) and then respecting relative shortenings, which are estimated from cross-sections along thrust fronts.

The displacement direction and magnitude of individual point-locations within blocks are evaluated. Thereafter, algorithms of ESRI ArcGIS are used to create a smooth interpolation between point-locations. Different interpolation al-

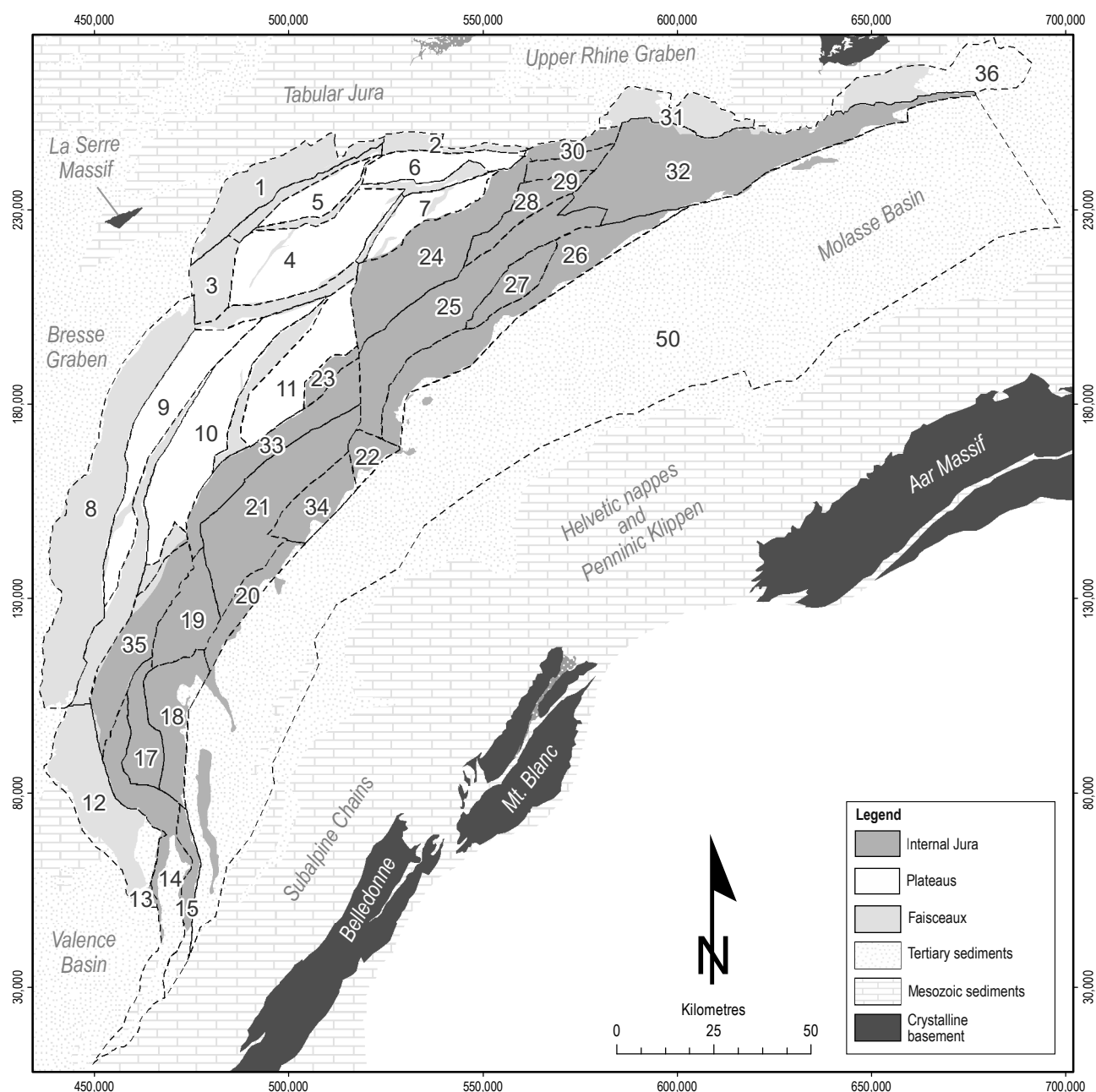


Fig. B.4 – Principal division and numbering of blocks in the Jura Mountains and detached Molasse Basin (Block 50).

gorithms are used depending on the structural type of a dynamic block. For example, plateau blocks show rather homogeneous displacement, with few internal deformation. Therefore, these blocks are preferably modelled with polynomial algorithms, whereas faisceaux and Internal Jura nappes show more heterogeneous displacements (“squeezing”), favourably interpolated with spline or local polynomial algorithms.

Block 1 – Faisceau des Avant-Monts: Neither Philippe et al. (1996) nor Affolter and Gratier (2004) cover this zone since it was not defined as detached Jura before (Madritsch et al. 2008). Hence the frontal displacement vectors needed to be defined. I used cross-section reconstruction to estimate a frontal displacement magnitude of roughly 1.75 km at the centre of Block 1. Eastern displacements must be smaller in order to maintain consistency with smaller displacement magnitudes in the south. The displacement model of Affolter and Gratier (2004) was used to define displacement vectors at the southern limit of Block 1.

Block 2 – Faisceau de Lomont: Block 2 was kept consistent in the south with Block 6. Apparently, there is more displacement in the west than in the east. Displacement directions fit palaeostress estimated from documented strike-slip faults and displacement magnitudes are similar to Block 6.

Table B.3 – Displacement magnitudes and directions with mean values for each block. IJ: Internal Jura.

Block No.	Name	Magnitude [km]			Forward direction [°]			Restoration direction [°]		
		Min.	Max.	Mean	Min.	Max.	Mean	Min.	Max.	Mean
1	Faisceau des Avant-Monts	1.1	2.9	2.0	309	329	322	129	149	142
2	Faisceau de Lomont	0.1	2.5	1.4	339	354	348	159	174	168
3	Faisceau de Quingey	1.9	8.2	4.1	306	312	310	126	132	130
4	Plateau de Montrond / Ornans s.s.	1.9	7.0	5.3	326	345	336	146	165	156
5	Plateau de Bouclans	1.7	5.4	3.3	344	359	349	164	179	169
6	Plateau de Sancey	0.4	2.9	1.8	338	359	350	158	179	170
7	Plateau de Pierrefontaine	1.6	5.6	3.7	326	342	333	146	162	153
8	Faisceau lédonien	1.2	9.6	6.1	268	314	286	88	134	106
9	Plateau lédonien	8.0	9.7	9.2	296	314	307	116	134	127
10	Plateau de Champagnole / Levier	9.4	10.8	10.0	300	312	306	120	132	126
11	Plateau de Nozeroy	9.4	11.5	10.2	300	312	307	120	132	127
12	Faisceau de Bugey / Ambérieu S	0.7	8.5	4.3	258	282	267	78	102	87
14	IJ, Southern Jura front	1.1	16.4	7.2	258	310	289	78	130	109
15	IJ, Mont Chat	6.5	19.3	9.3	295	295	295	115	115	115
17	IJ, Planachat	13.8	15.0	14.4	281	293	287	101	113	107
18	IJ, Grand Colombier	20.5	25.1	23.0	290	297	294	110	117	114
19	IJ, Tacon	13.5	23.2	17.9	289	300	293	109	120	113
20	IJ, Mont Credo	25.7	32.2	29.5	301	304	303	121	124	123
21	IJ, Risoux	19.2	24.1	22.1	301	317	308	121	137	128
22	IJ, Pontarlier triangle	28.6	32.2	31.3	305	305	305	125	125	125
23	IJ, Pontarlier W	10.8	12.2	11.5	310	312	311	130	132	131
24	IJ, Doubs	1.9	14.7	7.0	313	327	320	133	147	140
25	IJ, Mont Soleil	9.1	29.0	15.3	312	331	321	132	151	141
26	IJ, Chasseral	11.2	29.9	19.0	311	331	320	131	151	140
27	IJ, Val de Ruz	13.5	17.6	15.2	312	338	331	132	158	151
28	IJ, Goumois	3.6	11.8	5.9	318	333	325	138	153	145
29	IJ, Clos du Doubs	1.8	2.5	2.1	325	334	330	145	154	150
30	IJ, Roche d'Or	1.1	1.6	1.5	326	334	328	146	154	148
31	IJ, Ferrette Zone	0.0	1.9	1.0	331	351	339	151	171	159
32	IJ, Eastern Jura	0.3	12.3	5.3	331	340	334	151	160	154
33	IJ, Central front	11.3	17.8	13.8	296	309	301	116	129	121
34	IJ, Mont Tendre	29.2	32.0	30.7	299	306	302	119	126	122
35	IJ Oyonnax	6.8	12.4	8.9	285	293	291	105	113	111
36	Vorfaltenzone	0.0	1.6	0.8	335	335	335	155	155	155
50	Molasse Basin	1.1	33.2	17.4	302	335	323	122	155	143
Min. / Max. / Mean of all blocks		0.0	33.2	10.6	258	359	314	78	179	134

Block 3 – Faisceau de Quingey: The displacement magnitudes of Affolter and Gratier (2004) correspond to estimations from own cross-section construction. The model of Philippe et al. (1996) fails to explain north–south striking folds since the displacement is sub-parallel to them. Therefore, Affolter and Gratier (2004) is used for displacement directions.

Block 4-5 – Plateau de Montrond and Plateau de Bouclans: In the east and centre of Block 4, directions from Affolter and Gratier (2004) fail to explain sinistral faults – displacement directions are perpendicular to these faults. Philippe et al. (1996) indicates directions that are 60° oblique to Affolter and Gratier (2004). Both authors suggest a clockwise rotation of Block 4 and 5 during the evolution of the Jura. Therefore, displacements are presumed to be somewhat counter-clockwise rotated in comparison to palaeostress trends. The left hand side of Block 4 does not agree with palaeostress directions. Displacement directions, defined according rotation point of Blocks 4 to 7, are more similar to Philippe et al. (1996) than to Affolter and Gratier (2004). The finally evaluated displacement directions are able to explain observed sinistral faults.

Block 6 – Plateau de Sancey: North-east directions agree with Philippe et al. (1996) and Affolter and Gratier (2004). Directions are in agreement with documented sinistral strike-slip faults. Philippe et al. (1996) defines roughly 2.6 km displacement in the west. Displacement grids were interpolated using a 2nd order polynomial algorithm.

Block 7 – Plateau de Pierrefontaine: Cross-sections running across this block are from Fig. 5.3, Affolter and Gratier (2004) and Burkhard (1990). Displacements were mainly defined by estimations on Fig. 5.3 and a linear decrease towards 0 at the rotational point. Directions were defined by assuming a clockwise rotation of the block. Directions are perpendicular to folds in the centre of the block. I used a 2nd order polynomial algorithm to calculate both displacement direction and magnitude grids.

Block 8 – Faisceau lédonien: From own reconstructions, a displacement of 3 km is inferred close to the front of this block, north of Lons-le-Saunier. At Lons-le-Saunier, the displacement is rather higher, about 4-5 km, which agrees with Chauve et al. (1988). South of Lons-le-Saunier, thrust amounts from cross-sections are rather smaller, between 2-3 km (various cross-sections). Displacement magnitudes in the Plateau lédonien are ~10 km in the north and less to the south (min. 7.5 km) from own cross-section constructions. Displacement magnitudes of Affolter and Gratier (2004) correspond closely to estimated magnitudes in the front of Block 8. However, the magnitudes of Philippe et al. (1996) are in better agreement with own estimations and therefore, displacement values of Affolter and Gratier (2004) are considered an underestimate. Displacement directions of both Philippe et al. (1996) and Affolter and Gratier (2004) can be justified at the front with identified conjugate faults. However, directions of Affolter and Gratier (2004) at the Plateau lédonien are rather parallel to dextral faults, which suggests to use Philippe et al. (1996) for the Plateau lédonien.

Block 9 – Plateau lédonien: To the north of Block 9, about 10 km displacement are estimated from own cross-sections (matching Philippe et al. 1996) and to the south, at least 7.5 km displacement is estimated. Directions of Affolter and Gratier (2004) are at very high angles to identified sinistral faults (70-80°) and almost parallel to presumed dextral faults, hence rather improbable. The block rotates counter clockwise during restoration.

Block 10 – Plateau de Champagnole: The block rotates counter clockwise during restoration. The estimated displacements of 8.5-10 km roughly correspond to values of Philippe et al. (1996).

Block 11 – Plateau de Nozeroy: Philippe et al. (1996) and Affolter and Gratier (2004) show similar restoration directions with a mean of roughly 127°. The Plateau de Nozeroy rotates counter clockwise during palinspastic restoration. The northern part of the Plateau de Nozeroy shows deformation structures which are not included in the model (no compression of this area).

Block 12 – Faisceau de Bugey and Faisceau d'Ambérieu S: The restoration direction of this block is ENE in Affolter and Gratier (2004) and Philippe et al. (1996). The block is therefore supposed to be pushed sideways by blocks of the Internal Jura. Displacements from Philippe (1994) suggest that the front is thrust 3 km onto Tertiary sediments of the Bresse Graben and 1.5 km onto the Ile Crémieu.

Block 14 – IJ, Southern Jura front: There is no data from Affolter and Gratier (2004) for the southern portion of this block. From cross-sections of Philippe et al. (1996), I estimate 3.3 km thrusting of Block 15 onto Block 14 (Echelles thrust) and finally 2.5 km thrusting of Block 14 onto the BG. Displacements were roughly estimated from Philippe (1994) and Philippe et al. (1996) cross-sections. Displacement magnitudes are consistent with adjacent Blocks 15, 17 and 18. Affolter and Gratier (2004) indicate SE displacement to the directions in the southern part of Block 14. These directions are rather improbable considering structures that are observed and more east-wards displacement directions are considered, that closely correspond to Philippe et al. (1996).

Block 15 – IJ, Mont Chat: Philippe et al. (1996) apparently estimated displacements directions perpendicular to fold axes, whereas the model of Affolter and Gratier (2004) tries to avoid too much lateral extension. I decided to use 115° as mean restoration direction. This value is consistent with the Culoz-fault and shows a favourable orientation to explain supposed sinistral faults (the directions of Affolter and Gratier 2004 point too far southwards to explain some of these faults).

Block 17 – IJ, Planachat: Displacement directions were estimated between 108-110° in Affolter and Gratier (2004), which is consistent with conjugate fault systems. These values also roughly agree with Philippe et al. (1996) who indicates slightly lower directions of ~105-110°. The front of the Planachat Anticline is thrust about 2 km onto the Hauteville syncline, which is estimated on behalf of cross-sections of Philippe (1994). The Grand Colombier thrust (Block 18 front) shows shortening between 5-7.5 km, estimated from cross-sections in Philippe (1994).

Block 18 – IJ, Grand Colombier: Estimated shortening at the thrust of the Grand Colombier anticline from cross-sections in Philippe (1994) is 3.45 km in the south and 7.3 km in the north. The northernmost portion of Block 18 (Mt Crédo, Philippe et al. 1996), is thrust roughly 5 km on Block 19.

Block 19 – IJ, Tacon: The block is made of several imbricates, with the Credo-Vuache fault cross-cutting the structures. From the cross-section of Philippe et al. (1996), following estimations are made: shortening at Puthod thrust is 1.1 km, 1.2 km at the Cruchon thrust and 5.7 km at the Cruchon backthrust (total of 8 km shortening). The displacement directions of Affolter and Gratier (2004) are coherent with observed structures. The Tacon Thrust shows a shortening of 5.2 to 7.7 km, estimated from a cross-section of Wildi and Huggenberger (1993).

Block 20 – IJ, Mont Crédo: Estimations in the cross-sections of Philippe et al. (1996) for the Mont Credo reveal roughly 3 to 4.2 km shortening. A shortening of 3 km is given in Affolter and Gratier (2004) and 3.8 km follow from own cross-section constructions. The southern part of this block is estimated at 32 km displacement acc. Philippe et al. (1996). The left hand side of the block needs slightly more displacement in order to form the Septmoncel sinistral fault.

Block 21 – IJ, Risoux: From own cross-sections, I estimate max. 23 km displacement at the SE boundary of this block and the shortening at the Mont Risoux thrust (duplication) is estimated at about 11 to 13 km. The Risoux frontal thrust disappears almost completely to the east.

Block 22 – IJ, Pontarlier – La Sarraz triangle: The displacement direction is estimated to be rather oblique to the sinistral Pontarlier fault and subparallel to the La Sarraz dextral fault (oblique ramps are recognised on the Pontarlier fault and rather pure dextral displacement is suggested for the La Sarraz fault). The front of the block is suggested to thrust roughly 4 km onto Block 21.

Block 23 – IJ, Pontarlier W: Indicated directions of Philippe et al. (1996) and Affolter and Gratier (2004) are similar. Philippe et al. (1996) indicates 16 km displacement to the north, whereas Affolter and Gratier (2004) indicates a mere 5.3 km, which is not enough to keep the block consistent with more frontal displacements.

Block 24 – IJ, Doubs: At the northern end of the cross-section of Rime et al. (2019) displacement is about 9 km. Directions from Affolter and Gratier (2004) for the left hand side of the block are consistent with strike-slip faults.

Block 25 - IJ, Mont Soleil: Displacement directions in the west of Block 25 are taken from Affolter and Gratier (2004), which is consistent with observed conjugate fault systems and palaeostress trends (Homberg et al. 2002; Laubscher 1972). To the east, especially at the Ferrière fault, directions from both models (Affolter and Gratier 2004; Philippe et al. 1996) are rather improbable since they tend to be 90° to documented strike-slip faults. I estimate a restoration direction of 151° for the east end of the block (gradual increase from west to east). Using Rime et al. (2019), 3 km shortening across the block is estimated and 5.5 km thrusting onto Block 24.

Block 26 – IJ, Chasseral: Two rather good fix points are given in Philippe et al. (1996) from balanced cross-sections. The east of the block shows a displacement of 12 km whereas 21 km are given for the west. A rather minor shortening of 0.5 to 1 km across the block itself is estimated from cross-sections of Sommaruga (1997) and Philippe et al. (1996).

Block 27 – IJ, Val de Ruz: Displacement directions of Philippe et al. (1996) are roughly parallel to principal palaeostress directions from fault-slip data (Homberg et al. 2002). Displacement directions of Affolter and Gratier (2004) are considered improbable.

Block 28 – IJ Goumois: For the displacement direction of this block, directions of Philippe et al. (1996) are considered (between 137°-141°). Directions of Affolter and Gratier (2004) (123°) are almost perpendicular to strike-slip faults which is considered improbable. It seems that the left hand side of the block experienced more displacement, resulting in a counter-clockwise rotation during restoration.

Block 29/30 - IJ, Clos du Doubs / Roche d'Or: Cross-sections from Caër (2016), Nussbaum et al. (2017) and Philippe et al. (1996) were used for displacement magnitudes. The displacement at the front of the block varies between 1.1 and 2.8 km.

Block 31 – Ferrette Zone: Displacements of this block are well constrained by balanced cross-sections of Ustaszewski and Schmid (2006).

Block 32 – IJ, Eastern Jura: Shortenings of the southern limit are estimated from balanced cross-sections Philippe et al. (1996). In the east, cross-sections of Nagra (Madritsch and Deplazes 2014) are used to constrain displacement magnitudes. The north is defined by balanced cross-sections of Caër (2016) and Nussbaum et al. (2017) as well as Ustaszewski and Schmid (2007). A restoration direction of about 150° is used, which is consistent with conjugate fault systems. To the east, a 160° displacement direction is defined to justify observed fault systems. Note that the displacement model of Philippe et al. (1996) indicates a 130° restoration direction.

Block 33 – IJ, Central front: At the rear, Block 33 has 14 km displacement (estimated from shortenings in the Risoux cross-sections) and roughly 12 km at the front. The 16 km displacement given by Philippe et al. (1996) is considered an overestimate, whereas 6.5 km of Affolter and Gratier (2004) is decidedly too short to maintain consistency with surrounding blocks.

Block 34 – IJ, Mont Tendre: The displacement estimated from own cross-section construction corresponds to the roughly 32 km displacement given by Philippe et al. (1996). About 9 km shortening are estimated on the Mont Tendre thrust (which constitutes the front of the block). A substantial shortening of 12 to 13 km is estimated for the Risoux anticline.

Block 35 – IJ, Oyonnax: The Oyonnax block constitutes the front of the Internal Jura. Both previous displacement models (Affolter and Gratier 2004; Philippe et al. 1996) agree on a displacement direction of $\sim 110^\circ$. The displacement on the Oyonnax backthrust is estimated at 3.5 to 4 km (Philippe 1994, 1995).

Block 36 – Vorfaltenzone: Displacements are based on cross-sections of Madritsch and Deplazes (2014). Displacements are moderate, between 100 to 1500 m at maximum. The restoration direction is set at a constant 155° .

Block 50 – Molasse basin: Directions are set according conjugate faults. A somewhat fan shaped forward displacement field results, with directions between 302° in the SW and up to 335° in the E (Table B.3). The displacement magnitudes at the Alpine front are estimated from Burkhard (1990) in the east of Block 50. Generally, displacements across this block (the Molasse Basin) are not verified and a result of interpolation between adjacent blocks (of the Internal Jura) and estimations from previous studies for the Subalpine Molasse.

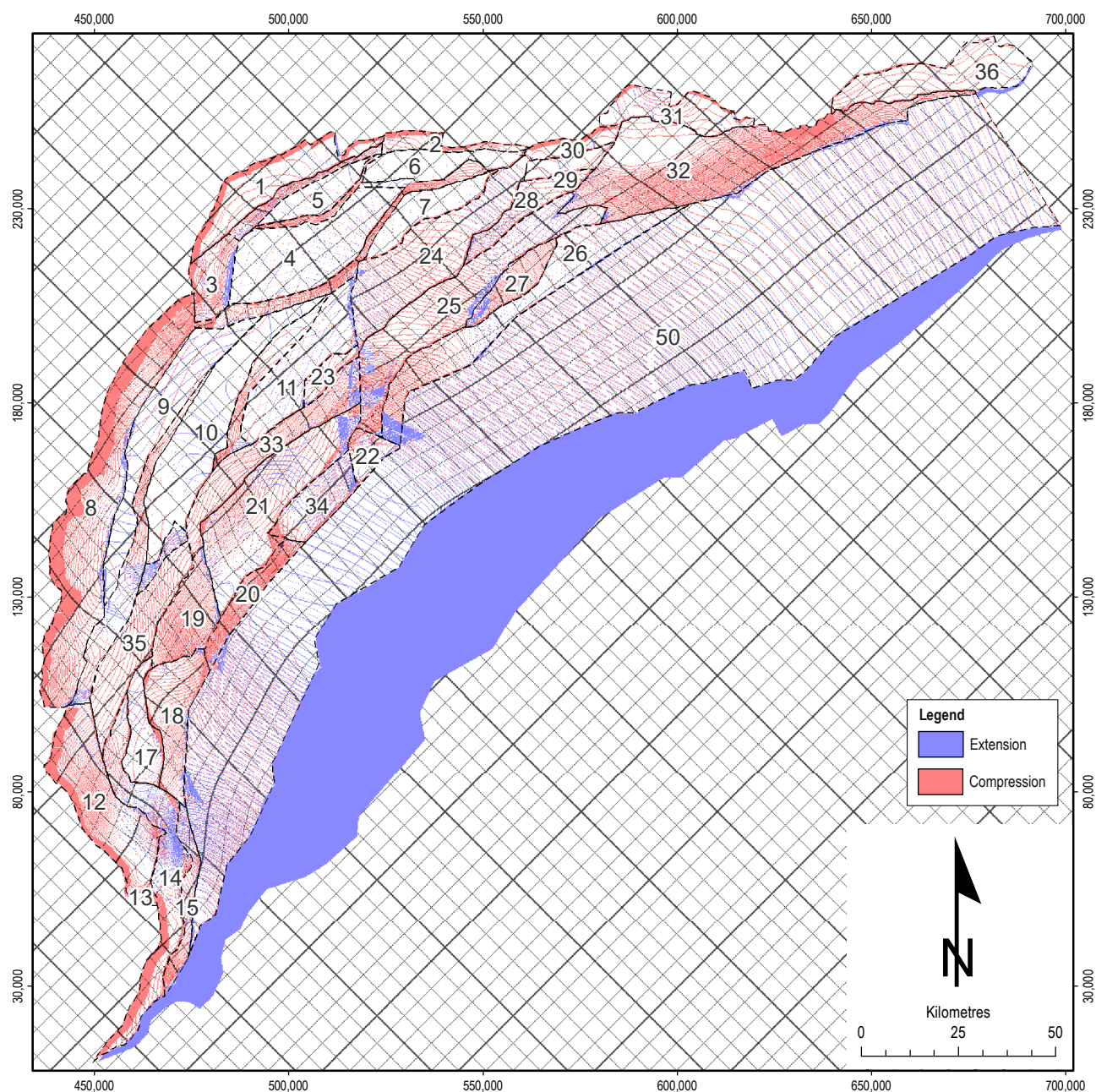


Fig. B.5 – Analysis of forward model. Forward modelling scripts are used to mark compression (indicating folding and/or thrusting) and extension (blue). The blue area south of Block 50 (the detached Molasse Basin) is a result of the modelling boundary and has no geological meaning. Blue areas within the Jura (e.g. Pontarlier fault zone or Faisceau de Quingey, Block 3) are interpreted as inconsistencies of the current model, since extension in these areas is rather improbable. The reference grid is rotated 45° and reference lines are therefore NW–SE (roughly parallel to the mean transport direction of the JFTB, see Table B.3) and NE–SW.

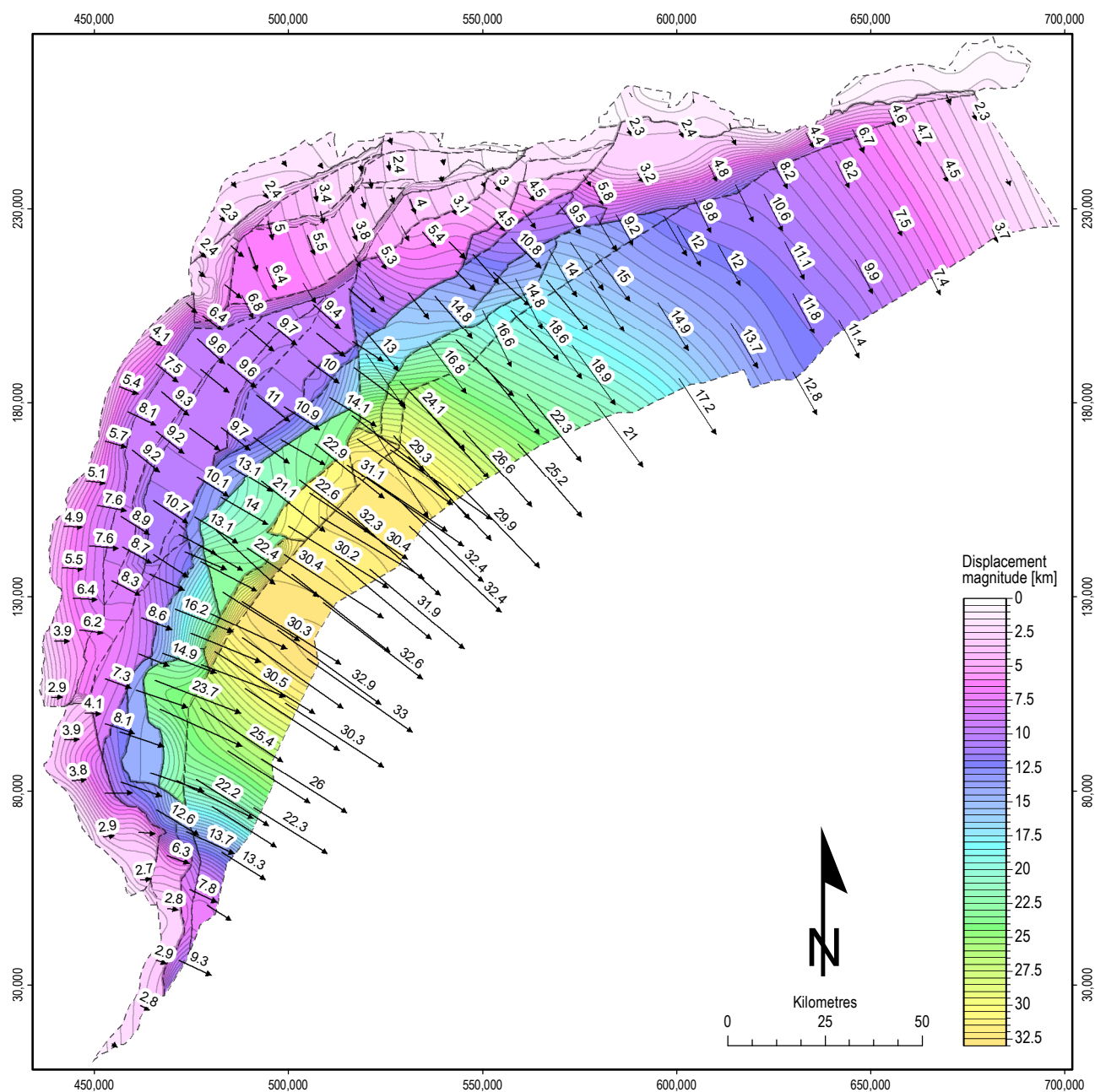


Fig. B.6 – Restoration model with isolines for displacement magnitudes. The highest displacement magnitudes in the Jura occur at the Mont Tendre block (Block 32, ~32 km), west of the Pontarlier system. The plateaus of the Southern Jura (Blocks 9, 10 and 11 corresponding to the Plateau lédonien, Plateau de Champagnole, Plateau de Levier and Plateau de Nozeroy, respectively) rotate counter-clockwise during restoration and show displacements between 9 and 11 km whereas the Plateau d’Ornans s.l. (Blocks 4 to 7, also rotating counter-clockwise) shows 1.5 – 6 km displacement.

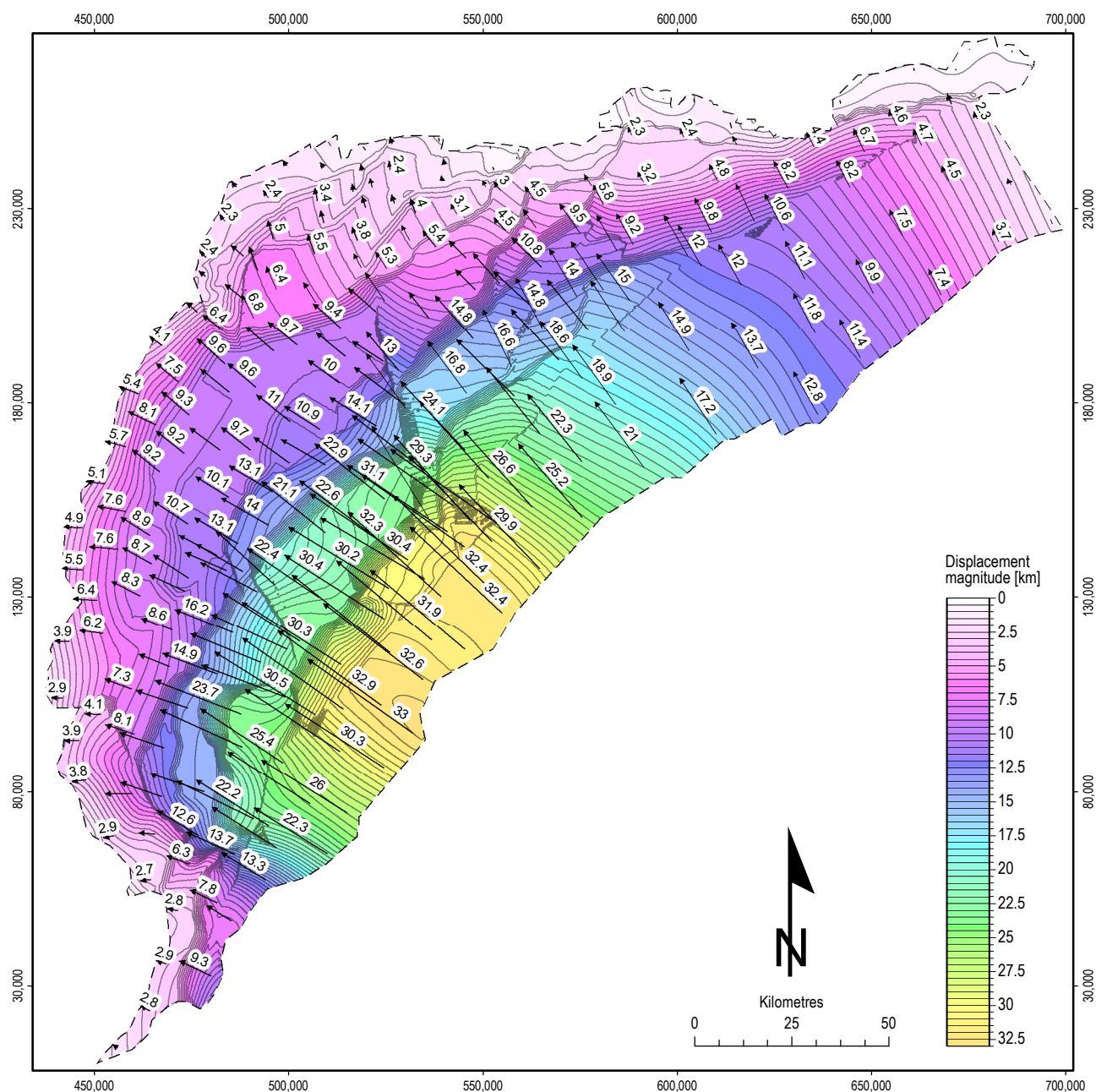


Fig. B.7 – Forward model displacement field. The forward model is calculated from restoration of the initial direction and magnitude grids. Gaps received due to restoration are filled with a spline interpolation.

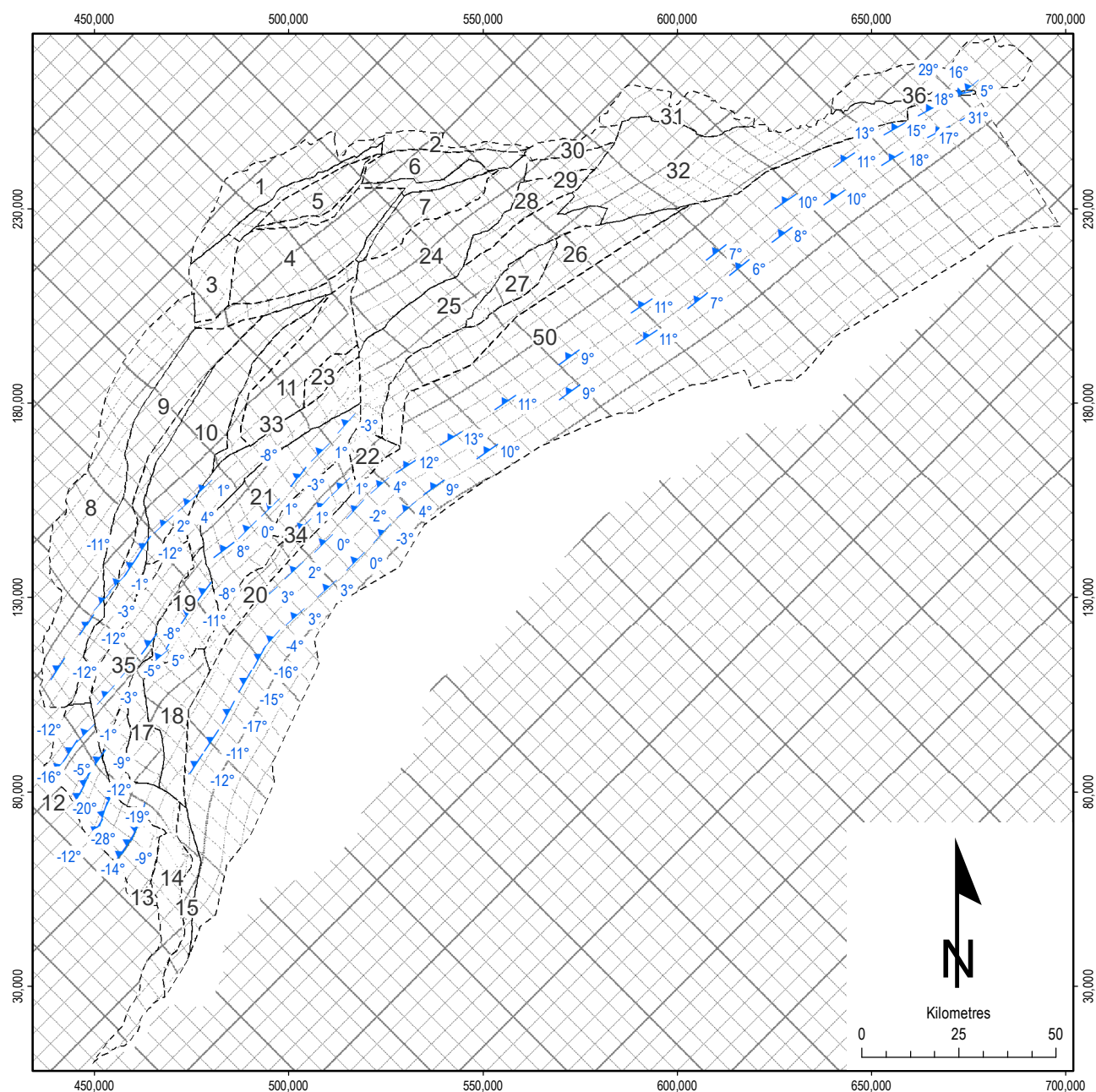


Fig. B.8 – Rotation analysis of the displacement model, showing a reference grid (with NW-SE and NE-SW lines), which is deformed during forward modelling. Differential displacement causes rotation of the reference grid, counter-clockwise (negative value) in the west and clockwise (positive value) in the east. Rotations are consistent with palaeomagnetic data (e.g. Gehring et al. 1991) as compiled in Affolter and Gratier (2004).

B.4 LINEAMENT RESTORATION AND INTERPRETED BASEMENT FAULTS

A palinspastic restoration of lineaments in the cover of the JFTB is conducted in here. Lineaments in the JFTB are lines that connect various oblique structures of the detached cover (Laubscher 2008a,b; Meier 2010; Steinmann 1892) or extensional structures such as normal faults and grabens (pincée according Glangeaud 1944), which are presumed to be restricted to the cover of the JFTB. The Eastern Jura reveals several NNE–SSW (Rhenish) striking lineaments (Fig. B.9), which are documented in Laubscher (2008b) and Meier (2010). The Central and Southern Jura also shows ENE–WSW (Erzgebirgian) as well as NW–SE (Hercynian) striking lineaments (Fig. B.9). These lineaments are supposed to be connected to faults in the Pre-Mesozoic basement, which controlled deformation during Mio-Pliocene formation of the JFTB (chapter 8 and Schori et al. 2021). Fig. B.9 shows interpreted lineaments and the corresponding restoration vectors from the displacement model (Appendix B.3), whereas Fig. B.10 shows the deduced position of basement faults after the palinspastic restoration of lineaments.

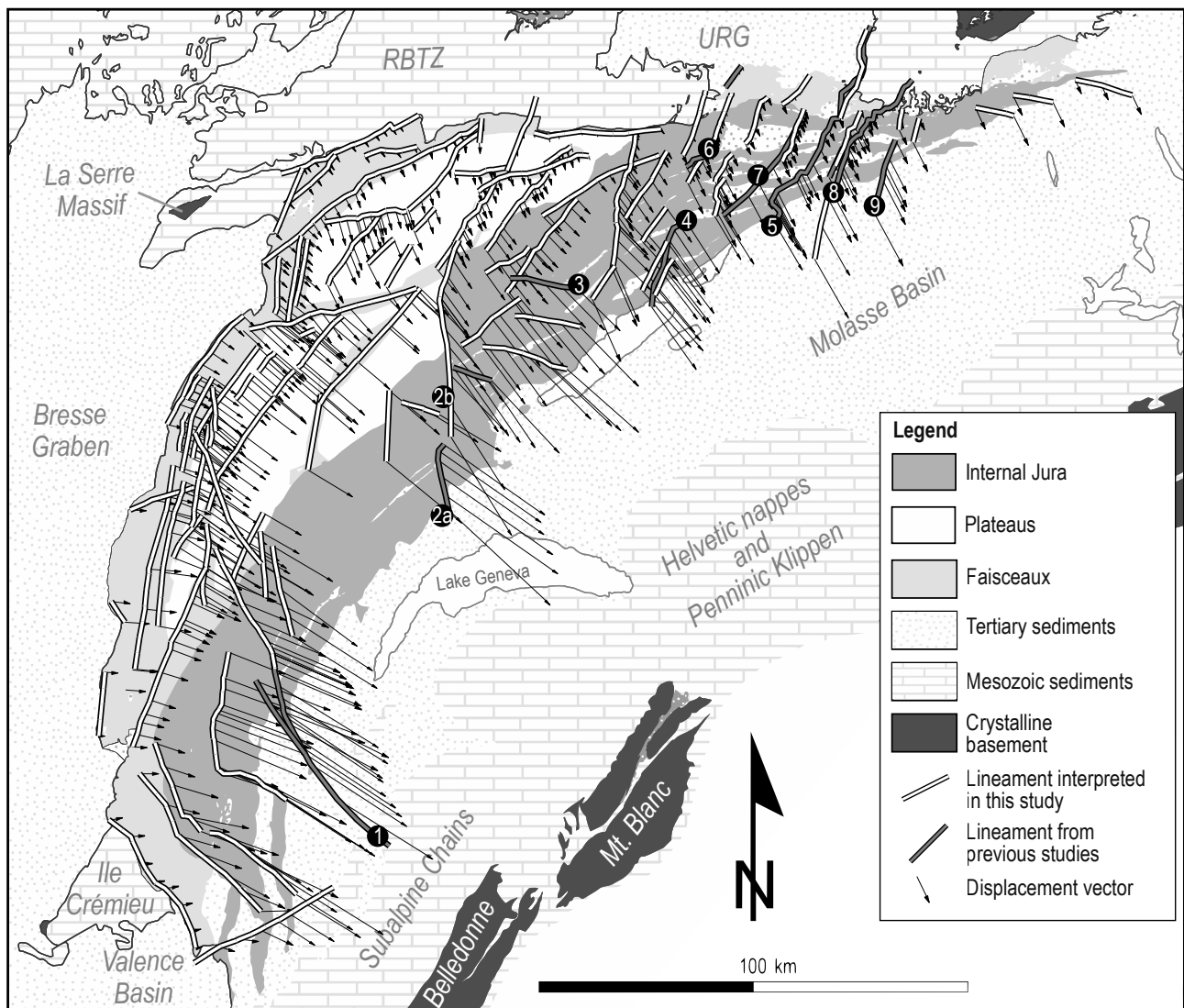


Fig. B.9 – Overview of lineaments interpreted from structures in the JFTB. Grey lineaments are from literature, whereas white lineaments are interpretations of this study. Lineaments are 1: Vuache lineament, 2a: Southern Pontarlier lineament, 2b: Northern Pontarlier lineament, 3: lineament proposed by Philippe (1995), 4: Chasseral lineament (corresponding to southern Vicques line in Meier 2010), 5: Schwarzwald lineament (Laubscher 2008a; Steinmann 1892), 6: Caquerelle lineament (Meier 2010), 7: Vicques lineament (Laubscher 2008b), 8: Wehrtal–Zeiningen–Scheltenpass lineament (Laubscher 2008b), 9: Mümliswil–Eptingen lineament (Meier 2010).

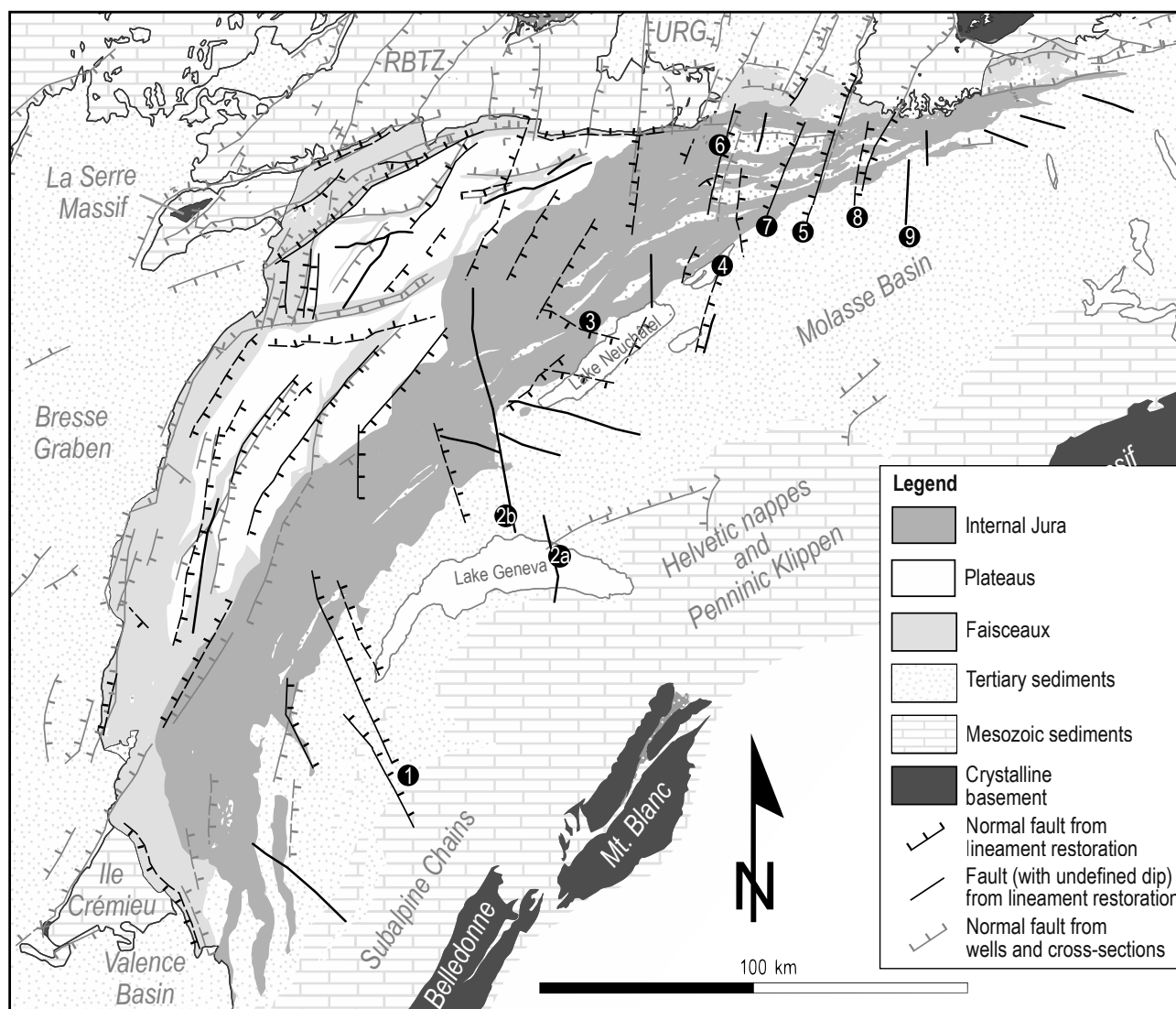


Fig. B.10 – Basement faults in the Jura Mountains and surroundings. Grey faults show fault zones in the basement that are deduced from boreholes, cross-sections and seismic lines. These faults are used in the top basement model (Fig. 6.2). Black faults are interpreted from palinspastic restoration of lineaments (Fig. B.9) using the displacement model in Appendix B.3 on page 182. In the restored position, the vergence of faults is concluded from cross-sections and previously identified basement faults (grey faults). Shifts between grey and black faults arise from misestimated displacement vectors (Appendix B.3 on page 182) and insecurities of lineament placement. Restored basement faults are numbered according to their connection to lineaments in Fig. B.9, which are 1: Vuache lineament, 2a: Southern Pontarlier lineament, 2b: Northern Pontarlier lineament, 3: lineament proposed by Philippe (1995), 4: Chasseral lineament (corresponding to southern Vicques line in Meier 2010), 5: Schwarzwald lineament (Laubscher 2008a; Steinmann 1892), 6: Caquerelle lineament (Meier 2010), 7: Vicques lineament (Laubscher 2008b), 8: Wehrtal–Zeiningen–Scheltenpass lineament (Laubscher 2008b), 9: Mümliswil–Eptingen lineament (Meier 2010).

B.5 DUPLEX STRUCTURES IN THE BASAL DÉCOLLEMENT

The basal décollement of the detached NAF happens in Triassic evaporites and concentrates in salt layers when present (Laubscher 1961). Triassic evaporites occur locally, concentrated within the Middle Triassic to Upper Triassic series and they seem to be both active in some regions (Jordan 1992). In many seismic lines and in some outcrops (Riepel quarry), the Triassic series reveals duplexing structures (Sommaruga et al. 2017). The following model (Fig. B.11) illustrates the formation of such duplexes and the structural consequences in the hanging wall.

The geometric forward model in Fig. B.11 illustrates structures resulting from the interaction between two detachment levels within a décollement zone. The sediment package in the initial state lies flat and in the layer at the bottom, two relatively incompetent horizons (e.g. clay, evaporites shown in dash-dot-dash lines) occur (Fig. B.11a). After two kilometres of displacement (Fig. B.11b), detachments develop within the two incompetent horizons, which are connected by ramps. The ramps become inactive after a while and new ramps form, which results in duplex structures (ramps appear as oblique reflectors on seismic lines). In this model (Fig. B.11), at any defined point and moment along the décollement zone, either the lower or the upper detachment is active. The two detachments are never superposed and contemporaneously active at any defined location along the section. The active basal décollement keeps a simple flat-ramp-flat geometry over time (Fig. B.11b), but new ramps are continuously added towards the front and inactive ramps are transported passively.

Note that the hanging wall shows buckle folding and more regional tectonic uplift, which is connected to the stratigraphic height difference (h) between the two incompetent horizons (Fig. B.11). The unit at the bottom, representing the Upper and Middle Triassic units of the detached NAF, is tectonically thickened.

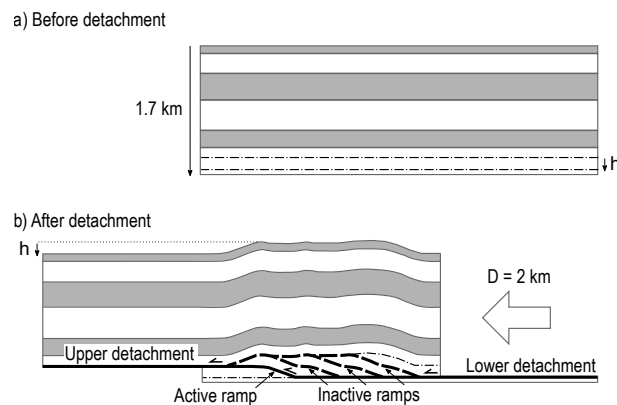
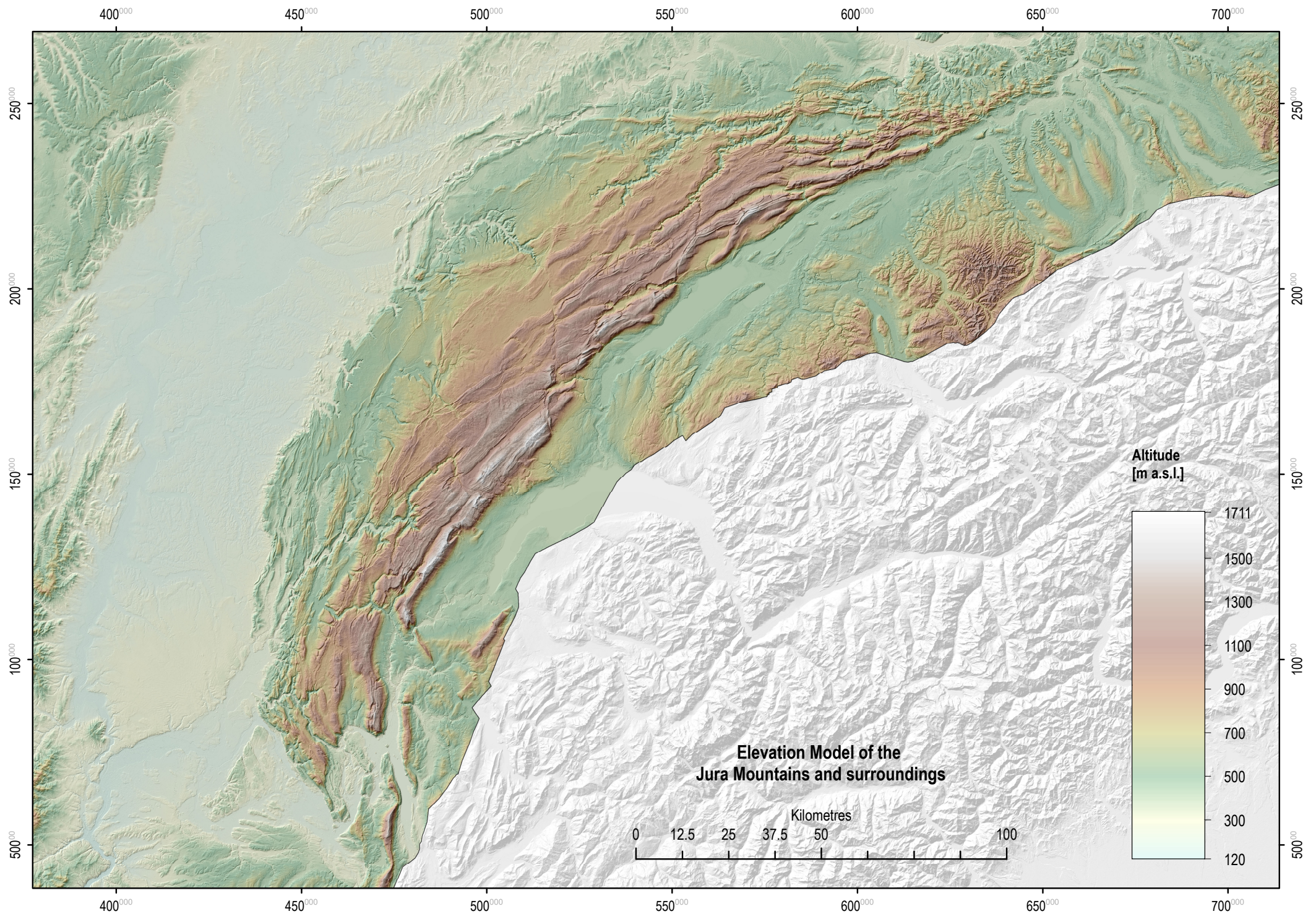


Fig. B.11 – Forward model illustrating duplexing. a) Undeformed sediments with a total thickness of 1.7 km, b) Duplex structures after 2 km horizontal displacement.

C - OVERVIEWS







INTERNATIONAL CHRONOSTRATIGRAPHIC CHART

www.stratigraphy.org

International Commission on Stratigraphy

v 2020/01



Eonothem / Eon Erathem / Era System / Period	Series / Epoch	Stage / Age	GSSP	numerical age (Ma)
Phanerozoic	Quaternary	Holocene	U/L M L/E U/L M L/E	present 0.0042 0.0062 0.0117
		Pleistocene		0.129 0.774
	Pliocene	Chibanian		1.80
		Calabrian		2.58
		Piacenzian		3.600
	Neogene	Zanclean		5.333
		Messinian		7.246
		Tortonian		11.63
		Serravallian		13.82
		Langhian		15.97
		Burdigalian		20.44
		Aquitanian		23.03
		Chattian		27.82
		Rupelian		33.9
		Priabonian		37.8
	Paleogene	Bartonian		41.2
		Lutetian		47.8
		Ypresian		56.0
		Thanetian		59.2
	Paleocene	Selandian		61.6
		Danian		66.0
	Cretaceous	Maastrichtian		72.1 ± 0.2
		Campanian		83.6 ± 0.2
		Santonian		86.3 ± 0.5
		Coniacian		89.8 ± 0.3
		Turonian		93.9
		Cenomanian		100.5
		Albian		~ 113.0
		Aptian		~ 125.0
		Barremian		~ 129.4
		Hauterivian		~ 132.6
		Valanginian		~ 139.8
		Berriasian		~ 145.0

Eonothem / Eon Erathem / Era System / Period	Series / Epoch	Stage / Age	GSSP	numerical age (Ma)
Phanerozoic	Jurassic	Tithonian		152.1 ± 0.9
		Kimmeridgian		157.3 ± 1.0
		Oxfordian		163.5 ± 1.0
		Callovian		166.1 ± 1.2
		Bathonian		168.3 ± 1.3
		Bajocian		170.3 ± 1.4
		Aalenian		174.1 ± 1.0
		Toarcian		182.7 ± 0.7
		Pliensbachian		190.8 ± 1.0
		Sinemurian		199.3 ± 0.3
	Triassic	Hettangian		201.3 ± 0.2
		Rhaetian		~ 208.5
		Norian		~ 227
		Carnian		~ 237
		Ladinian		~ 242
		Anisian		247.2
		Olenekian		251.2
		Induan		251.902 ± 0.024
		Changhsingian		254.14 ± 0.07
		Wuchiapingian		259.1 ± 0.5
	Permian	Capitanian		265.1 ± 0.4
		Wordian		268.8 ± 0.5
		Roadian		272.95 ± 0.11
		Kungurian		283.5 ± 0.6
		Artinskian		290.1 ± 0.26
		Sakmarian		293.52 ± 0.17
		Asselian		298.9 ± 0.15
		Gzhelian		303.7 ± 0.1
		Kasimovian		307.0 ± 0.1
		Moscovian		315.2 ± 0.2
	Carboniferous	Bashkirian		323.2 ± 0.4
		Serpukhovian		330.9 ± 0.2
		Visean		346.7 ± 0.4
		Tournaisian		358.9 ± 0.4

Eonothem / Eon Erathem / Era System / Period	Series / Epoch	Stage / Age	GSSP	numerical age (Ma)
Phanerozoic	Devonian	Famennian		372.2 ± 1.6
		Frasnian		382.7 ± 1.6
		Givetian		387.7 ± 0.8
		Eifelian		393.3 ± 1.2
		Emsian		407.6 ± 2.6
		Pragian		410.8 ± 2.8
		Lochkovian		419.2 ± 3.2
		Pridoli		423.0 ± 2.3
		Ludlow		425.6 ± 0.9
		Gorstian		427.4 ± 0.5
	Silurian	Homerian		430.5 ± 0.7
		Sheinwoodian		433.4 ± 0.8
		Telychian		438.5 ± 1.1
		Aeronian		440.8 ± 1.2
		Rhuddanian		443.8 ± 1.5
		Hirnantian		445.2 ± 1.4
		Katian		453.0 ± 0.7
		Sandbian		458.4 ± 0.9
		Darriwilian		467.3 ± 1.1
		Dapingian		470.0 ± 1.4
	Ordovician	Floian		477.7 ± 1.4
		Tremadocian		485.4 ± 1.9
		Stage 10		~ 489.5
		Jiangshanian		~ 494
		Paibian		~ 497
		Guzhangian		~ 500.5
		Drumian		~ 504.5
		Wuliuan		~ 509
		Stage 4		~ 514
		Stage 3		~ 521
	Cambrian	Stage 2		~ 529
		Fortunian		541.0 ± 1.0

Eonothem / Eon Erathem / Era System / Period	Series / Epoch	Stage / Age	GSSP	numerical age (Ma)
Precambrian	Proterozoic	Ediacaran		~ 635
		Cryogenian		~ 720
		Tonian		1000
	Meso-proterozoic	Stenian		1200
		Ectasian		1400
		Calymmian		1600
	Paleo-proterozoic	Statherian		1800
		Orosirian		2050
		Rhyacian		2300
		Siderian		2500
		Neo-archean		2800
	Archean	Meso-archean		3200
		Paleo-archean		3600
		Eo-archean		4000
	Hadean			~ 4600

Units of all ranks are in the process of being defined by Global Boundary Stratotype Section and Points (GSSP) for their lower boundaries, including those of the Archean and Proterozoic, long defined by Global Standard Stratigraphic Ages (GSSA). Italic fonts indicate informal units and placeholders for unnamed units. Versioned charts and detailed information on ratified GSSPs are available at the website <http://www.stratigraphy.org>. The URL to this chart is found below.

Numerical ages are subject to revision and do not define units in the Phanerozoic and the Ediacaran; only GSSPs do. For boundaries in the Phanerozoic without ratified GSSPs or without constrained numerical ages, an approximate numerical age (–) is provided.

Ratified Subseries/Subepochs are abbreviated as U/L (Upper/Late), M (Middle) and L/E (Lower/Early). Numerical ages for all systems except Quaternary, upper Paleogene, Cretaceous, Triassic, Permian and Precambrian are taken from 'A Geologic Time Scale 2012' by Gradstein et al. (2012), those for the Quaternary, upper Paleogene, Cretaceous, Triassic, Permian and Precambrian were provided by the relevant ICS subcommissions.

Colouring follows the Commission for the Geological Map of the World (www.cgmw.org)



Chart drafted by K.M. Cohen, D.A.T. Harper, P.L. Gibbard, J.-X. Fan (c) International Commission on Stratigraphy, January 2020

To cite: Cohen, K.M., Finney, S.C., Gibbard, P.L. & Fan, J.-X. (2013; updated) The ICS International Chronostratigraphic Chart. Episodes 36: 199-204.

URL: <http://www.stratigraphy.org/ICSChart/ChronostratChart2020-01.pdf>

D - CURRICULUM VITAE

ACADEMIC EDUCATION

- 2016–2021 *Doctoral programme in structural geology*, University of Fribourg, Department of Sciences and Medicine - Earth Sciences, Fribourg, Switzerland.
- 2011–2014 *Master programme in Earth Sciences with special qualification in Geology*, University of Bern, Institute of Geological Sciences, Bern, Switzerland.

PUBLICATIONS

- 2021 Schori, M., F. Zwaan, G. Schreurs, J. Mosar. Pre-existing Basement Faults Controlling Deformation in the Jura Mountains Fold-and-Thrust Belt: Insights from Analogue Models, article, *Tectonophysics* (814), 1-27, DOI 10.1016/j.tecto.2021.228980.
- 2020 Schori, M., F. Zwaan, G. Schreurs, J. Mosar. Supplementary Material - Pre-existing basement faults controlling deformation in the Jura Mountains fold-and-thrust belt: insights from analogue models, online material, *Mendeley Data*, Version 2, DOI 10.17632/6pm5zwjv9w.2.
- 2019 Rime, V., A. Sommaruga, M. Schori, J. Mosar. Tectonics of the Neuchâtel Jura Mountains: insights from mapping and forward modelling, article, *Swiss Journal of Geosciences* (112), 563-578, DOI 10.1007/s00015-019-00349-y.
- 2017 Sommaruga, A., J. Mosar, M. Schori, M. Gruber. The role of the Triassic evaporites underneath the North Alpine foreland. Book chapter in: *Permo-Triassic salt provinces of Europe, North Africa and the Atlantic Margins*, J. I. Soto, J. Flinch and G. Tari (Eds.), 447-466, DOI 10.1016/b978-0-12-809417-4.00021-5.
- 2015 Schori, M., G. Schreurs, J. Mosar. Multiple detachments during thin-skinned deformation of the Swiss Central Jura, article, *Swiss Journal of Geosciences* (108), 327-343, DOI 10.1007/s00015-015-0196-x.
- 2014 Schori, M. Combined structural field investigations and remote sensing analysis of the Combe Grède area (Chasseral, Central Jura), *Master Thesis*, University of Bern, unpublished.

CONFERENCES

- 2020 Schori, M., A. Sommaruga, S. Borderie, L. Hauvette, J. Mosar. Towards a model of the pre-Mesozoic basement beneath the Jura Mountains fold-and-thrust belt, digital poster, *Swiss Geoscience Meeting (SGM)*, online meeting.
- 2019 Schori, M., F. Zwaan, G. Schreurs, J. Mosar. Mimicking structures in the Jura Mountains fold-and-thrust belt: dynamics at pre-existing basement faults from analogue models, oral presentation, *European Geosciences Union (EGU)*, Vienna, Austria.

- 2018 Schori, M. The Palaeozoic Legacy of the Jura Mountains: Basement-Cover Interaction during Late Miocene, oral presentation, *Conférence des Universités de Suisse occidentale (CUSO) meeting*, Fribourg, Switzerland.
- 2017 Schori, M., J. Mosar. Basement-cover interaction in the Jura Mountains: Where, how and to what degree?, poster, *Swiss Geoscience Meeting (SGM)*, Davos, Switzerland.
- 2016 Schori, M., A. Sommaruga, J. Mosar. Triassic thickness compared to topography of the Swiss-French Alpine Foreland (Jura and Molasse Basin), poster, *Swiss Geoscience Meeting (SGM)*, Geneva, Switzerland.